BIOLOGY-INSPIRED ENGINEERING AND ENGINEERING-INSPIRED BIOLOGY

EDITED BY: Jan-Matthias Braun, Poramate Manoonpong and Xiaofeng Xiong

PUBLISHED IN: Frontiers in Neurorobotics

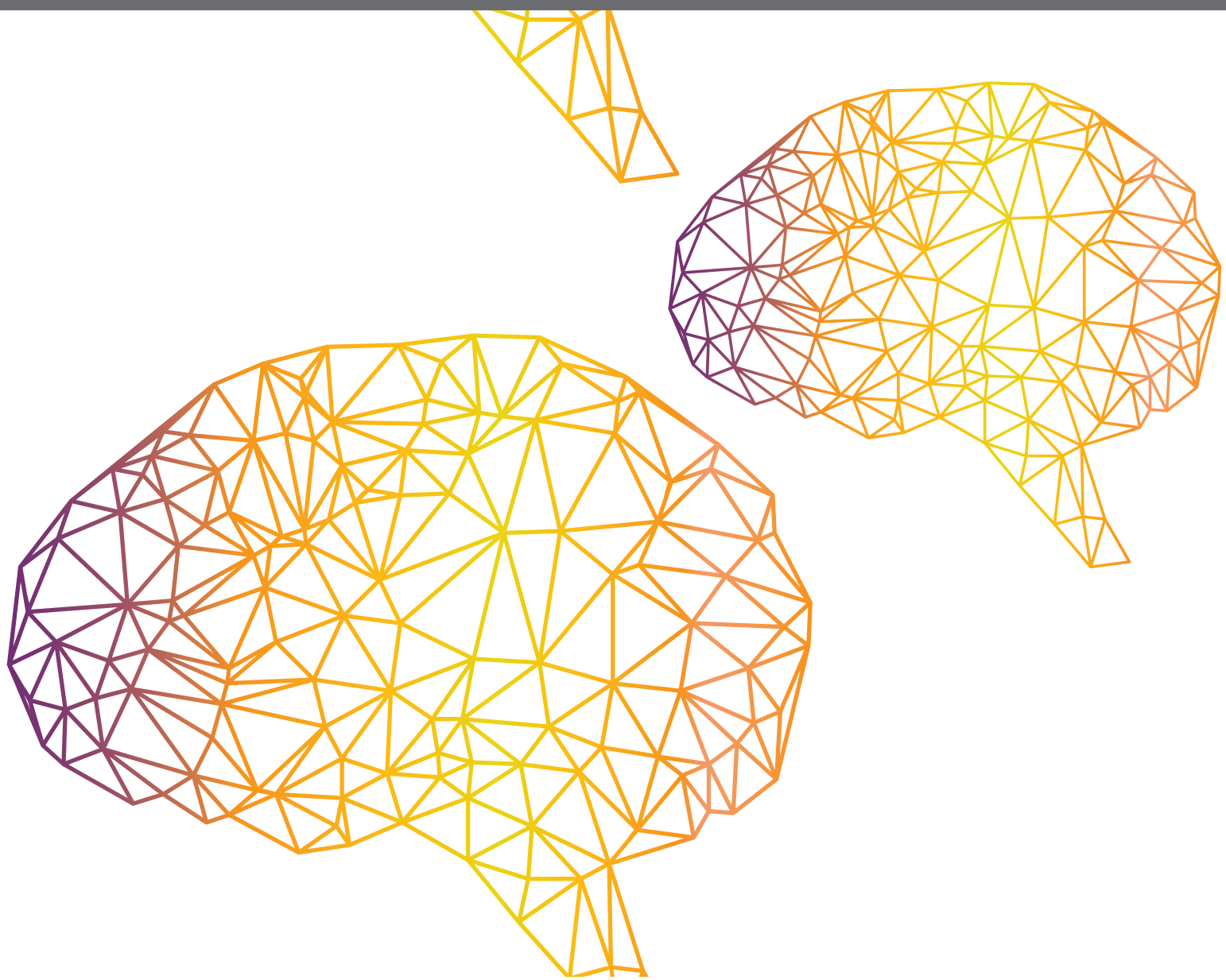

frontiers Research Topics

ISSN 1664-8714
ISBN 978-2-88966-340-8
DOI 10.3389/978-2-88966-340-8

About Frontiers

Frontiers is more than just an open-access publisher of scholarly articles: it is a pioneering approach to the world of academia, radically improving the way scholarly research is managed. The grand vision of Frontiers is a world where all people have an equal opportunity to seek, share and generate knowledge. Frontiers provides immediate and permanent online open access to all its publications, but this alone is not enough to realize our grand goals.

Frontiers Journal Series

The Frontiers Journal Series is a multi-tier and interdisciplinary set of open-access, online journals, promising a paradigm shift from the current review, selection and dissemination processes in academic publishing. All Frontiers journals are driven by researchers for researchers; therefore, they constitute a service to the scholarly community. At the same time, the Frontiers Journal Series operates on a revolutionary invention, the tiered publishing system, initially addressing specific communities of scholars, and gradually climbing up to broader public understanding, thus serving the interests of the lay society, too.

Dedication to Quality

Each Frontiers article is a landmark of the highest quality, thanks to genuinely collaborative interactions between authors and review editors, who include some of the world's best academicians. Research must be certified by peers before entering a stream of knowledge that may eventually reach the public - and shape society; therefore, Frontiers only applies the most rigorous and unbiased reviews.
Frontiers revolutionizes research publishing by freely delivering the most outstanding research, evaluated with no bias from both the academic and social point of view. By applying the most advanced information technologies, Frontiers is catapulting scholarly publishing into a new generation.

What are Frontiers Research Topics?

Frontiers Research Topics are very popular trademarks of the Frontiers Journals Series: they are collections of at least ten articles, all centered on a particular subject. With their unique mix of varied contributions from Original Research to Review Articles, Frontiers Research Topics unify the most influential researchers, the latest key findings and historical advances in a hot research area! Find out more on how to host your own Frontiers Research Topic or contribute to one as an author by contacting the Frontiers Editorial Office: researchtopics@frontiersin.org

BIOLOGY-INSPIRED ENGINEERING AND ENGINEERING-INSPIRED BIOLOGY

Topic Editors:
Jan-Matthias Braun, University of Southern Denmark, Denmark
Poramate Manoonpong, University of Southern Denmark, Denmark
Xiaofeng Xiong, University of Southern Denmark, Denmark

Citation: Braun, J.-M., Manoonpong, P., Xiong, X., eds. (2021). Biology-Inspired Engineering and Engineering-Inspired Biology. Lausanne: Frontiers Media SA. doi: 10.3389/978-2-88966-340-8

Table of Contents

frontiers in Neurorobotics

EDITORIAL
published: 13 November 2020
doi: 10.3389/fnbot.2020.614683

Editorial: Biology-Inspired Engineering and Engineering-Inspired Biology

Jan-Matthias Braun[1,2]*, *Poramate Manoonpong*[2,3] *and Xiaofeng Xiong*[2]

[1] *Applied AI & Data Science, The Mærsk Mc-Kinney Møller Institute, University of Southern Denmark, Odense, Denmark,* [2] *Embodied AI and Neurorobotics Lab, SDU Biorobotics, The Mærsk Mc-Kinney Møller Institute, University of Southern Denmark, Odense, Denmark,* [3] *Bio-Inspired Robotics and Neural Engineering Lab, School of Information Science and Technology, Vidyasirimedhi Institute of Science and Technology, Rayong, Thailand*

Keywords: biology-inspired engineering, engineering-inspired biology, bio-inspired computation, bio-inspired sensors, bio-inspired materials, bio-inspired structure

Editorial on the Research Topic

Biology-Inspired Engineering and Engineering-Inspired Biology

The term biology-inspired engineering refers to the fact that biology has been an important inspiration for developments in all aspects of engineering, for example the design of robots. Bio-inspired computation (Manoonpong and Tetzlaff, 2018; Manoonpong et al., 2020), sensors (Steffen et al.), actuators (Vanderborght et al., 2013; Dicker et al., 2017; Lee and Oh, 2019; Lund et al., 2019), structures (Tramsen et al., 2018; Tan et al., 2019; Shao et al., 2020), and materials (Rafsanjani et al., 2018; Wang et al., 2020) have enabled robots to produce robust and comparable behaviors to their biological counterparts. Owing to the biologically comparable behaviors, interdisciplinary biologists tend to flip the approach, i.e., engineering-inspired biology, whereby engineering systems and principles are utilized to initiate and test new hypotheses in biological research. For example, robots have been used as tools to investigate and test animal functions (Ijspeert, 2014; Dürr et al.; Wei et al.). This special issue reports the results and reviews of biology-inspired engineering and engineering-inspired biology research.

OPEN ACCESS

Edited and reviewed by:
Florian Rhrbein, Independent Researcher, Munich, Germany

***Correspondence:**
Jan-Matthias Braun
j-mb@mmmi.sdu.dk

Received: *06 October 2020*
Accepted: *22 October 2020*
Published: *13 November 2020*

Citation:
Braun J-M, Manoonpong P and Xiong X (2020) Editorial: Biology-Inspired Engineering and Engineering-Inspired Biology. Front. Neurorobot. 14:614683. doi: 10.3389/fnbot.2020.614683

1. BIOLOGY-INSPIRED ENGINEERING

In Schiller et al., a gecko-inspired soft robot was developed to climb inclined, flat surfaces. By reducing the volume and increasing the self-reinforcing effect of the bending actuators of the robot and using gecko inspired locomotion, they can reduce the energy consumption of the robot, and at the same time, improve the robot climbing ability and the movement speed. Results show that the robot with its straight gait can climb slopes of up to 84 degrees. In the horizontal plane, it can achieve a locomotion speed of 6 cm/s. In Zhu et al., neurobiologically inspired control for the coordinated behavior and coupled locomotion of a multi-joint bionic robot was developed. It is based on central pattern generators (i.e., σ-Hopf oscillators) with an undistorted synchronization method. Results show that the control approach can be used for the locomotion control of a bionic parallel waist of a legged robot, which is a highly coupled system. In principle, the approach can benefit the transition and transformation of the locomotion and makes the coupling motion more flexible; thereby it can be applied to not only legged robots but also flying, and swimming robots, etc. In Dai et al., an affine transformation based on an artificial bee colony algorithm was proposed to greatly improve the positioning precision under large initial errors condition.

The affine transformation is applied to the initialization and evolutionary processes of the algorithm. The proposed algorithm provides a novel way to increase the matching accuracy of gravity aided inertial navigation systems. In Sun et al., a new modular, small-sized, bio-inspired quadruped robot called Lilibot was introduced. Its modular components can be flexibly reconfigured to obtain features, such as different leg orientations for investigating the effectiveness and generalization of bio-inspired self-organized locomotion control. It has multiple sensory feedback to support bio-inspired vestibular reflexes and compliant control mechanisms for body posture stabilization and compliant behavior, respectively. Lilibot was evaluated through a bio-inspired adaptive neural controller. Results show that it can autonomously perform various adaptive behaviors including self-organized locomotion under different leg orientations, adaptive body posture stabilization on a tiltable plane, and adaptive leg compliance for unexpected external load negotiation. The results suggest that Lilibot can be considered as a friendly and generic quadrupedal platform for biology-inspired engineering and engineering-inspired biology studies. Specifically, it can be used as a tool to develop bio-inspired control in engineering research and to investigate and test animal functions as well as new hypotheses in biological research.

Going under water, Plum et al. presents a biologically inspired underwater vehicle with a soft and compliant exoskeleton. It is controlled by a shallow neural network, trained by a genetic algorithm. The compliant exoskeleton reduces accelerations induced by collisions dramatically, thus reducing stress on the vehicles components as well as reaction forces on the vehicles surroundings. Employing a segmented structure, the spherical exoskeleton does not limit the use of cameras, sensors, or manipulators. This study shows how a versatile vehicle can achieve protection against severe damage of often fragile underwater surroundings, like coral reefs, or of accompanying humans by means of biologically inspired engineering. It thereby presents a convincing, practical application in a very complex environment, which is achieved by basic changes to the structure, instead of costly changes to components and even more complex control algorithms.

Steffen et al. focuses on biology-inspired vision. For the review, sensors and algorithms for event-based stereo vision were investigated. These biologically plausible vision systems add time as additional constraint to solve the correspondence problem, i.e., for finding matching points in the two images of a stereo vision system. The event based nature of the vision sensors makes them perfect for further processing in spiking neural networks. The review covers conventional electrical as well as biological sensors, depth perception, and thus enables a thorough understanding of how biologically-plausible vision systems were developed, how their data can be processed, how they can improve future applications of vision systems, but also where there are still shortcomings in this very dynamic field of neuromorphic processing of sensory data.

Based on experiments to determine the maximum cooperative grasping mass and diameter of the human thumb and index finger, Chen et al. present non-linear regression models which relate these variables to age, gender, sum of thumb and index finger lengths, the ratio of index finger to thumb, and the hand used. The authors were successfully applying these two models to design the optimal size of robotic hands to reproduce the experiments. With this research, the authors not only demonstrate how biological findings can be used to determine relevant properties of a robotic model, they also argue that their models can be applied to hand rehabilitation. Thereby, they close the loop from biology-inspired engineering back to engineering-inspired biology, showing that both research directions are inherently intertwined.

2. ENGINEERING-INSPIRED BIOLOGY

In Kano, Kanauchi, Aonuma et al., the mechanism how brittle stars make decisions about their moving direction in decentralized nervous systems is developed by capturing behavioral findings in a phenomenological mathematical model. The authors propose a decision making process based on self-organization, which can autonomously determine the moving direction and move toward it adaptively. Based on the model, simulations verify that the model is able to reproduce the behavioral observations. This work is extended in Kano, Kanauchi, One et al., where a brittle star-like robot was introduced and exploited as a tool to realize an autonomous control mechanism underlying the locomotion and adaptation of brittle stars. According to this, the decentralized control mechanism can autonomously generate the inter-arm and intra-arm coordination for locomotion and adapt to unexpected physical damages, in one or several arms, by automatically coordinating the still responsive arms, in a way similar to brittle stars. On one hand, the study demonstrated that an engineering-inspired biology approach can be used to reveal the essence of the inter- and intra-arm coordination mechanism in brittle stars. On the other hand, it paves the way to develop robot control that can coordinate a large number of bodily degrees of freedom and adapt to unpredictable circumstances in real-time. In Dürr et al., the six legged robot HECTOR was developed for integrative biomimetics research of hexapedal locomotion. HECTOR has 18 highly sensorized compliant actuators, a light-weight exoskeleton, a distributed and expandable hardware architecture, as well as a proper dynamic simulation framework. These characteristics enable HECTOR to be an appropriate robot for investigating insect locomotion intelligence (e.g., muscle compliance and distributed proprioception). In Wei et al., a bio-inspired robot was built to validate the assumption that the flapping wings and leg burrs of locusts have an influence on their jumping performance. The validation has shown that the leg burrs and flapping wings make the locusts jump longer and improve their landing stability.

3. CONCLUDING REMARKS

The articles collected in this research topic present an overview of recent developments reflecting the 2-fold interaction between

engineering and biology. In biology-inspired engineering, we see how innovative solutions can result from research on their biological counterparts. Approaches span a broad range from mimicking material properties to re-engineering a biological mechanism based on an abstract principle. In engineering-inspired biology, the articles do not only showcase how engineering solutions can demonstrate the level or depth of our understanding of a mechanism, but also how they allow us to validate or reveal possible mechanisms in the biological counterpart. The success of this two-fold interaction makes it likely that in the future we will see more research that transfers not only in one direction, but that shows mutual inspirations and direct interactions between biological research and engineering applications, as for example in healthcare, rehabilitation, search and rescue, inspection, and space exploration.

AUTHOR CONTRIBUTIONS

All authors listed have made a substantial, direct and intellectual contribution to the work, and approved it for publication.

ACKNOWLEDGMENTS

We thank all authors contributing with their work to this Research Topic. We acknowledge funding by the H2020-FETPROACT project Plan4Act (no. 732266). PM acknowledges support from Vidyasirimedhi Institute of Science and Technology (VISTEC)-research funding (Thailand) on Bio-inspired Robotics and from the Human Frontier Science Program under grant agreement no. RGP0002/2017. The funders had no role in study design, data collection and analysis, decision to publish, or preparation of the manuscript.

REFERENCES

Dicker, M. P. M., Baker, A. B., Iredale, R. J., Naficy, S., Bond, I. P., Faul, C. F. J., et al. (2017). Light-triggered soft artificial muscles: molecular-level amplification of actuation control signals. *Sci. Rep.* 7:9197. doi: 10.1038/s41598-017-08777-2

Ijspeert, A. J. (2014). Biorobotics: using robots to emulate and investigate agile locomotion. *Science* 346, 196–203. doi: 10.1126/science.1254486

Lee, C., and Oh, S. (2019). Development, analysis, and control of series elastic actuator-driven robot leg. *Front. Neurorobot.* 13:17. doi: 10.3389/fnbot.2019.00017

Lund, S. H. J., Billeschou, P., and Larsen, L. B. (2019). High-bandwidth active impedance control of the proprioceptive actuator design in dynamic compliant robotics. *Actuators* 8:71. doi: 10.3390/act8040071

Manoonpong, P., and Tetzlaff, C. (2018). Editorial: neural computation in embodied closed-loop systems for the generation of complex behavior: from biology to technology. *Front. Neurorobot.* 12:53. doi: 10.3389/fnbot.2018.00053

Manoonpong, P., Xiong, X., and Larsen, J. C. (2020). Closed-loop dynamic computations for adaptive behavior (articles based on sab2018 conference). *Adapt. Behav.* 28, 125–127. doi: 10.1177/1059712319888814

Rafsanjani, A., Zhang, Y., Liu, B., Rubinstein, S. M., and Bertoldi, K. (2018). Kirigami skins make a simple soft actuator crawl. *Sci. Robot.* 3:eaar7555. doi: 10.1126/scirobotics.aar7555

Shao, D., Chen, J., Ji, A., Dai, Z., and Manoonpong, P. (2020). "Hybrid soft-rigid foot with dry adhesive material designed for a gecko-inspired climbing robot," in *2020 3rd IEEE International Conference on Soft Robotics (RoboSoft)* (New Haven, CT: IEEE), 578–585.

Tan, N., Sun, Z., Brahmananthan, N., Mohan, R. E., Venkataraman, S., Sosa, R., et al. (2019). A system-of-systems bio-inspired design process: conceptual design and physical prototype of a reconfigurable robot capable of multi-modal locomotion. *Front. Neurorobot.* 13:78. doi: 10.3389/fnbot.2019.00078

Tramsen, H. T., Gorb, S. N., Zhang, H., Manoonpong, P., Dai, Z., and Heepe, L. (2018). Inversion of friction anisotropy in a bio-inspired asymmetrically structured surface. *J. R. Soc. Interface* 15:20170629. doi: 10.1098/rsif.2017.0629

Vanderborght, B., Albu-Schaeffer, A., Bicchi, A., Burdet, E., Caldwell, D., Carloni, R., et al. (2013). Variable impedance actuators: a review. *Robot. Auton. Syst.* 61, 1601–1614. doi: 10.1016/j.robot.2013.06.009

Wang, L., Hui, Y., Fu, C., Wang, Z., Zhang, M., and Zhang, T. (2020). Recent advances in gecko-inspired adhesive materials and application. *J. Adhes. Sci. Technol.* 34, 2275–2291. doi: 10.1080/01694243.2020.1760478

Conflict of Interest: The authors declare that the research was conducted in the absence of any commercial or financial relationships that could be construed as a potential conflict of interest.

frontiers in Neurorobotics

ORIGINAL RESEARCH
published: 08 May 2019
doi: 10.3389/fnbot.2019.00019

Solving Gravity Anomaly Matching Problem Under Large Initial Errors in Gravity Aided Navigation by Using an Affine Transformation Based Artificial Bee Colony Algorithm

Tian Dai, Lingjuan Miao, Haijun Shao and Yongsheng Shi*

School of Automation, Beijing Institute of Technology, Beijing, China

Gravity aided inertial navigation system (GAINS), which uses earth gravitational anomaly field for navigation, holds strong potential as an underwater navigation system. The gravity matching algorithm is one of the key factors in GAINS. Existing matching algorithms cannot guarantee the matching accuracy in the matching algorithms based gravity aided navigation when the initial errors are large. Evolutionary algorithms, which are mostly have the ability of global optimality and fast convergence, can be used to solve the gravity matching problem under large initial errors. However, simply applying evolutionary algorithms to GAINS may lead to false matching. Therefore, in order to deal with the underwater gravity matching problem, it is necessary to improve the traditional evolutionary algorithms. In this paper, an affine transformation based artificial bee colony (ABC) algorithm, which can greatly improve the positioning precision under large initial errors condition, is developed. The proposed algorithm introduces affine transformation to both initialization process and evolutionary process of ABC algorithm. The single-point matching strategy is replaced by the strategy of matching a sequence of several consecutive position vectors. In addition, several constraints are introduced to the process of evolution by using the output characteristics of the inertial navigation system (INS). Simulations based on the actual gravity anomaly base map have been performed for the validation of the proposed algorithm.

Keywords: gravity aided navigation, bio-inspired navigation, navigation systems, optimization, underwater vehicle, evolutionary algorithm

OPEN ACCESS

Edited by:
Xiaofeng Xiong,
University of Southern Denmark, Denmark

Reviewed by:
Ning Sun,
Nankai University, China
Chin-Shiuh Shieh,
National Kaohsiung First University of Science and Technology, Taiwan

****Correspondence:***
Tian Dai
daitian@bit.edu.cn

Received: *16 November 2018*
Accepted: *17 April 2019*
Published: *08 May 2019*

Citation:
Dai T, Miao L, Shao H and Shi Y (2019) Solving Gravity Anomaly Matching Problem Under Large Initial Errors in Gravity Aided Navigation by Using an Affine Transformation Based Artificial Bee Colony Algorithm. Front. Neurorobot. 13:19. doi: 10.3389/fnbot.2019.00019

INTRODUCTION

It is well known that inertial navigation systems (INSs) typically used on underwater vehicles tend to develop accumulated errors. Above water, the INS data can be corrected by the use of global navigation satellite system (GNSS) (Bishop, 2002). However, due to the rapid attenuation of higher frequency signals and the unstructured nature of the undersea environment, GNSS signals can only propagate within short distance under water (Paull et al., 2013). As a passive navigation system, the gravity aided inertial navigation system (GAINS) holds strong potential as an auxiliary navigation system (Canciani and Raquet, 2017). GAINS obtains a gravity anomaly measurements by using gravimeters installed on a vehicle. These measurements are matched with a priori digital

map of the gravity anomaly, to estimate the vehicle position. GAINSs are completely passive and difficult to interfere with. These advantages are totally meet the requirement of underwater vehicles (Rice et al., 2004).

A GAINS consists of a priori gravity anomaly database (gravity anomaly map), a measurement unit (gravimeter), and a navigation algorithm. There are two types of GAINSs: filtering algorithms based GAINSs (Li et al., 2013; Claus and Bachmayer, 2015; Copp and Subbarao, 2015; Allotta et al., 2016) and matching algorithms based GAINSs (Zhao et al., 2014; Wu et al., 2015; Zhu et al., 2015; Han et al., 2016; Song et al., 2016). Filtering algorithms, which take use of simplified dynamic mathematical model of the vehicle, have a good performance in real-time. In filtering algorithms based GAINSs, commonly used filters are the extended Kalman filter (EKF), the particle filter (PF) and the Rao-Blackwellized particle filter (RBPF). EKF is more effective for low nonlinear estimation problems. PF can effectively handle highly non-linear or non-Gaussian estimation problems. RBPF is a hybrid filter combining EKF and PF (Simanek et al., 2015; Kim T. et al., 2018; Kim Y. et al., 2018). However, the application of filtering algorithms is limited since the precise model of gravity anomaly is difficult to establish (Han et al., 2016). The matching algorithm is a key factor in matching algorithms based GAINSs (Hegrenaes and Hallingstad, 2011; Wu et al., 2017). Terrain contour matching (TERCOM) (Affleck and Jircitano, 1990) algorithm and iterative closest contour point (ICCP) (Kamgarparsi and Kamgarparsi, 1999) algorithm are two conventional matching algorithms in GAINSs. TERCOM algorithm is realized via group correlation analysis. Most of the improvements to the TERCOM algorithm (Zhao et al., 2014; Han et al., 2016) are proposed to solve bad real-time performance and heavy computational complexity problem. However, TERCOM algorithm is sensitive to angular error of the INS-indicated segment, which is difficult to improve. ICCP algorithm, which uses rigid transformation to matching the multilateral arc, has a high matching accuracy. Over the past decade, a number of improved ICCP algorithm have been suggested. Among them, a part of researches were developed for improving the real-time performance (Tong et al., 2011; Wang et al., 2013). Other studies adopted affine transformation to deal with the scale error (Xu et al., 2014; Song et al., 2016). However, the mismatching of ICCP algorithm is easily included when the initial position errors of INS are large (Han et al., 2016). Both TERCOM-based algorithms and ICCP-based algorithms cannot guarantee the matching accuracy when initial errors are large. TERCOM-based algorithms are sensitive to angular errors of the INS-indicated segments and ICCP-based algorithms are sensitive to position errors. Therefore, a matching algorithm that maintain high matching precision under large initial errors is needed. Evolutionary algorithms (Quan and Fang, 2010; Gao et al., 2014; Hidalgo-Paniagua et al., 2016; Teymourian et al., 2016; Li et al., 2017) are a good choice because most of them have the ability of both global optimality and fast convergence.

The evolutionary algorithms have emerged as a powerful tool for finding optimum solutions of complex optimization problems. In the past few decades, a number of evolutionary algorithms have been used extensively to obtain optimal designs and overcome the computational drawbacks of traditional mathematical optimization methods (Abrao, 2013; Yildiz, 2013). Jaesung and Kim improved the genetic algorithm so solve robot path planning problem (Lee and Kim, 2016). An improved intelligent water drops algorithm and an advanced cuckoo search algorithm are proposed to solve the capacitated vehicle routing problem (Teymourian et al., 2016). Improved bee colony algorithm is applied to the color image segmentation, assigning the optimal coordinates of seeds and determining similarity differences (Sag and Çunkaş, 2015).

Gravity matching problem can be regarded as an optimization problem (Wu et al., 2017). Therefore, evolutionary algorithms can be directly applied to the gravity matching problem. Gao et al. proposed an improved artificial bee colony (ABC) algorithm and obtained a good performance on gravity matching under small initial errors (Gao et al., 2014). However, there exists a lot of similarity feature points in matching area when initial errors are large. Although the improved ABC algorithm can be implemented on navigation systems under large initial errors, the mismatching of position is easily included. In this paper, we consider a challenging gravity matching problem of achieving high precision under large initial errors. To solve this problem, we propose an affine transformation based ABC algorithm. Firstly, In order to avoid mismatching caused by similarity feature points, we apply sequence matching strategy to the proposed algorithm. Secondly, Scaling transformation, rotation transformation, and translation transformation are introduced to both initialization process and evolutionary process to increase the convergence speed. In addition, we constrain the affine transformation by utilizing the output characteristics of INS.

The rest of the paper is organized as follows. The second part introduces the ABC algorithm. INS error propagation model and the constraints of affine transformation are provided in the third part. The fourth part of this paper presents the procedure of affine transformation based artificial bee colony algorithm. A comprehensive discussion on the experimental settings and simulation results are provided in the fifth part. Conclusions are given in the last part.

ARTIFICIAL BEE COLONY ALGORITHM

The ABC algorithm (Karaboga and Basturk, 2007) is one of the most recently introduced swarm-based search methods (Akay and Karaboga, 2012; Akbari et al., 2012; Sag and Çunkaş, 2015; Li et al., 2016). It contains three groups of bees: employed bees, onlookers, and scouts. In ABC algorithm, the position of a food source represents a possible solution of the optimization problem and the nectar amount of a food source corresponds to the quality (fitness) of the associated solution. The more a solution has high fitness, the more possibility of being selected of this solution by onlooker bees. The number of the employed bees or the onlooker bees is equal to the number of solutions in the population. The initial swarm composed of employed bees are generated by (1):

$$\boldsymbol{x}_i^j = \boldsymbol{x}_{\min}^j + rand(0,1)(\boldsymbol{x}_{\max}^j - \boldsymbol{x}_{\min}^j) \tag{1}$$

Where x_i^j indicates the jth parameter of ith solution in the population, $i = \{1, 2, \cdots, SN\}$ and SN is the size of population, $j = \{1, 2, \cdots, D\}$ and D is the number of parameters in a solution. $x_{\min}^j$ and $x_{\max}^j$ are, respectively, the lower bound and the upper bound of jth parameter. $rand(0, 1)$ generates a real number between 0 and 1.

After initialization, fitness values of solutions are calculated by (2):

$$fit_i = \begin{cases} 1/(1+f_i) & f_i \geq 0 \\ 1 + |f_i| & f_i < 0 \end{cases} \tag{2}$$

Where f_i is the objective function value of ith solution in the population. fit_i is the fitness value of ith solution in the population. The employed bee evaluates the quality of food sources and determines a new one according to the fitness value. If the nectar amount of new source is better than the old source, employed bee will update its memory with new source. The employed bees update their sources according to the following equation:

$$v_i^j = x_i^j + rand(-1, 1)(x_i^j - x_{neighbor}^j) \tag{3}$$

Where $x_{neighbor}^j$ is the neighbor solution selected randomly, neighbor $\in \{1, 2, \cdots, i-1, i+1, \cdots, SN\}$. v_i^j represents new solution.

After new food sources have been explored, onlookers select an employed bee for guidance. For this purpose, roulette wheel is used to calculate the probabilities:

$$p_i = \frac{fit_i}{\sum_{q=1}^{SN} fit_q} \tag{4}$$

After the onlooker bees select a food source as a guide, the candidate food source is calculated by (3). Afterwards, the greedy selection process is applied for the onlooker bees. The best solution achieved so far is memorized. In addition, a food source will be abandoned when limit, a control parameter, is exceeded for the source. So it is replaced with randomly produced solution by (1).

For the gravity matching problem, denote $\boldsymbol{x}$ as the position of vehicle and f as the gravity objective function. Then ABC algorithm can be directly used to find the optimal position. However, simply applying ABC algorithm to the gravity matching problem may lead to false matching (Gao et al., 2014). There exists a lot of similarity gravity feature points in gravity database, which means single-point matching process may easily convergence at the wrong position.

SEQUENCE MATCHING STRATEGY

To solve the mismatching problem, the single-point matching strategy in basic ABC is replaced by strategy of matching a sequence of several consecutive position vectors. Considering the short-term high-precision characteristics of the INS (Wu et al., 2015), affine transformation could be used to describe the relationship between the sequence to be matched and the INS-indicated sequence. Specifically, these transformations include scaling transformation, rotation transformation, and translation transformation. The range of affine transformations can be estimated by an INS error propagation model.

INS Error Propagation Model

Affine transformation is constrained by the output characteristics of the INS. Therefore, an INS error propagation model (Yan et al., 2008) is employed in this paper. In Yan et al. (2008), i-reference frame is the fixed inertial frame; e-reference frame is the Terrestrial reference frame (TRF); n-reference frame has its origin on the surface and its axes pointing East, North, and Up (ENU reference frame); b-reference frame is centered in the center of gravity of the vehicle, with the y-axis pointing in the direction of the forward motion of the vehicle, the z-axis pointing up and the x-axis completing a right-handed reference frame. However, GAINSs are commonly used in underwater environments. In which case n-reference frame adopts North, East and Down (NED) reference frame; b-reference frame is centered in the center of gravity of the vehicle, with the x-axis pointing in the direction of the forward motion of the vehicle, the z-axis pointing down and the y-axis completing a right-handed reference frame (Allotta et al., 2016). Hence the INS error propagation model in Yan et al. (2008) needs to be modified.

In actual case, there exist rotation errors between n-reference frame (ideal mathematics platform) and n'-reference frame (actual mathematics platform). n'-reference frame can be gained after rotating 3 times of n-reference frame. Let α_z, α_y, α_x be the three rotational angles and $\boldsymbol{\alpha} = [\alpha_x \ \alpha_y \ \alpha_z]$, the rotation matrixes can be expressed as:

$$\begin{aligned} \boldsymbol{C}_{\alpha_z} &= \begin{bmatrix} \cos\alpha_z & -\sin\alpha_z & 0 \\ \sin\alpha_z & \cos\alpha_z & 0 \\ 0 & 0 & 1 \end{bmatrix} \\ \boldsymbol{C}_{\alpha_y} &= \begin{bmatrix} \cos\alpha_y & 0 & -\sin\alpha_y \\ 0 & 1 & 0 \\ \sin\alpha_y & 0 & \cos\alpha_y \end{bmatrix} \\ \boldsymbol{C}_{\alpha_x} &= \begin{bmatrix} 1 & 0 & 0 \\ 0 & \cos\alpha_x & \sin\alpha_x \\ 0 & -\sin\alpha_x & \cos\alpha_x \end{bmatrix} \end{aligned} \tag{5}$$

Then, the coordinate transformation matrix from n-reference frame to n'-reference frame is derived:

$$\boldsymbol{C}_{\mathrm{n}}^{\mathrm{n}'} = \boldsymbol{C}_{\alpha_x} \boldsymbol{C}_{\alpha_y} \boldsymbol{C}_{\alpha_z} \tag{6}$$

Denoting with $\boldsymbol{\omega}_{\mathrm{nn}'}^{\mathrm{n}'}$ the relative angular velocity of n'-reference frame in n-reference frame, the following equation has been derived:

$$\boldsymbol{\omega}_{\mathrm{nn}'}^{\mathrm{n}'} = \boldsymbol{C}_{\alpha_x} \boldsymbol{C}_{\alpha_y} \begin{bmatrix} 0 \\ 0 \\ \dot{\alpha}_z \end{bmatrix} + \boldsymbol{C}_{\alpha_x} \begin{bmatrix} 0 \\ \dot{\alpha}_y \\ 0 \end{bmatrix} + \begin{bmatrix} \dot{\alpha}_x \\ 0 \\ 0 \end{bmatrix} = \boldsymbol{C}_{\omega} \begin{bmatrix} \dot{\alpha}_x \\ \dot{\alpha}_y \\ \dot{\alpha}_z \end{bmatrix} \tag{7}$$

Hence, the differential equation of Euler platform error angles can be expressed as follows:

$$\dot{\boldsymbol{\alpha}}=\boldsymbol{C}_{\omega}^{-1}\boldsymbol{\omega}_{\mathrm{nn}'}^{\mathrm{n}'} \tag{8}$$

Here $\mathbf{C}_{\omega}$ and $\mathbf{C}_{\omega}^{-1}$ are calculated by the following expressions:

$$\begin{aligned}\boldsymbol{C}_{\omega}&=\begin{bmatrix}1 & 0 & -\sin\alpha_y\\ 0 & \cos\alpha_x & \sin\alpha_x\cos\alpha_y\\ 0 & -\sin\alpha_x & \cos\alpha_x\cos\alpha_y\end{bmatrix}\\ \boldsymbol{C}_{\omega}^{-1}&=\frac{1}{\cos\alpha_y}\begin{bmatrix}\cos\alpha_y & \sin\alpha_x\sin\alpha_y & \cos\alpha_x\sin\alpha_y\\ 0 & \cos\alpha_x\cos\alpha_y & -\sin\alpha_x\cos\alpha_y\\ 0 & \sin\alpha_x & \cos\alpha_x\end{bmatrix}\end{aligned} \tag{9}$$

Denoting with $\boldsymbol{\omega}_{\mathrm{ie}}^{\mathrm{n}}$ the rotational angular velocity of the earth. L and h are, respectively, latitude, and depth. R_{M} is the local radius of curvature in meridian and R_{N} is the local radius of curvature in prime vertical. $\hat{L}=L+\delta L$, $\hat{h}=h+\delta h$. In addition, δL and δh are slight errors. The following equations have been derived:

$$\boldsymbol{\omega}_{\mathrm{ie}}^{\mathrm{n}} = \left[\omega_{\mathrm{ie}}\cos L \;\; 0 \;\; -\omega_{\mathrm{ie}}\sin L\right]^{\mathrm{T}} \tag{10}$$

$$\boldsymbol{\omega}_{\mathrm{en}}^{\mathrm{n}} = \left[\frac{v_{\mathrm{E}}^{\mathrm{n}}}{R_{\mathrm{N}}-h} \;\; -\frac{v_{\mathrm{N}}^{\mathrm{n}}}{R_{\mathrm{M}}-h} \;\; -\frac{v_{\mathrm{E}}^{\mathrm{n}}}{R_{\mathrm{N}}-h}\tan L\right]^{\mathrm{T}} \tag{11}$$

$$\delta\boldsymbol{\omega}_{\mathrm{ie}}^{\mathrm{n}} = \begin{bmatrix}-\omega_{\mathrm{ie}}\sin\hat{L}\delta L\\ 0\\ -\omega_{\mathrm{ie}}\cos\hat{L}\delta L\end{bmatrix} \tag{12}$$

$$\delta\boldsymbol{\omega}_{\mathrm{en}}^{\mathrm{n}} = \begin{bmatrix}\delta v_{\mathrm{E}}^{\mathrm{n}}/\left(\hat{R}_{\mathrm{N}}-\hat{h}\right)\\ -\delta v_{\mathrm{N}}^{\mathrm{n}}/\left(\hat{R}_{\mathrm{M}}-\hat{h}\right)\\ -\left(\tan\hat{L}\delta v_{\mathrm{E}}^{\mathrm{n}}+\hat{v}_{\mathrm{E}}^{\mathrm{n}}\sec^2\hat{L}\delta L\right)/\left(\hat{R}_{\mathrm{N}}-\hat{h}\right)\end{bmatrix} \tag{13}$$

$\boldsymbol{\omega}_{\mathrm{in}}^{\mathrm{n}}$ and $\delta\boldsymbol{\omega}_{\mathrm{in}}^{\mathrm{n}}$ can be expressed as follows:

$$\omega_{\mathrm{in}}^{\mathrm{n}} = \boldsymbol{\omega}_{\mathrm{ie}}^{\mathrm{n}}+\boldsymbol{\omega}_{\mathrm{en}}^{\mathrm{n}} \tag{14}$$

$$\delta\boldsymbol{\omega}_{\mathrm{in}}^{\mathrm{n}} = \delta\boldsymbol{\omega}_{\mathrm{ie}}^{\mathrm{n}}+\delta\boldsymbol{\omega}_{\mathrm{en}}^{\mathrm{n}} \tag{15}$$

On the basis of these formulas, the INS attitude error and velocity error have been derived (Yan et al., 2008):

$$\dot{\boldsymbol{\alpha}} = \boldsymbol{C}_{\omega}^{-1}\left[\left(\mathbf{I}-\boldsymbol{C}_{\mathrm{n}}^{\mathrm{n}'}\right)\hat{\boldsymbol{\omega}}_{\mathrm{in}}^{\mathrm{n}}+\boldsymbol{C}_{\mathrm{n}}^{\mathrm{n}'}\delta\boldsymbol{\omega}_{\mathrm{in}}^{\mathrm{n}}-\boldsymbol{C}_{\mathrm{b}}^{\mathrm{n}'}\delta\boldsymbol{\omega}_{\mathrm{ib}}^{\mathrm{b}}\right] \tag{16}$$

$$\begin{aligned}\delta\dot{\boldsymbol{v}}^{\mathrm{n}} = &\left[\boldsymbol{I}-\left(\boldsymbol{C}_{\mathrm{n}}^{\mathrm{n}'}\right)^{\mathrm{T}}\right]\boldsymbol{C}_{\mathrm{b}}^{\mathrm{n}'}\hat{\boldsymbol{f}}_{\mathrm{sf}}^{\mathrm{b}}+\left(\boldsymbol{C}_{\mathrm{n}}^{\mathrm{n}'}\right)^{\mathrm{T}}\boldsymbol{C}_{\mathrm{b}}^{\mathrm{n}'}\delta\boldsymbol{f}_{\mathrm{sf}}^{\mathrm{b}}-\left(2\delta\boldsymbol{\omega}_{\mathrm{ie}}^{\mathrm{n}}+\delta\boldsymbol{\omega}_{\mathrm{en}}^{\mathrm{n}}\right)\\ &\times\left(\hat{\boldsymbol{v}}^{\mathrm{n}}-\delta\boldsymbol{v}^{\mathrm{n}}\right)-\left(2\hat{\boldsymbol{\omega}}_{\mathrm{ie}}^{\mathrm{n}}+\hat{\boldsymbol{\omega}}_{\mathrm{en}}^{\mathrm{n}}\right)\times\delta\boldsymbol{v}^{\mathrm{n}}+\delta\boldsymbol{g}^{\mathrm{n}}\end{aligned} \tag{17}$$

Where $\delta\boldsymbol{\omega}_{\mathrm{ib}}^{\mathrm{b}}$ is the measurement error of gyroscope, $\delta\boldsymbol{\omega}_{\mathrm{in}}^{\mathrm{n}}$ is the calculation error of $\boldsymbol{\omega}_{\mathrm{in}}^{\mathrm{n}}$. $\delta\boldsymbol{f}_{\mathrm{sf}}^{\mathrm{b}}$ is the measurement error of accelerometer. In addition, $\delta\boldsymbol{\omega}_{\mathrm{ib}}^{\mathrm{b}}$ are mainly consist of a constant bias $\boldsymbol{\varepsilon}^{\mathrm{b}}$ and zero mean Gaussian white noise $\mathbf{w}_{\mathrm{g}}^{\mathrm{b}}$. $\delta\boldsymbol{f}_{\mathrm{sf}}^{\mathrm{b}}$ are mainly consist of a constant bias ∇^{b} and zero mean Gaussian white noise $\mathbf{w}_{\mathrm{a}}^{\mathrm{b}}$. Besides, $\delta\boldsymbol{g}^{\mathrm{n}}$could be ignored. Hence, the INS error propagation model used in underwater environment is defined by the following equations:

$$\begin{cases}\delta\dot{L}=\frac{\delta v_{\mathrm{N}}^{\mathrm{n}}}{R_{\mathrm{M}}-h}+\delta h\frac{v_{\mathrm{N}}^{\mathrm{n}}}{(R_{\mathrm{M}}-h)^2}\\ \delta\dot{\lambda}=\frac{\delta v_{\mathrm{E}}^{\mathrm{n}}}{R_{\mathrm{N}}-h}\sec L+\delta L\frac{v_{\mathrm{E}}^{\mathrm{n}}}{R_{\mathrm{N}}-h}\tan L\sec L+\delta h\frac{v_{\mathrm{E}}^{\mathrm{n}}\sec L}{(R_{\mathrm{N}}-h)^2}\\ \delta\dot{h}=\delta V_{\mathrm{D}}\\ \dot{\boldsymbol{\alpha}}=\boldsymbol{C}_{\omega}^{-1}\left[\left(\boldsymbol{I}-\boldsymbol{C}_{\mathrm{n}}^{\mathrm{n}'}\right)\hat{\boldsymbol{\omega}}_{\mathrm{in}}^{\mathrm{n}}+\boldsymbol{C}_{\mathrm{n}}^{\mathrm{n}'}\delta\boldsymbol{\omega}_{\mathrm{in}}^{\mathrm{n}}-\boldsymbol{C}_{\mathrm{b}}^{\mathrm{n}'}\boldsymbol{\varepsilon}^{\mathrm{b}}\right]-\boldsymbol{C}_{\omega}^{-1}\boldsymbol{C}_{\mathrm{b}}^{\mathrm{n}'}\boldsymbol{w}_{\mathrm{g}}^{\mathrm{b}}\\ \delta\dot{\boldsymbol{v}}^{\mathrm{n}}=\left[\boldsymbol{I}-\left(\boldsymbol{C}_{\mathrm{n}}^{\mathrm{n}'}\right)^{\mathrm{T}}\right]\boldsymbol{C}_{\mathrm{b}}^{\mathrm{n}'}\hat{\boldsymbol{f}}_{\mathrm{sf}}^{\mathrm{b}}+\left(\boldsymbol{C}_{\mathrm{n}}^{\mathrm{n}'}\right)^{\mathrm{T}}\boldsymbol{C}_{\mathrm{b}}^{\mathrm{n}'}\nabla^{\mathrm{b}}-\left(2\delta\boldsymbol{\omega}_{\mathrm{ie}}^{\mathrm{n}}+\delta\boldsymbol{\omega}_{\mathrm{en}}^{\mathrm{n}}\right)\\ \times\left(\hat{\boldsymbol{v}}^{\mathrm{n}}-\delta\boldsymbol{v}^{\mathrm{n}}\right)-\left(2\hat{\boldsymbol{\omega}}_{\mathrm{ie}}^{\mathrm{n}}+\hat{\boldsymbol{\omega}}_{\mathrm{en}}^{\mathrm{n}}\right)\times\delta\boldsymbol{v}^{\mathrm{n}}+\left(\boldsymbol{C}_{\mathrm{n}}^{\mathrm{n}'}\right)^{\mathrm{T}}\boldsymbol{C}_{\mathrm{b}}^{\mathrm{n}'}\boldsymbol{w}_{\mathrm{a}}^{\mathrm{b}}\\ \dot{\boldsymbol{\varepsilon}}^{\mathrm{b}}=0\\ \dot{\nabla}^{\mathrm{b}}=0\end{cases} \tag{18}$$

Range of Scaling Transformation

Through the INS error propagation model (18), the range of rotation transformation and translation transformation can be estimated. However, the range of scaling transformation cannot be directly calculated. To better describe the scaling transformation, the INS-indicated distance and the actual distance in a short period are expressed by the following equations:

$$d_{k-1,k}^{\mathrm{INS}}=\frac{\left\|\boldsymbol{v}_{k-1}^{\mathrm{INS}}+\boldsymbol{v}_{k}^{\mathrm{INS}}\right\|}{2}\cdot\Delta t \tag{19}$$

$$d_{k-1,k}^{\mathrm{real}}\approx\frac{\left\|\boldsymbol{v}_{k-1}^{\mathrm{real}}+\boldsymbol{v}_{k}^{\mathrm{real}}\right\|}{2}\cdot\Delta t \tag{20}$$

$d_{k-1,k}^{\mathrm{INS}}$ and $d_{k-1,k}^{\mathrm{real}}$ are, respectively, the INS-indicated distance and the actual distance between k-1th sampling point and kth sampling point. $\boldsymbol{v}_{k}^{\mathrm{INS}}$ and $\boldsymbol{v}_{k}^{\mathrm{real}}$ are the INS-indicated linear velocity and the actual linear velocity of kth sampling point. Δt is the sampling period of the discrete time system.

Then, the relationship between $d_{k-1,k}^{\mathrm{INS}}$and $d_{k-1,k}^{\mathrm{real}}$ is derived:

$$\frac{d_{k-1,k}^{\mathrm{real}}}{d_{k-1,k}^{\mathrm{INS}}}=\frac{\left\|\boldsymbol{v}_{k-1}^{\mathrm{real}}+\boldsymbol{v}_{k}^{\mathrm{real}}\right\|}{\left\|\boldsymbol{v}_{k-1}^{\mathrm{INS}}+\boldsymbol{v}_{k}^{\mathrm{INS}}\right\|} \tag{21}$$

Where $\boldsymbol{v}_{k}^{\mathrm{INS}}$is described by an equation in the form:

$$\boldsymbol{v}_{k}^{\mathrm{INS}}=\boldsymbol{v}_{k}^{\mathrm{real}}+\delta\boldsymbol{v}_{k} \tag{22}$$

Here $\delta\boldsymbol{v}_{k}$ is the INS accumulated velocity error of kth sampling point. Accordingly, (21) is developed into the following form:

$$\frac{d_{k-1,k}^{\mathrm{real}}}{d_{k-1,k}^{\mathrm{INS}}}=\frac{\left\|\boldsymbol{v}_{k-1}^{\mathrm{INS}}+\boldsymbol{v}_{k}^{\mathrm{INS}}-\delta\boldsymbol{v}_{k-1}-\delta\boldsymbol{v}_{k}\right\|}{\left\|\boldsymbol{v}_{k-1}^{\mathrm{INS}}+\boldsymbol{v}_{k}^{\mathrm{INS}}\right\|} \tag{23}$$

Denoting with N the number of sampling points on matching sequence, the constraint of scale transform has been derived:

$$S=\frac{\sum_{k=2}^{N} d_{k-1,k}^{\text{real}}}{\sum_{k=2}^{N} d_{k-1,k}^{\text{INS}}}=\frac{\sum_{k=2}^{N}\left\|\boldsymbol{v}_{k-1}^{\text{INS}}+\boldsymbol{v}_{k}^{\text{INS}}-\delta\boldsymbol{v}_{k\text{-}1}-\delta\boldsymbol{v}_{k}\right\|}{\sum_{k=2}^{N}\left\|\boldsymbol{v}_{k-1}^{\text{INS}}+\boldsymbol{v}_{k}^{\text{INS}}\right\|} \tag{24}$$

AFFINE TRANSFORMATION BASED ABC ALGORITHM

In order to achieve high positioning accuracy under large initial errors, this paper proposes an affine transformation based ABC algorithm. The proposed algorithm is specifically presented to deal with the gravity matching problem for underwater navigation system. The affine transformation based ABC algorithm introduces affine transformation to both initialization process and evolutionary process of ABC algorithm. In addition, the affine transformation satisfies the constraint conditions provided by the output characteristics of the INS.

Objective Function and Initialization

The proposed algorithm use mean absolute difference (MAD) function as the objective function:

$$f(\boldsymbol{x})=\frac{1}{N}\sum_{k=1}^{N}\left|g_k^{\text{obs}}-g_k^{\boldsymbol{x}}\right| \tag{25}$$

Where $\boldsymbol{x}$ indicates a sequence of several consecutive position vectors. g_k^{obs} is the measured gravity anomaly value of kth sampling point and $g_k^{\boldsymbol{x}}$ is the corresponding gravity anomaly value on gravity anomaly base map of kth sampling point. $f(\boldsymbol{x})$ is the objective function.

fit $(\boldsymbol{x})$, the fitness value of $\boldsymbol{x}$, is calculated by (26):

$$fit(\boldsymbol{x})=\frac{1}{1+f(\boldsymbol{x})} \tag{26}$$

Initialization process is the first step of the proposed algorithm. In ABC algorithm, the initial swarm composed of employed bees are given by (1). But the lower bound and the upper bound of the $\boldsymbol{x}$ in sequence matching are difficult to acquire. Thus, the initialization method should be redefined.

The proposed algorithm applies scaling transformation, rotation transformation, and translation transformation on the INS-indicated sequence to implement initialization. Translation transformation is implemented by choosing a random first element of initial swarm:

$$x_{i,1}^{L}=x_{\min}^{L}+rand(0,1)(x_{\max}^{L}-x_{\min}^{L}) \tag{27}$$

$$x_{i,1}^{\lambda}=x_{\min}^{\lambda}+rand(0,1)(x_{\max}^{\lambda}-x_{\min}^{\lambda}) \tag{28}$$

Where $x_{i,1}^{L}$ and $x_{i,1}^{\lambda}$ indicate the latitude and longitude of the first sampling point on sequence i, $i=\{1,2,\cdots,SN\}$ and SN is the size of population. $x_{\max}^{L}$ and $x_{\min}^{L}$ are, respectively, the upper bound and the lower bound of latitude in search scope. $x_{\max}^{\lambda}$ and $x_{\min}^{\lambda}$ are, respectively, the upper bound and the lower bound of longitude in search scope.

Let S_i^{ini} be the scale factor used for initialization sequence i. The value of S_i^{ini} is calculated by (29):

$$S_i^{\text{ini}}=\begin{cases} rand(1,S), & S\geq 1 \\ rand(S,1), & S<1 \end{cases} \tag{29}$$

The expression of S is obtained from (24). The rotation angle used for initialization sequence i can be calculated by the following equation:

$$\beta_i^{\text{ini}}=rand(\beta_{\min}^{\text{ini}},\beta_{\max}^{\text{ini}}) \tag{30}$$

Where $\beta_{\min}^{\text{ini}}$ and $\beta_{\max}^{\text{ini}}$ are the minimum angle error and the maximum angle error of a segment in INS-indicated trajectory. Thus, the rotation matrix used for initialization sequence i have been derived:

$$\boldsymbol{R}_i^{\text{ini}}=\begin{bmatrix}\cos\beta_i^{\text{ini}} & -\sin\beta_i^{\text{ini}} \\ \sin\beta_i^{\text{ini}} & \cos\beta_i^{\text{ini}}\end{bmatrix} \tag{31}$$

Let $\boldsymbol{X}^{\text{INS}}=\left\{\boldsymbol{x}_1^{\text{INS}},\boldsymbol{x}_2^{\text{INS}},\ldots,\boldsymbol{x}_N^{\text{INS}}\right\}$ be the INS-indicated trajectory and $\boldsymbol{X}_i^{\text{ini}}=\left\{\boldsymbol{x}_{i,1}^{\text{ini}},\boldsymbol{x}_{i,2}^{\text{ini}},\ldots,\boldsymbol{x}_{i,N}^{\text{ini}}\right\}$ be the ith initialization sequence. After above mentioned transformations have been performed, the initial swarm is obtained:

$$\boldsymbol{X}_i^{\text{INS}\prime}=S_i^{\text{ini}}\boldsymbol{R}_i^{\text{ini}}\boldsymbol{X}^{\text{INS}} \tag{32}$$

$$\boldsymbol{T}_i^{\text{ini}}=\boldsymbol{x}_{i,1}^{\text{ini}}-\boldsymbol{x}_1^{\text{INS}\prime} \tag{33}$$

$$\boldsymbol{X}_i^{\text{ini}}=\boldsymbol{X}_i^{\text{INS}\prime}+\boldsymbol{T}_i^{\text{ini}} \tag{34}$$

Where $\boldsymbol{X}_i^{\text{INS}\prime}$ is the intermediate sequence, $\boldsymbol{x}_1^{\text{INS}\prime}$ is the first point in $\mathbf{X}_i^{\text{INS}\prime}$. Additional translation vector need to be applied on generated trajectories if they are out of range. Let $init_{\min}^{L}$ and $init_{\max}^{L}$ be the maximum and minimum latitude of initial trajectory. $init_{\min}^{\lambda}$ and $init_{\max}^{\lambda}$ are the maximum and minimum longitude of initial trajectory. $\mathbf{T}=\left\{T^{L},T^{\lambda}\right\}$, the translation vector, can be expressed as:

$$T^{L}=\begin{cases} x_{\min}^{L}-init_{\min}^{L}, & init_{\min}^{L}<x_{\min}^{L} \\ x_{\max}^{L}-init_{\max}^{L}, & init_{\max}^{L}>x_{\max}^{L} \\ 0, & \text{other}\end{cases} \tag{35}$$

$$T^{\lambda}=\begin{cases} x_{\min}^{\lambda}-init_{\min}^{\lambda}, & init_{\min}^{\lambda}<x_{\min}^{\lambda} \\ x_{\max}^{\lambda}-init_{\max}^{\lambda}, & init_{\max}^{\lambda}>x_{\max}^{\lambda} \\ 0, & \text{other}\end{cases} \tag{36}$$

Employed Bee Phase

With the initialization complete, an employed bee updates its food source in the neighborhood. Suppose $\boldsymbol{X}_i^{\text{ini}}$ is the sequence to be updated, $\boldsymbol{X}_j^{\text{ini}}=\left\{\boldsymbol{x}_{j,1}^{\text{ini}},\boldsymbol{x}_{j,2}^{\text{ini}},\ldots,\boldsymbol{x}_{j,N}^{\text{ini}}\right\}$ is selected randomly in the neighborhood of $\boldsymbol{X}_i^{\text{ini}}$, $j\in\{1,2,\cdots,i-1,i+1,\cdots,SN\}$ and SN is the size of population. The evolution equation is derived through the relation between $\boldsymbol{X}_i^{\text{ini}}$ and $\boldsymbol{X}_j^{\text{ini}}$.

Denoting with $\boldsymbol{Q}$ the covariance matrix:

$$\boldsymbol{Q}=\begin{bmatrix}Q_{11} & Q_{12} \\ Q_{21} & Q_{22}\end{bmatrix}=\sum_{k=1}^{N}\left(\boldsymbol{x}_{i,k}^{\text{ini}}-\tilde{\boldsymbol{x}}_i^{\text{ini}}\right)\left(\boldsymbol{x}_{j,k}^{\text{ini}}-\tilde{\boldsymbol{x}}_j^{\text{ini}}\right)^{\text{T}} \tag{37}$$

Where $\tilde{\boldsymbol{x}}_i^{\text{ini}}$ and $\tilde{\boldsymbol{x}}_j^{\text{ini}}$ are, respectively, the average value of all sampling points in $\boldsymbol{X}_i^{\text{ini}}$ and $\boldsymbol{X}_j^{\text{ini}}$. The eigenvalues of $\boldsymbol{Q}$ and the rotation angle from $\boldsymbol{X}_i^{\text{ini}}$ to $\boldsymbol{X}_j^{\text{ini}}$ are calculated through quaternion algorithm (Berthold, 1987):

$$\begin{aligned}\lambda_{1,2} &= \pm\left[(Q_{11}+Q_{22})^2+(Q_{21}-Q_{12})^2\right]^{1/2}\\ \lambda_{3,4} &= \pm\left[(Q_{11}-Q_{22})^2+(Q_{21}+Q_{12})^2\right]^{1/2} \qquad (38)\\ tg(\frac{\tau}{2}) &= (Q_{11}+Q_{22}-\lambda_{\text{m}})/(Q_{12}-Q_{21}) \qquad (39)\end{aligned}$$

Where λ_μ (μ= {1, 2, 3, 4}) are four eigenvalues of $\boldsymbol{Q}$. λ_{m} is the maximum eigenvalue. τ is the rotation angle from $\boldsymbol{X}_i^{\text{ini}}$ to $\boldsymbol{X}_j^{\text{ini}}$. Then, the rotation angle used for $\boldsymbol{X}_i^{\text{ini}}$ during employed bee phase is calculated by the following equations:

$$\beta_i^{\text{em}}=rand(-|\tau|,|\tau|) \qquad (40)$$

Notice that the angle between $\boldsymbol{X}_i^{\text{ini}}$ and $\boldsymbol{X}^{\text{INS}}$ after rotation should be in the range $(\beta_{\min}^{\text{ini}},\beta_{\max}^{\text{ini}})$. Denoting with η be the rotation angle from $\boldsymbol{X}_i^{\text{ini}}$ to $\boldsymbol{X}^{\text{INS}}$, β_i^{em} should meet the following in equation:

$$\beta_{\min}^{\text{ini}}+\eta<\beta_i^{\text{em}}<\beta_{\max}^{\text{ini}}+\eta \qquad (41)$$

Then, the following expression is obtained by (40) and (41):

$$\beta_i^{\text{em}}=rand\left(\max(-|\tau|,\beta_{\min}^{\text{ini}}+\eta),min(|\tau|,\beta_{\max}^{\text{ini}}+\eta)\right) \qquad (42)$$

Thus, the rotation matrix used for $\boldsymbol{X}_i^{\text{ini}}$ during employed bee phase is calculated by (43):

$$\boldsymbol{R}_i^{\text{em}}=\begin{bmatrix}\cos\beta_i^{\text{em}} & -\sin\beta_i^{\text{em}}\\ \sin\beta_i^{\text{em}} & \cos\beta_i^{\text{em}}\end{bmatrix} \qquad (43)$$

Let L_i^{ini} and L_j^{ini} be the length of $\boldsymbol{X}_i^{\text{ini}}$ and $\boldsymbol{X}_j^{\text{ini}}$. L^{ins} is the length of INS-indicated trajectory. The scale factor used for $\boldsymbol{X}_i^{\text{ini}}$ during employed bee phase is calculated by the following equations:

$$S_i^{\text{em}}=rand(\min(\frac{L_j^{\text{ini}}}{L_i^{\text{ini}}},\frac{L_i^{\text{ini}}}{L_j^{\text{ini}}}),max(\frac{L_j^{\text{ini}}}{L_i^{\text{ini}}},\frac{L_i^{\text{ini}}}{L_j^{\text{ini}}})) \qquad (44)$$

Notice that the scale factor between $\boldsymbol{X}_i^{\text{ini}}$ and $\boldsymbol{X}^{\text{INS}}$ after scaling transformation should meet the range on the right side of (29):

$$\begin{cases}1\cdot L^{\text{ins}}<L_i^{\text{ini}}\cdot S_i^{\text{em}}<S\cdot L^{\text{ins}}, & S\geq 1\\ S\cdot L^{\text{ins}}<L_i^{\text{ini}}\cdot S_i^{\text{em}}<1\cdot L^{\text{ins}}, & S<1\end{cases} \qquad (45)$$

Denoting with $S_{\min}^{\text{em}}$ and $S_{\max}^{\text{em}}$ the lower bound and the upper bound of S_i^{em}. According to (44) and (45), S_i^{em} is updated by (46):

$$\begin{aligned}S_i^{\text{em}} &= rand\left(S_{\min}^{\text{em}},S_{\text{m ax}}^{\text{em}}\right) \qquad (46)\\ S_{\min}^{\text{em}} &= \begin{cases}\max(min(\frac{L_j^{\text{ini}}}{L_i^{\text{ini}}},\frac{L_i^{\text{ini}}}{L_j^{\text{ini}}}),\frac{L^{\text{ins}}}{L_i^{\text{ini}}}), & S\geq 1\\ \max(min(\frac{L_j^{\text{ini}}}{L_i^{\text{ini}}},\frac{L_i^{\text{ini}}}{L_j^{\text{ini}}}),S\cdot\frac{L^{\text{ins}}}{L_i^{\text{ini}}}), & S<1\end{cases} \qquad (47)\\ S_{\max}^{\text{em}} &= \begin{cases}\min(\max(\frac{L_j^{\text{ini}}}{L_i^{\text{ini}}},\frac{L_i^{\text{ini}}}{L_j^{\text{ini}}}),S\cdot\frac{L^{\text{ins}}}{L_i^{\text{ini}}}), & S\geq 1\\ \min(\max(\frac{L_j^{\text{ini}}}{L_i^{\text{ini}}},\frac{L_i^{\text{ini}}}{L_j^{\text{ini}}}),\cdot\frac{L^{\text{ins}}}{L_i^{\text{ini}}}), & S<1\end{cases}\end{aligned}$$

$\boldsymbol{X}_i^{\text{ini}}$ is converted to $\boldsymbol{X}_i^{\text{ini}\prime}$ after rotation transformation and scaling transformation have been performed:

$$\mathbf{X}_i^{\text{ini}\prime}=S_i^{\text{em}}\mathbf{R}_i^{\text{em}}\mathbf{X}_i^{\text{ini}} \qquad (48)$$

Let $\tilde{\boldsymbol{x}}_i^{\text{ini}\prime}$ be the average value of all sampling points in $\boldsymbol{X}_i^{\text{ini}\prime}$ and the translation vector is calculated by (49):

$$\boldsymbol{T}_i^{\text{em}}=(\tilde{\boldsymbol{x}}_j^{\text{ini}}-\tilde{\boldsymbol{x}}_i^{\text{ini}\prime})\cdot rand(-1,1) \qquad (49)$$

Then, the employed bees update their sources according to the following equation:

$$\boldsymbol{X}_i^{\text{em}}=\boldsymbol{X}_i^{\text{ini}\prime}+\boldsymbol{T}_i^{\text{em}} \qquad (50)$$

If the fitness value of $\boldsymbol{X}_i^{\text{em}}$ is larger than the fitness value of $\boldsymbol{X}_i^{\text{ini}}$, $\boldsymbol{X}_i^{\text{ini}}$ will be replaced by $\boldsymbol{X}_i^{\text{em}}$. At the end of the employed bee phase, all of current sequences are denoted by $\boldsymbol{X}^{\text{em}}$.

Onlooker Bee Phase and Scout Bee Phase

The probability of each sequence to be selected by the onlooker bee is calculated by (4). Suppose $\boldsymbol{X}_i^{\text{em}}$ is the sequence selected by onlooker bee, the rotation matrix $\boldsymbol{R}_i^{\text{on}}$, the scale factor S_i^{on}, and the translation vector $\boldsymbol{T}_i^{\text{on}}$ used on $\boldsymbol{X}_i^{\text{em}}$ during onlooker bee phase can be calculated by (43), (46),and (49). Thus, the onlooker bees update their sources according to the following equation:

$$\boldsymbol{X}_i^{\text{on}}=S_i^{\text{on}}\boldsymbol{R}_i^{\text{on}}\boldsymbol{X}_i^{\text{em}}+\boldsymbol{T}_i^{\text{on}} \qquad (51)$$

If the fitness value of $\boldsymbol{X}_i^{\text{on}}$ is larger than the fitness value of$\boldsymbol{X}_i^{\text{em}}$, $\boldsymbol{X}_i^{\text{em}}$ will be replaced by $\boldsymbol{X}_i^{\text{on}}$. The best solution achieved so far is memorized. In addition, a sequence will be abandoned when limit, a control parameter, is exceeded for the source during scout bee phase. So it is replaced with randomly produced solution by (34). The pseudo of the proposal is given below.

Procedure of the proposal

Begin

1. confirm search scope

2. initialize a matching sequence $\mathbf{X}_i^{\text{ini}}$ at generation $t=0$ with $trial(i)=0$ using (34) for i = 1,2,…,SN

3. evaluate $f\left(\mathbf{X}_i^{\text{ini}}\right)$ for i = 1,2,…,SN and set the best solution as $\mathbf{X}_{\text{best}}$

4. **while** termination condition is not reached **do**

//**employed bee phase**

1) set $k=1$, **while** k<SN+1 **do**

Produce a new solution $\mathbf{X}_k^{\text{em}}$ for $\mathbf{X}_k^{\text{ini}}$ using (50)

if $f\left(\mathbf{X}_k^{\text{ini}}\right)>f\left(\mathbf{X}_k^{\text{em}}\right)$, $\mathbf{X}_k^{\text{ini}}=\mathbf{X}_k^{\text{em}}$, trial($i$) = 0

else $trial(i)=trial(i)$+1

end if

$k=k$+1

end while

2) all of current sequences are denoted by $\mathbf{X}^{\text{em}}$

//**onlooker bee phase**

3) set $k=1$, **while** k<SN+1 **do**

Select a sequence $\mathbf{X}_i^{\text{em}}$ based on its probability of selection calculated using (4) and produce a new solution $\mathbf{X}_i^{\text{on}}$ using (51)

If $f\left(\mathbf{X}_i^{\text{em}}\right) > f\left(\mathbf{X}_i^{\text{on}}\right)$, $\mathbf{X}_i^{\text{em}} = \mathbf{X}_i^{\text{on}}$, $trial(i) = 0$

else $trial(i) = trial(i)+1$

end if

$k = k+1$

end while

4) all of current sequences are denoted by $\mathbf{X}^{\text{on}}$

//scout bee phase

5) denote the best solution in $\mathbf{X}^{\text{on}}$ as $\mathbf{X}_{\text{best}}{}'$

if $f\left(\mathbf{X}_{\text{best}}\right) > f\left(\mathbf{X}_{\text{best}}{}'\right)$, $\mathbf{X}_{\text{best}} = \mathbf{X}_{\text{best}}{}'$

end if

6) reinitialize ith sequence if $trial(i) > limit$

7) $t = t+1$

8) all of current sequences are denoted by $\mathbf{X}^{\text{ini}}$

end while

5. output $\mathbf{X}_{\text{best}}$

End

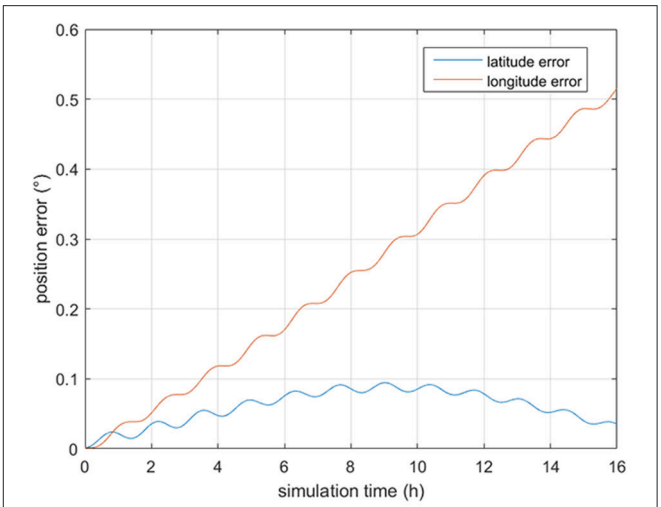

FIGURE 1 | The INS position error.

TABLE 1 | Simulation condition of INS.

Parameters	Quantity	Unit
Gyro constant drift	0.02	°/h
Gyro random drift (1σ)	0.02	°/h
Accelerometer constant bias	100	μg
Accelerometer random bias (1σ)	100	μg
Velocity	7.71	m/s
Acceleration	0	m/s
Initial angle error	0	°
Azimuth angle	60	°
Initial longitude error	0.1	′
Initial latitude error	0.1	′
Simulation time	16	h

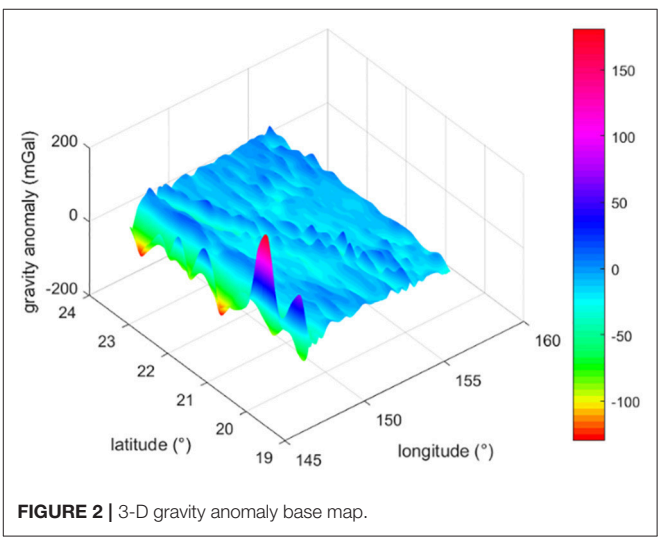

FIGURE 2 | 3-D gravity anomaly base map.

SIMULATION AND ANALYSIS

Simulation Parameters

In order to test the feasibility of our approach, numerous simulation experiments have been performed. An INS indicated trajectory start from (156°E, 20°N) is generated and the INS relevant parameters are listed in **Table 1**. The INS position error is shown in **Figure 1 (Supplementary Data Sheet 1)**. As seen from **Figure 1**, the position error of the generated trajectory exhibits a Scuhler oscillation of 84.4 min.

In order to evaluate the algorithm presented in this work, a gravity anomaly base map is required. In the simulations tests, goco05c model (Fecher et al., 2017) is used to calculate the gravity anomaly in the area from (147.6°E, 19.5°N) to (156.6°E, 24°N). After interpolated, the grid step is converted to 0.3′. The 3-D map of the gravity anomaly data is shown in **Figure 2 (Supplementary Data Sheet 1)**. The gravity anomaly relevant parameters are shown in **Table 2**.

TABLE 2 | Parameters of gravity anomaly base map.

Model name	Goco05c
Number of grid points	900 × 1800
Grid step	0.3′
Minimum value	−130. 039 mGal
Maximum value	180. 902 mGal
Mean	−15.246 mGal

Figure 3 shows the angle error of a segment in INS-indicated trajectory. It is obtained that the angle error is vary in a small range and the maximum segment angle error is 15°. Thus, $\beta_{\text{min}}^{\text{ini}}$ and $\beta_{\text{max}}^{\text{ini}}$ are set as −15°and 15°, respectively. The proposed algorithm uses the 3σ principle to confirm the search scope (Han et al., 2016). **Table 3** shows the configuration of the proposed algorithm. In this paper, optimal parameter values of affine transformation based ABC are obtained based on experience.

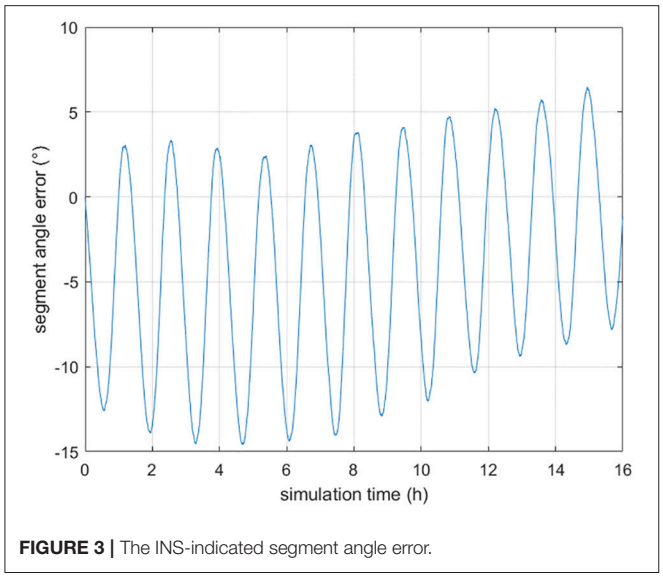

FIGURE 3 | The INS-indicated segment angle error.

TABLE 3 | Configuration of the proposed algorithm.

Maximum iterations	500
Limit	20
Population size	10
Number of sampling points per sequence	12
Sampling interval	5 min
The variance of gravity anomaly measurement noise	1 mGal

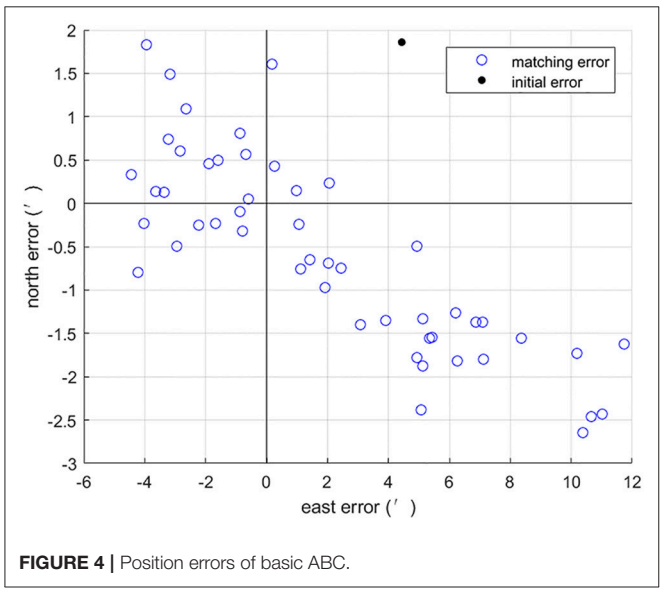

FIGURE 4 | Position errors of basic ABC.

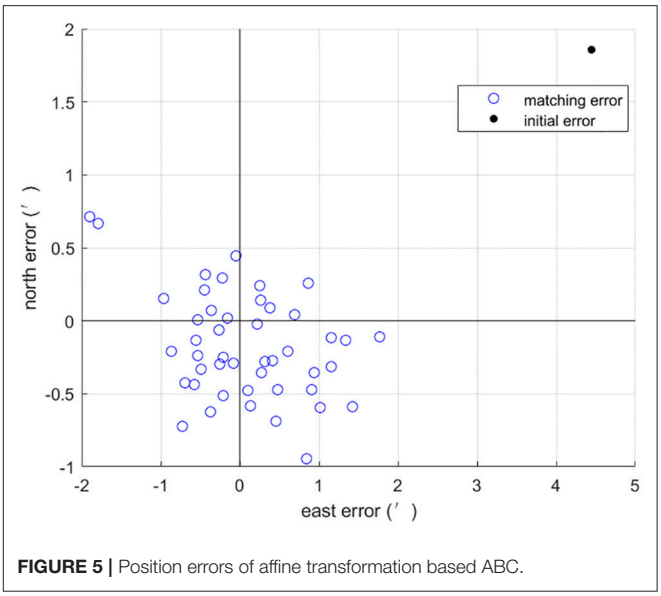

FIGURE 5 | Position errors of affine transformation based ABC.

TABLE 4 | Comparison of 50 Mont Carlo simulation results between basic ABC and affine transformation based ABC.

Algorithm	Initial error (′)	Mean error (′)	Matching probability (%)
Basic ABC	4.82	4.22	28
Affine transformation based ABC	4.82	0.73	96

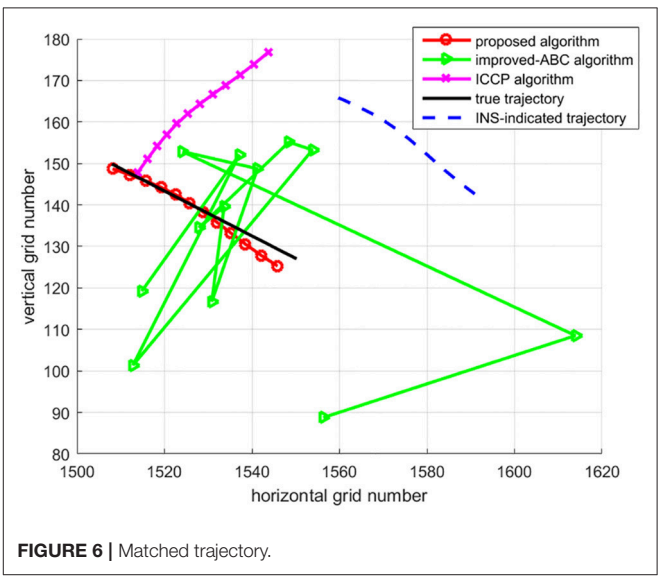

FIGURE 6 | Matched trajectory.

Comparison Between Basic ABC and Affine Transformation Based ABC

Based on the parameters above, the first set of 50 Mont Carlo simulation tests were done on the trajectory after 3 h of sailing. Simulation results of introducing sequence matching strategy into ABC algorithm has better positioning precision and matching probability than the basic ABC, as shown in **Figures 4, 5**. Statistical results of simulation tests are given in **Table 4**. In **Table 4**, a matching result is considered to be a successful matching if the position error is within 2′.

Comparison Between ICCP, Improved-ABC and Affine Transformation Based ABC

Due to ICCP is a widely used gravity matching algorithm and improved-ABC algorithm (Gao et al., 2014) is presented to tackle the similar problem. We use these algorithms as references, comparing the results of ICCP algorithm and improved-ABC algorithm with the proposed algorithm.

To test algorithms under large initial position errors, the second set of 50 Mont Carlo simulation tests were done on the trajectory after 7 h of sailing using the above three algorithms. Trajectories of matching results are shown in **Figure 6**, each trajectory is a typical one in 50 Mont Carlo simulations. **Figure 7** indicates the average error of longitude and latitude of each sampling point in 50 Mont Carlo simulations. In order to better evaluate the proposed algorithm, the statistical results of all the three algorithms are given in **Table 5**.

Simulation results in **Figures 6**, **7**, and **Table 5** show that the matching accuracy of the proposed algorithm is significantly superior to the other two algorithms under large initial position errors.

To better observe the effect of initial errors on these three algorithms, matching results of the whole trajectory within 16 h are shown in **Figure 8** and **Table 6**. The results are divided into three time periods for statistic. In **Table 6**, a matching

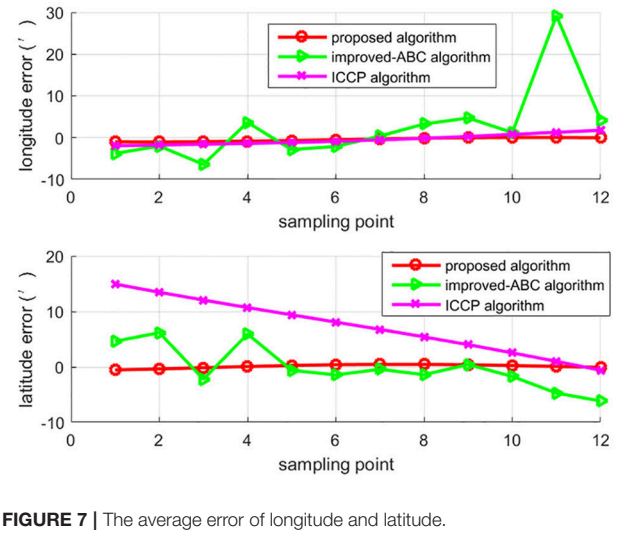

FIGURE 7 | The average error of longitude and latitude.

TABLE 5 | Statistical results of the matching errors.

Algorithm	Initial position error (km)	Mean error (km)	Standard deviation (km)
ICCP	22.47	25.85	0
Improved-ABC	22.47	15.95	8.70
Proposed algorithm	22.47	2.05	0.55

TABLE 6 | Statistical results within 16 h.

Time period	Algorithm	Average matching time (s)	Mean error (′)	Matching probability (%)
0–5 h	Improved-ABC	0.05	5.96	57
	ICCP	0.67	3.71	67
	Proposed algorithm	0.21	1.00	100
5–10 h	Improved-ABC	0.04	14.71	20
	ICCP	3.41	9.22	30
	Proposed algorithm	0.82	3.23	82
10–16 h	Improved-ABC	0.05	27.47	9
	ICCP	9.88	22.33	0
	Proposed algorithm	1.75	6.63	73

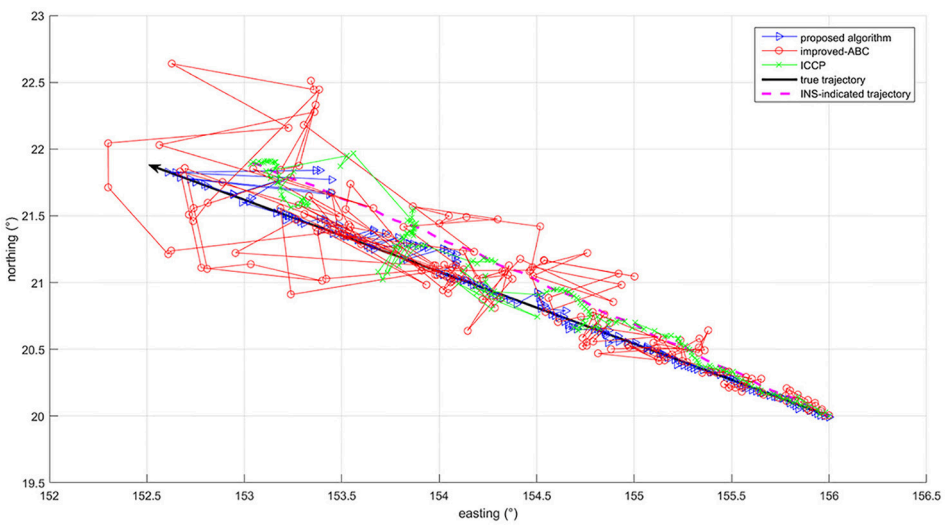

FIGURE 8 | Matching results of the whole trajectory.

result is considered to be a successful matching if the position error is within 5′. It can be concluded that the convergence speed of ICCP algorithm decreases a lot with the increase of initial position errors. While the convergence speed of improved-ABC algorithm is not affected by initial position errors. The proposed algorithm converge slower than improved-ABC algorithm and much faster than ICCP algorithm under large initial errors. In **Figure 8**, at the beginning, all of the three algorithms can hold high positioning accuracy. But with the initial errors and the search scope increase, the accuracy of ICCP algorithm and improved-ABC algorithm decrease significantly, whereas the proposed algorithm can guarantee much higher matching accuracy.

CONCLUSION

Gravity aided inertial navigation system can solve the problem of INS error accumulation and ensure the concealment of INS. However, there are still many problems in the field of gravity aided navigation system. In this paper, we focus on the problem of how to ensure the matching accuracy under the large initial errors condition. In order to avoid mismatching under large initial errors, an affine transformation based ABC algorithm is adopted. The simulation results show that the proposed algorithm can achieve high matching precision under the condition of large initial errors.

In addition to ABC algorithm, other evolutionary algorithms can also be used to solve the gravity matching problem. How to introduce the sequence matching strategy in other evolutionary algorithms? How are the effects of these algorithms after introducing the sequence matching strategy? These need to be further studied in the future. What's more, the matching accuracy of gravity matching algorithm is highly correlated with the precision and resolution of the gravity anomaly base map. This paper focuses on the matching algorithm for large initial errors. How to perform a gravity matching algorithm in the area with low uniqueness should be discussed in the next step.

AUTHOR CONTRIBUTIONS

TD and LM designed the study. TD, LM, and HS performed the simulations. All of the authors analyzed the data. All authors contributed to the writing and editing of the manuscript.

FUNDING

This work was supported by the National Natural Science Foundation of China (grant number 61473039).

SUPPLEMENTARY MATERIAL

The Supplementary Material for this article can be found online at: https://www.frontiersin.org/articles/10.3389/fnbot.2019.00019/full#supplementary-material

Supplementary Data Sheet 1 | Gravity base map and the INS data.

REFERENCES

Abrao, T. (2013). *Search Algorithms for Engineering Optimization: Chapter 8-Application of Harmony Search Algorithm in Power Engineering, Chapter Book-Chapter 8*. Crovatia: InTech Open Access Publishing.

Affleck, C. A., and Jircitano, A. (1990). "Passive gravity gradiometer navigation system," in *Proceedings of IEEE Position Location and Navigation Symposium* (Las Vegas, NV), 60–66.

Akay, B., and Karaboga, D. (2012). A modified artificial bee colony algorithm for real-parameter optimization. *Inform. Sci.* 192, 120–142. doi: 10.1016/j.ins.2010.07.015

Akbari, R., Hedayatzadeh, R., Ziarati, K., and Hassanizadeh, B. (2012). A multi-objective artificial bee colony algorithm. *Swarm Evol. Comput.* 2, 39–52. doi: 10.1016/j.swevo.2011.08.001

Allotta, B., Caiti, A., Costanzi, R., Fanelli, F., Fenucci, D., Meli, E., et al. (2016). A new AUV navigation system exploiting unscented Kalman filter. *Ocean Eng.* 113, 121–132. doi: 10.1016/j.oceaneng.2015.12.058

Berthold, K. P. H. (1987). Closed-form solution of absolute orientation using unit quaternions. *J. Opt. Soc. Am. A* 4, 629–642.

Bishop, G. C. (2002). Gravitational field maps and navigational errors [unmanned underwater vehicles]. *IEEE J. Ocean. Eng.* 27, 726–737. doi: 10.1109/JOE.2002.1040954

Canciani, A., and Raquet, J. (2017). Airborne magnetic anomaly navigation. *IEEE Trans. Aerosp. Electron. Syst.* 53, 67–80. doi: 10.1109/TAES.2017.2649238

Claus, B., and Bachmayer, R. (2015). Terrain-aided navigation for an underwater glider. *J. Field Robot.* 32, 935–951. doi: 10.1002/rob.21563

Copp, B., and Subbarao, K. (2015). Nonlinear adaptive filtering in terrain-referenced navigation. *IEEE Trans. Aerosp. Electron. Syst.* 51, 3461–3469. doi: 10.1109/TAES.2015.140826

Fecher, T., Pail, R., and Gruber, T. (2017). Goco05c: a new combined gravity field model based on full normal equations and regionally varying weighting. *Surv. Geophys.* 38, 571–590. doi: 10.1007/s10712-016-9406-y

Gao, W., Zhao, B., Zhou, G., Wang, Q., and Yu, C. (2014). Improved artificial bee colony algorithm based gravity matching navigation method. *Sensors* 14, 12968–12989. doi: 10.3390/s1407 12968

Han, Y., Wang, B., Deng, Z., and Fu, M. (2016). An improved TERCOM-based algorithm for gravity-aided navigation. *IEEE Sens. J.* 16, 2537–2544. doi: 10.1109/JSEN.2016.2518686

Hegrenaes, O., and Hallingstad, O. (2011). Model-aided INS with sea current estimation for robust underwater navigation. *IEEE J. Ocean. Eng.* 36, 316–337. doi: 10.1109/JOE.2010.2100470

Hidalgo-Paniagua, A., Vega-Rodríguez, M., and Ferruz, J. (2016). Applying the MOVNS (multi-objective variable neighborhood search) algorithm to solve the path planning problem in mobile robotics. *Expert Syst. Appl.* 58, 20–35. doi: 10.1016/j.eswa.2016.03.035

Kamgarparsi, B., and Kamgarparsi, B. (1999). Vehicle localization on gravity maps. *Proc. SPIE.* 3693, 182–191.

Karaboga, D., and Basturk, B. (2007). A powerful and efficient algorithm for numerical function optimization: artificial bee colony (ABC) algorithm. *J. Glob. Optimization* 39, 459–471. doi: 10.1007/s10898-007-9149-x

Kim, T., Kim, J., and Byun, S. W. (2018). A comparison of nonlinear filter algorithms for terrain-referenced underwater navigation. *Int. J. Control Autom. Syst.* 16, 2977–2989. doi: 10.1007/s12555-017-0504-5

Kim, Y., Hong, K., and Bang, H. (2018). Utilizing out-of-sequence measurement for ambiguous update in particle filtering. *IEEE Trans. Aerosp. Electron. Syst.* 54, 493–501. doi: 10.1109/TAES.2017.2741878

Lee, J., and Kim, D. W. (2016). An effective initialization method for genetic algorithm-based robot path planning using a directed acyclic graph. *Inf. Sci. (NY).* 332, 1–18. doi: 10.1016/j.ins.2015.11.004

Li, H., Liu, M., and Zhang, F. (2017). Geomagnetic navigation of autonomous underwater vehicle based on multi-objective evolutionary algorithm. *Front. Neurorobot.* 11, 1–8. doi: 10.3389/fnbot.2017.00034

Li, J., Pan, Q., and Duan, P. (2016). An improved artificial bee colony algorithm for solving hybrid flexible flowshop with dynamic operation skipping. *IEEE Trans. Cybern.* 46, 1311–1324. doi: 10.1109/TCYB.2015.2444383

Li, T., Zhao, D., and Huang, Z. (2013). A wavelet-based grey particle filter for self-estimating the trajectory of manoeuvring autonomous underwater vehicle. *Trans. Inst. Meas. Control* 36, 321–335. doi: 10.1177/0142331213500981

Paull, L., Saeedi, S., Seto, M., and Li, H. (2013). AUV navigation and localization: a review. *IEEE J. Ocean. Eng. 2013* 39, 131–149. doi: 10.1109/JOE.2013.2278891

Quan, W., and Fang, J. (2010). A star recognition method based on the adaptive ant colony algorithm for star sensors. *Sensors* 10, 1955–1966. doi: 10.3390/s100301955

Rice, H., Kelmenson, S., and Mendelsohn, L. (2004). "Geophysical navigation technologies and applications," in *Proceedings of IEEE Position Location and Navigation Symposium* (Monterey, CA), 618–624.

Sag, T., and Çunkaş, M. (2015). Color image segmentation based on multiobjective artificial bee colony optimization. *Appl. Soft Comput.* 34, 389–401. doi: 10.1016/j.asoc.2015.05.016

Simanek, J., Reinstein, M., and Kubelka, V. (2015). Evaluation of the EKF-based estimation architectures for data fusion in mobile robots. *IEEE ASME Trans. Mech.* 20, 985–990. doi: 10.1109/TMECH.2014.2311416

Song, Z., Zhang, J., Zhu, W., and Xi, X. (2016). The vector matching method in geomagnetic aiding navigation. *Sensors* 16:1120. doi: 10.3390/s16071120

Teymourian, E., Kayvanfar, V., Komaki, G. H. M., and Zandieh, M. (2016). Enhanced intelligent water drops and cuckoo search algorithms for solving the capacitated vehicle routing problem. *Inf. Sci. (NY).* 334, 354–378. doi: 10.1016/j.ins.2015.11.036

Tong, Y., Bian, S., Jiang, D., and Xiao, S. (2011). Gravity matching simulation of real-time iccp algorithm. *J. Chin. Inertial Technol.* 19, 340–343.

Wang, X., Su, M., Liu, P., and Ding, S. (2013). Application of improved ICCP algorithm in gravity matching aided navigation. *Sci. Surv. Mapp.* 207. 38, 36–39

Wu, L., Wang, H., Chai, H., Hsu, H., and Wang, Y. (2015). Research on the relative positions-constrained pattern matching method for underwater gravity-aided inertial navigation. *J. Navigation* 68, 937–950. doi: 10.1017/S0373463315000235

Wu, L., Wang, H., Chai, H., Zhang, L., Hsu, H., and Wang, Y. (2017). Performance evaluation and analysis for gravity matching aided navigation. *Sensors* 17:769. doi: 10.3390/s17040769

Xu, X., Wu, J., Xu, S., Wang, L., and Li, P. (2014). ICCP algorithm for underwater terrain matching navigation based on affine correction. *J. Chin. Inertial Technol.* 22, 362–367. doi: 10.13695/j.cnki.12-1222/o3.2014.03.016

Yan, G., Yan, W., and Xu, D. (2008). Application of simplified UKF in SINS initial alignment for large misalignment angles. *J. Chin. Inertial Technol.* 16, 253–264. doi: 10.13695/j.cnki.12-1222/o3.2008.03.006

Yildiz, A. R. (2013). Comparison of evolutionary-based optimization algorithms for structural design optimization. *Eng. Appl. Artif. Intell.* 26, 327–333. doi: 10.1016/j.engappai.2012.05.014

Zhao, L., Gao, N., Huang, B., Wang, Q., and Zhou, J. (2014). A novel terrain-aided navigation algorithm combined with the TERCOM algorithm and particle filter. *IEEE Sens. J.* 15, 1124–1131. doi: 10.1109/JSEN.2014.2360916

Zhu, Z., Guo, Y., and Yang, Z. (2015). Study on initial gravity map matching technique based on triangle constraint model. *J. Navigation* 69, 353–372. doi: 10.1017/S0373463315000661

Conflict of Interest Statement: The authors declare that the research was conducted in the absence of any commercial or financial relationships that could be construed as a potential conflict of interest.

frontiers in Neurorobotics

REVIEW
published: 28 May 2019
doi: 10.3389/fnbot.2019.00028

Neuromorphic Stereo Vision: A Survey of Bio-Inspired Sensors and Algorithms

Lea Steffen[1]*, *Daniel Reichard*[1], *Jakob Weinland*[1], *Jacques Kaiser*[1], *Arne Roennau*[1] and *Rüdiger Dillmann*[1,2]

[1] FZI Research Center for Information Technology, Karlsruhe, Germany, [2] Humanoids and Intelligence Systems Lab, Karlsruhe Institute of Technology (KIT), Karlsruhe, Germany

Any visual sensor, whether artificial or biological, maps the 3D-world on a 2D-representation. The missing dimension is depth and most species use stereo vision to recover it. Stereo vision implies multiple perspectives and matching, hence it obtains depth from a pair of images. Algorithms for stereo vision are also used prosperously in robotics. Although, biological systems seem to compute disparities effortless, artificial methods suffer from high energy demands and latency. The crucial part is the correspondence problem; finding the matching points of two images. The development of event-based cameras, inspired by the retina, enables the exploitation of an additional physical constraint—time. Due to their asynchronous course of operation, considering the precise occurrence of spikes, Spiking Neural Networks take advantage of this constraint. In this work, we investigate sensors and algorithms for event-based stereo vision leading to more biologically plausible robots. Hereby, we focus mainly on binocular stereo vision.

Keywords: bio-inspired 3D-perception, neuromorphic visual sensors, cooperative algorithms, event-based technologies, brain-inspired robotics, human-like vision

OPEN ACCESS

Edited by:
Jan-Matthias Braun, University of Southern Denmark, Denmark

Reviewed by:
Sio Hoi Ieng, Université Pierre et Marie Curie, France
Yulia Sandamirskaya, University of Zurich, Switzerland

***Correspondence:**
Lea Steffen
steffen@fzi.de

Received: *03 January 2019*
Accepted: *07 May 2019*
Published: *28 May 2019*

Citation:
Steffen L, Reichard D, Weinland J, Kaiser J, Roennau A and Dillmann R (2019) Neuromorphic Stereo Vision: A Survey of Bio-Inspired Sensors and Algorithms. Front. Neurorobot. 13:28. doi: 10.3389/fnbot.2019.00028

1. INTRODUCTION

As the visual sense and any visual sensor loose one dimension when mapping the 3D-world onto a 2D-representation, the ability to recover depth is crucial for biological and artificial vision systems. Stereo-vision refers to the method recovering depth information from both eyes, or in the artificial context, two sensors. In biology this is possible due to the laterally shifted eyes, gaining slightly different versions of a scene. The brain matches the corresponding points of both images and computes their disparity.

While biology computes disparities seemingly effortless, current approaches computing stereo in real-time are too computationally expensive. This is mainly caused by acquiring and processing huge amounts of redundant data. Hence, frame-based data acquisition implies computational limitations (Rogister et al., 2012). Furthermore, with increasing complex scenes and noise the computational expense of common machine vision system increases significantly. That has negative effects on the speed, size, and efficiency of the hardware (Osswald et al., 2017). Finding the corresponding dots in both images is hereby the bottleneck. This computationally complex issue is referred to as the correspondence problem. With the development of neuromorphic visual sensors (Lichtsteiner et al., 2008), a new physical constraint is now also applicable in artificial vision: time (Kogler et al., 2011a; Rogister et al., 2012; Dikov et al., 2017). Similar to retinal

output cells, event-based sensors transmit information asynchronously as a continuous stream of events (Rogister et al., 2012). A comprehensive scientific investigation of the neural code of the retina is provided in Meister and Berry (1999).

Spiking Neural Networks are a natural match for event-based sensors due to their asynchronous operation principle. Thus, SNNs are a popular choice for many systems using silicon retinas like the work of Orchard et al. (2013), Orchard et al. (2015), and Haessig et al. (2017). Examples for event-based stereo vision applications applying networks with spiking neurons are Dikov et al. (2017), Osswald et al. (2017), Rebecq et al. (2017), and Haessig et al. (2019).

As self-driving cars are already a very promising application of artificial depth perception, they are also an interesting field of use for event-based 3D-vision. An approach combining event-based vision and deep learning for steering prediction for autonomous vehicles is introduced in Maqueda et al. (2018). Furthermore, event-based vision is changing technologies and algorithms in fields such as health-care, security, surveillance, entertainment and industrial automation (Brandli, 2015). In Mafrica (2016), EBS for robotic and automotive applications are investigated.

Scientists in the field of computer vision and 3D-imaging strive for the sophisticated model posed by nature. Nevertheless, a comprehensive review, not only about human inspired sensors but also biologically plausible algorithms and the synergy of both, is still missing. This paper surveys the advances of event-based techniques and algorithms, especially developed for neuromorphic visual sensors, researchers have made to this day. As stereo vision is a large topic many different techniques such as radar, ultrasonic sensors, light section, structured light, and depth from defocus/focus exist. However, this manuscript is mainly focusing on binocular stereo vision.

For this purpose, conventional machine stereo vision is reviewed briefly and vision in nature is elaborated in more depth. Subsequently, the evolution and a comparison of event-based sensors is presented, followed by an investigation of cooperative algorithms and their alternatives for event-driven stereo vision.

2. TECHNICAL AND BIOLOGICAL BACKGROUND

Machine stereo vision, also referred to as stereoscopic vision, has been an active field of research for decades. It has been widely investigated before the arise of event-based sensors. However, biology understands a scene faster than computers and at lower energy budget (Martin et al., 2018). It works reliable in human vision and error robustness and energy efficiency are sophisticated. Hence, nature can be used as an inspiration for more efficient and robust sensors and algorithms. This section covers standard cameras and their mechanics as well as the human retina and depth perception in nature.

2.1. Conventional Cameras and Their Principle of Operation

Customary cameras commonly use a sensor constituted of a 2D-Array of pixels, where each pixel is sensitive to light intensity. Data is selected synchronously from all pixels at fixed time steps. The generated pixel data at one time is called frame and thus the frequency of the read-out is called frame rate (Mahowald, 1992; Akolkar et al., 2015). These sensors are limited in their performance by their course of action. Imaging and information transfer at a fixed frame rate, unrelated to the dynamics of the observed scene, causes two opposed issues. For one, important information might get lost leading to a decrease in temporal resolution. This is less crucial but still true for relatively high frame rates, since events might always occur between these two time steps. The complementary problem is an inevitably high redundancy. Data transfer of all pixels, even in case of no or small local changes, increase the data transfer and volume needlessly. This problem is magnified as changes usually only affect a small part of the scene, like a subset of pixels, and rarely the whole image (Posch et al., 2014).

2.2. Depth Perception in Machine Vision

There are a lot of techniques to obtain 3D-data of a scene. Active representatives are electro-optical distance measurements such as LIDAR (light detection and ranging), TOF cameras (time-of-flight), radar, ultrasonic sensors, light section, and structured light. In addition there are passive techniques such as SfM (Structure from motion), shape from shading and stereopsis. However, most of these technologies are slow, computation-intensive and resource-gobbling. In case of LIDAR the 3D-generation itself is rather cheap but it outputs a lot of points that are expensive to handle. These drawbacks are problematic for many applications using 3D-data, like navigation, path planning, and robotic motion control. Cameras are a good option because they produce dense data in real time. However, since cameras represent the 3D-environment in 2D-data, depth information must be gained supplementary. The obvious way is stereoscopy, a form of sensor fusion in which the same scene is recorded from at least two different points of view and the data is combined into a sole representation. If you have the matching dots from both images, the depth can be determined since it is inversely proportional to the disparity. Disparity is the displacement along the epipolar line.

According to Lucas and Kanade (1981) the 3D-position of an object is reconstructable if enough of its dots can be found and matched from at least two images, taken from slightly differing perspectives. This requires four steps; (1) finding of objects and features in the image, (2) matching the points found, (3) estimating the camera parameter, and (4) determining the distance from the camera objects represented by the dots. This process is called image registration and the basic problem of finding points that belong together in two images of the same scene is called the correspondence problem. **Figure 1** shows why this problem is not trivial. In this case the solution is particularly difficult because the four depicted objects are indistinguishable. Hence, further methods are necessary to determine correct correspondences.

Stereo vision is a very well-investigated research area in the field of machine vision. In Marr and Poggio (1976), the authors laid the foundation for research in this field at an early stage. In Barnard and Fischler (1982), Dhond and Aggarwal (1989),

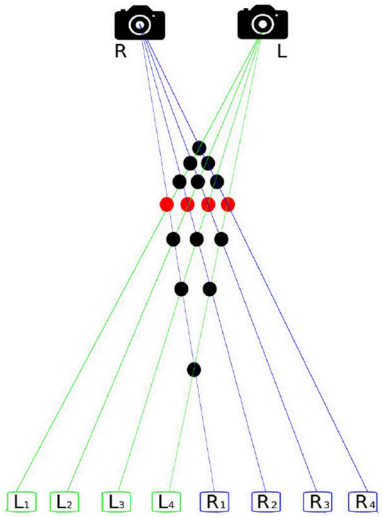

FIGURE 1 | The correspondence problem. The scene comprises four identical objects, recorded from two perspectives. *R* is the right and *L* the left camera. The rectangles L_1–L_4 represent the imaging of *L* and R_1–R_4 of *R*. There are 16 possible matches, visualized by dots, showing how the shots of *L* and *R* might correspond to each other. Only four of them, accentuated in red, are correct matches.

and Scharstein et al. (2002) different approaches to overcome the stereo correspondence problem are presented and in Scharstein et al. (2002) a general taxonomy is proposed two-frame stereo methods regarding comparison of multi-view 3D-reconstruction methods, differentiating their key properties. In Seitz et al. (2006), this In Seitz et al. (2006), this taxonomy is expanded and refined. On this basis six algorithms (Kolmogorov and Zabih, 2002; Pons et al., 2005; Goesele et al., 2006; Vogiatzis et al., 2007; Furukawa, 2008) for reconstruction of dense objects with calibrated cameras are calibrated cameras are evaluated. The authors of Seitz et al. (2006) measure accuracy (how close the reconstruction truth model) and completeness (how much of the ground truth model is successfully reconstructed) of all methods to provide a good comparison. It is stated that except (Goesele et al., 2006), all evaluated techniques are complete. evaluated techniques are complete. Hernández Esteban and Schmitt (2004) achieves the highest accuracy, with 90% of its ground truth mesh. It is also worth mentioning, that the runtimes vary drastically. The fastest approach is drastically. The fastest approach is Pons et al. (2005) and the slowest one is Goesele et al. (2006). A quite general review about the broad range of 3D-reconstruction techniques, is provided in Butime et al. (2006). Here, the camera-based approaches.

Methods for artificial stereoscopy can be divided into two groups, sparse and dense scene representation. Sparse approaches include especially early, often feature-based, work. Many of those use edge detectors or interest operators to detect promising areas of the image and find their correspondences. Newer approaches from this area extract very reliable characteristics and use them as seeds to determine further correspondences (Szeliski, 2010). The second group, dense methods, although more complex, are more popular nowadays. In Scharstein et al. (2002), a taxonomy for these approaches is presented, defining the four steps, (1) matching cost computation, (2) cost (support) aggregation, (3) disparity computation/optimization, and (4) disparity refinement as the basis of such algorithms. Most of the approaches in this group can be subdivided into these sections, although a subgroup of these points can already form a full-fledged algorithm. A further differentiation results in local and global methods (Szeliski, 2010). With the local approach only intensity values within a finite range are considered for the calculation of the disparities of a point. Many local algorithms, such as the sum-of-squared-differences (SSD), consist of steps 1–3, but a few consist only of steps 1 & 2. In contrast, global methods are based on smoothness assumptions and usually refer to the entire image. They usually do not use aggregation and often consist of steps 1, 3, & 4. To optimize the outcome simulated annealing, expectation maximization or graph cuts are often applied. Additionally to global and local methods there are also iterative algorithms (Scharstein et al., 2002; Szeliski, 2010) including the biologically motivated approach of Marr and Poggio (1976). In the case of increasingly complex scenes and in the case of noisy image data, the classical approaches for stereoscopic vision quickly reach their limits and also the computational effort is disproportionately large. This has a huge impact on the size, speed, power consumption, throughput, and efficiency of the hardware used and makes their integration difficult (Osswald et al., 2017).

2.3. The Retina

The retina, also known as the fundus, is a highly developed system consisting of photosensitive cells that contain approximately 100 million black-and-white photoreceptors and nearly 4 million color receptors (Boahen, 1996). It is a multi-layered neuronal network responsible for the acquisition and preprocessing of visual information. As shown in **Figure 2** the retina is divided into three main layers, the photoreceptor layer, the outer plexiform layer, and the inner plexiform layer (Posch et al., 2014). These layers include, with the photoreceptors, the bipolar cells, and the ganglion cells, the three most important cell types.

Photoreceptors are the actually light-sensitive cell type of the retina and can be divided into two types that react to different wavelengths of light. Cones for color recognition and sharp vision, as well as rods for vision under bad lighting conditions (Rodieck, 1998). These sensory cells convert incident light into an electrical signal which influences the release of neurotransmitters and thus triggers a chain reaction (Posch et al., 2014). In darkness, the non-excited normal state, photoreceptors secrete neurotransmitter exciting the bipolar cells. Subsequently, the stimulated bipolar cells also release neurotransmitters inhibiting the ganglion cells. This means that when no light penetrates the eye, photoreceptors, and bipolar cells are active and ganglion cells are inactive. If the illumination increases significantly, the depicted process drives the ganglion cells creating action potentials that reach the visual center of the brain via the optic nerve (Ganong, 1972; Goldstein, 2015).

The sensory cells of the outer as well as the inner plexiform layer, by name the bipolar cells and the ganglion cells, can

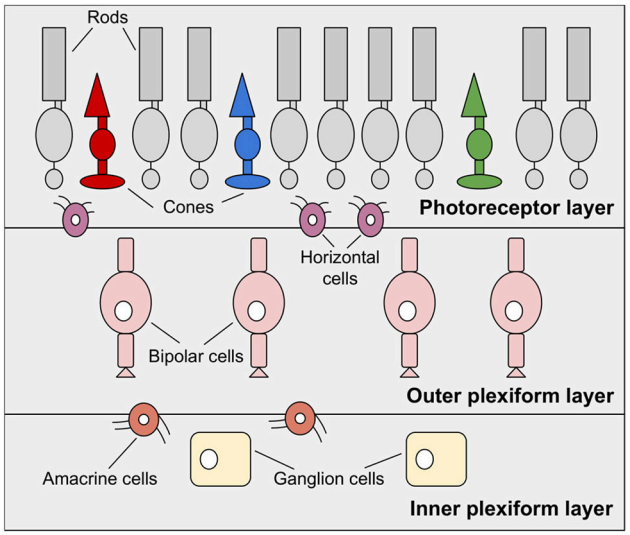

FIGURE 2 | The human retina, reduced to essential layers for neuromorphic visual sensors. The photoreceptor layer, the outer plexiform layer including bipolar cells and the inner plexiform layer made up of ganglion cells. Additionally, horizontal cells and amacrine cells connect these layers.

be divided into *ON-* and *OFF-types*. The ON-bipolar cells code for bright and the OFF-bipolar cells for dark time-space differences. In the absence of a stimulus both cells generate a few random spikes. However, if the illumination is increasing, the ON-cell increases its firing rate when not stimulated while the OFF-cell no longer generates any pulses at all. In the case of a negative change in illumination, if it gets darker, this effect reverses (Rodieck, 1998). This effect is achieved by comparing individual signals of the photoreceptors with time-space average values, determined by means of horizontal cells. Horizontal cells interconnect photoreceptors and bipolar cells laterally. Respectively, the diverse amacrine cells mediate signal transmission between bipolar cells and ganglion cells (Posch et al., 2014). Amacrine cells are inhibitory interneurons and therefore regulate other cells by repression. There are at least 33 subgroups which are mainly characterized by their diameter and thus in their sphere of influence. The smallest variety, narrow-field amacrine cell (NA), is only about 70 μm in diameter. In addition, there are medium-field (MA), with about 70 μm, and wide-field amacrine cells (WA), with about 350 μm diameter (Balasubramanian and Gan, 2014).

1. **Local automatic gain control (*DP 1*)** at the photoreceptor and network level is the preprocessing by means of time-space bandpass filtering and adaptive sampling. As a result, the receptors are independent of absolute values and instead measure the changes of illumination with an adaptive accuracy. This leads to a larger dynamic range of the input without increasing the output unnecessarily. The dynamic range is defined as the ratio between maximum processable signal and background noise in darkness (Posch et al., 2011).
2. **Bandpass spatio-temporal filtering (*DP 2*)** in the outer plexiform layer limits the frequencies in both directions. By suppressing low frequencies, redundancies are discarded and inhibiting high frequencies reduces noise in moving objects. In addition, high-pass filters of the inner plexiform layer emphasize this effect.
3. **The equalization of the signal (*DP 3*)** by means of ON- and OFF-types lowers the spike rate. Without this separation, a significantly higher coding rate would be required in order to encode positive and negative values on one channel.
4. **High spatial and temporal resolution (*DP 4*)** of the entire signal is simulated by the distribution of sustainable parvocellular cells (P-cells) and the volatile magnocellular cells (M-cells) in the retina. In fact, in the center of the visual field the spatial resolution is high and the temporal resolution low. At the edge region it is the other way around. The effect is further enhanced by precise fast eye movement.

DP 1 & DP 2 are implemented in the outer and DP 3 & DP 4 in the inner retinal layer Posch et al. (2014). The retina is responsible for converting spatio-temporal illumination information into pulses. This information is then transmitted via the optical nerve to the visual cortex. The four design principles, above all adaptive filtering and sampling, allow flexible, high-quality signal processing, and efficient coding maximizing the information content (Boahen, 1996, 2000; Posch et al., 2014).

2.4. Biological Depth Perception

In biological imaging, the 3D-environment is projected onto a 2D-representation and thus the precise position of objects in space is lost. Safe navigation in unknown surroundings, as well as the estimation of distances is only possible for humans, because we can reconstruct depth from 2D-information and are thus capable of 3D-perception.

An important part for depth perception, is *a priori knowledge*. That refers to the ability of humans to consider past stimuli. Hence, the brain can see 3D even if it is not receiving any depth information just now, but did so a second ago. The principle is similar to the core idea of event-based vision; to not acquire the current depth, only changes in local depth.

Apart from *a priori knowledge*, the techniques for depth perception can be roughly divided into oculomotor and visual stimuli (Ganong, 1972; Goldstein, 2015). For oculomotor depth criteria, also referred to as oculomotor cues the position of the eyes and the tension of the eye muscles are decisive. The eye position is used to measure the distance of the focused object. In addition, the muscles are tense for near objects and relaxed for distant ones. Oculomotor cues are useful for vision at close range until approximately one arm's length from the eye and are created in two different ways. The first is the convergence (up to 600 cm) resulting from the movement of the eyes toward the center, when objects located nearby, are observed. On the other hand it concerns accommodation (20–300 cm) caused by the change in shape of the eye lens when objects at different distances are focused (Ganong, 1972; Cutting, 1997).

Visual depth criteria are further divided monocular and binocular vision. Monocular refers to all depth information that can be obtained by one eye alone, and binocular means that two eyes are required. Monocular vision therefore refers to all the information we can extract from a simple 2D-signal in order to understand a scene. For one this concerns static monocular cues like the knowledge about the common shape and size of known objects, as well as texture and shadow as well as the fact that people can segment objects well on the basis of context. Furthermore, based on the perspective and scene continuity and the assumption that objects either stay in place or move according to physical laws we can derive more information. In addition to static, there is dynamic monocular vision. It is created by movement-induced depth stimuli, which are produced by head and eye movements. This includes the covering and uncovering of objects as well as the parallax. The latter occurs when several objects are located at different distances from the observer, who is moving parallel to them. The near objects move, in the perspective of the observer faster than the more distant ones (Ganong, 1972; Cutting, 1997; Goldstein, 2015).

According to Rose (1980), binocular sensitivity is higher than monocular sensitivity. Additionally, a comparison of monocular and binocular stimuli states that binocular have shorter latencies than monocular responses (Adachi-Usami and Lehmann, 1983). Binocular vision distinguishes between simultaneous vision, fusion and stereopsis. Under simultaneous vision one understands that certain visual impressions are captured by both eyes simultaneously. This serves for the suppression of false visual sensation caused for instance by illnesses related to strabismus. The dual perception of simultaneous vision helps to avoid disturbing effects. The merging of the two separately recorded signals of both eyes, is named fusion and it is necessary to not permanently see double (Ganong, 1972; Goldstein, 2015). The basis of stereopsis is disparity and is caused by the fact that, although both visual fields overlap for the most part, corresponding points differ slightly due to a view angle shifted by ∼6 cm. Disparity, the horizontal displacement, is inversely proportional to the depth. This coherence is the basis of the correspondence problem in binocular vision shown graphically in **Figure 1** (Julesz, 1960; Ganong, 1972; Goldstein, 2015). Julesz showed by means of a simple experiment how our brain can reliably solve the correspondence problem (Julesz, 1960, 1964). For this purpose, random dot diagrams were shown to a group of participants. He used two graphics of dots which are identical except for a slightly shifted square in the center. The participants were able to see a depth map representing the offset square. This effect occurs because the brain tries to reconcile both signals, but there is a difference in elevation. Research based on random dot diagrams led to one of the most influential books (Julesz, 1971) in cognitive sciences and the basic work for stereo vision. How exactly the brain establishes the connection between two points of the retina, and thus solves the correspondence problem, is still an active field of research. In Cumming and Parker (1997), theories are investigated to what extent the signals of cortical neurons are related to conscious binocular depth perception.

3. EVENT-BASED VISUAL SENSORS

In Delbrück et al. (2010), the utopian features of a perfect camera are identified as an infinitely high resolution, an infinitely wide contrast range and an infinite number of frames per second. At the same time, this ideal sensor has a pixel size of zero and effectively no power consumption. Since nature is much closer to this ideal than conventional cameras, scientists started to imitate biological systems. Biologically inspired camera systems absorb light just like their biological counterparts. In biology, photoreceptors are used therefore and for the artificial afterimage electrical circuits containing photodiodes are applied. The data processing of such a perfect sensor would of course be enormously computationally demanding, but nature also has a solution for this; retinas take over a large part of the processing and thus only transmit relevant information to the brain (Delbrück et al., 2010). Artificial retinas also take this aspect into account. They acquire and transmit information according to the dynamics of the recorded scene. They are asynchronous in their course of transmission, and therefore do not output a fixed number of data packets per second. Instead they broadcast information independently for individual pixels if their illumination changes significantly. This is a great derivation from the rigid control and transmission mechanisms of conventional sensors and implies considerable advantages for many applications. Particularly worth mentioning is the latency in the microsecond range, the extremely high contrast range and the avoidance of motion blur. A profound survey of neuromorphic sensors is given in Posch et al. (2014). Hence, section 3.1 refers to this work to some extent.

Spiking Neural Networks (SNN) are members of the family of Artificial Neural Networks (ANN) but spiking neurons provide a closer and more accurate model of biological neurons. The unique characteristic of SNNs is continuous input over time and they are referred to as the third generation of ANNs. For a comprehensive introduction to SNNs see Maass (1997), Vreeken (2003), and Grüning and Bohte (2014). However, their asynchronous principle of operation is perfectly suited for processing even-based data, as the natural output of EBS is the required form of input for SNNs. A biological introduction, and a survey of how SNNs can be used for robotics is given in Bing et al. (2018). A discussion of the advantages of combining EBS and SNN is done in Akolkar et al. (2015).

However, as parallelism is a key component of EBS and SNN, they require dedicated hardware to run efficiently. Neuromorphic hardware as SpiNNaker (Furber et al., 2006, 2014), ThrueNorth (Merolla et al., 2014), Spikey (Pfeil et al., 2013), and Loihi (Davies et al., 2018) model the massively parallel structure of the brain. Algorithms including spike and event-based communication often enhance their performance when run on neuromorphic hardware. Energy efficiency, scalability, and real-time interfacing with the environment caused by high parallelism are advantages of this technology (Furber et al., 2014; Davies et al., 2018). Furthermore, fault tolerance is a huge benefit of this brain inspired hardware. Much like neural structures in nature, neuromorphic systems cope well with the failure of single components.

In the field of machine learning, it was shown several times that neuromorphic hardware can be applied successfully to biologically inspired algorithms. For instance, in Neftci et al. (2014) a Restricted Boltzmann Machine using leaky integrate-and-fire neurons with STDP synapses is used for learning a generative model of the MNIST dataset of hand-written digits. Another example is shown in Bogdan et al. (2018). The authors implement a technique for topographic map formation on SpiNNaker. Eventhough stereo vision applications have not been implemented on neuromorphic systems a lot. Although first approaches like (Dikov et al., 2017; Andreopoulos et al., 2018) exist, implying that there is potential. Furthermore, running event-based stereo vision algorithms on neuromorphic hardware creates a complete event-based chain from the data acquisition to the processing.

3.1. The Silicon Retina—Emergence and Fundamentals

Over the last 50 years, scientists have developed visual sensors, so-called silicon retinas, modeled after the biological retina and thus employing neurobiological principles. Many of the technologies developed are based on the principles of *very large scale integration(VLSI)*. Pioneers for silicon retinas are Mahowald and Mead who had already introduced their *Silicon VLSI Retina* in 1991 (Mahowald and Mead, 1991; Mahowald, 1994). This sensor has adaptable photoreceptors and a network capable of spatial smoothing (Lichtsteiner et al., 2008). It is a sensor chip with a 2D hexagonal grid of pixels. In this sensor they replicated some cell types of biological retinas. This concerns the photoreceptors, bipolar cells and horizontal cells discussed in chapter 2.3. The interaction of the three components and their affiliation to their biological model is visualized in **Figure 3**. The artificial photoreceptor (P) is modeled based on the cone and consists of two components, a time-continuous light sensor and an adaptive circuit (Mahowald and Mead, 1991; Mahowald, 1992; Douglas et al., 1995; Posch et al., 2014).

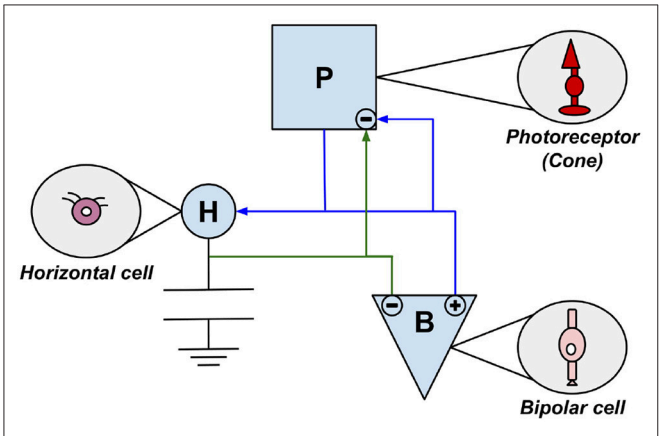

FIGURE 3 | The three components of Mahowalds silicon retina are modeled on photoreceptor cells, bipolar cells, and horizontal cells. Every module is marked by the first letter of its biological paragon.

The layer of horizontal cells (H) located between the photoreceptor layer and the outer plexiform layer (see **Figure 2**) is represented by a network of adjustable MOS resistors (Posch et al., 2014). The circuits representing bipolar cells (B) amplify differences between the values measured by P and the local average. The component B additionally converts these signals into ON- and OFF-values (Mahowald, 1994; Posch et al., 2014). Since this sensor represents merely the photoreceptor layer, the outer plexiform layer and their connecting layer, thus the inner layers of the retina, only DP 3 & DP 4 from chapter 2.3 are converted. This sensor was used exclusively for test and demonstration purposes proofing biological theses (Lichtsteiner et al., 2008).

In contrast, the *Parvo-Magno Retina* by Zaghloul and Boahen considers five retinal layers. It comprises the three main layers shown in **Figure 2** and both intermediate layers of horizontal and amacrine cells (Boahen, 2005; Zaghloul and Boahen, 2006). This technology emphasizes the realistic imitation of P-cells (sustainable parvocellular cells) and M-cells (volatile magnocellular cells) of both plexiform layers. The Parvo-Magno Retina is superior to the Silicon VLSI Retina by the implementation of the outer retinal layers. In addition to DP 3 & DP4, it implements two further properties of biological retinas: adaptation to lighting conditions and local contrast (see DP 1 in chapter 2.3) and flexible spatio-temporal filtering (see DP 2 in chapter 2.3).

Despite its promising structure, the Parvo-Magno Retina from Zaghloul and Boahen is difficult to apply for practical use-cases. This is mainly due to the lack of correspondences between the response characteristics of the pixels (Posch et al., 2014). This concerns strongly fluctuating spike rates of the pixels as well as many non-sensitive pixels which do not react even with comparatively high stimuli (contrast up to 50%) (Lichtsteiner et al., 2008). However, this feature does not mark down this sensor compared to other models of its time. Many early representatives of the silicon retina are not suitable for any real applications. This is mostly down to the fact that their developers were mainly biologists rather than engineers and their motivation was to verify neurobiological models. Common weaknesses of these technologies are an extremely complex circuit (see **Figure 4**), a large retinal area and a low filling factor. On top of that they are susceptible to noise and VLSI implementations tend to have device conflicts. These issues prevented their use in practice so far (Posch et al., 2014). A few years ago, however, there was a turnaround. More and more developers with a technical background, practice-oriented motivation and the necessary knowledge, became involved. The scientific team around Ruedi developed one of the first sensors with a stronger focus on applicability (Ruedi et al., 2003). His team focused mainly on spatial and only subordinately on temporal contrast. After a period of global integration the system weighted events according to the strength of their spatial contrast. This implies a big advantage since events with high contrast are prioritized for transmission during a period of high data throughput. This ensures that despite limited bandwidth and high data volumes, no important information will be lost. The sensor is characterized by a large contrast range, but suffers greatly from temporal

redundancies and a temporal resolution which, due to global integration, is limited by the frame rate (Lichtsteiner et al., 2008).

The approach of Mallik et al. (2005) goes in a similar direction. Here, too, typical event-based technologies, such as the communication protocol presented in chapter 3.2, are used for synchronous image acquisition. The active pixel sensor (APS) CMOS is modified in such a way that absolute exposure changes are detected. The advantages of an APS with small pixels are put into perspective by the small contrast range and the absolute exposure measurement. Therefore, good results can only be achieved with uniform illumination of the scene (Lichtsteiner et al., 2008).

The sensors of Ruedi et al. (2003) as well as Mallik et al. (2005) are, regarding their technical implementation, far superior to the cameras of Mahowald and Mead (1991) and Boahen (2000). What they gain in practical applicability, however, they lose in biological plausibility, mainly due to their synchronous mode of action.

Today's representatives of the silicon retina, represent a compromise of biological and technical aspects. They implement all the design principles of biological retinas presented in chapter 2.3 at the pixel level, as did the Parvo-Magno retina. This concerns local gain control (1.DP: amplification), pre-processing by spatio-temporal bandpass filtering (2.DP: processing), adaptive sampling (3.DP: detection), and continuous perception (4.DP: quantification) (Boahen, 1996). Delbrück and Posch are to be emphasized on their technical achievements. Their work is discussed in more detail in Chapter 3.3 (Lichtsteiner et al., 2008; Liu and Delbrück, 2010; Chen et al., 2011; Posch et al., 2011).

In Delbrück et al. (2010) criteria for the classification of biologically inspired sensors are introduced. These are summarized in **Table 1**. Sensors that fall under the category

TABLE 1 | Three criterions to classify EBS.

Criterion	Name	Benefits
Spatial	Spatial contrast (*SC*)	Reducing spatial redundancies makes it well suited for unsteady lighting conditions.
	Spatial difference (*SD*)	Cheap
Temporal	Temporal contrast (*TC*)	Reducing temporal redundancies makes it well suited for uneven lighting conditions.
	Temporal difference (*TD*)	Easy to implement
Data acquisition	Frame event (*FE*)	Cheap hardware and easy to implement
	Asynchronous event (*AE*)	Low latency, requires relatively few computing power

The categories (Spatial) and (Temporal) differentiate between relative contrast and absolute differences. Its flexible and adaptive nature makes relative contrast beneficial in case of unsteady and uneven lightning conditions.

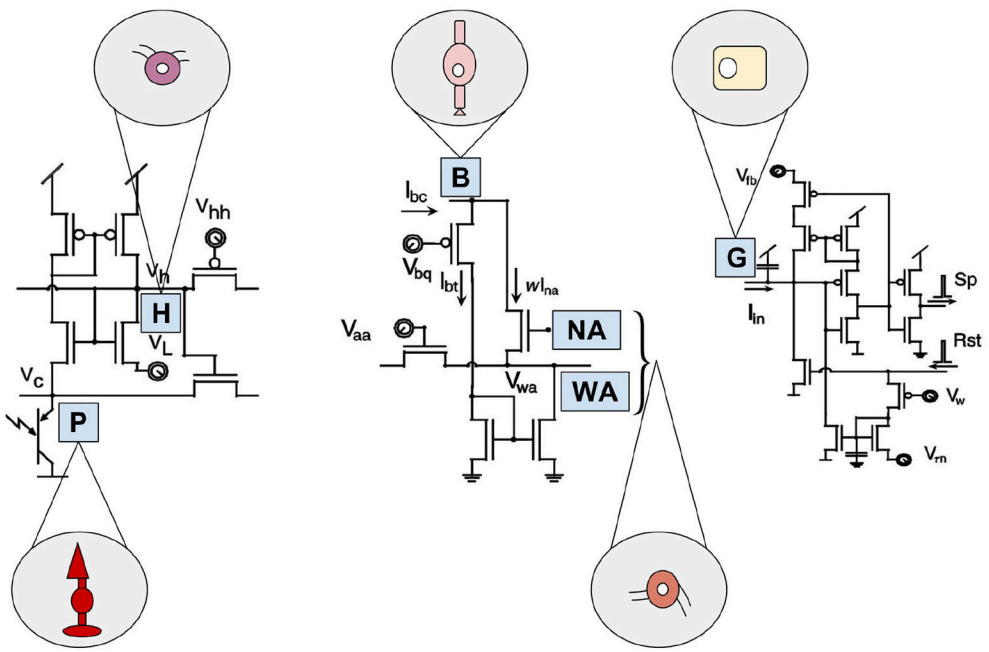

FIGURE 4 | Artificial building blocks and their biological models of the Parvo-Magno Retina from Zaghloul and Boahen. The left circuit shows the outer retinal layer. A phototransistor takes current via an nMOS transistor. Its source is connected to V_C, representing the biological photoreceptor (P). Its gate is connected to V_h, portraying horizontal cells (H). The circuit in the center represents the amacrine cell modulation. A bipolar terminal B excites a network of wide-field amacrine cells (WA) and also narrow-field amacrine cells (NA) through a current mirror. The amacrine cells, in turn have an inhibitory effect on B. By the right circuit the spiking ganglion cells are represented. Current I_in from the inner retinal circuit charges up a membrane capacitor G, based on biological ganglion cells. If its membrane voltage crosses a threshold a spike (Sp) is emitted and a reset (Rst) discharges the membrane. Inspired by Zaghloul and Boahen (2006).

spatial contrast (SC) instead of *spatial difference (SD)* can handle temporal variations with regard to scene lighting better. This is because the use of relative intensity ratios instead of absolute intensity differences suppresses spatial redundancies. Respectively, cameras from the category *temporal contrast (TC)*, compared to *temporal difference (TD)*, are better in respect to dealing with uneven, spatially varying lighting conditions. The reason for this is that relative instead of absolute intensity changes are considered and thus temporal redundancies are suppressed. This criteria is also applied in **Table 2** of chapter 3.3, the comparison of current event-based sensors.

The four design principles of biological vision and their implementation in conventional and event-based cameras is as follows:

- **Amplification:** While automatic gain control is global in conventional cameras it is realized locally in the retina.
- **Preprocessing:** Preprocessing is not applied in standard sensors but the retina uses band-pass filters.
- **Detection:** Since standard cameras make use of integrating detectors, such as CCD, resets are often required.
- **Quantization:** While fixed in standard cameras in retinas quantization is adaptable to the frequency of change and the distribution of the input signal. Event-based sensors privilege time, while classic cameras privilege precise pixel intensity.

The main distinguishing features are the lack of frames, low latency, low processing power and a high contrast range.

TABLE 2 | Comparison of event-based sensors.

	DVS	DAVIS	ATIS
Major function	Asynchronous detection of temporal contrast	See DVS + synchronuos imaging	See DVS + Intensity measurement for every single event
Resolution	128 × 128	240 × 180	304 × 240
Gray-scale value	✗	Synchronous	Asynchronous
Circuits per pixel	1	1	2
Exposure time	✗	Uniform	Uneven
Latency	15 μs	3 μs	4 μs
Noise	Very strong (2.1%)	Strong (APS: 0.4%, DVS: 3.5%)	Medium (0.25%)
Dynamic range	120 dB	130 dB	143 dB
Pixel size	0.35 × 0.35 μm	0.18 × 0.18 μm	0.30 × 0.30 μm
Costs	2,590/2,250 €	4,140/3,630 €	5,000/4,000 €
Contrast sensitivity	15%	11%	30%
Date of publication	2008	2013	2011
Application	Dynamic scenes	Dynamic scenes	Surveillance
Classification regarding Table 1			
	SC TD AE	SC TD APS: FE DVS: AE	SC TD & TC AE

As costs the standard and the reduced costs for scientific and educational purpose is listed. Information originates from Posch et al. (2014), Dong-il and Tae-jae (2015), and Cohen et al. (2017).

3.2. Address Event Representation

In nature, data transfer from the eye to the brain is carried out by approximately one million axons of ganglion cells. For a realistic technical imitation, each pixel of the camera needed its own cable. Since any practical chip wiring makes this impossible, VLSI-technologies employ a workaround (Posch et al., 2014).

To bundle the data traffic on these lines, an event-based data protocol Address Event Representation (AER) is used. The research and development that is leading to this technology was largely pioneered in the late 80s by Sivilotti (1990) and Mahowald (1992). Both scientists were part of the Caltech group of Carver Mead. AER is an event-controlled, asynchronous point-to-point communication protocol for neuromorphic systems. It allows spikes to be transferred from neurons of one chip to neurons of a second chip (Boahen, 1998, 2000). The basic idea is based on the addressing of pixels or neurons, with their *x*- and *y-value*, within their array (Lichtsteiner et al., 2008).

For a long time, this technology has only been used by a small group of researchers, such as Boahen (1996) for prototypes of the Silicon Retina. It was not until after the turn of the millennium that a broader public took notice of it. In addition to the development of many more biological camera systems, AER also found its way into other contexts, such as biological hearing and wireless networking (Posch et al., 2014).

The basic functionality of AER is implemented, as illustrated visually in **Figure 5**, by two address encoder and a digital bus. The bus system implements a multiplex strategy so that all neurons and pixels transmit their information, time-coded, on the same line. The address encoder (AE) of the sending chip generates a unique binary address for each element in case of a change. This can be either a neuron that generates a spike or a pixel on which an event (exposure change) occurs. The AER bus transmits this address at high speed to the receiving chip, whose address encoder (AD) then determines the correct position and generates a spike on the respective neuron. AER uses streams of events to communicate between chips. An event is defined as a tuple $Event(x, y, t, p)$, whereby the pixel reference of the event is given by x and y. The timestamp is given by t and the polarity is represented by p. The polarity is either positive or negative and thus indicates whether the lighting intensity has increased or decreased. The event in question will then be displayed as an ON-event, in positive, or OFF-event, in negative case.

It is easily possible to extend this technique, since on the one hand, events from different senders can be combined, and on the other hand, forwarding to multiple recipients is feasible (Lazzaro and Wawrzynek, 1995). This means that all connection types are possible; *many to one*, *one to many*, and *many to many*. In addition, arbitrary connections and new connections and transformations can easily be implemented with the help of this digital address system. An important advantage is that due to the asynchronous character calculations are fast and efficient.

3.3. Comparison of the Best-Known Exponents: DVS—DAVIS—ATIS

All modern, event-based sensors are based on the technology introduced in section 3.1. They have independent pixels that generate asynchronous events depending on exposure changes. In addition, all sensors of this type use AER (see section 3.2) for communication. The large contrast range of these cameras is based on the logarithmic compression of the photoreceptor circuits and the local, event-based quantization (Lichtsteiner et al., 2008). The best known sensor of this kind, the Dynamic Vision Sensor (DVS), was developed at ETH Zurich in 2008. The circuit diagram in **Figure 6** introduces the pixel design of the DVS which forms the basis of all other sensors in this section. The design decisions are based on the three main objectives; high contrast range, low error rate, and low latency (Lichtsteiner et al., 2008). To avoid unwanted oscillations there is a subdivision

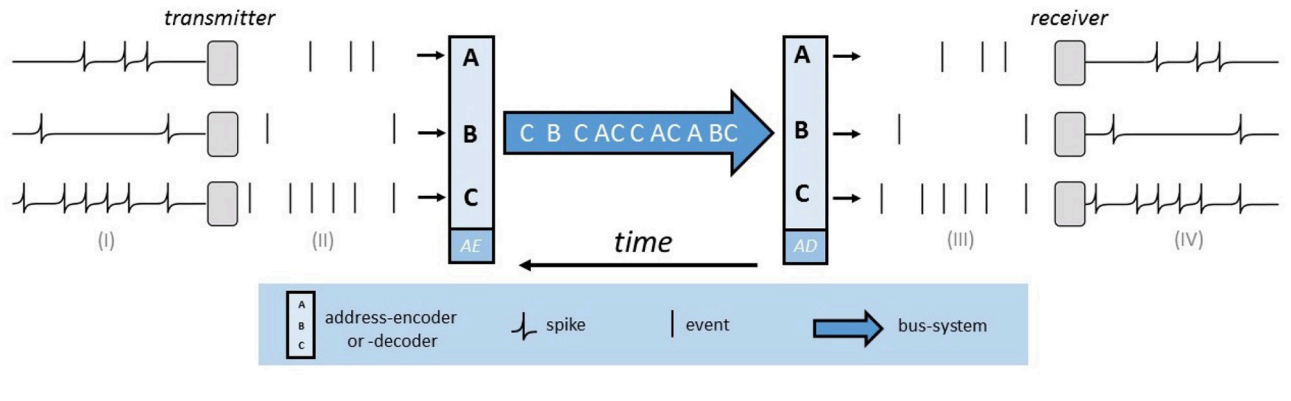

FIGURE 5 | The AER-bus-system. Three neurons on the sending chip produce spikes [see (I)]. These are interpreted as binary events [see (II)] and by means of the address encoder (AE), a binary address is generated. This address is transmitted via the bus-system and the address decoder (AD) determines the correct position on the receiving chip [see (III)]. Hence a spike is emitted on the affected neuron of the receiver [see (IV)].

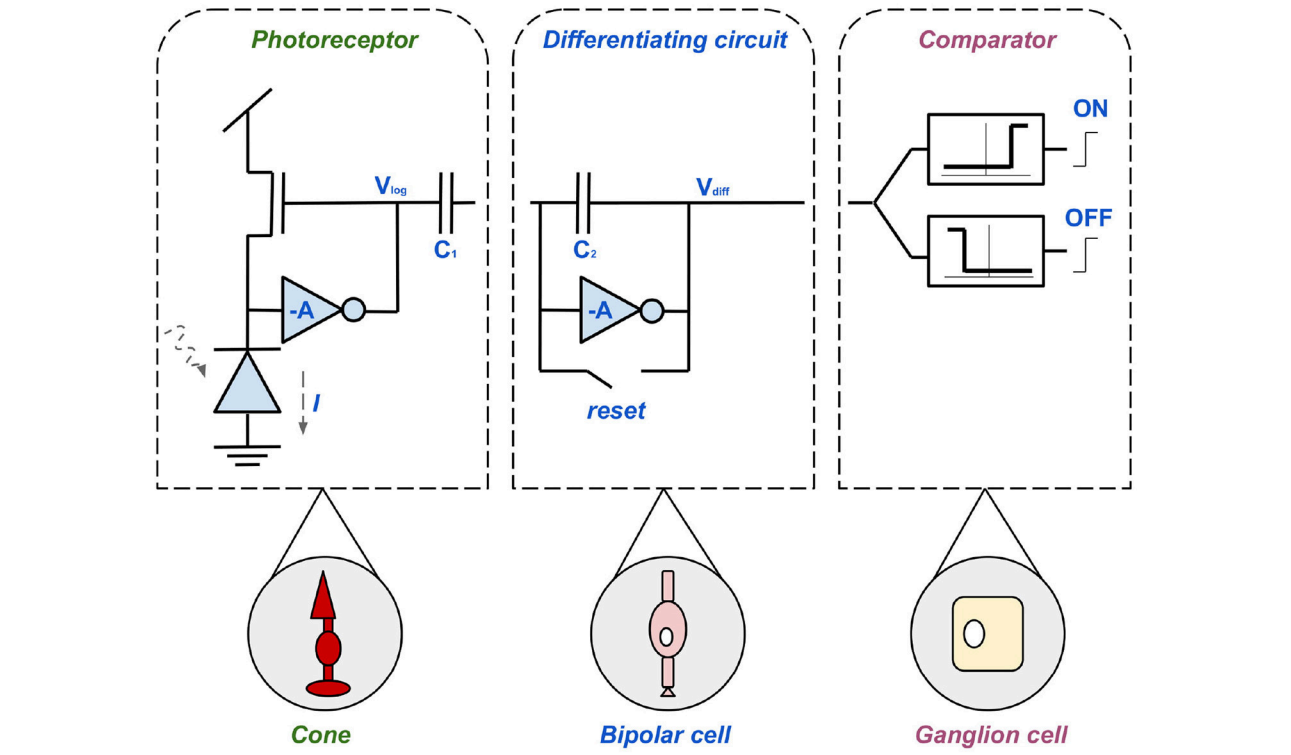

FIGURE 6 | The three-layered pixel circuit of the DVS, consisting of a photoreceptor, inspired by the biological cones, a differential circuit, based on the bipolar cell and a comparator modeled after the ganglion cell.

into sub-circuits (Brandli, 2015), as shown in **Figure 6**. Firstly, the left component represents the cone, a fast, logarithmic photoreceptor. Due to its logarithmic mode of operation, growth in individual pixels is effectively controlled without delaying the reaction time to exposure changes. The disadvantage of this photoreceptor set-up is that if the output is to be used without post-processing, calibration is necessary. This is due to fluctuations between the thresholds of the transistor. Secondly, the mid-component is based on the bipolar cell. Its task is to precisely amplify changes and avoid errors, generated by direct coupling (DC mismatch), through resets after each event. The third component of the DVS is the comparator consisting of two transistors. The transistors represent the ON- and OFF-ganglion cells (Lichtsteiner et al., 2008). The synergy of the components is as follows; light information is obtained by a photodiode which thus generates the current intensity *I*. Photoreceptors (cones) convert *I* into a logarithmic voltage V_p. This voltage is inversely amplified by the factor $A = C_1/C_2$. Also a positive or negative event V_{diff} is generated by the differential circuit (bipolar cell), depending on the polarity of the photocurrent. Subsequently, the pulses are collected, divided into ON- and OFF-events and forwarded by the comparator (ganglion cell) (Posch et al., 2014). The logarithmic effect and the suppression of DC makes the sensor so sensitive to contrast in the time domain (Lichtsteiner et al., 2008). Hence, it takes well into account dynamic, fleeting scene information, just like biological magno-cellular structures. The functionality of P-cells, necessary for sustainable information (see chapter 2.3) is neglected (Posch et al., 2011).

Posch and his team developed the Asynchronous Time-Based Image Sensor (ATIS) Posch et al. (2011). Their exponent is even closer to the biological model and also a more practically applicable sensor. The ATIS extends the basic principle of the DVS by a further photodiode to measure the time difference between two events and thus gain event-based intensity values in addition to the temporal contrast values of the event stream. As visualized in the upper part of **Figure 7**, the conventional change detector (CD) circuit is used to detect changes in the event stream. A circuit for exposure measurement (EM) is added. From a biological perspective, the CD-component, implemented in the DVS and the ATIS, is a magno-cellular structure. The additional EM-component embodies biological P-cells and is thus responsible to gather sustainable information. In other words, the magno-cellular CD, answers the question *"where?,"* while the parvo-cellular EM is responsible to solve *"what?."* The application of the EM makes it possible to create gray-scale images from the events. Hereby, the intensity is given by $I = 1/t$, implying that the amount of the temporal difference between two events of a pixel determines its gray-level value. As visualized under *gray-value determination* in the lower part of **Figure 7**, a big temporal difference leads to a dark gray-value, and a small difference to a brighter one. The CD circuit triggers the activity in the EM circuit. Hence, the measurement of a new exposure time and consequently a new gray-scale value is initiated if the illumination varies (Posch et al., 2014). In **Figure 7** this coherence is illustrated by the gray arrow with the label *triggers*. This process ensures that the EM circuit is also asynchronous and the corresponding gray-value is updated for each event (Posch et al., 2011, 2014; Brandli, 2015). The development of ATIS showed scientists for the first time the possibility to combine frame-based with frame-free approaches to obtain static and dynamic image information in parallel. The resulting duality also opens up a large number of new processing capabilities, since many conventional machine vision algorithms do not work with asynchronous event streams. The special design and operating principle of the ATIS also offers further advantages, some of which have direct applications; for example, video compression at sensor level can be achieved by suppressing temporal redundancies. In addition, the extremely high temporal resolution and the dynamic range of 143 dB are remarkable. ATIS owes its wide dynamic range to the fact that it encodes its intensity values time based. Conventional sensors use fixed integration times for the complete array and are thus highly dependent on light levels. Time based encoding naturally leads to separate integration times for each pixel implying the wide dynamic range and a more light independent sensor. However, this leads to uneven exposure times, which causes problems with near and slow objects (Posch et al., 2014).

It was in this context that the motivation for developing the Dynamic and Active-pixel Vision Sensor (DAVIS) came about. Besides the DVS and ATIS it is the third major event-based sensor. DAVIS, introduced in Berner et al. (2013), is a hybrid of DVS and APS. As shown in **Figure 8**, the DVS-circuit, responsible for the asynchronous detection of logarithmic intensity changes, for generating dynamic scene information, is supplemented. Thus, all three modern event-based cameras have the same circuit as a basis. The second component of the DAVIS is an APS and, similar to the EM of ATIS, responsible for absolute exposure measurement and generating gray-scale images in addition to the event stream. In contrast to ATIS, however, the additional component of DAVIS is not asynchronous. The APS circuit receives static scene information by frame-based sampling of the intensities. This makes it very close in its operating principle to the APS component of conventional cameras. The obvious advantage of being able to use decades of research, is impaired by the existing disadvantages of frame-based cameras, such as redundancy, high latency etc. (Berner et al., 2013; Posch et al., 2014; Cohen et al., 2017).

Table 2 takes all three sensors into account. In addition to technical criteria, such as resolution, pixel size and dynamic range the costs and fields of application are also regarded. DVS is the predecessor of the other two sensors. It is the smallest and least expensive one, but has clear disadvantages in comparison. For example its low resolution of 128×128, its noise problems and its inability to generate intensity or gray-value information. The other two sensors each have different strengths and weaknesses. The ATIS convinces with a contrast range of 143 dB, caused by not mapping intensity values to a fixed voltage range. However, this also leads to uneven exposure times and thus to motion artifacts. The DAVIS has less problems with motion artifacts because it uses even exposure times. The synchronous mode of operation of the DAVIS, for intensity measurement and gray-value images, causes a large redundancy but also leads to independent processes which do not interfere with each other. ATIS has the highest resolution

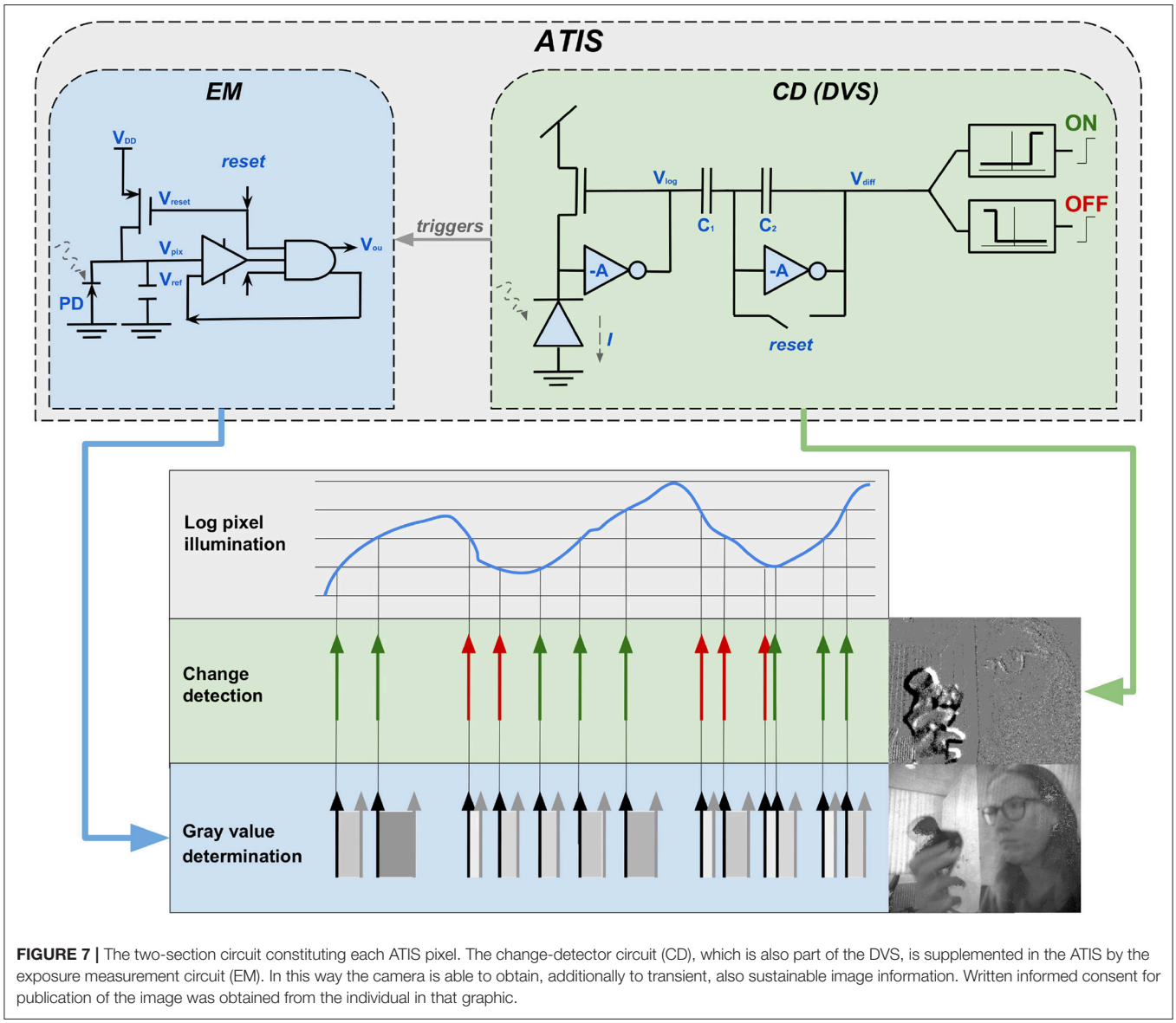

FIGURE 7 | The two-section circuit constituting each ATIS pixel. The change-detector circuit (CD), which is also part of the DVS, is supplemented in the ATIS by the exposure measurement circuit (EM). In this way the camera is able to obtain, additionally to transient, also sustainable image information. Written informed consent for publication of the image was obtained from the individual in that graphic.

of 304 × 240, which offers considerable advantages in confusing scenes with many objects. Since the DAVIS has smaller pixels it better represents fine granular image areas with a high level of detail. As a result, ATIS is better suited for monitoring and the DAVIS for dynamic scenes with fast movements. ATIS, due to its completely asynchronous character and the fact that the theoretical basis of P-cells is taken into account, is superior in biological plausibility. DAVIS leads in practical applicability. On the one hand this is due to their small pixel size, but on the other hand also because it is better at handling darkness and near, slow objects.

3.4. Additional Models of Event-Based Sensors

Alongside the three best-known representatives of neuromorphic cameras, discussed in chapter 3.3, there are other models worth mentioning[1]. In 2007, long before the development of the ATIS and virtually at the same time as the DVS was created, Christoph Posch, a co-developer of DVS and ATIS, invented the Dynamic Line Sensor (DLS). This sensor was presented in Posch et al. (2007) and is quite unusual; its resolution is 2 × 256 and thus it consists of only two series of pixel. Despite this characteristic, which makes it a niche solution, the sensor has interesting properties. For example, its pixel size is with 15μm smaller than that of all the sensors presented in **Table 2**. Additionally its high temporal resolution is noteworthy (Posch et al., 2007).

Color perception is a fundamental characteristic of biological vision. However, for long there have been no applicable event-based sensors implementing color vision (Delbrück et al., 2010; Posch et al., 2014). Experiments in this direction suffered

[1] An overview of neuromorphic sensors and their applications is given here: https://github.com/biphasic/event-based_vision_resources

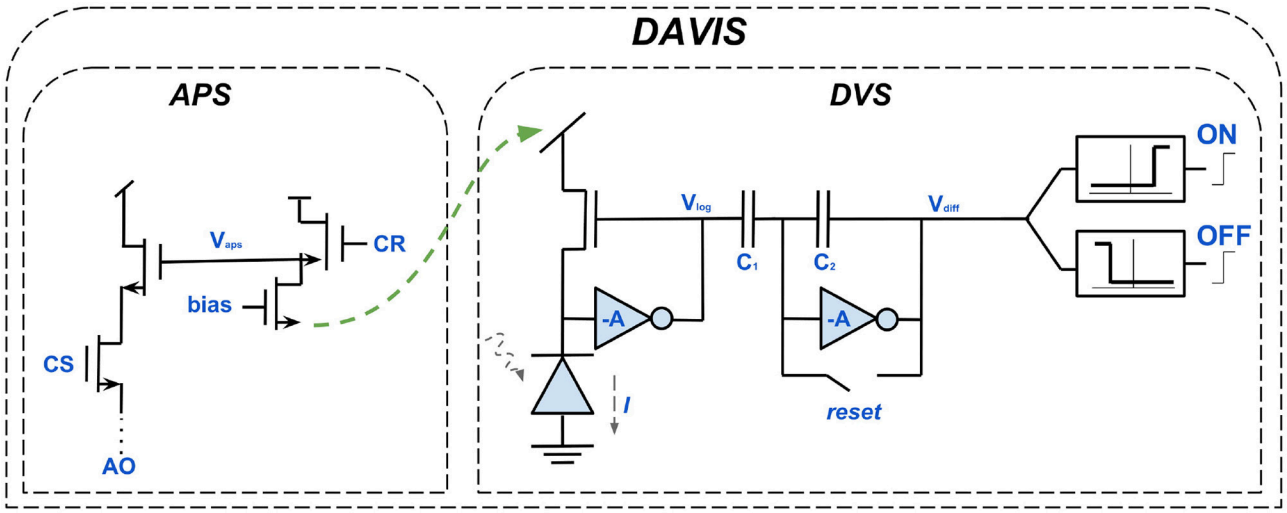

FIGURE 8 | The circuits building up the DAVIS. Each of its pixels is a hybrid of the DVS-circuit and an active-pixel-sensor (APS). Like the ATIS sensor, the additional component of the DAVIS is capable of generating gray-scale images. However, the principle of operation of the APS is synchronous and thus similar to conventional vision sensors, distinguishing both sensors severely.

from weak color discrimination (Berner and Delbrück, 2011; Leñero-Bardallo et al., 2014) and also had either extremely large circuits (Berner and Delbrück, 2011) or large pixels (Leñero-Bardallo et al., 2014). This was fundamentally different with the color dynamic and active-pixel vision sensor (C-DAVIS) from Li et al. (2015). It combines slightly modified pixel circuits of the DAVIS with a special type of Bayer sensor, a photosensor with color filter. The C-DAVIS generates in parallel synchronous color images and asynchronous event streams that do not receive color information. Thus, the coloring is created in the conventional part of the camera.

EBS have been continuously improved in the last years. Alongside research institutes, private companies, like Prophesee, Samsung, and HillHouse, contributed to this progress. Therefore, some of the newer models are less accessible to academia. With Samsung's DVS, a representative of neuromorphic cameras, constructed outside the academic world, was introduced for the first time in Son et al. (2017). The motivation was clearly make EBS marketable. The developers focused on reducing the pixel size to 9 μm and lower the energy consumption (Yaffe et al., 2017). This VGA dynamic vision sensor embodies a digital as well as an analog implementation. The resolution was increased to 640 × 480 and AER was extended to G-AER (Group Address Event Representation) to compress data throughput. G-AER handles massive events in parallel by binding the neighboring 8 pixels into a group. This technique allows easier control of pixel biases and event thresholds (Son et al., 2017).

Another recent model is the Celex, developed at Nanyang Technological University, Singapore (NTU Singapore) (Huang et al., 2017, 2018) and distributed by the company HillHouse[2]. This sensor has a dynamic range of >120 dB and like the ATIS the Celex provides absolute brightness with every event. It is also noteworthy that the Celex IV , an event-based HD sensor is announced.

4. EVENT-DRIVEN STEREOSCOPY

Although all depth stimuli depicted in section 2.4 are used in combination to enable 3D-perception in humans, binocular perception is by far the most revealing one. The other techniques sometimes provide only relative positions and are often imprecise. Binocular vision, in contrast, produces absolute values with very high accuracy (Mallot, 1998). As a result, the vast majority of event-based approaches to stereoscopy are based on binocular depth stimuli. A stereo set-up made of EBS is usually used for this purpose. To obtain disparities and thus depth information from the event streams, the individual events of both sensors must be assigned to each other. Despite the extremely high temporal resolution of EBS (Lichtsteiner et al., 2008; Posch et al., 2011), noise, faulty calibration, different contrast sensitivity of the sensors or pixels lead to deviations of several milliseconds in reality. As a result, determining matching events of both sensors with exclusively temporal aspects leads, in addition to the right ones, also to false correspondences. This is shown in **Figure 9**.

4.1. Cooperative Algorithms

To suppress false correspondences cooperative algorithms can be applied. The neurons of a SNN, that implements a cooperative algorithm, communicate according to certain rules. The research of Marr and Poggio (1976, 1977, 1979) and Marr (1982) forms the beginning of these algorithms.

To exploit the advantages of an approach based on SNN and EBS, the implementations of event-based cooperative algorithms

[2]More information about HillHouse: http://www.hillhouse-tech.com

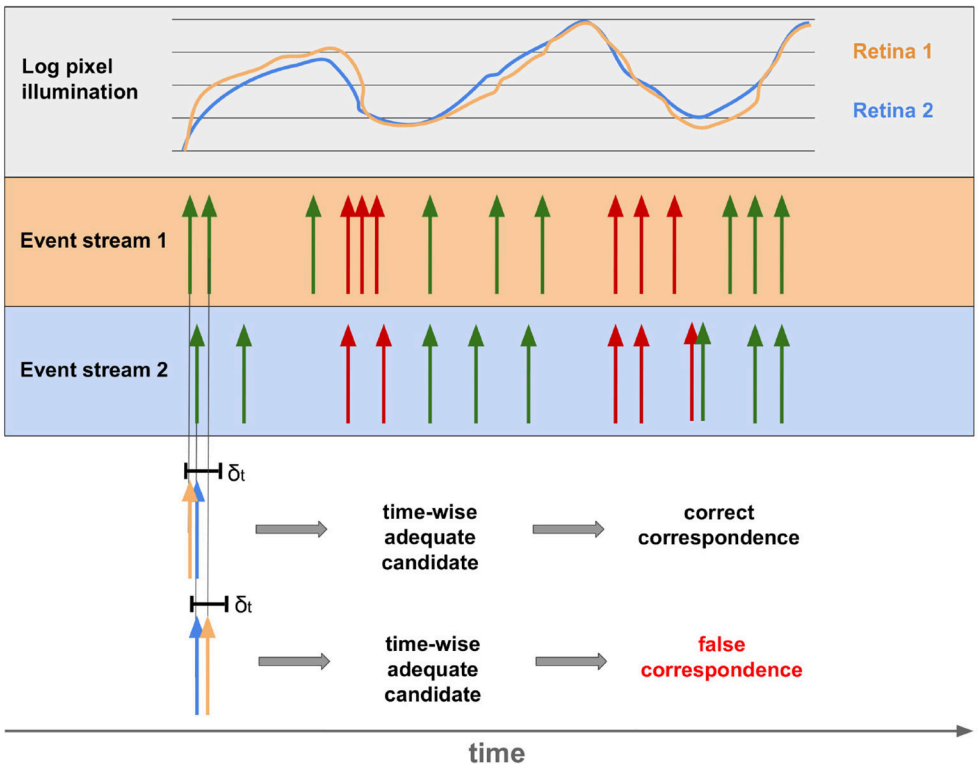

FIGURE 9 | Event streams of two sensors for the same point of the real world. The top row shows the deviation of illumination between the two corresponding pixels of two retinas. The resulting streams of OFF and ON events are shown below. Below it can be seen that events of both sensors occurring within the timeframe δ_t can be both, correct and incorrect correspondences.

is compatible with neuromorphic hardware. In the case of Dikov et al. (2017) and Kaiser et al. (2018) this is SpiNNaker.

4.1.1. Matching Constraints

All approaches based on Marr and Poggio (1977) use two event-based sensors as input of a neural network and are therefore confronted with the correspondence problem. The naming, *cooperative algorithms*, is derived from the fact that rules are defined how the neurons of the network communicate with each other. The purpose of the communication rules is to solve the correspondence problem. Since the neurons are able to measure disparities by applying these rules, they are called disparity sensitive neurons (DSN). According to Marr and Poggio (1977), there are three steps in measuring stereo disparities: (S1) Determination of the point of interest (POI) in the first image; (S2) identification of the POI in the second image; (S3) measurement of the disparity of the two pixels. Since wrong correspondences cause problems, physical properties of solid bodies are considered in order to obtain additional constraints. These are the following two properties: (P1) is the *uniqueness* of each point in a scene at a given time. (P2) is the *continuity* of matter meaning it is continuous and divided into objects. The surfaces of objects are generally perceived as smooth (Marr, 1982). The three rules for communication between DSNs, referred to as matching constraints, are derived from P1 and P2:

- *Uniqueness Constraint* (C_1): Derived from P1, for each point of the image of the first eye/camera there is at most one corresponding hit in the image of the second eye/camera. Therefore C_1 inhibits the communication between DSNs in vertical and horizontal direction (Marr and Poggio, 1979; Marr, 1982).
- *Continuity Constraint* (C_2): According to P2, physical matter is cohesive and smooth. Hence, C_2 has a stimulating effect when it comes to communication in diagonal direction with the same disparity. So if a disparity of neighboring neurons is consistent, it is more likely to be correct and the corresponding signal is thus amplified (Marr and Poggio, 1979; Marr, 1982).
- *Compatibility Constraint* (C_3): Is derived from the thesis of Marr and Poggio (1977), that *black dots can only match black dots*. It states that similar characteristics in the same region are more likely than completely different ones. In practice, it causes ON-events and OFF-events occurring temporally and spatially dense to inhibit each other. There is a greater probability of incorrect correspondences since contrasting changes in lighting are less common for neighboring pixels (Marr and Poggio, 1977; Marr, 1982).

4.1.2. Extension to Pulse-Coupled, Event-Based Technologies

The principles presented in chapter 4.1.1 are transferred into an event-based implementation in Firouzi and Conradt (2016).

However, it does not use spiking neurons and is thus not exploiting the event-based data ideally. In Dikov et al. (2017) and Osswald et al. (2017), SNNs and the corresponding neuromorphic hardware are combined with this approach. Compared to conventional synchronous methods, these models use a further constraint to suppress false correspondences, *time* (Dikov et al., 2017). This brings a great novelty to the old approach; the network input is not composed of static images but instead spike-trains containing spatio-temporal information. The network implemented in Osswald et al. (2017) consists of three essential parts; retina coordinates, represented by OFF- and ON-neurons, coincidence detectors and disparity detectors. The aim is to amplify correct correspondences and to suppress wrong ones in order to generate a correct disparity measurement. The retina coordinates generate a spike for each change in illumination at a specific point in space. The random detectors signal simultaneous spikes for possible layers. The cells are arranged so that each spike represents the position of a possible disparity. Since coincidence detectors are sensitive for right but also for wrong correspondences, all possible hits are gathered here. Within the connections of the neurons of coincidence detectors and disparity detectors rules of binocular vision are implemented. In greater detail, C2 and C3 are realized by stimulating and inhibiting compounds. The uniqueness rule C1, is implemented subsequently through recurrent, inhibitory connections of the disparity detectors.

In Osswald et al. (2017), the effects of this approach are analyzed. The authors compare the spike rates of the random detectors with those of the disparity detectors. The conclusion is that wrong correspondences are detected significantly more often without matching constraints.

In case, one of the sensors of the stereo set-up is exposed to high-frequency stimuli, false correspondences can arise. This is because the DSN, which collects the signals of both retina coordinates, exceeds its threshold, although only one of the sensors sends a pulse and the other does not. To overcome this issue, the basic technique was extended in Dikov et al. (2017) by micro-ensembles. Hereby, neuronal micro-ensembles are used that implement the behavior of a logical &. For this purpose, as shown in **Figure 10**, two blocking neurons are connected between the retinal coordinates and the integrating DSN. In case the left retina neuron receives a spike, it excites both, the integrating and the left blocker neuron. At the same time it inhibits the right blocker neuron. If now the right retina neuron does not receive a spike and therefore does not inhibit the left blocker neuron, this prevents the integrating neuron from generating a spike. This mechanism ensures that the integrating neuron is only capable of spiking if both blocker neurons of the ensemble are inhibited. Hence the integrating neuron only emits a pulse if both retina neurons are spiking (Dikov et al., 2017; Kaiser et al., 2018). In Dikov et al. (2017) and Osswald et al. (2017) disparities are calculated merely from dynamic scenes. This is simply to the fundamental technology of event-based cameras that perceive only changes in lighting and are thus not perceiving static scenes continuously. In Kaiser et al. (2018), this approach, including EBS, is extended to static scenes by applying synchronous microsaccades. In biology, microsaccades are extremely fast and very small eye movements with low amplitude. This artificial dynamic allows the network to extract disparities from static scenes. For the practical implementation, a robot head has been constructed which is capable of carrying out vertical and horizontal tilt movements independently and simultaneously.

4.1.3. Network Architecture

On an abstract level, the network receives signals from two EBSs processing the data and extracting the disparities. The simplified structure of the SNN is as follows; events of two EBS that are on the same epipolar plane of the real world are input of the same 2D-plane of the network, as shown in **Figure 10**. These 2D-layers are stacked to form the 3D-SNN. Each 2D-layer calculates the disparities for a pixel row of both DVS. The neurons of the output layer generate a pulse when the corresponding point of the real world changes from occupied to unoccupied or vice versa (Dikov et al., 2017; Osswald et al., 2017; Kaiser et al., 2018).

However, the special structure of the network and its internal connections are essential for solving the correspondence problem. Therefore, the structure of the network is discussed in more detail; a disparity is indicated by a DSN that exceeds its threshold. Each DSN describes, by its x- and y-position in combination with the disparity for which it is sensitive, a specific point in space. There are two ways to arrange these neurons so that they represent the replicated scene of the real world. The naive way is that each DSN represents a point of the real world and all neurons are equally distributed, as are their real counterparts. We call this the dynamic path because the DSNs are not assigned fixed retina coordinates. For this approach, the cameras must be calibrated very accurately, their exact position and orientation must be known, and their focus line must be taken into account throughout. These conditions are difficult to implement in practice. Alternatively, each DSN represents a fixed neuron from both populations of retina coordinates. Thus same two pixels of the respective sensor are always connected with each other. This is the static method which is much less error-prone.

4.2. Extensions of Cooperative Algorithms

The formalisms of cooperative algorithms already eliminate the majority of false correspondences. However, some scientists found ways to combine this basic approach with an entirely different approach in order to obtain even more accurate results. In the following methods are shown that complement cooperative algorithms.

4.2.1. Gaborfilters

In Camuñas-Mesa et al. (2014a,b) and Reverter Valeiras et al. (2016), the authors show how to extend cooperative algorithms extended by a new component, a supplementary constraint. On top of the known matching constraints such as time and polarity, the authors use Gabor filters to extract information about the object edges that generate the events. This is working well because EBS create events when objects, and thus their edges, move. Events that belong together refer to the same edge and should therefore have the same orientation.

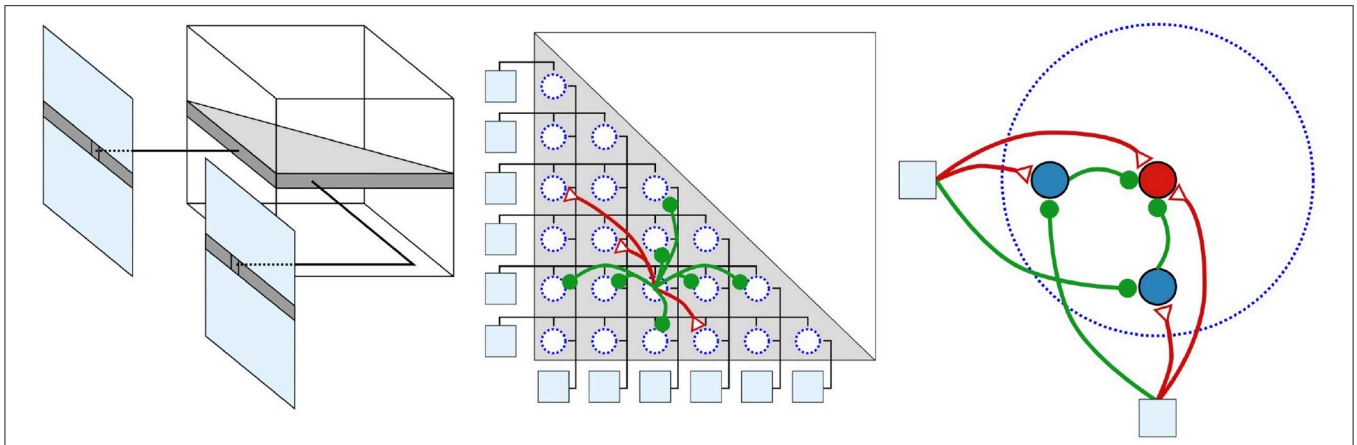

FIGURE 10 | Structure of the network inspired by Dikov et al. (2017) with increasing degree of detail. The network's 3D-structure is represented in the left part; An entire row of pixels is mapped from both EBS to one plane of the SNN. This 2D-layer is where the disparities of the affected pixels are calculated. The center shows the neurons of a 2D-layer, connected according to the constraints of cooperative algorithms, outlines in chapter 4.1.1. Green represents inhibiting and blue exciting synapses. In the right part the outline of micro ensembles are visualized. The cooperative manner of this network relies on micro-ensembles. The retina coordinates are visualized as light blue squares, the blocking neurons as blue circles and the collecting neuron as a red circle. Reprinted by permission from Springer Artificial Neural Networks and Machine Learning (Kaiser et al., 2018).

The authors of Camuñas-Mesa et al. (2014a) use Gabor filters, with different angles and scales, on the original event streams of both cameras. The results are used as input for a cooperative algorithm.

The work of Reverter Valeiras et al. (2016) is based on the *HFirst-approach* of Orchard (Orchard et al., 2015), which uses a hierarchical, h-max-inspired SNN-architecture and a neuromorphic camera for object recognition. In Reverter Valeiras et al. (2016), an ATIS (see chapter 3.3) is applied. The approach describes itself as actually event driven, as each new event renews the 3D-pose estimation.

4.2.2. Belief Propagation

A new completely event-based approach to depth perception is presented in Xie et al. (2017). It is based on *Belief Propagation* (BP), a subset of the *message-passing* algorithms. These algorithms are used to solve derivation, optimization and condition fulfillment problems. Bayesian networks or Markov Random Fields are often applied for preprocessing in this context. BP then calculates the marginal distribution of each unobserved node. Hence, the correspondence problem is seen as a labeling problem. The labels refer to the disparity and their quality is measured as a cost function. By use of maximum a posteriori probability (MAP), labels are determined that minimize the cost function. The method consists of four steps; preprocessing, adjustment, Belief Propagation, and output of disparities. The pre-processing consists of noise filtering and correction of the input images. For correction it is transformed so that each pixel row of the two images refers to the same points. The matching determines whether two events are potential partners. Correct matches are from different sensors, occur within a time window, have the same polarity and occur in the same or adjacent rows. This implementation of Belief Propagation is based on Felzenszwalb and Huttenlocher (2004). The algorithm does not synchronously renew all disparity estimates, but always the neighborhoods of new events. The output of the algorithm is a *belief vector* for each node. The label, thus the disparity, is then chosen so that it minimizes the cost function.

Kogler, who tried for a long time to apply classical algorithms to event-based data, offers in Kogler et al. (2014) an alternative realization of event-based stereo vision with Belief Propagation. He complements this with a subsequent filtering in two phases.

4.2.3. Combining Spatial and Temporal Aspects With Luminance and Motion

In the discussed approaches of this chapter, as well as in chapter 4.1, the correspondence problem is commonly solved by spatial constraints and luminance. According to the authors of Ieng et al. (2018), disparities are thus not reliably detected in uncontrolled lighting conditions and unstructured scenes. Therefore, Ieng et al. (2018) presents an entirely time-based method that exploits the unique characteristics of neuromorphic sensors, such as high temporal resolution, even more. For this purpose, the ATIS presented in chapter 3.3 is applied, which in addition to change events also uses the luminance encoded in the form of temporal differences. This approach does not represent a completely new method, but rather an extension of known approaches. Hereby, the precise timing of Kogler et al. (2011a) is combined with the local motion consistency of Benosman et al. (2012) and the temporal consistency of the luminance from Posch et al. (2011). By additional luminance information wrong correspondences are reduced. This means that the unique principle of operation of the ATIS, which in contrast to DAVIS works completely asynchronously, leads to new results. Due to the consideration of many different approaches and theoretical considerations, the algorithm is extremely complex. Spatial, temporal, generalized temporal, and motion criteria are combined.

4.3. Alternatives to Cooperative Algorithms

The approaches presented so far (see chapter 4.1 and 4.2) are all based on the biological theories of binocular vision investigated by Marr and Poggio (1979). An alternative implementation of a cooperative network compatible with their research is given in Piatkowska et al. (2013). Piatkowska developed an adaptive, cooperative algorithm adjusting the disparity estimation with each new event. In Piatkowska et al. (2017), the approach is enhanced and the error rate, determined by MME, can be reduced by 50%. For this purpose the normalization is altered and a noise filter is used. The authors also surrogate the applied DVS through ATIS.

This chapter introduces other methods for stereo viewing with event-based cameras, beside cooperative algorithms.

4.3.1. Conventional, Perspective-Based, and Active Techniques

In Schraml et al. (2007), a conventional, area-based approach to solving the correspondence problem is transferred to event-based cameras. Area-based approaches use the neighboring pixels to find correspondences between the two images for groups of pixels. The authors tested classical cost functions such as Normalized Cross-Correlation (NCC), Normalized Sum of Absolute Differences (NSAD), and Sum of Squared Differences (SSD). It is questionable whether it makes sense to implement such an algorithm with EBS because the pre-processing consists of reconstructing gray-value images from the events. In addition, such a classical algorithm was compared by Kogler in Kogler et al. (2011a) to a time-based approach and did much worse, especially because of its error rate of 4.91%. In Kogler et al. (2009), the area-based approach is combined with a feature-based approach for EBS. This work, combining classical algorithms with event-based technology, is also pursued in Dominguez-Morales et al. (2011) and Belbachir et al. (2012). The researchers around around Kogler, however, state in Kogler et al. (2011b) that classical approaches to stereoscopic vision do not take account the advantages of silicon retinas and that the reconstruction of images leads to a loss of temporal accuracy. Based on this consideration, an algorithm is developed in Kogler et al. (2011b) focusing on the temporal correlation of events. This approach is considered by the developers themselves to be far superior to their previous experiments.

A separate class of algorithms for event-based stereoscopy are the perspective approaches (Benosman et al., 2011; Rogister et al., 2012), which are to be clearly separated from the classical methods and often serve as a basis for advanced algorithms. Epipolar geometry is used as a constraint in order to allow to reconstruct 3D-structures. Events are reconstructed, within a time window, and based on their distance to the epipolar line. Wrong correspondences are additionally eliminated by considering polarity, orientation and order. In Carneiro et al. (2013), this is enhanced by applying a Bayesian filter.

Quite different solutions to recover depth from event-based data are shown in Martel et al. (2018) and Haessig et al. (2019). These are active techniques and require additional hardware, setting them apart from most investigated methods. In Haessig et al. (2019), the known method to estimate depth from the amount of defocus at the focal plane is transferred to neuromorphic sensors and hardware. This is a simple yet elegant solution, whereby the camera alters its focal distance in a steady manner and a SNN computes the time of the best focus for each pixel, creating a depth map. This approach requires a specific liquid lenses, as an adjustable focal distance is necessary to allow a variable focus. According to the authors the low power consumption and computation times guarantee a real-time application. Complementing the event-based stereo setup, two mirrors and a mirror-galvanometer driven laser are used in Martel et al. (2018). This equipment allows the creation of *light spots* in the scene, where contrast varies a lot. Two DAVIS capture these contrast changes, detecting the laser-induced events enabling a resource-efficient matching. Events are clustered by space-density, using a simple mean-shift algorithm, high-density filter and triangulation using a direct linear transform in the overlap field of both sensors. A rare feature of this method is that sensor synchronization is not required.

4.3.2. Event-Based 3D-Perception Through Monocular Cues

In Rebecq et al. (2017), Rebecq presents a method for Event-based Multi-View Stereo (EMVS). The approach is based on *dense* methods (see chapter 2.2) for conventional cameras. These approaches, determine dense 3D-structures from known angles. EMVS, which is based on the work of Space-Sweep Approach (Collins, 1996), estimates semi-dense 3D-structures with only one event-based camera. The camera is thereby moved on a known trajectory. The moving sensor obtains edge detection and continuous measurement data. The algorithm comprises three sub-steps; (1) events are projected back in the form of beams. (2) These beams are counted in a voxel grid to measure the spatial density of the beams. (3) A semi dense reconstruction of the edges is possible due to local maxima. A unique characteristic of this approach is that only one sensor is used for depth perception and no additional aids are applied. Also, the camera is not fixed but moves on a given trajectory. The authors report that their method handles noise, fast movements and poor lighting well.

Further approaches to monocular depth perception are presented in Brandli et al. (2014) and Matsuda et al. (2015). These methods distinguish themselves from EMVS by using complementary hardware and not relying merely on the data of one camera. In Brandli et al. (2014), a pulsed line laser is used in railing reconstruction whose asynchronous operating principle can be easily combined with an event-based algorithm. In Matsuda et al. (2015), the EBS is supplemented by Structured Light.

5. CONCLUSION

Neuromorphic systems have enormous potential, yet they are rarely used in a non-academic context. Particularly, there are no industrial employments of these bio-inspired technologies. Nevertheless, event-based solutions are already far superior to conventional algorithms in terms of latency and energy efficiency.

Potential consequences and the future of such technologies and processes are discussed in this chapter.

5.1. Remaining Issues of Silicon Retinas

Although much research with biologically inspired sensors has taken place in recent decades, there are still plenty of unresolved issues and open questions in the field. Techniques based on Mahowald's VLSI-retina are in some respects quite similar to the structures of the human brain and eyes, which they are imitating. At the same time, however, there are many biological mechanisms and structures that are not, or only partly, implemented artificially. A popular example of this is the *wiring problem* in biological neural 3D-structures (Posch et al., 2014). Although 3D-wiring has been regarded as the more efficient technology for more than 20 years (Milenkovic and Milutinovic, 1998), there are still only a few immature approaches (Kurino et al., 2000; Culurciello and Andreou, 2005).

Another fundamental feature of biological vision is color perception. C-DAVIS, a neuromorphic sensor capable of color recognition, has been available since 2015, but color perception is only implemented in the synchronous and not in the event-based part of the camera (Li et al., 2015). Sensors that encode color information in the events do not yet exist. However, it can be argued that color and motion perception is also processed separately in biological vision, by means of cones and rods, and therefore a division of the mechanisms is justified.

Furthermore, the problem of spatial redundancies and how they can be effectively reduced remains unsolved. Moreover, even the relatively high resolution of DAVIS and ATIS is much too small for industrial purposes and their already strongly reduced pixel size are still too large (Posch et al., 2014).

5.2. Artificial Stereoscopy—A Comparison

The comparatively low dynamic range and the limited frequency of conventional camera systems form a bottleneck for classical approaches to stereoscopy. In addition, these methods are very unreliable under uncontrolled lighting conditions. In Akolkar et al. (2015), the advantages of event-based sensors for pattern recognition are discussed in detail. This can essentially be transferred to stereoscopy. Motion artifacts and object displacement of synchronous image acquisition are the reason why asynchronous imaging is sophisticated in stereo vision.

However, the use of EBS is not sufficient, which is indicated by the fact that the algorithms have very different results. For example, approaches based on classical methods for stereo vision cannot compete with cooperative algorithms. The authors, of the methods introduced in section 4.1, state that range-based and feature-based approaches have significantly worse results than simple algorithms using temporal correlation. This is especially interesting since temporal correlation is only the most basic criterion of the cooperative algorithms in chapter 4.1. Cooperative algorithms are the gold standard, which can also be seen by the fact that they have been used successfully by several independent research groups (Dikov et al., 2017; Osswald et al., 2017; Piatkowska et al., 2017; Kaiser et al., 2018). The approach of section 4.2.3 introduced in Ieng et al. (2018) was published in summer 2018 and is therefore quite new. In addition, it builds on many previous works. As a result, it is very progressive and combines many benefits of the research it is based on. Also noteworthy are the results of Martel et al. (2018) and Haessig et al. (2019). Hereby, active approaches requiring additional hardware are introduced. However, these techniques are resource-efficient allowing a real-time application.

5.3. Outlook

Algorithms are based on SNNs and EBS only develop their potential when they are applied on neuromorphic hardware (Khan et al., 2008). Although there are already some implementations of networks on neuromorphic hardware (Dikov et al., 2017; Andreopoulos et al., 2018; Kaiser et al., 2018), research in this area is not that far yet. However, this will probably change rapidly in the next few years which will make the existing approaches much more powerful.

The application of DAVIS or ATIS in contrast to DVS has already significantly improved the outcome of several approaches like (Reverter Valeiras et al., 2016; Piatkowska et al., 2017; Andreopoulos et al., 2018; Ieng et al., 2018). In particular responsible for this progress is the higher resolution of these sensors. Even though solutions from industry, such as Samsung's DVS (Son et al., 2017), are not yet mature, this could alter drastically within the next few years. A likely consequence is that the costs of these cameras will decrease. This development is further strengthened by the fact that several scientists, which had an important part in the development of DVS, DAVIS and ATIS, are transferring their expertise to the industry by founding companies. Examples for this are Insightness[3], Prophesee[4], and iniVation[5]. This trend suggests that many problems of current algorithms can be solved by better sensors and respective technologies.

AUTHOR CONTRIBUTIONS

LS, DR, AR, and RD are responsible for the idea, the core concept, and the architecture of this paper. LS, JW, DR, and JK did the research and wrote the paper.

FUNDING

This research has received funding from the Baden-Württemberg Stiftung under the research program *Neurorobotik* as well as the European Union's Horizon 2020 Framework Programme for Research and Innovation under the Specific Grant Agreement No. 785907 (Human Brain Project SGA2).

[3]More information about Insightness: http://www.insightness.com
[4]More information about Prophesee: https://www.prophesee.ai/
[5]More information about iniVation: https://inivation.com

REFERENCES

Adachi-Usami, E., and Lehmann, D. (1983). Monocular and binocular evoked average potential field topography: upper and lower hemiretinal stimuli. *Exp. Brain Res.* 50, 341–346. doi: 10.1007/BF00239198

Akolkar, H., Meyer, C., Clady, X., Marre, O., Bartolozzi, C., Panzeri, S., et al. (2015). What can neuromorphic event-driven precise timing add to spike-based pattern recognition? *Neural Comput.* 27, 561–593. doi: 10.1162/NECO_a_00703

Andreopoulos, A., Kashyap, H. J., Nayak, T. K., Amir, A., and Flickner, M. D. (2018). "A low power, high throughput, fully event-based stereo system," in *The IEEE Conference on Computer Vision and Pattern Recognition (CVPR)*. (Salt Lake City, UT), 7532–7542.

Balasubramanian, R., and Gan, L. (2014). Development of retinal amacrine cells and their dendritic stratification. *Curr. Ophthalmol. Rep.* 2, 100–106. doi: 10.1007/s40135-014-0048-2

Barnard, S. T., and Fischler, M. A. (1982). Computational stereo. *ACM Comput. Surv.* 14, 553–572. doi: 10.1145/356893.356896

Belbachir, A., Litzenberger, M., Schraml, S., Hofstätter, M., Bauer, D., Schön, P., et al. (2012). "Care: A dynamic stereo vision sensor system for fall detection," in *IEEE International Symposium on Circuits and Systems* (Seoul), 731–734.

Benosman, R., Ieng, S., Rogister, P., and Posch, C. (2011). Asynchronous event-based hebbian epipolar geometry. *IEEE Trans. Neural Netw.* 22, 1723–1734. doi: 10.1109/TNN.2011.2167239

Benosman, R., Ieng, S. H., Clercq, C., Bartolozzi, C., and Srinivasan, M. (2012). Asynchronous frameless event-based optical flow. *Neural Netw.* 27, 32–37. doi: 10.1016/j.neunet.2011.11.001

Berner, R., Brandli, C., Yang, M., Liu, S.-C., and Delbrück, T. (2013). "A 240x180 120db 10mw 12us-latency sparse output vision sensor for mobile applications," in *Proceedings of the International Image Sensors Workshop* (Kyoto), 41–44.

Berner, R., and Delbrück, T. (2011). Event-based pixel sensitive to changes of color and brightness. *IEEE Trans. Circ. Syst. I* 58, 1581–1590. doi: 10.1109/TCSI.2011.2157770

Bing, Z., Meschede, C., Rhrbein, F., Huang, K., and Knoll, A. C. (2018). A survey of robotics control based on learning-inspired spiking neural networks. *Front. Neurorobot.* 12:35. doi: 10.3389/fnbot.2018.00035

Boahen, K. (2005). Neuromorpic microchips. *Sci. Am.* 292, 56–63. doi: 10.1038/scientificamerican0505-56

Boahen, K. A. (1996). A retinomorphic vision system. *IEEE Micro* 16, 30–39. doi: 10.1109/40.540078

Boahen, K. A. (1998). "Communicating neuronal ensembles between neuromorphic chips," in *Neuromorphic Systems Engineering*. The Springer International Series in Engineering and Computer Science (Analog Circuits and Signal Processing), ed T. S. Lande (Boston, MA: Springer) doi: 10.1007/978-0-585-28001-1_11

Boahen, K. A. (2000). Point-to-point connectivity between neuromorphic chips using address events. *IEEE Trans. Circ. Syst. II* 47, 416–434. doi: 10.1109/82.842110

Bogdan, P. A., Rowley, A. G. D., Rhodes, O., and Furber, S. B. (2018). Structural plasticity on the spinnaker many-core neuromorphic system. *Front. Neurosci.* 12:434. doi: 10.3389/fnins.2018.00434

Brandli, C., Mantel, T., Hutter, M., Höpflinger, M., Berner, R., Siegwart, R., et al. (2014). Adaptive pulsed laser line extraction for terrain reconstruction using a dynamic vision sensor. *Front. Neurosci.* 7:275. doi: 10.3389/fnins.2013.00275

Brandli, C. P. (2015). *Event-based machine vision*. (Ph.D. thesis). ETH Zurich, Zurich.

Butime, J., Gutierez, I., Corzo, L., and Espronceda, C. (2006). "3D reconstruction methods, a survey," in *Proceedings of the First International Conference on Computer Vision Theory and Applications* (Setúbal), 457–463.

Camuñas-Mesa, L. A., Serrano-Gotarredona, T., Ieng, S. H., Benosman, R., and Linares-Barranco, B. (2014a). On the use of orientation filters for 3d reconstruction in event-driven stereo vision. *Front. Neurosci.* 8:48. doi: 10.3389/fnins.2014.00048

Camuñas-Mesa, L. A., Serrano-Gotarredona, T., Linares-Barranco, B., Ieng, S., and Benosman, R. (2014b). "'Event-driven stereo vision with orientation filters," *2014 IEEE International Symposium on Circuits and Systems (ISCAS)* (Melbourne, VIC), 257–260.

Carneiro, J., Ieng, S., Posch, C., and Benosman, R. (2013). Event-based 3D reconstruction from neuromorphic retinas. *Neural Netw.* 45, 27–38. doi: 10.1016/j.neunet.2013.03.006

Chen, D. G., Matolin, D., Bermak, A., and Posch, C. (2011). Pulse-modulation imaging–review and performance analysis. *IEEE Trans. Biomed. Circ. Syst.* 5, 64–82. doi: 10.1109/TBCAS.2010.2075929

Cohen, G., Afshar, S., van Schaik, A., Wabnitz, A., Bessell, T., Rutten, M., et al. (2017). "Event-based sensing for space situational awareness," in *Proceedings of the Advanced Maui Optical and Space Surveillance (AMOS) Technologies Conference* (Maui).

Collins, R. T. (1996). "A space-sweep approach to true multi-image matching," in *Proceedings CVPR IEEE Computer Society Conference on Computer Vision and Pattern Recognition* (San Francisco, CA), 358–363.

Culurciello, E., and Andreou, A. G. (2005). "Capacitive coupling of data and power for 3D silicon-on-insulator VLSI," in *2005 IEEE International Symposium on Circuits and Systems* (Kobe), 4142–4145.

Cumming, B. G., and Parker, A. J. (1997). Responses of primary visual cortical neurons to binocular disparity without depth perception. *Lett. Nat.* 389, 280–283. doi: 10.1038/38487

Cutting, J. E. (1997). High-performance computing and human vision 1. *Behav. Res. Methods Instrum. Comput.* 29, 27–36.

Davies, M., Srinivasa, N., Lin, T., Chinya, G., Cao, Y., Choday, S. H., et al. (2018). Loihi: A neuromorphic manycore processor with on-chip learning. *IEEE Micro* 38, 82–99. doi: 10.1109/MM.2018.112130359

Delbrück, T., Linares-Barranco, B., Culurciello, E., and Posch, C. (2010). "Activity-driven, event-based vision sensors," in *Proceedings of 2010 IEEE International Symposium on Circuits and Systems (ISCAS)* (Paris), 2426–2429.

Dhond, U., and Aggarwal, J. (1989). Structure from stereo - a review. *IEEE Trans. Syst. Man Cybern.* 19, 1489–1510. doi: 10.1109/21.44067

Dikov, G., Firouzi, M., Röhrbein, F., Conradt, J., and Richter, C. (2017). Spiking cooperative stereo-matching at 2ms latency with neuromorphic hardware. *Front. Neurosci.* 10384, 119–137. doi: 10.1007/978-3-319-63537-8_11

Dominguez-Morales, M., Cerezuela-Escudero, E., Jimenez-Fernandez, A., Paz-Vicente, R., Font-Calvo, J. L., Iigo-Blasco, P., et al. (2011). "Image matching algorithms in stereo vision using address-event-representation: a theoretical study and evaluation of the different algorithms," in *Proceedings of the International Conference on Signal Processing and Multimedia Applications* (Seville), 1–6.

Dong-il, C., and Tae-jae, L. (2015). A review of bioinspired vision sensors and their applications. *Sens. Mater.* 27, 447–463.

Douglas, R., Mahowald, M., and Mead, C. (1995). Neuromorphic analogue VLSI. *Annu. Rev. Neurosci.* 18, 255–281.

Felzenszwalb, P. F., and Huttenlocher, D. R. (2004). "Efficient belief propagation for early vision," in *Proceedings of the 2004 IEEE Computer Society Conference on Computer Vision and Pattern Recognition, 2004*, (Washington, DC).

Firouzi, M., and Conradt, J. (2016). Asynchronous event-based cooperative stereo matching using neuromorphic silicon retinas. *Neural Process. Lett.* 43, 311–326. doi: 10.1007/s11063-015-9434-5

Furber, S., Temple, S., and Brown, A. (2006). "High-performance computing for systems of spiking neurons," in *Proceedings of AISB'06: Adaptation in Artificial and Biological Systems* (Bristol, UK), 29–36.

Furber, S. B., Galluppi, F., Temple, S., and Plana, L. A. (2014). The spinnaker project. *Proc. IEEE* 102, 652–665. doi: 10.1109/JPROC.2014.2304638

Furukawa, Y. (2008). *High-fidelity image-based modeling*. (Ph.D. thesis). Champaign, IL, United States, Graduate College of the University of Illinois at Urbana-Champaign.

Ganong, W. F. (1972). *Medizinische Physiologie*. Berlin; Heidelberg: Springer-Verlag.

Goesele, M., Curless, B., and Seitz, S. M. (2006). Multi-view stereo revisited. *IEEE Comput. Vis. Pattern Recogn.* 2, 2402–2409. doi: 10.1109/CVPR.2006.199

Goldstein, E. B. (2015). *Wahrnehmungspsychologie*. Berlin; Heidelberg: Springer-Verlag.

Grüning, A., and Bohte, S. M. (2014). "Spiking neural networks: principles and challenges," in *ESANN 2014 Proceedings, European Symposium on Artificial Neural Networks, Computational Intelligence and Machine Learning* (Bruges).

Haessig, G., Berthelon, X., Ieng, S., and Benosman, R. (2019). A spiking neural network model of depth from defocus for event-based neuromorphic vision. *Sci. Rep.* 9:3744. doi: 10.1038/s41598-019-40064-0

Haessig, G., Cassidy, A., Alvarez-Icaza, R., Benosman, R., and Orchard, G. (2017). Spiking optical flow for event-based sensors using ibm's truenorth neurosynaptic system. *CoRR*. abs/1710.09820.

Hernández Esteban, C., and Schmitt, F. (2004). Silhouette and stereo fusion for 3d object modeling. *Comput. Vis. Image Understand.* 96, 367–392. doi: 10.1016/j.cviu.2004.03.016

Huang, J., Guo, M., and Chen, S. (2017). "A dynamic vision sensor with direct logarithmic output and full-frame picture-on-demand," in *2017 IEEE International Symposium on Circuits and Systems (ISCAS)* (Baltimore, MD), 1–4. doi: 10.1109/ISCAS.2017.8050546

Huang, J., Guo, M., Wang, S., and Chen, S. (2018). "A motion sensor with on-chip pixel rendering module for optical flow gradient extraction," in *2018 IEEE International Symposium on Circuits and Systems (ISCAS)* (Florence), 1–5.

Ieng, S., Carneiro, J., Osswald, M., and Benosman, R. (2018). Neuromorphic event-based generalized time-based stereovision. *Front. Neurosci.* 12:442. doi: 10.3389/fnins.2018.00442

Julesz, B. (1960). Binocular depth perception of computer-generated patterns. *Bell Syst. Tech. J.* 39, 1125–1162. doi: 10.1002/j.1538-7305.1960.tb03954.x

Julesz, B. (1964). Binocular depth perception without familiarity cues. *Science* 145, 356–362.

Julesz, B. (1971). *Foundations of Cyclopean Perception*. Chicago, IL: University of Chicago Press.

Kaiser, J., Weinland, J., Keller, P., Steffen, L., Vasquez Tieck, C., Reichard, D., et al. (2018). "Microsaccades for neuromorphic stereo vision," in *Artificial Neural Networks and Machine Learning – ICANN 2018* (Rhodes), 244–252.

Khan, M. M., Lester, D. R., Plana, L. A., Rast, A., Jin, X., Painkras, E., et al. (2008). "Spinnaker: Mapping neural networks onto a massively-parallel chip multiprocessor," in *2008 IEEE International Joint Conference on Neural Networks (IEEE World Congress on Computational Intelligence)* (Hong Kong), 2849–2856.

Kogler, J., Eibensteiner, F., Humenberger, M., Sulzbachner, C., Gelautz, M., and Scharinger, J. (2014). Enhancement of sparse silicon retina-based stereo matching using belief propagation and two-stage post-filtering. *J. Electron. Imaging* 23:43011. doi: 10.1117/1.JEI.23.4.043011

Kogler, J., Humenberger, M., and Sulzbachner, C. (2011a). "Event-based stereo matching approaches for frameless address event stereo data," in *Advances in Visual Computing - 7th International Symposium, ISVC 2011* (Las Vegas, NV).

Kogler, J., Sulzbachner, C., Humenberger, M., and Eibensteiner, F. (2011b). "Advances in Theory andApplications of Stereo Vision," in *Address-Event Based Stereo Vision with Bio-inspired Silicon Retina Imagers* 165–188. doi: 10.5772/12941

Kogler, J., Sulzbachner, C., and Kubinger, W. (2009). "Bio-inspired stereo vision system with silicon retina imagers," in *Proceedings of the 7th International Conference on Computer Vision Systems: Computer Vision Systems* (Liège), 174–183.

Kolmogorov, V., and Zabih, R. (2002). "Multi-camera scene reconstruction via graph cuts," in *Computer Vision ECCV 2002* (Copenhagen), 8–40.

Kurino, H., Nakagawa, M., Wook Lee, K., Nakamura, T., Yamada, Y., Tae Park, K., et al. (2000). "Smart vision chip fabricated using three dimensional integration technology," in *Advances in Neural Information Processing Systems 13, Papers from Neural Information Processing Systems (NIPS) 2000* (Denver, CO), 720–726.

Lazzaro, J., and Wawrzynek, J. (1995). "A multi-sender asynchronous extension to the aer protocol," in *16th Conference on Advanced Research in VLSI* (Chapel Hill, NC), 158–169.

Leñero-Bardallo, J. A., Bryn, D. H., and Häfliger, P. (2014). Bio-inspired asynchronous pixel event tricolor vision sensor. *IEEE Trans. Biomed. Circ. Syst.* 8, 345–357. doi: 10.1109/TBCAS.2013.2271382

Li, C., Brandli, C., Berner, R., Liu, H., Yang, M., Liu, S., et al. (2015). "Design of an RGBW color VGA rolling and global shutter dynamic and active-pixel vision sensor," in *2015 IEEE International Symposium on Circuits and Systems (ISCAS)* (Lisbon), 718–721.

Lichtsteiner, P., Posch, C., and T., D. (2008). A 128 x 128 120 db 15 us latency asynchronous temporal contrast vision sensor. *IEEE J. Solid-State Circ.* 43, 566–576. doi: 10.1109/JSSC.2007.914337

Liu, S., and Delbrück, T. (2010). Neuromorphic sensory systems. *Curr. Opin. Neurobiol.* 20, 288–295. doi: 10.1016/j.conb.2010.03.007

Lucas, B. D., and Kanade, T. (1981). "An iterative image registration technique with an application to stereo vision," in *Proceedings of the 7th international joint conference on Artificial intelligence* (Vancouver, BC), 674–679.

Maass, W. (1997). Networks of spiking neurons: the third generation of neural network models. *Neural Netw.* 9, 1659–1671.

Mafrica, S. (2016). *Bio-inspired visual sensors for robotic and automotive applications*. (Ph.D. thesis). Marseille, Aix-Marseille Université.

Mahowald, M. (1992). *VLSI analogs of neuronal visual processing: a synthesis of form and function*. (Ph.D. thesis). California Institute of Technology, Pasadena, CA, United States.

Mahowald, M. (1994). *An Analog VLSI System for Stereoscopic Vision*. New York, NY: Springer Science+Business Media.

Mahowald, M., and Mead, C. (1991). The silicon retina. *Sci. Am.* 264, 76–82.

Mallik, U., Clapp, M., Choi, E., Cauwenberghs, G., and Etienne-Cummings, R. (2005). "Temporal change threshold detection imager," *IEEE ISSCC Digest of Technical Papers* (Baltimore, MD: Johns Hopkins University), 362–603.

Mallot, H. A. (1998). *Sehen und die Verarbeitung Visueller Information: Eine Einführung*. Wiesbaden: Vieweg+Teubner Verlag.

Maqueda, A. I., Loquercio, A., Gallego, G., García, N., and Scaramuzza, D. (2018). Event-based vision meets deep learning on steering prediction for self-driving cars. *CoRR*. arXiv:1804.01310. doi: 10.1109/CVPR.2018.00568

Marr, D. (1982). *Vision: A Computational Investigation into the Human Representation and Processing of Visual Information*. New York, NY: Henry Holt and Co., Inc.

Marr, D., and Poggio, T. (1976). Cooperative computation of stereo disparity. *Science* 194, 283–287. doi: 10.1126/science.968482

Marr, D., and Poggio, T. (1977). *A Theory of Human Stereo Vision.* Technical report, Cambridge, MA: Massachusetts Institute of Technology.

Marr, D., and Poggio, T. (1979). A computational theory of human stereo vision. *Proc. R. Soc. Lond. Ser. B Biol. Sci.* 204, 301–328. doi: 10.1098/rspb.1979.0029

Martel, J. N. P., Müller, J., Conradt, J., and Sandamirskaya, Y. (2018). "An active approach to solving the stereo matching problem using event-based sensors," in *2018 IEEE International Symposium on Circuits and Systems (ISCAS)* (Florence), 1–5.

Martin, J. G., Davis, C. E., Riesenhuber, M., and Thorpe, S. J. (2018). Zapping 500 faces in less than 100 seconds: evidence for extremely fast and sustained continuous visual search. *Sci. Rep.* 8:12482. doi: 10.1038/s41598-018-30245-8

Matsuda, N., Cossairt, O., and Gupta, M. (2015). "Mc3d: Motion contrast 3d scanning," *2015 IEEE International Conference on Computational Photography (ICCP)* (Houston, TX), 1–10.

Meister, M., and Berry, M. J. (1999). The neural code of the retina. *Neuron* 22, 435–450. doi: 10.1016/S0896-6273(00)80700-X

Merolla, P. A., Arthur, J. V., Alvarez-Icaza, R., Cassidy, A., Sawada, J., Akopyan, F., et al. (2014). A million spiking-neuron integrated circuit with a scalable communication network and interface. *Science* 345, 668–673. doi: 10.1126/science.1254642

Milenkovic, A., and Milutinovic, V. (1998). A quantitative analysis of wiring lengths in 2D and 3D VLSI. *Microelectron. J.* 29, 313–321. doi: 10.1016/S0026-2692(97)00043-8

Neftci, E., Das, S., Pedroni, B., Kreutz-Delgado, K., and Cauwenberghs, G. (2014). Event-driven contrastive divergence for spiking neuromorphic systems. *Front. Neurosci.* 7:272. doi: 10.3389/fnins.2013.00272

Orchard, G., Benosman, R., Etienne-Cummings, R., and Thakor, N. (2013). "A spiking neural network architecture for visual motion estimation," in *2013 IEEE Biomedical Circuits and Systems Conference (BioCAS)* (Rotterdam), 298–301.

Orchard, G., Meyer, C., Etienne-Cummings, R., Posch, C., Thakor, N., and Benosman, R. (2015). Hfirst: a temporal approach to object recognition. *IEEE Trans. Pattern Anal. Mach. Intell.* 37, 2028–2040. doi: 10.1109/TPAMI.2015.2392947

Osswald, M., Ieng, S., and Benosman, R.and Indiveri, G. (2017). A spiking neural network model of 3D perception for event-based neuromorphic stereo vision systems. *Sci. Rep.* 7:40703. doi: 10.1038/srep 44722

Pfeil, T., Grübl, A., Jeltsch, S., Müller, E., Müller, P., Petrovici, M. A., et al. (2013). Six networks on a universal neuromorphic computing substrate. *Front. Neurosci.* 7:11. doi: 10.3389/fnins.2013.00011

Piatkowska, E., Belbachir, A. N., and Gelautz, M. (2013). "Asynchronous stereo vision for event-driven dynamic stereo sensor using an adaptive cooperative approach," in *2013 IEEE International Conference on Computer Vision Workshops* (Sydney, NSW), 45–50.

Piatkowska, E., Kogler, J., Belbachir, N., and Gelautz, M. (2017). "Improved cooperative stereo matching for dynamic vision sensors with ground truth evaluation," in *2017 IEEE Conference on Computer Vision and Pattern Recognition Workshops (CVPRW)* (Honolulu, HI), 370–377.

Pons, J., Keriven, R., and Faugeras, O. (2005). "Modelling dynamic scenes by registering multi-view image sequences," in *2005 IEEE Computer Society Conference on Computer Vision and Pattern Recognition (CVPR'05)* (San Diego, CA), 822–827. doi: 10.1109/CVPR.2005.227

Posch, C., Hofstätter, M., Matolin, D., Vanstraelen, G., Schön, P., Donath, N., et al. (2007). "A dual-line optical transient sensor with on-chip precision time-stamp generation," in *2007 IEEE International Solid-State Circuits Conference. Digest of Technical Papers* (San Francisco, CA), 500–618.

Posch, C., Matolin, D., and Wohlgenannt, R. (2011). A QVGA 143 dB dynamic range frame-free PWM image sensor with loss-less pixel-level video compression and time-domain CDS. *IEEE J. Solid-State Circ.* 46, 259–275. doi: 10.1109/JSSC.2010.2085952

Posch, C., Serrano-Gotarredona, S., Linares-Barranco, B., and Delbrück, T. (2014). Retinomorphic event-based vision sensors: bioinspired cameras with spiking output. *Proc. IEEE* 102, 1470–1484. doi: 10.1109/JPROC.2014.2346153

Rebecq, H., Gallego, G., Mueggler, E., and Scaramella Perez, D. (2017). EMVS: Event-based multi-view stereo - 3D reconstruction with an event camera in real-time. *Int. J. Comput. Vis.* 126, 1394–1414. doi: 10.1007/s11263-017-1050-6

Reverter Valeiras, D., Orchard, G., Ieng, S., and Benosman, R. B. (2016). Neuromorphic event-based 3D pose estimation. *Front. Neurosci.* 9:522. doi: 10.3389/fnins.2015.00522

Rodieck, R. (1998). *The First Steps in Seeing*. Sunderland, MA: Sinauer Associates.

Rogister, P., Benosman, R., Ieng, S., Lichtsteiner, P., and Delbrück, T. (2012). Asynchronous event-based binocular stereo matching. *IEEE Trans. Neural Netw. Learn. Syst.* 23, 347–353. doi: 10.1109/TNNLS.2011.2180025

Rose, D. (1980). The binocular: monocular sensitivity ratio for movement detection varies with temporal frequency. *Perception* 9, 577–580. doi: 10.1068/p090577

Ruedi, P., Heim, P., Kaess, F., Grenet, E., Heitger, F., Burgi, P., et al. (2003). A 128 /spl times/ 128 pixel 120-db dynamic-range vision-sensor chip for image contrast and orientation extraction. *IEEE J. Solid-State Circ.* 38, 2325–2333. doi: 10.1109/JSSC.2003.819169

Scharstein, D., Szeliski, R., and Zabih, R. (2002). "A taxonomy and evaluation of dense two-frame stereo correspondence algorithms," in *Proceedings IEEE Workshop on Stereo and Multi-Baseline Vision*. (Kauai, HI).

Schraml, S., Schön, P., and Milosevic, N. (2007). "Smartcam for real-time stereo vision - address-event based embedded system," in *Proceedings of the Second International Conference on Computer Vision Theory and Applications - Volume 2: VISAPP* (Barcelona), 466–471.

Seitz, S., Curless, B., Diebel, J., Scharstein, D., and Szeliski, R. (2006). "A comparison and evaluation of multi-view stereo reconstruction algorithms," in *Proceedings of the 2006 IEEE Computer Society Conference on Computer Vision and Pattern Recognition* (New York, NY), 519–528.

Sivilotti, M. A. (1990). *Wiring considerations in analog VLSI systems, with application to field-programmable networks*. (Ph.D. thesis). California Institute of Technology, Pasadena, CA, United States.

Son, B., Suh, Y., Kim, S., Jung, H., Kim, J., Shin, C., et al. (2017). "A 640×480 dynamic vision sensor with a 9μ pixel and 300meps address-event representation," in *2017 IEEE International Solid-State Circuits Conference (ISSCC)* (San Francisco, CA), 66–67.

Szeliski, R. (2010). *Computer Vision: Algorithms and Applications*. London: Springer Verlag.

Vogiatzis, G., Hernández Esteban, C., Torr, P., and Cipolla, R. (2007). Multiview stereo via volumetric graph-cuts and occlusion robust photo-consistency. *IEEE Trans. Pattern Anal. Mach. Intell.* 29, 2241–2246. doi: 10.1109/TPAMI.2007.70712

Vreeken, J. (2003). *Spiking Neural Networks, an Introduction*. Utrecht University: Information and Computing Sciences.

Xie, Z., Chen, S., and Orchard, G. (2017). Event-based stereo depth estimation using belief propagation. *Front. Neurosci.* 11:535. doi: 10.3389/fnins.2017.00535

Yaffe, Y., Levy, N., Soloveichik, E., Derhy, S., Keisar, A., Rozin, E., et al. (2017). "Dynamic vision sensor - the road to market," in *ICRA'17*. Singapore.

Zaghloul, K. A., and Boahen, K. (2006). A silicon retina that reproduces signals in the optic nerve. *J. Neural Eng.* 3:257. doi: 10.1088/1741-2560/3/4/002

Conflict of Interest Statement: The authors declare that the research was conducted in the absence of any commercial or financial relationships that could be construed as a potential conflict of interest.

frontiers in Neurorobotics

ORIGINAL RESEARCH
published: 02 August 2019
doi: 10.3389/fnbot.2019.00059

Synchronization of Non-linear Oscillators for Neurobiologically Inspired Control on a Bionic Parallel Waist of Legged Robot

Yaguang Zhu, Shuangjie Zhou, Dongxiao Gao and Qiong Liu*

Key Laboratory of Road Construction Technology and Equipment of MOE, Chang'an University, Xi'an, China

Synchronization of coupled non-linear oscillators inspired by a central pattern generator (CPG) can control the bionic robot and promote the coordination and diversity of locomotion. However, for a robot with a strong mutual coupled structure, such neurobiological control is still missing. In this contribution, we present a σ-Hopf harmonic oscillator with decoupled parameters to expand the solution space of the locomotion of the robot. Unlike the synchronization of original Hopf oscillators, which has been fully discussed, the asymmetric factor of σ-Hopf oscillator causes a deformation in oscillation waveform. Using the non-linear synchronization theory, we construct the transition state model of the synchronization process to analyze the asymmetrical distortion, period change and duty ratio inconsistency. Then a variable coupling strength is introduced to eliminate the waveform deformation and maintain the fast convergence rate. Finally, the approach is used for the locomotion control of a bionic parallel waist of legged robot, which is a highly coupled system. The effectiveness of the approach in both independent and synthesis behavior of four typical motion patterns are validated. The result proves the importance of controllability of the oscillation waveform and the instantaneous state of the synchronization, which benefits the transition and transformation of the locomotion and makes the coupling motion more flexible.

Keywords: bionic parallel waist, locomotion control, synchronization, transition state, σ-Hopf oscillator

OPEN ACCESS

Edited by:
Poramate Manoonpong, University of Southern Denmark, Denmark

Reviewed by:
Arash Ahmadi, University of Windsor, Canada
Chengju Liu, Yangpu Hospital, Tongji University, China
Horacio Rostro Gonzalez, University of Guanajuato, Mexico

****Correspondence:***
Yaguang Zhu
zhuyaguang@chd.edu.cn

Received: *27 April 2019*
Accepted: *11 July 2019*
Published: *02 August 2019*

Citation:
Zhu Y, Zhou S, Gao D and Liu Q (2019) Synchronization of Non-linear Oscillators for Neurobiologically Inspired Control on a Bionic Parallel Waist of Legged Robot. Front. Neurorobot. 13:59. doi: 10.3389/fnbot.2019.00059

INTRODUCTION

Legged robot technique has made remarkable progress in the past few decades, and produced a series of very famous achievements: StarlETH (Hutter et al., 2012), ANYmal (Hutter et al., 2016; Hwangbo et al., 2019), HyQ series (Semini et al., 2011, 2016), MIT Cheetah series (Seok et al., 2013; Wensing et al., 2017), Boston Dynamics Spotmini series[1]. Great contribution has been made in the aspects of leg structure (Ananthanarayanan et al., 2012), leg control (Barasuol et al., 2013), limb coordination (Gehring et al., 2016), compliance control (Eich et al., 2009), balance control (Raibert and Tello, 1986), adaptive control (Manoonpong et al., 2013), and so on (Schwendner et al., 2014; Gehring et al., 2016), which continuously improve the flexibility, stability, coordination and intelligence of robots in related fields.

[1]https://www.bostondynamics.com/robots.

No robot has been able to act as flexibly and as animal-like as cat or a dog until today. The control strategy is not the only reason for this, as there are many differences between the structure of natural creatures and robots. Inspired by biologists (Galis et al., 2014), along with demand for high-flexibility and high-speed robots, many scholars have carried out in-depth research on the bionic torso (Albiez et al., 2006). The bionic torso structure can be divided into two types: torso with active joint (Khoramshahi et al., 2013; Satoh and Fujimoto, 2018) and with passive joint (Takuma et al., 2010; Haynes et al., 2012). An additional active joint on a torso can effectively improve the motion range and dexterity of a robot. Most passive joints use elastic elements to collect energy during movement and to improve compliance. However, the function of a biological torso for load capacity, movement, coordination and other aspects is obviously much more than these. Therefore, this paper builds a bionic parallel waist to replace the original rigid torso for the advantages of strong carrying capacity and high control accuracy of the parallel structure. Actually, the parallel robot has been widely used in the industry fields (Dallej et al., 2006; Cong et al., 2011; He et al., 2015). Its structure (Villarreal-Cervantes et al., 2010), kinematics (Plitea et al., 2013), dynamics (Staicu, 2009), control (Liu et al., 2018b), and so on have all been studied before. Although the parallel structure has been directly applied to legged robot, showing better performance than serial structure (Kuehn et al., 2017), no bionical method is used on the parallel structure. This paper investigates the CPG-based network for neurobiologically inspired control of the bionic parallel waistf and discusses the related issues.

At present, CPG models have been applied in various robots (Donati et al., 2016; Santos et al., 2016; Liu et al., 2018a), and can be divided into two categories (Wu et al., 2009): neuron-based models and oscillatior-based models. Neuron-based models mainly include the Matsuoka neuron oscillator model (Matsuoka, 1985, 1987), the Kimura model (Kimura et al., 2001, 2002; Fukuoka et al., 2003), cellular neural network (CNNs) (Arena and Fortuna, 2000; Arena et al., 2001), and recurrent neural network (Rao and Kamat, 1995; Senda and Tanaka, 2000). The biological significance of the models is relatively clear. The oscillator-based models include the Kuramoto oscillator (Acebron et al., 2005), the Hopf harmonic oscillator (Righetti and Ijspeert, 2006; Righetti, 2008), the Van der Pol oscillator (Van der Pol and Van der Mark, 1928; Dutra et al., 2003), and more. These oscillator-based models can periodically generate non-linear oscillation signals and are widely used as CPG oscillation units since they contain a fewer number of parameters and have sophisticated background implementation theories. All of these above can be used for robot control and the networks with oscillators will not differ too much within the same robot, with respect to the architecture and coupling topology, which are related to the physical structure and control frame. In terms of waveforms that determine what trajectories will actually be performed by each joint during a cycle, the oscillator must be selected cautiously. In some robots with simple structure, waveform has a relatively small effect on the movement of single joint and whole body. Therefore, for the parallel platform in this paper, the spatial mechanism with six degrees of freedom is related to six coupling limbs. The movement of each limb directly affects the smoothness and stability of overall system, so we have to focus on the transition smoothness, transformation quickness, and velocity/acceleration impact of the oscillator.

Synchronization means an exact match of the scaled amplitude with a desired phase difference (Chung and Dorothy, 2010). Different phase lead or lag has already been performed in the oscillators with the same frequency to manipulate different locomotion of various robots (Ijspeert, 2008). There are two points that need to be figured out. One is the stability of the synchronization. The stable theory of the coupled oscillator system can help to determine the exact parameters, and they are the constraints that make the system converge at final moment (Buchli and Ijspeert, 2004; Kopell et al., 2006). This consideration has been fully discussed both in architectural symmetries and diffusion-like couplings (Buono and Golubitsky, 2001; Ashwin, 2003; Ramezani et al., 2017). Another point is that the transition process needs to be clear and controllable, since it concerns the trajectory of every movement of the limbs and joints. An unreasonable transition between two perfect stable states will also lead to an unexpected locomotion. In fact, in the premise of synchronization stability, the transition process in both joint space and Cartesian space should be taken into serious consideration. In this paper, the transition state of coupled non-linear oscillators is analyzed in detail to guarantee the rational locomotion in every single moment.

In our previous work, we have researched on legged robot about trajectory planning (Zhu and Guo, 2016; Zhu et al., 2018a), deviation correction (Zhu et al., 2016, 2017), force control (Zhu et al., 2015; Zhu and Jin, 2016), energy optimization (Jin et al., 2013; Zhu et al., 2014), and locomotion diversity (Zhu et al., 2018b), aiming to achieve excellent coordination and flexibility of legged robot. The bionic parallel waist is supposed to be a good choice for the issue from both a biological and a robotic point of view. At present, the majority of parallel robots utilize the model control theory (Jin et al., 2014). Each angle of joint with the strong coupling and structure constraints needs to be calculated, since all joint actuators are involved in the locomotion of parallel robots at the same time. All trajectories (position, velocity, acceleration, and torque) have to be designed for accurate control and high speed. Although these methods can be used in the bionic robot, we are more inclined to the bionic control method, for it is hard to design every possible movement in the solution space in advance. Thus, synchronization of σ-Hopf oscillators for the bionic parallel waist of a legged robot is proposed to realize neurobiologically inspired control. The paper is organized as follows. Materials and Method introduces the bionic parallel robot system and the method. In Analysis of Synchronization, synchronization of σ-Hopf oscillators is analyzed. Neurobiologically Inspired Control and Results illustrates CPG-Based locomotion control and results. The performances and findings are discussed and concluded in Simulation.

MATERIALS AND METHODS

For the coordinated locomotion of a legged robot, a bionic parallel waist is developed for the method proposed in this paper. We will introduce the system of the parallel waist and synchronization method of coupled σ-Hopf oscillators in the following part: sections Platform and System, σ-Hopf Harmonic Oscillator, Network, and Synchronization of σ-Hopf Oscillators.

Platform and System

In mammals, the waist (both bone and muscle) plays an extraordinary role in movement (Grondin and Potvin, 2009), and researchers found that robots with waists performed better than those with a rigid body (Coros et al., 2011). The parallel platform in this paper is used as the waist of the four-legged robot to obtain better coordination ability. Its structure is shown in **Figure 1A**. The moving platform at the waist connects the front legs, while the rear legs are linked to the stationary platform. The whole parallel platform is supposed to be the robot torso and can achieve shift, rotation, and synthesis movements. Six identical limbs connecting the moving platform to the stationary platform are the actuating mechanism of the waist. There are two spherical joints between coupler links, and one rotation joint for the connection of an input rod and the motor. So, the moving platform can move with 6 spatial degrees of freedom effectively under the actuation of 6 brushless DC motors. The magnet encoders are mounted next to the input rods and are connected by gears. They are shown in **Figure 1B**. Force sensors are mounted on the long linkages and used for the payload calculation. All information obtained through encoders and force sensors are sent to the controller for locomotion generation.

Most existing legged robots without waist structures adjust the action of the rigid torso by controlling the leg movement (Cao and Poulakakis, 2016; Zhang et al., 2016). Some others enhance the movement ability by active or passive joints. But the presented parallel waist has far more flexibility and larger load capacity, which can easily assist the robot to achieve pitching, stretching, and torsion of the torso. Therefore, the robot equipped with a bionic waist needs to carry out overall behavior planning including torso and legs, so as to generate motion rhythm and control parameters for the waist. With the bionic control method, these parameters will be used to adjust the CPG oscillator and synchronous network, and then generate the control signal for the motor driver, which is shown in **Figure 1C**.

σ-Hopf Harmonic Oscillator

The important role of CPG in bionic control is self-evident and the details have been investigated in the field of biology (Macintosh et al., 1993; Jorgensen et al., 2003), neuroscience (Grillner et al., 2007; Jean-Xavier and Perreault, 2018), and robotics (Wang et al., 2012). Especially in the application of multi-degree-of-freedom or multi-joint robots, it is particularly prominent due to the coupling and synchronization ability of CPG signals, which can form a signal transmission network similar to natural creature. However, no matter how complex the network is or what change post-processing makes, the controllability of the original signal generated by CPG affects the control performance of robots directly. Then we must control CPG signal at every single moment. That is to say, if CPG is regarded as a simple control wave, we should not only pay attention to its frequency and amplitude, but also control its offset, the speed of ascending, and descending (shape of the signal). They are not problems in the model control (Jin et al., 2014), since all of the required control variables can be "designed out." CPG waveform in the bionic control is subject to the control of oscillation and coupling property, and cannot be changed easily (Zhu et al., 2018b). In the present paper, the σ-Hopf oscillator is proposed [σ is one special parameter to distinguish it from the orignal Hopf oscillator (Drazin, 2008)] for two reasons. One is the Stability. The symmetric limit circle prevents the classical problem of instability due to switching between two stable systems and the stability of coupled Hopf oscillators has also been previously discussed (Pham and Slotine, 2005; Kato and Kamimura, 2008). The other reason is the consideration for excellent locomotion diversity and smoothness by changing amplitude, frequency, phase, and waveform, which has been fully investigated in our published paper (Zhu et al., 2018b). Its features and characteristics will be introduced in the following. The form of synchronous coupling of σ-Hopf is

$$\dot{\upsilon} = \begin{bmatrix} \dot{x} \\ \dot{y} \end{bmatrix} = \begin{bmatrix} \sigma_1(x-a) - \sigma(y-b) \\ \sigma_1(y-b) + \sigma(x-a) \end{bmatrix} + \mathbf{g}(t) + \mathbf{u}(t) \tag{1}$$

where,

$$\begin{cases} \sigma = \pi/(\rho \cdot (e^{-\lambda y} + 1) \cdot \varphi) + \pi/((1-\rho) \cdot (e^{\lambda y} + 1) \cdot \varphi) \\ \sigma_1 = -\alpha((x-a)^2 + (y-b)^2 - \mu) \end{cases} \tag{2}$$

Equivalently,

$$\dot{\upsilon} = \mathbf{f}(\upsilon, \alpha, \mu, \sigma(\rho, \lambda, t)) + \mathbf{g}(t) + \mathbf{u}(t) \tag{3}$$

where x and y are the state variables; a, b is the center of the limit cycle; μ is amplitude of the oscillations. The bifurcation parameter α can switch from -1 to 1 such that this would change the stable limit cycle dynamics to the dynamics with a globally stable equilibrium point (Strogatz, 2015). In the $\boldsymbol{\sigma}(\rho, \lambda, t)$, λ is strength and φ is the period factor; $0<\rho<1$ denotes the duty factor and determines the transformation speed between the ascending and descending phases. In (2), the parameters φ and ρ are uncorrelated. That means that the movement period will not be influenced by a change in the duty factor. $\mathbf{g}(t)$ is coupling input, for a single oscillator $\mathbf{g}(t) = 0$. $\mathbf{u}(\mathrm{t}) = -\mathrm{sign}(y)u$ is the external input to control the oscillation signal by the external sensing information (i.e., contact detection in the legged robot; Righetti, 2008; Aoi et al., 2013). The coverage coefficient and frequency were always coupled together and cannot be controlled independently. Therefore, we decoupled it and induced the duty factor ρ so that the frequency and shape of the waveform can be controlled independently (Zhu et al., 2018b). The presence of $\boldsymbol{\sigma}(\mathrm{t})$ here is different from the original Hopf oscillator and plays an important role in changing the oscillation waveform. We will later see that they can be useful for different patterns of locomotion. In the next

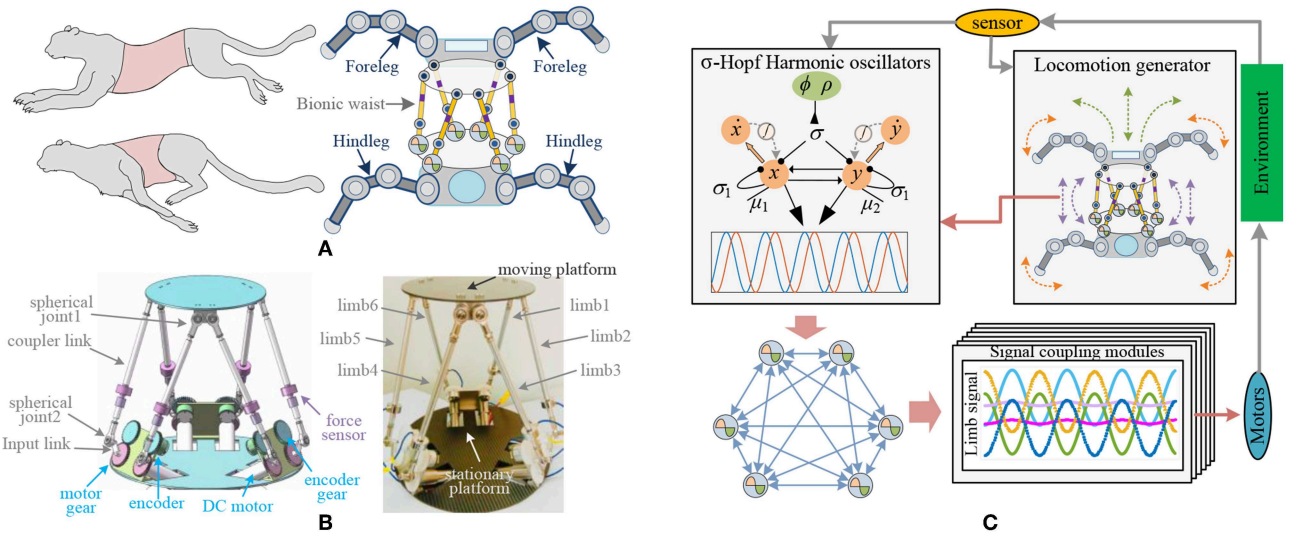

FIGURE 1 | Architecture of bio-inspired legged robot with parallel waist. **(A)** Mechanical structure of bio-inspired robot. **(B)** Mechanical structure of bionic waist. **(C)** Framework of robot system, including locomotion generator of the robot, σ-Hopf oscillators, synchronous network, and coupling signal modules.

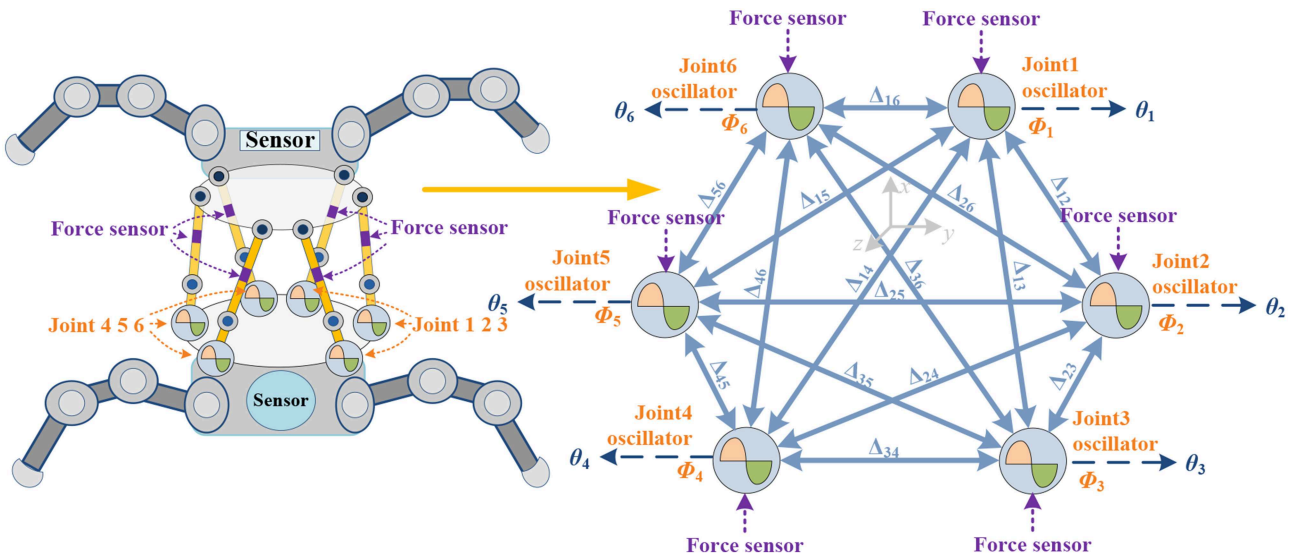

FIGURE 2 | Two-way ring architecture network. Every limb composes of 2 links, 2 spherical hinges, 1 actuator, and 1 force sensor. Φ_i is denoted as oscillation phase of *i*th joint, θ_i is the control signal of *i*th joint. Geometric structure is shown in Appendix (**Supplementary Material**).

section, we present how to construct a stable synchronization of σ-Hopf oscillators for the purpose of diverse locomotion pattern modulation.

Network

Synchronization permits different actuators to oscillate with a prescribed phase lead or lag to regulate different movement patterns. On the basis of the joint number, structure connection and behavioral characteristics of different robots [legged robot (Kalouche et al., 2015; Bjelonic et al., 2016; Owaki and Ishiguro, 2017), snake robot (Wang et al., 2016), swimming robot (Stefanini et al., 2006), and flying robot (Corke et al., 2003; Ramezani et al., 2017)], the behavior control networks are also different. The type of oscillator (Wang et al., 2018) and phase difference (Aoi et al., 2011) formation method are also important factors. The specific network architecture is shown in **Figure 2**. The parallel waist platform adopts the same control frame as the leg of the robot, and each limb is driven by an oscillator. The full coupled two-way ring architecture is constructed, since it has better transition performance than one-way ring architecture (Chung and Dorothy, 2010). For the coupled σ-Hopf oscillators in this paper, (3) can be rewritten with a diffusive coupling with

the phase-rotated neighbor

$$\dot{\boldsymbol{v}}_i = \mathbf{f}(\boldsymbol{v}_i, \mu_i, \boldsymbol{\sigma}_i(\rho_i, \lambda, t)) - k(t)\sum_{j\in\mathfrak{N}_i}^{n_i}(\boldsymbol{v}_i - \frac{\mu_i}{\mu_j}\mathbf{R}(\Delta\Phi_{ij})\boldsymbol{v}_j) + \mathbf{u}(t) \quad (4)$$

$$\mathbf{R}(\Delta\Phi) = [\cos(\Delta\Phi) - \sin(\Delta\Phi); \sin(\Delta\Phi)\cos(\Delta\Phi)] \quad (5)$$

in which, the positive scalar k(t) denotes the coupling gain and can be time-varying for different locomotion. $\mathbf{R}(\Delta\Phi)\mathcal{SO}(2)$ is a 2-D rotational transformation of the phase difference $\Delta\Phi_{ij}$ between the ith and jth oscillators. The desired phase offset $\Delta\Phi_{ij}$ guides υ_i to synchronize with υ_j. N_i denotes the set that contains only the local neighbors of the ith σ-Hopf oscillator, and n_i is the number of the neighbors. Both N_i and $n_i$depend on the coupled σ-Hopf oscillators and network architecture. Since the coordination motion pattern of the bionic waist is determined by the relative phase between the oscillators, the phase offset matrix $\Delta\Phi_{ij}$ is the key in the network. Generally, $\Delta\Phi_{ij} = \Phi_i - \Phi_j$ ($i, j = 1,\ldots,6$, $0 \le \Delta\Phi_{ij} \le 2\pi$), $\Delta\Phi_{ij} = -\Delta\Phi_{ji}$, $\Delta\Phi_{ij} = \Delta\Phi_{ik} + \Delta\Phi_{kj}$ and $\Delta\Phi_{ii} = 0$ ($i, j = 1,\ldots,6$). So, the locomotion of the waist is determined by [$\Delta\Phi_{12}$, $\Delta\Phi_{23}$, $\Delta\Phi_{34}$, $\Delta\Phi_{45}$, $\Delta\Phi_{56}$, $\Delta\Phi_{61}$], which can be written as [Δ_{12}, Δ_{23}, Δ_{34}, Δ_{45}, Δ_{56}, Δ_{61}] for simplification. The full coupled network with $\Delta\Phi$ is shown in **Figure 2**.

Theoretically, a 6RSS parallel platform can realize the independent and coupled locomotion of three translational and three rotational motions in the Cartesian coordinate system (Ahmet and Koksal, 2014) In this paper, four main torso movements of the mammals (Rossignol, 2004) are discussed: Stretching and flexing along Z axial (motion pattern A), lateral movement along X axial (motion pattern B), pitch around Y axial (motion pattern C), and torsion around Z axial (motion pattern D). According to the symmetry of motion and the established coordinate system shown in Appendix (**Supplementary Material**), the oscillators always operate synchronously. From a lateral perspective, all mentioned actions are symmetrical along the X axial except rotation movement around the Z axial. The joint 1–6, 2–5, and 3–4 have the opposite turning direction to guarantee the symmetric loading, so $\Delta_{16} = \Delta_{25} = \Delta_{34} = 180^\circ$ (for the rotation around the Z axial, $\Delta_{16} = \Delta_{25} = \Delta_{34} = 0^\circ$). The oscillator amplitude is also symmetric along the X axial. Vertically, in the motion pattern A, oscillators on the same side along the X axial keep same pace, then $\Delta_{12} = \Delta_{23} = 0^\circ$and $\Delta_{65} = \Delta_{54} = 0^\circ$; in motion pattern B, there are $\Delta_{12} = \Delta_{65} = 0^\circ$ and $\Delta_{23} = \Delta_{54} = 180^\circ$according to the asymmetric structure along the Y axial; in motion pattern C, there are $\Delta_{16} = \Delta_{25} = \Delta_{34} = 180^\circ$, $\Delta_{12} = \Delta_{65} = 180^\circ$ and $\Delta_{23} = \Delta_{54} = 0^\circ$, since the actuator 1 and 6 are located in the positive half of X axial and joint 2 (or 3) and 5 (or 4) are located in the negative half; in motion pattern D, all actuators have the same rotational direction, so $\Delta_{16} = \Delta_{25} = \Delta_{34} = 0^\circ$, $\Delta_{12} = \Delta_{65} = 180^\circ$, $\Delta_{23} = \Delta_{54} = -180^\circ$ and $\Delta_{13} = \Delta_{64} = 0^\circ$. Other independent or coupled locomotions can be obtained by similar analysis, even if they never occur in vertebrates. Additionally, the range of movements are associated with the amplitude control signals. We will illustrate these relationships in Neurobiologically Inspired Control and Results.

Synchronization of σ-Hopf Oscillators

The neurobiological approach to an engineered bionic waist is to produce the analytical model of oscillators that matches the real need of bioinspired legged robot. It will benefit the coordinated locomotion between the waist and leg joints, but the limit-cycle dynamics, synchronization of the coupled oscillator and feedback signals integration have to be taken into consideration (Ijspeert, 2008; Seo et al., 2010). Thus, we have proposed (1) with period parameter ϕ, amplitude μ, coupled input $\boldsymbol{g}$(t), and feedback input $\boldsymbol{u}$(t). This is the base for the bionic waist to perform agile maneuvering in decoupled, symmetric or unsymmetric locomotion in Cartesian space. For the synchronization of a network, we rewrite the coupled Hopf oscillators with the related concern:

$$\dot{\boldsymbol{v}}_i = \mathbf{f}(\boldsymbol{v}_i, \mu_i, \boldsymbol{\sigma}_i(\rho_i)) - k(t)\sum_{j\in\mathfrak{N}_i}^{n_i}(\upsilon_i - \frac{\mu_i}{\mu_j}\mathbf{R}(\Delta\Phi_{ij})\boldsymbol{v}_j). \quad (6)$$

If the external sensing input u(t) is taken as some initial state of the oscillator, its value will not affect the stability. If σ equals to a constant or $\rho = 0.5$, ascending and descending will equal to each other, it will be the standard Hopf oscillator, and its stability with a diffusive coupling has been proved (Pham and Slotine, 2005). When $\rho \neq 0.5$, the σ-Hopf oscillation waveform is asymmetrical. Although the total time in one period is still unchanged, it presents different frequencies ($\pi/(\rho\cdot(e^{-\lambda y}+1)\cdot\varphi)$ for ascending and $\pi/((1\text{-}\rho)\cdot(e^{\lambda y}+1)\cdot\phi)$ for descending), and leads to asymmetrical oscillation signals. Thus, to demonstrate the synchronization of the modified oscillators, $\{\dot{\bar{\boldsymbol{v}}}\}$ is denoted for the symmetric oscillators (with $\rho = 0.5$). According the stable theory of phase synchronization, we construct (6) into

$$\{\dot{\bar{\boldsymbol{v}}}\} = \mathbf{f}(\{\bar{\boldsymbol{v}}\}, \mu, \boldsymbol{\sigma}^{\rho=0.5}) - k(t)\mathbf{G}\{\bar{\boldsymbol{v}}\} \quad (7)$$

where $\rho \in \mathbb{R}^n$, and different ρ makes synchronization of oscillators with different wave shape possible. Specially, if $\rho = 0.5$, the shape of waveform will equal to the original waveform. The matrix $\mathbf{G}$ is a Laplacian matrix with phase shifts $\mathbf{R}(\Delta\boldsymbol{\Phi}_{ij})$. Considering instantaneous deformation, $\{\bar{\upsilon}_0\}$ is denoted for the original oscillators signal without synchronization, $\{\bar{\upsilon}\}$ is for the original oscillators signal with synchronization, and$\{\Delta\bar{\upsilon}_s\}$ is the change between them. So

$$\bar{\upsilon} = \bar{\upsilon}_0 + \Delta\bar{\upsilon}_s(\mathbf{G}(\bar{\upsilon}_0)) \quad (8)$$

For simplicity, $\Delta\bar{\upsilon}_s(\mathbf{G}(\bar{\upsilon}_0))$is written as$\Delta\bar{\upsilon}_s$,

$$\begin{aligned}\{\dot{\bar{\boldsymbol{v}}}\} &= \mathbf{f}(\{\bar{\boldsymbol{v}}\}, \mu, \boldsymbol{\sigma}^{\rho=0.5}) - k(t)\mathbf{G}\{\bar{\boldsymbol{v}}\} = \mathbf{f}(\{\bar{\boldsymbol{v}}_0\}, \mu, \boldsymbol{\sigma}^{\rho=0.5}) \\ &+ \mathbf{f}(\{\Delta\bar{\boldsymbol{v}}_s\}, \mu, \boldsymbol{\sigma}^{\rho=0.5}) - k(t)\mathbf{G}\{\bar{\boldsymbol{v}}_0\} - k(t)\mathbf{G}\{\boldsymbol{\Delta}\bar{\boldsymbol{v}}_s\} \\ &= \mathbf{f}(\{\bar{\boldsymbol{v}}_0\}, \mu, \boldsymbol{\sigma}^{\rho=0.5}) + \mathcal{G}\{\mathbf{G}(\bar{\boldsymbol{v}}_0), k(t)\} \quad (9)\end{aligned}$$

$$\begin{aligned}\mathcal{G}\{\mathbf{G}(\bar{\upsilon}_0), k(t)\} &= \mathbf{f}(\{\Delta\bar{\upsilon}_s\}, \mu, \sigma^{\rho=0.5}) - k(t)\mathbf{G}\{\bar{\upsilon}_0\} \\ &- k(t)\mathbf{G}\{\Delta\bar{\upsilon}_s\}. \quad (10)\end{aligned}$$

When finally it gets stable, $\{\boldsymbol{v}\} \to \{\boldsymbol{v}_0\}$. Then,

$$\{\dot{\bar{\boldsymbol{v}}}\} = \mathbf{f}(\{\bar{\boldsymbol{v}}_0\}, \mu, \boldsymbol{\sigma}^{\rho=0.5}) + \mathcal{G}\{\bar{\boldsymbol{v}}_0, k(t)\}$$

$$\begin{cases} \{\Delta\bar{\boldsymbol{v}}_s\} = 0 \\ \mathbf{f}(\{\Delta\bar{\boldsymbol{v}}_0\}, \mu, \boldsymbol{\sigma}^{\rho=0.5}) = 0 \\ \mathcal{G}\{\mathbf{G}(\bar{\boldsymbol{v}}_0), k(t)\} = 0 \end{cases} \tag{11}$$

So

$$\mathcal{G}\{\mathbf{G}(\bar{\boldsymbol{v}}_0), k(t)\} \begin{cases} \neq 0, transitionstate \\ = 0, steadystate \end{cases} \tag{12}$$

It shows that the signals of oscillators with synchronization in the transition state are different from that of original oscillators, but they will turn back to their original form after the convergence.

The modified signals of oscillators (with $\rho \neq 0.5$) without synchronization is denoted as $\{\hat{\boldsymbol{v}}_0\}$ and $\{\Delta\boldsymbol{v}_0\}$is the deviation between $\{\bar{\boldsymbol{v}}_0\}$ and $\{\hat{\boldsymbol{v}}_0\}$. According to (8), for modified signal with synchronization

$$\hat{\boldsymbol{v}}_0 = \bar{\boldsymbol{v}}_0 + \Delta\hat{\boldsymbol{v}}_0 \tag{13}$$

$$\hat{\boldsymbol{v}} = \hat{\boldsymbol{v}}_0 + \Delta\hat{\boldsymbol{v}}_s(\hat{\boldsymbol{v}}_0) = \hat{\boldsymbol{v}}_0 + \Delta\hat{\boldsymbol{v}}_s(\bar{\boldsymbol{v}}_0, \Delta\hat{\boldsymbol{v}}_0). \tag{14}$$

$\Delta\hat{\boldsymbol{v}}_s(\bar{\boldsymbol{v}}_0, \Delta\hat{\boldsymbol{v}}_0)$ is written as $\Delta\hat{\boldsymbol{v}}_s$. For $\{\dot{\hat{\boldsymbol{v}}}\}$, we have

$$\{\dot{\hat{\boldsymbol{v}}}\} = \{\dot{\bar{\boldsymbol{v}}}_0\} + \{\Delta\dot{\hat{\boldsymbol{v}}}_0\} + \{\Delta\dot{\hat{\boldsymbol{v}}}_s\} = \{\dot{\hat{\boldsymbol{v}}}_0\} + \{\Delta\dot{\hat{\boldsymbol{v}}}_s\} \tag{15}$$

$$\{\dot{\bar{\boldsymbol{v}}}_0\} = \mathbf{f}(\{\bar{\boldsymbol{v}}_0\}, \mu, \boldsymbol{\sigma}^{\rho=0.5}) - k(t)\mathbf{G}\{\bar{\boldsymbol{v}}_0\} \tag{16}$$

$$\{\Delta\dot{\hat{\boldsymbol{v}}}_0\} = \mathbf{f}(\{\Delta\hat{\boldsymbol{v}}_0\}, \mu, \boldsymbol{\sigma}^{\rho=0.5}) - k(t)\mathbf{G}\{\Delta\hat{\boldsymbol{v}}_0\} \tag{17}$$

$$\{\Delta\dot{\hat{\boldsymbol{v}}}_s\} = \mathbf{f}(\{\Delta\hat{\boldsymbol{v}}_s\}, \mu, \boldsymbol{\sigma}^{\rho\neq0.5}) - k(t)\mathbf{G}\{\Delta\hat{\boldsymbol{v}}_s\} \tag{18}$$

$$\{\dot{\hat{\boldsymbol{v}}}_0\} = \mathbf{f}(\{\bar{\boldsymbol{v}}_0\}, \mu, \boldsymbol{\sigma}^{\rho=0.5}) - k(t)\mathbf{G}\{\bar{\boldsymbol{v}}_0\} + \mathbf{f}(\{\Delta\hat{\boldsymbol{v}}_0\}, \mu, \boldsymbol{\sigma}^{\rho=0.5}) - k(t)\mathbf{G}\{\Delta\hat{\boldsymbol{v}}_0\} \tag{19}$$

$$\{\dot{\hat{\boldsymbol{v}}}\} = \mathbf{f}(\{\bar{\boldsymbol{v}}_0\}, \mu, \boldsymbol{\sigma}^{\rho=0.5}) + \mathbf{f}(\{\Delta\hat{\boldsymbol{v}}_0\}, \mu, \boldsymbol{\sigma}^{\rho=0.5}) + \mathcal{G}'\{\bar{\boldsymbol{v}}_0, \Delta\hat{\boldsymbol{v}}_0, k(t)\} \tag{20}$$

$$\mathcal{G}'\{\bar{\boldsymbol{v}}_0, \Delta\hat{\boldsymbol{v}}_0, k(t)\} = \mathbf{f}(\{\Delta\hat{\boldsymbol{v}}_s\}, \mu, \boldsymbol{\sigma}^{\rho\neq0.5}) - k(t)\mathbf{G}\{\bar{\boldsymbol{v}}_0\} - k(t)\mathbf{G}\{\Delta\hat{\boldsymbol{v}}_0\} - k(t)\mathbf{G}\{\Delta\hat{\boldsymbol{v}}_s\}. \tag{21}$$

Remark:

1. If $\Delta\hat{\boldsymbol{v}}_0 \neq 0$ and $k(t) \neq 0$, the process will be signal synchronization of modified Hopf oscillators. For any fixed parameters, the deformation $\Delta\hat{\boldsymbol{v}}_0$ of $\hat{\boldsymbol{v}}_0$ and $\bar{\boldsymbol{v}}_0$ will be a constant, so $\mathbf{G}\{\Delta\hat{\boldsymbol{v}}_0\} \neq 0$. The related $\Delta\hat{\boldsymbol{v}}_s(\bar{\boldsymbol{v}}_0, \Delta\hat{\boldsymbol{v}}_0)$ will be determined by $k(t)\mathbf{G}\{\bar{\boldsymbol{v}}_0\} + k(t)\mathbf{G}\{\Delta\hat{\boldsymbol{v}}_0\}$ and the amplitude is also fixed, so $\mathcal{G}'$ is not equal to 0. Under the influence of $\mathcal{G}'$, modified oscillators signal with synchronization will be different from original signal ($\rho = 0.5$), and the deformation depends on the specific parameters ρ and k. Also, for any parameter $k(t)$ satisfying the stability condition (Pham and Slotine, 2005), $\hat{\boldsymbol{v}}_0$ will have a corresponding stable state.
2. If $\Delta\hat{\boldsymbol{v}}_0 = 0$, $k(t) \neq 0$, thus $\hat{\boldsymbol{v}}_0 = \bar{\boldsymbol{v}}_0$ and $\{\dot{\hat{\boldsymbol{v}}}\} = \{\dot{\bar{\boldsymbol{v}}}_0\}$, it means they are original oscillators signal with synchronization, $k(t)\mathbf{G}\{\bar{\boldsymbol{v}}_0\} + k(t)\mathbf{G}\{\Delta\hat{\boldsymbol{v}}_0\}$ will 0, then $\Delta\hat{\boldsymbol{v}}_s(\bar{\boldsymbol{v}}_0, \Delta\hat{\boldsymbol{v}}_0) = 0$, $\mathcal{G}'$ is equal to $\mathcal{G}$, and suitable $k(t)$ will make it global stable.
3. Usually, in the synchronization, the convergence strength $k(t) \neq 0$. But if $k(t)$ is approaching 0 gradually and the time is long enough for stabilization with a certain value of it, things will be different. We assume that $k_{n+1} < k_n$ for $\forall\, n$, Then, every part of $\mathcal{G}'$ in (21) can be constructed in stable amplitude form[n]

$$\mathcal{H}^n_{\mathcal{G}} = \mathcal{H}^n_{\mathbf{f}} - \mathcal{H}^n_G - \mathcal{H}^n_0 - \mathcal{H}^n_s, \tag{22}$$

$$\mathcal{H}^n_{\mathbf{f}} \propto \left(\mathcal{H}^n_0, \mathcal{H}^n_s\right) \text{ and } \mathcal{H}^n_G = 0. \tag{23}$$

Then,

$$k \to 0 \Rightarrow \mathcal{H}_0, \mathcal{H}_s \to 0 \Rightarrow \mathcal{H}_{\mathbf{f}} \to 0 \Rightarrow \mathcal{H}^n_{\mathcal{G}}. \tag{24}$$

So every change of k will have a new $\mathcal{H}^n_G$ and it will never equal to 0 before stable. It seems very hard to let $\mathcal{H}^n_G \to 0$, since it is hard to know how long it needs to get stable. But if the small deformation of waveform is acceptable, large convergence rate will be achieved. Thus, there is a trade off between convergence rate and final deformation, and the details will be discussed as follows.

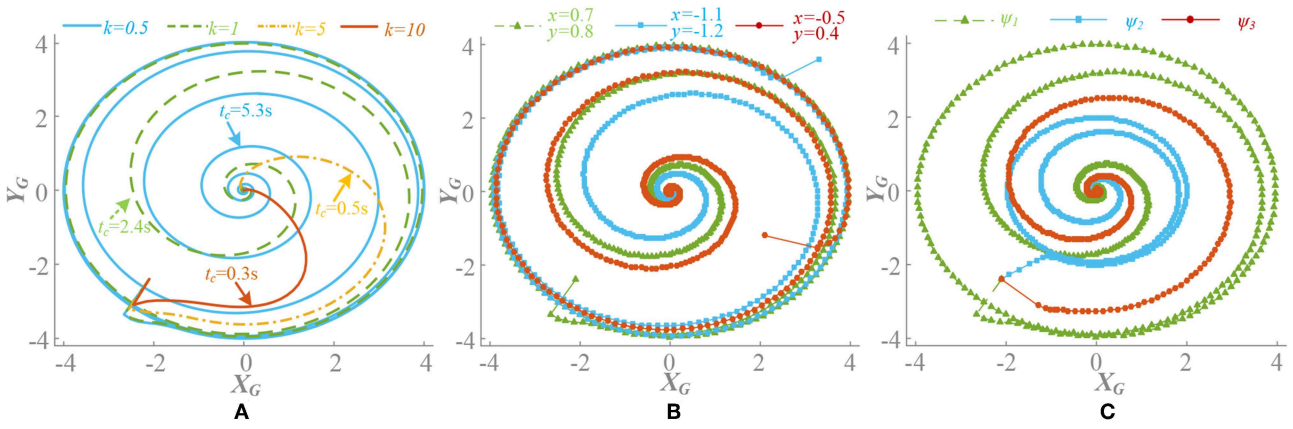

FIGURE 3 | Convergence process of $\mathcal{G}\{G(\bar{v}_0), k(t)\}$with influence of different parameter ($\rho = 0.5$). Signal of limb 1 is selected. **(A)** Different value of k(t), phase factors $\psi_i = \Phi_i/2\pi$, ψ = [0, 0.5, 0.5, 0, 0, 0.5], initial point is (0.7, 0.8). Different k(t) leads a different convergence rate. **(B)** Different initial points (x_0, y_0), k(t) = 1, ψ = [0, 0.5, 0.5, 0, 0, 0.5]. Initial point has little influence on convergence rate, but is important to synchronization process. **(C)** Different phase factors ψ_1 = [0, 0.5, 0.5, 0, 0, 0.5], ψ_2 = [0, 0.5, 0, 0.5, 0, 0.5], ψ_3 = [0.2, 0.4, 0.6, 0.1, 0.9, 0.7]. k(t) = 1, initial point is (0.7, 0.8). A different phase factor means a different synchronization process.

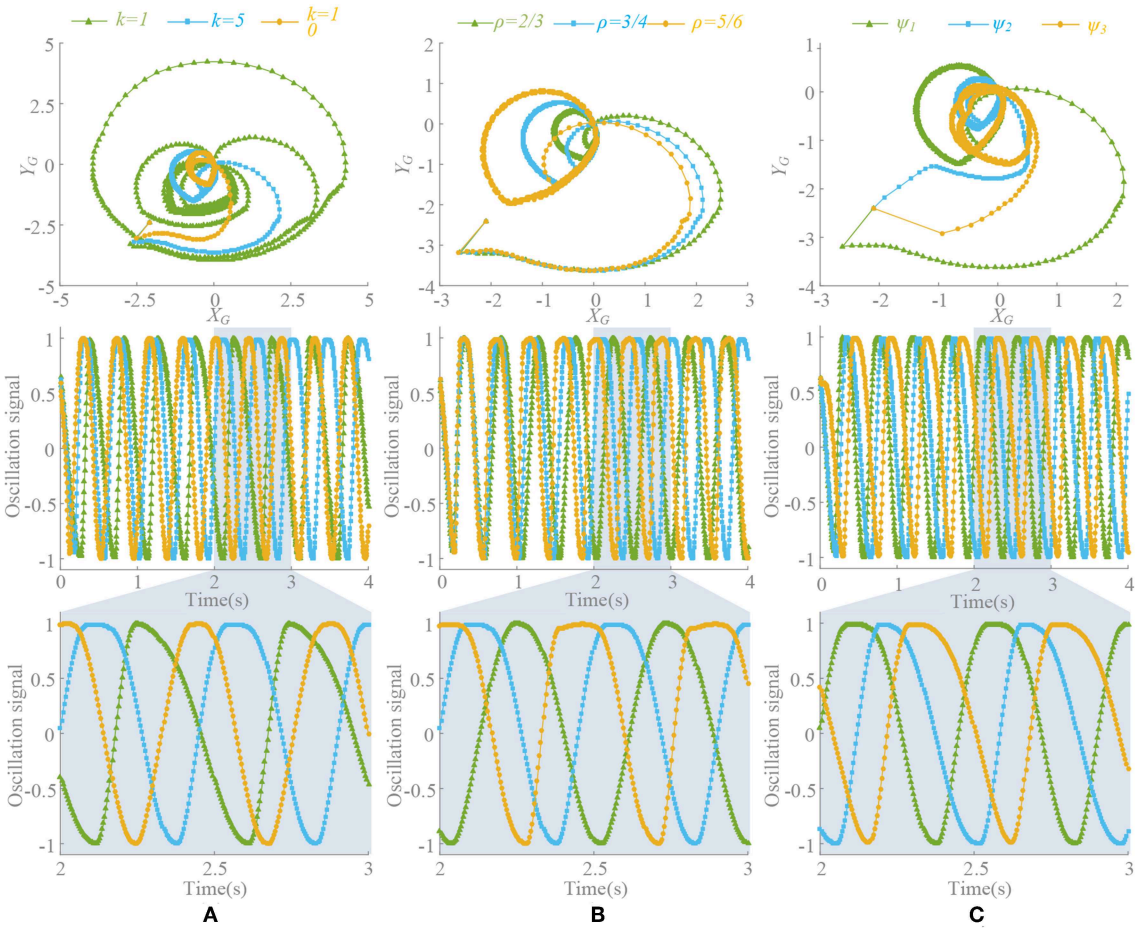

FIGURE 4 | Influence of different parameters with $\rho \neq 0.5$. Signal of limb 1 is selected. **(A)** Different value of k(t), phase factors $\psi_i = \Phi_i/2\pi$, ψ = [0, 0.5, 0.5, 0, 0, 0.5], $\rho = 3/4$ and initial point (0.7, 0.8). Different k(t) leads a different limit circle scale of $G\{\bar{v}_0\}$ and the deformation is directly related to $k(t)G\{\bar{v}_0\}$. **(B)** Different $\boldsymbol{\rho}$ = [2/3, 3/4, 5/6], initial point (0.7, 0.8), and k(t) = 5. Large ρ leads to large deformation. **(C)** Different phase factors ψ_1 = [0, 0.5, 0.5, 0, 0, 0.5], ψ_2 = [0, 0.5, 0, 0.5, 0, 0.5], ψ_3 = [0.2, 0.4, 0.6, 0.1, 0.9, 0.7], k(t) = 5, initial point (0.7, 0.8), and $\rho = 3/4$. Different motion pattern has different limit circle of $G\{\bar{v}_0\}$.

ANALYSIS OF SYNCHRONIZATION

Through the transition state analysis of the synchronization process, k(t) is the only parameter which can be adjusted, which determines the convergence rate and the steady state of the oscillator synchronization. For the original symmetric hopf oscillator, k(t) can be large to meet the requirement of rapid convergence, while for σ-hopf oscillator, whose waveform can be asymmetric, the process will be different and specific analysis is required.

1. When $\rho = 0.5$, there is $\Delta\hat{\boldsymbol{v}}_0 = 0$. k(t) is convergence strength and $\mathcal{G}\{\mathbf{G}(\bar{\boldsymbol{v}}_0), k(t)\}$ converges to zero. The different value of k(t), initial points and phase factors will cause different convergence rates. The convergence process of $\mathcal{G}\{\mathbf{G}(\bar{\boldsymbol{v}}_0), k(t)\}$is shown in **Figure 3**. Generally speaking, on the premise of global stable, the larger k(t) leads to faster convergence rate, as well as motion pattern transformation. If the initial point is designed close to the limit cycle with the concern of synchronization, it also contributes to the fast convergence rate. The phase factors reflect the synchronization relation of the oscillators and determine the phase difference at steady state.
2. When $\rho \neq 0.5$, there is $\Delta\hat{\boldsymbol{v}}_0 \neq 0$. Through the separate adjustment of k, ρ and phase factors, $\mathbf{G}\{\bar{\boldsymbol{v}}_0\}$ whose trend is consistent with $\mathcal{G}'\{\mathbf{G}(\bar{\boldsymbol{v}}_0), k(t)\}$, is analyzed. The different process of approaching to a steady state is shown in **Figure 4**. As in the previous analysis, $k(t)\mathbf{G}\{\bar{\boldsymbol{v}}_0\}$ does not equal 0 in a steady state and it also stabilizes to a non-circular asymmetrical limit cycle, which brings about an asymmetrical oscillation waveform as analyzed by (21). For a certain motion pattern with fixed coupling parameter, only the effects of the k and ρ on the oscillator need to be analyzed. For example, in motion pattern B, the oscillators on the left and right side along the X axial are symmetrical, so taking the oscillator 1 as a representative. The convergence rate, asymmetry rate (the difference between the positive and negative areas, 0 means no difference), period change and duty ratio (the ratio of ascending part in one period cycle, 0.5 represents

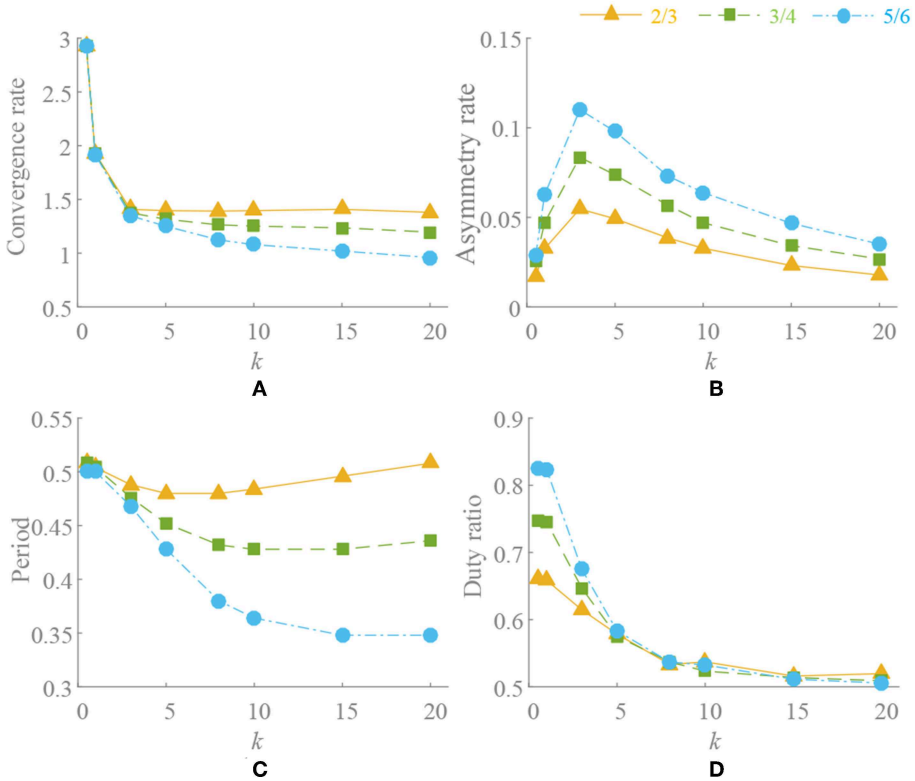

FIGURE 5 | Convergence and deformation of waveform. Oscillation period is set to $T = 0.5$s. $\boldsymbol{k} = [0.5, 1, 3, 5, 8, 10, 15, 20]$, $\boldsymbol{\rho} = [2/3, 3/4, 5/6]$. **(A)** Convergence rate. **(B)** Asymmetry rate. **(C)** Period change. **(D)** Duty ratio.

the symmetry waveform) of the steady-state waveforms with different k and ρ are shown in **Figure 5**. The convergence rate is mainly determined by k. The convergence is very slow in $k < 1$ with almost no distortion, fast in $k = 1$–5 with a little distortion and extremely fast in $k > 5$ with large distortion and period change. After k=10, convergence rate should have been <1 s (steady state is judged by checking the change of peak values in adjacent period). Besides, there are two findings: (1) large ρ value brings about large distortion, as shown in **Figures 4B**, **5B**. (2) In the raise of k value, the waveform tends to be symmetrical (asymmetry rate tends to 0 and the duty ratio tends to 0.5) with period shrinking. That means the entire waveform is changed to be "small" and "smooth," which is much different from expected, as shown in **Figures 4A**, **5C,D**.

Since the value of k(t) determines the convergence rate and the magnitude of the distortion, a function k_e(t) is proposed:

$$k_e(t) = \kappa e^{-\eta\cdot(t-t_0)} \tag{25}$$

in which, η is the descend factor and related to time. κ is the initial strength. t_0 is the begin moment. A little time will be taken for large convergence strength and long for a small value. So, the convergence process is mainly determined by the state of k_e(t) > = 1, then the effective time $T_{effective}$ of convergence can be solved by

$$e^{-\eta\cdot(t-t_0)} \geq 1/\kappa \tag{26}$$

$$T_{effective} = (t - t_0) \geq \ln(\kappa)/\eta\ . \tag{27}$$

Therefore, in the steady state, when $k(t) = 0$, the distortion vanishes and the period recovers to normal. The problem of oscillation deformation caused by the asymmetry factor is solved. However, the adjustment capability of synchronization is not available at this moment. If the phase difference is inaccurate as required before $k(t) = 0$, it cannot be adjusted any more. Therefore, choosing the right parameters to ensure fast and stable convergence is important. It can be seen from the **Figure 6** that κ and η are approximately linearly correlated. According to the finds above, when κ is too large, deformation must not be ignored. Then κ and η are better taking values within [1, 10]. In this paper, $\kappa = \eta = 5$ and the convergence time is 0.32 s. Finally, the σ-Hopf oscillators with synchronization used in the system is

$$\dot{\boldsymbol{v}}_i = \mathbf{f}(\boldsymbol{v}_i, \mu_i, \boldsymbol{\sigma}_i(\rho_i, \lambda, t)) - \kappa e^{-\eta\cdot(t-t_0)}\cdot \sum_{j\in\mathfrak{N}_i}^{n_i} (\boldsymbol{v}_i - \frac{\mu_i}{\mu_j}\mathbf{R}(\Delta\Phi_{ij})\boldsymbol{v}_j) + \mathbf{u}(t) \tag{28}$$

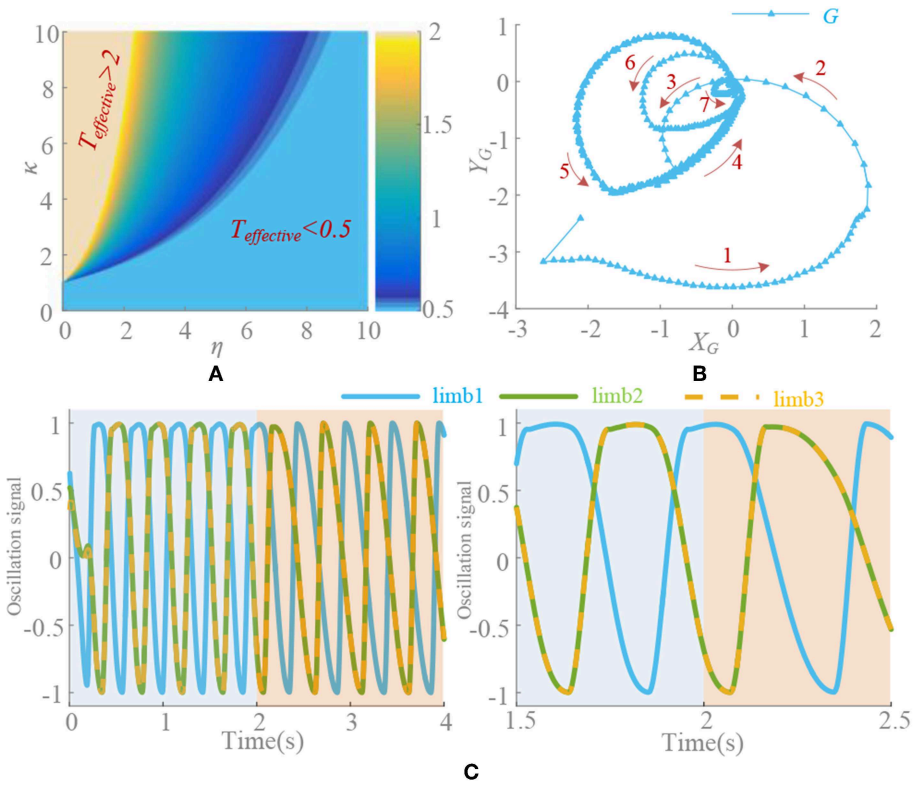

FIGURE 6 | (A) Effective time surface of k_e(t). $T_{effective}$>2s and $T_{effective}$ <0.5s is marked. $T = 0.5$s. **(B)** Convergence process. Red arrow is the direction of limit circle. **(C)** Deformation elimination. k(t) = 5 in 0–2 s and changes to k_e(t) at 2 s ($t_0 = 2$ s). $\rho = 5/6$, $\kappa = \eta = 5$, $t_0 = 2$ s, $\psi = [0, 0.5, 0.5, 0, 0, 0.5]$ and signal of limb 1, 2, and 3 are selected.

in which, the positive scalar κ denotes the coupling gain and can be time-varying for different locomotion, η denotes the descend factor, and t_0 is the start point.

NEUROBIOLOGICALLY INSPIRED CONTROL AND RESULTS

The forward and inverse kinematics of parallel robots is a cumbersome task, and there are a lot of related researches (Merlet and Pmerlet, 2006; Li and Wen, 2011; Huang et al., 2013). So, the presented CPG signal processing and network construction is used for parallel bionic waists in this section. It can effectively avoid complex solving processes and achieve coordinated bionic behavior. But the formation and construction of coupling bionic behavior of such parallel structures is still unknown. The waist is mainly composed of lumbar bones and muscles. It helps the torso to achieve multi-directional bending and axial torsion and transmits (spinal) nerve signals and loads of legs (Hashemirad et al., 2009; Galis et al., 2014). The proposed parallel waist can achieve identical functions, which provide a structural basis for the control strategy. In this paper, four main movements: stretch, lateral shift, pitch and torsion (motion pattern A, B, C, and D) are discussed. In order to prove the effectiveness of the method, the range deviation, motion transformation characteristics, and position error of the waist will be analyzed from the amplitude, phase, and deformation of the oscillation signal, respectively.

Amplitude and Frequency

According to the bionic waist structure and coupling network established in Materials and Method, the phase relationship of the six oscillation signals is shown in **Figure 7A**. These signals will be directly used to drive the limbs of the platform. Due to the problem of multiple solutions in the inverse kinematics of parallel robots (Ahmet and Koksal, 2014), repeat movements occur in the full rotation range of the actuator. That is to say, the different configurations of actuator can result in the same position of the moving platform, so the appropriate range of joint rotation must be selected, which satisfies both the maximum movement space and the requirement of smooth locomotion. Compared to the series structure, it is not so simple to achieve independent movement in the parallel bionic waist, since the movement of a single actuator will cause multiple degrees of freedom of the moving platform. Learning from the forward and inverse kinematics of the parallel robot and the structural characteristics of the bionic waist (see Appendix in **Supplementary Material**), the amplitude and offsets of the oscillation signal are tuned. The control waveform shown in **Figure 7B** is a result of the amplitude and phase adjustment for the range and direction of the locomotion.

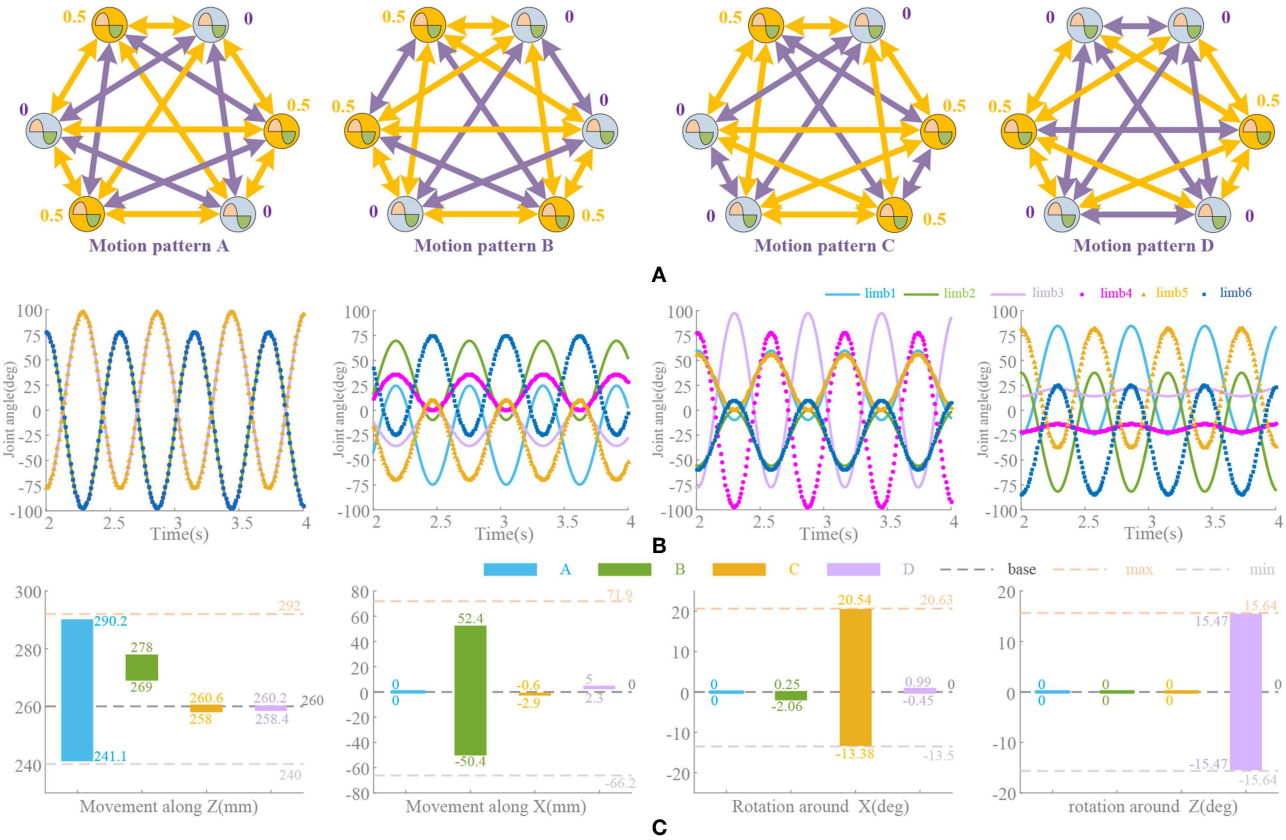

FIGURE 7 | Different motion patterns in different directions. **(A)** Network configuration. Coupling factors are set according to Materials and Method. Yellow arrows link oscillators with 180° phase difference. Phase factors ($\psi_i = \Phi_i/2\pi$) is marked. Purple arrows mean no phase difference. **(B)** Amplitude and offset of oscillation signals. **(C)** Deviations between neurobiologically inspired control and kinematics solution [the forward and inverse kinematics formula and structure parameters are shown in Appendix (**Supplementary Material**)]. Movement along and around axial Y is not taken into consideration for the symmetry of structure and movement.

In order to verify the effectiveness of the motion synthesis, the limit range of movement under CPG based control is compared with that obtained by kinematics solution. The deviations of the main motions are shown in **Figure 7C**. Among them, the actuator range is referenced to the maximum motion position and distributed according to the oscillator waveform (approximate linear distribution). However, the actual parallel platform motion is decomposed into a rotation of 6 actuators with strong non-linear coupling property, which depends on the complexity of motion synthesis, so there are movements in other directions besides the main control directions, i.e., almost every motion pattern will cause movements along axial Z. If the pre-processing module or network is used for non-linear mapping and planning, this phenomenon can be improved and more complicated locomotion can be realized, but in this paper the limbs are directly driven by the oscillation signals at present.

With regard to frequency, most of the motions in quadruped mammals are in low frequencies, and even high-speed running will not carry out in too high frequency. The frequency transition problem has been discussed in detail (Nachstedt et al., 2017). Since the parallel waist frequency does not change too much and has no abrupt change, it will not cause waveform deformation and position deviation. Of course, in order to improve the adaptability, optimization and adaptive methods can be used for frequency adjustment, and there are many methods (Righetti et al., 2006; Nachstedt et al., 2017).

Phase

According to the foregoing illustration, the phase differences in the four typical motions have been determined by the structure and the motion state. In nature, such states in mammals are very easy to transform, i.e., the stretching (motion pattern A) of the torso is easy to transform into a lateral shifting motion (motion pattern B) or a pitching motion (motion pattern C). While the motion pattern D is relatively independent. Generally, it is necessary to return to the initial state before performing other locomotion. According to the symmetric distribution of the actuators ($\Delta_{16} = \Delta_{25} = \Delta_{34} = 180°$), the motion patterns A, B, and C can be simplified to consider the phase difference of the single-sided actuator 1–2–3. According to **Figure 8**, three changes are conducted: A→C, C→B, and A→B. A→C and C→B can be supposed as similar locomotion, since only one group of oscillators needs to change phase, indicating that most of the actuators have similar movements in the two motion patterns.

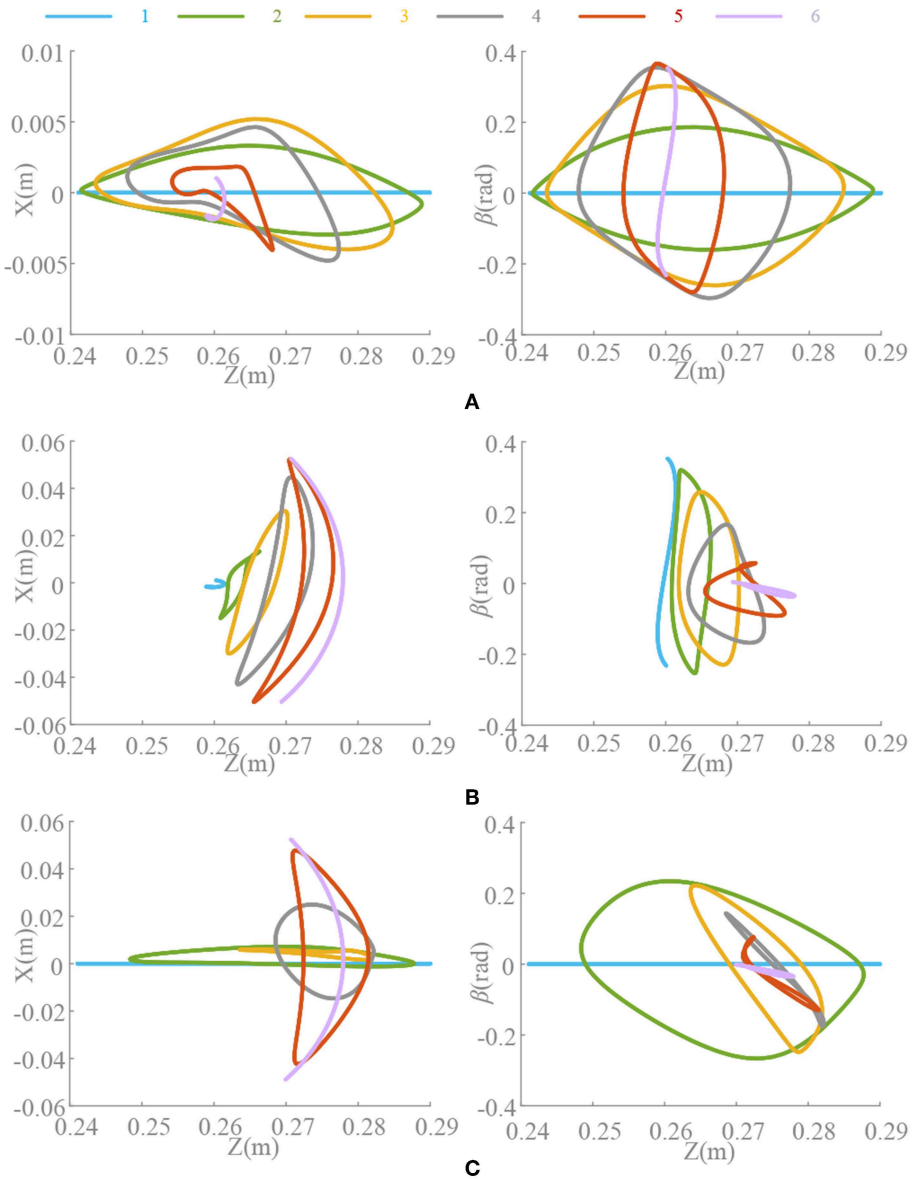

FIGURE 8 | Transformation of different motion patterns. β is the pitch angle round Y. **(A)** Motion pattern A→ motion pattern C. **(B)** Motion pattern C→ motion pattern B. **(C)** Motion pattern A→ motion pattern B. All transformation is conducted in 5 steps. Both phase and amplitude changes linearly.

Therefore, the transformation should be very smooth. But A→B needs to change two sets of oscillators which cannot be a similar motion. If a transformation like A→B is unavoidable, it is best to change through similar motion, such as A→C→B through a bending motion or A→AB→B through a coupling transition. It is recommended to change state between adjacent motion patterns. Otherwise, it will cause large deviation and even malfunction. In the transformation, the oscillation amplitude should be adjusted at the same time, since it is related to both the changing process and result.

CPG-based locomotion control with phase difference adjustment enables fast transformation between motion patterns and formation of several coupling motions. Without a doubt, most of the mammalian movements are a synthesis of simple movements, i.e., the running process is the synthesis of motion pattern A and motion pattern C. In addition, it is worth mentioning that the motion pattern of the parallel waist is not only determined by the phase difference of the oscillator, but also by the amplitude.

Duty Factor ρ

The significance of introducing σ is to make an asymmetrical duty cycle in oscillation, so that the locomotion is more controllable and coordinated, such as the leg swinging of walking robot (Xiong et al., 2017), the wings flapping of flying robot (Briod et al., 2014), and the fin swaying of underwater robots (Wang et al., 2019). But the asymmetry oscillation always brings about deformation of the waveform as well as the period changes,

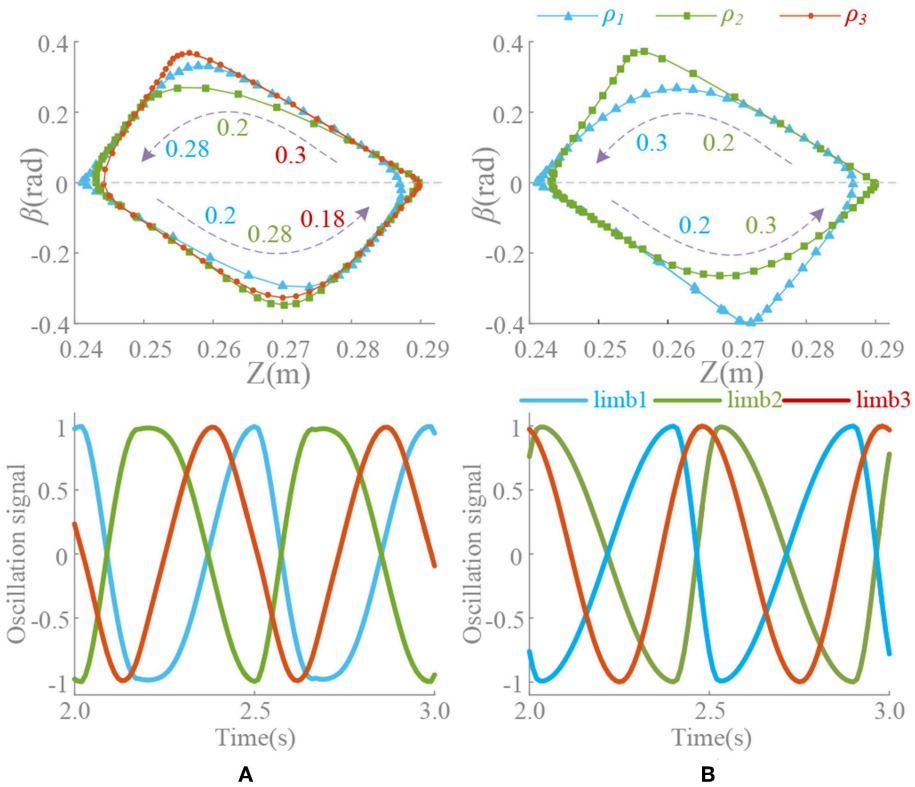

FIGURE 9 | Position trajectory and waveform of coupling motion. $T = 0.5$ s, $\psi = [0, 0.5, 0.2, 0.3, 0, 0.5]$, $\rho_1 = [3/4, 1/4, 0.55, 0.45, 3/4, 1/4]$, $\rho_2 = [1/4, 3/4, 0.45, 0.55, 1/4, 3/4]$, $\rho_3 = [3/4, 1/4, 3/4, 1/4, 3/4, 1/4]$. Forward duration (below zero line) and back duration (above zero line) are influenced by ρ^{limb3}, which is corresponding to limb 3 and Δ_{13}. β is the pitch angle round Y. **(A)** Constant coupling strength, $k(t) = 5$. **(B)** Proposed coupling strength $k(t) = k_e(t)$.

which has been discussed in Materials and Method and Analysis of Synchronization. And we noticed that selection of ρ is also influenced by the phase difference, i.e., in the Z-direction motion, the difference between the oscillator 1 and the oscillator 2 is 180°. Therefore, in order to maintain the consistent action, if the ρ of the oscillator 1 is 3/4, the ρ of the oscillator 2 should be 1/4. Thus, the locomotion coordination can be ensured. So, if the motion transformation is performed, the value of ρ must also be changed correspondingly. A fixed ρ value may not satisfy the phase difference requirement. The coupling motion of motion pattern A and C is analyzed in **Figure 9**. In the transformation from motion pattern A to C ($\Delta_{13} = 0 \rightarrow \Delta_{13} = 0.5$), ρ should do the same change.

During the above motion, the existence $\mathcal{G}'\{\mathbf{G}(\bar{v}_0), k(t)\}$ in the (21) leads an unexpected change on period of oscillation signal in the steady state. Unsuitable ρ will make it worse. ρ^{limb3} keeping unchange ($\rho^{limb3} = 3/4$) through the transformation ($\Delta_{13} = 0.2$) leads an unpredictable forward-back duration ratio shown in **Figure 9A**. This effect cannot be eliminated if k is non-zero, which reduces the control ability of ρ to the waveform. Moreover, the effect or the change is actually difficult to detect or predict. The method of this paper can control the waveforms of each oscillator as well as the ρ and phase difference, so that some special motion points even can control effectively shown in **Figure 9B**. The value of ρ should be adjusted timely according to the phase difference to make the transformation more coordinated and less impact. Furthermore, precise control and smooth motion are to be further improved by optimizing control and learning, evolution and other methods.

SIMULATION

To investigate the effects of neurobiologically inspired control method on bionic parallel waist, we conducted co-simulation by MATLAB/ADAMS. The parameters of the parallel platform are shown in the Appendix (**Supplementary Material**). The control frame is presented in Platform and System and shown in **Figure 1C**. With the bionic control method, control signals for the motor driver are generated by the oscillators and synchronous network. Specifically, we set 3 transition states for magnitude (S_M), phase (S_P), and coupling strength (S_C) to evaluate the performance of the method. Oscillation signals, joint angles, and moving platform locomotion trajectories including movements and rotations are shown in **Figure 10**. Before 2.5 s, the platform performs in motion pattern A, so there are only movements along Z axial. The magnitudes are regulated by

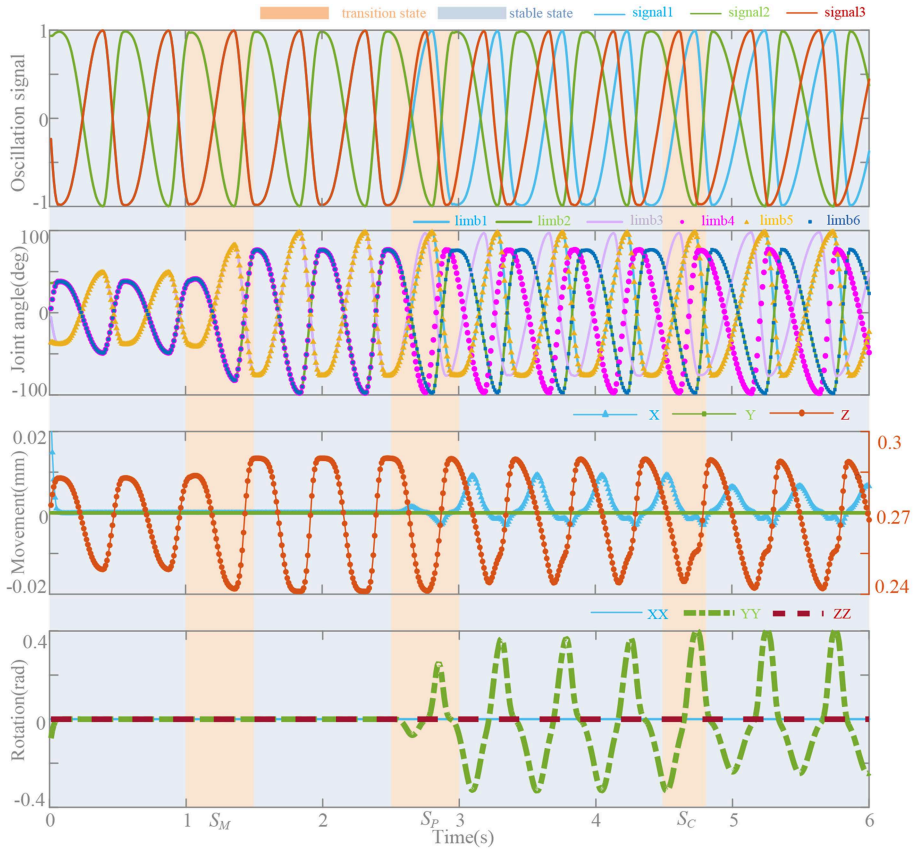

FIGURE 10 | Oscillation signals, joint angles, and locomotion trajectories. $T = 0.5$ s, $k(t) = 5$, $\psi = [0, 0.5, 0, 0.5, 0, 0.5]$, and $\rho = [1/4, 3/4, 1/4, 3/4, 1/4, 3/4]$. Magnitude transition ($S_M$): movement Z (0.25, 0.28 mm)→ (0.241, 0.292 mm). Phase transition (S_P): $\psi \rightarrow [0, 0.5, 0.2, 0.7, 0, 0.5]$. Coupling strength transition (S_C), $k(t) = 5 \rightarrow k(t) = k_e(t)$.

linear transformation in 0.5 s and they make the moving distance change from 0.25–0.28 mm to 0.241–0.292 mm. To perform a bending movement (rotation around Y axial), $\boldsymbol{\psi}$ is gradually set from [0, 0.5, 0, 0.5, 0, 0.5] to [0, 0.5, 0.2, 0.7, 0, 0.5] in 0.5 s from the moment at 2.5 s to regulate the phases of limb 3 and 4. This leads the moving platform to rotate around Y axial and slight movements along X axial. In the coupling strength transition at 4.5 s, coupling strength $k(t) = 5$ turns to $k(t) = k_e(t)$ and signals become stable in 0.32 s according to the effective time surface of k_e(t). The duty factor is set constant as $\rho = [1/4, 3/4, 1/4, 3/4, 1/4, 3/4]$ and the distortion begin to diminish at 3.5 s when $k(t) = k_e(t)$. Influence on the movements and rotations of this factor also can be seen in **Figure 9**.

CONCLUSION

A synchronous bionic control strategy based on σ-Hopf for a bionic parallel waist is proposed. To identify and evaluate waveform distortion of asymmetry σ-Hopf oscillation in synchronization, the transition state is analyzed. The variable coupling strength is raised to eliminate distortion and ensure effective and stable synchronization simultaneously. On this basis, the bionic control network for the parallel waist is constructed to realize the typical behavior. The effects of amplitude, frequency, phase, and duty factor on the behavioral deviation, motion pattern transformation, and forward-back duration adjustment are discussed. The main contributions of this paper are:

1. σ-Hopf oscillator has a symmetrical circular limit cycle and the waveform is regular and stable. Different from other oscillators, its frequency, amplitude, and duty ratio can be adjusted independently, which contribute to the control of different moving speeds, motion range, and forward-back duration. These advantages can enhance behavioral diversity and agility of bionic robot, which is of great significance for bionic control.
2. The waveform characteristics of σ-Hopf oscillator makes the synchronization process more complicated than symmetric oscillator. Our analysis and methods show a way to eliminate the deformation and ensure the fast convergence. Thus, without changing the characteristics of σ-Hopf oscillator, synchronization process is achieved and can be used for the coordinated behavior and coupled locomotion of the multi-joint bionic robot.

3. The σ-Hopf oscillator based neurobiologically inspired control is put forward to enhance the controllability for the bionic waist, which has really strong coupling characteristics. Not only the initial and final state of motion, but also the intermediate state and instantaneous state can be controlled precisely. This will benefit the transition and transformation of the locomotion and makes the coupling motion more flexible.

In this paper we provide a waveform-controllable oscillator and an undistorted synchronization method for the bionic robot, i.e., legged robot, flying robot, and swimming robot, etc. In the future, we will build the entire motion control network of the quadruped robot with bionic waist for coordinated motion. As the network architecture becomes more complex, the proposed method will make more sense for the controllable locomotion and synchronization process.

DATA AVAILABILITY

All datasets generated for this study are included in the manuscript and/or the **Supplementary Files**.

AUTHOR CONTRIBUTIONS

YZ designed the method. YZ, SZ, DG, and QL designed and performed the simulations. YZ and SZ analyzed the data and wrote the paper.

FUNDING

This research was funded by the National Natural Science Foundation of China (No. 51605039), the Thirteenth 5-Year Plan Equipment Pre-research Field Fund (No. 61403120407), the China Postdoctoral Science Foundation (No. 2018T111005 and 2016M592728), Fundamental Research Funds for the Central Universities, CHD (No. 300102259308, 300102258203, and 300102259401).

SUPPLEMENTARY MATERIAL

The Supplementary Material for this article can be found online at: https://www.frontiersin.org/articles/10.3389/fnbot.2019.00059/full#supplementary-material

REFERENCES

Acebron, J., Bonilla, L. L., Pérez-Vicente, C. J., Ritort, F., and Spigler, R. (2005). The Kuramoto model: a simple paradigm for synchronization phenomena. *Rev. Mod. Phys.* 77, 137–185. doi: 10.1103/RevModPhys.77.137

Ahmet, D., and Koksal, E. (2014). Modeling and trajectory tracking control of 6-DOF RSS type parallel manipulator. *Robotica* 32, 643–657. doi: 10.1017/S0263574713000908

Albiez, J., Luksch, T., Dilmann, R., and Berns, K. (2006). "A behaviour network concept for controlling walking machines," in *Adaptive Motion of Animals and Machines*, eds H. Kimura, K. Tsuchiya, A. Ishiguro, and H. Witte (Tokyo: Springer), 237–244. doi: 10.1007/4-431-31381-8_21

Ananthanarayanan, A., Azadi, M., and Kim, S. (2012). Towards a bio-inspired leg design for high-speed running. *Bioinspir Biomim.* 7:046005. doi: 10.1088/1748-3182/7/4/046005

Aoi, S., Katayama, D., Fujiki, S., Tomita, N., Funato, T., Yamashita, T., et al. (2013). A stability-based mechanism for hysteresis in the walk-trot transition in quadruped locomotion. *J. R. Soc. Interface* 10:20120908. doi: 10.1098/rsif.2012.0908

Aoi, S., Yamashita, T., and Tsuchiya, K. (2011). Hysteresis in the gait transition of a quadruped investigated using simple body. *Phys. Rev. E Stat. Nonlin. Soft. Matter. Phys.* 83(6 Pt 1):061909. doi: 10.1103/PhysRevE.83.061909

Arena, P., and Fortuna, L. (2000). Collective behavior in cellular neural networks to model the central pattern generator. *Int. J. Syst. Sci.* 31, 827–841. doi: 10.1080/002077200406561

Arena, P., Fortuna, L., Frasca, M., and Marchese, C. (2001). "Multi-template approach," in *IEEE International Symposium on Circuits and Systems* (Sydney, NSW: IEEE), 37–40. doi: 10.1109/ISCAS.2001.921240

Ashwin, P. (2003). *The Symmetry Perspective: From Equilibrium to Chaos in Phase Space and Physical Space (Progress in Mathematics), Vol. 35.* Basel: Bulletin of the London Mathematical Society, 430–431.

Barasuol, V., Buchli, J., Semini, C., Frigerio, M., Pieri, E. R. D., and Caldwell, D. G. (2013). "A reactive controller framework for quadrupedal locomotion on challenging terrain," in *Proceedings of IEEE International Conference on Robotics and Automation* (Karlsruhe: ICRA), 2554–2561. doi: 10.1109/ICRA.2013.6630926

Bjelonic, M., Kottege, N., and Beckerle, N. P. (2016). "Proprioceptive control of an over-actuated hexapod robot in unstructured terrain," in *IEEE/RSJ International Conference on Intelligent Robots and Systems* (Daejeon: IEEE). doi: 10.1109/IROS.2016.7759321

Briod, A., Kornatowski, P., Zufferey, J., and Floreano, D. (2014). A Collision-resilient Flying Robot. *J. Field Robot.* 31, 496–509. doi: 10.1002/rob.21495

Buchli, J., and Ijspeert, A. J. (2004). "Distributed central pattern generator model for robotics application based on phase sensitivity analysis biologically inspired approaches to advanced information technology," in *First International Workshop* (Lausanne). doi: 10.1007/978-3-540-27835-1_25

Buono, P. L., and Golubitsky, M. (2001). Models of central pattern generators forquadruped locomotion. I. Primary gaits. *J. Math. Biol.* 42, 291–326. doi: 10.1007/s002850000058

Cao, Q., and Poulakakis, I. (2016). Quadrupedal running with a flexible torso: control and speed transitions with sums-of-squares verification. *Art. Life Robot.* 21, 384–392. doi: 10.1007/s10015-016-0330-5

Chung, S. J., and Dorothy, M. (2010). Neurobiologically inspired control of engineered flapping flight. *J. Guidance Control Dyn.* 33, 440–453. doi: 10.2514/1.45311

Cong, M., Liu, D., Du, Y., Wen, H., and Wu, Y. (2011). Application of triune parallel serial robot system for full mission tank training. *Ind. Robot.* 38, 533–544. doi: 10.1108/01439911111154108

Corke, P. I., Peterson, R. A., and Rus, D. (2003). "Networked robots: flying robot navigation using a sensor net," in *Robotics Research. The Eleventh International Symposium* (Siena: ISRR). doi: 10.1007/11008941_25

Coros, S., Karpathy, A., Jones, B., Reveret, L., and Panne, M. (2011). Locomotion skills for simulated quadrupeds. *ACM T GRAPHIC.* 30, 1–12. doi: 10.1145/2010324.1964954.

Dallej, T., Andreff, N., Mezouar, Y., and Martinet, P. (2006). "3D pose visual servoing relieves parallel robot control from joint sensing," in *IEEE/RSJ International Conference on Intelligent Robots and Systems* (Beijing), 4291–4297. doi: 10.1109/IROS.2006.281959

Donati, E., Indiveri, G., and Stefanini, C. (2016). "A novel spiking CPG-based implementation system to control a lamprey robot," in *IEEE International Conference on Biomedical Robotics and Biomechatronics* (Singapore), 1364. doi: 10.1109/BIOROB.2016.7523822

Drazin, P. G. (2008). *Nonlinear Systems (Cambridge Texts in Applied Mathematics).* Cambridge: Cambridge Univ. Press.

Dutra, M. S., De Pina Filho, A. C., and Romano, V. F. (2003). Modeling of a bipedal locomotor using coupled nonlinear oscillators of Van der Pol. *Biol. Cybern*. 88, 286–292. doi: 10.1007/s00422-002-0380-8

Eich, M., Grimminger, F., and Kirchner, F. (2009). Adaptive compliance control of a multi-legged stair-climbing robot based on proprioceptive data. *Industr. Robot* 36, 331–339. doi: 10.1108/01439910910957084

Fukuoka, Y., H., and Kimura, A. H., Cohen (2003). Adaptive dynamic walking of a quadruped robot on irregular terrain based on biological concepts. *Int. J. Robot. Res.* 22, 187–202. doi: 10.1177/0278364903022003004

Galis, F., Carrier, D. R., Van Alphen, J., Mije, S. V. D., Van Dooren, T. J. M., Metz, J., et al. (2014). Fast running restricts evolutionary change of the vertebral column in mammals. *Process Natl Acad Sci U.S.A*. 111, 11401–11406. doi: 10.1073/pnas.1401392111

Gehring, C., Coros, S., Hutler, M., Bellicoso, D., Huter, M., Bellicoso, D., et al. (2016). Practice makes perfect: an optimization-based approach to controlling agile motions for a quadruped robot. *IEEE Robot. Autom. Mag.* 23, 34–43. doi: 10.1109/MRA.2015.2505910

Grillner, S., Wallén, P., Saitoh, K., Kozlov, A., and Robeertson, B. (2007). Neural bases of goal-directed locomotion in vertebrates—an overview. *Brain Res. Rev*. 57, 2–12. doi: 10.1016/j.brainresrev.2007.11.005

Grondin, D. E., and Potvin, J. R. (2009). Effects of trunk muscle fatigue and load timing on spinal responses during sudden hand loading. *J. Electromyogr. Kinesiol*. 19, e237–45. doi: 10.1016/j.jelekin.2008.05.006

Hashemirad, F., Talebian, S., Hatef, B., and Kahlaee, A. H. (2009). The relationship between flexibility and EMG activity pattern of the erector spinae muscles during trunk flexion–extension. *J. Electromyogr. Kinesiol*. 19, 746–753. doi: 10.1016/j.jelekin.2008.02.004

Haynes, G. C., Pusey, J., Knopf, R., Johnson, A. M., and Koditschek, D. (2012). "Laboratory on legs: an architecture for adjustable morphology with legged robots," in *SPIE Defense, Security, and Sensing* (Baltimore, MD: International Society for Optics and Photonics), 786–796. doi: 10.1117/12.920678

He, B., Zhang, P., and Hou, S. (2015). Accuracy analysis of a spherical 3-DOF parallel underactuated robot wrist. *Int. J. Adv. Manuf. Tech*. 79, 395–404. doi: 10.1007/s00170-015-6837-4

Huang, J., Chen, Y., and Zhong, Z. (2013). Udwadia-kalaba approach for parallel manipulator dynamics. *J. Dyn. Syst. Measur. Control*. 135:061003. doi: 10.1115/1.4024600

Hutter, M., Gehring, C., Bloesch, M., Hoepflinger, M., Remy, C. D., and Siegwart, R. (2012). "Starleth a compliant quadrupedal robot for fast, efficient, and versatile locomotion," in *International Conference on Climbing & Walking Robot-Clawar* (Baltimore, MD:), 1–8. doi: 10.1108/01439911311309942

Hutter, M., Gehring, C., Jud, D., Lauber, A., Bellicoso, D., Tsounis, V., et al. (2016). "ANYmal - a highly mobile and dynamic quadrupedal robot," in *IEEE/RSJ International Conference on Intelligent Robots & Systems* (Daejeon), 483–490. doi: 10.1109/IROS.2016.7758092

Hwangbo, J., Lee, J., Dosovitskiy, A., Bellicoso, D., Tsounis, V., Koltun, V., et al. (2019). Learning agile and dynamic motor skills for legged robots. *Sci. Robot*. 4:eaau5872. doi: 10.1126/scirobotics.aau5872

Ijspeert, A. J. (2008). Central pattern generators for locomotion control in animals and robots: a review. *Neural Netw*. 21, 642–653. doi: 10.1016/j.neunet.2008.03.014

Jean-Xavier, C., and Perreault, M. C. (2018). Influence of brain stem on axial and hindlimb spinal locomotor rhythm generating circuits of the neonatal mouse. *Front. Neurosci*. 12:53. doi: 10.3389/fnins.2018.00053

Jin, B., Chen, C., and Li, W. (2013). Power consumption optimization for a hexapod walking robot. *Intell. Robot. Syst.* 71, 195–209. doi: 10.1007/s10846-012-9771-9

Jin, Y., Chanal, H., and Paccot, F. (2014). "Robotics and automation," in *Handbook of Manufacturing Engineering and Technology, Parallel Robot*, ed A. Nee (London: Springer).

Jorgensen, M. J., Marras, W. S., and Gupta, P. (2003). Cross-sectional area of the lumbar back muscles as a function of torso flexion. *Clin. Biomech*. 18, 280–286. doi: 10.1016/s0268-0033(03)00027-5

Kalouche, S., Rollinson, D., and Choset, H. (2015). "Modularity for maximum mobility and manipulation: control of a reconfigurable legged robot with series-elastic actuators," in *IEEE International Symposium on Safety, Security, and Rescue Robotics (SSRR)* (West Lafayette, IN: IEEE). doi: 10.1109/SSRR.2015.7442943

Kato, N., and Kamimura, S. (2008). *Bio-mechanisms of Swimming and Flying Fluid Dynamics, Biomimetic Robots, and Sports Science*. Berlin: Springer.

Khoramshahi, M., Spröwitz, A., Tuleu, A., Ahmadabadi, M. N., and Ljspeert, A. J. (2013). "Benefits of an active spine supported bounding locomotion with a small compliant quadruped robot," in *IEEE International Conference on Robotics and Automation* (Karlsruhe), 3329–3334. doi: 10.1109/ICRA.2013.6631041

Kimura, A., Fukuoka, Y., Konaga, K., Hada, Y., and Takase, K. (2001). "Adaptive dynamic walking of a quadruped robot on irregular terrain using a neural system model," in *Proceedings of IEEE/Rsj International Conference on Intelligent Robots and Systems, Vol. 4* (Maui, HI: IEEE), 2312–2317. doi: 10.1007/3-540-36460-9_10

Kimura, H. Y., Fukuoka, Y., and Hada, Takase, K. (2002). "Three-dimensional adaptive dynamic walking of a quadruped-rolling motion feedback to CPGs controlling pitching motion," in *Proceeding of 2002 IEEE International Conference of Robotics and Automation* (Washington, DC), 2228–2233. doi: 10.1109/ROBOT.2002.1013563

Kopell, N., Ermentrout, G. B., and Williams, T. L. (2006). On chains of oscillators forced at one end: SIAM journal on applied mathematics. *Soc. Industr. Appl. Math*. 51, 1397–1417. doi: 10.2307/2101972

Kuehn, D., Schilling, M., Stark, T., Zenzes, M., and Kirchner, F. (2017). System design and testing of the hominid robot charlie. *J. Field Robot*. 34, 666–703. doi: 10.1002/rob.21662

Li, K., and Wen, R. (2011). "Active vibration isolation of 6-RSS parallel mechanism using integrated force feedback controllor," in *Proceedings of the 2011 Third International Conference on Measuring Technology and Mechatronics Automation* (Shangshai), 314–317. doi: 10.1109/ICMTMA.2011.80

Liu, C., Li, X., Zhang, C., and Chen, Q. (2018a). Multi-layered CPG for adaptive walking of quadruped robots. *J. Bionic. Eng.* 15, 341–355. doi: 10.1007/s42235-018-0026-8

Liu, X., Han, G., Xie, F., Meng, Q., and Zhang, S. (2018b). A novel parameter optimization method for the driving system of high-speed parallel robots. *ASME. J. Mech. Robot*. 10:041010. doi: 10.1115/1.4040028

Macintosh, J. E., Bogduk, N., and Pearcy, M. J. (1993). The effects of flexion on the geometry and actions of the lumbar erector spinae. *SPINE* 18, 884–893. doi: 10.1097/00007632-199306000-00013

Manoonpong, P., Parlitz, U., and Wörgötter, F. (2013). Neural control and adaptive neural forward models for insect-like, energy-efficient, and adaptable locomotion of walking machines. *Front. Neural Circ*. 7:12. doi: 10.3389/fncir.2013.00012

Matsuoka, K. (1985). Sustained oscillations generated by mutually inhibiting neurons with adaptation. *Biol. Cybern*. 52, 367–376. doi: 10.1007/BF00449593

Matsuoka, K. (1987). Mechanism of frequency and pattern control in the neural rhythm generators. *Biol. Cybern*. 56, 345–353.

Merlet, J., and Pmerlet, J. P. (2006). *Parallel Robots (Solid Mechanics and Its Applications), 2nd Edn*. Berlin: Springer. doi: 10.1115/1.2900773

Nachstedt, T., Tetzlaff, C., and Manoonpong, P. (2017). Fast dynamical coupling enhances frequency adaptation of oscillators for robotic locomotion control. *Front. Neurorobot*.11:14. doi: 10.3389/fnbot.2017.00014

Owaki, D., and Ishiguro, A. (2017). A quadruped robot exhibiting spontaneous gait transitions from walking to trotting to galloping. *Sci. Rep*. 7:277. doi: 10.1038/s41598-017-00348-9

Pham, Q. C., and Slotine, J. J. (2005). Stable concurrent synchronization in dynamic system networks. *Neural Netw*. 20, 62–77. doi: 10.1016/j.neunet.2006.07.008

Plitea, N., Lese, D., Pisla, D., and Vaida, C. (2013). Structural design and kinematics of a new parallel reconfigurable robot. *Robot. Com. Int. Manuf*. 29, 219–235. doi: 10.1016/j.rcim.2012.06.001

Raibert, M. H., and Tello, E. R. (1986). Legged robots that balance. *IEEE*. 1, 89–89. doi: 10.1109/MEX.1986.4307016

Ramezani, A., Chung, S. J., and Hutchinson, S. (2017). A biomimetic robotic platform to study flight specializations of bats. *Sci. Robot*. 2:aal2505. doi: 10.1126/scirobotics.aal2505

Rao, D. H., and Kamat, H. V. (1995). "Artificial neural networks for the emulation of human locomotion patterns," in *Conference of the Biomedical Engineering Society of India, in Proceedings of the First Regional Conference IEEE, Vol. 2*, (New Delhi), 80–81. doi: 10.1109/RCEMBS.1995.532167

Righetti, L. (2008). "Pattern generators with sensory feedback for the control of quadruped locomotion," in *IEEE International Conference on Robotics and Automation* (Pasadena, CA: IEEE), 819–824. doi: 10.1109/ROBOT.2008.4543306

Righetti, L., Buchli, J., and Ijspeert, A. J. (2006). Dynamic hebbian learning in adaptive frequency oscillators. *Phys. D Nonlinear Phenomena*. 216, 269–281. doi: 10.1016/j.physd.2006.02.009

Righetti, L., and Ijspeert, A. J. (2006). *Design Methodologies for Central Pattern Generators: An Application to Crawling Humanoids*. Philadelphia, PA: Robotics: Science and Systems Ii, August, University of Pennsylvania, DBLP.

Rossignol, S. (2004). Adaptive mechanisms of spinal locomotion in cats. *Integr. Comp. Biol*. 44, 71–79. doi: 10.1093/icb/44.1.71

Santos, C. P., Alves, N., and Moreno, J. C. (2016). Biped locomotion control through a biomimetic CPG-based controller. *J. Intell. Robot. Syst*. 85, 1–24. doi: 10.1007/s10846-016-0407-3

Satoh, S., and Fujimoto, K. (2018). Gait generation for a biped robot with knees and torso via trajectory learning and state-transition estimation. *Artif Life Robot*. 23, 489–497. doi: 10.1007/s10015-018-0476-4

Schwendner, J., Joyeux, S., and Kirchner, F. (2014). Using embodied data for localization and mapping. *J. Field Robot*. 31, 263–295. doi: 10.1002/rob.21489

Semini, C., Barasuol, V., Goldsmith, J., Frigerio, M., Focchi, M., Gao, Y., et al. (2016). Design of the hydraulically actuated, torque-controlled quadruped robot HyQ2Max. *IEEE/ASME Trans. Mech*. 99, 635–646. doi: 10.1109/TMECH.2016.2616284

Semini, C., Tsagarakis, N. G., Guglielmino, E., Focchi, M., Cannella, F., and Caldwell, D. G. (2011). Design of HyQ - a hydraulically and electrically actuated quadruped robot. *Proc. Inst. Mech. Eng. Part I J. Syst. Control Eng*. 225, 831–849. doi: 10.1177/0959651811402275

Senda, K., and Tanaka, T. (2000). *On Nonlinear Dynamic that Generates Rhythmic Motion with Specific Accuracy*. Montreal, QC: Animals and Machines (AMAM), 8–12.

Seo, K., Chung, S. J., and Slotine, J. J. E. (2010). CPG-based control of a turtle-like underwater vehicle. *Auton. Robot*. 28, 247–269. doi: 10.1007/s10514-009-9169-0

Seok, S., Wang, A., Chuah, M. Y., Otten, D., Lang, J., and Kim, S. (2013). "Design principles for highly efficient quadrupeds and implementation on the MIT Cheetah robot," in *IEEE International Conference on Robotics & Automation* (Karlsruhe), 3307–3312. doi: 10.1109/ICRA.2013.6631038

Staicu, S. (2009). Inverse dynamics of the 3-PRR planar parallel robot. *Robot. Autonom. Syst*. 57, 556–563. doi: 10.1016/j.robot.2008.09.005

Stefanini, C., Orlandi, G., Menciassi, A., Ravier, Y., Spina, G. L., Grillner, S., et al. (2006). "A mechanism for biomimetic actuation in lamprey-like robots," in *IEEE/RAS-EMBS International Conference on Biomedical Robotics and Biomechatronics* (Pisa). doi: 10.1109/BIOROB.2006.1639151

Strogatz, S. H. (2015). Nonlinear dynamics and chaos: with applications to physics, biology, chemistry, and engineering. *Comput. Phys.* 8, 532. doi: 10.1063/1.4823332

Takuma, T., Ikeda, M., and Masuda, T. (2010). "Facilitating multi-modal locomotion in a quadruped robot utilizing passive oscillation of the spine structure," in *International Conference on Intelligent Robots and Systems* (Taipei: IEEE), 4940–4945. doi: 10.1109/IROS.2010.5649134

Van der Pol, B., and Van der Mark, J. (1928). The heartbeat considered as a relaxation oscillation, and an electrical model of the heart. *Philos. Mag.* 6, 763–775. doi: 10.1080/14786441108564652

Villarreal-Cervantes, M. G., Cruz-Villar, C. A., Alvarez-Gallegos, J., and Flores, E. A. P. (2010). Differential evolution techniques for the structure-control design of a five-bar parallel robot. *Eng. Optimiz.* 42, 535–565. doi: 10.1080/03052150903325557

Wang, R., Wang, S., Wang, Y., Tan, M., and Yu, J. (2019). A paradigm for path following control of a ribbon-fin propelled biomimetic underwater vehicle. *IEEE Tran. Syst. Man Cybernet. Syst*. 49, 482–493. doi: 10.1109/TSMC.2017.2705340

Wang, X., Li, M., Wang, P., Guo, W., and Sun, L. (2012). Bio-inspired controller for a robot cheetah with a neural mechanism controlling leg muscles. *J. Bionic. Eng*. 9, 282–293. doi: 10.1016/S1672-6529(11)60120-0

Wang, Y., Xue, X., and Chen, B. (2018). Matsuoka's CPG with desired rhythmic signals for adaptive walking of humanoid robots. *IEEE Trans. Cybernet*. 48, 1–14. doi: 10.1109/TCYB.2018.2870145

Wang, Z., Gao, Q., and Zhao, H. (2016). CPG-inspired locomotion control for a snake robot basing on nonlinear oscillators. *J. Intell. Robot. Syst*. 85, 1–19. doi: 10.1007/s10846-016-0373-9

Wensing, P., Kim, S., and Slotine, J. J. E. (2017). Linear matrix inequalities for physically consistent inertial parameter identification: a statistical perspective on the mass distribution. *IEEE Robot. Autom. Lett*. 3, 60–67. doi: 10.1109/LRA.2017.2729659

Wu, Q. D., Liu, C. J., Zhang, J. Q., and Chen, Q. (2009). Survey of locomotion control of legged robots inspired by biological concept. *Sci. China Ser. F Inform. Sci*. 52, 1715–1792. doi: 10.1007/s11432-.009-0169-7

Xiong, X., Worgotter, F., and Manoonpong, P. (2017). Adaptive and energy efficient walking in a hexapod robot under neuromechanical control and sensorimotor learning. *IEEE Trans. Cybernet*. 46, 2521–2534. doi: 10.1109/TCYB.2015.2479237

Zhang, G., Rong, X., Chai, H., Li, Y., and Li, B. (2016). Torso motion control and toe trajectory generation of a trotting quadruped robot based on virtual model control. *Adv. Robot*. 30, 284–297. doi: 10.1080/01691864.2015.1113889

Zhu, Y., Chen, L., Liu, Q., Qin, R., and Jin, B. (2018a). Omnidirectional jump of a legged robot based on the behavior mechanism of a jumping spider. *Appl. Sci.* 8:51. doi: 10.3390/app8010051

Zhu, Y., and Guo, T. (2016). Galloping trajectory generation of a legged transport robot based on energy consumption optimization. *J. Robot*. 2016, 1–9. doi: 10.1155/2016/9645730

Zhu, Y., Guo, T., Liu, Q., Zhu, Q., Zhao, X., and Jin, B. (2017). Turning and radius deviation correction for a hexapod walking robot based on an ant-inspired sensory strategy. *Sensors* 17:2710. doi: 10.3390/s17122710

Zhu, Y., and Jin, B. (2016). Compliance control of a legged robot based on improved adaptive control: method and experiments. *Int. J. Robot. Autom*. 31, 366–373. doi: 10.2316/Journal.206.2016.5.206-4536

Zhu, Y., Jin, B., and Li, W. (2015). Leg compliance control of a hexapod robot based on improved adaptive control in different environments. *J. Cent. South Univ*. 22, 904–913. doi: 10.1007/s11771-015-2600-0

Zhu, Y., Jin, B., Li, W., and Li, S. (2014). Optimal design of hexapod walking robot leg structure based on energy consumption and workspace. *Trans. Can. Soc. Mech. Eng*. 38, 305–317. doi: 10.1139/tcsme-2014-0022

Zhu, Y., Jin, B., Wu, Y., Guo, T., and Zhao, X. (2016). Trajectory correction and locomotion analysis of a hexapod walking robot with semi-round rigid feet. *Sensors* 16:E1392. doi: 10.3390/s16091392

Zhu, Y., Wu, Y., Liu, Q., Guo, T., Qin, R., and Hui, J. (2018b). A backward control based on σ-Hopf oscillator with decoupled parameters for smooth locomotion of bio-inspired legged robot. *Robot. Auton. Syst*. 106, 165–178. doi: 10.1016/j.robot.2018.05.009

Conflict of Interest Statement: The authors declare that the research was conducted in the absence of any commercial or financial relationships that could be construed as a potential conflict of interest.

frontiers in Neurorobotics

BRIEF RESEARCH REPORT
published: 23 August 2019
doi: 10.3389/fnbot.2019.00066

Decentralized Control Mechanism for Determination of Moving Direction in Brittle Stars With Penta-Radially Symmetric Body

Takeshi Kano[1]*, *Daichi Kanauchi*[1], *Hitoshi Aonuma*[2], *Elizabeth G. Clark*[3] and *Akio Ishiguro*[1]

[1] *Research Institute of Electrical Communication, Tohoku University, Sendai, Japan,* [2] *Research Center of Mathematics for Social Creativity, Research Institute for Electronic Science, Hokkaido University, Sapporo, Japan,* [3] *Department of Geology and Geophysics, Yale University, New Haven, CT, United States*

A brittle star, an echinoderm with penta-radially symmetric body, can make decisions about its moving direction and move adapting to various circumstances despite lacking a central nervous system and instead possessing a rather simple distributed nervous system. In this study, we aimed to elucidate the essential control mechanism underlying the determination of moving direction in brittle stars. Based on behavioral findings on brittle stars whose nervous systems were lesioned in various ways, we propose a phenomenological mathematical model. We demonstrate via simulations that the proposed model can well reproduce the behavioral findings. Our findings not only provide insights into the mechanism for the determination of moving direction in brittle stars, but also help understand the essential mechanism underlying autonomous behaviors of animals. Moreover, they will pave the way for developing fully autonomous robots that can make decisions by themselves and move adaptively under various circumstances.

Keywords: brittle star, decentralized control, autonomous robot, locomotion, determination of moving direction

OPEN ACCESS

Edited by:
Jan-Matthias Braun, University of Southern Denmark, Denmark

Reviewed by:
Malte Schilling, Bielefeld University, Germany
Valery E. Karpov, National Research University Higher School of Economics, Russia

***Correspondence:**
Takeshi Kano
tkano@riec.tohoku.ac.jp

Received: *05 March 2019*
Accepted: *05 August 2019*
Published: *23 August 2019*

Citation:
Kano T, Kanauchi D, Aonuma H, Clark EG and Ishiguro A (2019) Decentralized Control Mechanism for Determination of Moving Direction in Brittle Stars With Penta-Radially Symmetric Body. Front. Neurorobot. 13:66. doi: 10.3389/fnbot.2019.00066

1. INTRODUCTION

Most robots are designed to perform given tasks in predefined environments and lack the ability to autonomously determine and move toward their moving direction while adapting to various unpredictable situations. In contrast, animals can feasibly adapt to the unpredictable real-world and move toward their desired direction. Interestingly, this ability is not unique to higher organisms with sophisticated brains, but is inherent even in primitive living organisms (Meyer et al., 2017). This fact suggests that decisions are not made solely by a central controller, i.e., brain, and that decentralized control plays a significant role in animal locomotion. Many studies have been devoted to elucidate the decentralized control mechanism underlying animals' adaptive locomotion (Kimura et al., 2007; Schilling et al., 2013; Kano et al., 2017a,c), yet they have not succeeded in achieving both autonomous determination of moving direction and adaptation to unpredictable circumstances simultaneously. Clarifying it will help understand the mechanism of autonomous behaviors of animals as well as develop fully autonomous robots that can make decisions by themselves and behave adaptively and reasonably on this basis.

Brittle stars, a group of echinoderms that locomote on the sea floor, are a suitable model for addressing the above-mentioned issue. They have a penta-radially symmetric body in which five arms radiate from the central disc and are capable of moving omni-directionally (**Figure 1**) (Arshavskii et al., 1976b; Astley, 2012; Kano et al., 2012; Watanabe et al., 2012). They lack a central nervous system but instead possess a rather simple distributed nervous system consisting of radial nerves along the arms, which join a circumoral nerve ring at the disc (**Figure 1**) (Cobb and Stubbs, 1981). Despite such a simple nervous system, they can make decisions about their own movement (e.g., to escape from predators or to approach food), and once the decision is made, they locomote by coordinating their arm movements in real time (Arshavskii et al., 1976a,b; Astley, 2012; Matsuzaka et al., 2017; Clark et al., 2019). Moreover, they have outstanding resilience to bodily damage. Even after arbitrary loss of their arms, they promptly determine their moving direction and reorganize the coordination of the remaining arms to resume locomotion (Arshavskii et al., 1976a; Kano et al., 2017b).

It is likely that the moving direction is determined in the circumoral nerve ring by integrating sensory information detected at the arms. However, previous works on the locomotion of brittle stars (Arshavskii et al., 1976a,b; Astley, 2012; Kano et al., 2012, 2017b; Watanabe et al., 2012) did not elucidate the essential mechanism for the determination of moving direction. Recently, we have investigated the role of the circumoral nerve ring in the determination of moving direction through behavioral experiments (Clark et al., 2019). In particular, we observed the locomotion of brittle stars whose circumoral nerve ring was transected at various points. We found that brittle stars tended to move toward the direction opposite to the transected points, and that arms do not coordinate when the neural connection between the arms is lost by the transection. It is expected that these findings impart important insights into the determination of moving direction.

In this study, we propose a mathematical model that explains the behavioral findings on the nerve ring transection to deepen the understanding of the mechanism for the determination of moving direction in brittle star locomotion. In particular, based on our previous model for the adaptive inter-arm coordination of trimmed-arm brittle stars (Kano et al., 2017b), the extended model is proposed wherein the moving direction is modeled phenomenologically with an analogy of water tanks connected by tubes. We demonstrate via simulations that the proposed model well reproduces the results of the behavioral experiments.

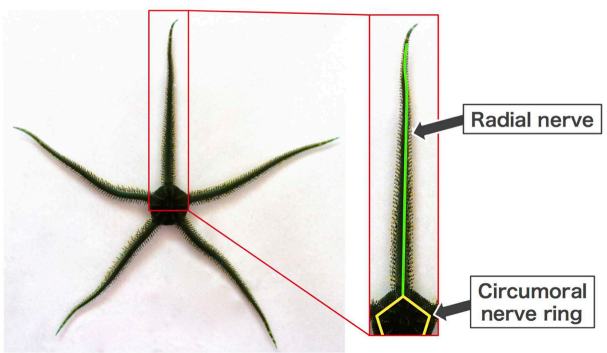

FIGURE 1 | Body and nerve structure of a brittle star (*Ophiarachna incrassata*).

2. BEHAVIORAL FINDINGS

In this section, we present representative results of the behavioral experiments in which the circumoral nerve ring was transected in various ways (Clark et al., 2019). In particular, here we present the following four cases (**Figure 2**):

- Experiment 1. The nerve ring was cut in one place.
- Experiment 2. The nerve ring was cut in two places, with each arm retaining at least one nerve ring connection with an adjacent arm.
- Experiment 3. The nerve ring connection between each arm was cut (i.e., five separations). Moreover, an aversive stimulus was added to one of the arms.
- Experiment 4. The nerve ring was cut in two places but on both sides of the same arm. Moreover, an aversive stimulus was added to one of the neurally connected arms.

Note that in all experiments, we first observed the behavior of intact brittle stars for 10 min. Then, we cut the nerve rings and observed the behavior for a further 10 min. We used potassium chloride (KCL) solution as the aversive stimuli. Detailed procedures and the results of the experiments are provided in the work by Clark et al. (2019).

The results are shown in **Figure 2**. In Experiment 1, brittle stars tended to move in the direction opposite to the point where the nerve ring was cut (**Figure 2A** and **Supplementary Movie 1**). In Experiment 2, the arms connected by the nerve ring tended to coordinate; however, neurally disconnected arms did not tend to coordinate. Namely, it was often observed that the two connected arms coordinated to move in a certain direction, whereas the other three arms coordinated to move in the opposite direction (**Figure 2B** and **Supplementary Movie 2**). In Experiment 3, the arms did not coordinate and, thus, locomotion was not observed. When a stimulus was applied to one of the arms, only the stimulated arm responded whereas the other arms did not respond (**Figure 2C** and **Supplementary Movie 3**). In Experiment 4, the four neurally connected arms coordinated to move away from the stimulus, whereas the neurally isolated arm did not coordinate with the other arms and, thus, did not contribute to locomotion (**Figure 2D** and **Supplementary Movie 4**).

In summary, the following findings were obtained from the above experiments.

1. Brittle stars tend to move to a direction opposite to the point where the nerve ring was cut.
2. Neurally isolated arms cannot coordinate with other arms.
3. Sensory input (i.e., stimulus) is transmitted to neurally connected arms and enables them to coordinate.

Thus, it is likely that neural connection in the nerve ring plays an important role in the determination of moving direction.

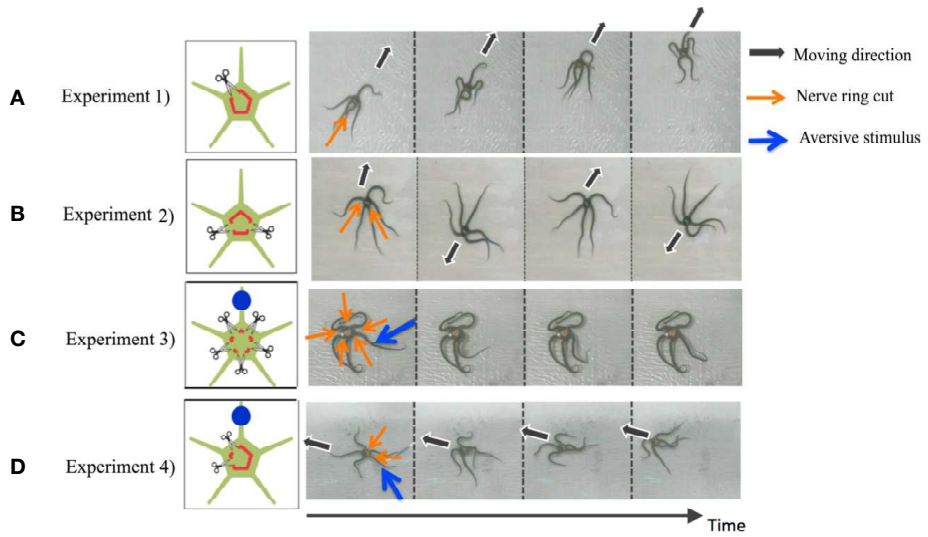

FIGURE 2 | Results of the behavioral experiments: **(A)** Experiment 1, **(B)** Experiment 2, **(C)** Experiment 3, and **(D)** Experiment 4. Points where the nerve ring is cut and points where an aversive stimulus is added are indicated by scissors and blue circles, respectively. In the snapshots, the moving direction, points where the nerve ring is cut, and points where an aversive stimulus is added are indicated by black, orange, and blue arrows, respectively. Except for **(B)**, data was taken from the work by Clark et al. (2019).

3. MODEL

Based on the above findings, we propose a mathematical model. We have previously proposed a decentralized control model for the inter-arm coordination and succeeded in reproducing the locomotion patterns of brittle stars in which several arms were amputated (Kano et al., 2017b). This model was implemented in a brittle star-like robot, and it adapted to physical damages like real brittle stars; thus, it likely captures the essence of brittle star locomotion. However, the moving direction is determined by the central command. Thus, we here modify our previous model so that the moving direction is determined in a self-organized manner at the nerve ring. We review our previous model in section 3.1, and then we propose the modified model in section 3.2.

3.1. Review of Our Previous Work

The schematic of the body system in our previous model (Kano et al., 2017b) is shown in **Figure 3A**. The body consists of a pentagonal central disc and five arms radiating from its vertices. Each arm has only two degrees of freedom, i.e., yaw and pitch joints. Each arm can detect the ground reaction force parallel to the ground. The reaction forces acting on the right- and left-hand sides of the ith arm are denoted by $F_{R,i}$ and $F_{L,i}$, respectively.

It is assumed that the desired moving direction of the center of the body is predetermined and is denoted by the vector $\mathbf{d}$. On this basis, parameters a_i $(i = 1, 2, 3, 4, 5)$ are defined as

$$a_i = \mathbf{r}_i \cdot \mathbf{d}, \tag{1}$$

where $\mathbf{r}_i$ denotes the vector pointing the proximal end of the ith arm from the viewpoint of the center of the disc. Thus, a_i is large when the proximal end of the ith arm is oriented toward the direction of motion from the viewpoint of the center of the central disc (**Figure 3B**).

Using the a_i values, each arm can evaluate whether the detected reaction force assists with propulsion toward the desired moving direction or not. In particular, $U_{R,i}$ and $U_{L,i}$, which are defined as

$$\begin{aligned} U_{R,i} &= \max[a_i - a_{i-1}, 0]F_{R,i}, \\ U_{L,i} &= \max[a_i - a_{i+1}, 0]F_{L,i}, \end{aligned} \tag{2}$$

represent to what extent the detected reaction force from the right/left assists with propulsion toward the desired moving direction, and the ith arm can make the evaluation on the basis of the values of $U_{R,i}$ and $U_{L,i}$. For example, let us consider the case in which the ith arm is oriented toward the moving direction, i.e., $a_{i-1} > a_i > a_{i+1}$ (**Figure 3C**). When the ith arm experiences a reaction force from the left, $U_{L,i}$ is positive and, thus, the reaction force assists with propulsion. Meanwhile, when the ith arm receives a reaction force from the right, $U_{R,i}$ is zero and, thus, the reaction force does not assist with propulsion.

Based on the above, the torque generated at each joint is determined according to the following rule (**Figure 3D**). First, each arm moves randomly to detect the reaction force against the ground (**Figure 3Di**). If the reaction force assists with propulsion toward the desired moving direction, the arm pushes against the ground, i.e., a power stroke begins (**Figure 3Dii**). Then, a recovery stroke begins when the joint angle reaches a certain threshold (**Figures 3Diii,iv**). On the other hand, if the reaction force impedes propulsion toward the desired moving direction, no action is generated (**Figure 3Dv**). Detailed mathematical formulas are provided in the **Appendix** and Kano et al. (2017b)

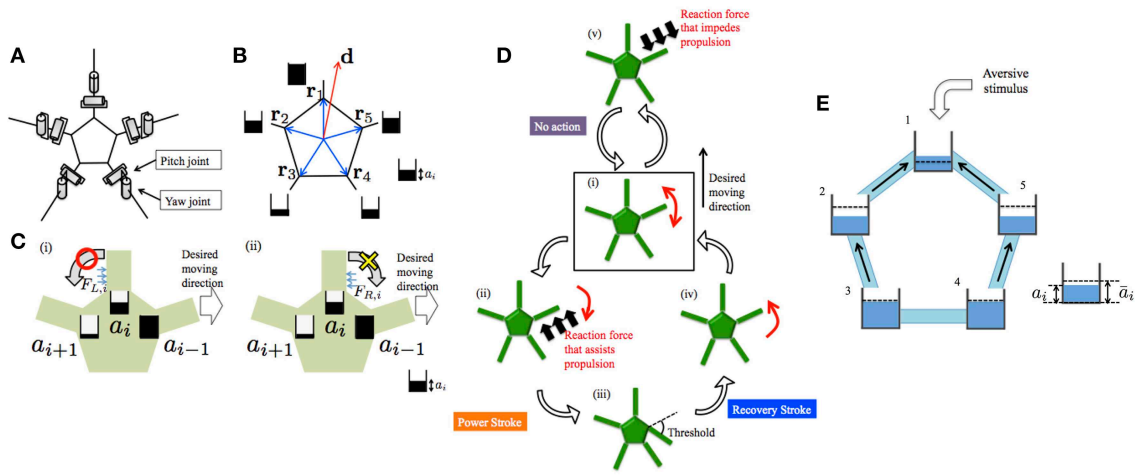

FIGURE 3 | Schematics of the previous model (Kano et al., 2017b) and the proposed model. **(A)** Body system. **(B)** Definitions of **d** and $\mathbf{r}_i$. The a_i values are also shown schematically. **(C)** Evaluation of reaction force from the environment when $a_{i-1} > a_i > a_{i+1}$. **(D)** Outline of the decentralized control mechanism. Detailed explanations are provided in the main text. **(E)** Schematic of the proposed model. Five water tanks are connected by tubes. Water level denotes a_i. Dashed lines denote $\bar{a}_i$. Black arrows indicate water flow. Schematics in **(A,C,D)** were reproduced from Kano et al. (2017b).

3.2. Proposed Model

In the above-mentioned model, a_i is determined by using the predetermined desired moving direction **d** (Equation 1). However, because real brittle stars likely determine their moving direction by integrating sensory information detected at each body part, it is natural to consider that a_i is determined in a self-organized manner. Hence, here we modify the model, focusing on how to control a_i.

Unfortunately, a neurophysiological basis for the determination of a_i is lacking at the present stage. Hence, we model a_i phenomenologically: we control a_i by considering an analogy with water tanks connected with tubes (**Figure 3E**). In this analogy, five water tanks, each of which corresponds to each arm, are located on a plane and they are connected with tubes. The water level of the ith tank represents the value of a_i. The water levels between adjacent tanks tend to decrease because water flows from a tank with higher level to that with lower level; thus, a_i evolves in a diffusive manner. In each tank, water is added or removed so that the water level approaches the target level. The target level increases and decreases when attractant and aversive stimuli are added to the corresponding arm, respectively.

Thus, the time evolution of a_i is described as follows:

$$\tau \dot{a}_i = \bar{a}_i - a_i + D(a_{i-1} + a_{i+1} - 2a_i), \tag{3}$$

where τ is a time constant and D denotes the diffusion coefficient, which is related to the diameter of the tubes in **Figure 3E**. The target water level $\bar{a}_i$ is given by

$$\bar{a}_i = c_0 + s_i, \tag{4}$$

where c_0 is a positive constant and s_i denotes the stimulus applied to the ith arm, which is positive and negative in the case of attractant and aversive stimulus, respectively.

It is assumed in our model that a nerve ring cut corresponds to a tube cut and that water outflows from the cross-section of the cut tube. Thus, in the case of a nerve ring cut at the place between the ith and $(i+1)$th arms, for example, the time evolution of a_i is calculated by replacing a_{i+1} on the right-hand side of Equation (3) with zero.

We note that the definitions of $U_{R,i}$ and $U_{L,i}$ are slightly changed from Equation (2) as follows:

$$\begin{aligned} U_{R,i} &= \tanh\{\kappa_u(\max[a_i - a_{i-1}, 0]F_{R,i})\}, \\ U_{L,i} &= \tanh\{\kappa_u(\max[a_i - a_{i+1}, 0]F_{L,i})\}. \end{aligned} \tag{5}$$

The hyperbolic tangent functions are introduced to make the parameter tuning feasible and to well mimic the behavioral findings, yet this change is not essential for the determination of moving direction.

4. SIMULATION

To validate the proposed model, we performed simulation experiments. Experimental conditions the same as Experiments 1–4 in section 2 were examined. The parameter values, which were determined by trial-and-error, are as follows: $\tau = 0.2$ s, $c_0 = 1.0$, $D = 1.0 \times 10^3$, $\lambda = 2.0\ \mathrm{s}^{-1}$, $\beta_{\mathrm{yaw}} = 2.0$, $\beta_{\mathrm{pitch}} = 30.0$, $\gamma_{\mathrm{yaw}} = 5.0$, $\gamma_{\mathrm{pitch}} = 10.0$, $\kappa_u = 1.0 \times 10^2$, $\gamma_s = 80.0$, $\theta_{th} = \pi/6$ rad. The proportional gains of the yaw and joints are 1.5 and 0.7 kgs^{-2}, respectively, while the derivative gains of the yaw and pitch joints are 0.6 and 0.0 kgs^{-1}, respectively.

The results are shown in **Figure 4**. In Experiment 1, the simulated brittle star tended to move in the direction opposite to the point where the nerve ring was cut (**Figure 4A** and **Supplementary Movie 5**). In Experiment 2, the connected two arms coordinated to move in a certain direction, whereas the other three arms coordinated to move in the opposite direction

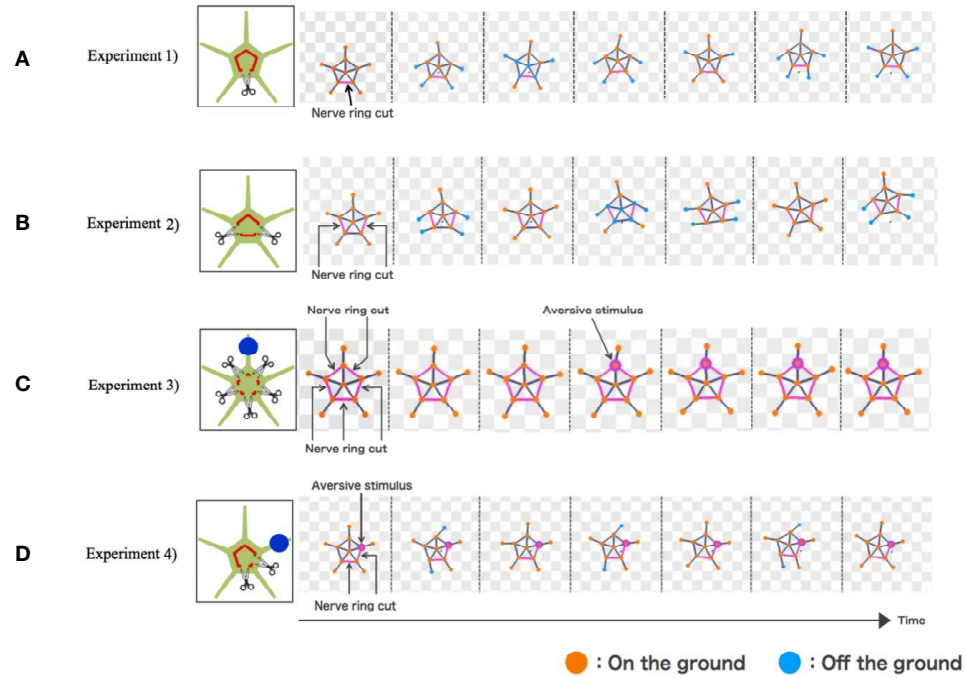

FIGURE 4 | Simulation results: **(A)** Experiment 1, **(B)** Experiment 2, **(C)** Experiment 3, and **(D)** Experiment 4. Points where the nerve ring is cut and points where an aversive stimulus is added are indicated by scissors and blue circles, respectively. In the snapshots, points where the nerve ring is cut are indicated by pink lines. Points where aversive stimuli are added are indicated by pink circles. Mass points are colored orange and blue when they contact with and lift off the ground, respectively.

(**Figure 4B** and **Supplementary Movie 6**). In Experiment 3, the arms did not coordinate and, thus, locomotion was not observed. Locomotion was not initiated even when a stimulus was applied to one of the arms (**Figure 4C** and **Supplementary Movie 7**). In Experiment 4, the four neurally connected arms coordinated to move away from the stimulus, whereas the neurally isolated arm did not coordinate with other arms and, thus, did not contribute to locomotion (**Figure 4D** and **Supplementary Movie 8**). Thus, the behaviors of real brittle stars shown in section 2 were generally well reproduced by the proposed model.

However, there still exists a difference between the simulated and real brittle stars. Each arm of the brittle star in Experiment 3 and the neurally isolated arm in Experiment 4 looked relaxed and did not actively push against the ground (**Figures 2C,D**). Meanwhile, in the simulation, these arms generate torques and actively pushed themselves against the ground (**Figures 4C,D**). This is because the terms $\max[a_i - a_{i-1}]$ and $\max[a_i - a_{i+1}]$ in Equation (5) are always positive for the neutrally isolated arm.

5. CONCLUSION AND FUTURE WORK

In this study, we have focused on a brittle star which can autonomously determine the moving direction and move toward it adaptively under various circumstances by using its primitive distributed nervous system. Based on behavioral findings from the locomotion of brittle stars whose nerve rings were cut in various ways (Clark et al., 2019), we proposed a phenomenological mathematical model in which the direction of movement is determined in a self-organized manner, using an analogy with water tanks connected by tubes. We demonstrated via simulations that the behavioral findings can be well reproduced. Thus, our model likely captures the essence for the determination of moving direction in brittle stars.

We believe that this study imparts deep insights to biologists. While the previous models on animal locomotion (Kimura et al., 2007; Schilling et al., 2013; Kano et al., 2017a,c) focused on adaptation to various circumstances, the proposed model enables autonomous determination of the moving direction as well as adaptation. Thus, it will help understand the mechanism underlying autonomous behaviors of animals. Moreover, from an engineering perspective, the proposed control mechanism will be helpful in designing fully autonomous robots that can determine their moving direction as well as adapt to the circumstances encountered in real time, and it can potentially be used for disaster scenarios.

However, several problems still remain. First, a biological basis for the proposed model is still lacking. In particular, the physical meaning of a_i from a neurophysiological basis is unclear. Second, there still exists a discrepancy between the simulated and real brittle stars. Third, it is still unclear how the control mechanism of brittle star locomotion is related to that of other animals. Further neurophysiological studies and mathematical modeling on this basis are needed in the future. Extension of the proposed model to describe the coupling between the inter- and intra-arm coordination also remains as a future work.

DATA AVAILABILITY

The raw data supporting the conclusions of this manuscript will be made available by the authors, without undue reservation, to any qualified researcher.

AUTHOR CONTRIBUTIONS

TK and AI: contributed the initial conception. TK, DK, HA, and EC: proposed the mathematical model. DK: performed simulations. TK: wrote the manuscript. DK, HA, EC, and AI: contributed to manuscript revision.

FUNDING

This work was supported in part by the Japan Science and Technology Agency, CREST (JPMJCR14D5) and by a Grant-in-Aid for Scientific Research (B) (No. 16KT0099) from the Ministry of Education, Culture, Sports, Science, and Technology (MEXT), Japan.

ACKNOWLEDGMENTS

The authors would like to thank Dr. Akira Fukuhara, Kotaro Yasui, Shura Suzuki, and Taishi Mikami of Tohoku University for their helpful suggestions.

SUPPLEMENTARY MATERIAL

The Supplementary Material for this article can be found online at: https://www.frontiersin.org/articles/10.3389/fnbot.2019.00066/full#supplementary-material

Supplementary Movie 1 | The behavior of a brittle star in Experiment 1.

Supplementary Movie 2 | The behavior of a brittle star in Experiment 2.

Supplementary Movie 3 | The behavior of a brittle star in Experiment 3.

Supplementary Movie 4 | The behavior of a brittle star in Experiment 4.

Supplementary Movie 5 | Simulation result for Experiment 1.

Supplementary Movie 6 | Simulation result for Experiment 2.

Supplementary Movie 7 | Simulation result for Experiment 3.

Supplementary Movie 8 | Simulation result for Experiment 4.

REFERENCES

Arshavskii, Y., Kashin, S., Litvinova, N., Orlovskii, G., and Fel'dman, A. (1976a). Coordination of arm movement during locomotion in ophiurans. *Neurophysiology* 8, 404–410. doi: 10.1007/BF01063603

Arshavskii, Y., Kashin, S., Litvinova, N., Orlovskii, G., and Fel'dman, A. (1976b). Types of locomotion in ophiurans. *Neurophysiology* 8, 398–404. doi: 10.1007/BF01063602

Astley, H. (2012). Getting around when you're round: quantitative analysis of the locomotion of the blunt-spined brittle star, *ophiocoma echinata*. *J. Exp. Biol.* 215, 1923–1929. doi: 10.1242/jeb.068460

Clark, E., Kanauchi, D., Kano, T., Aonuma, H., Briggs, D., and Ishiguro, A. (2019). The function of the ophiuroid nerve ring: how a decentralized nervous system controls coordinated locomotion. *J. Exp. Biol.* 222:jeb192104. doi: 10.1242/jeb.192104

Cobb, J., and Stubbs, T. (1981). The giant neurone system in ophiuroids I. The general morphology of the radial nerve cords and circumoral nerve ring. *Cell Tissue Res.* 219, 197–207. doi: 10.1007/BF00210028

Kano, T., Sakai, K., Yasui, K., Owaki, D., and Ishiguro, A. (2017a). Decentralized control mechanism underlying interlimb coordination of millipedes. *Bioinspir. Biomimet.* 12:036007. doi: 10.1088/1748-3190/aa64a5

Kano, T., Sato, E., Ono, T., Aonuma, H., Matsuzaka, Y., and Ishiguro, A. (2017b). A brittle star-like robot capable of immediately adapting to unexpected physical damage. *R. Soc. Open Sci.* 4:171200. doi: 10.1098/rsos.171200

Kano, T., Suzuki, S., Watanabe, W., and Ishiguro, A. (2012). Ophiuroid robot that self-organizes periodic and non-periodic arm movements. *Bioinspir. Biomimet.* 7:034001. doi: 10.1088/1748-3182/7/3/034001

Kano, T., Yoshizawa, R., and A., I. (2017c). Tegotae-based decentralised control scheme for autonomous gait transition of snake-like robots. *Bioinspir. Biomimet.* 12:046009. doi: 10.1088/1748-3190/aa7725

Kimura, H., Fukuoka, Y., and Cohen, A. (2007). Dynamic walking of a quadruped robot on natural ground based on biological concepts. *Int. J. Robot. Res.* 26, 475–490. doi: 10.1177/0278364907078089

Matsuzaka, Y., Sato, E., Kano, T., Aonuma, H., and Ishiguro, A. (2017). Non-centralized and functionally localized nervous system of ophiuroids: evidence from topical anesthetic experiments. *Biol. Open* 6, 425–438. doi: 10.1242/bio.019836

Meyer, B., Ansorge, C., and Nakagaki, T. (2017). The role of noise in self-organized decision making by the true slime mold *physarum polycephalum*. *PLoS ONE* 12:e0172933. doi: 10.1371/journal.pone.0172933

Schilling, M., Hoinville, T., Schmitz, J., and Cruse, H. (2013). Walknet, a bio-inspired controller for hexapod walking. *Biol. Cybern.* 107, 397–419. doi: 10.1007/s00422-013-0563-5

Watanabe, W., Kano, T., Suzuki, S., and Ishiguro, A. (2012). A decentralized control scheme for orchestrating versatile arm movements in ophiuroid omnidirectional locomotion. *J. R. Soc. Interf.* 7, 102–109. doi: 10.1098/rsif.2011.0317

Conflict of Interest Statement: The authors declare that the research was conducted in the absence of any commercial or financial relationships that could be construed as a potential conflict of interest.

APPENDIX

The joint torque is determined according to proportional-derivative control, and the time evolution of the target joint angles of the *i*th arm is defined as follows:

$$\dot{\Phi}_i = \lambda(\Xi_i + \mathbf{P}_i + \mathbf{R}_i - \Phi_i), \tag{A1}$$

where λ is a positive constant and $\Phi_i = [\phi_{\mathrm{yaw},i}, \phi_{\mathrm{pitch},i}]^{\mathrm{T}}$ with $\phi_{\mathrm{yaw},i}$ and $\phi_{\mathrm{yaw},i}$ being the target angles for the yaw and pitch joints, respectively. Note that the signs of the yaw and pitch joint angles are taken as positive when the arm bends leftward and upward with respect to the central disc, respectively. The vectors Ξ_i, $\mathbf{P}_i$, and $\mathbf{R}_i$ contribute to the generation of the noise, power stroke, and recovery stroke, respectively. Hereafter, we describe mathematical formulas for these terms.

The noise vector Ξ_i is defined as

$$\Xi_i = \begin{bmatrix} \alpha_{\mathrm{yaw}}\xi_{\mathrm{yaw},i} \\ \alpha_{\mathrm{pitch}}\xi_{\mathrm{pitch},i} \end{bmatrix}, \tag{A2}$$

where α_{yaw} and α_{pitch} are positive constants and $\xi_{\mathrm{yaw},i}$ and $\xi_{\mathrm{pitch},i}$ are uniform random numbers in the range $[-1, 1]$, which vary with a fixed interval. It should be noted that the noise is essential because the robot cannot interact with the environment in the absence of the noise. Namely, if the noise is absent, the driving force of the robot does not exist, and the robot cannot detect the reaction force against the ground.

The power stroke vector, $\mathbf{P}_i$ is defined as

$$\mathbf{P}_i = \begin{bmatrix} -\beta_{\mathrm{yaw}}(U_{R,i} - U_{L,i}) \\ -\beta_{\mathrm{pitch}}(U_{R,i} + U_{L,i}) \end{bmatrix}, \tag{A3}$$

where β_{yaw} and β_{pitch} are positive constants, and $U_{R,i}$ and $U_{L,i}$ are defined in Equation (2) in the main text.

The recovery stroke vector $\mathbf{R}_i$ is defined as

$$\mathbf{R}_i = \begin{bmatrix} \gamma_{\mathrm{yaw}}(S_{R,i} - S_{L,i}) \\ \gamma_{\mathrm{pitch}}(S_{R,i} + S_{L,i}) \end{bmatrix}, \tag{A4}$$

where γ_{yaw} and γ_{pitch} are positive constants, and $S_{R,i}$ and $S_{L,i}$ are given by

$$\begin{aligned} S_{R,i} &= \frac{1}{2}[1 + \tanh\{\kappa_s(-\theta_{\mathrm{yaw},i} - \theta_{th})\}], \\ S_{L,i} &= \frac{1}{2}[1 + \tanh\{\kappa_s(\theta_{\mathrm{yaw},i} - \theta_{th})\}], \end{aligned} \tag{A5}$$

where κ_s is a positive constant, and $\theta_{\mathrm{yaw},i}$ is the yaw joint angle of the *i*th arm. When the joint angle reaches the threshold angle θ_{th} or $-\theta_{th}$, $S_{L,i}$ or $S_{R,i}$ increases, respectively; thus, the target joint angle changes, causing the *i*th arm to move in the opposite direction by lifting off from the ground.

In summary, the noise vector Ξ_i is essential for detecting the reaction force against the ground (**Figure 3Di**). The power stroke vector $\mathbf{P}_i$ is **0** unless the *i*th arm detects a reaction force that assists with propulsion; however, $\mathbf{P}_i$ acts in such a way that the *i*th arm can push against the ground when it detects an assistive reaction force (**Figure 3Dii**). The recovery stroke vector $\mathbf{R}_i$ is nearly equal to **0** unless the yaw joint angle of the *i*th arm exceeds the threshold $\pm\theta_{th}$; however, $\mathbf{R}_i$ acts in such a way that the *i*th arm moves itself forward when the yaw joint angle reaches the threshold (**Figures 3Diii,iv**).

frontiers in Neurorobotics

REVIEW
published: 23 October 2019
doi: 10.3389/fnbot.2019.00088

Integrative Biomimetics of Autonomous Hexapedal Locomotion

Volker Dürr[1,2], Paolo P. Arena[3], Holk Cruse[2], Chris J. Dallmann[1,2], Alin Drimus[4], Thierry Hoinville[1,2], Tammo Krause[5], Stefan Mátéfi-Tempfli[4†], Jan Paskarbeit[2], Luca Patanè[3], Mattias Schäffersmann[2], Malte Schilling[2], Josef Schmitz[1,2], Roland Strauss[5], Leslie Theunissen[1,2], Alessandra Vitanza[3†] and Axel Schneider[2,6]*

[1]Department of Biological Cybernetics, Faculty of Biology, Bielefeld University, Bielefeld, Germany, [2]Cognitive Interaction Technology: Center of Excellence, Bielefeld University, Bielefeld, Germany, [3]DIEEI: Dipartimento di Ingegneria Elettrica Elettronica e Informatica, Università degli Studi di Catania, Catania, Italy, [4]Mads Clausen Institute, University of Southern Denmark, Sønderborg, Denmark, [5]Institut für Entwicklungsbiologie und Neurobiologie, Johannes Gutenberg-Universität, Mainz, Germany, [6]Institute of System Dynamics and Mechatronics, Bielefeld University of Applied Sciences, Bielefeld, Germany

OPEN ACCESS

Edited by:
Xiaofeng Xiong,
University of Southern Denmark, Denmark

Reviewed by:
Tjeerd V. Olde Scheper,
Oxford Brookes University, United Kingdom
Yaguang Zhu,
Chang'an University, China

***Correspondence:**
Volker Dürr
volker.duerr@uni-bielefeld.de

†Present address:
Stefan Mátéfi-Tempfli
European Campus Rottal-Inn, Deggendorf Institute of Technology, Pfarrkirchen, Germany
Alessandra Vitanza
Institute of Cognitive Sciences and Technologies (ISTC), National Research Council (CNR), Rome, Italy

Received: 09 July 2019
Accepted: 07 October 2019
Published: 23 October 2019

Citation:
Dürr V, Arena PP, Cruse H, Dallmann CJ, Drimus A, Hoinville T, Krause T, Mátéfi-Tempfli S, Paskarbeit J, Patanè L, Schäffersmann M, Schilling M, Schmitz J, Strauss R, Theunissen L, Vitanza A and Schneider A (2019) Integrative Biomimetics of Autonomous Hexapedal Locomotion. Front. Neurorobot. 13:88. doi: 10.3389/fnbot.2019.00088

Despite substantial advances in many different fields of neurorobotics in general, and biomimetic robots in particular, a key challenge is the integration of concepts: to collate and combine research on disparate and conceptually disjunct research areas in the neurosciences and engineering sciences. We claim that the development of suitable robotic integration platforms is of particular relevance to make such integration of concepts work in practice. Here, we provide an example for a hexapod robotic integration platform for autonomous locomotion. In a sequence of six focus sections dealing with aspects of intelligent, embodied motor control in insects and multipedal robots—ranging from compliant actuation, distributed proprioception and control of multiple legs, the formation of internal representations to the use of an internal body model—we introduce the walking robot HECTOR as a research platform for integrative biomimetics of hexapedal locomotion. Owing to its 18 highly sensorized, compliant actuators, light-weight exoskeleton, distributed and expandable hardware architecture, and an appropriate dynamic simulation framework, HECTOR offers many opportunities to integrate research effort across biomimetics research on actuation, sensory-motor feedback, inter-leg coordination, and cognitive abilities such as motion planning and learning of its own body size.

Keywords: motor control, walking, compliance, leg coordination, proprioception, load sensing, internal model, motor learning

INTRODUCTION

In neurorobotics, animals are more than just a source of inspiration. They also serve as reference systems for many, apparently disparate computational competences such as: (i) reliable, resource-efficient, parallel and/or de-centralized computing in real time; (ii) autonomous, fast and robust decision-making in complex environments; and (iii) flexible coordination and control of many degrees of freedom (e.g., Ijspeert, 2014). To date, research has tended to all of these computational competences of animals, and neurorobotics has seen many successful abstractions and implementations of selected neural mechanisms.

Natural locomotion behavior of multi-legged animals is an example of intelligent interactive behavior where all of the mentioned competences are equally relevant. With regard to bio-inspired walking robots with six or more legs, early research concentrated on mechanical design (e.g., Pfeiffer et al., 1995) and force control (e.g., Devjanin et al., 1983; Schneider et al., 1995). This line of research has been developed further continuously, including bio-inspired approaches to system design such as evolutionary optimization (e.g., Bartsch et al., 2012). Concerning control, the implemented biomimetic approaches may be assigned to one of two major streams.

The first of these streams emphasized the principle of modular sensorimotor control with a focus on sensory feedback (e.g., Pfeiffer et al., 1995; Espenschied et al., 1996; Schneider et al., 2006). In many cases, the sensorimotor control modules were implemented by use of artificial neural networks (e.g., Berns et al., 1994; Schmitz et al., 2008; von Twickel et al., 2012), thus requiring learning prior to operation (e.g., Ilg and Berns, 1995) and/or during operation (e.g., Manoonpong et al., 2008). For example, the performance on difficult terrain can be improved through machine learning techniques (e.g., Bartsch et al., 2012; Goldschmidt et al., 2014).

The second stream of biomimetic approaches emphasized experimental findings on biomechanics and neural oscillators and implemented different forms of rhythmic pattern generators for hopping (e.g., Altendorfer et al., 2001) or walking (e.g., Arena et al., 2012), including highly modular approaches based on mechanical coupling alone (Owaki et al., 2017). A more theoretical approach within this stream of research also succeeded in exploiting chaotic properties of neural oscillatory networks (Steingrube et al., 2010). Both streams of research have at least partially included results derived from behavioral experiments, either by implementing particular motion patterns (e.g., Klaassen et al., 2002) or a continuum of free gaits based on the rules governing inter-leg coordination (e.g., Espenschied et al., 1996; Schmitz et al., 2008), but also theoretically derived criteria (e.g., Fielding and Dunlop, 2004). This plethora of approaches has been reviewed with respect to the mutual benefits of biology and engineering in general (e.g., Ritzmann et al., 2000; Ayers et al., 2002), and adaptive control strategies for multi-legged robots in particular (e.g., Arena and Patanè, 2009; Aoi et al., 2017).

In spite of the remarkable achievements of individual research efforts, the integration of multiple, equally well-developed competences in a single robotic platform is still a challenge. Here, we argue that a key challenge of neurorobotics is the necessity to integrate concepts from different fields of engineering and neuroscience—and the ensuing necessity to have appropriate robotic integration platforms. To illustrate how we envisage such collaborative, multi-competence effort on a single robotic integration platform, we use the hexapedal walking robot HECTOR (**Figure 1**; Schneider et al., 2014; Paskarbeit et al., 2015). As a research platform, HECTOR is special because it offers many opportunities for integrating concepts of neuroscience and engineering alike. It has 18 highly sensorised, compliant actuators, a light-weight exoskeleton (**Figures 1D,E**), and a hardware architecture that is suitable for de-centralized control. Together with a summary of our current understanding of motor flexibility in HECTOR's biological paragon, the stick insect (**Figure 1A**), we provide examples of various aspects of natural motor control. In doing so, we close the loop between multiple embodied sensory systems and compliant actuators by different sensorimotor mechanisms of inter-leg coordination, including cognitive abilities such as motion planning.

The results presented in this article are grouped into six sections, with each section focusing on a different aspect of intelligent adaptive walking systems in biology and technology. Together, these sections provide an integrative view of a biomimetic walking system, ranging from: (I) compliant actuation; (II) distributed proprioception of posture and load; to (III) the particular role of body-substrate interaction; (IV) spatial coordination of multiple legs. Based on these aspects of de-centralized control, we (V) discuss different modular control concepts for adaptive coordination of multiple legs, including the role of internal models in context-dependent coordination of a complex body. Finally, we expand the cognitive repertoire of HECTOR by (VI) a neural network model that can form an internal body-representation for decision-making on the grounds of learned own motor abilities. Each one of the six facets will be introduced by a current view on biological systems and emphasize the behavioral relevance for an animal. This will be complemented by a specific suggestion on how to abstract biological insights and implement at least some of them in a technological framework. Last but not least, each section will point out why the contribution is relevant for an integrative hardware model of multi-legged locomotion and, thus, a holistic view on flexibility and robustness of multi-legged walking in animals and machines.

MUSCLES AND COMPLIANT ACTUATION

All biological locomotion systems are compliant, simply for the fact that biological actuators (i.e., muscles and tendons) are made of deformable macromolecular structures that may drive deformation of tissues or move adjacent limb segments connected by articulated joints. A common view is that muscle-tendon systems in animals are tuned to serve a particular purpose, either in accelerating or decelerating a body part or by transmitting forces efficiently (Dickinson et al., 2000; Alexander, 2003). As such, compliance in biological motion may store and release energy in a passive manner but may also contribute actively to improve movement efficiency. While both passive and active compliance is relevant for resource efficiency, a further benefit of passive compliance is safety in the sense that it allows dissipation of energy, for example during the impact of a foot at touch-down.

Compliance of Muscle

A muscle can be thought of as a force generator that is controlled by the central nervous system (CNS). The forces actively generated by the respective muscles, as well as the resulting torques at the actuated joints, are non-linear functions of the activation and contraction dynamics of muscles

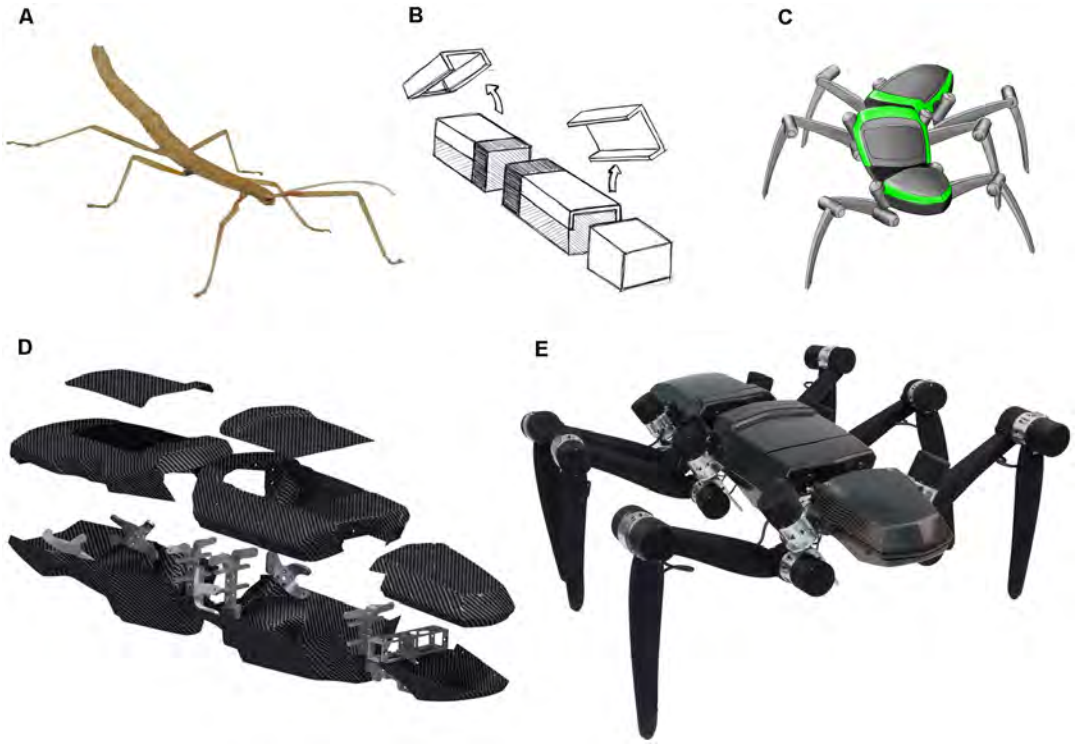

FIGURE 1 | HECTOR—from bio-inspiration to a physical robot. **(A)** The Indian stick insect *Carausius morosus* served as a template for the robot design. Especially, the relative distances of the leg onsets, the alignment of leg joint axes and the subdivision into three body segments were transferred during the design process. **(B)** Early abstraction of the three body segments prothorax, mesothorax and metathorax as compartments for the accommodation of "head-related" sensors, embedded computer system and battery, respectively. **(C)** First design sketch (Folkwang University of the Arts, Essen, Germany) of the hexapod robot considering the general shape demands from panels **(A,B)**. **(D)** 3D-CAD-rendering of the light-weight, self-supporting body segments with an exoskeleton made of carbon fiber composites (manufactured at the Leibniz-Institute of Polymer Research in Dresden, Germany). Only few metal parts are included for directing the leg forces into the housings. **(E)** Photo of HECTOR. The body length of the assembled robot is 95 cm. The total mass is 13 kg. Approximately 7 kg of the mass comes from the 18 compliant joint drives in the legs.

(Zajac, 1989; Zakotnik et al., 2006), as well as of the mechanical integration of the musculotendinous complex into the joint. The activation dynamics represents the time course of the chemical activation processes within muscle fibers (e.g., calcium dynamics). In case of vertebrate muscle, where muscle activation is largely dependent on the number of motoneurons recruited, muscle activation dynamics is typically described by a first-order non-linear differential equation (Zajac, 1989; Buchanan et al., 2004). In insects, where muscles are often innervated by very few motoneurons and single twitches can last very long, higher-order nonlinearities are used (Zakotnik et al., 2006; Wilson et al., 2013; Harischandra et al., 2019). The contraction dynamics represents the influence of muscle length and shortening velocity on the active force generation of a muscle (Hill, 1938; Aubert, 1956; Zajac, 1989; Romero and Alonso, 2016). Activation dynamics and contraction dynamics are assumed to be independent of each other although this has been discussed controversially (Rack and Westbury, 1969). Muscles are connected to segments *via* soft tissue e.g., tendons which also show a non-linear compliant behavior for which different formulations have been proposed (e.g., Hatze, 1974; van Soest and Bobbert, 1993; Thelen, 2003). The mechanical effect of muscle forces onto a joint is further influenced by the dependence of the lever arm length on joint angle, and non-linear damping due to the soft tissue in which the actuator is embedded.

Since muscles can generate active forces in one direction only, joint actuation has to be accomplished at least by an antagonistic pair of muscles in which one of the players can also be replaced by a passive elastic structure. Due to the presence of at least two muscles per joint and due to additional degrees of freedom arising from nervous activation of muscles, the mechanical function of any muscle-tendon system may vary greatly depending on the timing and magnitude of its recruitment (e.g., Sawicki et al., 2015). The level of co-activation of antagonistic muscles allows the regulation of joint stiffness (Hogan, 1984; Gribble et al., 2003; Zakotnik et al., 2006). The mixture of co- and reciprocal activation, for instance, allows an almost separate adjustment of compliance and joint angle, at least in certain intervals of the angular working range (Annunziata et al., 2011; Annunziata and Schneider, 2012).

Therefore, with regard to a particular motor task, the CNS is responsible for controlling not only the movement itself, but also the compliance of the system, particularly for maintaining

stability during interaction tasks that involve impacts or other interaction forces between the body and an external object (e.g., as in manipulation tasks).

Compliance in Biomimetic Actuators

In the technical domain, a variety of damped and undamped compliant actuation systems have been developed that can be subsumed under the term "variable impedance actuators." Recently, Vanderborght et al. (2013) have categorized this family of actuators into "*active impedance by control*," "*inherent compliance*" (passive compliance), "*inherent damping*" and "*inertial*" actuators. Of these, *inherent compliance* and *inherent damping* actuators have the advantage of not requiring any active control of compliance (e.g., by a second actuator for adjusting joint stiffness), at the cost of having a mechanically fixed impedance behavior.

Inherent damping means that a passive visco-elastic element reduces oscillations of the compliant system when mechanically excited, for example in response to a collision with an obstacle. In contrast to *active impedance by control* actuators, passive actuator systems have no bandwidth-limitation of the elastic effect. In order to exploit the advantages of adjustable impedance, passive actuators may be operated in a "hybrid fashion," where compliance can be adjusted by control, as opposed to modification of the mechanical properties. In this way, mechanically passive actuator systems may be used to implement muscle-like actuation (Annunziata and Schneider, 2012), even though muscles are not passive systems. The combination of inherent compliance and inherent damping leads to a well manageable behavior of HECTOR's joint drives. However, it must be stressed that the control of compliant structures with high dynamic bandwidth, in general, is challenging. Solution approaches contain passivity based impedance control (Albu-Schäffer et al., 2007), classical impedance control (Hogan, 1985) or hybrid impedance control (Anderson and Spong, 1988).

The Compliant Joint Drives of HECTOR

The ability of physical interaction with the environment is a key feature of animal locomotion, involving repeated impacts of the feet on the ground, mechanical coupling of a variable number of legs through body and substrate and, as a consequence, discontinuous changes of force- and torque interactions among the individual joint actuators. The manifold of mechanosensory information arising through these bodily interactions is a foundation for sensory, (event)-driven walking controllers such as Walknet (as originally described by Cruse et al., 1995, see below). For the control of mechanical interaction of body and substrate, a reliable estimate of joint torques during resisted actuation is desirable. Much like the force estimate of isometric muscle contractions requires the combination of Golgi tendon organs and the compliant tendon, here, the combination of a sensor and the serial elasticity of the compliant actuator is needed.

The compliant actuators of HECTOR belong to the *inherent compliance* category: they use an elastomer coupling as the compliant element. Because the elastomer has visco-elastic properties, it introduces an *inherent damping* component into the actuator, too, other than a set of steel springs would do. **Figure 2A** shows a sectional view of the fully integrated, compact and compliant drive system which is used in each one of the 18 leg joints of HECTOR. **Figure 2B** shows a photo of the drive. The weight of each drive is below 0.4 kg. As a result, about 55% (7.2 kg) of the robot's total weight (13.0 kg) is constituted by its joint actuators. The drive includes small-scale electronics, integrated as a PCB stack (**Figure 2F**). The PCB stack contains power-, communication- and control-electronics. It is software-controlled by an integrated 8-bit microcontroller. The core of the actuator is a brush-less DC motor, driving a light-weight harmonic drive gearbox. The short installation length of motor and gearbox allows for the small dimensions of the entire system (length ∼90 mm, diameter ∼50 mm). Motor and gearbox are followed by an elastomer coupling (**Figures 2C–E**), making it a serial elastic actuator (Pratt and Williamson, 1995). The main reason for favoring an elastomer coupling over a steel spring coupling was the fact that it can be scaled down to a diameter of 20 mm, allowing for compact integration (**Figure 2D**). The input flange with its hub is attached to the output of the gearbox. The output flange of the coupling with its hub is mechanically connected to the output of the joint. The torsion between input and output hub is mediated by two sets of three teeth (photo in **Figure 2E**), gearing into the six lobes of the elastomer star. The elastomer star was used as an inlay, i.e., not bonded to the metal teeth of the hubs. In principle, it can be bonded to the teeth as well. For torsion measurements at the elastomer coupling, it is equipped with a magnet and Hall sensor ensemble. A second one of these ensembles measures the output angle of the drive. A characterization of the non-linear behavior of the compliant element as well as a suitable fit function for a system model can be found in Paskarbeit et al. (2013).

DISTRIBUTED PROPRIOCEPTION OF POSTURE AND LOAD

All animals physically interact with their environment, as any overt behavior requires the generation of force: force to accelerate the own body's center of mass (locomotion), force to deform or displace external structures (manipulation), and force to accelerate a limb in order to generate or acquire information through limb movement (signaling and active sensing). As a consequence, the control of force is a fundamental requirement of purposeful, interactive behavior. The sensory modality involved is proprioception, the mechanoreception of force and posture (for review, see Tuthill and Azim, 2018). Two hallmarks of proprioception are: (i) the intimate relationship between the process of sensory transduction and the biomechanics of the surrounding body tissue; and (ii) its distributed nature, i.e., the fact that each and every body part is equipped with different mechanoreceptors. The combination of these two aspects implies that the entire body of an animal essentially serves as one complex proprioceptive organ. In the following section, we will review some general aspects of distributed proprioception in insects, with a focus on load sensing in

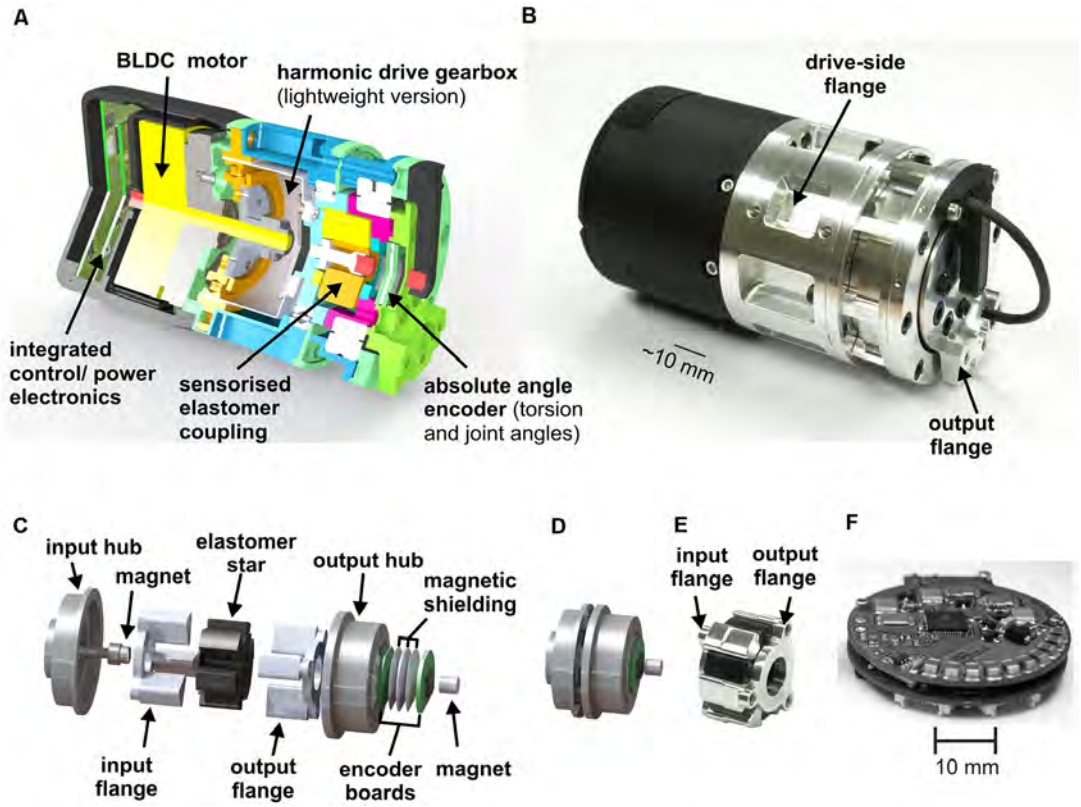

FIGURE 2 | Compliant joint drive with elastomer coupling. **(A)** The section view of an elastic joint drive of HECTOR. It contains a power- and control-electronics stack, a brushless DC motor, a light-weight harmonic drive gearbox, and a sensorised elastomer coupling with two position encoders. **(B)** Photographic depiction of the elastic joint drive with mounting points for adjacent segments. Stable force transmission is achieved by the positive locking of segment and seating (input flange and output flange). **(C)** Explosion view of the coupling shown in panel **(D)**. The input flange is linked to the output of the gearbox. It connects to the input hub that carries three teeth, each of which extends into a corresponding notch of the elastomer. The remaining three notches in the elastomer are held by the three teeth of the output hub which, in turn, is fixed to the output flange. The elastic torsion of the elastomer and the resulting twist between input and output hubs is measured by a Hall-effect position sensor (after Paskarbeit et al., 2013, with permission). **(D)** View of the elastomer coupling, as integrated into the drive. **(E)** Photo of input and output flange, together with elastomer star. **(F)** Image of the power- and control-electronics stack which is mounted in the back of the drive (after Paskarbeit et al., 2013, with permission).

locomotion. In conjunction with these considerations, we will explain the concept of distributed proprioception in HECTOR.

Distributed Proprioception in Insects

Taking an evolutionary view, most insect mechanoreceptors are derived from ciliated epithelium tissue. As such, they are either embedded within or immediately attached to the cuticle of the exoskeleton. As the cuticle covers the entire insect body, cuticular mechanoreceptors may be found on all body segments, with particularly high density on legs, wings and feelers. The basic type of these epithelial mechanoreceptors is a tactile hair that is innervated by a single mechanosensory cell (*Sensillum chaeticum*). Groups of such tactile hairs are often located near the joints, forming patches or rows of hairs that may get deflected during movement of the adjacent joint. These hair plates serve as joint angle sensors (**Figure 3C**). A more derived version of epithelial mechanoreceptor is the *Sensillum campaniformium*, in which only a small cap- or dome-shaped structure can be seen externally. Like hairs, they typically come in groups, as indicated by the yellow, magenta and purple circles in **Figure 3C**. Campaniform sensilla (CS) are located at strategic locations for monitoring strains in the exoskeleton, usually near the joint at the base of a segment, where skeletal strain may be immediately related to a load imposed to the end of the segment. For example, at the base of the leg, cuticular strains can arise due to: (i) self-generated forces and torques (contraction of proximal leg muscles); (ii) constant body load; (iii) shifts in body load due to altered body orientation and/or slipping of legs; and (vi) externally applied loads. Indeed, the structure that is of particular relevance to load sensing in insects is the trochanter, a short leg segment that, in many insects, is firmly attached to the base of the femur, i.e., the first long leg segment (**Figures 3A,C**). The trochanter carries a number of proprioceptive organs that signal load and positional information. For example, **Figure 3C** shows a posture-encoding hair plate (white circle) and three groups of load-encoding CS groups (colored circles).

Because coxa-trochanter (CTr) and femur-tibia joints are hinge joints with nearly parallel joint axes, they cause the leg

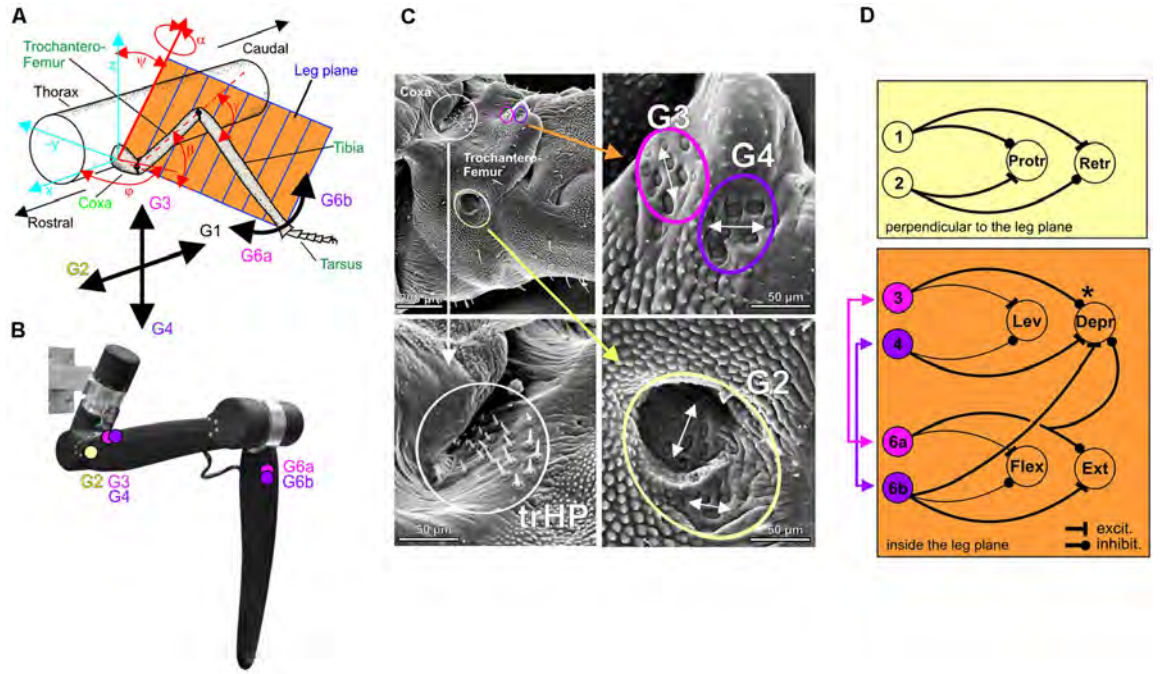

FIGURE 3 | Distributed proprioception in the insect walking system. **(A)** Schematic of the reference frame for force detection by campaniform sensilla (CS) of an insect leg. For a given axis orientation (Φ, Ψ) and joint angle (α) of the thorax-coxa joint, all other leg joints move the leg within the leg plane (orange). The black arrows indicate the directional selectivity of four trochanteral CS groups (G1 to G4) and two tibial CS groups (G6a and G6b) in the stick insect. Owing to their location on the leg and to their physiology, four of these groups signal loading and unloading either within (G3, G4, G6a, G6b) or orthogonal (G1, G2) to the plane of leg movement. For example, G1 responds strongest to posteriorly directed forces. **(B)** Analogous sites for biomimetic strain measurements on the leg of HECTOR. **(C)** Scanning electron micrograph of the trochanter of a stick insect hind leg, with three enlarged sections showing the dorsal trochanteral hair plate (trHP, white circle), and trochanteral CS groups G2 (yellow), G3 (magenta) and G4 (purple). White double-arrows indicate the different preferred strain direction of each sensilla group. **(D)** Putative wiring diagram of known reflex loops involving trochanteral and tibial CS in a standing stick insect, indicating target and sign of the sensory-motor couplings mediated by individual CS groups. Thick lines represent verified sensory-motor couplings, thin lines are presumed on the basis of cursory observations. The schematic motor neuron pools are arranged according to their actions on joints either within the leg plane of movement (orange: levator/depressor system of the Coxa-Trochanter (CTr) joint and flexor/extensor system of the femur-tibia joint) or perpendicular to this plane (yellow: protractor/retractor system). Note that the excitatory connection from tibial CS group G6b to the depressor of the trochantero-femur establishes a muscle synergy through inter-joint coupling within the leg plane. The asterisk at the inhibitory connection of CS group G3 to the depressor indicates that a sign reversal is known to occur during walking.

to move in a plane (see **Figure 3A**). The high density of CS groups on the trochanter ensures that loads are monitored at the proximal end of this leg plane, where force magnitudes are largest and, hence, resolution is maximal. The CS groups not only reliably encode magnitude and rate of change of force increments and decrements (e.g., Zill et al., 2011), their exact location and orientation in the exoskeleton also make them directionally selective. For example, CS groups G3/G4 are most sensitive to loads applied within the joint plane, whereas CS groups G1/G2 are most sensitive to loads applied perpendicularly to the leg plane. Other CS groups, e.g., G6a/G6b on the base of the tibia, supply further information about loads applied within the leg plane (**Figures 3A,C**). The tuning curves of these CS groups thus constitute a reference frame of load encoding that is aligned with the movement plane of the leg (Zill et al., 2012).

Owing to this alignment, the reference frame of load encoding is also congruent with the actions of the leg muscles. For example, protractor/retractor muscles of the thorax-coxa joint will cause actions that impose loads in the direction perpendicular to the leg plane. This is monitored by CS groups G1 and G2. Indeed, our current knowledge of the local reflex circuitry in walking legs suggests that each CS group affects the activity of those muscles that may alter their own sensory reading (**Figure 3D**). For example, activation of individual G4 receptors in a quiescent stick insect induces depressor activity, whereas activation of G3 receptors reduces the activity of that same muscle. In both cases, the resulting change in muscle activity resulted in force changes driving leg movement within the leg plane (for more details on CS activity and muscle synergies, see Zill et al., 2015, 2017).

Whereas this framework of distributed reflexes stabilizes the posture of a standing animal against perturbation, the situation becomes more complicated during locomotion. This is because the reflex effects of a given CS group may reverse during active motion. This is reminiscent of a force enhancement mechanism known from vertebrates (Prochazka et al., 1997a,b; Donelan and Pearson, 2004), where afferences from Golgi tendon organs are involved in a positive force feedback loop. The state-dependent reversal of the motor effects of CS groups G1/G2 on the protractor/retractor muscle

system in stick insects suggests a similar mechanism in insect locomotion (Akay et al., 2007; for a similar effect on G3/G4, see Zill et al., 2012).

Figure 3D summarizes the motor effects of load sensors distributed on a stick insect leg. Note that connections indicate the target and sign of a reflex, not necessarily an identified monosynaptic neural connection. In a standing animal, this circuitry constitutes a set of negative feedback loops that may serve to limit excessive forces (Schmitz, 1993; Haberkorn et al., 2019). For example, combined excitement of CS groups G3 and G6a (magenta combination in **Figure 3D**) might be caused by large depressor forces, acting to push the leg downwards and outwards. The joint inhibition of extensor and depressor muscle activity will reduce the strain sensed by these CS groups on both the femur and the tibia. In active animals, the sign of at least some reflex actions may reverse (e.g., marked by asterisks in **Figure 3D**). In this case, a depressor force will lead to further enhancement of depressor force, thus forming a positive force feedback loop. This may aid sustaining the body weight during walking.

Distributed Proprioception in HECTOR

Given our current knowledge on distributed proprioception in insects and its relevance for adaptive coordination of multiple joints and legs, it is compelling to transfer some of its principles to technical walking machines. Structurally, the carbon-fiber-enhanced, light-weight exoskeleton of HECTOR is well-suited to be equipped with mechanoreceptors at various locations. For example, the principles of distributed load sensing in an insect leg may be mimicked by corresponding pairs of strain gauges placed at the locations indicated in **Figure 3B**. The matched pairs of loading/unloading-sensitive CS groups, e.g., G6a/G6b (Zill et al., 2011), could be abstracted by a pair of corresponding strain gauges on opposite sides of the same leg segment. This has been done for a single leg of HECTOR as indicated in **Figure 4A**. All strain gauge pairs are connected to a strain gauge board (**Figure 4B**) which communicates the strain information *via* the bus system of HECTOR (see below). **Figure 4C** shows a close-up of the α- and β-pair glued to the carbon fiber rod of the femur.

Figures 4D,E compare the α-torsion of the elastomer coupling in the α-joint drive with the output of the respective α-pair of strain gauges (**D**) and the β-torsion of the elastomer coupling in the β-joint drive with the output of the β-pair of strain gauges (**E**). Results show representative measurements for a single step of the leg which was mounted to a frame that allowed passive sliding of the leg base in the upward and forward direction during stance (gray areas in **Figures 4D,E**). The results show that both information sources, joint torsion and segmental strain, are analogous to each other but show different temporal response components due to different material properties of the measurement substrate (nitrile rubber in the elastomer coupling; carbon fiber rod at the femur). Strain gauges, however, potentially allow the measurement of strain also in directions which are not picked up by the elastomer couplings.

Irrespective of whether load distribution among legs is measured inside the joint drives or *via* bending forces, several sensor elements need to be read out simultaneously, or at least with similar data acquisition rates. In insects, this requirement is met by the distributed organization of the CNS, where most afferents from sensory organs of a given segment project into the specific ganglion of that body segment. For example, all afferents from trichoid hairs or CS on a middle leg project to the ganglion of the mesothorax. Since each segmental ganglion can be considered a stage of local information processing, including the circuitry for generating motor commands, sensory-motor control is highly distributed and de-centralized (see also "Modularity of Insect Motor Control" section).

In a robot with multiple limbs, a de-centralized control concept could be implemented in different ways: one extreme would be to assemble a network of multiple de-centralized hardware modules; another extreme would be the use of a single central processing unit running several separate but interacting software modules. In the case of HECTOR, a mix of these concepts has been implemented: a large number of sensors is read out by a set of only three bus master boards, each representing the information node in one body segment (a fourth bus master was integrated for later communication with the body segment drives). At the same time, a single central controller, located in the mesothorax, receives all sensory information from the bus masters and emulates the distributed control network in software. As shown in **Figure 5**, HECTOR's main body consists of three segments, each of which carries two legs. The three compliant actuators per leg contain their own controller electronics (**Figure 2F**), including local sensors of various kinds (see leg details in **Figure 5**). Using a custom communication protocol that is based on an RS-485 interface in the hardware layer, the wiring in the legs can be reduced considerably (for details, see Schneider et al., 2012). The *BioFlex* bus master connects both legs of that body segment, including all its sensors and actuators, with the central controller. At present, the sensory equipment of each joint of HECTOR comprises eight different sensor types, supplying a total of 12 measurements per joint. These include the joint angle, the torsion of the integrated elastomer coupling, 3D-acceleration and orientation vectors, etc. (see leg details in **Figure 5**). Potentially, the central controller can thus exploit 216 measurements from the 18 leg joint drives alone, not including strain gauges (**Figure 4**), foot tip sensors (see "Multi-Taxel Touch Sensor for HECTOR Foot" section), vision or touch (see Hoinville et al., 2014).

The connection between the central controller and the bus masters is realized by USB, thus combining the universal availability of USB with a computationally efficient bus protocol. The efficiency of the bus protocol is especially important for the embedded microcontrollers in the joint drives since they are also responsible for the communication with the motors and must keep up a hard-real-time schedule. Since USB uses differential signaling too, the error rate is very low despite the fact that the communication lines run close to brushless DC motors and power lines. To further reduce the cabling, a common power supply is used for all electronics on board. All segments are supplied with 20–40 V from the battery pack in the rear segment (metathorax in **Figure 5**).

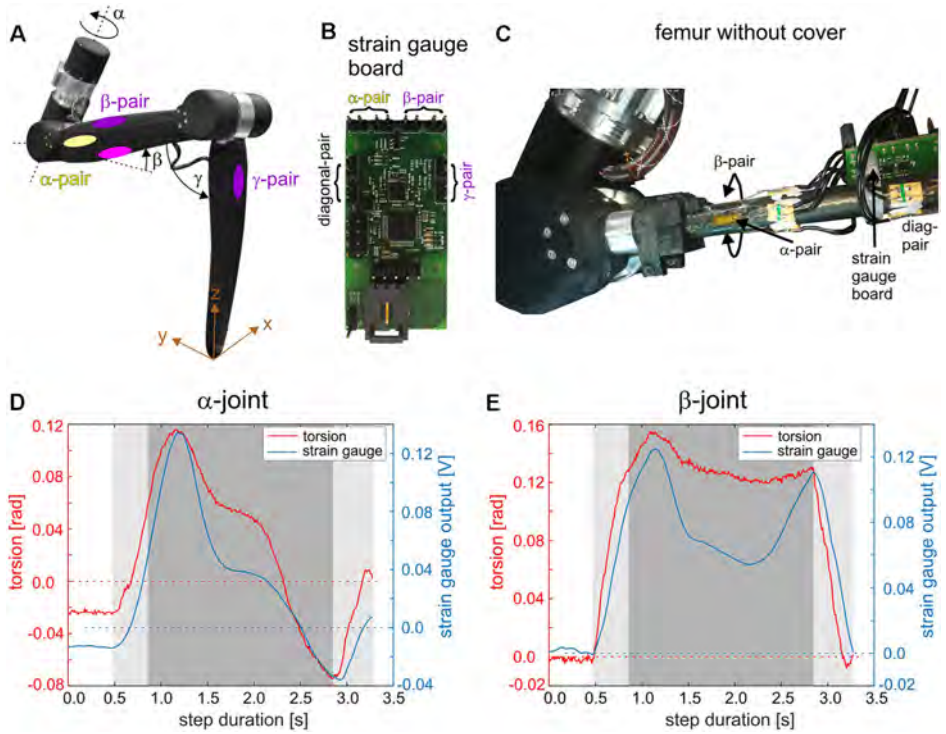

FIGURE 4 | Distributed proprioception in a leg of HECTOR. **(A)** A single leg of HECTOR with elastic α-, β-, and γ-joint drives (equivalent to the thorax-coxa, CTr, and femur-tibia joints of insects). Yellow and purple/magenta ellipses on the femur segment indicate locations for application of strain gauge pairs on the carbon fiber rod under the femur cover. Each strain gauge pair is named according to the joint axis which is predominantly responsible for the bending of the respective pair (colors as in **Figure 3**). The γ-pair is situated on the tibia segment. **(B)** Small-scale strain gauge board for the processing of four strain gauge pairs. The board can be mounted on the femur segment and connects to all strain gauges used on the leg structure. It can also be connected to the BioFlex bus of the robot communication infrastructure (see **Figure 5**). **(C)** Femur segment of the leg without cover, revealing the strain gauge pairs glued to the carbon fiber rod. The diagonal pair is sensitive to torsion of the femur and has no obvious biological equivalent. **(D)** Time courses of the α-joint torsion and the corresponding reading of the α-strain gauge pair during a single step. During the experiment, the leg was mounted to a sliding tether that simulated body movement by allowing the leg to push its own base forward and upward during stance (x and z directions in **A**). The dark gray area highlights the time interval during which the leg base was actively lifted and during which the leg had to carry its own weight. The light gray area indicates loading and unloading. **(E)** Same as **(D)** but for β-joint torsion and β-strain gauge pairs.

GROUND CONTACT AND LOAD-DEPENDENT COORDINATION

With regard to distributed mechanoreception, the foot is a special case. Because the foot is the main contact zone of the insect body, forces and motions of the foot are immediately related to events occurring at the interface between body and substrate. Even if a considerable part of substrate adhesion may be passive, it is important for animals to detect the onset and offset of ground contact, and to control the muscle forces necessary to achieve, maintain and terminate a firm engagement of the foot with its substrate. In particular when walking on rough terrain with potential step-to-step variation in surface structure and orientation of the substrate, detecting and encoding the properties of ground contact and substrate engagement are essential for postural stability, motion efficiency and, in case of a walking machine, safety.

Ground Reaction Forces in Insect Walking

A look at the forces acting on a foot during a step cycle immediately reveals that "having ground contact" is not a simple binary state, not even when walking on a perfectly flat horizontal surface. For example, **Figure 6** shows mean foot trajectories for the stance phases of all leg types in an unrestrained, straight and planar walking stick insect. Additionally, it shows the mean magnitude and direction of the horizontal ground reaction forces (GRF), as measured in the study of Dallmann et al. (2016) at a given time of the normalized stance movement. Clearly, GRF vary strongly throughout the step cycle and differ a lot among leg types. Whereas the "breaking phase" with forward-directed (thus decelerating) force vectors is common to all legs, only middle and hind legs show a clear "propulsion phase" with significant rearward directed force vectors. Inward directed force vectors are also common to all legs, though with different timing and magnitude. In front and middle legs, breaking forces can last up to more than 50% of the stance phase (red and blue vectors in **Figure 6**). In contrast, a hind leg begins to contribute to propulsion much earlier, i.e., after about 25% of its stance phase (light blue vectors in **Figure 6**).

Given the fact that a stick insect foot has five tarsomeres, all of which are moved by the same muscle-tendon complex (i.e., with a single degree of freedom for control only), the complex GRF

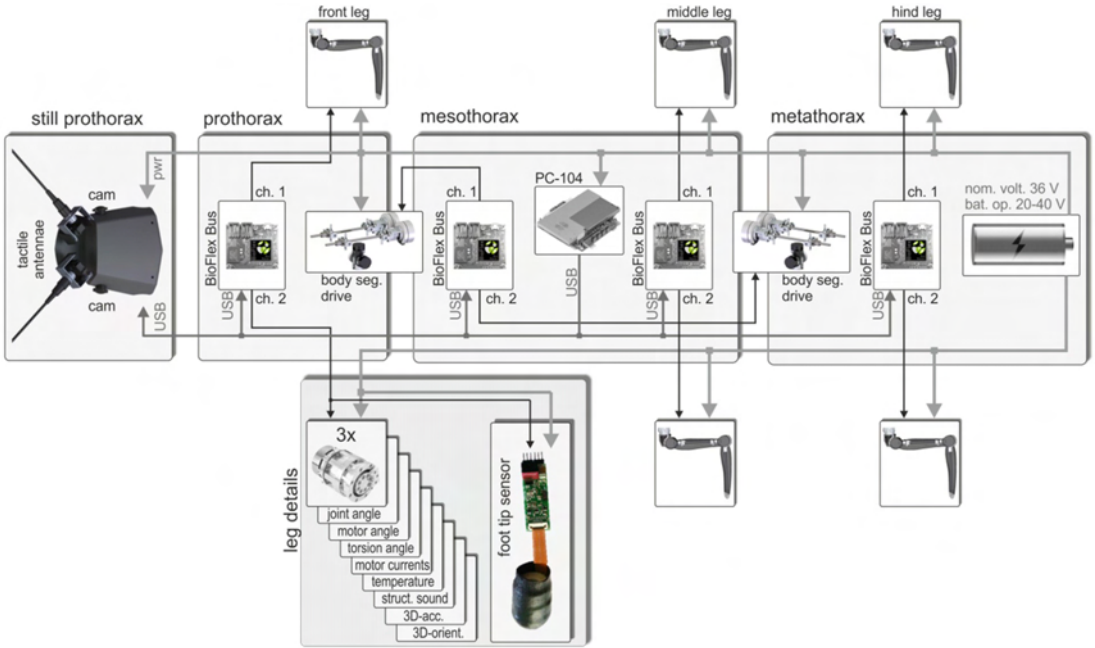

FIGURE 5 | Communication scheme and location of main electronic parts of HECTOR. The robot has three body segments (pro-, meso-, and metathorax), each one of which carries a pair of legs. The front segment looks like a head as it carries eyes (cameras) and antennae (tactile probes) (Hoinville et al., 2014). Each leg comprises three compliant joint drives that communicate with a bus master (BioFlex Bus) in the respective body segment. Each bus master has two channels (2 Mbit/s each) to connect to a maximum of 250 clients which are polled by the bus master to allow real-time operation. The box for the left front leg lists the 12 sensor readings provided by the integrated electronics board of each joint drive and shows the multi-taxel foot tip sensor of a front leg. The bus masters are connected to the host computer (PC/104) in the mesothorax *via* high-speed USB. A fourth bus master in the mesothorax is dedicated to the two spindle drive setups for the inter-segmental joints.

pattern in **Figure 6** suggests strong changes in passive forces acting on the foot. Since the tarsomeres are equipped with a variety of mechanoreceptors, including tactile hairs and CS, it is conceivable that they can monitor magnitude and orientation of force vectors as well as size and orientation of the contact area. Indeed, tarsal sensilla have been shown to reliably encode rate and amplitude of loads and resisted muscle forces at the tarsus (Zill et al., 2014, 2017), and to contribute to activation of both the tarsal retractor muscles and the more proximal flexor muscles involved in pulling the leg inward (Zill et al., 2015). This suggests that tarsal sensilla are involved in the establishment and maintenance of substrate engagement.

In addition, signals from tarsal CS could be suitable for detecting increments and decrements of vertical load in the process of triggering transitions from stance to swing (see "Load-Dependent Coordination" section). However, several studies have demonstrated that complete loss of the distal part of a leg does not impair proper step cycle transitions as long as the trochanteral CS groups are intact (Wendler, 1964; Keller et al., 2007). This finding indicates that the CS groups at the base of the leg are sufficient to detect ground contact. Moreover, the sensitivity, orientation, and locations of CS groups 1–4 (**Figure 3C**) are well-suited to monitor the GRF at the endpoint of the leg. The extensive sensorization of the insect foot could, of course, add more fidelity to the encoding of GRF by trochanteral CS groups. Moreover, it is likely to be relevant for the control of the foothold, in particular for encoding grip force or detecting slip. This is reminiscent of the integration of cutaneous and muscle receptors in vertebrates, where it has been argued that sensory monitoring of the ground contact conditions is relevant for understanding walking and for devising biologically inspired walking models (Frigon and Rossignol, 2006).

Multi-Taxel Touch Sensor for HECTOR Foot

With regard to our knowledge on foot sensorization in walking insects, the design of a sensorised foot for HECTOR was guided by two main goals: (i) the pressure distribution on the foot tip should be monitored at multiple measurement points, allowing to estimate both the magnitude and the spatial direction of the force vector; and (ii) the sensor array should yield a tactile image of the contact surface, potentially allowing for further analysis and/or classification of the substrate. Once achieved, the combination of these two properties would be of immediate relevance to the use of the foot tip as a sensorised gripper.

For a touch-sensitive foot tip of HECTOR, we chose to use piezo-resistive rubbers because of their smooth dependence of measured resistance on applied pressure (Drimus et al., 2014b). Other important advantages of this material are flexibility, overload robustness and low cost. The material can withstand pressure up to approximately 6 MPa (or 860 psi) for millions of actuations. By using a multiplexing algorithm, we could address multiple sensing elements with a small number of wires. As a

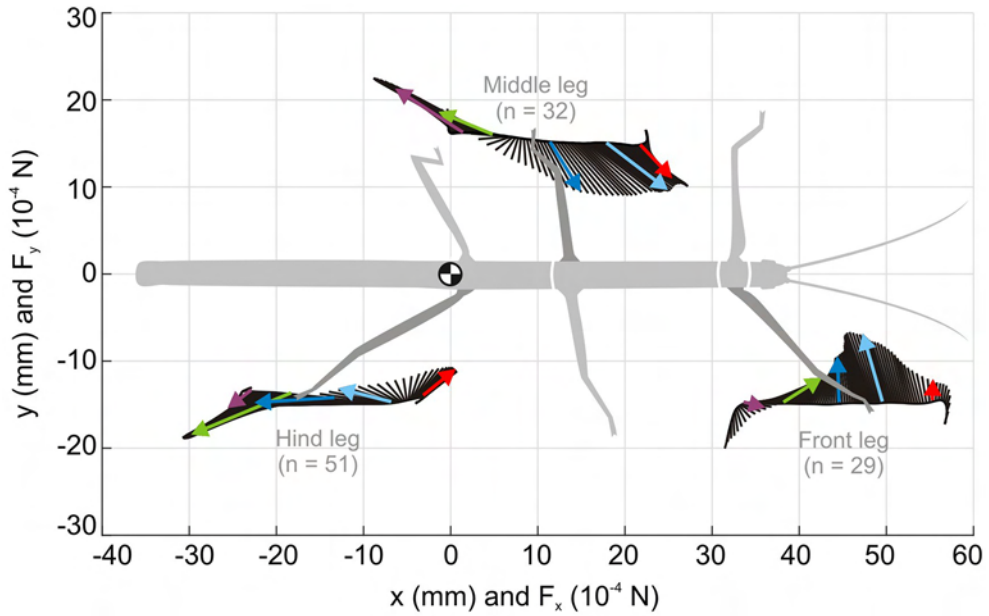

FIGURE 6 | Horizontal ground reaction forces (GRF) during unrestrained locomotion. Average horizontal force vectors of an unrestrained forward walking stick insect on a planar surface (drawn as inverted ground reaction force vectors). The vectors are mapped onto the position trajectories of the respective tarsus in a body-centered coordinate system (origin: the center of mass, being located at the rear end of the metathorax). Data from one representative animal, with separate measurements per leg, normalized to the duration of the stance phase. Black lines show force vectors every 1% of stance duration. Colored arrows indicate magnitude and direction of the horizontal force components at specific times of stance (red: 10%, cyan: 30%, blue: 50%, green: 70%, purple: 90%). Walking direction is from left to right. For details on ground reaction force measurements, see Dallmann et al. (2016).

result, we could acquire a tactile image by iterating through all possible combinations of matrix columns and rows, yielding a spatial array of measured values at any given moment.

A semi-spherical tip covered with as many tactile cells (taxels) as possible ensured that movements of the end-effector were not constrained by the sensor, while contact information could be acquired for most poses. For a foot tip diameter of 2 cm, a radial array structure of 12 sectors and five rings was chosen as the best compromise between manufacturing difficulties, cell size and spatial resolution (see sensor layout in **Figure 7B**). This determined the spatial resolution as 30° azimuth and 15° elevation for the force direction estimate in polar coordinates, with 60 taxels per tactile image. Among various electrode types, Drimus et al. (2014b) obtained the best results by using *Flex PCB* designs with high-conductivity finish and conductive epoxies (**Figure 7**). Also, permanent electrical contact between the electrodes and the piezo-resistive rubber patch was avoided, as this reduces the sensitivity for the low-force sensing range.

In order to build a sensor array over a curved surface, we started with a plastic mold of the end effector tip, into which five concentric electrode rings were integrated, that were made of conductive silver epoxy (thickness apporoximately 0.5 mm; 8,331 Silver Conductive Epoxy Adhesive, MGChemicals) yielding a resistivity of 0.017 Ωcm. On top of this bottom layer, we cut a flower-like shape of conductive rubber, uniformly covering the effector tip. The top layer consisted of a custom-developed *Flex PCB* that covered the conductive rubber. With its 12 electrodes, it provided a perpendicular overlap with the epoxy electrodes. Both the epoxy and the *Flex PCB* electrodes were connected to *Flex FFC* connectors over a total of 18 signal wires (ground, 12 top and five bottom electrodes). A final thin protective layer of polyurethane-impregnated textile was applied, not unlike a sock, as shown in **Figure 7B**. For a detailed description of the manufacturing process, see Drimus et al. (2014a). The finalized prototypes, together with the electronics modules, are shown in **Figure 7C**.

The basic mechanism for measuring the pressure exerted on each rubber taxel is based on a voltage divider principle as described in Drimus et al. (2014b). Therefore the electronics for data acquisition consisted of a multichannel ADC, multiplexers, power supply and an RS-485 transceiver for integration into HECTOR's *Bioflex* bus system, along with an Atmel UC3L064 microcontroller. Temporal resolution may be up to 500 tactile images per second. The microcontroller can reply requests *via* the *Bioflex* bus regarding force, pressure or angle estimates, as well as full tactile images with 8-bit values per taxel. According to model calculations, accurate estimates can be obtained for forces as low as 0.1 N. Below that, accuracy deteriorates due to contact resistance uncertainties within the piezo-resistive rubber (Drimus et al., 2014a).

The sensorised foot tip was tested by applying forces up to 30 N at different tilt angles, as illustrated in **Figure 8D**, along with the corresponding tactile images. The results show that the identity of the taxels triggered, as well as the force distribution gives an intuitive estimate of both force magnitude and direction. For incipient contacts (e.g., columns 2 and 4 in **Figure 8D**), only

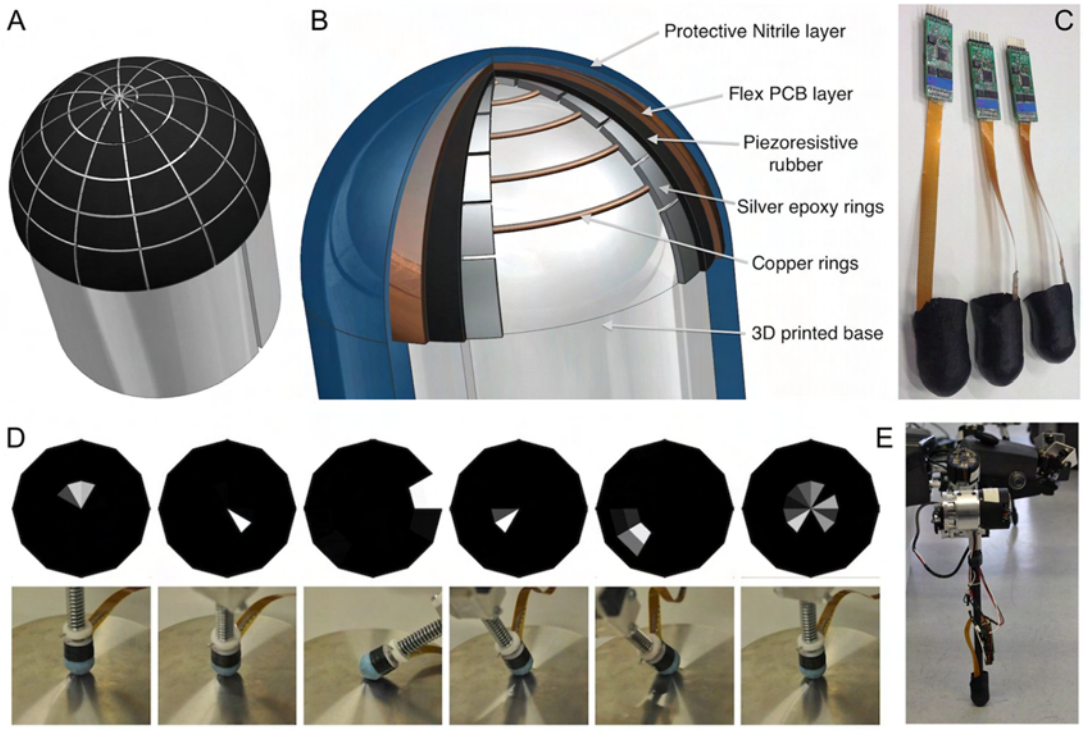

FIGURE 7 | Multi-taxel foot tip sensor. **(A)** Tactile cell distribution across the foot tip surface. There are five concentric rings with 12 sensing cells per ring. **(B)** The section cut through the sensorized foot tip, revealing the layered construction of sensor. **(C)** Finished prototypes with electronics. Lower panel: directional sensitivity of the foot tip sensor. **(D)** Tactile images (top) and corresponding test situations (bottom) for six different end-effector poses. The more slanted the pose, the more marginal is the location of mean activity in the tactile image (adapted from Drimus et al., 2014a, with permission). **(E)** Sensorized end-effector mounted on HECTOR.

single taxels are triggered, whereas high contact forces result in the triggering of more cells (e.g., 3rd column in **Figure 8D**). Previous experiments with similar constructed tactile sensor arrays have shown very good classification rates for palpation procedures with a parallel gripper (Drimus et al., 2014b), as well as classifying different types of cylindrical terrains when used in combination with a compliant robot foot (Borijindakul et al., 2018). The sensorised end-effector mounted on HECTOR is shown in **Figure 7E** (see also **Figure 5**). For the presented foot tip sensor, preliminary experiments on substrate classification in response to a vertical contact event were successful for substrates as different as gravel, sand or a solid plane. Furthermore, surface sensing with a flexible leg prototype that was covered with similar piezo-resistive rubber showed promising results in the classification of different types of pipe substrate such as PVC, hard paper and sponge when used in a planar array (Borijindakul et al., 2018).

Load-Dependent Coordination

Due to their sensitivity and their arrangement at the leg segments, CS lend themselves to monitor distant events, such as lift-off or touch-down events of neighboring legs. The footfall patterns of stick insects reveal a metachronal wave of swing moments from back to front ensuring temporal coordination. Middle legs, for example, start their swing shortly after the touch-down of the ipsilateral hind leg. From behavioral studies (Cruse, 1985) it is known that, besides position parameters, the loading state of the leg is critical for the decision when to switch from stance to swing. Since all legs in stance are mechanically coupled *via* body and ground, the middle leg should be unloaded as the ipsilateral hind leg touches down and starts to take on some body load. In principle, this unloading of the middle leg could be detected by the G3/G4 group of trochanteral CS (**Figure 3C**).

Given our knowledge of the sensory-motor loops involving trochanteral CS (**Figure 3D**), one can anticipate that afferent activity from G3 during stance should enhance the activity of the trochanteral depressor muscle, whereas unloading caused by touch-down of the neighboring hind leg terminates G3 activity and leads to G4 activity instead. Afferent activity from G4, in turn, activates the levator motoneurons (**Figure 8B**). Moreover, recordings of afferent activity from middle legs of free walking cockroaches already suggested that some CS are sensitive to unloading of the middle leg were activated upon touchdown of the neighboring hind leg (Zill et al., 2009, 2012). Using combined motion capture, ground reaction force measurements and parallel electromyographic (EMG recordings of the antagonist levator/depressor muscles of the middle leg in a stick insect (**Figure 8A**), Dallmann et al. (2017) showed that: (i) the sensitivity of the G3/G4 CS is sufficiently high to sense the torque change at the CTr joint upon unloading of the leg;

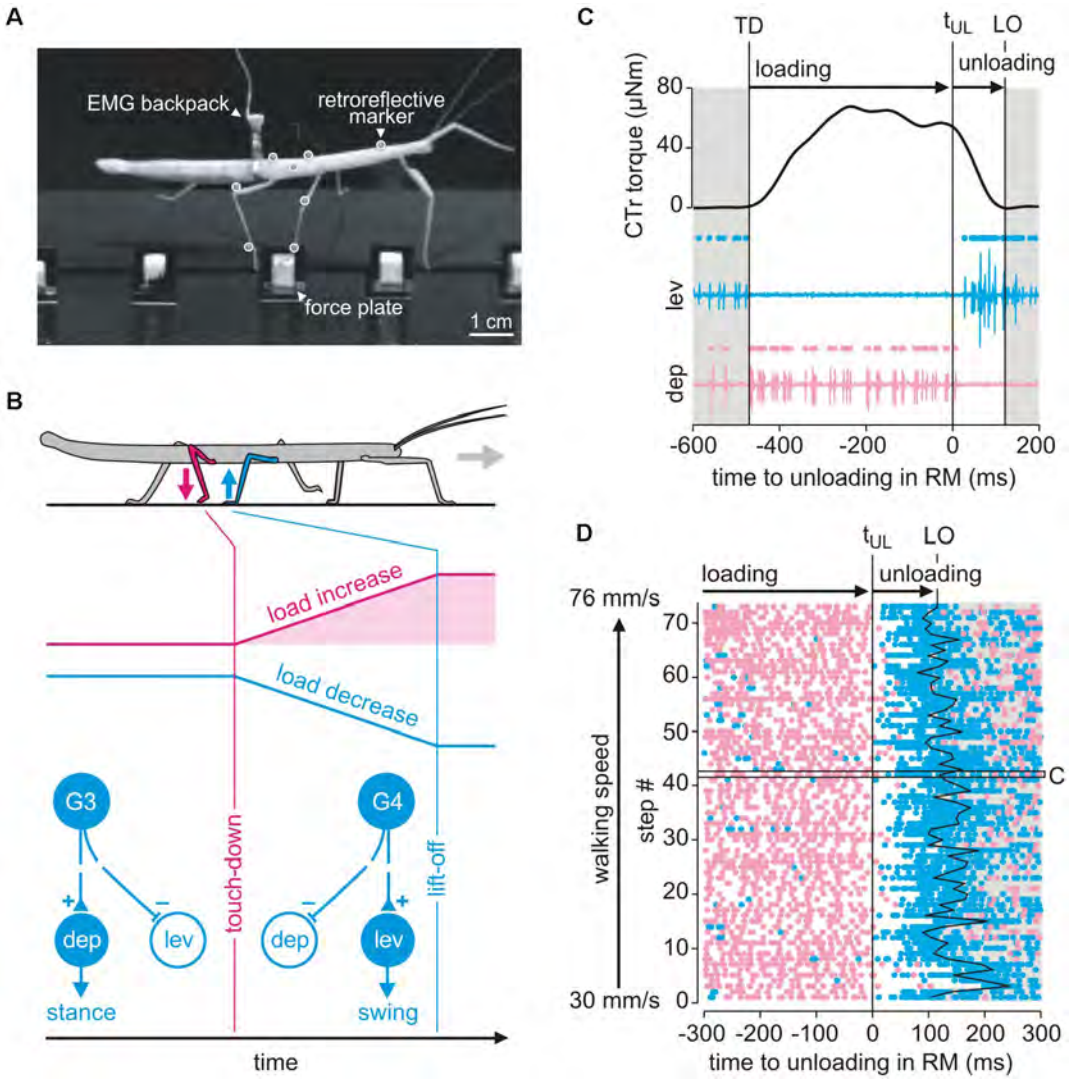

FIGURE 8 | Load-based inter-leg coordination in an insect. **(A)** Experimental setup for the simultaneous measurement of kinematics, GRF and muscle activity. Side view of an animal carrying a light-weight EMG backpack and motion capture markers (white circles) while standing on a force plate with its right middle (RM) leg just as the right hind leg is about to touch down. **(B)** Graphical summary of the putative mechanism underlying the transition from swing to stance in the RM leg after touch-down of the ipsilateral hind leg. CS groups G3 and G4 on the dorsal trochanter are highly sensitive to cuticular strains in the trochantero-femur of that leg. G3 is activated when dorsad bending torques increase, as by loading of the leg during stance. G4 activity signals a decrease of dorsad bending, as during unloading. Schematic of the G3/G4 reflex pathways onto coxal muscles in active animals. Broken lines indicate functional motor effects. G3 afferent activity excites (+) the depressor, i.e., a stance muscle, and inhibits (–) the levator, i.e., a swing muscle (Zill et al., 2012). G4 afferent activity is assumed to have the opposite effect. Unloading induced by a neighboring leg may reverse afferent activity from G3 to G4, thereby promoting the leg's stance-to-swing transition. **(C)** Unloading of the middle leg coincides with a cessation of depressor activity. CTr torque of the RM leg and simultaneously recorded activity of the levator muscle (blue) and depressor muscle (red) of an example step. Dots above EMG traces indicate muscle spikes detected based on amplitude. TD: touch-down; LO: lift-off; t_{UL}: time of unloading. **(D)** Raster plot of detected muscle spikes aligned to t_{UL} of the RM leg (n = 73 steps from N = 8 animals). Walking speed corresponds to the mean speed of the center of mass during stance. The black box marks the step shown in **(C)**. Note that the depressor activity stops at the time of unloading while levator activation shows a considerable time delay and cannot account for the onset of unloading of the middle leg. This holds true for the entire range of walking speeds tested (adapted from Dallmann et al., 2017, with permission).

(ii) the termination of depressor activity coincided with the time of unloading (**Figures 8C,D**, pink traces); and that (iii) unloading is not due to the onset of levator activity (**Figures 8C,D**, blue traces). The latter was revealed by the finding that the levator muscle becomes active only with considerable delay to unloading (**Figure 8D**, white region between pink and blue dots). A model of the animal in static equilibrium allowed the estimation of what may be called the unloading efficacy of a particular leg. Strong differences between unloading efficacy among legs revealed that the ipsilateral hind leg is the most likely candidate for unloading the middle leg with respect to both amplitude and timing (Dallmann et al., 2017). These results indicate that, when a leg

touches down on ground during walking, it effectively takes on body load and thus unloads a specific neighboring leg. Given that a leg can detect the unloading reliably, this can locally trigger its transition from stance to swing, thus contributing to temporal coordination of a specific pair of neighboring legs. Since this mechanism of inter-segmental coordination is mediated by the mechanical information flow, it may be a robust, fast, and computationally cheap augmentation to neural mechanisms involving inter-segmental interneurons. Moreover, it is to date the only mechanism that was shown to implement a behavioral coordination rule proposed by Cruse and Schwarze (1988), Cruse (1990), rule 2 in Cruse et al. (1995). As it exploits interaction forces occurring between the legs and the substrate it is an inherently embodied, adaptive control mechanism and, therefore, well-suited for implementation in multi-legged robots.

SPATIAL COORDINATION OF LIMBS AND OMNIDIRECTIONAL AGILITY

Spatial Coordination of Limbs in Insects

Recent research on inter-leg coordination in animals has been somewhat biased towards aspects of temporal coordination, to the analysis and modeling of gaits in particular (flies: Wosnitza et al., 2013; Isakov et al., 2016; ants: Wahl et al., 2015; cockroach: Bender et al., 2011; Weihmann et al., 2017; stick insect: Grabowska et al., 2012; Szczecinski et al., 2018). While temporal coordination and its speed-dependent transitions certainly are of general importance to our understanding of steady-state locomotion—particularly regarding considerations of optimality (Weihmann, 2018), it does not account for the control of foot placement. This, however, may be of critical importance for climbing animals. Goats and their relatives provide for extreme examples of this, as they may even climb trees (see Figure 1 in Delibes et al., 2017), and several species inhabit rocky and/or alpine habitats (e.g., Lewinson and Stefanyshyn, 2016) where slipping and falling may cause deadly injuries. In insects, impact-induced injuries will be less critical due to their small mass. Moreover, fast-running insects are known to compensate for mechanical disturbances (Jindrich and Full, 2002) through viscoelastic properties (Dudek and Full, 2006), thus making foot-placement less important. Nevertheless, accurate foot placement will be of behavioral relevance whenever accurate control of limb posture and/or efficient climbing performance will affect fitness, e.g., in foraging, escape or camouflage behaviors.

Given the proprioceptor types of insects (Horridge, 1965; McIver, 1985; Tuthill and Azim, 2018) and their distinct afferent projection regions in the ventral nerve cord (Tsubouchi et al., 2017), it is plausible to assume distinct neural circuits for the control of force and load on the one hand (see sections above) and the control of limb posture on the other. Moreover, the impressive flexibility of motor behavior in insects suggests flexible recruitment of sensory-motor feedback mechanisms as required for a particular behavioral goal (Dürr et al., 2018). Studies on several behavioral paradigms have shown that limb posture may be set by exteroceptive encoding, e.g., through vision or touch, or by proprioceptive encoding. Examples for visual control of limb posture range from attentive behavior such as antennal tracking of visual objects (Honegger, 1981) to turning-related changes in the movement direction of front legs (Dürr and Ebeling, 2005; Rosano and Webb, 2007) and visually guided foot placement or reaching (Niven et al., 2010, 2012) to decision-making in climbing (Pick and Strauss, 2005). Tactually guided foot-placement occurs in stick insects that use their front legs to reach for a location that was touched by the ipsilateral antenna (Schütz and Dürr, 2011). Accurate foot placement in three dimensions through proprioceptive encoding has been shown in freely climbing stick insects (Theunissen et al., 2014), where foot contact locations of a trailing leg are systematically shifted according to the last foot contact of the leading leg (for review, see Dürr et al., 2018).

Compelling evidence that postural cues may strongly affect or even override otherwise rhythmic mechanisms comes from a simple experiment on the stance-to-swing transition in stick insects. In tethered walking stick insects, a single leg may be taken out of the stepping rhythm by placing the foot on a spatially fixed platform, while the other five legs continue coordinated walking. In this case, the position of the platform strongly affects the likelihood of foot lift-off and the re-emergence of rhythmic stepping of the sixth leg (Cruse and Epstein, 1982; see Supplementary Video 1 of Dürr et al., 2004). Other evidence for the relevance of postural cues in the control of stepping comes from goal-directed turning, e.g., in jumping spiders (Land, 1972). Generally, sensory-induced state transitions in stepping have been included in many models of inter-leg coordination in insects (Cruse et al., 1995; Ekeberg et al., 2004) and mammals (Ekeberg and Pearson, 2005) alike, and all of these examples include postural effects (note that postural cues such as leg retraction angle may co-vary strongly with cues related to interaction force, such as the decrease of load during late stance; see "Load-Dependent Coordination" section).

In insects, postural effects are particularly relevant in limb movements that are not mechanically coupled to the movement of other limbs, i.e., whenever the limb is not in contact with the substrate. For example, removal of a proprioceptive hair field on the trochanter strongly affects the height of the swing movement during in unrestrained walking stick insects (Theunissen et al., 2014), as well as the angular range of single-leg searching-movements in stationary animals (Berg et al., 2013). Removal of the same hair fields also raises the likelihood of intermittent searching movements during free walking (Theunissen et al., 2014). This is in line with an artificial neural network model of "apparent sequencing" of swing and searching movements (Dürr, 2001) that assumes that both movements are controlled by the same recurrent network and that the cyclic foot trajectory occurs whenever the swing movement is not interrupted by ground contact (for a detailed discussion of this matter, see Dürr et al., 2018).

Similarly, cyclic grooming of the hind wing in locusts (Berkowitz and Laurent, 1996) can be modulated by shifting a tactile stimulus such that the foot follows stimulus position (Matheson, 1998). Indeed, the lack of a position-dependent transition from one movement pattern to another (Dürr and Matheson, 2003), the robustness of grooming position against

changes in load (Matheson and Dürr, 2003) and the strong effect of sensory manipulation on grooming position (Page and Matheson, 2009) indicate that a continuum of cyclic movement patterns, i.e., grooming at various spots on the body surface, is under postural control.

Finally, tactually guided, targeted reaching movements of front legs initiate climbing in stick insects (Schütz and Dürr, 2011). In conjunction with the spatial coordination of foot placement between front and middle legs and between middle and hind legs (Theunissen et al., 2014), there appears to be a chain of coordinate transformations from anterior segments to posterior limbs in stick insects. By reaching towards antennal contact locations with the front leg and subsequently placing middle and hind leg feet in very close locations, stick insects appear to exploit prior knowledge of established foot contacts. That way, spatial coordination of ipsilateral limbs can keep locomotion efficient in a variable environment. Such transfer of postural information from one leg to the other can be modeled by a simple feed-forward Artificial Neural Network (ANN, Dean, 1990). This has been exploited in several versions of Walknet, a model of decentralized control of hexapedal walking (Cruse et al., 1995; Dürr et al., 2004; Schilling et al., 2013). Recently, we expanded on the idea of transfer of spatial information among limbs, including antennae and walking legs (Dürr and Schilling, 2018). Based on a large sample of behavioral data, we first determined the size and shape of the volume comprising all positions that are within reach of any limb (**Figure 9A**). In analogy to the psychophysics of human reaching, this volume was termed the "peripersonal space" of a stick insect. A subspace of peripersonal space was then defined as the set of all foot positions that may be reached by at least two limbs. Within this "affordance space" (**Figure 9B**) accurate transfer of spatial contact information can be modeled by sets of small feed-forward ANNs (with neuron numbers within a physiologically realistic range; Dürr and Schilling, 2018). With regard to the neural representation of near-range space, these results show that a behaviorally relevant form of representation may not require the existence of a map-like, topological representation of external space, but may be implemented as a simple, direct posture mapping among pairs of limbs instead.

A second important aspect of spatial coordination in insects concerns the thoracic joints. Whereas the three thorax segments are firmly merged in the basic bauplan of several insect orders (e.g., in Diptera and Hymenoptera), it is a characteristic of some others that at least one thorax segment can be moved relative to the others. This may be in favor of agile use of the head in carnivorous staphylinid beetles or snakeflies (Raphidioptera), and/or the agile use of the front legs in mantids and mantispids. In the mentioned cases, only the prothorax appears to be moved actively, while the winged meso- and metathorax are firmly fixed to each other. In contrast, several stick insect species can actively move the meta-mesothorax joint as well (Theunissen et al., 2015). This is likely to improve agility during climbing, e.g., by considerable augmentation of the working range of front legs. Although the mesothorax is very long in stick insects, movement of the meso-methathorax joint hardly displaces the middle legs because they are located at the rear end of the segment and support the metathorax together with the hind legs. **Figure 9C** shows how the stick insect *Carausius morosus* uses its thorax joints during climbing, where the meta-mesothorax and meso-prothorax joints (**Figure 9C**, green and blue, respectively) cover mean ranges of 20–30 degrees as the animal climbs a stair approximately three times the body height. Movement of the mesothorax alone thus accounted for an increase of working range of the front leg tarsus by more than 8 mm, equivalent to about 30% of the leg length.

A third major role of spatial coordination is to control the magnitude and direction of the force vector for propulsion, i.e., the net force accelerating the center of mass. Since all joints of the legs in stance are mechanically coupled in parallel closed kinematic chains (at least when assuming no slip of the feet), a torque generated at any joint within this parallel set of closed kinematic chains will affect most (if not all) of the other joints. Whereas in animals this aspect of spatial coordination mainly concerns the efficient coordination of joint torques and, therefore, energy requirement, in engineering it is also a matter of avoiding high tensions that could harm the electronic actuators.

In curve-walking insects, spatial coordination affects the direction of the stance trajectory (Jander, 1985; Jindrich and Full, 1999; Dürr and Ebeling, 2005; Gruhn et al., 2009) and a modification of the spatial coordination of touch-down and lift-off positions between leading and trailing legs (Jindrich and Full, 1999; Ebeling and Dürr, 2006). The associated, transient changes in gait during turning are, at least in part, a consequence of the altered stance directions and step lengths. This view draws support from genetic manipulation experiments on *Drosophila*, showing that the proprioception of interaction forces is crucial for maintaining course (Isakov et al., 2016).

Owing to the distinct control problems for mechanically un-coupled swing, search and/or reaching movements as opposed to mechanically coupled stance movements, several modeling approaches have suggested to treat the two problems with separate control modules (e.g., Cruse et al., 1995; Espenschied et al., 1996). It is important to note that this separation of swing and stance control is mainly a conceptual one, and does not imply these control modules correspond to distinct physiological networks (Dürr et al., 2018). For example, early versions of the distributed neural network controller Walknet suggested a high-pass-filtered positive-feedback mechanism for the coordination of retraction and depression among multiple legs in stance (Cruse et al., 1998) that was inspired by state-dependent reflex reversal from resistance to assistance reflexes (for review, see Pearson, 1995; Büschges and El Manira, 1998).

From an engineering perspective, the adaptive modulation of local reflexes has been applied very early to six-legged (e.g., Berns et al., 1994; Ilg and Berns, 1995) and four-legged (e.g., Albiez et al., 2003) walking machines. In particular, the concept of local positive velocity feedback has been applied successfully for coordinating multiple legs in stance (Schneider et al., 2006). Based on these proofs of principle, it can be concluded that the distributed proprioception and the adaptive

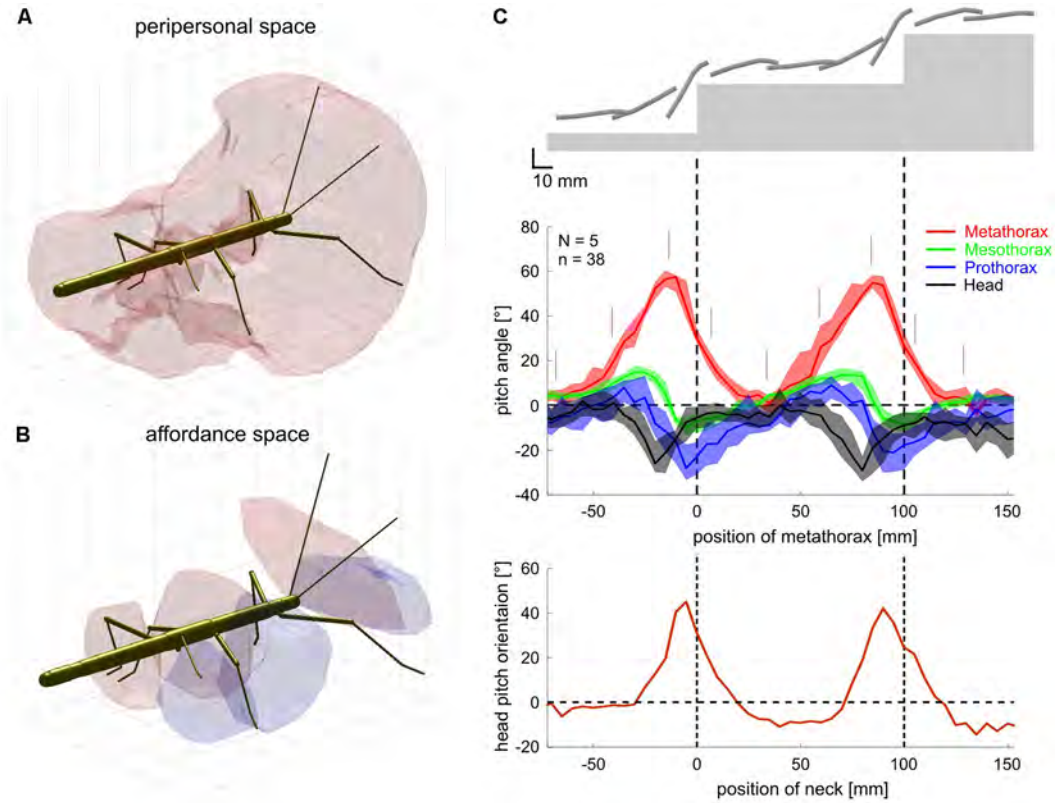

FIGURE 9 | Spatial coordination in insects. **(A)** Active movements of antennae and walking legs of a stick insect delimit a volume around the body within which the limbs may touch an object. Since this volume comprises that part of the ambient space within which motor activity, proprioceptive and tactile sensory input may coincide, it may be called the peripersonal space of an insect. **(B)** Transfer of spatial contact information can work only in those parts of peripersonal space where at least two limbs may reach the same position in space. Since for all such positions, a contact experience of one limb indicates a potential contact position on another limb, an affordance is generated: a limb may reach a contact location on another limb. This was proposed as affordance space by Dürr and Schilling (2018). **(C)** Top: schematic postures of head and thorax as a stick insect climbs a sequence of two stairs. Middle: the inclination of the metathorax changes strongly (red; plotted as a function of metathorax position) and the head and all thorax segments move relative to each other. The head is pitched relative to the prothorax (black), the prothorax relative to the mesothorax (blue) and the mesothorax against the metathorax (green). Gray lines indicate the instants corresponding to the schematic postures above. Bottom: head pitch angle as a function of head position [adapted from Dürr and Schilling, 2018 (**A,B**; CC BY 4.0) and Theunissen et al., 2015 **(C)**, with permission].

modulation of multiple local reflex circuits are sufficient for the control of a multi-legged robot locomotion (Schmitz et al., 2008). As yet, it is a complex problem, requiring either careful tuning or autonomous learning of multiple reflex pathways.

Omnidirectional Walking in HECTOR

Walking in HECTOR is organized in a computing framework that consists of four main software modules. The actual *walking controller module* was implemented in Python 3 with some time-critical routines like kinematics calculations and stability checks written in C++ and integrated *via* Swig. The *dynamics simulation module* was implemented in C++ using ODE. The *walking controller module* can either be connected to the *dynamics simulation module* or to a *middleware module* (if real robot operation is desired), both *via* TCP/IP. The *middleware module* (implemented in C++) translates control messages from the *walking controller module* and sends the required commands to the bus master boards in the body segments of the robot (see **Figure 5**). Details of the framework and a flow chart of the overall control sequence for walking can be found in Paskarbeit, 2017 (p. 42 and p. 124).

The walking controller of HECTOR implements distributed control with each leg being considered a separate agent that locally controls the alternation of stance and swing movements. The transitions from stance to swing and *vice versa* are governed by local rules acting between adjacent legs (Cruse, 1990; Cruse et al., 1995). For reasons of robustness, however, the spatial coordination of foot trajectories during turning is not controlled by modulation of distributed reflex loops. Instead, the central directional control of the whole robot is combined with the concept of local leg coordination as illustrated in **Figure 10**. The movement of the central body axis is considered (blue line in **Figure 10A**). This axis runs from a point $\mathbf{p}_0$ between the hind legs to a point $\mathbf{p}_1$ between the front legs with a center point in the middle (**Figure 10B**). These points can be used as "pull points" at which a pull vector **h** can be applied to initiate movement of the central body. By varying **h**, the robot may navigate into a desired direction. The example shown in **Figures 10A–C** uses

only a single pull vector $\mathbf{h}_1$ at the front of the robot. Knowing $\mathbf{h}_1$, one can compute both the rotation angle ω and the displacement vector $\mathbf{d}$ to describe the intended movement by means of a transformation matrix. Assuming that the legs remain at their position before the displacement but the body is shifted towards the new positions $\mathbf{p}_0'$ and $\mathbf{p}_1'$ the inverse of the transformation matrix can be applied to the foot positions of all legs on the ground to calculate the individual leg trajectories for the next time step of a stance movement (**Figure 10C**). In the current example, constant application of pull vector $\mathbf{h}_1$ would move the body of the robot as indicated in **Figure 10D**. As an alternative to the explicit calculation of the inverse transformation matrix, an internal body model as described in "Modularity and the Decentralized Coordination of Multiple Limbs" section may be used for an implicit determination of the stance movements of each leg in the next time step. Since the pull vector $\mathbf{h}_1$ may be oriented in any direction the stance movements of individual legs need no longer be aligned with the fore-aft-axis of the robot as in straight walking or in slight curves.

As a consequence of this framework, the swing-to-stance transition does not take place at a specified posterior extreme position of the leg (see PEP in Cruse et al., 1995). Instead, the stance movement needs to be restricted in any direction with respect to the workspace of the individual leg during omnidirectional walking. The limit of the workspace is formulated in terms of an unrestrictedness measure (Paskarbeit, 2017) which has been derived from the complementary concept of restrictedness as formulated by Fielding and Dunlop (2004). An example for such a limited area is shown in **Figure 10E**. At the start position of stance, the leg conducts a stance trajectory according to the desired movement of the central body as described above. The course and curvature of the stance trajectory is extrapolated beyond the current position to yield a test point in each control cycle. The test point is then checked for its unrestrictedness value: if the value lies below zero, a swing movement may be elicited, otherwise the leg remains in stance. The target position of a swing movement is set to the intersection point where the backward extension of the last stance trajectory, laid out from a home position of the leg, crosses the unrestrictedness boundary (**Figure 10F**). This ensures that the leg can continue the last stance movement after touch-down.

The boundary for each leg results from a projection of a volumetric representation of unrestrictedness. The basic unrestrictedness measure is a scalar value that ranges from zero to one. Any volume in the workspace of a leg which has unrestrictedness values within this numeric interval can be reached by the leg. If a point in space has an unrestrictedness value below zero, it is restricted by definition and should not be entered by the leg. Hence, this can serve as a trigger for a stance-to-swing transition. Note that the conditional definition of the unrestrictedness volume is similar to the affordance volume described in conjunction with **Figure 9B**, except that there the boundary depends on a condition involving two legs, not just one. Indeed, unrestrictedness values can be described for various aspects of a leg that could potentially restrict leg movement. **Figure 11** shows three examples for the left middle leg of HECTOR: the joint angle unrestrictedness $u_{\alpha\beta\gamma}$ (**Figure 11A**), the singularity unrestrictedness u_s (**Figure 11B**) and the torque unrestrictedness u_τ (**Figure 11C**). Since the values run between zero and one, multiple unrestrictedness values can be combined by computing the product (see **Figure 11D**). In different walking situations, different kinds of unrestrictedness measures may be considered. For instance, the torque unrestrictedness may be neglected during a swing movement, whereas in stance the torque limits of the drives must be maintained. A further useful unrestrictedness measure is the smallest distance between the geometric envelopes of two adjacent legs. As suggested by **Figures 11E,F**, this may be used to tell collision from non-collision constellations among legs.

Example trajectories of HECTOR's body segments during curve walking based on this control approach are shown in **Figure 13E** with the respective podogram in **Figure 13F**. Here, it becomes evident, that regular gait patterns are exceptions in walking situations with constant heading, speed and environmental conditions. A fixed gait pattern during curve walking is neither necessary in insect walking (**Figures 13A,B**), nor in robotic walking with moveable body segment joints (**Figures 13C,D**) or in the control case discussed above (**Figures 13E,F**).

MODULARITY AND THE DECENTRALIZED COORDINATION OF MULTIPLE LIMBS

Modularity of Insect Motor Control

Despite the importance of central brain structures such as the Central Complex for the selection, control and maintenance of heading (e.g., Strauss, 2002; Neuser et al., 2008; Seelig and Jayaraman, 2013; see also "Conclusions" section), and the significance of small sets of descending interneurons for specific behaviors such as sensory-induced turning (e.g., Zorović and Hedwig, 2013), backward walking (Bidaye et al., 2014) or landing (Ache et al., 2019; for review, see Bidaye et al., 2017), the control of locomotion in insects is highly decentralized. For example, there is no single region or network that governs the execution of a particular gait. Rather, step cycle parameters such as duty factor or stance duration vary continuously with velocity, resulting in a continuum of gaits (for review, see Dürr et al., 2018). Accordingly, there appear to be several network "modules" that interact to give rise to the overall behavior. Anatomically, the modularity of motor control networks in insects is reflected already by the segmental architecture of the CNS, with the ventral nerve cord comprising one ganglion per body segment, connected by nerves that may cover distances of up to several millimeters between the thoracic ganglia (note that thoracic ganglia are fused in more derived taxa such as flies). Each one of the thoracic ganglia contains the complete set of motoneurons that drive the two legs of the corresponding thorax segment.

As a result of pharmacological activation studies, each thoracic ganglion is thought to comprise distinct neural oscillator circuits for different leg joints, thus forming the basis of alternating activity of antagonistic muscles acting on the same joint (Bässler and Büschges, 1998). In stick insects, pharmacological activation appears to induce only

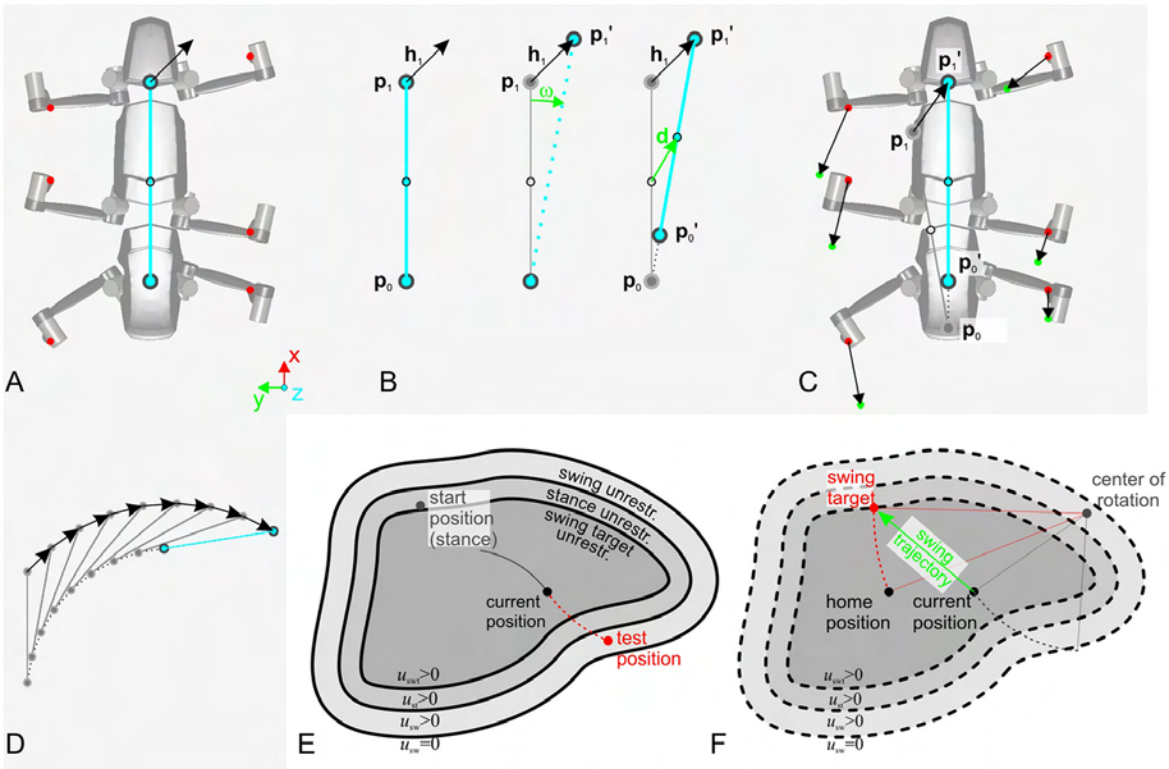

FIGURE 10 | Spatial coordination in HECTOR. To direct the robot into a desired direction, two "pull points" may be used. **(A)** The two pull points, p_0 and p_1 are defined on the virtual body midline (blue circles). Foot positions are shown as red dots. **(B)** Concept for the computation of the rotation angle ω and the displacement vector d. Based on these two values, a transformation matrix can be constructed. The inverse of this matrix is applied to the leg tips in order to calculate the leg trajectories for the next time step which is shown in **(C)**. Panel **(D)** indicates the movement of the pull points and the robot midline for a sequence of transformations. **(E)** During the resulting stance movement of a single foot on the ground, the leg must not leave its physically limited working area. In HECTOR this limit is formulated in terms of an unrestrictedness measure. For an ongoing stance movement, the current trajectory is extrapolated beyond the current position, yielding a test point that is checked for its unrestrictedness value. If this value lies below zero, a swing movement is elicited. **(F)** The target of the swing movement is set to a point on the unrestrictedness boundary. It is the intersection point with the backward extension of the current robot movement (red dotted line, attached to the home position of the leg). Instead of explicit transformation matrices, the internal body model may be used as well to estimate the respective movements of the feet.

little coordination of oscillatory activity among different leg joints (e.g., Büschges et al., 1995), whereas persistent coupling among leg joints has been reported for other insects (e.g., Ryckebusch and Laurent, 1993). Similarly, pharmacologically induced rhythmic antennal movements in stick insects show the same pattern of inter-joint coupling if proprioceptive feedback is still present (Krause et al., 2013). Although the neural components of the local oscillator networks in the walking system of insects remain elusive until today, the idea of coupled oscillators can be applied successfully in modeling of rhythmic intra-leg (e.g., Daun-Gruhn and Tóth, 2011) and inter-leg coordination (e.g., Tóth et al., 2015). As yet, only modeling approaches that emphasize sensory coupling between joints (Ekeberg et al., 2004) and between legs (Szczecinski et al., 2014, 2017) in addition to central oscillator activity can account for insect-like motor flexibility (Dürr et al., 2018). Correspondingly, several robotic approaches that were based on coupled oscillator networks have used sensory input for switching between distinct states in motor behavior (e.g., Ijspeert et al., 2007) or the entrainment of coordinated limb-movements (Owaki et al., 2013) over a range of walking speeds (Owaki and Ishiguro, 2017).

Owing to the distributed and de-centralized organization of proprioception (see "Distributed Proprioception of Posture" and "Load and Ground Contact and Load-Dependent Coordination" sections), inclusion of any proprioceptive feedback adds a "degree of de-centralization." A purely proprioceptive-feedback driven and, thus, strictly de-centralized approach in the modeling of insect locomotion is Walknet (Cruse et al., 1998; Schilling et al., 2013). This distributed Artificial Neural Network controller implements behaviorally derived rules of inter-leg coordination (Cruse, 1990). To do so, it strictly separates the control of mechanically coupled as opposed to mechanically uncoupled limb movements (Dürr et al., 2004). As a consequence, mechanically uncoupled swing or search movements purely rely on postural feedback (three joint angles per leg, see also "Spatial Coordination of Limbs in Insects" section), whereas mechanically coupled movements are governed by ground contact (postural information is used too, but ground contact causes a switch between control modes). Since Walknet is a

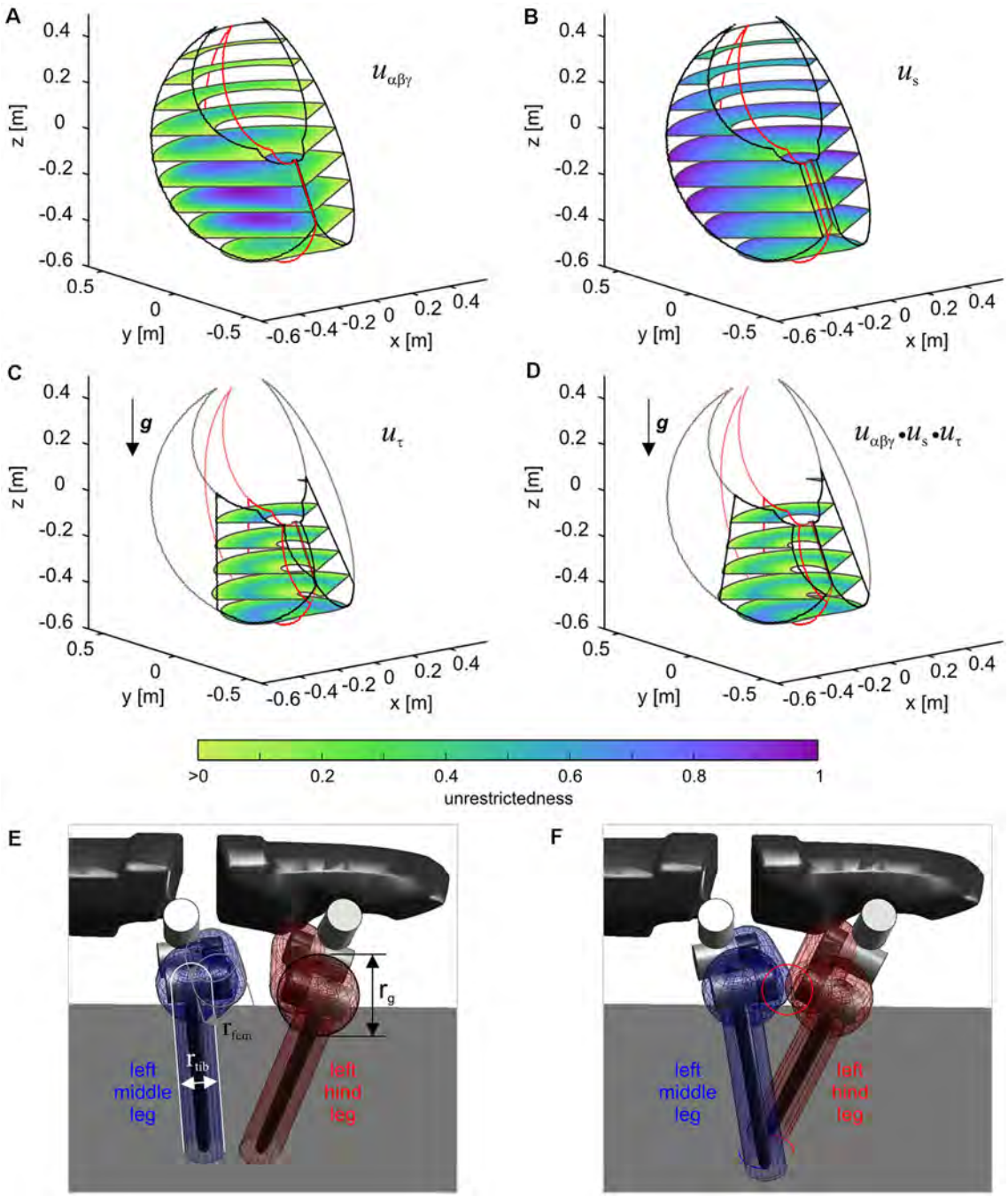

FIGURE 11 | The unrestrictedness measure in HECTOR. Volumetric representation of unrestricedness values for the left middle leg of HECTOR. The horizontal slices are set at distances of 0.1 m in z-direction. Panel **(A)** shows the joint angle unrestrictedness. Black and red contour lines are given for α-angles of 0 and $\pm$ 1 rad. **(B,C)** The singularity unrestrictedness **(B)** and the torque unrestrictedness **(C)** for a vertically directed gravity vector. **(D)** Combination (product) of the three unrestrictednes measures of **(A–C)**. Any unrestrictedness value larger than 0 indicates a position which can be reached safely. Panels **(E,F)** show a non-collision and a collision situation between two neighboring legs, respectively. The distance between the enveloping geometric primitives can also be used for a further unrestrictedness measure.

kinematic controller, it does not consider interaction forces. In analogy to the considerations of load-dependent inter-leg coordination (see "Load-Dependent Coordination" section), a ground contact signal may be considered a binarized version of an interaction force signal (for further discussion, see Dürr et al., 2018).

Given the considerations about spatial coordination of multiple legs in stance ("Spatial Coordination of Limbs in

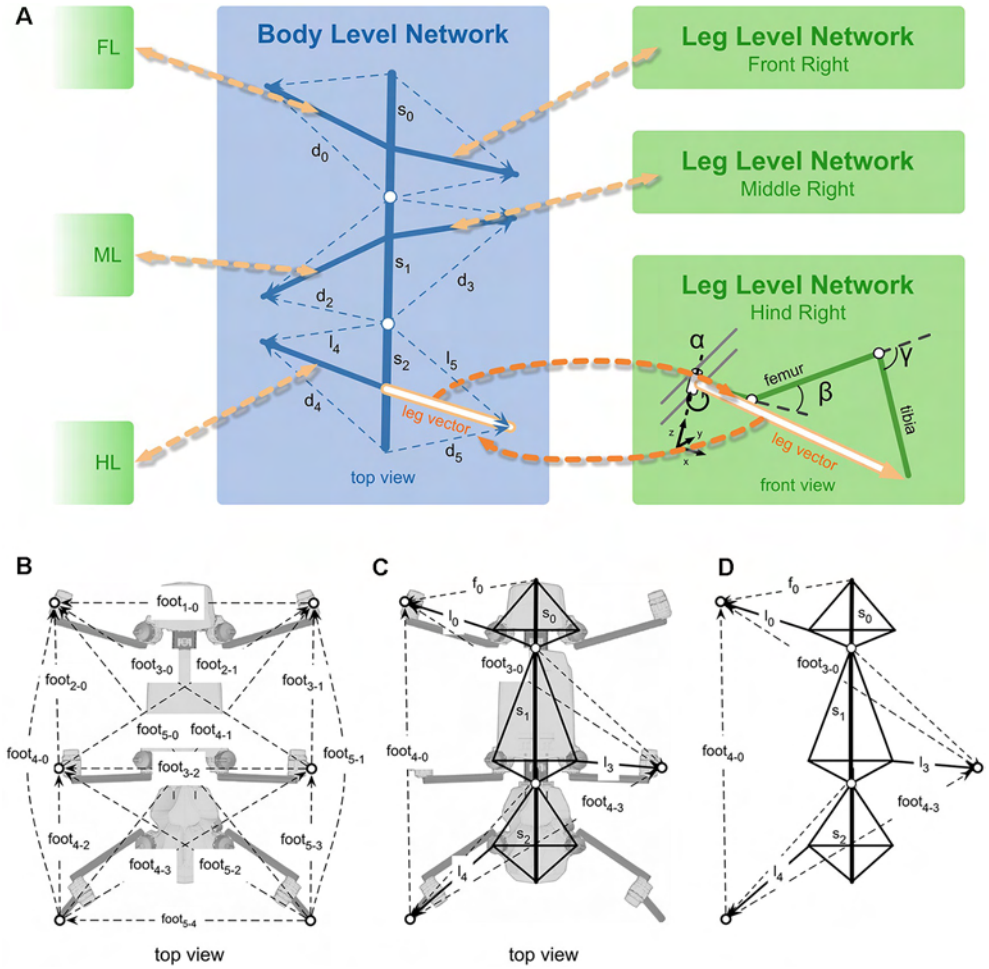

FIGURE 12 | Hierarchical internal body model. **(A)** The body model comprises a body level network (blue) and six subordinate leg level networks (green). Left: the body level network controls the six leg vectors, l_0 to l_5, and the three main body segment vectors, s_0 to s_2. Right: each one of the six leg level networks controls a leg with three joints and segments. The two levels are inter-connected *via* the shared representation of the leg vector (white arrow) (adapted from Schilling and Cruse, 2012, CC BY 4.0). **(B)** Higher level of the internal body model. Arrows show all constituting vectors that are used to construct the local equations and relationships used to set up an Mean of Multiple Computations (MMC) network for the control of HECTOR. **(C,D)** One specific walking situation of a tripod gait, with the left front and hind leg on the ground together with the RM leg (with and without the underlying robot schematic). During the control of stance only those leg vectors are considered that are interacting with the ground, thus potentially contributing to propulsion, balance and steering. Legs that are currently in swing are suppressed within the body model (adapted from Schilling et al., 2012, © 2012 IEEE).

Insects" section), we propose that sensory information about ground contact or substrate engagement determines the control mode of a given leg. However, as an alternative to the two control schemes of the stance movement discussed earlier, i.e., state-dependent modulation of proprioceptive reflexes and the inverse-kinematics approach described in conjunction with **Figure 12A**, we introduced an internal, hierarchical body model that can coordinate the movement of all joints which are part of at least one closed kinematic chain. The hierarchical model has been introduced for the control of six-legged walking on flat terrain in dynamic simulation, including negotiating curves (Schilling et al., 2012). This model captured movements of the robot body in two dimensions, only. The model was extended and applied to have the robot HECTOR to climb stairs and to walk across rubble (Paskarbeit et al., 2015). The extension uses a singular-value decomposition approach to control the height of the body (and leg bases) over ground, thus relieving the constraint to two dimensions.

The hierarchical body model approach follows the idea of the passive motion paradigm (Mussa-Ivaldi et al., 1988). It is realized as a recurrent neural network that implements the *Mean of Multiple Computations* (MMC) principle that allows the combined solution of forward and inverse kinematics problems (Steinkühler and Cruse, 1998; Schilling, 2011). MMC networks implement a redundant set of kinematic equations, where each equation describes the triangular geometry of one part of the leg or body. As such, an MMC network maintains the decentralized and modular nature of motor control despite the fact that all equations and, thus, all partial kinematic problems are solved in conjunction by iterating a recurrent neural network. In the

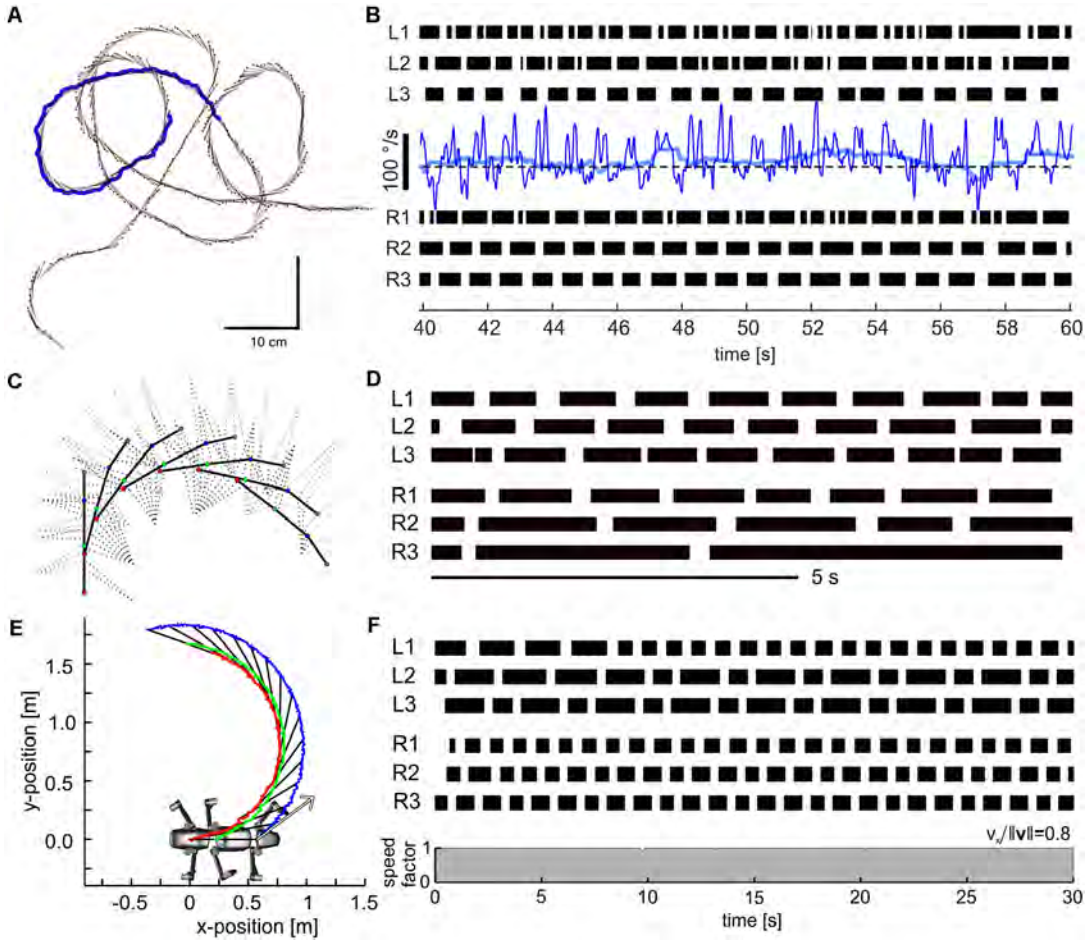

FIGURE 13 | Curve walking in stick insects and HECTOR with and without a body model. **(A)** Sequence of a free walking, blindfolded stick insect on a horizontal plane. Black line segments and red dots show body axis and head every 200 ms (duration: 106 s; median speed was 35 mm/s at the beginning and 25 mm/s at the end). Bold blue line labels the part shown in the podogram. **(B)** Podogram with black lines showing stance episodes of all six legs (L1 to L3: left front to hind legs; R1 to R3: right front to hind legs) and corresponding yaw rotation of the body axis. Blue lines show median rotational velocity per 60 ms window (thin dark blue) and per 1 s window (thick light blue). **(C)** Snapshots of the simulated HECTOR turning to the right using the internal body model of **Figure 12**. The internal body model was constantly pulled to the front and the right. Snapshots show one body posture per second and four leg postures per second (Figure 8B from Schilling et al., 2013, CC BY 4.0). **(D)** Podogram of the complete run shown corresponds to a turn of about 180°. The lower bar corresponds to 5 s of real time, or 500 iterations of the simulation time (adapted from Figure 7 from Schilling et al., 2013; CC BY 4.0). **(E,F)** Trajectories **(E)** and corresponding podogram **(F)** of the HECTOR simulation using the restrictedness measure as described in **Figure 10**, but not the body model. Red, green and blue lines in **(E)** show trajectories of the hind, middle and front segment, respectively. Gray arrow shows the pull vector.

following, the basic characteristics of the model will be explained in order to address how this integrates into the embodied control approach.

A Hierarchical but Decentralized Body Model Based on the MMC Approach

A key principle of an MMC network is that the kinematics constrain the attractor space of the recurrent neural network. Because of these constraints, the activation of the network always corresponds to a correct spatial configuration—or posture—of the modeled body. In a multi-legged agent, considering all possible interactions between the joints that are mechanically coupled at any given instant in time poses a computational problem: the computational effort increases exponentially with the number of joints. In order to reduce the computational complexity of the problem, we proposed a hierarchical body model that allows the distribution of the computational task on two levels (**Figure 12A**). In this scheme, the lower "leg level" comprises the detailed kinematics of a given leg (green panels in **Figure 12A**). The higher level or "body level" (blue panel in **Figure 12A**) comprises the description of the main body segments. In case of HECTOR, the body level comprises the three thorax segments and their relations to the subordinate instantiations of multiple legs. At the body level, there is no detailed information about leg joints. Instead, the leg is represented as a three-dimensional vector that captures the leg's contribution to support the body. In **Figure 12A**, this is shown by vectors connecting the main body segments (s_0 to s_2) to the

feet of the six legs (l_0 to l_5), i.e., the ground contact locations. The two levels are connected through shared representations that are present on both levels. This is indicated by the white arrow in **Figure 12A**. Essentially, this leg target vector "summarizes" the kinematics of the entire leg while, at the body level, it may be regarded as the desired relation between the body and substrate.

On the leg level of the MMC model, each leg is described by a set of three joints and three segments, corresponding to the coxa, trochantero-femur and tibia of an insect leg. As shown in **Figure 12A**, each leg is described by a kinematic chain with a single degree of freedom per joint, where the α joint sets the orientation of the leg plane, while the β and γ joints move the foot within this leg plane. In HECTOR, as in the stick insect (**Figure 3A**), the joint axis of the α joint is slanted, causing a change in pronation/supination of the leg plane as the leg is retracted/protracted (see Theunissen et al., 2015; for time courses of this pronation/supination angle, and Dallmann et al., 2016; for consequences on individual joint torque contributions to propulsion and body support).

Other than standard approaches to inverse and forward kinematics of manipulators MMC networks do not suffer the problem of singularities that may prevent finding a suitable and unique solution for the inverse kinematics problem (for details, see Schilling, 2011). This is because for each triangular relation within the MMC network the optimal solution is easily computable. Moreover, multiple equations (one for each triangular relation) contribute to the convergence properties of an MMC network, thus exploiting a redundant description of the body kinematics for computing a mean solution (hence the acronym MMC for *Mean of Multiple Computations*).

In the hierarchical structure shown in **Figure 12A**, the body and leg levels share the description of the foot positions. At the leg level, this is achieved by describing the posture simultaneously and equivalently by a set of joint angles and by Cartesian coordinates of the foot position relative to the body (along with some mediating diagonal variables). At the body level, each leg with ground contact and all body segments are represented by a vector encoding the foot position. The body model is used differently in the control of swing and stance. As a consequence, only the legs that potentially contribute to propulsion, balance and steering through body-substrate interactions are considered at the upper level of the body model. With regard to the legs in swing, all corresponding equations within the MMC network are disregarded, as if being inhibited. As a result, the equations concerning legs in swing are not taking part in the multiple computations that will determine the posture at the next time step. For example, **Figures 12C,D** show a typical posture of HECTOR occurring in a tripod gait: only three legs have ground contact at this instant, and only the corresponding three-leg vectors can be used to compute the motion of the parallel closed kinematic chains formed by body, legs and substrate. For determining the posture of the next instant in time, the MMC network implements all possible combinations of connected leg segment vectors, along with additional diagonal vectors describing the interaction of the legs *via* the substrate (**Figure 12B**). From these, only the vectors shown in **Figure 12C** are "active" during a tripod stance episode. Much like described for the computations at the leg level, each variable can be computed in multiple ways, using a set of kinematic relations (for details on how to set up these equations, see Schilling et al., 2012).

Controlling Multiple, Mechanically Coupled Limbs Through a Body Model

Much like what has been described in conjunction with **Figure 12A**, the control of stance is induced by a passive movement of the front end, as if pulling the body into a given direction. Owing to the recurrent structure of the MMC network, this disturbance of the body model network propagates to all variables contained in the equations for the connected segments. Most notably, this includes all foot positions of the legs in stance. As a result, these variables are adjusted in a way, which complements the enforced movement. Moreover, as foot positions are shared by the body level and the leg level, the induced changes "spread" down into the leg level networks so as to adjust the variables of individual legs. As a consequence, all joint angles of the closed kinematic chains are adjusted in a cooperative way, supporting the overall body movement. The procedure of making these adjustments lasts for multiple iterations, as the network converges into a stable state. Then the resulting leg and segment vectors can be applied to control the actuators. The main difference between the concepts illustrated in **Figures 10**, **12** concerns the consideration of postural safety in **Figure 10**, and the simultaneous iteration of all posture control variables in **Figure 12**.

The body level allows for continuous changes of body orientation. In our simulations and on the robot HECTOR we found that already a single iteration step of the body level is sufficient to come up with good approximations for all leg vectors concerned. When the body level has converged to a particular leg vector, this leg vector serves as an input to the leg level network (**Figure 12A**, see dashed arrow from left to right connecting the higher with the lower level) ensuing subsequent iterations of these networks and converging to a suitable set of joint angles. In the opposite direction, sensory information acquired by a leg may be used to update the model continuously, thus integrating additional sensory information (Schilling et al., 2012).

The internal body model has been successfully implemented in simulation and on HECTOR. Using dynamic simulations, we first tested the body model in curve walking (**Figure 13B**; Schilling et al., 2012). It allowed HECTOR to navigate quite narrow curves, with markedly prolonged stance movements of the inner hind leg (R3 in **Figure 13B**) much like those reported for visually induced tight turns of tethered walking stick insects (Dürr and Ebeling, 2005). When walking slight curves, stick insects show much less asymmetry between inner and outer leg stance durations (**Figure 13A**) but this strongly increases with increasing curvature of the walked path. As the model simulation was pulled at the front and forced into tight curves, the body level came up with the complementing leg target vectors while exploiting the two inter-segmental drives of HECTOR (see **Figure 5**). The results suggested that the body model can be used for simultaneous active control of the inter-segmental drives and all legs on ground, allowing for complementary contributions in the negotiation of tight curves. During these simulations, the

leg level networks provided robust and stable solutions to the inverse kinematics problems posed by the foot position vector input from the body level. Following the successful application in simulation, the body model has been used on the physical robot as well. There, it has been extended for situations on uneven and rough terrain through a mechanism that adapts the control of body height (Paskarbeit et al., 2015).

Internal Simulation of Movements and Planning

During its use in the control of stance, the body model essentially serves as a dynamic internal representation of body postures. Its convergence properties allow the flexible use of the same body model to generate appropriate reactive movements to a number of different types of disturbances (e.g., inducing a turn or a change in body clearance). When decoupling the body model from the actual joint drives, the same dynamic internal body model may also be used for movement prediction and planning. Recently, we applied it as an internal simulator to forecast the consequences of different alternative behaviors as a form of planning ahead (Schilling and Cruse, 2017). In this series of simulations, the model served a dual purpose, exploiting its full flexibility in motor control and planning. Besides its application for the control of multiple limbs in stance, as described above, the predictive capabilities of the system were used whenever the system ran into a novel, problematic situation. In a form of trial-and-error search, it was used to test possible behaviors, providing an estimate of their outcomes. These estimates allowed to decide whether the chosen behavior would lead to instability or else might help to overcome the problematic situation. Only if the internal simulation proved successful, the internally simulated behavior was applied to the actuators of the system (Schilling and Cruse, 2017). This shows how an embodied internal model may be grounded in lower-level motor control and can be used flexibly for a cognitive task such as planning ahead (Cruse and Schilling, 2016).

INTERNAL MODELS FOR BODY-SIZE LEARNING

The relation between the body and the brain is a crucial aspect of embodied robotics (e.g., Nabeshima et al., 2005; Pfeifer et al., 2007). Modern robotic systems are often requested to be very versatile and may even be designed in a completely reconfigurable way. To deal with such complexity, there is a growing demand for simple techniques that allow a robot to autonomously learn the capability of its body without human intervention (Sturm et al., 2008). The MMC model outlined in "Modularity and the Decentralized Coordination of Multiple Limbs" section is based on a predefined set of kinematic equations that is not subject to adaptation or learning at run-time. As a geometric sensory-motor representation of the body, it serves as a body model under the assumption of no growth or damage. In the following section we will consider the plastic use of such an internal body representation in a life-long memory of *Drosophila melanogaster*, implementing a simple form of body model based on recent experimental findings (Krause, 2015; Krause et al., 2019).

Biological Evidence on Body-Size Learning in Flies

Walking fruit flies can visually estimate the width of a gap in their walkway and engage in energy-consuming climbing behavior only when they see a chance to surmount the chasm (Pick and Strauss, 2005). Since the body size of adult fruit flies depends in part on environmental factors like food quality and temperature during larval stages, there can be considerable size variation among flies of the same genetic background. Therefore, an adaptation process is needed after hatching from the pupal case so that each fly can learn about its own body size. Indeed, visually deprived flies—both freshly hatched flies (Kienitz, 2010) and flies reared in a featureless environment (Krause, 2015)—try to surmount insurmountably wide gaps, whereas flies kept in structured environments with light later take decisions adapted to their body size (Krause et al., 2019).

Experienced small flies abandon attempts on gaps that their larger siblings from the same vials still attempt to climb. The default state of freshly hatched flies before calibrating their size memory is "very large." They calibrate their body-size estimate to their actual body size by gathering visual feed-back from the retinal images of contrast edges during normal locomotion (parallax motion). The act of physically climbing across gaps is not required for this calibration process. Neurogenetic manipulation revealed that body-size learning requires the cAMP cascade. Learning mutants of the cAMP cascade do not adapt to their individual size. Instead, they try to overcome chasms, which are clearly impossible to cross. Mutant analysis and differential rescue experiments *via* the GAL4/UAS-system revealed that the information is stored in projection systems of the protocerebral bridge (PB) of the central complex (CX, **Figure 14A**). Furthermore, we have identified the biochemical learning cascade for this life-long body size memory, but the neural circuitry remains to be determined.

A Computational Model for Body-Size Learning

To simulate the neurobiological findings on gap-climbing *Drosophila melanogaster* flies, we developed a spiking neural network model for body-size learning using parallax-motion information. The model has been implemented and evaluated in a dynamic simulation of HECTOR navigating through a multi-chamber environment. HECTOR has a number of properties that make it a perfect platform for implementing cognitive functions that require embodiment with distributed, multimodal sensory information. One can make use of the embedded distributed sensory system consisting of six pressure sensors located in the tip of each leg, a complete inertial module on the main body and an omnidirectional vision system used to extract the relevant information from the objects located in the environment.

Following the neural structure of the fly brain, the relevant neural assemblies that constitute the Central Complex model are shown in **Figure 14A**. A neuronal lattice captures the essence of the visual system and is used to acquire spatial

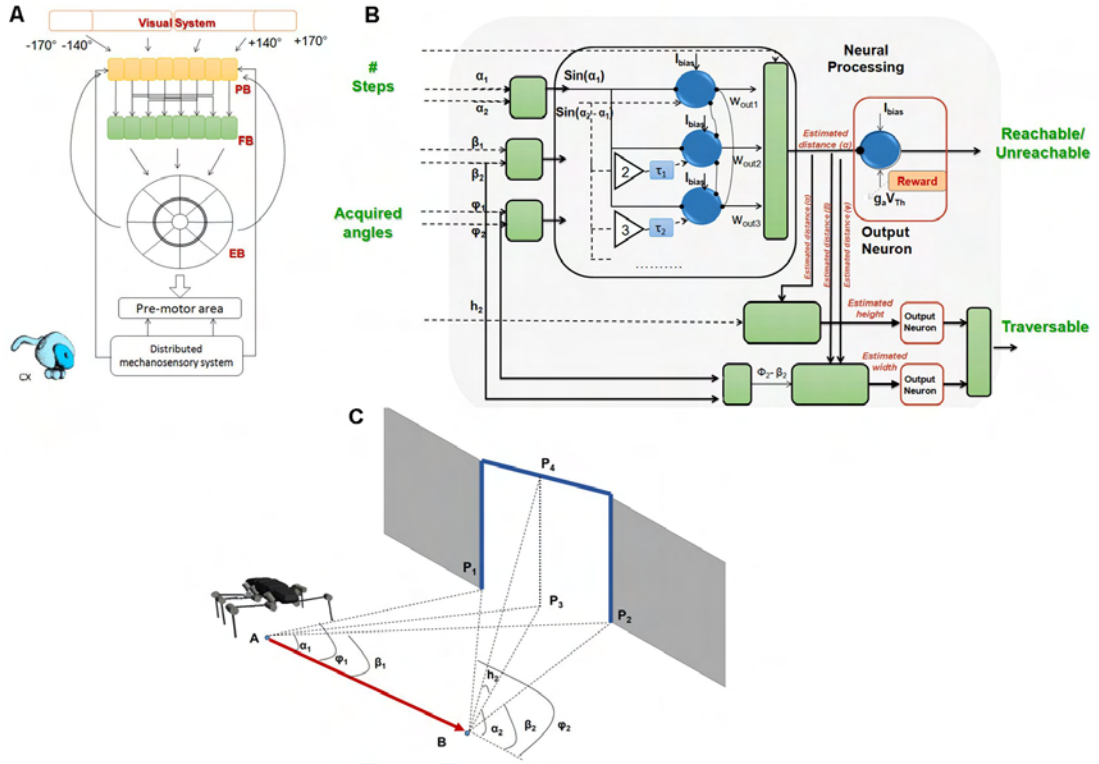

FIGURE 14 | Navigation control structure inspired by the *Drosophila* Central Complex. **(A)** Block scheme of the control structure. The visual system transfers information to the protocerebral bridge (PB) that is involved in body-size learning. The fan-shaped body (FB) participates in visual learning and orientation control whereas the ellipsoid body (EB) is in charge of spatial memory formation. **(B)** Scheme of the network devoted to learning whether an object is reachable within a certain number of steps and whether it is traversable depending on the acquired visual inputs. The green boxes represent simple mathematical transformations, whereas the blue circles represent spiking neurons. The learning process is performed at the level of the output neurons (red boxes). **(C)** Scheme of the angular positions acquired by the visual system as the robot moves forward from point **(A)** to point **(B)**. The object of interest is a gate where different points of interest are detected. Different angles are acquired from the visual system to be processed by the network in **(B)** (adapted by permission from Patané et al., 2018 © 2018).

information about angular directions of the objects of interest and the heading of the robot. This visual information is transferred to the PB and the Fan-shaped Body (FB), which extract the *where* and *what* for heading control and visual learning, respectively. Moreover, it is mediated to the Ellipsoid Body (EB) for the formation of spatial memory (Neuser et al., 2008; Kuntz et al., 2017). Previous studies have tested this model design in the context of direction control, spatial memory and other capabilities (Soto et al., 2009; Arena et al., 2013b). Here, we report its extension to include the formation of body-size knowledge.

Within the dynamic simulation environment, the robot walks around and detects the position of visible objects of interest. The angular position of an object is acquired through a uniformly distributed ring of neurons that have a one-to-one match with the ommatidia of the eye (about 4.8° opening angle each) distributed in a range of about 300°. The output of the stimulated neuron is modulated with a post-synaptic weight that corresponds to the sinusoidal function of the angular position of the neuron. After forward motion from point A to B as shown in **Figure 14C** (equivalent to four robot steps in the experiments described here), the robot evaluates the new angular position of the object of interest. This second acquisition is used to estimate the distance between the robot and the object through parallax, i.e., the angular difference in the position of the same object from two different viewpoints.

The distance between the robot and the object is directly proportional to the distance traveled during the parallax-motion estimation, and the coefficient of proportionality depends on the initial acquired angle and its variation when acquired afterward. Starting from this mathematical formulation, a spiking neural network has been designed and implemented to yield similar results (Arena et al., 2013a). A block scheme of the proposed model is shown in **Figure 14B**. The information about object position acquired in two different time steps is discretized and weighted. An array of Class I Izhikevich neurons (Izhikevich, 2004) is then used to evaluate the ratio between the two acquired sinusoidally modulated inputs.

An array of synaptic gains is used to find the correct match: in the end, excitatory inputs should compensate the inhibitory ones in order to allow the neuron to fire. A bias current was added, making each neuron able to fire with a minimal additional input current. A series of time delays (τ_i) was included to

evaluate the neuronal responses in sequence. Each neuron is connected with the others through inhibitory synapses forming a winner-takes-all network topology. The first active neuron (i.e., winning neuron) strongly inhibits the others and produces an output that is proportional to its corresponding gain factor. Assuming that the system knows the distance traveled between the two instants of acquisition (e.g., in terms of number of steps), the outcome of the first part of the network is a signal that is proportional to the estimated object distance. The last processing stage consists of an output neuron that is subject to a threshold adaptation learning process. Depending on an internally generated reward signal, the threshold level is adapted to either facilitate or reduce the spike rate of the neuron. Threshold adaptation can be considered a consequence of the nonlinearities present in the membrane dynamics of a neuron (Izhikevich, 2004). The threshold adaptation process can be modeled as a voltage-dependent current that is introduced as an additional input to the decision neuron. It can be expressed as $I_A = -g_A{}^*V_{Th}$, defining g_A as an activation conductance and V_{Th} as a dynamic threshold that is being learned. The current can be modified to hyperpolarize or depolarize neurons. The output neuron thus acts as a gate: its firing indicates that an object is reachable, whereas a silent state corresponds to unreachable ones. Therefore, the decision neuron will provide a prediction of reachability or unreachability that has to be verified by the robot.

At the beginning of an experiment, every object is assumed to be reachable, and in each trial, the robot walks towards a selected target. A reward is generated if the object can be reached within twelve steps. This distance may be considered the maximum energy or time available to fulfil the task. The threshold is then modified depending on the coherence between the reinforcement signal and the internal prediction that is provided by the network. If the prediction is correct, the threshold V_{Th} remains unchanged. Otherwise, if the robot's assumption of reachability (or unreachability) is not confirmed during the approach, the threshold V_{Th} is increased (or decreased) by a value ΔV_{Th} so as to hyperpolarize (or depolarize) the output neuron accordingly. As the entity of the threshold variation represents a compromise between the speed of the learning process and the precision required, the learning phase will end as soon as the threshold value reaches a steady state condition.

Further details on the mathematical description of the network and learning process can also be retrieved in Arena et al. (2013a, 2018), where the proposed network was applied to learn the reachability space in roving and walking robots. In applying this control structure to HECTOR, we adopted the same paradigm for the network structure and the learning algorithm. Through acquiring further sensory information from the visual system, body size learning could be extended to include additional capabilities, allowing the robot to estimate not only the distance of an object but also its height and the width through the selection of points of interest (e.g., center of mass, vertex and others). This was exploited in the experimental test of body-size learning, where the size of gates had to be judged depending on the learned body size (**Figure 14C**). The scenario of the simulated environment is shown in **Figure 15A**. It consists of four rooms that are connected by gates of different sizes. At the beginning of the learning phase, the robot was placed in one of these rooms and started to evaluate the estimated distance, height and width of the gates through parallax motion. In a sequence of approaches, the robot first chooses a particular gate at random and then tries to traverse it. Depending on the success of the approach, a reward signal is triggered to adapt the threshold V_{Th} of the output neuron accordingly, thereby tuning the internal body-size representation. Traversable passages were placed between two adjacent rooms, while all the other gates were too small to be used. Therefore, the robot was confined to the four rooms (**Figure 15A**) while allowing for continuous, autonomous learning. **Figures 15B,C** show a typical walking trajectory of the robot while exploring the environment.

Since the distance of the robot to the gates varies, the robot opts for different behavioral choices depending on the capabilities of its own body. **Figure 15D** shows the percentages of selected behaviors depending on the real distance between the robot and the gate. It can be noticed that for low distance values the chosen behavior is an attempt to reach the gate, and the result matches the hypothesis. For distances longer than the reachability threshold, the robot performs a correct give-up (i.e., a change of "interest" in favor of other objects), whereas in the intermediate region, next to the critical distance value, a series of unsuccessful attempts and incorrect give-ups are performed in accord with *Drosophila* experiments (Krause, 2015; Krause et al., 2019).

When the learning process of the output-neuron threshold converges to a stable solution, the robot can use the learned body-size model in the decision-making process. The robot is now capable of identifying gates that can be reached and traversed without getting stuck in a passage that is too narrow to pass. The trajectory performed by the robot at the end of the learning phase is shown in **Figure 15C**. After learning, attempts to pass through not traversable gates are absent.

To evaluate how the body-size knowledge is related to the actual robot size, the simulated HECTOR robot was modified by shortening the tibia of each leg, thus reducing the "reachability threshold" for a given number of steps. This was done for both a 10% and 30% length reduction of the tibia. The results are shown in **Figure 15E**, indicating that each robot learns different body-size models, according to the leg length and the corresponding reachability threshold. The maximum number of unsuccessful attempts differs according to the reachability threshold, such that the distribution peaks of the robots with shortened tibiae occurred at shorter distances. In summary, we could show that a spiking neural network model inspired by the *Drosophila* central complex can learn the body size of the robot through interaction with the environment, and in particular by comparing self-generated estimates of working range with the actual behavioral performance.

CONCLUSIONS

The sections "Muscles and Compliant Actuation," "Distributed Proprioception of Posture and Load," "Ground Contact and Load-Dependent Coordination," "Spatial Coordination of Limbs and Omnidirectional Agility," and "Modularity and the

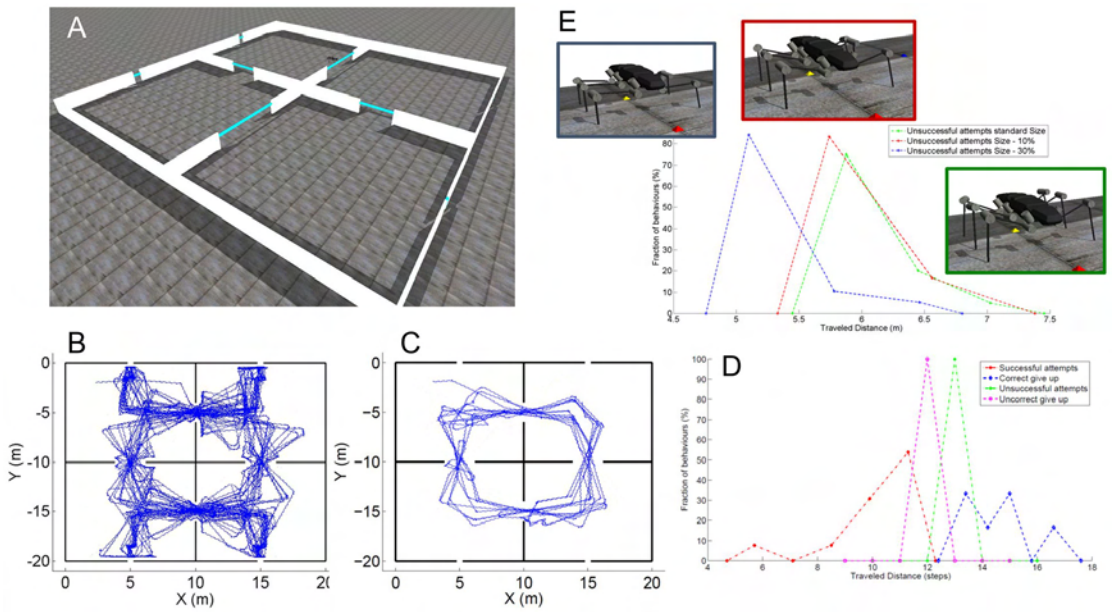

FIGURE 15 | Demonstration of body-size learning. **(A)** The simulation environment consists of four rooms, each one containing three potential passages of different width and height. Each room is 10 × 10 m^2, the gates facing outside are too small to be passed (width: 0.6–0.8 m, height: 0.3–0.4 m) whereas the other gates are large enough (width: 1.5–2.4 m, height: 0.7–1.0 m). **(B)** Trajectory walked by the simulated robot while exploring the environment during the learning phase. During the learning phase, the robot acquires the knowledge needed for the formation of the internal body-size model. **(C)** Trajectory walked by the robot during the test phase. The body-size model is now used to select and pass the suitable gates while avoiding the others. **(D)** Distribution of the possible behavioral choices made on the basis of the distance output neuron. When the traveled distance is next to the maximum reachable value (i.e. 12 steps) the robot, as in the biological counterpart, can either try to attempt unsuccessfully or to give up incorrectly. **(E)** Comparison between the unsuccessful attempts in three simulations, where the HECTOR model was changed by reducing the tibia segment by 10% (red) and 30% (blue).

Decentralized Coordination of Multiple Limbs" provided an overview of the potential for integration of multiple lines of research on a common robotic research platform for biomimetic motor behavior, ranging from compliant actuation to cognitive functions. It has been proposed in the past that the goal of biomimetic robots is to "take inspiration from biological principles to design robots that match the agility of animals, and to use robots as scientific tools to investigate animal adaptive behavior" (Ijspeert, 2014). Here, we argue that a further, equally important goal is *to collate and combine biomimetics research on disparate and conceptually disjunct research areas in the neurosciences and engineering sciences in order to integrate insights and concepts on a common platform*. An important step in this direction was initiated with the *iCub* platform of the Italian Institute of Technology, that was introduced as an open platform for research on cognitive robotics, the role of embodiment for cognitive functions in particular (Metta et al., 2008, 2010). Regarding shared research on robot locomotion, a similarly prominent initiative was centered around the quadruped walking robot *LittleDog* of the company Boston Dynamics. Much like *iCub*, *LittleDog* was used by a number of labs to conduct research on the same platform (Murphy et al., 2010). In both of these cases, the research was mainly focusing on computer science topics in cognitive robotics (in case of iCub) or robust controller software for adaptive locomotion (in case of *LittleDog*). Arguably, the outcome of these very successful research networks was mainly in engineering (e.g., cognitive robotics, robot control).

In the case of the hexapod walking robot HECTOR, three properties proved to be particularly important for integrative research. The first of these properties is the highly decentralized hardware architecture (**Figure 5**) that allows to read out and combine a large number of measurements from different clients ("Distributed Proprioception in HECTOR" section). In the examples provided above, these include 18 sensorised actuators with twelve sensor readings per motor ("The Compliant Joint Drives of HECTOR" section), up to three strain sensor clients ("Distributed Proprioception in HECTOR" section) and one multi-taxel foot tip ("Multi-Taxel Touch Sensor for HECTOR Foot" section) per leg. Together with the second property, the room for additional components inside the exoskeleton (see **Figure 1D**), the decentralized hardware architecture allowed inclusion of a hardware-accelerated vision system (Meyer et al., 2016) or the use of the prothorax segment as a "head unit" hosting a visuo-tactile system. Finally, the availability of a dynamic simulation environment for HECTOR has allowed researchers from different labs to develop and test components while simulating the use of HECTOR's hardware properties. To this end, we have concentrated on research regarding three overarching topics in biomimetic locomotion: (i) the particular significance of distributed load sensing; (ii) the emergence of gaits from local coordination rules (or constraints); and (iii) the

formation and exploitation of internal representations of body posture and size.

Load vs. Posture

Three essential variables need to be controlled in legged locomotion: propulsion, stability and heading. All three of these control variables concern the appropriate acceleration of the center of mass (CoM), which, in turn, implies the generation of appropriate forces and torques causing the desired acceleration. Given the physical limitations of the body and its legs, propulsion, stability and heading can only be maintained through coordinated interaction of the limbs with the substrate. At first sight, monitoring the force/torque distribution across the joints of the limbs, and particularly the interaction forces acting on the feet appears to be the most direct way of controlling CoM accelerations. As yet, the effect of a change in torque at a particular joint drive on the CoM can be predicted only, if: (i) the posture of the limb that contains this particular drive is known; (ii) foot contact is sufficiently firm to transmit forces to the substrate without slip; and (iii) all other legs in ground contact give way appropriately in order not to counteract the intended effect. As a consequence, any controller that is to coordinate the movement of multiple legs during stance has to take account of the current body posture. In HECTOR, the measurement of individual joint torques is possible ("The Compliant Joint Drives of HECTOR" section). The three conditions for estimating effects of single drive torques on the CoM can be met by: (i) joint angle readings from the joint drives ("The Compliant Joint Drives of HECTOR" section) and/or the use of a kinematic internal body model ("Controlling Multiple, Mechanically Coupled Limbs Through a Body Model" section); by (ii) monitoring interaction forces with a multi-taxel foot tip sensor ("Multi-Taxel Touch Sensor for HECTOR Foot" section); and by (iii) monitoring strain forces on leg segments ("Distributed Proprioception in HECTOR" section) and a range of control concepts as discussed in "Omnidirectional Walking in HECTOR" and "Controlling Multiple, Mechanically Coupled Limbs Through a Body Model" sections.

Regarding the various sources of distributed sensory feedback that are available during locomotion, recent findings on freely walking stick insects suggest that load-sensing may be beneficial to monitor load transfer among legs and, thus, to determine the appropriate time for a stance-to-swing transition (Dallmann et al., 2017). Similarly, distributed monitoring of load signals have been used successfully for temporal coordination of multiple legs in robots (e.g., Owaki et al., 2013; Owaki and Ishiguro, 2017). Moreover, the normal and tangential components of the ground reaction force vector as experienced (or measured) by an animal provide an immediate link between stability and propulsion. Accordingly, freely walking stick insects adjust the relative activation of antagonist muscles according to altered load distributions when walking on slopes (Dallmann et al., 2019). Finally, the high spatial resolution of a sensorised foot tip can help to extract detailed contact patterns per foot and potentially serve to judge substrate properties (Borijindakul et al., 2018), thus linking locomotion and near-range exploration (for further discussion of this issue see Dürr et al., 2018).

Despite the multiple potential use of distributed force and load measurements, it remains to be shown whether and how insects integrate these distributed measurements for a global control of CoM acceleration. To date, several experimental results suggest that force/load measurements are mainly used for local control, i.e., for assistance and resistance reflexes at single joints (e.g., Akay et al., 2007; for review, see Zill et al., 2004) and, probably, to support temporal coordination of neighboring legs (Dallmann et al., 2017). Recently, it was shown that postural variables stay remarkably unaffected in stick insects that walk up or down steep slopes, despite the fact that this required substantial adjustment of single-joint torques (Dallmann et al., 2019). This suggests that stick insects tend to adjust muscle force so as to maintain a preferred body posture, rather than to adjust body posture so as to optimize force transfer to the substrate.

Gaits

Unlike in many other walking robots, the gait of HECTOR is not pre-programmed or governed by coupled central oscillators. Instead, the gait emerges from a combination of sensory-motor feedback that regulates limb posture, and/or pairwise coupling of neighboring legs through coordination rules (Cruse, 1990; Cruse et al., 1995). Owing to this approach, a persistent rhythm, i.e., one that characterizes a particular gait, can emerge only once the system enters a steady state. In contrast, transitions in speed, attitude, posture or direction are marked by discontinuities. The most basic types of discontinuity in legged locomotion are the local destabilizing and stabilizing transitions from stance to swing (lift-off) and swing to stance (touch-down), respectively (Dürr et al., 2004). In steady-state locomotion, these step-to-step "local discontinuities" define the overall rhythm or gait. Moreover, they effectively gate the information flow from load and force sensors. This is because strain-sensitive campaniform sensilla afferents of insects fire only if muscle forces are resisted, e.g., during stance (Zill et al., 2012).

In this context, it is important to decide on the function of a swing movement. In the most simple case (and common case in robotics), swing movements are but return strokes of the limb that serve to execute the next stance movement in very much the same way as the preceding one. Essentially, this reduces the control of a swing movement to the inversion of action at every single joint upon lift-off, and a delayed depression in order to re-gain ground contact. In walking insects, however, touch-down locations appear to be under postural control (e.g., Cruse, 1979; Theunissen et al., 2014), and on-going swing movements may be "re-targeted" towards locations detected by the visual (e.g., Niven et al., 2010) or tactile systems (Schütz and Dürr, 2011). Although the latter findings do not concern the stance-to-swing transition, they raise the question as to whether "global discontinuities" such as changes in body inclination or heading could be initiated by swing movements, or need to be initiated during stance. This is not clear because a targeted swing movement and the ensuing altered touch-down location could initiate a new "pulling direction" of the respective leg and, thus, affect the overall acceleration of the CoM during the subsequent stance movement.

In stick insects, the timing of various kinematic parameters suggests that the initiation of visually-induced turning occurs by a change in stance direction of the front legs, both in response to large-field visual cues (Dürr and Ebeling, 2005) and in turning responses towards visual landmarks (Rosano and Webb, 2007). At the same time, the persistent timing of yaw rotation velocity and stance movements of the hind legs during sustained curve walking (**Figure 13A**) indicates that in turning stick insects the function of the legs may differ between initiating (by front legs) and maintaining rotation (by hind legs). Similar to stick insects, HECTOR translates an intended change of heading into appropriate changes in foot trajectories, either by "global" use of an internal body model that moderates the transitions among the participating legs in stance (**Figure 13B**), or by "local" use of inverse kinematics (**Figure 13C**). In both cases, the foot trajectories during stance are terminated depending on postural cues (**Figure 12**; "Controlling Multiple, Mechanically Coupled Limbs Through a Body Model" section) and/or the combination of various posture and torque measures into a single estimator of unrestrictedness (**Figure 11**; "Omnidirectional Walking in HECTOR" section). As a consequence, the timing of lift-off very much depends on posture, thus mixing issues of spatial and temporal coordination in the resulting gait.

Therefore, we argue that gaits should be considered a matter of optimality of steady-state locomotion, rather than a matter of control. This view gains support from theoretical considerations of optimal phase shifts in multi-legged locomotion, so as to minimize energy by restraining vertical oscillations of the CoM (Weihmann, 2018). For closed-loop control of locomotion, a fixed gait imposes limitations that are undesirable for locomotion engineering, and probably inefficient for animal locomotion in a variable environment. Accordingly, we propose that gaits should emerge from a control scheme that ensures not only efficient propulsion and stability, but also sufficient adaptiveness in the face of step-to-step changes in body-substrate interaction, and flexibility in the function of particular limbs as behavioral goals change (Dürr et al., 2018). In HECTOR, we achieve this by a combination of de-centralized control and loose, pairwise coupling among limbs through coordination rules and/or the inclusion of internal spatial representations.

Multiple Spatial Representations

In this study, three kinds of internal spatial representations were considered. Perhaps the most simple form concerned postural mappings between neighboring limbs ("Spatial Coordination of Limbs in Insects" section). This pairwise mapping was originally proposed to model spatial targeting of touch-down locations in ipsilateral pairs of legs by (Dean, 1990), and introduced into the de-centralized walking controller Walknet (Cruse et al., 1995). Such mappings may serve as a distributed representation of the "space within reach" for at least two limbs. The corresponding pairwise posture mappings do not encode spatial information as such, but may serve to transfer spatial contact information to a neighboring limb in a behaviorally relevant manner. As a result, each posture mapping defines an affordance volume (**Figure 9**) within which a receiver leg can exploit the prior experience of a sender leg (Dürr and Schilling, 2018).

An extension of this approach implements a recurrent neural network to combine postural information about all limbs for the coordination of legs in stance. This was originally proposed by Kindermann and Cruse (2002) and later formulated in a more versatile form by Schilling (2011). The architecture of so-called MMC networks incorporates the geometric constraints of many joint positions in a redundant manner, and converges on solutions that meet these constraints, given a nearly arbitrary set of sensory inputs (see "Controlling Multiple, Mechanically Coupled Limbs Through a Body Model" section). The MMC architecture is not grounded on particular properties of physiological neural networks, except that it uses distributed proprioceptive input and implements recurrent neural connections. A possible neurobiological interpretation of its ability to coordinate the kinematics of parallel closed kinematic chains is that recurrent neural networks with rich proprioceptive input and appropriate connectivity may converge on stable states that should be considered an internal representation of body posture.

Finally, a spiking neural network was proposed that can exploit the consequences of own body actions to form an internal representation of body size ("Internal Models for Body-Size Learning" section). The model takes inspiration from findings on the central complex of the fruit fly *Drosophila melanogaster* (Strauss, 2002; Krause et al., 2019). So far, it is the only part of the described HECTOR project that is devoted to online learning. In essence, it deals with the problem that any internal spatial representation needs to be calibrated to the overall body size or limb proportions (for example, a simulated HECTOR with shorter or longer legs; **Figure 15D**). In more general terms, whenever body morphology changes during life-time, or cannot be known at a time suitable for pre-programming, there will always be the need to scale internal mappings.

Integrative Biomimetics

As most other biomimetic robots, HECTOR is not a scaled hardware model of any particular animal species, despite the fact that its original design was inspired by thorax and leg proportions of a stick insect (**Figure 1**). As outlined in all sections above, the technical issues tackled have their counterparts in experimental neuroscience, despite the fact that none of the implementations on HECTOR come even close to being a one-to-one model of the biological counterpart. The proposed solutions are thus conceptual models that reflect system properties of their biological counterpart rather than their physiological implementation. With regard to integration of different lines of research, we find that it can be advantageous to combine conceptual models because individual subsystems do not have to be adjusted to the particular implementations of other subsystems, as long as they can be interfaced. In relation to Marr's three levels of analysis (Marr and Poggio, 1976), this loosely corresponds to an integration at the algorithmic level.

Moreover, the different methodologies that were applied in the neurobiological experiments conducted in conjunction with this article (e.g., reflex circuits in **Figure 3**, ground reaction forces in **Figure 6**, muscle activity in **Figure 8**, behavioral physiology of unrestrained locomotion in **Figure 9**,

and neurogenetics of higher-order motor behavior in **Figure 14**) are paralleled by equally different methodologies in the engineering developments (e.g., mechatronics in **Figure 2**; sensor technology in **Figure 7**, modeling of recurrent neural networks in **Figure 12**, and of spiking neural networks in **Figure 14**). Since all of these methodologies—both in neuroscience and in engineering—require very different and potentially disjunct areas of expertise, we believe that it not only takes collaborative effort of different research labs to bring these areas of expertise together but that it is absolutely essential to have a common research integration platform like HECTOR and a corresponding dynamic simulation environment to do so.

AUTHOR CONTRIBUTIONS

VD, PA, HC, AD, MSchi, JS, RS, and AS: conceived the project. VD, PA, RS, and AS: acquired funding. VD, PA, SM-T, JS, RS, and AS: coordinated the subprojects. CD, AD, TH, TK, JP, LP, MSchä, MSchi, JS, LT, and AV: conducted the experiments. VD, PA, HC, CD, AD, TK, JP, LP, MSchä, MSchi, JS, RS, LT, AV, and AS: analyzed the data and prepared figures. VD, PA, AD, LP, MSchi, JS, RS, and AS: wrote the manuscript.

FUNDING

This work was funded by FP7 Information and Communication Technologies (FP7 ICT) Grant No. 270182, entitled "Embodied Motion Intelligence for Cognitive, Autonomous roBots" (EMICAB) awarded to VD, AS, PA, and RS, and the large-scale project "Embodied Intelligence as a Core of Cognitive Intelligence" (EICCI) awarded to VD and AS as part of Deutsche Forschungsgemeinschaft (DFG) grant EXC 277 (CITEC).

ACKNOWLEDGMENTS

We thank Olivier Da Costa, Holger Krapp and Gurvinder Virk for supportive and constructive criticism throughout the initial phase of this collaborative project. The electronics boards for reading out the strain gauge pairs shown in **Figure 4** were kindly designed and manufactured by the Cognitronics and Sensor Systems group of the Technical Faculty of Bielefeld University. We thank Nalin Harischandra, Andre F. Krause for their contributions during the EMICAB project, and Yannick Günzel for technical assistance.

REFERENCES

Ache, J. M., Namiki, S., Lee, A., Branson, K., and Card, G. M. (2019). State-dependent decoupling of sensory and motor circuits underlies behavioral flexibility in *Drosophila*. *Nat. Neurosci.* 22, 1132–1139. doi: 10.1038/s41593-019-0413-4

Akay, T., Ludwar, B. C., Göritz, M. L., Schmitz, J., and Büschges, A. (2007). Segment specificity of load signal processing depends on walking direction in the stick insect leg muscle control system. *J. Neurosci.* 27, 3285–3294. doi: 10.1523/JNEUROSCI.5202-06.2007

Albiez, J. C., Luksch, T., Ilg, W., Berns, K., and Dillmann, R. (2003). Reactive reflex based control for a four-legged walking machine. *Rob. Auton. Syst.* 44, 181–189. doi: 10.1016/s0921-8890(03)00068-x

Albu-Schäffer, A., Ott, C., and Hirzinger, G. (2007). A unified passivity based control framework for position, torque and impedance control of flexible joint robots. *Int. J. Rob. Res.* 26, 23–39. doi: 10.1177/0278364907073776

Alexander, R. M. (2003). *Principles of Animal Locomotion.* Princeton, NJ: Princeton University Press.

Altendorfer, R., Moore, N., Komsuolu, H., Buehler, M., Brown, H. B., McMordie, D., et al. (2001). RHex: a biologically inspired hexapod runner. *Auton. Robots* 11, 207–213. doi: 10.21236/ada438814

Anderson, R. J., and Spong, M. W. (1988). Hybrid impedance control of robotic manipulators. *IEEE J. Robot. Autom.* 4, 549–556. doi: 10.1109/56.20440

Annunziata, S., Paskarbeit, J., and Schneider, A. (2011). Novel bioinspired control approaches to increase the stiffness variability in multi-muscle driven joints. *Bioinspir. Biomim.* 6:045003. doi: 10.1088/1748-3182/6/4/045003

Annunziata, S., and Schneider, A. (2012). Physiologically based control laws featuring antagonistic muscle co-activation for stable compliant joint drives. *Appl. Bionics Biomech.* 9, 249–266. doi: 10.1155/2012/503818

Aoi, S., Manoonpong, P., Ambe, Y., Matsuno, F., and Wörgötter, F. (2017). Adaptive control strategies for interlimb coordination in legged robots: a review. *Front. Neurorobot.* 11:39. doi: 10.3389/fnbot.2017.00039

Arena, E., Arena, P., and Patanè, L. (2012). "CPG-based locomotion generation in a *Drosophila* inspired legged robot," in *Proceedings of the 2010 4th IEEE RAS/EMBS International Conference on Biomedical Robotics and Biomechatronics* (Roma: IEEE), 1341–1346.

Arena, P., Di Mauro, G., Krause, T., Patanè, L., and Strauss, R. (2013a). "A spiking network for body size learning inspired by the fruit fly," in *Proceedings of the International Joint Conference on Neural Networks* (Dallas, TX: IEEE), 1251–1257.

Arena, P., Marceo, S., Patanè, L., and Strauss, R. (2013b). "A spiking network for spatial memory formation: towards a fly-inspired ellipsoid body model," in *International Joint Conference on Neural Networks* (Dallas, TX: IEEE), 1245–1250.

Arena, P., and Patanè, L. (2009). *Spatial Temporal Patterns for Action Oriented Perception in Roving Robots.* Berlin: Springer.

Arena, P., Patanè, L., Sanalitro, D., and Vitanza, A. (2018). "Insect-inspired body size learning model on a humanoid robot," in *Proceedings of the 7th IEEE International Conference on Biomedical Robotics and Biomechatronics (Biorob)*, (Enschede, Netherlands: IEEE), 1127–1132.

Aubert, X. (1956). *Le Couplage Énergetique de la Contraction Musculaire.* Brussels: Université Catholique de Louvain. Doctoral Dissertation.

Ayers, J., Davis, J., and Rudolph, A. (2002). *Neurotechnology for Biomimetic Robots.* Cambridge, MA: MIT Press.

Bartsch, S., Birnschein, T., Rommermann, M., Hilljegerdes, J., Kuhn, D., and Kirchner, F. (2012). Development of the six-legged walking and climbing robot SpaceClimber. *J. Field Robot.* 29, 506–532. doi: 10.1002/rob.21418

Bässler, U., and Büschges, A. (1998). Pattern generation for stick insect walking movements—multisensory control of a locomotor program. *Brain Res. Rev.* 27, 65–88. doi: 10.1016/s0165-0173(98)00006-x

Bender, J. A., Simpson, E. M., Tietz, B. R., Daltorio, K. A., Quinn, R. D., and Ritzmann, R. E. (2011). Kinematic and behavioral evidence for a distinction between trotting and ambling gaits in the cockroach *Blaberus discoidalis*. *J. Exp. Biol.* 214, 2057–2064. doi: 10.1242/jeb.056481

Berg, E. M., Büschges, A., and Schmidt, J. (2013). Single perturbations cause sustained changes in searching behavior in stick insects. *J. Exp. Biol.* 216, 1064–1074. doi: 10.1242/jeb.076406

Berkowitz, A., and Laurent, G. (1996). Central generation of grooming motor patterns and interlimb coordination in locusts. *J. Neurosci.* 16, 8079–8091. doi: 10.1523/JNEUROSCI.16-24-08079.1996

Berns, K., Cordes, S., and Ilg, W. (1994). "Adaptive, neural control architecture for the walking machine lauron," in *Proceedings of the IEEE/RSJ International Conference on Intelligent Robots and Systems* (München: IEEE), 1172–1177.

Bidaye, S. S., Bockemühl, T., and Büschges, A. (2017). Six-legged walking in insects: how CPGs, peripheral feedback, and descending signals generate coordinated and adaptive motor rhythms. *J. Neurophysiol.* 119, 459–475. doi: 10.1152/jn.00658.2017

Bidaye, S. S., Machacek, C., Wu, Y., and Dickson, B. J. (2014). Neuronal control of *Drosophila* walking direction. *Science* 344, 97–101. doi: 10.1126/science.1249964

Borijindakul, P., Jinuntuya, N., Drimus, A., and Manoonpong, P. (2018). "Cylindrical terrain classification using a compliant robot foot with a flexible tactile-array sensor for legged robots," in *Proceedings of the From Animals to Animats 15th International Conference on Simulation of Adaptive Behavior, SAB 2018* (Frankfurt: Springer VS), 136–146.

Buchanan, T. S., Lloyd, D. G., Manal, K., and Besier, T. F. (2004). Neuromusculoskeletal modeling: estimation of muscle forces and joint moments and movements from measurements of neural command. *J. Appl. Biomech.* 20, 367–395. doi: 10.1123/jab.20.4.367

Büschges, A., and El Manira, A. (1998). Sensory pathways and their modulation in the control of locomotion. *Curr. Opin. Neurobiol.* 8, 733–739. doi: 10.1016/s0959-4388(98)80115-3

Büschges, A., Schmitz, J., and Bässler, U. (1995). Rhythmic patterns in the thoracic nerve cord of the stick insect induced by pilocarpine. *J. Exp. Biol.* 198, 435–456.

Cruse, H. (1979). The control of the anterior extreme position of the hindleg of a walking insect, *Carausius morosus*. *Physiol. Entomol.* 4, 121–124. doi: 10.1111/j.1365-3032.1979.tb00186.x

Cruse, H. (1985). Which parameters control the leg movement of a walking insect? II. The start of the swing phase. *J. Exp. Biol.* 116, 357–362.

Cruse, H. (1990). What mechanisms coordinate leg movement in walking arthropods? *Trends Neurosci.* 13, 15–21. doi: 10.1016/0166-2236(90)90057-h

Cruse, H., Bartling, C., Dreifert, M., Schmitz, J., Brunn, D. E., Dean, J., et al. (1995). Walking: a complex behaviour controlled by simple networks. *Adapt. Behav.* 3, 385–418. doi: 10.1177/105971239500300403

Cruse, H., and Epstein, S. (1982). Peripheral influences on the movement of the legs in a walking insect *Carausius morosus*. *J. Exp. Biol.* 101, 161–170.

Cruse, H., Kindermann, T., Schumm, M., Dean, J., and Schmitz, J. (1998). Walknet—a biologically inspired network to control six-legged walking. *Neural Netw.* 11, 1435–1447. doi: 10.1016/s0893-6080(98)00067-7

Cruse, H., and Schilling, M. (2016). Mental states as emergent properties—from walking to consciousness *Open Mind, Philosophy and the Mind Sciences in the 21st Century. Vol 1*, eds T. Metzinger and J. M. Windt (Cambridge, MA: MIT Press), 349–419.

Cruse, H., and Schwarze, W. (1988). Mechanisms of coupling between the ipsilateral legs of a walking insect (*Carausius morosus*). *J. Exp. Biol.* 138, 455–469.

Dallmann, C. J., Dürr, V., and Schmitz, J. (2016). Joint torques in a freely walking insect reveal distinct functions of leg joints in propulsion and posture control. *Proc. R. Soc. B Biol. Sci.* 283:20151708. doi: 10.1098/rspb.2015.1708

Dallmann, C. J., Dürr, V., and Schmitz, J. (2019). Motor control of an insect leg during level and incline walking. *J. Exp. Biol.* 222:jeb188748. doi: 10.1242/jeb.188748

Dallmann, C. J., Hoinville, T., Dürr, V., and Schmitz, J. (2017). A load-based mechanism for inter-leg coordination in insects. *Proc. Biol. Sci.* 284:20171755. doi: 10.1098/rspb.2017.1755

Daun-Gruhn, S., and Tóth, T. I. (2011). An inter-segmental network model and its use in elucidating gait-switches in the stick insect. *J. Comput. Neurosci.* 31, 43–60. doi: 10.1007/s10827-010-0300-1

Dean, J. (1990). Coding proprioceptive information to control movement to a target: simulation with a simple neural network. *Biol. Cybern.* 63, 115–120. doi: 10.1007/bf00203033

Delibes, M., Castañeda, I., and Fedriani, J. M. (2017). Tree-climbing goats disperse seeds during rumination. *Front. Ecol. Environ.* 15, 222–223. doi: 10.1002/fee.1488

Devjanin, E. A., Gurfinkel, V. S., Gurfinkel, E. V., Kartashev, V. A., Lensky, A. V., Shneider, A. Y., et al. (1983). The six-legged walking robot capable of terrain adaptation. *Mechan. Mach. Theory* 18, 257–260. doi: 10.1016/0094-114x(83)90114-3

Dickinson, M. H., Farley, C. T., Full, R. J., Koehl, M. A. R., Kram, R., and Lehman, S. (2000). How animals move: an integrative view. *Science* 288, 100–106. doi: 10.1126/science.288.5463.100

Donelan, J. M., and Pearson, K. G. (2004). Contribution of force feedback to ankle extensor activity in decerebrate walking cats. *J. Neurophysiol.* 92, 2093–2104. doi: 10.1152/jn.00325.2004

Drimus, A., Jankovics, V., Gorsic, M., and Mátéfi-Tempfli, S. (2014a). "Novel high resolution tactile robotic fingertips," in *IEEE Sensors* (Valencia: IEEE), 791–794. doi: 10.1109/ICSENS.2014.6985118

Drimus, A., Kootstra, G., Bilberg, A., and Kragic, D. (2014b). Design of a flexible tactile sensor for classification of rigid and deformable objects. *Rob. Auton. Syst.* 62, 3–15. doi: 10.1016/j.robot.2012.07.021

Dudek, D. M., and Full, R. J. (2006). Passive mechanical properties of legs from running insects. *J. Exp. Biol.* 209, 1502–1515. doi: 10.1242/jeb.02146

Dürr, V. (2001). Stereotypic leg searching-movements in the stick insect: kinematic analysis, behavioural context and simulation. *J. Exp. Biol.* 204, 1589–1604.

Dürr, V., and Ebeling, W. (2005). The behavioural transition from straight to curve walking: kinetics of leg movement parameters and the initiation of turning. *J. Exp. Biol.* 208, 2237–2252. doi: 10.1242/jeb.01637

Dürr, V., and Matheson, T. (2003). Graded limb targeting in an insect is caused by the shift of a single movement pattern. *J. Neurophysiol.* 90, 1754–1765. doi: 10.1152/jn.00416.2003

Dürr, V., and Schilling, M. (2018). Transfer of spatial contact information among limbs and the notion of peripersonal space in insects. *Front. Comput. Neurosci.* 12:101. doi: 10.3389/fncom.2018.00101

Dürr, V., Schmitz, J., and Cruse, H. (2004). Behaviour-based modelling of hexapod locomotion: linking biology and technical application. *Arthropod Struct. Dev.* 33, 237–250. doi: 10.1016/j.asd.2004.05.004

Dürr, V., Theunissen, L. M., Dallmann, C. J., Hoinville, T., and Schmitz, J. (2018). Motor flexibility in insects: adaptive coordination of limbs in locomotion and near-range exploration. *Behav. Ecol. Sociobiol.* 72:15. doi: 10.1007/s00265-017-2412-3

Ebeling, W., and Dürr, V. (2006). Perturbation of leg protraction causes context-dependent modulation of inter-leg coordination, but not of avoidance reflexes. *J. Exp. Biol.* 209, 2199–2214. doi: 10.1242/jeb.02251

Ekeberg, Ö., Blümel, M., and Büschges, A. (2004). Dynamic simulation of insect walking. *Arthropod Struct. Dev.* 33, 287–300. doi: 10.1016/j.asd.2004.05.002

Ekeberg, Ö., and Pearson, K. G. (2005). Computer simulation of stepping in the hind legs of the cat: an examination of mechanisms regulating the stance-to-swing transition. *J. Neurophysiol.* 94, 4256–4268. doi: 10.1152/jn.00065.2005

Espenschied, K. S., Quinn, R. D., Beer, R. D., and Chiel, H. J. (1996). Biologically based distributed control and local reflexes improve rough terrain locomotion in a hexapod robot. *Rob. Auton. Syst.* 18, 59–64. doi: 10.1016/0921-8890(96)00003-6

Fielding, M. R., and Dunlop, G. (2004). Omnidirectional hexapod walking and efficient gaits using restrictedness. *Int. J. Robotics Res.* 23, 1105–1110. doi: 10.1177/0278364904047396

Frigon, A., and Rossignol, S. (2006). Experiments and models of sensorimotor interactions during locomotion. *Biol. Cybern.* 95, 607–627. doi: 10.1007/s00422-006-0129-x

Goldschmidt, D., Wörgötter, F., and Manoonpong, P. (2014). Biologically-inspired adaptive obstacle negotiation behavior of hexapod robots. *Front. Neurorobot.* 8:3. doi: 10.3389/fnbot.2014.00003

Grabowska, M., Godlewska, E., Schmidt, J., and Daun-Gruhn, S. (2012). Quadrupedal gaits in hexapod animals-inter-leg coordination in free-walking adult stick insects. *J. Exp. Biol.* 215, 4255–4266. doi: 10.1242/jeb.073643

Gribble, P. L., Mullin, L. I., Cothros, N., and Mattar, A. (2003). Role of cocontraction in arm movement accuracy. *J. Neurophysiol.* 89, 2396–2405. doi: 10.1152/jn.01020.2002

Gruhn, M., Zehl, L., and Büschges, A. (2009). Straight walking and turning on a slippery surface. *J. Exp. Biol.* 212, 194–209. doi: 10.1242/jeb.018317

Haberkorn, A., Gruhn, M., Zill, S. N., and Büschges, A. (2019). Identification of the origin of force-feedback signals influencing motor neurons of the thoraco-coxal joint in an insect. *J. Comp. Physiol. A* 205, 253–270. doi: 10.1007/s00359-019-01334-4

Harischandra, N., Clare, A. J., Zakotnik, J., Blackburn, L. M. L., Matheson, T., and Dürr, V. (2019). Evaluation of linear and non-linear activation dynamics models for insect muscle. *PLoS Comput. Biol.* 15:e1007437. doi: 10.1371/journal.pcbi.1007437

Hatze, H. (1974). "A model of skeletal muscle suitable for optimal motion problems," in *Biomechanics IV, International Society of Biomechanics in Sports Science*, eds R. C. Nelson and C. A. Mourehouse (Basel: Karger), 417–422.

Hill, A. V. (1938). The heat of shortening and the dynamic constants of muscle. *Proc. R. Soc. Lond. B Biol. Sci.* 126, 136–195. doi: 10.1098/rspb.1938.0050

Hogan, N. (1984). Adaptive control of mechanical impedance by coactivation of antagonist muscles. *IEEE Trans. Automat. Contr.* 29, 681–690. doi: 10.1109/tac.1984.1103644

Hogan, N. (1985). Impedance control: an approach to manipulation: part I-theory. *J. Dyn. Sys. Meas. Control* 107, 1–7. doi: 10.1115/1.3140702

Hoinville, T., Harischandra, N., Krause, A. F., and Dürr, V. (2014). "Insect-inspired tactile contour sampling using vibration-based robotic antennae," in *Biomimetic and Biohybrid Systems. Living Machines 2014. Lecture Notes in Computer Science*, eds A. Duff, N. F. Lepora, A. Mura, T. J. Prescott, and P. F. M. J. Verschure (Cham: Springer) 8608, 118–129. doi: 10.1007/978-3-319-09435-9_11

Honegger, H.-W. (1981). A preliminary note on a new optomotor response in crickets: antennal tracking of moving targets. *J. Comp. Physiol. A* 142, 419–421. doi: 10.1007/bf00605454

Horridge, G. A. (1965). "The arthropoda: part III insecta," in *Structure and Function in the Nervous System, Vol. II*, eds T. H. Bullock and G. A. Horridge (San Francisco, CA: Freeman), 1030–1055.

Ijspeert, A. J. (2014). Biorobotics: using robots to emulate and investigate agile locomotion. *Science* 346, 196–203. doi: 10.1126/science.1254486

Ijspeert, A. J., Crespi, A., Ryczko, D., and Cabelguen, J.-M. (2007). From swimming to walking with a salamander robot driven by a spinal cord model. *Science* 315, 1416–1420. doi: 10.1126/science.1138353

Ilg, W., and Berns, K. (1995). A learning achitecture based on reinforcement learning for adaptive-control of the walking machine LAURON. *Rob. Auton. Syst.* 15, 321–334. doi: 10.1016/0921-8890(95)00009-5

Isakov, A., Buchanan, S. M., Sullivan, B., Ramachandran, A., Chapman, J. K. S., Lu, E. S., et al. (2016). Recovery of locomotion after injury in *Drosophila* depends on proprioception. *J. Exp. Biol.* 219, 1760–1771. doi: 10.1242/jeb.133652

Izhikevich, E. M. (2004). Which model to use for cortical spiking neurons? *IEEE Trans. Neural Netw.* 15, 1063–1070. doi: 10.1109/TNN.2004.832719

Jander, J. P. (1985). "Mechanical stability in stick insects when walking straight and around curves," in *Insect Locomotion*, eds M. Gewecke and G. Wendler (Berlin: Paul Parey), 33–42.

Jindrich, D. L., and Full, R. J. (1999). Many-legged maneuverability: dynamics of turning in hexapods. *J. Exp. Biol.* 202, 1603–1623.

Jindrich, D. L., and Full, R. J. (2002). Dynamic stabilization of rapid hexapedal locomotion. *J. Exp. Biol.* 205, 2803–2823.

Keller, B. R., Duke, E. R., Aymer, A. S., and Zill, S. N. (2007). Tuning posture to body load: decreases in load produce discrete sensory signals in the legs of freely standing cockroaches. *J. Comp. Physiol. A* 193, 881–891. doi: 10.1007/s00359-007-0241-y

Kienitz, B. (2010). *Motorisches Lernen in Drosophila Melanogaster*. Mainz, Germany: Johannes Gutenberg Universität. Doctoral Dissertation.

Kindermann, T., and Cruse, H. (2002). MMC-a new numerical approach to the kinematics of complex manipulators. *Mech. Mach. Theory* 37, 375–394. doi: 10.1016/s0094-114x(01)00080-5

Klaassen, B., Linnemann, R., Spenneberg, D., and Kirchner, F. (2002). Biomimetic walking robot scorpion: control and modeling. *Rob. Auton. Syst.* 41, 69–76. doi: 10.1016/s0921-8890(02)00258-0

Krause, T. (2015). *Physiologie eines erlernten Körpermodells bei Drosophila melanogaster*. Mainz, Germany: Johannes Gutenberg Universität. Doctoral Dissertation.

Krause, T., Spindler, L., Poeck, B., and Strauss, R. (2019). *Drosophila* acquires a long-lasting body-size memory from visual feedback. *Curr. Biol.* 29, 1833.e3–1841.e3. doi: 10.1016/j.cub.2019.04.037

Krause, A. F., Winkler, A., and Dürr, V. (2013). Central drive and proprioceptive control of antennal movements in the walking stick insect. *J. Physiol. Paris* 107, 116–129. doi: 10.1016/j.jphysparis.2012.06.001

Kuntz, S., Poeck, B., and Strauss, R. (2017). Visual working memory requires permissive and instructive NO/cGMP signaling at presynapses in the *Drosophila* central brain. *Curr. Biol.* 27, 613–623. doi: 10.1016/j.cub.2016.12.056

Land, M. F. (1972). Stepping movements made by jumping spiders during turns mediated by the lateral eyes. *J. Exp. Biol.* 57, 15–40.

Lewinson, R. T., and Stefanyshyn, D. J. (2016). A descriptive analysis of the climbing mechanics of a mountain goat (*Oreamnos americanus*). *Zoology* 119, 541–546. doi: 10.1016/j.zool.2016.06.001

Manoonpong, P., Pasemann, F., and Wörgötter, F. (2008). Sensor-driven neural control for omnidirectional locomotion and versatile reactive behaviors of walking machines. *Rob. Auton. Syst.* 56, 265–288. doi: 10.1016/j.robot.2007.07.004

Marr, D., and Poggio, T. (1976). From understanding computation to understanding neural circuitry. *AI Memo* 357, 1–22.

Matheson, T. (1998). Contralateral coordination and retargeting of limb movements during scratching in the locust. *J. Exp. Biol.* 201, 2021–2032.

Matheson, T., and Dürr, V. (2003). Load compensation in targeted limb movements of an insect. *J. Exp. Biol.* 206, 3175–3186. doi: 10.1242/jeb.00534

McIver, S. B. (1985). "Mechanoreception," in *Comprehensive Insect Physiology, Biochemistry and Pharmacology*, eds G. A. Kerkut and L. I. Gilbert (Oxford, New York, NY: Pergamon Press), 71–132.

Metta, G., Natale, L., Nori, F., Sandini, G., Vernon, D., Fadiga, L., et al. (2010). The iCub-áhumanoid robot: an open-systems platform for research in cognitive development. *Neural Netw.* 23, 1125–1134. doi: 10.1016/j.neunet.2010.08.010

Metta, G., Sandini, G., Vernon, D., Natale, L., and Nori, F. (2008). "The iCub humanoid robot: an open platform for research in embodied cognition," in *Proceedings of the 8th Workshop on Performance Metrics for Intelligent Systems (PerMIS'08)*, (Gaithersburg, MD: ACM), 50–56. doi: 10.1145/1774674.1774683

Meyer, H. G., Bertrand, O. J. N., Paskarbeit, J., Lindemann, J. P., Schneider, A., and Egelhaaf, M. (2016). "A bio-inspired model for visual collision avoidance on a hexapod walking robot," in *Living Machines 2016: Biomimetic and Biohybrid Systems. 2016*, eds N. F. Lepora, A. Mura, M. Mangan, P. F. M. J. Verschure, M. Desmulliez, and T. J. Prescott (Cham: Springer International Publishing), 167–178.

Murphy, M. P., Saunders, A., Moreira, C., Rizzi, A. A., and Raibert, M. (2010). "The LittleDog robot," in *The International Journal of Robotics Research* (Anchorage, AK: IEEE) 30, 145–149.

Mussa-Ivaldi, F. A., Morasso, P., and Zaccaria, R. (1988). Kinematic networks. *Biol. Cybern.* 60, 1–16. doi: 10.1007/bf00205967

Nabeshima, C., Lungarella, M., and Kuniyoshi, Y. (2005). "Timing-based model of body schema adaptation and its role in perception and tool use: a robot case study," in *IEEE International Conference on Development and Learning (ICDL-05)*, (Osaka: IEEE), 7–12.

Neuser, K., Triphan, T., Mronz, M., Poeck, B., and Strauss, R. (2008). Analysis of a spatial orientation memory in *Drosophila*. *Nature* 453, 1244–1247. doi: 10.1038/nature07003

Niven, J. E., Buckingham, C. J., Lumley, S., Cuttle, M. F., and Laughlin, S. B. (2010). Visual targeting of forelimbs in ladder-walking locusts. *Curr. Biol.* 20, 86–91. doi: 10.1016/j.cub.2009.10.079

Niven, J. E., Ott, S. R., and Rogers, S. M. (2012). Visually targeted reaching in horse-head grasshoppers. *Proc. Biol. Sci.* 279, 3697–3705. doi: 10.1098/rspb.2012.0918

Owaki, D., Goda, M., Miyazawa, S., and Ishiguro, A. (2017). A minimal model describing hexapedal interlimb coordination: the Tegotae-based approach. *Front. Neurorobot.* 11:29. doi: 10.3389/fnbot.2017.00029

Owaki, D., and Ishiguro, A. (2017). A quadruped robot exhibiting spontaneous gait transitions from walking to trotting to galloping. *Sci. Rep.* 7:277. doi: 10.1038/s41598-017-00348-9

Owaki, D., Kano, T., Nagasawa, K., Atsushi, T., and Ishiguro, A. (2013). Simple robot suggests physical interlimb communication is essential for quadruped walking. *J. R. Soc. Interface* 10:20120669. doi: 10.1098/rsif.2012.0669

Page, K. L., and Matheson, T. (2009). Functional recovery of aimed scratching movements following a graded proprioceptive manipulation. *J. Neurosci.* 29, 3897–3907. doi: 10.1523/jneurosci.0089-09.2009

Paskarbeit, J. (2017). *Consider the Robot—Abstraction of Bioinspired Leg Coordination and its Application to a Hexapod Robot Under Consideration of Technical Constraints*. Bielefeld: Bielefeld University. Doctoral Dissertation.

Paskarbeit, J., Annunziata, S., Basa, D., and Schneider, A. (2013). A self-contained, elastic joint drive for robotics applications based on a sensorised elastomer

coupling—design and identification. *Sens. Actuators A Phys.* 199, 56–66. doi: 10.1016/j.sna.2013.04.028

Paskarbeit, J., Schilling, M., Schmitz, J., and Schneider, A. (2015). "Obstacle crossing of a real, compliant robot based on local evasion movements and averaging of stance heights using singular value decomposition," in *IEEE International Conference on Robotics and Automation (ICRA)*, (Seattle, WA: IEEE), 3140–3145.

Patané, L., Strauss, R., and Arena, P. (2018). "Nonlinear circuits and systems for neuro-inspired robot control," in *Springer Briefs in Nonlinear Circuits*, eds L. Fortuna, and G. Chen (Springer: Springer International Publishing), I–XII. doi: 10.1007/978-3-319-73347-0

Pearson, K. G. (1995). Proprioceptive regulation of locomotion. *Curr. Opin. Neurobiol.* 5, 786–791. doi: 10.1016/0959-4388(95)80107-3

Pfeifer, R., Lungarella, M., and Iida, F. (2007). Self-organization, embodiment, and biologically inspired robotics. *Science* 318, 1088–1093. doi: 10.1126/science.1145803

Pfeiffer, F., Eltze, J., and Weidemann, H. J. (1995). Six-legged technical walking considering biological principles. *Rob. Auton. Syst.* 14, 223–232. doi: 10.1016/0921-8890(94)00031-v

Pick, S., and Strauss, R. (2005). Goal-driven behavioral adaptations in gap-climbing *Drosophila*. *Curr. Biol.* 15, 1473–1478. doi: 10.1016/j.cub.2005.07.022

Pratt, G. A., and Williamson, M. M. (1995). "Series elastic actuators," in *Proceedings of the 1995 IEEE/RSJ International Conference on Intelligent Robots and Systems'95. Human Robot Interaction and Cooperative Robots* (Pittsburgh, PA: IEEE), 399–406.

Prochazka, A., Gillard, D., and Bennett, D. J. (1997a). Implications of positive feedback in the control of movement. *J. Neurophysiol.* 77, 3237–3251. doi: 10.1152/jn.1997.77.6.3237

Prochazka, A., Gillard, D., and Bennett, D. J. (1997b). Positive force feedback control of muscles. *J. Neurophysiol.* 77, 3226–3236. doi: 10.1152/jn.1997.77.6.3226

Rack, P. M., and Westbury, D. R. (1969). The effects of length and stimulus rate on tension in the isometric cat soleus muscle. *J. Physiol.* 204, 443–460. doi: 10.1113/jphysiol.1969.sp008923

Ritzmann, R. E., Quinn, R. D., Watson, J. T., and Zill, S. N. (2000). Insect walking and biorobotics: a relationship with mutual benefits. *BioScience* 50, 23–33. doi: 10.1641/0006-3568(2000)050[0023:iwabar]2.3.co;2

Romero, F., and Alonso, F. (2016). A comparison among different Hill-type contraction dynamics formulations for muscle force estimation. *Mech. Sci.* 7, 19–29. doi: 10.5194/ms-7-19-2016

Rosano, H., and Webb, B. (2007). A dynamic model of thoracic differentiation for the control of turning in the stick insect. *Biol. Cybern.* 97, 229–246. doi: 10.1007/s00422-007-0170-4

Ryckebusch, S., and Laurent, G. (1993). Rhythmic patterns evoked in locust leg motor-neurons by the muscarinic agonist pilocarpine. *J. Neurophysiol.* 69, 1583–1595. doi: 10.1152/jn.1993.69.5.1583

Sawicki, G. S., Robertson, B. D., Azizi, E., and Roberts, T. J. (2015). Timing matters: tuning the mechanics of a muscle-tendon unit by adjusting stimulation phase during cyclic contractions. *J. Exp. Biol.* 218, 3150–3159. doi: 10.1242/jeb.121673

Schilling, M. (2011). Universally manipulable body models—dual quaternion representations in layered and dynamic MMCs. *Auton. Robots* 30, 399–425. doi: 10.1007/s10514-011-9226-3

Schilling, M., and Cruse, H. (2012). What's next: recruitment of a grounded predictive body model for planning a robot's actions. *Front. Psychol.* 3:383. doi: 10.3389/fpsyg.2012.00383

Schilling, M., and Cruse, H. (2017). ReaCog, a minimal cognitive controller based on recruitment of reactive systems. *Front. Neurorobot.* 11:3. doi: 10.3389/fnbot.2017.00003

Schilling, M., Hoinville, T., Schmitz, J., and Cruse, H. (2013). Walknet, a bio-inspired controller for hexapod walking. *Biol. Cybern.* 107, 397–419. doi: 10.1007/s00422-013-0563-5

Schilling, M., Paskarbeit, J., Schmitz, J., Schneider, A., and Cruse, H. (2012). "Grounding an internal body model of a hexapod walker—control of curve walking in a biologically inspired robot," in *IEEE/RSJ International Conference on Intelligent Robots and Systems* (Vilamoura: IEEE), 2762–2768.

Schmitz, J. (1993). Load-compensating reactions in the proximal leg joints of stick insects during standing and walking. *J. Exp. Biol.* 183, 15–33.

Schmitz, J., Schneider, A., Schilling, M., and Cruse, H. (2008). No need for a body model: positive velocity feedback for the control of an 18-DOF robot walker. *Appl. Bionics Biomech.* 5, 135–147. doi: 10.1080/11762320802221074

Schneider, A., Cruse, H., and Schmitz, J. (2006). Decentralized control of elastic limbs in closed kinematic chains. *Int. J. Robotics Res.* 25, 913–930. doi: 10.1177/0278364906068941

Schneider, A., Paskarbeit, J., Schäffersmann, M., and Schmitz, J. (2012). "HECTOR, a new hexapod robot platform with increased mobility—control approach, design and communication," in *Advances in Autonomous Mini Robots—Proceedings of the 6-th AMiRE Symposium*, eds U. Rückert, S. Joaquin and W. Felix (Berlin: Springer), 249–264.

Schneider, A., Paskarbeit, J., Schilling, M., and Schmitz, J. (2014). "HECTOR, a bio-inspired and compliant hexapod robot," in *Proceedings of the Living Machines 2014*, eds A. Duff, N. F. Lepora, A. Mura, T. J. Prescott, and P. F. M. J. Verschure (Milan: Heidelberg, Springer. LNAI 8608), 427–429.

Schneider, A., Schmucker, U., and Ihme, T. (1995). "Force control in locomotion of legged vehicle and body movement for mounting operations," in *Proceedings of the 9th World Congress on the Theory of Machines and Mechanisms* (Milan, Italy), 2363–2367.

Schütz, C., and Dürr, V. (2011). Active tactile exploration for adaptive locomotion in the stick insect. *Philos. Trans. R. Soc. Lond. B Biol. Sci.* 366, 2996–3005. doi: 10.1098/rstb.2011.0126

Seelig, J. D., and Jayaraman, V. (2013). Feature detection and orientation tuning in the *Drosophila* central complex. *Nature* 503, 262–266. doi: 10.1038/nature12601

Soto, L. A., Morillas, S., Listán, J., Jiménez, A., Arena, P., Patanè, L., et al. (2009). "Embedding the AnaFocus' Eye-RIS vision system in roving robots to enhance the action-oriented perception," in *Proceedings of the SPIE 7365, Dresden, Germany, Bioengineered and Bioinspired Systems IV* (Dresden: SPIE Europe Microtechnologies for the New Millennium), 736509. doi: 10.1117/12.821634

Steingrube, S., Timme, M., Wörgötter, F., and Manoonpong, P. (2010). Self-organized adaptation of a simple neural circuit enables complex robot behaviour. *Nat. Phys.* 6, 224–230. doi: 10.1038/nphys1508

Steinkühler, U., and Cruse, H. (1998). A holistic model for an internal representation to control the movement of a manipulator with redundant degrees of freedom. *Biol. Cybern.* 79, 457–466. doi: 10.1007/s004220050495

Strauss, R. (2002). The central complex and the genetic dissection of locomotor behaviour. *Curr. Opin. Neurobiol.* 12, 633–638. doi: 10.1016/s0959-4388(02)00385-9

Sturm, J., Plagemann, C., and Burgard, W. (2008). "Adaptive body scheme models for robust robotic manipulation," in *Robotics: Science and Systems (Zürich, Switzerland)*, (MIT Press, Cambridge, Massachusetts), 1–8.

Szczecinski, N. S., Bockemühl, T., Chockley, A. S., and Büschges, A. (2018). Static stability predicts the continuum of interleg coordination patterns in *Drosophila*. *J. Exp. Biol.* 221:jeb189142. doi: 10.1242/jeb.189142

Szczecinski, N. S., Brown, A. E., Bender, J. A., Quinn, R. D., and Ritzmann, R. E. (2014). A neuromechanical simulation of insect walking and transition to turning of the cockroach *Blaberus discoidalis*. *Biol. Cybern.* 108, 1–21. doi: 10.1007/s00422-013-0573-3

Szczecinski, N. S., Hunt, A. J., and Quinn, R. D. (2017). A functional subnetwork approach to designing synthetic nervous systems that control legged robot locomotion. *Front. Neurorobot.* 11:37. doi: 10.3389/fnbot.2017.00037

Thelen, D. G. (2003). Adjustment of muscle mechanics model parameters to simulate dynamic contractions in older adults. *J. Biomech. Eng.* 125, 70–77. doi: 10.1115/1.1531112

Theunissen, L. M., Bekemeier, H. H., and Dürr, V. (2015). Comparative whole-body kinematics of closely related insect species with different body morphology. *J. Exp. Biol.* 218, 340–352. doi: 10.1242/jeb.114173

Theunissen, L. M., Vikram, S., and Dürr, V. (2014). Spatial co-ordination of foot contacts in unrestrained climbing insects. *J. Exp. Biol.* 217, 3242–3253. doi: 10.1242/jeb.108167

Tóth, T. I., Grabowska, M., Rosjat, N., Hellekes, K., Borgmann, A., and Daun-Gruhn, S. (2015). Investigating inter-segmental connections between thoracic

ganglia in the stick insect by means of experimental and simulated phase response curves. *Biol. Cybern.* 109, 349–362. doi: 10.1007/s00422-015-0647-5

Tsubouchi, A., Yano, T., Yokoyama, T. K., Murtin, C., Otsuna, H., and Ito, K. (2017). Topological and modality-specific representation of somatosensory information in the fly brain. *Science* 358, 615–623. doi: 10.1126/science.aan4428

Tuthill, J. C., and Azim, E. (2018). Proprioception. *Curr. Biol.* 28, R194–R203. doi: 10.1016/j.cub.2018.01.064

van Soest, A. J., and Bobbert, M. F. (1993). The contribution of muscle properties in the control of explosive movements. *Biol. Cybern.* 69, 195–204. doi: 10.1007/bf00198959

von Twickel, A., Hild, M., Siedel, T., Patel, V., and Pasemann, F. (2012). Neural control of a modular multi-legged walking machine: simulation and hardware. *Rob. Auton. Syst.* 60, 227–241. doi: 10.1016/j.robot.2011.10.006

Vanderborght, B., Albu-Schäffer, A., Bicchi, A., Burdet, E., Caldwell, D. G., Carloni, R., et al. (2013). Variable impedance actuators: a review. *Rob. Auton. Syst.* 61, 1601–1614. doi: 10.1016/j.robot.2013.06.009

Wahl, V., Pfeffer, S. E., and Wittlinger, M. (2015). Walking and running in the desert ant *Cataglyphis fortis*. *J. Comp. Physiol. A* 201, 645–656. doi: 10.1007/s00359-015-0999-2

Weihmann, T. (2018). Leg force interference in polypedal locomotion. *Sci. Adv.* 4:eaat3721. doi: 10.1126/sciadv.aat3721

Weihmann, T., Brun, P. G., and Pycroft, E. (2017). Speed dependent phase shifts and gait changes in cockroaches running on substrates of different slipperiness. *Front. Zool.* 14:54. doi: 10.1186/s12983-017-0232-y

Wendler, G. (1964). Laufen und stehen der stabheuschrecke: sinnesborsten in den beingelenken als glieder von regelkreisen. *Z. Vergl. Physiol.* 48, 198–250. doi: 10.1007/bf00297860

Wilson, E., Rustighi, E., Newland, P. L., and Mace, B. R. (2013). Slow motor neuron stimulation of locust skeletal muscle: model and measurement. *Biomech. Model. Mechanobiol.* 12, 581–596. doi: 10.1007/s10237-012-0427-2

Wosnitza, A., Bockemühl, T., Dübbert, M., Scholz, H., and Büschges, A. (2013). Inter-leg coordination in the control of walking speed in *Drosophila*. *J. Exp. Biol.* 216, 480–491. doi: 10.1242/jeb.078139

Zajac, F. E. (1989). Muscle and tendon: properties, models, scaling, and application to biomechanics and motor control. *Crit. Rev. Biomed. Eng.* 17, 359–411.

Zakotnik, J., Matheson, T., and Dürr, V. (2006). Co-contraction and passive forces facilitate load compensation of aimed limb movements. *J. Neurosci.* 26, 4995–5007. doi: 10.1523/jneurosci.0161-06.2006

Zill, S. N., Büschges, A., and Schmitz, J. (2011). Encoding of force increases and decreases by tibial campaniform sensilla in the stick insect, *Carausius morosus*. *J. Comp. Physiol. A* 197, 851–867. doi: 10.1007/s00359-011-0647-4

Zill, S. N., Chaudhry, S., Büschges, A., and Schmitz, J. (2015). Force feedback reinforces muscle synergies in insect legs. *Arthropod Struct. Dev.* 44, 541–553. doi: 10.1016/j.asd.2015.07.001

Zill, S. N., Chaudhry, S., Exter, A., Büschges, A., and Schmitz, J. (2014). Positive force feedback in development of substrate grip in the stick insect tarsus. *Arthropod Struct. Dev.* 43, 441–455. doi: 10.1016/j.asd.2014.06.002

Zill, S. N., Keller, B. R., and Duke, E. R. (2009). Sensory signals of unloading in one leg follow stance onset in another leg: transfer of load and emergent coordination in cockroach walking. *J. Neurophysiol.* 101, 2297–2304. doi: 10.1152/jn.00056.2009

Zill, S. N., Neff, D., Chaudhry, S., Exter, A., Schmitz, J., and Büschges, A. (2017). Effects of force detecting sense organs on muscle synergies are correlated with their response properties. *Arthropod Struct. Dev.* 46, 564–578. doi: 10.1016/j.asd.2017.05.004

Zill, S. N., Schmitz, J., and Büschges, A. (2004). Load sensing and control of posture and locomotion. *Arthropod Struct. Dev.* 33, 273–286. doi: 10.1016/j.asd.2004.05.005

Zill, S. N., Schmitz, J., Chaudhry, S., and Büschges, A. (2012). Force encoding in stick insect legs delineates a reference frame for motor control. *J. Neurophysiol.* 108, 1453–1472. doi: 10.1152/jn.00274.2012

Zorović, M., and Hedwig, B. (2013). Descending brain neurons in the cricket *Gryllus bimaculatus* (de Geer): auditory responses and impact on walking. *J. Comp. Physiol. A* 199, 25–34. doi: 10.1007/s00359-012-0765-7

Conflict of Interest: The authors declare that the research was conducted in the absence of any commercial or financial relationships that could be construed as a potential conflict of interest.

The handling Editor declared a shared affiliation, though no other collaboration, with several of the authors (AD, SM-T).

frontiers in Neurorobotics

ORIGINAL RESEARCH
published: 23 October 2019
doi: 10.3389/fnbot.2019.00087

Hybrid Inspired Research on the Flying-Jumping Locomotion of Locusts Using Robot Counterpart

Dunwen Wei[1], *Tao Gao*[1,2]*, *Zhaoxin Li*[1], *Xiaojuan Mo*[3], *Shuqin Zheng*[1] *and Cong Zhou*[1]

[1] School of Mechanical and Electrical Engineering, University of Electronic Science and Technology of China, Chengdu, China, [2] Faculty of Engineering, The China University of Petroleum-Beijing at Karamay, Karamay, China, [3] School of Mechanical Engineering, Northwestern Polytechnical University, Xi'an, China

Locusts are a kind of agile insects that can move and maneuver so efficiently in the unstructured terrain and complex environment. This marvel survivability of locusts benefits from their flying-jumping multi-modal locomotion. But until recently, the main influences of the locomotion performance are still a controversial and unknown issue. In this paper, the idea of hybrid inspired method that combines biologically inspired robot with robot inspired biology was proposed to explore the principle of flying-jumping locomotion of locusts. Firstly, we analyzed the influence of leg burrs and flapping wings on the jumping performance by the biological experiments. Nevertheless, individual heterogeneity and uncontrollability of locusts result in the unconvincing results of biological experiments. Therefore, according to the thought of robotics-inspired biology, we proposed and built a locust-inspired robot with flying-jumping locomotion via the principle of metamorphic mechanism based on the biological-inspired robot. Lastly, the preliminary robotic experiments were carried out to validate our thought that the flapping wings and leg burrs of locust have a great influence on the jumping performance. This robotics-inspired biology method remedied the shortcomings of biological experiments through the consistency and controllability of the robot experiments. Meanwhile, through the hybrid inspired research, the results show both the leg burrs and flapping wings can help the locust jump longer and improve the stability by adjusting the landing attitude to some extent, while the biological experiments dedicate that the locust with leg burrs and wings have the self-stability ability.

Keywords: hybrid inspiration, bioinspired robots, robotics-inspired biology, multi-modal locomotion, flying-jumping locomotion, locust

OPEN ACCESS

Edited by:
Xiaofeng Xiong, University of Southern Denmark, Denmark

Reviewed by:
Diansheng Chen, Beihang University, China
Mircea Ivanescu, University of Craiova, Romania

***Correspondence:**
Tao Gao
gaotao@uestc.edu.cn

Received: *31 July 2019*
Accepted: *07 October 2019*
Published: *23 October 2019*

Citation:
Wei D, Gao T, Li Z, Mo X, Zheng S and Zhou C (2019) Hybrid Inspired Research on the Flying-Jumping Locomotion of Locusts Using Robot Counterpart. Front. Neurorobot. 13:87. doi: 10.3389/fnbot.2019.00087

INTRODUCTION

The inspiration of biology as a well-known method has led to the design of biologically inspired robots (Meyer and Guillot, 2008). This category robots are also commonly called bioinspired robots (Iida and Ijspeert, 2016). Many bioinspired robots are inspired by the locomotion of animals to move and manipulate so effectively in their environment (Lu et al., 2018). But until recently, the main influences of determining the locomotion performance of different animals in different complex environments are still a controversial and unknown issue (Peyré-Tartaruga and Coertjens, 2018). The conventional method by biological experiments is the mainstream of exploring the locomotion principle of animals. The challenges of biological experiments are to snapshot the

focused locomotion state and keep the repeatability of experiments. However, because of the individual heterogeneity and uncontrollability of animals, the biological experiments result in the irregular, or unconvincing results. Therefore, the robot experiments are serving as an advanced replacement for the biological system to explore and discover the principles or mechanisms behind the biology (Karásek et al., 2018). This method of providing new scientific knowledge for biology is named as robot inspired biology (Gravish and Lauder, 2018). Biologically inspired robot and robot inspired biology are the cross-disciplinary research frontiers of engineers and scientists in the future of robotic and biological locomotion research (Romano et al., 2019).

In this paper, the idea of hybrid inspired research that combines biologically inspired robot with robot inspired biology was proposed and adopted to explore the principle of locust flying-jumping locomotion. According to the idea of the biologically inspired robot, we conducted the biological experiments for initially exploring the flying-jumping locomotion of locusts. Such biological experiment provides the idea for developing one locust-inspired flying-jumping robot. According to the idea of the robot inspired biology, we explored the influence of leg burrs, and flapping wings on the jumping performance by robot experiments. In the following parts, we first reviewed the state of arts of locust flying-jumping locomotion research from both locust biology aspect and locust-inspired robot aspect before we continue our hybrid inspired research.

From the biological perspective of locusts, it is well-known that the locusts are a kind of agile insects capable of performing multi-modal locomotion with both flying and jumping to efficiently navigate in the unstructured terrain and complex environment (Zaitsev et al., 2015). On the one hand, locusts take the typical jumping locomotion as the main physical strategy to travel rapidly on the ground and manipulate different obstacles. Benefiting from the long hind legs with enlarged femora, locusts have a greater mass of extensor tibiae muscles and have a long stretching distance for acceleration. On the other hand, because of the long period of biological evolution, locusts have evolved the jump to launch into flight, and the flying locomotion with wings is a means of rapid escape. The research about the jumping behavior and adopt a catapult mechanism (Burrows, 2016), in which of the hind legs contract to store energy in distortions of the exoskeleton, and then suddenly release the energy to power the hind legs' rapid movement. This flying-jumping locomotion has the advantage of overcoming large obstacles in unstructured terrains comparing with the other wheeled and crawling locomotion. And because of that, the jumping locomotion via the locust biological experiment has been studied for several decades, starting from the 1970s with some distinguished work (Camhi, 1970; Bennet-Clark, 1975; Heitler and Burrows, 1977). In recent years, Chen et al. (2015) examined the mechanism of air posture adjustment of locusts and declared that the wings and abdomen are mainly utilized for air posture adjustment. Mo et al. (2019) studied the influence of substrate roughness on the jumping performance and claimed that there was no significant relation between ground roughness and jumping success. In order to improve the accuracy and efficiency of biological experiments, Zhou et al. (2019) developed a jumping locomotion detection system named JumpDetector with automatic trajectory tracking and behavior analysis to evaluate the endurance jumping of locusts.

Despite decades of study, little is known about how leg burrs and flapping wings influent the jumping performance. However, in nature, the complexity of leg burrs and flapping wings interaction with the ground and air often rivals or even exceeds that of theoretical analysis. But an advanced understanding of leg-wing interaction and flying-jumping locomotion in complex terrain is relatively lacking. To overcome this challenge, we firstly performed the flying-jumping locomotion studies of how the locomotion performance depends on leg burrs, flying wing, and leg morphology.

In the aspect of the research of locust-inspired robot, multi-modal locomotion robotic systems are new concepts of bio-inspired robotics with two or more of locomotion (Low et al., 2015; Mintchev and Floreano, 2016). Such bio-inspired robotic systems may lack direct connectivity to their biological counterparts, but are useful for understanding the principles of mechanical design and control as well as for understanding the principles behind the biology. In the recent years, there are some proposed robots with the flying-jumping multi-modal locomotion (Fukuda et al., 2012). Inspired by the flying and jumping behaviors of the desert locust, Beck et al. (2017) recently developed a miniature jumping robot with spreading wings and a tail to assistant jump over 1.7 m. Woodward and Metin (2014) and Woodward (2017) built a biologically inspired jumping-gliding robot, named as Multi-bat, whose mass is only 100 g. This robot has two four-bar mechanisms flapping wings which can make the robot jump over meters. In order to increase the jump gliding distance and reduce the landing impact energy, Kovac et al. (2008), Kovač et al. (2011) designed a jump gliding mechanism and installed it on the small locust jumping robot. Li et al. (2012) improved the previously developed jumping robot Grillo (Scarfogliero and Stefanini, 2006), added the wings to increase the jumping distance and hovering time, and the tail swinging from left to right can adjust the gliding direction. Chen et al. (2015) designed an air attitude adjustment system for a locust-inspired robot through the asymmetric movement of wings to verify the mechanism of attitude adjustment. It proved that locusts adjust their attitude in the air through the asymmetric movement of their wings.

The current research mainly designed the static wings on the basis of jumping robot to enhance the stability during the takeoff, flight, and landing. However, the static wing can only increase the gliding distance but not provide enough lift force. Zhang et al. (2017) proposed a multi-modal locomotion robot with jumping-flapping locomotion to study the feasibility of jumping aided takeoff, but it is only a conceptual design. Therefore, it is necessary to add flapping-wing on the basis of jumping locomotion, and to develop a locust-inspired robot with flying-jumping multi-modal locomotion, therefore the robot can use the jumping motion to take off the ground, and use the flapping wings to fly after taking off, then it can flap wings slowly to buffer the impact when landing. In nature, there are many

insects that have similar locomotion modes like this. The locust is one of the insects that have both the flying and jumping locomotion. However, the influence of locust's leg burrs and flapping wings on jumping performance, the factors affecting the jumping performance and how the factors affect the jumping performance of locusts are still unknown. So, inspired by the locomotion of locusts, we built a flying-jumping bioinspired robot. We validated the deduction drawn from the biological experiment upon locusts by the robot prototype based on the idea of robotics-inspired biology.

Our contribution in this paper is to bridge this gap by the method of hybrid inspired research to discover the influence factors of locomotion performance, and use biological experiments and robot experiments to better understand biological movement and advance robotic mobility in the real world. On the aspect of biological experiments, we studied the animals' biology and locomotion behavior that influences the flying-jumping performance through some unique leg and/or wing surgeries for living locusts. On the aspect of robot physical experiment, we inspired from the locomotion of locusts to design and build new locust-inspired robots with the improved locomotor capabilities. Based on the locomotion mechanism of the locust legs coupled with its wings, the jumping mechanism and the flying mechanism were, respectively, designed and analyzed using the abundant force and trajectory characteristics of the gear-bar mechanism. Combined with the principles of metamorphic mechanism, the flying-jumping mechanism was designed by coupling the flapping-wing mechanism with the jump mechanism. We used robots as physical models to test hypotheses of the flying-jumping locomotion. These robots enable control and variation of influent parameters and allow precise, repeatable, and systematic experiments. The use of bio-inspired robots as physical models, rather than locust animals, provides a few advantages in studying the complex locomotion: (a) Biological experiments on locust animals can disrupt their lives and raise ethical questions, involving caging them and, if necessary, manipulating, or operating on them. (b) Biological experiments with animals vary from one individual to another and from one trial to another, and thus generate data with large variability, while robots are simpler than animals, with fewer degrees of freedom and more well-defined morphology and kinematics. Robots are much more repeatable. (c) Robots can often be modified more easily and allow easier parameter variation, whereas animals can be hard to modify without affecting their behavior.

This paper is arranged as follows. In section Locomotion Principle From Biological Experiments, we firstly investigated the influences of both the leg burrs and flapping wings on jumping performance by biological experiments, and then we made some biological deductions based on the biological experiment results. In section Design of Locust-Inspired Robot, we proposed one locust-inspired robot, which has flapping and jumping multi-modal locomotion based on the principles of the metamorphic mechanism. By the thought of robot inspired biology, we carried out the preliminary experiments to validate our thought that the flapping wings and leg burrs of locust have a great influence on the jumping performance.

LOCOMOTION PRINCIPLE FROM BIOLOGICAL EXPERIMENTS

Biological experiments on the characteristic and locomotion of locusts can accurately grasp the structural parameters and flying-jumping locomotion. The coupling principle of leg burrs, leg bounce, and flapping wings is the main factor that affects jumping performance. Therefore, exploring the mechanism between the leg and the flapping-wing are of great significance for the study of locomotion performance. In this section, the possible influencing factors, such as the number of leg burrs, the bounce legs, and the flapping-wing on the jumping performance are observed experimentally, and the mathematical model is used to calculate the influence on the jumping performance, to find out the factors affecting the jumping performance of the locusts, and to reveal the locust legs. The mechanism of motion coupled with the wing provides a theoretical basis for the study of robots with flying-jumping locomotion.

The mechanism of bionic locomotion is the basis and key point of research on the flying-jumping locomotion of locusts. From the perspective of biophysical structure, it is the inevitable trend of structural bionics. Based on the enlightenment from biological take-off, flight, and landing behavior, we explore the factors affecting the jumping performance of locusts and reveal the mechanism of stability affecting the takeoff, flight, and landing of locusts.

In order to study the influence of leg burrs and flapping wings of locusts on jumping performance, we conducted some biological experiments using one kind of wild east Asian migratory locusts living in China and analyzed their jumping and flying behavior. By observing the influence of the number of burrs in the legs, the flapping wings and the coupling of leg bouncing and flapping motion on the jumping performance, we try to find out the main factors that affect the jumping performance and reveal the mechanism of the coupling movement between the legs and wings.

Experimental Procedures of Locomotion

As shown in **Figure 1A**, the body structure diagram of locust consists of five parts, which are the head, the thorax, the abdomen, the wings, and the legs. Six legs are symmetrically distributed on both sides of the central axis of the body, which are two forelegs, two middle legs, and two hind legs. As shown in **Figure 1B**, the hind legs with many leg burrs are thicker and stronger than the forelegs and middle legs, which is good for the jump. Compared with the strong hind leg to promote the force, the forelegs and the middle legs are mainly used for crawling to provide the support force and the ground cushioning. The structure of flapping wings includes the forewings and hind wings, in which the leather of forewings is covered on the hind wings when not flying. The forewings, also known as the tegmina, have the tough wing veins and cover on the back of the body during crawling and protects the hind wing. When flying, the forewings can increase the contact area with air and increase the lift. The wing chord of hind wings is longer than the forewings. The texture of hind wings is soft and easy to deform. The hind

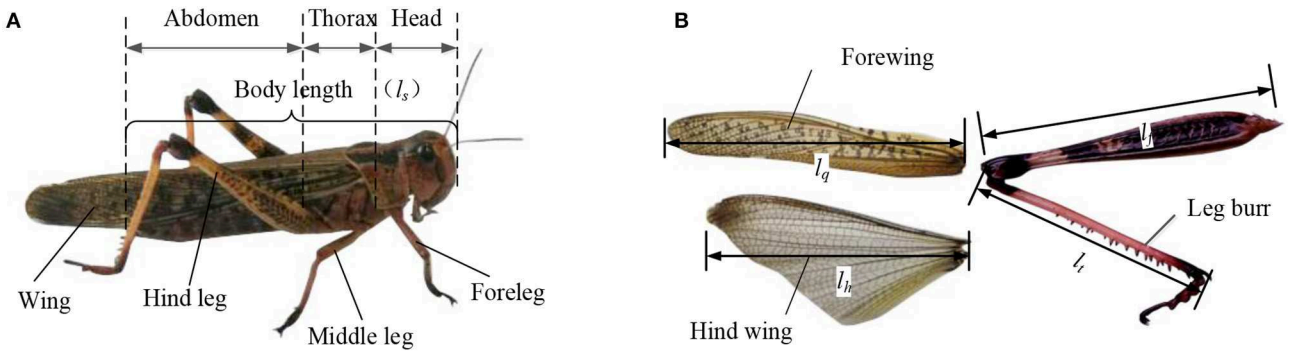

FIGURE 1 | The morphological characteristics of locusts **(A)** the body structure of locust consisting the head, chest, abdomen, wings, and legs; **(B)** flapping-wing and leg structure of locust.

wing, with film-like leather driven by the chest muscles, can be folded and shrunk.

The possible influencing factors, such as the number of leg burrs, the bounce legs, and the flapping-wing on the jumping performance are observed by experiments. The whole jumping performance of locusts is captured by cameras. The influences of different wing lengths and the number of leg burrs on the jumping performance are observed and analyzed. The biological experiment consists of the following five steps, namely, preparation, treatment, recovery, testing, and post-processing.

Preparation

In the preparation step, as shown in **Figure 2A**, in order to eliminate the influence of individual differences in biological experiments, we chose east Asian migratory locusts with similar body parameters (4∼5 cm body length), strong physique and complete limbs. The candidate locusts were feed with enough food and reared at a cuboid glass container with about 22 W light and 30 ± 2°C temperature.

Treatment

In order to study the effect of leg burrs and flapping wings on jumping performance, we conducted some treatments for the candidate locusts. This is probably the most delicate experimental process step by manual. We must manually operate the candidate locusts to the leg burrs and/or flapping wings. As shown in **Figure 2B**, we carried out the different operations for both flapping wings and leg burrs, respectively. For the treatment of the wings, we divided them into three groups; (a) normal locusts without any treatment for flapping wings; (b) the locusts with half of the wings being cut off; and (c) the locusts without wings. Similarly, we conducted some treatments for leg burrs under the same external conditions. We obtained three candidate groups; (a) locusts with the complete leg burrs and without any treatment; (b) locusts with some leg burrs being cut off; and (c) locusts with all burrs being cut off. The experiment conditions and experiment environment are the same as those in the wings experiment. After the treatment, seven groups of candidates were obtained and denoted by the connection lines shown as **Figure 2B**.

Recovery

Because the treatments for candidate locusts will more or less affect their behavior, it is hard to make the locusts we chose to perform equally without variability. As a result, we made the following efforts to make the experiment data more authentic. In order to make the locust in each group have the unique variable, we let the locusts have enough rest and enough time to recover after operation treatment such as cutting off the leg burrs and/or wings. During the period of resting and recovering, we fed them with the equal amount of food, and make them live in the appropriate environment to keep them in a well-health condition and reduce the influences of irrelevant variables and inconsistent condition.

Testing

In the experiment, we use the high-speed camera to record the motion trajectory. Meanwhile, we use the scale as a background to calculate jumping height and distance directly. In order to obtain more accurate experiment data, we tried our best to shorten the duration of the experiment. We also add a group of locusts that jump on the oily ground as a contrast, in which the locusts only slipped on the ground and couldn't perform any jumping. In order to reduce accidental error, we let the locusts in each group perform 10 times jumps and recorded the average value of the jumping height and the jumping length in each group.

Post-processing

The video files were input into MATLAB software, and the jumping performance of different groups was recorded. The locomotion parameters of the jumping behavior were analyzed on the basis of the experiment data.

Result Analysis of Biological Experiments

From the experiments, we found that the locust stores energy slowly and releases energy quickly through the structure of hind legs to jump and then fly by the flapping wings. There are four phases in its jumping process: leg contraction phase, take-off phase, flight phase, and landing phase. The first phase is to adjust the body posture by forelegs and middle legs, meanwhile, the

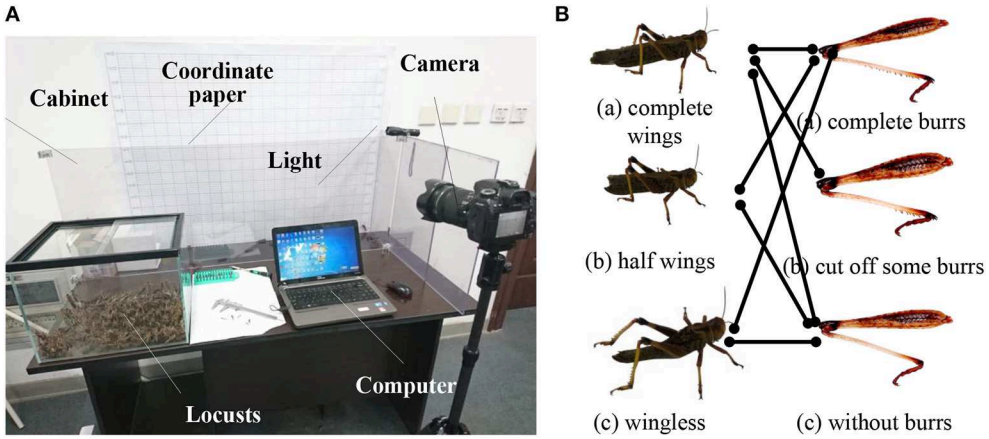

FIGURE 2 | Biological experiments **(A)** experimental setup; **(B)** group of different treatments for flapping wings and leg burrs.

hind legs constrict to store energy. Then the energy is released quickly in the take-off phase, phase to make the body take off the ground. In the third phase, the body moves forward through wing flapping motion. Then in the last phase locusts use slowly flapping motion to provide some lift and jump buffer of leg joints to reduce the contact impact force between leg and ground. Meanwhile, locusts use the leg burrs on tibia legs and appendages to increase the friction force between legs and ground, to prevent the tipping, slipping, or the rebounding that causes them bouncing off the ground when they are landing. The jumping and flying locomotion is mainly related to hind legs and wings, so we analyzed the leg burrs and wing integrity. By observing the effect of the number of leg burrs, the wing integrity, and the coupling of leg bouncing and wing-flapping motion on the jumping performance, we try to find out the factors that affect the jumping performance and reveal the mechanism of the coupling movement between the legs and wings.

In the leg contraction phase, as shown in **Figure 3** the force expression of the locust model is shown in the following equation:

$$\begin{cases} \sum_{i=1}^{3} F_{ixr} + \sum_{j=1}^{3} F_{jxl} = m\ddot{x} \\ \sum_{i=1}^{3} F_{iyr} + \sum_{j=1}^{3} F_{jyl} - mg = m\ddot{y} \, (ij = 1 \sim 3) \\ \sum_{i=1}^{3} F_{izr} + \sum_{j=1}^{3} F_{izl} = 0 \end{cases} \tag{1}$$

where F is the force from the ground. The subscript i and j of F express the 1st leg, 2nd leg, and 3rd leg (foreleg, middle leg and hind leg, respectively). The subscript x, y, and z of F denote the component forces along the x axis, y axis, and z axis. The subscripts r and l of F denote the right leg and the left leg. The x and y are the position of the center of mass (CoM) of the locust.

We assume the forces from the right leg and the left leg are equal. At the same time, the force on the hind leg is much larger than that of foreleg and middle leg.

$$\begin{cases} F_{ixr} = F_{ixl} \\ F_{iyr} = F_{iyl} \, (i = 1 \sim 3) \\ F_{izr} = F_{izl} \end{cases} \text{and} \begin{cases} F_{3xr} \gg F_{1xr} + F_{2xr} \\ F_{3yr} \gg F_{1yr} + F_{2yr} \end{cases} \tag{2}$$

when analyzing the take-off phase of locusts, the forces acting on the front and middle legs can be ignored. The Equation (1) can be simplified as:

$$\begin{cases} 2F_{3xr} = m\ddot{x} \\ 2F_{3yr} - mg = m\ddot{y} \end{cases} \tag{3}$$

The force F_{3yr} is provided by the ground along the coordinate axis y. When the leg of the locust and the ground do not slip, the force F_{3yr} multiplied by the friction factor is the maximum static friction force. Therefore, when the force in the x direction is less than or equal to the maximum static friction force, the leg of locusts does not slip. Then we obtained the following conditions.

$$\begin{cases} F_{ixr} \le \mu F_{iyr} \\ F_{ixl} \le \mu F_{iyl} \end{cases} and \mu \ge \frac{\ddot{x}}{\ddot{y} + g} \tag{4}$$

It is known that the friction factor between the ground and the legs of locusts affects the jumping performance of locusts. Therefore, the number of leg burrs of locust affects its jumping performance. The more the number, the better the jumping performance. When the number of leg burrs of locusts is relatively small, the friction between the ground and the legs of locusts is not enough to meet the acceleration condition of the body of locusts. At this time, the legs of locusts will slip to a certain extent, which will affect the jumping stability and jumping performance of locusts.

In the flight phase, the corresponding mathematical model was set up to analyze the influence of different flapping wings on

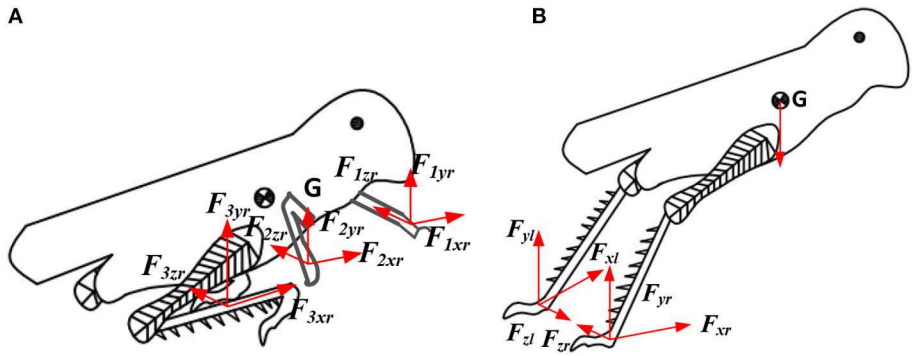

FIGURE 3 | Schematic diagram of locust jumping model. **(A)** Leg contraction phase; **(B)** the take-off phase.

the jumping performance of locusts. According to the work from Oertel (2010), we obtained the following equation:

$$F_s(t) = \frac{1}{2} C_s \rho_k S_c \left[r_s \dot{\theta}(t) \right]^2 \tag{5}$$

where C_s is the lift coefficient; $\rho_k$is the air density; wing parameters S_c and r_s are the area of the wing and the distance length from the point to wing root; $\theta(t)$ is the flapping angular velocity of flapping wings. According to the formula (5), it can be concluded that when air density ρ_k, lift coefficient C_s and wing flapping angular velocity $\theta(t)$ remain unchanged, the distance r_s from a certain point on the wing to the wing root and the area S_c of the wing decrease, which will lead to the decrease of lift provided by the insect flapping wing. It can be seen that after we clipped part of its wings, not only the area of the wings S_c decreased, but also the r_s decreased, then the lift provided by air to the locust wings would decrease, affecting the jumping height and distance. When the locust has no wings, that is, the area of the wings S_c and the r_s are both zero. At this time, the locust has no lift, but only the ground force when jumping, so the jumping height, and distance are greatly reduced.

According to the experimental data, we analyzed the jumping performance of the above seven groups. We calculated the mean value and standard deviation of the jumping height and jumping distance with 10 times jump of each group. Through analyzing the results described in **Figure 4**, we found that the jumping height and the jumping distance of locusts with complete leg burrs were reduced to some extent after the part of leg burrs were cut off, and the jump height and the jump distance were further reduced when all of the leg burrs were cut off. Therefore, it is thought that under certain ground conditions, the number of leg burrs affects the jumping performance. The more the number of leg burrs, the better the jumping performance. When the number of leg burrs in is relatively small, the friction between the ground and the legs of locusts is not enough to satisfy the acceleration conditions of pushing locusts' bodies. At this time, locusts will slip on the ground to a certain extent, which will affect the stability and jumping performance of locusts.

Under the same number of leg burrs, we compared the results of wingless locusts with that of half-wing locusts, their jumping height and jumping distance decreased significantly. Compared with the complete-wing locust, the jumping height, and jumping distance of the half-wing locusts also decreased to a certain extent. Under the same wing length parameter, the jump height and jump distance of locusts without leg burrs are reduced to some extent. We compared the locusts without leg burrs to the locusts with complete leg burrs. So, we deduce that the flapping-wing movement of locusts also has a certain impact on jumping height and distance. Flapping-wing can help locusts improve jumping distance and jumping height.

Because biological experiments with animals vary from one individual to another and from one trial to another, and thus generate data with large variability, the jumping height, and distance values of locusts are generally different. The deviation of dispersion degree directly expressed by standard deviation is unreasonable. Therefore, the concept of coefficient of variation is introduced to represent the dispersion degree between different groups, so as to eliminate the influence of measurement scale and dimension on the measurement results. For this paper, the greater the value of the coefficient of variation, the worse the jumping stability. The coefficient of variation can be expressed as:

$$CV = \frac{SD}{MN} \cdot 100\% \tag{6}$$

where SD is the sample standard deviation; MN is the sample mean.

As shown in **Figure 5**, the variation coefficient of jumping height and distance with different groups are different. The quantity of leg burr affects the CV of jump performance. The large value of the coefficient of variation indicates the instability of jumping. After comparing the value of CV, the results show the leg burr complete locust burr-free cut off part of the leg burr legs locusts with jumping height and distance of the coefficient of variation in turn increase, so the leg burrs affect stability, on the leg burr, the less the jump data dispersion degree that the greater the stability of the worse. Nevertheless, these factors include the following factors:

(1) Individual heterogeneity results in the unconvincing experimental results. While animals vary from one

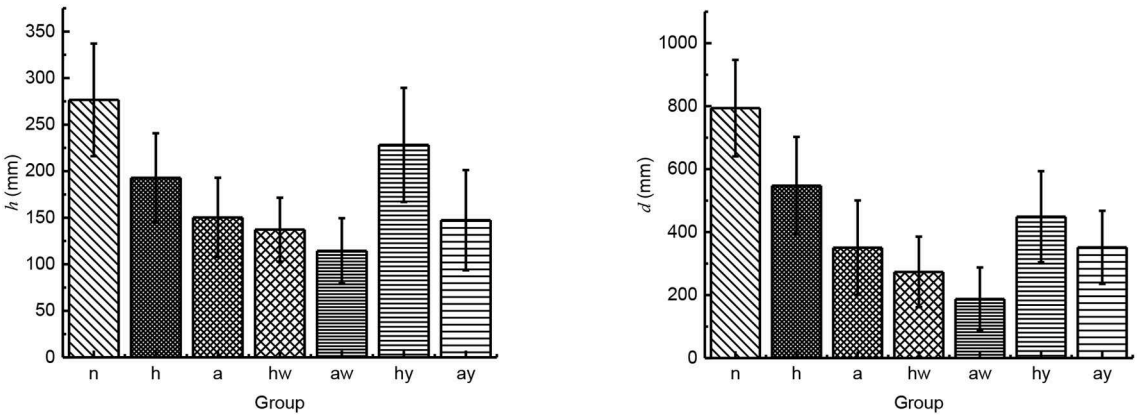

FIGURE 4 | The influence of leg burs and wings on jumping performance (*n* stands for the group of locusts with normal leg burrs and normal wings; *h* stands for the group of locusts with half-leg burrs cut off and normal wings; *a* stands for the group of locusts without leg burrs and with normal wings; *hw* stands for the group of locusts without leg burrs and with half wings; *aw* stands for the group of locusts without leg burrs and without wings; *hy* stands for the group of locusts with all leg burrs and half wings; *ay* stands for the group of locusts with all leg burrs and without wings).

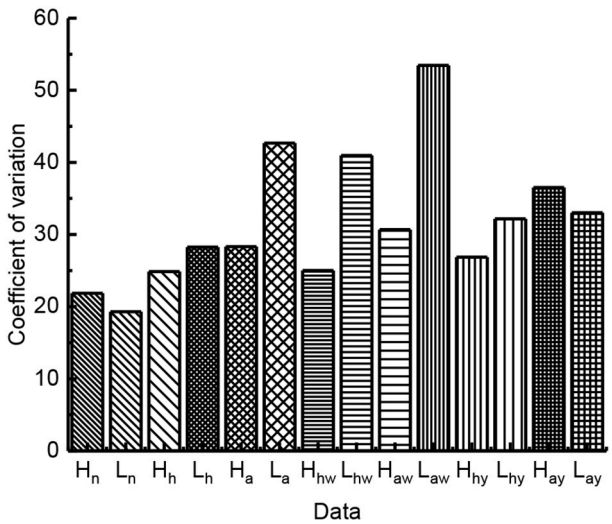

FIGURE 5 | The variation coefficient of jumping performance.

individual to another and from one trial to another and thus generate data with large variability.

(2) External stimulus is different and uncontrollable for locusts. Giving the same stimulus, the locusts may feel different incentives or they may be immune to stimuli over a long experimental period of time.

(3) Surgery has different effects on individuals. The effect of the operation surgery for different locust is more or less different because of the operator and locust itself.

DESIGN OF LOCUST-INSPIRED ROBOT

In the previous section, we carried out biological experiments and analyzed biological morphology and jumping performance. We preliminarily determined that the leg burrs and flapping wings of locusts have great influence on the jumping performance of living locusts. However, individual heterogeneity and uncontrollability of locusts resulted in the unconvincing experimental results. In this section, we proposed one robot prototype with flying, and jumping locomotion inspired by the locusts. This prototype has both flying and jumping locomotion based on metamorphic mechanism and lays a foundation for the study of robot inspired biology. In order to validate the deductions observed in the biological experiments and to remedy the shortcomings of biological experiments, we carried out some robot experiments for its consistency and controllability.

Jumping Mechanism

Inspired by the jumping structure of locust hind legs, we selected the torsion spring as the energy storage element to mimic the muscle of locusts. And the rope was selected to act as a tendon in the locust's legs. As shown in **Figure 6**, the mechanism proposed in this paper has the advantage in torque output. Specifically, a natural lever ratio can be obtained through the rotating shaft and the radius of the rope pulley, which results in the increase of the torque. The transmission ratio between the torsion spring and the rope pulley can be expressed as follow:

$$K = R/\left(l_t \cos\frac{\theta_s}{2}\right). \tag{7}$$

where l_t is the length of the tibia, R is the radius of the pulley, θ_s is the angle between l_t and l_f. The actual transmission ratio is between 1/5 and 1/10, which increases the pulley's torque by 5–10 times. At the beginning of energy storage stage, the pulling force required is the smallest while θ_s is the largest. At this time, K is the largest (about 1/5), and the minimum gained multiple is obtained. At the moment before the end of the energy storage stage, the pulling force required is the largest while the θ_s is the smallest. It is known that K is the smallest (about 1/10), and the maximum gained multiple is obtained. In the process of energy storage stage, the pull force and the gained multiple are both

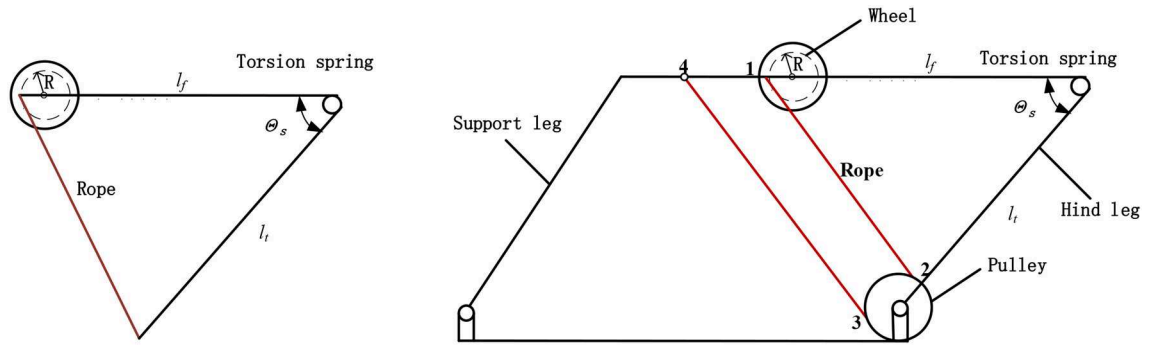

FIGURE 6 | Jumping mechanism. l_t is the length of tibial leg, l_f is the length of the femoral leg, R is the effective radius of the pulley, and θ_s is the angle between l_t and l_f.

increasing. Therefore, the minimum output torque of the motor can minimize to the greatest extent.

Another advantage of this design is that the torsion spring can reach a relatively large deformation angle about 100 degrees, which is more similar to the natural energy storage angle of the locust compared with other jumping robots. The gear system is driven by the motor, for the gear system can reduce the consumption of the motor and increase the output torque. Then the gear system drives the rope pulley to pull the rope and drive the rear leg to rotate. At the same time, torsion spring will be reversed and stores energy.

The motor is fixed on the central frame, and 6th gear is fixed coaxially with the rope pulley. The motor transmits the torque to the rope pulley through the speed-reduction gear system. One end of the rope is connected to the rope pulley, and the other end is connected to the 4th hole of the frame passing the movable pulley on the connecting rod which is at the end of the rear leg. And we made the rope 12 parallel to the rope 34. Because the movable pulley is installed on the connecting rod at the end of the hind leg, when the rope pulls the pulley, a torsion spring is given to the movable pulley through the connecting rod, which leads to saving half of the motor's force. According to the description of locusts' biological characteristics and the parameters of their limbs in chapter two, it can be seen that locust's femoral leg is almost as long as the tibial leg. So, we made $l_f = l_t$ in the jumping mechanism we design. And in order to improve the stability of the robot, a parallelogram mechanism is used to synchronize the front support leg and the rear support leg. This design method can further rise the barycentre of the robot.

As shown in **Figure 7**, when the energy storage stage begins, the main driving motor transmits the rotational motion to the pulley through the speed-reduction gear system. And the rope pulley drives the rope to shrink with the jumping leg rotating clockwise. When the torsion angle of the torsion spring is close to 100 degrees, the linear motor drives the axle sleeve to move downward. Resulting in 6th gear and 5th gear separate from each other instantly. At the same time, the linear motor stops operating.

Figure 7B is the trigger state. Because 6th gear suddenly loses meshing force, the rope wounded on the pulley will release rapidly under the force of torsional spring, then the jumping leg swings back quickly, and the robot will accelerate to complete the jumping motion. When the robot has landed on the land and is going to operate the next jump, the linear motor starts again and runs in another direction. Under the force of 1st pressure spring and 2nd pressure spring, 6th gear moves upward and meshes 5th gear again. Then torsion spring will store energy again to prepare for the next jump.

Flying Mechanism

The flapping mechanism we designed consists of two parts: biomimetic wings and driving mechanism. In consideration of the abundant motion and force transformation characteristics of the gear and connecting rod mechanism, we designed a pair of the symmetrical four-bar mechanism driving the wing support rod. The carbon fiber rod is inserted on the wing support rocker, and the wing is installed on the carbon fiber rod. When the wings begin to flap, the aerodynamic force produced by flapping up and down is unequal, so we designed the wings to flap up and down at a different speed. The mechanism is designed with quick return characteristic to make the flapping wing shoot up slowly and down rapidly. The flapping mechanism is shown in **Figure 8**. One end of the right connecting rod is connected with the 8th gear, the other end is connected with the swing rod. And both ends of the right connecting rod can rotate around the center of rotation, and the swing lever can rotate around the point O on the frame. The wing is mounted symmetrically on the left and right swing rods and the movements of the wings are the same.

Metamorphic Mechanism and Coupling Mechanism

The metamorphic mechanism can transform the mechanism from one mechanism to another instantly, and the number of effective components or degrees of freedom will change. In order to design a robotic mechanism with the characteristics of instantaneous energy release from legs, the fixed posture of legs and wing flapping motion during the flight, we designed a metamorphic mechanism which can let the components merge and separate instantaneously. And we chose the rope to realize the instantaneous merger and separation between 5th gear and 6th gear. We also added a coupling module to couple the bionic

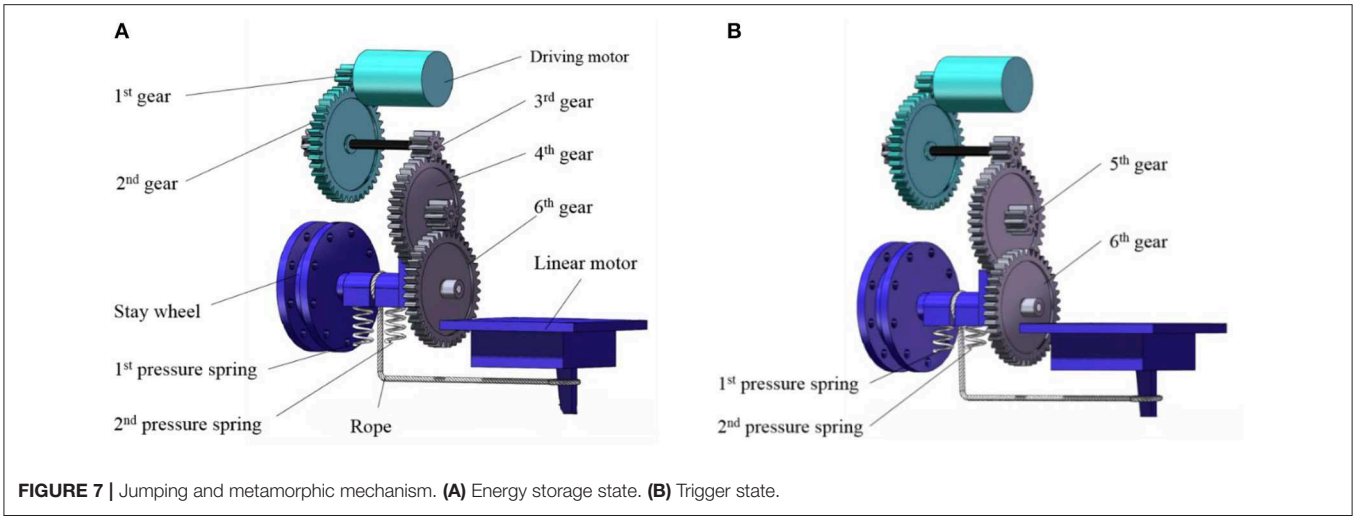

FIGURE 7 | Jumping and metamorphic mechanism. **(A)** Energy storage state. **(B)** Trigger state.

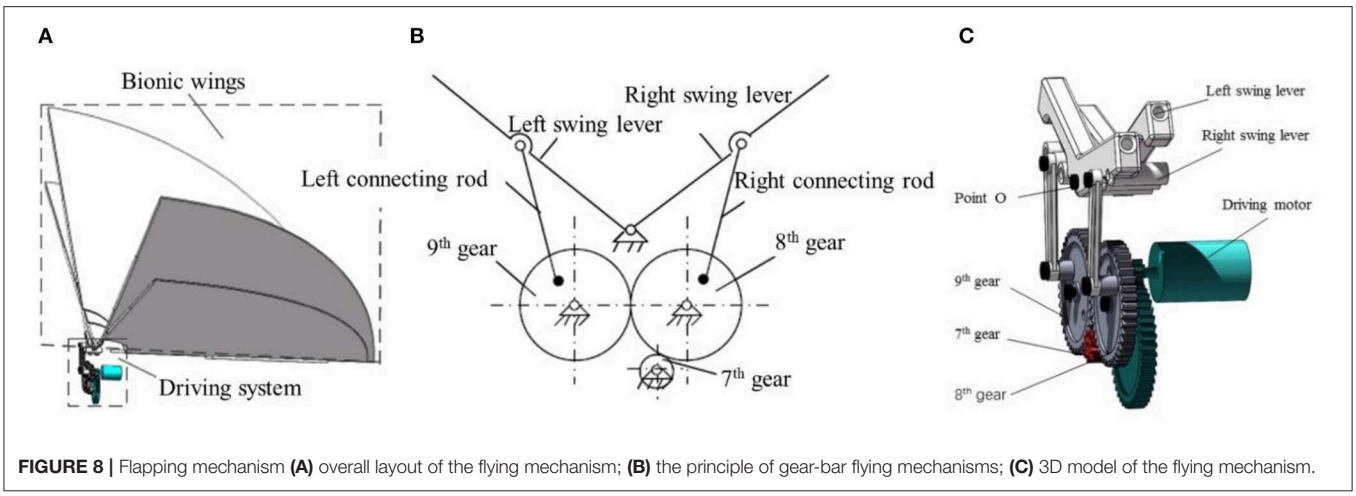

FIGURE 8 | Flapping mechanism **(A)** overall layout of the flying mechanism; **(B)** the principle of gear-bar flying mechanisms; **(C)** 3D model of the flying mechanism.

jumping mechanism with the bionic flapping mechanism based on the aforementioned bionic jumping and flapping mechanism. For the linear motion characteristic of the linear motor, we used it to control the coupling between the jumping mechanism and the flapping wing mechanism.

From the coupling picture of gear system shown in **Figure 7**, it can be seen that the main drive motor, 1st gear and 2nd gear are shared through the metamorphic mechanism. 7th gear meshes with 8th gear, and the symmetrically distributed 8th gear and 9th gear drives the wings to flapping motion. 3rd gear on the other side transfers the torque to the pulley, which drives the leg to store and release energy, and realizes the coupling of jumping and flapping motion by a single main motor. In this paper, the pressure spring with both the characteristics of rigidity and flexibility is chosen for the coupling mechanism. The rigidity characteristic is used to provide 6th gear with support force and the flexibility characteristic is used to let 6th gear separate from 5th gear under the traction of the liner motor. In order to ensure that rope pulley can reverse under the spring force after 6th gear and 5th gear is separated from each other; we installed a sleeve with clearance fit between rope pulley and 6th gear. This sleeve not only plays an accurate positioning role, but also can quickly reverse under torsional spring force when being pulled.

Figure 7A shows the combined state of the metamorphic mechanism, that is, the combined meshing state of 5th gear and 6th gear. **Figure 7B** shows the separation state of the metamorphic mechanism, that is, the demeshing state of 5th gear and 6th gear, and the robot completes the jumping process.

ROBOTICS-INSPIRED BIOLOGY

In this section, we built the robot prototype with flying-jumping locomotion inspired by the locusts. Based on the idea of robotics-inspired biology, we carried out some preliminary experiments to validate the influence of leg burrs and flapping wings on the jumping performance, which remedied the shortcomings of the inconsistency, and uncontrollability in the biological experiments. Through the jumping test with the different number of leg burrs and the experiment with the static and flapping wing states, the effects of leg burrs and flapping wings on the jumping performance are revealed.

Prototype of Locust Inspired Robot

The robot prototype shown in **Figure 9** was produced by the 3D printer, consisting of the gear-rod mechanism, gear transmission system, metamorphic mechanism, energy storage, and release mechanism. In order to make the robot achieve the best jumping performance, the weight of the robot should be as light as possible. The material we chose is presented in **Table 1**. We chose one hollow cup 820 DC motor with quite strong magnetic force and large torsion for aeromodelling which can achieve the non-load speed of 5,000 r/min with 3.7 V voltage and 0.1 A current.

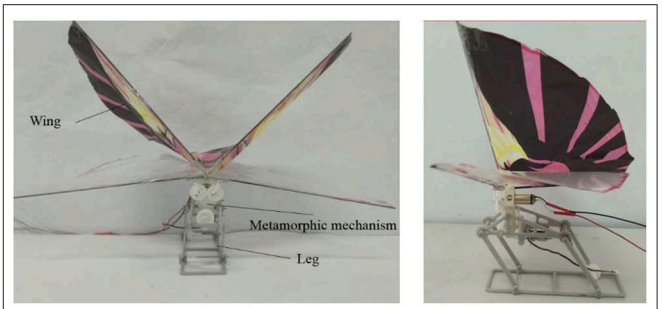

FIGURE 9 | Prototype of bioinspired flying-jumping robot.

TABLE 1 | Materials and their density g/cm^3.

Body part	Material	Density
Legs and external rack	PLA	1.26
Central support	ABS	1.05
Pulley	Nylon	1.15
Sole	PLA	1.26
Wing sport	PLA	1.26

The Workflow of the Prototype

Figure 10 is the experiment platform. Similar to the locomotion mode of the locusts, the designed robot has four stages in its flying-jumping process. The motion sequences of flying-jumping locomotion with the proposed bioinspired robot. **Figure 11** is the motion sequences of flying-jumping locomotion with the proposed bioinspired robot. The first stage is called the jumping preparing stage. Firstly, the main motor begins to run, and the rope pulley is driven to rotate by the gear transmission system to wound the rope around the rope pulley. Then the tibia leg is driven by the rope to gradually approach the external frame. At the same, the torsion spring generates the torsion angle to store the energy needed for jumping. In this stage, the flapping wing mechanism flaps slowly. The second stage is called the jumping stage. In this stage the torsion angle of the torsion spring reaches 100 degrees, then the linear motor starts to run to separate the two gears from meshing, and the rope wound on the pulley is released instantaneously under the force of the torsion spring force, which makes the robot jump off the ground instantaneously. The third stage is called the flying stage. In this stage the linear motor stops running and keeps the gears five and six out of mesh to prevent legs from swinging, at the same time, the wings flap quickly to provide lift force. The fourth stage is called the landing stage. In this stage, the rotating speed of the main motor is reduced, with the wings flapping slowly. And the deformation of torsion spring absorbs the impact energy when touching the ground.

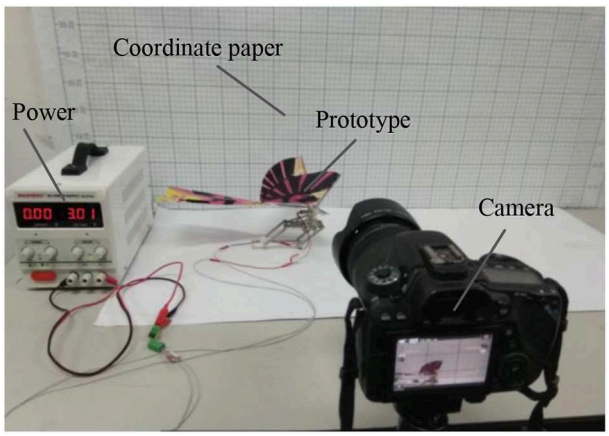

FIGURE 10 | The experiment platform.

Experimental Verification

In this section, we have carried out experiments to validate the influence of leg burrs and flapping-wing on jumping performance. We also compared the data that we got from the experiments on the prototype with the data of the biological experiments.

In the experiment on the influence of leg burrs on jumping performance, we removed the wings and conducted two groups of experiments. The robot in the first group jumps with burrs stuck to the foot and the robot in the second group jumps without burrs on its foot. The average value of the jumping performance in each group is presented in **Figure 12**. We can find that the maximum jumping height of the prototype without burrs is 330 mm; the longest jumping distance is 335 mm; the jumping height is about 3.1 times of the body length and the distance is about 3.1 times. The maximum jumping height of the prototype with burrs is 392 mm; the longest jumping distance is 305 mm; the jumping height is about 3.8 times of the body and the distance is about 3.2 times. It can be seen that leg burrs can increase jumping distance, jumping height, and jumping stability, which is consistent with the previous deduction derived from the biological experiment on the locusts.

In the experiment on the influence of flapping-wing on jumping performance, we conducted two groups of experiments. The first group jumps without wing-flapping motion. The second group jumps with wing-flapping motion. The average value of the jumping performance in each group is presented in **Figure 12**. We found that the maximum jumping height of the static wing is 270 mm. The longest jumping distance is 250 mm. The jumping height is about 2.6 times of the body length and the distance is about 2.6 times. The maximum jumping height of flapping wing prototype is 240 mm; the longest jumping distance is 780 mm;

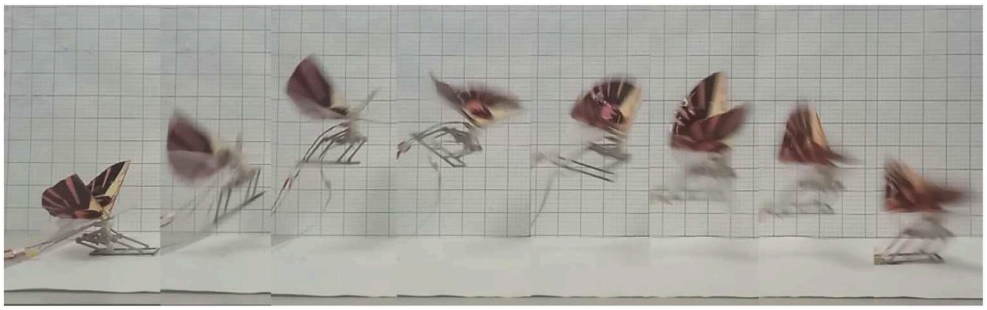

FIGURE 11 | The motion sequences of flying-jumping locomotion with the proposed bioinspired robot.

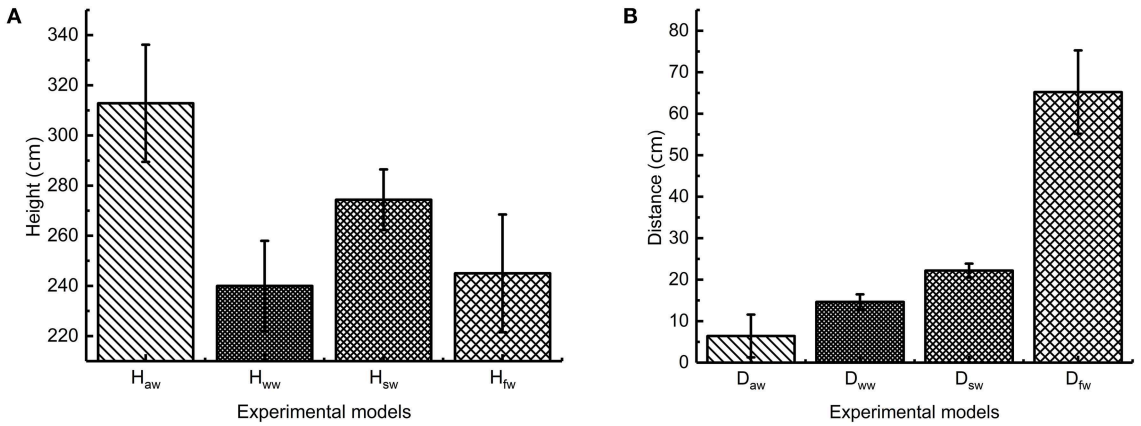

FIGURE 12 | Jumping performance of locust bioinspired robot **(A)** jumping height **(B)** jumping distance H_{aw} stands for the average jumping height with burrs and without wings; H_{ww} stands for the average jumping height without burrs and wings; H_{sw} stands for the average jumping height with burrs and with static wings; H_{fw} stands for the average jumping height with burrs and flapping-wings; D_{aw} stands for the average jumping distance with burrs and without wings; D_{ww} stands for the average jumping distance without burrs and wings; D_{sw} stands for the average jumping distance with burrs and static wings; D_{ww} stands for the average jumping distance with burrs and flapping wings.

the height is about 2.3 times of the body length and the distance is about 8.2 times. According to the analysis of the experiment, it is not easy for the flapping-wing robot prototype to flip in the air during the jumping process, which greatly increases the jumping stability of the robot and reduces the damage to the robot. By comparing the results of data, it can be seen that the jump distance of the flapping-wing robot is greatly increased compared with that of the static wing robot, and the jumping height data are basically the same, which is consistent with the analysis of locust. Through the comparison of data results, it can be seen that compared with the robot with stationary wings, the jumping height, and jumping distance of the robot with flapping wings is greatly increased, and the flapping-wing flying motion exists in addition to the inertia force in the jumping and flying stage.

In order to analyze the influence of leg burrs and flapping wing on the jumping stability, according to the formula (6), the coefficients of variation were calculated based on the experimental results. As shown in **Figure 13**, we analyzed the coefficients of variation of the jumping performance including jumping height and jumping distance. The results dedicate that the coefficient of variation of the robot with leg burrs is relatively smaller than these of the robot without burrs. That is, the jumping locomotion of the robot with leg burrs is relatively stable, which is consistent with the results of biological experiments. Meanwhile, the robot with static wings has the smallest coefficient of variation compared with those experiments of robots (a) without burrs (b) with burrs (d) with flapping wings. This phenomenon indicates the wings greatly increases the jumping stability and reduces the damage to the robot. The jumping height data were basically equal, which was consistent with the analysis of biological experiments.

The analysis of jumping height data shows that the jumping process of the prototype in this paper is controlled by simple equipment, and the jumping motion of the robot occurs instantaneously. If the wings beat too early, the robot will generate a certain lift when it does not jump, which will cause the foot to slide on the ground, and affect the jumping height of the prototype. Through the experiment of the prototype, the validity of the previous deduction is verified.

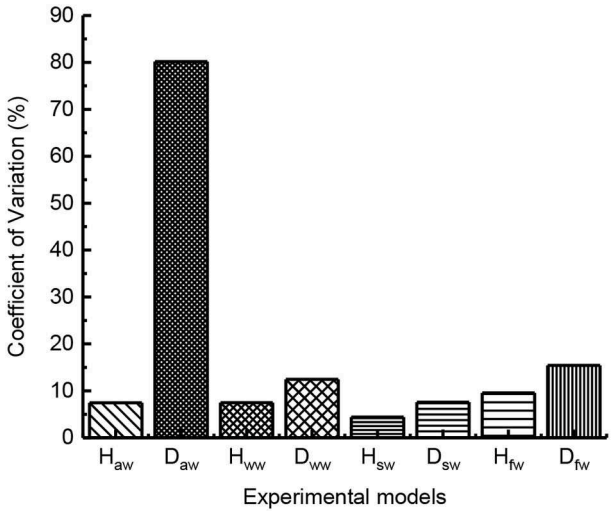

FIGURE 13 | The coefficient of variation of jumping performance with robot H_{aw} stands for the average jumping height with burrs and without wings; H_{ww} stands for the average jumping height without burrs and wings; H_{sw} stands for the average jumping height with burrs and with static wings; H_{fw} stands for the average jumping height with burrs and flapping-wings; D_{aw} stands for the average jumping distance with burrs and without wings; D_{ww} stands for the average jumping distance without burrs and wings; D_{sw} stands for the average jumping distance with burrs and static wings; D_{ww} stands for the average jumping distance with burrs and flapping wings.

CONCLUSION

In this paper, we performed systematic experiments to understand the influences between the locomotors (both locust animals and bioinspired robots) and their jumping performance. The integration of hybrid inspired research contributed to the discovery of biology principles and the creation of bioinspired robot model, which also has proven powerfully in understanding the complex phenomena and predicting the design and control of robots.

We developed one simple but comprehensive robot prototype to validate and explain our observations from the biological experiments. Compared with other prototypes, the proposed robot inspired by locusts has multi-modal locomotion including jumping and flying based on metamorphic mechanism, which makes it perform the locusts' locomotion. We also discovered the sensitive dependence of locomotion performance on these leg burrs and flapping wings. We found that the number of leg burrs and the wing integrity has great influence the jumping performance, and the more the leg burrs are and the more complete the wings are the better jumping performance will be. Overall, our studies provided novel principles for bioinspired robots with flying-jumping locomotion, and at the same time, our robot-inspired experiment provides the insight to discover some principles behind the flying-jumping locomotion of biology.

At the current stage, the degree of freedom of the legs and flapping wings in our proposed prototype is limited. Multi-degree of freedom legs and the flexible wings will provide the potential to mimic more similar biological locomotion. The biological experiment is also hard to discover the principles of the coupling motion between the legs and the flapping wings during taking-off, air flight, and landing-off. In future work, we will have a tendency to concentrate on those issues based on the idea of hybrid inspired research.

DATA AVAILABILITY STATEMENT

The raw data supporting the conclusions of this manuscript will be made available by the authors, without undue reservation, to any qualified researcher.

AUTHOR CONTRIBUTIONS

DW and TG contributed the initial conception and obtained funding support. TG, SZ, and CZ conducted the experiments and data curation. DW, XM, and ZL wrote the original draft manuscript. DW, TG, and XM contributed to manuscript revision.

FUNDING

This project was supported by the National Natural Science Foundation of China (Grant No. 51705066), Sichuan Science and Technology Program (Grant No. 2019YFG0343), and the Joint Foundation of China University of Petroleum-Beijing At Karamay (Grant No. DK2018B00002).

ACKNOWLEDGMENTS

This is a short text to acknowledge the contributions of specific colleagues, institutions, or agencies that aided the efforts of the authors.

REFERENCES

Beck, A., Zaitsev, V., Hanan, U. B., Kosa, G., Ayali, A., and Weiss, A. (2017). Jump stabilization and landing control by wing-spreading of a locust-inspired jumper. *Bioinspir. Biomim.* 12:066006. doi: 10.1088/1748-3190/aa8ceb

Bennet-Clark, H. C. (1975). The energetics of the jump of the locust *Schistocerca gregaria*. *J Exp Biol* 63, 53–83.

Burrows, M. (2016). Development and deposition of resilin in energy stores for locust jumping. *J. Exp. Biol.* 219, 2449–2457. doi: 10.1242/jeb.138941

Camhi, J. M. (1970). Yaw-correcting postural changes in locusts. *J. Exp. Biol.* 52, 519–531.

Chen, D., Chen, K., Zhang, Z., and Zhang, B. (2015). Mechanism of locust air posture adjustment. *J. Bio. Eng.* 12, 418–431. doi: 10.1016/S1672-6529(14)60133-5

Fukuda, T., Hasegawa, Y., Sekiyama, K., and Aoyama, T. (2012). *Multi-Locomotion Robotic Systems: New Concepts of Bio-Inspired Robotics*, Vol. 81. Berlin; Heidelberg: Springer.

Gravish, N., and Lauder, G. V. (2018). Robotics-inspired biology. *J. Exp. Biol.* 221:jeb138438. doi: 10.1242/jeb.138438

Heitler, W. J., and Burrows, M. (1977). The locust jump. I. The motor programme. *J. Exp. Biol.* 66, 203–219.

Iida, F., and Ijspeert, A. J. (2016). "Biologically inspired robotics," in *Springer Handbook of Robotics,* eds B. Siciliano, and O. Khatib (Cham: Springer), 2015–2034. doi: 10.1007/978-3-319-32552-1

Karásek, M., Muijres, F. T., De Wagter, C., Remes, B. D. W., and de Croon, G. C. H. E. (2018). A tailless aerial robotic flapper reveals that flies use torque coupling in rapid banked turns. *Science* 361, 1089–1094. doi: 10.1126/science.aat0350

Kovač, M., Wassim-Hraiz, Fauria, O., Zufferey, J. C., and Floreano, D. (2011). "The EPFL jumpglider: a hybrid jumping and gliding robot with rigid or folding wings," in *2011 IEEE International Conference on Robotics and Biomimetics*. Phuket. doi: 10.1109/ROBIO.2011.6181502

Kovac, M. M., Fuchs, A., Guignard, J., Zufferey, and Floreano, D. (2008). "A miniature 7g jumping robot," in *2008 IEEE International Conference on Robotics and Automation* (Pasadena, CA). doi: 10.1109/ROBOT.2008.4543236

Li, F., Weiting, L., Xin, F., Gabriella, B., Umberto, S., Cesare, S., et al. (2012). Jumping like an insect: design and dynamic optimization of a jumping mini robot based on bio-mimetic inspiration. *Mechatronics* 22, 167–176. doi: 10.1016/j.mechatronics.2012.01.001

Low, K. H., Hu, T., Mohammed, S., Tangorra, J., and Kovac, M. (2015). Perspectives on biologically inspired hybrid and multi-modal locomotion. *Bioinspir. Biomim.* 10:020301. doi: 10.1088/1748-3190/10/2/020301

Lu, H., Zhang, M., Yang, Y., Huang, Q., Fukuda, T., Wang, Z., et al. (2018). A bioinspired multilegged soft millirobot that functions in both dry and wet conditions. *Nat. Commun.* 9:3944. doi: 10.1038/s41467-018-06491-9

Meyer, J. A., and Guillot, A. (2008). "Biologically inspired robots," in *Springer Handbook of Robotics,* eds B. Siciliano, and O. Khatib (Berlin, Heidelberg: Springer), 1399–1422. doi: 10.1007/978-3-540-30301-5_61

Mintchev, S., and Floreano, D. (2016). Adaptive morphology: a design principle for multimodal and multifunctional robots. *IEEE Robot. Autom. Mag.* 23, 42–54. doi: 10.1109/MRA.2016.2580593

Mo, X., Ge, W., Romano, D., Donati, R., Benelli, G., Dario, P., et al. (2019). Modelling jumping in Locusta migratoria and the influence of substrate roughness. *Entomol. Gener.* 317–332. doi: 10.1127/entomologia/2019/0607

Oertel, H. (2010). "Properties of liquids and gases," in *Prandtl-Essentials of Fluid Mechanics* (New York, NY: Springer), 15–42.

Peyré-Tartaruga, L. A., and Coertjens, M. (2018). Locomotion as a powerful model to study integrative physiology: efficiency, economy, and power relationship. *Front. Physiol.* 9:1789. doi: 10.3389/fphys.2018.01789

Romano, D., Donati, E., Benelli, G., and Stefanini, C. (2019). A review on animal–robot interaction: from bio-hybrid organisms to mixed societies. *Biol. Cybern.* 113, 201–225. doi: 10.1007/s00422-018-0787-5

Scarfogliero, U. C., Stefanini, C and Dario, P. (2006). "A bioinspired concept for high efficiency locomotion in micro robots: the jumping Robot Grillo," in *Proceedings 2006 IEEE International Conference on Robotics and Automation, 2006* (Orlando, FL: ICRA). doi: 10.1109/ROBOT.2006.1642322

Woodward, M. A. (2017). *MultiMo-Bat: Biologically Inspired Integrated Multi-Modal Locomotion*. Pittsburgh, PA: Carnegie Mellon University.

Woodward, M. A., and Metin, S. (2014). Multimo-bat: a biologically inspired integrated jumping–gliding robot. *Int. J. Rob. Res.* 33, 1511–1529. doi: 10.1177/0278364914541301

Zaitsev, V., Gvirsman, O., Ben Hanan, U., Weiss, A., Ayali, A., and Kosa, G. (2015). A locust-inspired miniature jumping robot. *Bioinspir. Biomim.* 10:066012. doi: 10.1088/1748-3190/10/6/066012

Zhang, J. C., Dong, C., and Song, A. (2017). "Jumping aided takeoff: Conceptual design of a bio-inspired jumping-flapping multi-modal locomotion robot," in *2017 IEEE International Conference on Robotics and Biomimetics (ROBIO)* (Pasadena, CA). doi: 10.1109/ROBIO.2017.8324390

Zhou, F., Kang, L., and Wang, X. H. (2019). JumpDetector: an automated monitoring equipment for the locomotion of jumping insects. *Insect Sci.* doi: 10.1111/1744-7917.12668

Conflict of Interest: The authors declare that the research was conducted in the absence of any commercial or financial relationships that could be construed as a potential conflict of interest.

frontiers in Neurorobotics

BRIEF RESEARCH REPORT
published: 05 November 2019
doi: 10.3389/fnbot.2019.00092

Investigation on the Cooperative Grasping Capabilities of Human Thumb and Index Finger

Xiaojing Chen[1,2], Zhiguo Li[1], Yuqing Wang[2], Jizhan Liu[3] and Dezong Zhao[4]*

[1] College of Mechanical and Electronic Engineering, Northwest A&F University, Yangling, China, [2] School of Mechanical and Power Engineering, Henan Polytechnic University, Jiaozuo, China, [3] School of Agricultural Equipment Engineering, Jiangsu University, Zhenjiang, China, [4] Department of Aeronautical and Automotive Engineering, Loughborough University, Loughborough, United Kingdom

The maximum cooperative grasping mass and diameter of the human thumb and index finger were investigated by 7560 grasp-release trials on various masses of solid cylinders and various sizes of rings. The maximum grasping mass of the participants' thumb-index finger depended on gender, age and the sum of thumb-index finger lengths ($P < 0.05$), but not on the hand-used and ratio of index finger to thumb length ($P > 0.05$). The maximum grasping diameter of the participants' thumb-index finger depended on the age, sum of thumb-index finger lengths and ratio of index finger to thumb length ($P < 0.05$), but not on the gender and hand-used ($P > 0.05$). There was a non-linear regression model for the dependence of the maximum grasping mass on gender, age and the sum of thumb-index finger lengths and another non-linear regression model for the dependence of the maximum grasping diameter on the age, sum of thumb-index finger lengths and ratio of index finger to thumb length. Two regression models were useful in the optimal size design of robotic hands intending to replicate thumb-index finger grasping ability. This research can help to define not only a reasonable grasp mass and size for a bionic robotic hand, but also the requirements for hand rehabilitation.

Keywords: thumb and index finger, object mass and diameter, human characteristics, cooperative grasping capabilities, robotic hand

OPEN ACCESS

Edited by:
Florian Röhrbein, Technical University of Munich, Germany

Reviewed by:
Yuqing Lin, Beijing Institute of Technology, China
Zhijun Zhang, South China University of Technology, China
Lufeng Luo, Foshan University, China

****Correspondence:***
Zhiguo Li
lizhiguo0821@163.com

Received: *27 April 2019*
Accepted: *23 October 2019*
Published: *05 November 2019*

Citation:
Chen X, Li Z, Wang Y, Liu J and Zhao D (2019) Investigation on the Cooperative Grasping Capabilities of Human Thumb and Index Finger. Front. Neurorobot. 13:92. doi: 10.3389/fnbot.2019.00092

INTRODUCTION

By comparing with multi-fingered dexterous hands, two-finger bionic hand has simple mechanical structure and is easy for motion planning, so it is always used in the fruit harvesting robots (Bac et al., 2017; Silwal et al., 2017). However, the work environment of the fruit harvesting robots is extremely complex, such as the fruits in a plant are difference in size, shape, posture, and position (Li et al., 2019a,b), and the existing two-finger bionic hands are difficult to meet the grasping requirements of fruit harvesting (Li et al., 2013), so the robots are still not used for practical fruit harvesting so far. With the assistance of brain and eye coordination, individuals are always considered reliable performers when able to complete the tasks of grasping, moving and releasing a target fruit by using only the thumb and index finger, and the overall performance of this stable manipulation system is reasonable. The human hand is a powerful multifunctional tool, and exploration of its capabilities helps researchers to define a reasonable grasp mass and size for a bionic robotic hand, intending to replicate its abilities (Feix et al., 2014; Chen et al., 2019). From the viewpoint of ergonomics, fruit harvesting robot designers need to understand the cooperative grasping capabilities of the human thumb-index finger and the quantitative correlation between

finger-length and grasping capabilities for newly designed two-finger bionic hands so as to improve their grasping performance (Yussof and Ohka, 2012; Wang and Ahn, 2017).

Studies highlighting the human thumb-index finger grasping behaviors have been published during the last decade. Some researchers revealed that the grasp stability during manipulation was primarily affected by the object weight, the relative curvature and friction force between the fingertips and object surface, and the distance between two contact points when an object was pinched by the thumb-index finger (Li et al., 2013; Luciw et al., 2014). Biegstraaten et al. (2006) concluded that the reaching and lifting movements were quite independent when an object was grasped with a precision grip (Biegstraaten et al., 2006). Vigouroux et al. (2011) proposed that when the human thumb-index finger grasped objects having different widths then the finger joint postures, muscle force and grip force varied significantly according to the object width, and an interesting result was that the muscle force/grip force ratios of the major flexor muscles remain particularly stable with respect to the width, whereas other muscle ratios differed widely. Furthermore, various research studies have also been carried out on human five-finger grasping capabilities (Vigouroux et al., 2011). Eksioglu (2004) demonstrated that the optimum grip span relative to an individual's hand anthropometry was about 2 cm shorter than his modified thumb crotch length based on the judgment criteria of maximum voluntary isometric grip force, muscular activity and subjective rating. Seo and Armstrong (2008) illustrated that when cylindrical handles were grasped in a power grip posture, the ratio of the handle diameter to hand length can explain 62%, 57%, and 71% of the variances in grip force, normal force and contact area, respectively, Seo and Armstrong (2008). Li et al. (2010) anticipated that the hand circumference, among several anthropometric parameters such as height, weight, wrist, and forearm, lengths of hand and palm, had the strongest correlation with the maximal grip strength. Bansode et al. (2014) revealed that the dominant hand's grip strength in males and females had significant positive correlation with the age, height, weight and body mass index and the span of the dominant hand, while it had no obvious correlation with the waist circumference and waist to hip ratio. Feix et al. (2014) found that the optimum grasping capability of the human hand was less than 500 g in terms of mass, and the width of the object at the grasp location was less than 7 cm.

In summary, significant progress has been made in this field. Nevertheless, less attention has been paid to the cooperative grasping capability of human thumb and index finger and its influencing factors. This means there is a technical gap for the ergonomic design of robotic hands intending to replicate the ability of the human hand. Therefore, on the basis of the existing literature data, we carried out studies in an effort to investigate the effect of human body characteristics (e.g., age, gender, stature, hand-used, sum of thumb and index finger lengths and ratio of index finger to thumb length) on the thumb-index finger grasping capabilities, namely, the maximum grasping mass and diameter of the thumb-index finger using a multiple non-linear regression analysis method.

MATERIALS AND METHODS

Material

To investigate the cooperative grasp capabilities of human thumb-index finger, 20 different masses of solid cylinders and 15 different external diameters of rings were manufactured as grasped objects in August 2017. The solid cylinders with a diameter d_c of 40 mm were made of C45 carbon steel having the following characteristics: density of 7.85 g/cm^3 and surface roughness R_a = 0.1 μm (**Figure 1A**). The rings with a height h_r of 40 mm were made of acrylic and had a density of 1.2 g/cm^3 and a surface roughness R_a = 0.05 μm (**Figure 1B**). The operative parameters of the solid cylinders and rings such as their heights, diameters and masses are listed in **Table 1**. The solid cylinders were used to study the effects of human body characteristics on the maximum mass of objects that can be grasped with the thumb-index finger, while the rings were used to study the effects of human body characteristics on the maximum diameter of objects that can be grasped with the thumb-index finger. Multi-factor grasp-release tests were performed within 72 h at room temperature (24 ± 1°C, 50–55% RH).

Participants

A total of 108 volunteers (54 males and 54 females) were recruited from Henan Polytechnic University, *HPU* Kindergarten and *Hexiang* Primary School to participate in the grasp-release tests in this study. Their characteristics were as follows {mean [standard deviation (SD)]}: age, 11.9 (6.8) years; height, 141.5 (23.8) cm; thumb length, 41.9 (7.7) mm and index-finger length, 56.6 (10.0) mm. All the contributors were provided with a detailed description of the objectives and requirements of the experiment and then written informed consent was obtained from the participants over the age of 16 and from the parents of the participants under the age of 16. All the volunteers were right-handed, with normal hearing and corrected-to-normal vision, and had no history of injuries to their hands, mental illness or physical disabilities. This study was carried out in accordance with the principles of the Basel Declaration and recommendations of the Establishment of Institutional Ethics Committees in China.

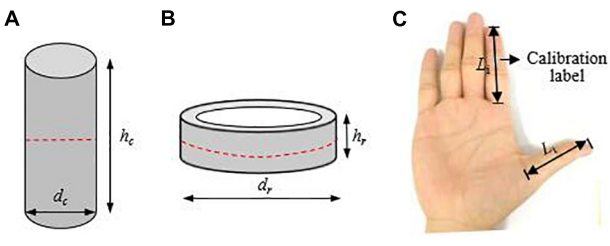

FIGURE 1 | Grasped object sizes and hand sizes: **(A)** solid cylinder, where d_C and h_C denote the diameter and height, **(B)** ring, where d_r and $h_r$denote the external diameter and height, **(C)** hand sizes, L_i – index finger length, L_t – thumb length.

TABLE 1 | Geometric characteristics of grasped objects.

No.	Solid cylinder			Ring		
	Height h_c/mm	Diameter d_c/mm	Mass m_c/g	Height h_r/mm	Diameter d_r/mm	Mass m_r/g
1	20	40	197.2	40	30	12.2
2	30	40	295.8	40	40	16.7
3	40	40	394.4	40	50	21.3
4	50	40	493.0	40	60	25.8
5	60	40	591.6	40	70	30.3
6	70	40	690.2	40	80	34.8
7	80	40	788.8	40	90	39.3
8	90	40	887.4	40	100	43.9
9	100	40	986.0	40	110	48.4
10	110	40	1084.6	40	120	52.9
11	120	40	1183.2	40	130	57.4
12	130	40	1281.7	40	140	61.9
13	140	40	1380.3	40	150	66.5
14	150	40	1478.9	40	160	71.0
15	200	40	1971.9	40	170	75.5
16	250	40	2464.9			
17	500	40	4929.8			
18	750	40	7394.7			
19	1000	40	9859.6			
20	1250	40	12324.5			

Procedures

The participants washed their hands with soap and water and dried them with a towel about 5 min before tests. The stature of each participant was measured using a folding ruler to an accuracy of 1 mm. Each participant was facilitated with a calibration label patching on his hands, and his thumb and index finger were opened to take a photo with a digital camera (Canon IXUS 95IS) from the top of the palm (**Figure 1C**). The captured images were transmitted into the computer and then processed by the Digimizer Version 4.2.6.0 to extract the lengths of the two fingers. The lengths of the thumb and index finger were measured by the distance from proximal flexion crease of the finger to the tip of the respective finger (**Figure 1C**), which was in agreement with Kanchan and Krishan (2011), Ishak et al. (2012) and Jee et al. (2015). Subsequently, the grasped objects were placed on a table, and each participant was directed to sit in an office chair in front of the table with the right upper arm parallel to the trunk, the elbow resting on his/her right thigh and the forearm extended anteriorly. The participant was asked to lift and move an object from one position to another using the thumb and index finger of the right hand naturally. 15 s later the participant moved the object back using the thumb and index finger of the left hand. During grasping, the middle finger, ring finger, little finger and palm could not touch the object.

The cooperative grasping process of human thumb and index finger was a hand-brain-eye coordination behavior and can be divided into five steps (**Figure 2**). 1st step: location and sensing an object by vision system with guide of brain; 2nd step: the brain processes information obtained from vision system and makes a strategic decision (e.g., pre-grasp type, grasp force, and grasp position) for stable grasping; 3rd step: the brain commands hand to reach and grasp the object; 4th step: the tactile sensory information was feedbacked to the brain for further decision-making and if necessary the posture and force of grasp will be adjusted with the command of brain; 5th step: the hand grasps the object stably and moves it into another position.

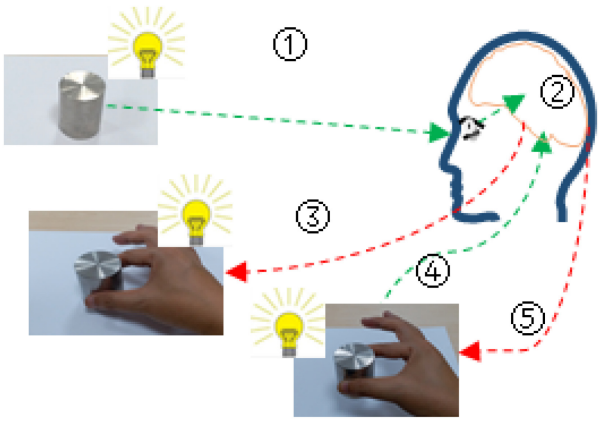

FIGURE 2 | Cooperative grasping behavior of human thumb and index finger.

In this experiment, the grasped objects were solid cylinders of various masses (**Figure 1A**) and rings of various sizes (**Figure 1B**). Each participant grasped the solid cylinders based on its mass from light to heavy in order and then grasped the rings based on their external diameter from small to large in order. The maximum grasping mass of the human thumb-index finger

indicated the maximum mass of objects that can be grasped with the thumb-index finger. The maximum grasping diameters of the human thumb-index finger indicated the maximum diameter of objects that can be grasped with the thumb-index finger. After each grasping task, the grasping result, namely, success or failure, was recorded carefully by a skilled observer. A grasp trial was characterized as successful if the grasp-release process was stable and no relative slip occurred between the index finger, thumb and object; otherwise, it was characterized as a failed trial. In total, there were 7560 grasp trials (108 volunteers × 2 hands × 20 solid cylinders + 108 volunteers × 2 hands × 15 rings) in the experiment.

Non-linear Regression Analysis

In this study, a non-linear regression analysis method is used to find two potential mathematical models of the relationships between the dependent variables (namely, the maximum grasping mass, and diameter of the thumb-index finger) and a set of independent variables (e.g., age, gender, hand-used, and sum of thumb-index finger lengths, ratio of index finger to thumb length). Because human thumb and index finger are co-existed and their lengths exist multicollinearity, two relative independent parameters: sum of thumb and index finger lengths and ratio of index finger to thumb length were selected to characterize the thumb and index finger lengths in the regression analysis. In consideration of the strong correlation between the stature and finger-length sum which was anticipated by Abdel-Malek et al. (1990), the finger-length sum was considered in the following regression analysis but the stature was not considered. Human body characteristics such as age and sum of thumb-index finger lengths were regarded as the original independent variables, and the maximum grasping mass and diameter of the thumb-index finger were set as the first and second dependent variables, respectively. After the experiments, the linear (e.g., $y = kx$) and non-linear (e.g., $y = kx^2$, $y = k\ln x$) functional relationships between age and maximum grasping mass, between the sum of thumb-index finger lengths and maximum grasping mass, between age and maximum grasping diameter, and between the sum of thumb-index finger lengths and maximum grasping diameter, were estimated using the "curve estimation" of IBM SPSS Statistics 24.0 (version 24.0, IBM Corporation, United States) and then compared in order to select an optimal functional relationship between the two variables based on the adjusted coefficient of determination R^2. A larger R^2 indicated that the corresponding function relationship is more suitable for fitting the experimental data between the two variables. The constant was not included in each regression equation.

After the optimal functions between the original quantitative independent variables and the dependent variables were obtained, each non-linear function was regarded as a new independent variable to be used in the following multiple linear regression analysis and the significance level was set at 0.05. Because gender and the hand-used were categorical variables, before linear regression analysis, the two levels of gender, namely, male, and female, were coded as "0" and "1," respectively, and the two levels of the hand-used, namely, left hand and right hand, were also coded as "0" and "1," respectively. Finally, a multiple linear regression analysis was used to construct two potential mathematical models. The constant was not included in each regression model. The goodness-of-fit test was used to measure how well the observed data correspond to each regression model, the *F*-test was used to test the overall significance of each regression model, and the *t*-test was used to determine whether an independent variable had a statistically significant effect on the dependent variable in each model.

RESULTS AND DISCUSSION

Descriptions of Experimental Results

Figure 3 shows the maximum grasping masses of the human thumb-index finger under different human body characteristics conditions (e.g., gender, hand-used, age, and sum of thumb-index finger lengths). In this study, the maximum grasping masses of the thumb-index finger of participants ranged from 690.2 to 9859.6 g. The maximum grasping masses of the thumb-index finger of male participants were 5057.6 ± 2695.6 g (Mean ± Standard Deviation), significantly higher than those of female participants 3265.5 ± 1853.5 g (**Figure 3A**). However, there was no significant difference in the maximum grasping masses of the thumb-index finger in the left and right hands of participants; the maximum grasping masses of the thumb-index finger of the left hand were 4102.7 ± 2449.4 g, slightly lower than those of the right hand 4220.5 ± 2513.1 g (**Figure 3B**). In this study, the age of participants ranged from 3∼27 years old and the sum of the thumb and index finger lengths ranged from 56.9 to 132.6 mm. Obviously, the maximum grasping masses of the thumb-index finger of participants had a non-linear (e.g., quadratic function, logarithmic function) increased trend with increasing age and the sum of the thumb and index finger lengths (**Figures 3C,D**).

Figure 4 shows the maximum grasping diameters of the human thumb-index finger under different human body characteristics conditions (e.g., gender, hand-used, age, and sum of thumb-index finger lengths). In this study, the maximum grasping diameters of the thumb-index finger of participants ranged from 70 to 170 mm. The maximum grasping diameters of the thumb-index finger of male participants were 129.0 ± 22.2 mm, slightly larger than those of female participants 119.9 ± 25.2 mm (**Figure 4A**). The maximum grasping diameters of the thumb-index finger of the left hand were 124.0 ± 24.1 mm, almost equal to that of the right hand (**Figure 4B**). Similar to **Figures 3C,D**, the maximum grasping diameters of the thumb-index finger of participants also showed a non-linear (e.g., quadratic function, logarithmic function) increased trend with increasing age and the sum of the thumb and index finger lengths (**Figures 4C,D**).

Table 2 lists the adjusted coefficients of determination of the linear and non-linear regression models between the quantitative independent and dependent variables. By comparing the adjusted coefficients of determination of three types of functions, the linear function provided the optimal functional relationship between age and maximum grasping mass, and between sum of thumb-index finger lengths and maximum grasping diameter; the

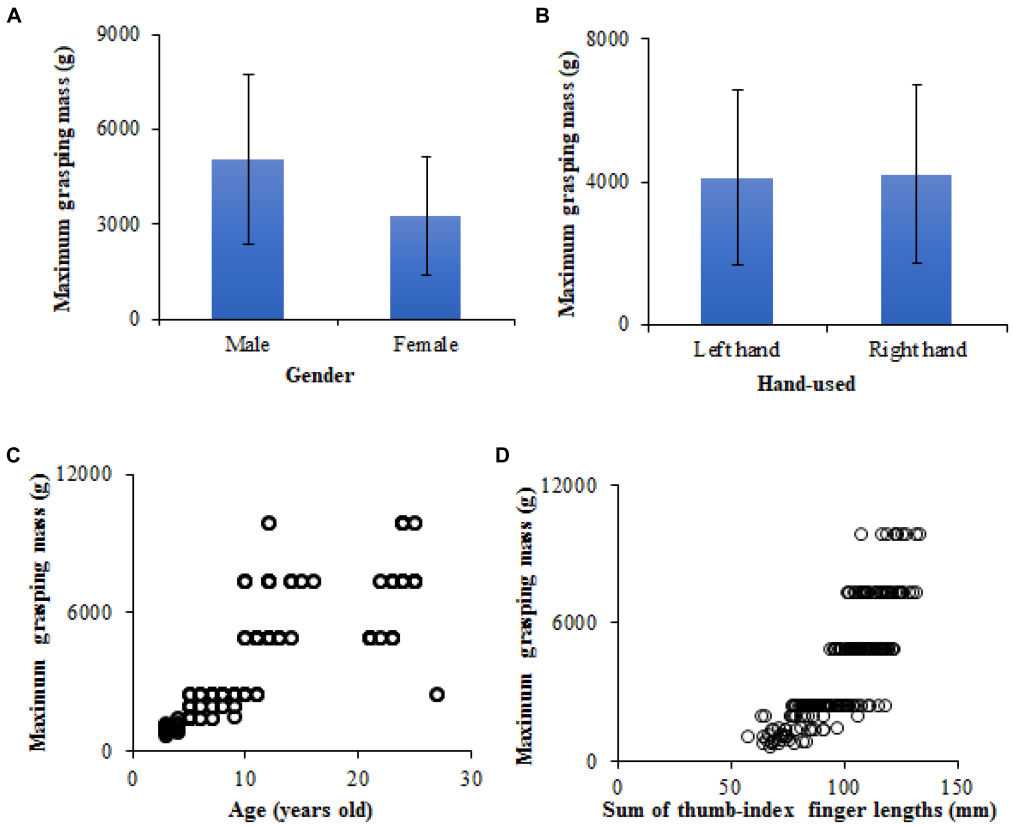

FIGURE 3 | Maximum grasping masses of the human thumb-index finger under different human body characteristics conditions: **(A)** Relationship between gender and maximum grasping mass (Mean ± Standard Deviation), **(B)** relationship between hand-used and maximum grasping mass (Mean ± Standard Deviation), **(C)** relationship between age and maximum grasping mass, **(D)** relationship between sum of thumb-index finger lengths and maximum grasping mass.

quadratic function yielded the optimal functional relationships between sum of thumb-index finger lengths and maximum grasping mass; and the logarithmic function provided the optimal functional relationship between age and maximum grasping diameter. These results were used in the following regression analysis.

Factors Affecting the Maximum Grasping Mass of Human Thumb-Index Finger

The non-linear regression model for the dependence of the maximum grasping mass on gender, age and sum of thumb-index finger lengths is presented in Eq. 1. The adjusted coefficient of determination, which is denoted as R^2, was 0.97, which suggests that the model fitted the data well and indicates that this model can explain 97% of the variance in the maximum grasping mass that was predicted by the gender, age and sum of thumb-index finger lengths. It was concluded from the *F*-test that the overall fit was significant ($P < 0.05$). *t*-tests demonstrated that the maximum mass of the objects that the participants could grasp using the thumb-index finger depended on gender, age and the sum of thumb-index finger lengths ($P < 0.05$), but not on the hand-used and ratio of index finger to thumb length ($P > 0.05$).

$$M_{\max} = 127.1 \times A + 0.32 \times L_o^2 - 1070.5 \times G \quad (1)$$

where $M_{\max}$ – maximum grasping mass, g; G – gender; A – age of participants, years; and L_o – finger-length sum, mm.

The age of participants ranged from 3∼27 years old, which is at the stage of growth and development of human muscle (Lexell et al., 1992), so the age showed a positive significant effect on the maximum grasping mass of the human thumb-index finger. The sum of thumb and index finger lengths was positively related to the maximum grasping mass of the human thumb-index finger, the reason being that participants with big hands have long fingers and tend to have high muscular strength (Seo and Armstrong, 2008). The values $G = 0$ or 1, namely, male or female, were substituted into Eq. 1 to describe the maximum grasping masses of the participants. The difference in the maximum grasping masses of the thumb-index finger of males and females was 1070.5 g. Similar research results demonstrated that the grip strength of males was significantly higher than that of females (Puh, 2009) and the hand length had a significant effect on the grasp strength of human five-fingers (Li et al., 2010). The significant relationship between gender and the maximum grasping mass of two fingers can be attributed to the maximal voluntary contraction force of males being always greater than that of females of similar height (Shurrab et al., 2017). Therefore, increasing the maximal voluntary contraction force can improve the maximum grasping mass of human two-fingers. The grip

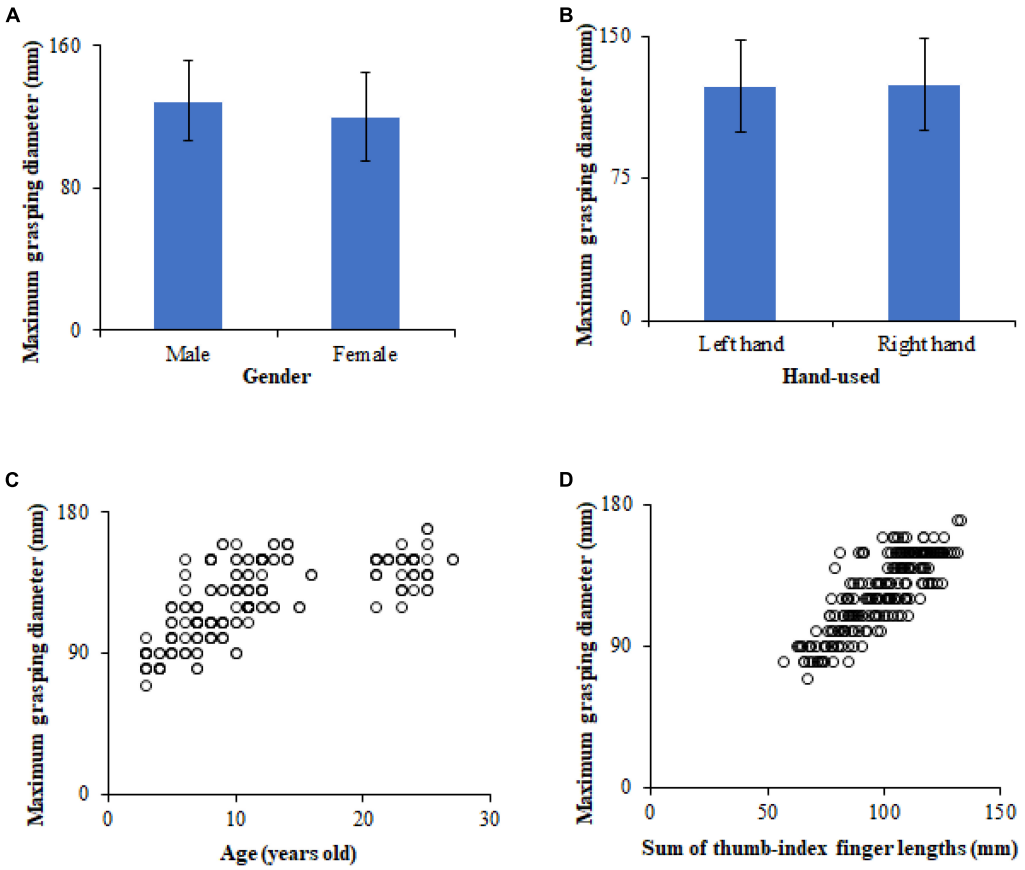

FIGURE 4 | Maximum grasping diameters of the human thumb-index finger under different human body characteristics conditions: **(A)** Relationship between gender and maximum grasping diameter (Mean ± Standard Deviation), **(B)** relationship between hand-used and maximum grasping diameter (Mean ± Standard Deviation), **(C)** relationship between age and maximum grasping diameter, **(D)** relationship between sum of thumb-index finger lengths and maximum grasping diameter.

TABLE 2 | Adjusted coefficients of determination of regression models between independent and dependent variables.

Function	$M_{max} = f(A)$	$M_{max} = f(L_0)$	$D_{max} = f(A)$	$D_{max} = f(L_0)$
$y = k\,x$	0.89	0.84	0.84	0.99
$y = k\,x^2$	0.72	0.91	0.56	0.96
$y = k \ln x$	0.88	0.77	0.97	0.98

M_{max}-maximum grasping mass; D_{max}-maximum grasping diameter; A-age; L_0-sum of thumb and index finger lengths.

strength is a similar parameter to the maximum grasping mass for measuring the grasping capacity of human fingers. These findings illustrated that the finger-length sum and the maximal voluntary contraction force would jointly affect the maximum grasping mass of thumb-index finger, which suggested that the two factors should be considered together for improving the maximum grasping mass of robotic hands during ergonomic design.

Factors Affecting the Maximum Grasping Diameter of Human Thumb-Index Finger

The non-linear regression model for the dependence of the maximum grasping diameter on the age, sum of thumb-index finger lengths and ratio of index finger to thumb length is presented in Eq. 2. The adjusted coefficient of determination, which is denoted as R^2, was 0.99, which demonstrates that the model fitted the data well and this model can explain 99% of the variance in the maximum grasping diameter that was predicted by the age, sum of thumb-index finger lengths and ratio of index finger to thumb length. It was concluded from the F-test that the overall fit was significant ($P < 0.05$). t-tests showed that the maximum diameter of the objects that the participants could grasp using the thumb-index finger depended on the age, sum of the thumb-index finger lengths and ratio of index finger to thumb length ($P < 0.05$), but not on the gender and hand-used ($P > 0.05$).

$$D_{\max} = 6.58 \times Ln\left(\text{Age}\right) + 0.98 \times L_{\text{o}} + 9.67\, L_{\text{r}} \qquad (2)$$

where $D_{\max}$ – maximum grasping diameter, mm; L_{o} – sum of thumb-index finger lengths, mm; L_{r} – ratio of index finger to thumb length.

The sum of the thumb and index finger lengths ranged from 56.9 to 132.6 mm and the ratio of index finger to thumb length ranged from 1.09 to 1.65. The sum of the thumb and index finger lengths was positively proportional to the maximum grasping

diameter. The longer the sum of the thumb-index finger lengths, the larger the span between two fingertips; hence, the larger the maximum grasping diameter of the participants using the thumb-index finger. When the sum of the thumb and index finger lengths increased by 1 mm, the maximum grasping diameter of thumb-index finger increased by 0.98 mm. When the ratio of index finger to thumb length increased by 0.01, the maximum grasping diameter of thumb-index finger increased by 0.0967 mm. The ratio of index finger to thumb length was positively related to the maximum grasping diameter, which indicated that the combination of a short thumb and a long index-finger would increase the maximum grasping diameter of the thumb-index finger. The main reason is that as an object is grasped by two fingers, especially with the power-grasp type, the short thumb easily serves as a supporting point to match the long index finger in enveloping the object contour to form a force closure plane. The short thumb is not easy to be constrained by the object shape and a force-closure stable grasp can be achieved in the contact plane based on the grasp stability criterion that were reported by Li et al. (2013). There is little information on this topic in the literature.

DISCUSSION

The Eq. 1 in see section "Factors Affecting the Maximum Grasping Mass of Human Thumb-Index Finger" quantitatively described the relationship between the sum of thumb and index finger lengths and the maximum grasping mass. When developing a two-finger bionic robotic hand, if the masses of potential target objects are given, an optimal length design of robotic thumb and index finger can be deduced using the Eq. 1 and an additional condition: the average ratio of index finger to thumb length is 1.36. Similarly, the Eq. 2 in Section "Factors Affecting the Maximum Grasping Diameter of Human Thumb-Index Finger" quantitatively described the relationship between the sum of thumb and index finger lengths, the ratio of index finger to thumb length and the maximum grasping diameter. When developing a two-finger bionic robotic hand, if the diameters of potential target objects are given, a suitable length design of robotic thumb and index finger can be deduced using the Eq. 2. Hence, the two non-linear regression models were useful in the optimal size design of robotic hands intending to replicate thumb-index finger grasping ability. When manipulating a novel object, sensory feedback provides us with information about its physical properties such as mass and then the brain is thought to select the most appropriate model maintained in our central nervous system for the current task (Lemon et al., 1995; Davidson and Wolpert, 2004). According to the maximum grasping mass set of thumb-index finger, a deep learning algorithm can be developed to justify whether some objects in an unstructured working environment meet the grasping requirements of bionic robotic hands. Furthermore, if there are some irregular objects (e.g., mug) in the unstructured environment, the maximum grasping diameter set of thumb-index finger can be used to make grasp planning algorithms for selecting the optimal grasping locations on an irregular object surface for a bionic robotic hand. Additionally, many time-varying problems always exist in the kinematic control problems of robotic fingers and the varying-parameter convergent differential neural network would be an efficient and accurate method for solving this grasping planning problem (Zhang et al., 2018a,b).

CONCLUSION

In this study, the maximum cooperative grasping mass and diameter of the human thumb and index finger in a wide range of unstructured tasks were investigated. The age of participants ranged from 3∼27 years old and the sum of their thumb and index finger lengths ranged from 56.9 to 132.6 mm. The results showed that the maximum grasping masses and diameters of the participants' thumb-index finger ranged from 690.2 to 9859.6 g and 70 to 170 mm. The maximum grasping mass of the participants' thumb-index finger depended on gender, age and the sum of thumb-index finger lengths ($P < 0.05$), but not on the hand-used and ratio of index finger to thumb length ($P > 0.05$). The maximum grasping diameter of the participants' thumb-index finger depended on the age, sum of the thumb-index finger lengths and ratio of index finger to thumb length ($P < 0.05$), but not on the gender and hand-used ($P > 0.05$).

There was a non-linear regression model for the dependence of the maximum grasping mass on gender, age and the sum of thumb-index finger lengths and another non-linear regression model for the dependence of the maximum grasping diameter on the age, sum of thumb-index finger lengths and ratio of index finger to thumb length. Two regression models were useful in the optimal size design of robotic hands intending to replicate thumb-index finger grasping ability. This research can help to define not only a reasonable grasp mass and size for a bionic robotic hand, but also the requirements for hand rehabilitation.

DATA AVAILABILITY STATEMENT

All datasets generated for this study are included in the article/supplementary material.

AUTHOR CONTRIBUTIONS

XC and ZL designed and performed the experiments and wrote the manuscript. YW, JL, and DZ reviewed and supervised the work.

FUNDING

This work was supported by a European Marie Curie International Incoming Fellowship (326847 and 912847), a Special Foundation for Talents of Northwest A&F University (Z111021801), a Shaanxi Project of Science and Technology Activities for Returning from Overseas (2018030), and a Key Research and Development Plan of Shaanxi Province (2019NY-172).

REFERENCES

Abdel-Malek, A. K., Ahmed, A. M., El Sharkawi, S. A., and El Hamid, N. A. (1990). Prediction of stature from hand measurements. *Forensic Sci. Int.* 46, 181–187. doi: 10.1016/0379-0738(90)90304-h

Bac, W., Hemming, J., Barth, R., and Wais, E. (2017). Performance evaluation of a harvesting robot for sweet pepper. *J. Field Robot.* 34, 1123–1139. doi: 10.1002/rob.21709

Bansode, D. G., Borse, L. J., and Yadav, R. D. (2014). Study of correlation between dominant hand's grip strength and some physical factors in adult males and females. *Int. J. Pharm. Res. Health Sci.* 2, 316–323.

Biegstraaten, M., Smeets, J. B. J., and Brenner, E. (2006). The relation between force and movement when grasping an object with a precision grip. *Exp. Brain Res.* 171, 347–357. doi: 10.1007/s00221-005-0271-z

Chen, X., Li, Z., Wang, Y., and Liu, J. (2019). Effect of fruit and hand characteristics on thumb-index finger power-grasp stability during manual fruit sorting. *Comput. Electron. Agric.* 157, 479–487. doi: 10.1016/j.compag.2019.01.032

Davidson, P. R., and Wolpert, D. M. (2004). Internal models underlying grasp can be additively combined. *Exp. Brain Res.* 155, 334–340. doi: 10.1007/s00221-003-1730-z

Eksioglu, M. (2004). Relative optimum grip span as a function of hand anthropometry. *Int. J. Ind. Ergonom.* 34, 1–12. doi: 10.1016/j.ergon.2004.01.007

Feix, T., Bullock, I., and Dollar, A. M. (2014). Analysis of human grasping behavior: object characteristics and grasp type. *IEEE Trans. Haptics* 7, 311–323. doi: 10.1109/TOH.2014.2326871

Ishak, N. I., Hemy, N., and Franklin, D. (2012). Estimation of sex from hand and handprint dimensions in a Western Australian population. *Forensic Sci. Int.* 221, 154.e1–154.e6. doi: 10.1016/j.forsciint.2012.04.017

Jee, S. C., Bahn, S., and Yun, M. H. (2015). Determination of sex from various hand dimensions of Koreans. *Forensic Sci. Int.* 257, 521.e1–521.e10. doi: 10.1016/j.forsciint.2015.10.014

Kanchan, T., and Krishan, K. (2011). Anthropometry of hand in sex determination of dismembered remains - a review of literature. *J. Forensic Leg. Med.* 18, 14–17. doi: 10.1016/j.jflm.2010.11.013

Lemon, R. N., Johansson, R. S., and Westling, G. (1995). Corticospinal control during reach, grasp, and precision lift in man. *J. Neurosci.* 15, 6145–6156. doi: 10.1523/jneurosci.15-09-06145.1995

Lexell, J., Sjostrom, M., Nordlund, A. S., and Taylor, C. C. (1992). Growth and development of human muscle: a quantitative morphological study of whole vastus lateralis from childhood to adult age. *Muscle Nerve* 15, 404–409. doi: 10.1002/mus.880150323

Li, K., Hewson, D. J., Duchene, J., and Hogrel, J. Y. (2010). Predicting maximal grip strength using hand circumference. *Man. Ther.* 15, 579–585. doi: 10.1016/j.math.2010.06.010

Li, Z., Li, P., Yang, H., and Wang, Y. (2013). Stability tests of two-finger tomato grasping for harvesting robots. *Biosyst. Eng.* 116, 163–170. doi: 10.1016/j.biosystemseng.2013.07.017

Li, Z., Miao, F., Yang, Z., Chai, P., and Yang, S. (2019a). Factors affecting human hand grasp type in tomato fruit-picking: a statistical investigation for ergonomic development of harvesting robot. *Comput. Electron. Agric.* 157, 90–97. doi: 10.1016/j.compag.2018.12.047

Li, Z., Miao, F., Yang, Z., and Wang, H. (2019b). An anthropometric study for the anthropomorphic design of tomato-harvesting robots. *Comput. Electron. Agric.* 163:104881. doi: 10.1016/j.compag.2019.104881

Luciw, M. D., Jarocka, E., and Edin, B. B. (2014). Multi-channel eeg recordings during 3,936 grasp and lift trials with varying weight and friction. *Sci. Data* 1:140047. doi: 10.1038/sdata.2014.47

Puh, U. (2009). Age-related and sex-related differences in hand and pinch grip stength in adults. *Int. J. Rehabil. Res.* 33, 4–11. doi: 10.1097/MRR.0b013e328325a8ba

Seo, N. J., and Armstrong, T. (2008). Investigation of grip force, normal force, contact area, hand size, and handle size for cylindrical handles. *Hum. Factors* 50, 734–744. doi: 10.1518/001872008x354192

Shurrab, M., Mandahawi, N., and Sarder, M. D. (2017). The assessment of a two-handed pinch force: quantifying different anthropometric pinch grasp patterns for males and females. *Int. J. Ind. Ergon.* 58, 38–46. doi: 10.1016/j.ergon.2017.02.006

Silwal, A., Davidson, J. R., Karkee, M., and Mo, C. (2017). Design, integration, and field evaluation of a robotic apple harvester. *J. Field Robot.* 34, 1–18.

Vigouroux, L., Domalain, M., and Berton, E. (2011). Effect of object width on muscle and joint forces during thumb-index finger grasping. *J. Appl. Biomech.* 27, 173–180. doi: 10.1123/jab.27.3.173

Wang, W., and Ahn, S. H. (2017). Shape memory alloy-based soft gripper with variable stiffness for compliant and effective grasping. *Soft Robot.* 4, 379–389. doi: 10.1089/soro.2016.0081

Yussof, H., and Ohka, M. (2012). Grasping strategy and control algorithm of two robotic fingers equipped with optical three-axis tactile sensors. *Procedia Eng.* 41, 1573–1579. doi: 10.1016/j.proeng.2012.07.352

Zhang, Z., Fu, T., Yan, Z., Jin, L., Xiao, L., Sun, Y., et al. (2018a). A varying-parameter convergent-differential neural network for solving joint-angular-drift problems of redundant robot manipulators. *IEEE ASME Trans. Mech.* 23, 679–689. doi: 10.1109/tmech.2018.2799724

Zhang, Z., Lu, Y., Zheng, L., Li, S., Yu, Z., and Li, Y. (2018b). A new varying-parameter convergent-differential neural-network for solving time-varying convex QP problem constrained by linear-equality. *IEEE Trans. Automat. Contr.* 63, 4110–4125. doi: 10.1109/tac.2018.2810039

Conflict of Interest: The authors declare that the research was conducted in the absence of any commercial or financial relationships that could be construed as a potential conflict of interest.

frontiers in Neurorobotics

ORIGINAL RESEARCH
published: 13 December 2019
doi: 10.3389/fnbot.2019.00104

Flexible Coordination of Flexible Limbs: Decentralized Control Scheme for Inter- and Intra-Limb Coordination in Brittle Stars' Locomotion

Takeshi Kano[1]*, *Daichi Kanauchi*[1], *Tatsuya Ono*[1], *Hitoshi Aonuma*[2] and *Akio Ishiguro*[1]

[1] Research Institute of Electrical Communication, Tohoku University, Sendai, Japan, [2] Research Center of Mathematics for Social Creativity, Research Institute for Electronic Science, Hokkaido University, Sapporo, Japan

Conventional mobile robots have difficulties adapting to unpredictable environments or performing adequately after undergoing physical damages in realtime operation, unlike animals. We address this issue by focusing on brittle stars, an echinoderm related to starfish. Most brittle stars have five flexible arms, and they can coordinate among the arms (i.e., inter-arm coordination) as well as the many bodily degrees of freedom within each arm (i.e., intra-arm coordination). They can move in unpredictable environments while promptly adapting to those, and to their own physical damages (e.g., arm amputation). Our previous work focused on the inter-arm coordination by studying trimmed-arm brittle stars. Herein, we extend our previous work and propose a decentralized control mechanism that enables coupling between the inter-arm and intra-arm coordination. We demonstrate via simulations and real-world experiments with a brittle star-like robot that the behavior of brittle stars when they are intact and undergoing shortening or amputation of arms can be replicated.

Keywords: brittle star, decentralized control, inter-limb coordination, intra-limb coordination, resilience

OPEN ACCESS

Edited by:
Poramate Manoonpong, University of Southern Denmark, Denmark

Reviewed by:
Jose De Jesus Rubio, National Polytechnic Institute, Mexico
Malte Schilling, Bielefeld University, Germany
Paolo Arena, University of Catania, Italy

***Correspondence:**
Takeshi Kano
tkano@riec.tohoku.ac.jp

Received: *08 October 2019*
Accepted: *29 November 2019*
Published: *13 December 2019*

Citation:
Kano T, Kanauchi D, Ono T, Aonuma H and Ishiguro A (2019) Flexible Coordination of Flexible Limbs: Decentralized Control Scheme for Inter- and Intra-Limb Coordination in Brittle Stars' Locomotion. Front. Neurorobot. 13:104. doi: 10.3389/fnbot.2019.00104

1. INTRODUCTION

Modern mobile robots are required to perform adequately in harsh environments such as disaster areas, distant planets, and deep oceans (Murphy, 2004; Antonelli et al., 2008; Sanderson, 2010; Nagatani et al., 2013; Patané, 2019). The challenge now is how to make the robots coordinate, in real-time, their numerous bodily degrees of freedom under unpredictable circumstances, including changes in the environment and unexpected physical damages to the robots' structure. Previous studies tackled this problem by using learning techniques (Bongard et al., 2006; Mahdavi and Bentley, 2006; Mostafa et al., 2010; Koos et al., 2013; Christensen et al., 2014; Ren et al., 2014; Rubio et al., 2018, 2019; Yen et al., 2018) and trial-and-error methods (Cully et al., 2015), however, the performance level of robots using these techniques is not satisfactory. Specifically, the previous robots could only adapt to predictable circumstances or required a considerably long adaptation time.

Drawing inspiration from animals could be one solution to the aforementioned problem. Indeed, animals, even primitive living organisms, do not lose their functionality under unstructured and unpredictable real-world constraints, and they can adapt to various environments in real-time

by coordinating their bodily degrees of freedom (Takamatsu et al., 2001; Schilling et al., 2013). This ability has been honed through evolutionary selection pressure, and it is likely that there is a sophisticated underlying mechanism. Owing to this, engineers have started implementing animal adaptation mechanisms in robots (Ijspeert, 2014).

Among the various animal species, in this paper, we focus on the locomotion of a brittle star; a variety in the phylum Echinodermata, which includes other varieties like starfish, sea cucumber, sea urchin etc. (Glaser, 1907; Arshavskii et al., 1976a,b; Wilkie, 1978; Cobb and Stubbs, 1981; Skold and Rosenberg, 1996; Carnevali, 2006; Astley, 2012; Kano et al., 2012, 2017; Watanabe et al., 2012; Matsuzaka et al., 2017; Clark et al., 2019). A brittle star has a central disc and five functionally interchangeable flexible arms that diverge radially from a central disc (**Figure 1A**), and it can move adaptively on unpredictable and unstructured terrains (Arshavskii et al., 1976b). Moreover, it has an outstanding adaptability to bodily damage; it can move even after losing most of its arms (Arshavskii et al., 1976a; Kano et al., 2017). It achieves this highly adaptive locomotion by real-time coordination of different arms (i.e., inter-arm coordination) and the many bodily degrees of freedom within each arm (i.e., intra-arm coordination) (Arshavskii et al., 1976a,b; Astley, 2012; Kano et al., 2012, 2017; Watanabe et al., 2012; Matsuzaka et al., 2017; Clark et al., 2019). Surprisingly, these coordinations are performed via an extremely simple decentralized nervous system along the arms, which join a circumoral nerve ring (**Figure 1B**, **Supplementary Movie**) (Cobb and Stubbs, 1981). Thus, brittle stars likely implement an ingenious autonomous decentralized control mechanism that enables adaptation to unexpected circumstances through the coordination of many body parts.

Thus far, the essential control mechanism underlying the brittle stars' locomotion had stayed elusive for a long time, although several studies analyzed the locomotion patterns of brittle stars (Arshavskii et al., 1976a,b; Astley, 2012). Recently, we have addressed this issue by adopting a synthetic approach to infer essential mechanisms, by constructing phenomenological mathematical models and robots (Kano et al., 2012, 2017; Watanabe et al., 2012). Therein, we proposed a simple decentralized control model for the inter-arm coordination, based on the locomotion of brittle stars whose arms were trimmed or amputated in various ways (Kano et al., 2017). We implemented this mechanism in a brittle star-like robot and demonstrated that it can immediately adapt to damages, in one or several arms, by automatically coordinating the still responsive arms, in a way similar to real brittle stars. However, as the trimmed-arm brittle stars were intensively analyzed, our previous works focused on the way different arms are coordinated (i.e., inter-arm coordination), but not on the ways multiple bodily degrees of freedom within each arm are coordinated (i.e., intra-arm coordination). Thus, it remained unclear how brittle stars move adaptively by coupling the inter- and intra-arm coordination.

Herein, we aim to elucidate the decentralized control mechanism that couples the inter- and intra-arm coordinations in brittle stars' locomotion. Based on findings of the behavior of brittle stars, with various morphologies (various arm lengths, different numbers of arms etc.) and in different environments, we propose a decentralized control model that incorporates both inter- and intra-arm coordination mechanisms. Given that we are motivated to capture the essential mechanism rather than to strictly mimic the locomotion of real brittle stars, the proposed mechanism is simple and describes the minimal requirement of the brittle stars' locomotion. The validity of the proposed control mechanism was investigated via simulations, and with an experimental robot. The results show that the proposed mechanism, despite its simplicity, can reproduce the behavior of brittle stars to some extent.

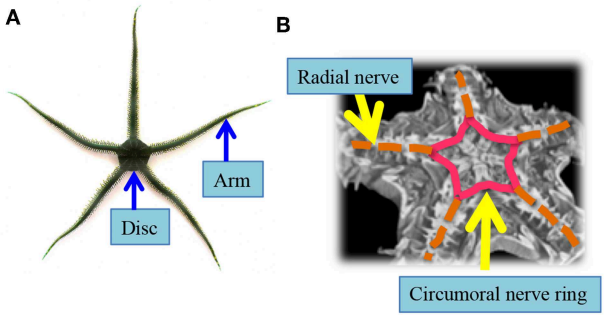

FIGURE 1 | Body and nerve structure of a real brittle star (*Ophiarachna incrassata*). **(A)** Overview of a brittle star. Five flexible arms radiate from a central disc. **(B)** Micro-computed tomography image of a brittle star. The nervous system is indicated by pink and orange lines. Radial nerves that innervate the arms (orange lines) are connected via a circumoral nerve ring located in the central disc (pink lines).

The remainder of this paper is structured as follows. In section 2, we briefly summarize behavioral findings on brittle stars. In section 3, we propose a model of brittle star locomotion. Specifically, we present a model of the mechanical system and the decentralized control mechanism for the inter- and intra-arm coordination, which was deduced from the behavioral findings. In sections 4, 5, we demonstrate that a simulated brittle star (section 4) and an experimental brittle star-like robot (section 5) reproduce the locomotion of real brittle stars. Finally, we draw our conclusions and indicate the scope of future work in section 6.

2. BEHAVIORAL FINDINGS

Herein we introduce locomotion patterns of real brittle stars (*Ophiarachna incrassata*) under various conditions. **Figure 2A** shows a typical locomotion pattern of an intact brittle star, which is called "breaststroke" (Arshavskii et al., 1976a). The brittle star assigns distinct roles to the arms. One arm is designated the center limb, another two are the forelimbs, and there are two hindlimbs. The center limb is pointing into the movement direction. The forelimbs are the primary structures that work in coordination to move the organism forward, and the hindlimbs have a minimal role in propulsion.

Figures 2B–E showed the snapshots of the locomotion of brittle stars when the number of arms, arm length,

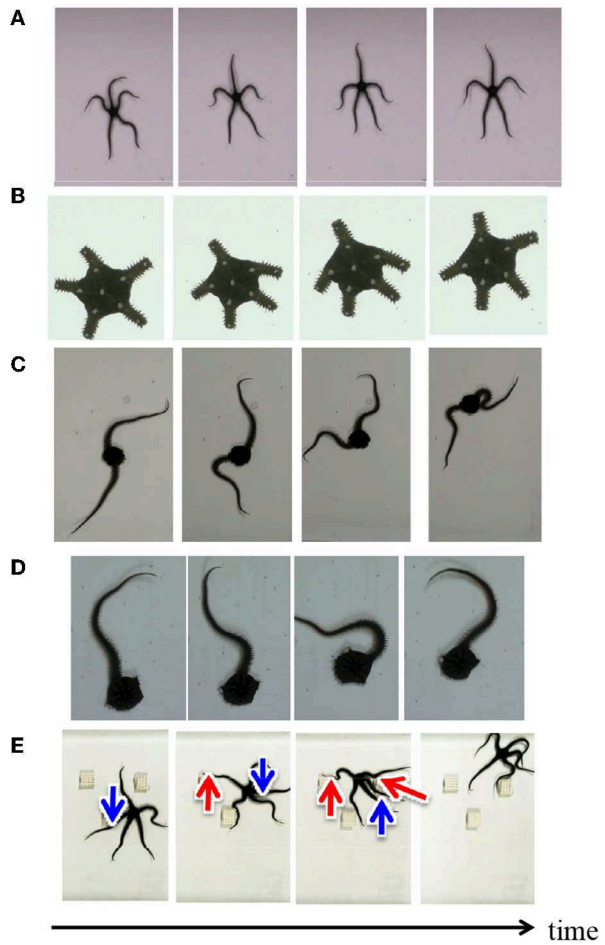

FIGURE 2 | Snapshots of locomotion of real brittle stars under various situations: **(A)** an intact brittle star on a flat terrain, **(B)** a brittle star with five shortened arms on a flat terrain, **(C)** a brittle star with two arms on a flat terrain, **(D)** a brittle star with one arm on a flat terrain, and **(E)** an intact brittle star on a terrain with several square objects. Red and blue arrows denote points where the arms exploit and avoid objects, respectively.

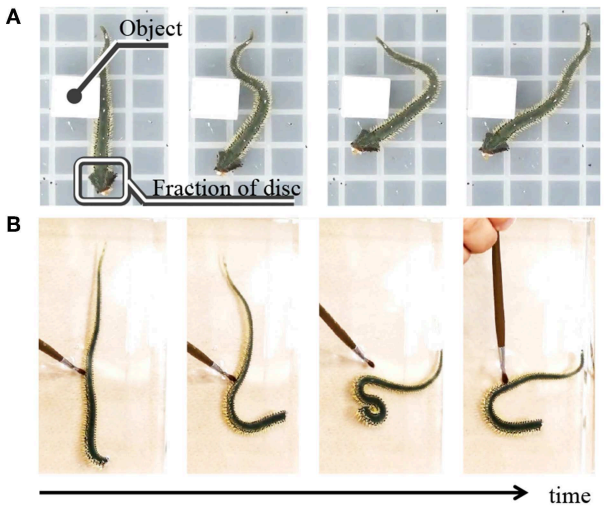

FIGURE 3 | Snapshots of motion of real brittle stars when only fraction of the body remains. **(A)** Locomotion of a brittle star with one arm and its proximal end of the disc on a terrain with a square object. **(B)** Motion of an arm without the disc. The arm was physically stimulated with an ink brush to induce motion.

and environment were changed in various ways (**Supplementary Movie**). When all the arms were shortened, the inter-arm coordination pattern was similar to the "breaststroke" of intact brittle stars (**Figure 2B**) (Kano et al., 2017). When some of the arms were removed, brittle stars moved by coordinating the bodily degrees of freedom in the remaining arms (**Figures 2C,D**). More specifically, the arms were often anchored to the ground and then they push themselves against the anchored points and effectively move. **Figure 2E** shows the locomotion of a brittle star on a terrain with several square objects. The arms push themselves against objects when they receive reaction forces that assist propulsion; meanwhile, they avoid the objects when they receive reaction forces that hinder propulsion.

We also performed the following behavioral experiments to specify the origin of the inter- and intra-arm coordinations (**Figure 3**, **Supplementary Movie**). **Figure 3A** shows snapshots when a brittle star, with only one arm and its proximal end of the disc, is placed on a terrain with a square object. Although only a fraction of the disc remained, the arm could move by exploiting the object; thus, locomotion was observed. **Figure 3B** shows the snapshots of the behavior of an arm, which was completely detached from the disc. In this case, the arm could not locomote by coordinating its body parts, although it responded to physical stimuli in a reflexive manner. These results suggest that the proximal ends of the arms in the central disk play important roles in locomotion through coordination of the body parts.

3. MODEL

Based on the findings described in section 2, we propose a minimal model of the body and the control system of a brittle star, aiming to capture the essence of the inter- and intra-arm coordination. We note that the model described in this section is used for simulations in section 4. The robot slightly differs from this model, due to technical reasons, as we will describe in section 5.

3.1. Body

A real brittle star comprises a central disc and five flexible arms. The arm comprises a series of segments, each containing a roughly discoidal vertebral ossicle surrounded by four muscles that connect adjacent ossicles (**Figure 4**) (Wilkie, 1978). The arm can bend horizontally as well as vertically by contracting these muscles. In a typical locomotion, horizontal movement is larger than that of vertical. However, vertical movement plays an important role in determining the points of ground contact.

Based on the above anatomical feature, the body is modeled as shown in **Figure 5**. The body is described by mass points, rigid links that connect mass points, and joints. The central disc forms

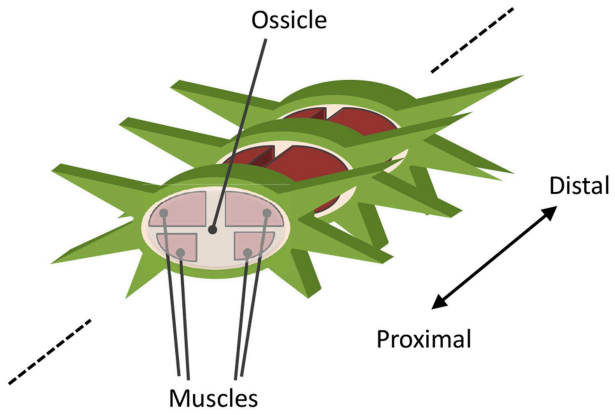

FIGURE 4 | Schematic for anatomical structure of an arm.

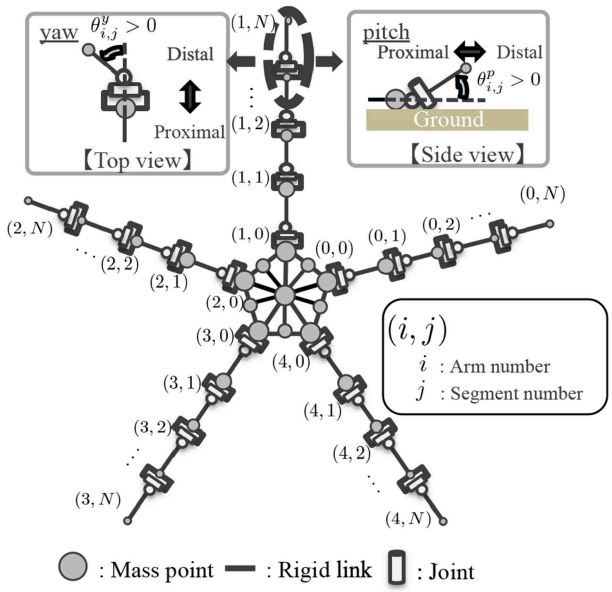

FIGURE 5 | Schematic of the body model. Definition of the joint angle is shown in the magnified view.

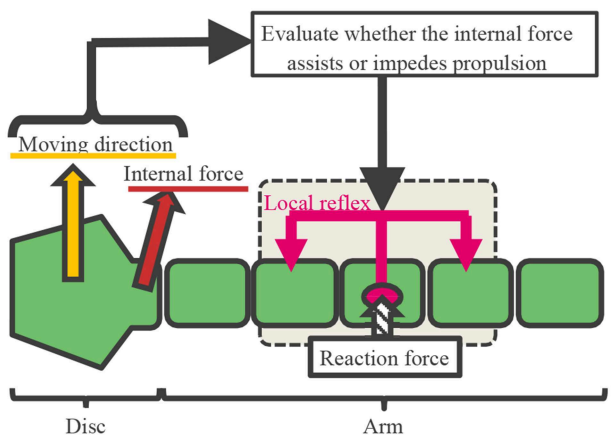

FIGURE 6 | A conceptual diagram of the proposed control mechanism.

a pentagon, and arms radiate from its apexes. In each arm, while intact, N mass points are concatenated in a one-dimensional array. Yaw and pitch joints are implemented between adjacent mass points. The arms are actuated by changing the target angles of these joints. The arms are enumerated by i, and the joints within each arm are enumerated by j. Considering that the distal side of real brittle stars' arms are thinner than the proximal side, the mass of the mass points in the arm $m_{i,j}$ is set to decrease as j increases. Specifically, $m_{i,j}$ is given by:

$$m_{i,j} = \alpha^j m_{\text{arm}}, \tag{1}$$

where m_{arm} and α are positive constants, where α is smaller than 1. The mass of the mass points in the disc is set to be a constant, denoted by m_{body}.

3.2. Arm Control Model

Based on the findings in section 2, we hypothesized that the arms are controlled according to the following procedure (**Figures 6**, **7** and **Supplementary Movie**):

1) Determining the moving direction: Although real brittle stars likely determine it by integrating stimuli received over the entire body, herein, we assume for simplicity (**Figure 6**) that it is given by a central command.
2) The internal force at the proximal end of each arm (namely, the force to which each arm pulls/pushes the central disc) is detected. Then, it is evaluated whether the detected force assists propulsion or not, and this information is sent to a lower level (i.e., peripheral side of the arms) (**Figure 6**).
3) The following local reflexive mechanisms work at the lower level, based on the result evaluated in 2).

   (a) When the force detected at the proximal end assists propulsion, we deduced that the following local reflexive mechanism works in real brittle stars: when a certain part of the arm receives a reaction force from the environment, several contralateral upper muscles on the distal side and ipsilateral lower muscles on the proximal side contract (**Figure 7A**). The muscle contraction of the distal segments works to increase the reaction force because it enables the arm to further push against the ground. Meanwhile, the muscle contraction of the proximal segments works to pull the central disc toward the contact point. Thus, the arm can exploit the environment to move effectively. This local reflexive mechanism can be expressed in the body model, as shown in **Figure 5**: When the arm receives a reaction force from the right(left)-hand side, several distal yaw segments bend to the left (right) while several proximal yaw segments bend to the right (left) (**Figure 7A**). At the same time, several distal pitch segments bend to push themselves against the ground while several proximal pitch segments bend to lift off the ground (**Figure 7A**).

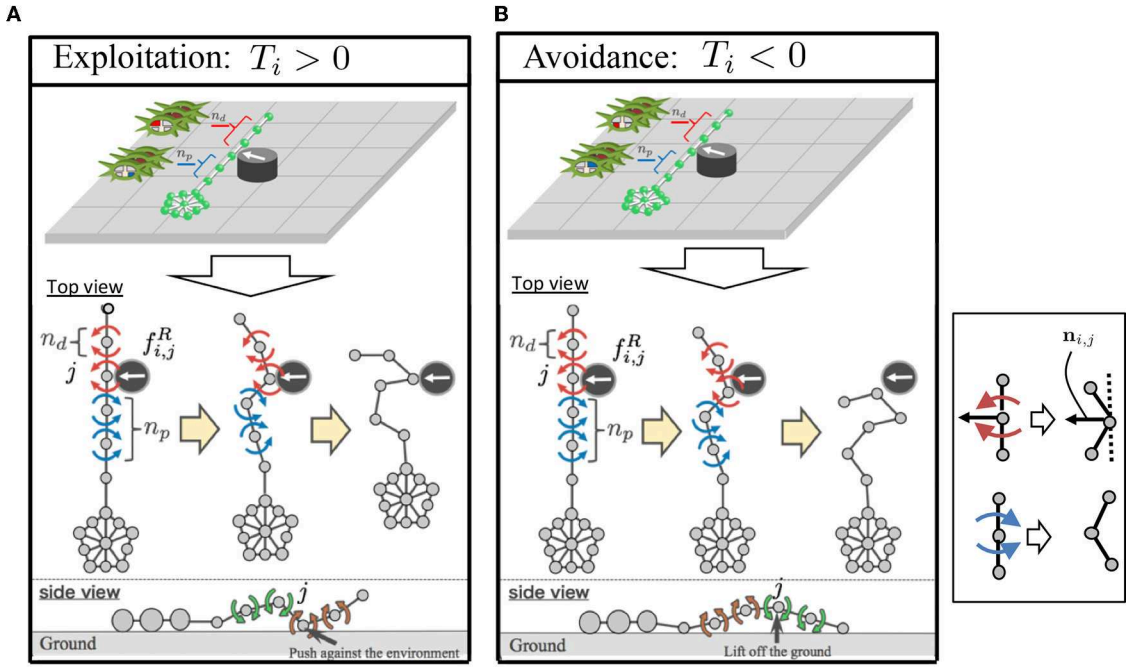

FIGURE 7 | Feedback mechanism: **(A)** exploitation and **(B)** avoidance. In the upper figures, muscles that contract due to the local reflexive mechanism are depicted in red and blue for the distal and proximal segments, respectively. This local reflexive mechanism was implemented in the proposed body model (**Figure 5**), as shown in the lower figures. The blue and red arrows represent the torques to bend the joints, as shown in the inset. The definition of the unit vector $\mathbf{n}_{i,j}$ is also shown in the inset.

(b) When the detected force at the proximal end impedes propulsion, we deduced that the following local reflexive mechanism works in real brittle stars: when a certain part of the arm receives a reaction force from the environment, several contralateral lower muscles on the distal side and ipsilateral upper muscles on the proximal side contract (**Figure 7B**). The muscle contraction of the proximal segments works to make the proximal part anchored to the ground. Meanwhile, the muscle contraction of the distal segments works to raise the arm and to carry it to the moving direction. Thus, the arm can move by reducing the resistive reaction force. This local reflexive mechanism can be expressed in the body model shown in **Figure 5**: When the arm receives a reaction force from the right(left)-hand side, several distal yaw segments bend to the left (right) while several proximal yaw segments bend to the right (left) (**Figure 7B**). At the same time, several distal pitch segments bend to lift off the ground while several proximal pitch segments bend to push themselves against the ground (**Figure 7B**).

The above-mentioned control mechanism is mathematically described as follows. The moving direction, which is assumed to be given as a central command, is denoted by the vector $\mathbf{D}$. Note that the absolute value $|\mathbf{D}|$ denotes the magnitude of the "will" of locomotion. The internal force at the proximal end of the ith arm is denoted by $\mathbf{F}_i$. Subsequently, the inner product of $\mathbf{D}$ and $\mathbf{F}_i$, denoted by T_i, is derived. Namely,

$$T_i = \mathbf{D} \cdot \mathbf{F}_i. \tag{2}$$

The detected force assists propulsion when T_i is positive, meanwhile, it impedes propulsion when T_i is negative. Then, the value of T_i is sent to the lower level.

The torque generated by the yaw and pitch joints, $\tau^y_{i,j}$ and $\tau^p_{i,j}$, are determined according to the proportional-derivative (PD) control (Rubio, 2016, 2018; Sun et al., 2018), namely,

$$\tau^y_{i,j} = \beta^j\{-k_y(\theta^y_{i,j} - \bar{\theta}^y_{i,j}) - c_y\dot{\theta}^y_{i,j}\}, \tag{3}$$
$$\tau^p_{i,j} = \beta^j\{-k_p(\theta^p_{i,j} - \bar{\theta}^p_{i,j}) - c_p\dot{\theta}^y_{i,j}\}, \tag{4}$$

where $\theta^y_{i,j}$ and $\theta^p_{i,j}$ are the real yaw and pitch joint angles, and $\bar{\theta}^y_{i,j}$ and $\bar{\theta}^p_{i,j}$ are the target yaw and pitch joint angles, k_y and k_p are the proportional gains for the yaw and pitch joints, c_y and c_p are the derivative gains for the yaw and pitch joints, respectively. The parameter β is a constant satisfying $0 < \beta < 1$, which were introduced so that the torque generated at the distal side becomes smaller than that at the proximal side, like real brittle stars. The target joint angles are determined according to the local reflexive mechanisms described in 3(a) and (b). Thus, $\bar{\theta}^y_{i,j}$ and $\bar{\theta}^p_{i,j}$ are given by the following differential equations:

$$\tau\dot{\bar{\theta}}^y_{i,j} = -\bar{\theta}^y_{i,j} + \xi^y + \sigma^y \tanh\left(\gamma|T_i|S^y_{i,j}\right), \tag{5}$$
$$\tau\dot{\bar{\theta}}^p_{i,j} = -\bar{\theta}^p_{i,j} + \xi^p + \sigma^p \tanh\left(\gamma T_i S^p_{i,j}\right), \tag{6}$$

where τ, σ^y, σ^p, and γ are positive constants; ξ^y and ξ^p denote the noise, which are implemented to actively interact

with the environment. The third terms on the right-hand side of Equations (5) and (6) denote the local reflexive mechanisms, where $S^y_{i,j}$ and $S^p_{i,j}$ are given by:

$$S^y_{i,j} = \sum_{s=\max\{0,j-n_d\}}^{j} (f^R_{i,s} - f^L_{i,s}) - \sum_{s=j+1}^{\min\{N,j+n_p\}} (f^R_{i,s} - f^L_{i,s}), \quad (7)$$

$$S^p_{i,j} = \sum_{s=\max\{0,j-n_d\}}^{j} (f^R_{i,s} + f^L_{i,s}) - \sum_{s=j+1}^{\min\{N,j+n_p\}} (f^R_{i,s} + f^L_{i,s}), \quad (8)$$

where n_d and n_p respectively denote the number of distal and proximal segments to which the detected force is fed back; $f^R_{i,j}$ and $f^L_{i,j}$ are defined as:

$$\begin{aligned} f^R_{i,j} &= \max\{\mathbf{f}_{i,j} \cdot \mathbf{n}_{i,j}, 0\} \\ f^L_{i,j} &= \max\{-\mathbf{f}_{i,j} \cdot \mathbf{n}_{i,j}, 0\} \end{aligned} \quad (9)$$

where $\mathbf{f}_{i,j}$ denotes the force vector acting to the jth mass point in the ith arm, and $\mathbf{n}_{i,j}$ is the unit vector perpendicular to the arm (**Figure 7**). Note that the max and min functions were introduced in Equations (7) and (8) so that the indexes do not go out of the allowed range. Thus, the feedback mechanisms described in 3(a) and (b) work when T_i is positive and negative, respectively.

Note that the proposed control mechanism is an extension of the control mechanism for inter-arm coordination we previously proposed (Kano et al., 2017). In fact, when each arm is shortened, the feedback to the proximal side operates in a similar manner as the local reflexive mechanism proposed in our previous work (Kano et al., 2017). Therefore, it is expected that the proposed control mechanism will enable inter-arm coordination. Additionally, the proposed control mechanism also enables the bending of long flexible arms in an appropriate manner, and thus, it is expected that intra-arm coordination can be achieved.

Given that the proposed control mechanism is based on self-organization, the theoretical analysis of the model is a challenge. Likewise, predicting its resulting behavior is also difficult. However, in the following sections, we will demonstrate the effectiveness of the proposed control mechanism and the manner in which this mechanism can reproduce the brittle stars' locomotion to a certain extent by utilizing the self-organization principle.

4. SIMULATION

We performed simulation experiments to validate the proposed model. The simulation source code is provided as **Data Sheet 1** in the Supplementary Material. In order to simplify the calculation; the three-dimensional dynamics of the body was derived by assuming that the yaw and pitch axis of the joints were perpendicular and parallel to the ground. The vector **D** which expresses the moving direction, was set to be a unit vector. The performance should be evaluated through the adaptability to either physical damage or environments rather than through the locomotion speed under a specific environment. Unfortunately, however, to the best of our knowledge, there is no index that can measure the adaptability, and it is difficult to quantitatively define fitness. Thus, we did not apply any optimization method but determined the parameters through trial-and-error. Ideally, common parameter values should be used for all experimental conditions. Unfortunately, they had to be individually adjusted for each condition, as shown in **Table 1**. Specifically, σ_y was set to be slightly smaller for the five flexible arms (**Figure 8A**) as compared to that in the other cases (**Figures 8B–E**). Doing so was necessary owing to the simplicity of the proposed model. Note that σ_p was set to be considerably smaller than σ_y because vertical arm movement is smaller than horizontal arm movement in real brittle stars. However, feedback to the pitch joints plays a significant role in locomotion, because points where the body anchors the ground are accurately determined with the use of this feedback mechanism.

The result is shown in **Figure 8** (**Supplementary Movie**). In the case of five flexible limbs (**Figure 8A**), the arms pushed themselves against the ground to move effectively (**Figure 2A**). When the five arms were shortened (**Figure 8B**), two forelimbs adjacent to the center limb tended to move synchronously, like "breaststroke" pattern of real brittle stars (**Figure 2B**). When two arms (**Figure 8C**) or only one arm (**Figure 8D**) remained, arms were often anchored to the ground, and then they pushed themselves against the anchored points to move effectively, like real brittle stars (**Figures 2C,D**). Finally, the simulated brittle star with one flexible arm moved on terrain with pegs. Then, the arm pushed against pegs and moved effectively when it received reaction forces that assisted propulsion, while objects were avoided if it received reaction forces that hinder propulsion (**Figure 8E**); this agrees with the behavioral findings (**Figure 2E**).

In the above-mentioned behaviors, inter- and intra-arm coordination was appropriately used to adapt to various circumstances. When the five arms were shortened (**Figure 8B**), the simulated brittle star moved through the coordination of different arms (i.e., inter-arm coordination). Meanwhile, when one arm (**Figure 8D**) remained, the simulated brittle star moved through the coordination of different parts within the arm

TABLE 1 | Parameter values employed in the simulation experiments.

Variable	Dimension	Figure 8A	Figures 8B–E
α		0.8	0.8
β		0.6	0.6
m_{body}	[kg]	1.9×10^{-3}	1.9×10^{-3}
m_{arm}	[kg]	1.3×10^{-3}	1.3×10^{-3}
k_y	[kgm^{2}s^{-2}]	6.9	6.9
k_p	[kgm^{2}s^{-2}]	5.4×10^{1}	5.4×10^{1}
c_y	[kgm^{2}s^{-1}]	3.2×10^{-3}	3.2×10^{-3}
c_p	[kgm^{2}s^{-1}]	3.2×10^{-3}	3.2×10^{-3}
σ^p	[deg]	1.6×10^{-1}	1.6×10^{-1}
σ^y	[deg]	0.8	1.2
n_d		2	2
n_p		4	4
γ	[kg^{-2}m^{-2}s^4]	4.3×10^{11}	4.3×10^{11}
τ	[s]	0.4	0.4

(i.e., intra-arm coordination). In other cases (**Figures 8A,C,E**), both inter- and intra-arm coordination were used. In summary, the simulated brittle star adapted to various circumstances by coupling the inter- and intra-arm coordination and qualitatively reproducing the locomotion of real brittle stars.

As additional data, we present the result when σ_y is 1.2, which is equal to the σ_y value in **Figures 8B–E** (**Table 1**), in the case of five flexible limbs (**Figure 9**). The arms are observed to be more vigorous than in the case of real brittle stars. This suggests that there was an excess amount of feedback, although the parameter is suitable for the other cases (**Figures 8B–E**).

5. ROBOT

In this section, we present an experimental brittle star-like robot (PENTABOT III) and the results.

5.1. Hardware

The overview of the robot is shown in **Figure 10A**. The robot consists of a central disc with five arms. The diameter of the central disc, the arm length, and the total weight was 0.22 m, 0.35 m, and 3.2 kg, respectively. Four yaw and three

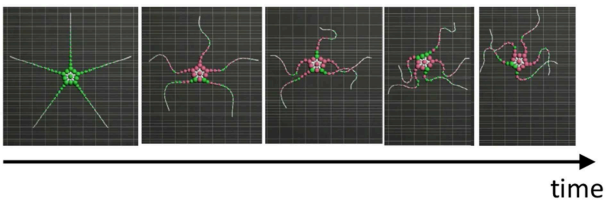

FIGURE 9 | Snapshots of the simulated brittle star in the case where the arms are intact and the body is on a flat terrain with $\sigma_y = 1.2$.

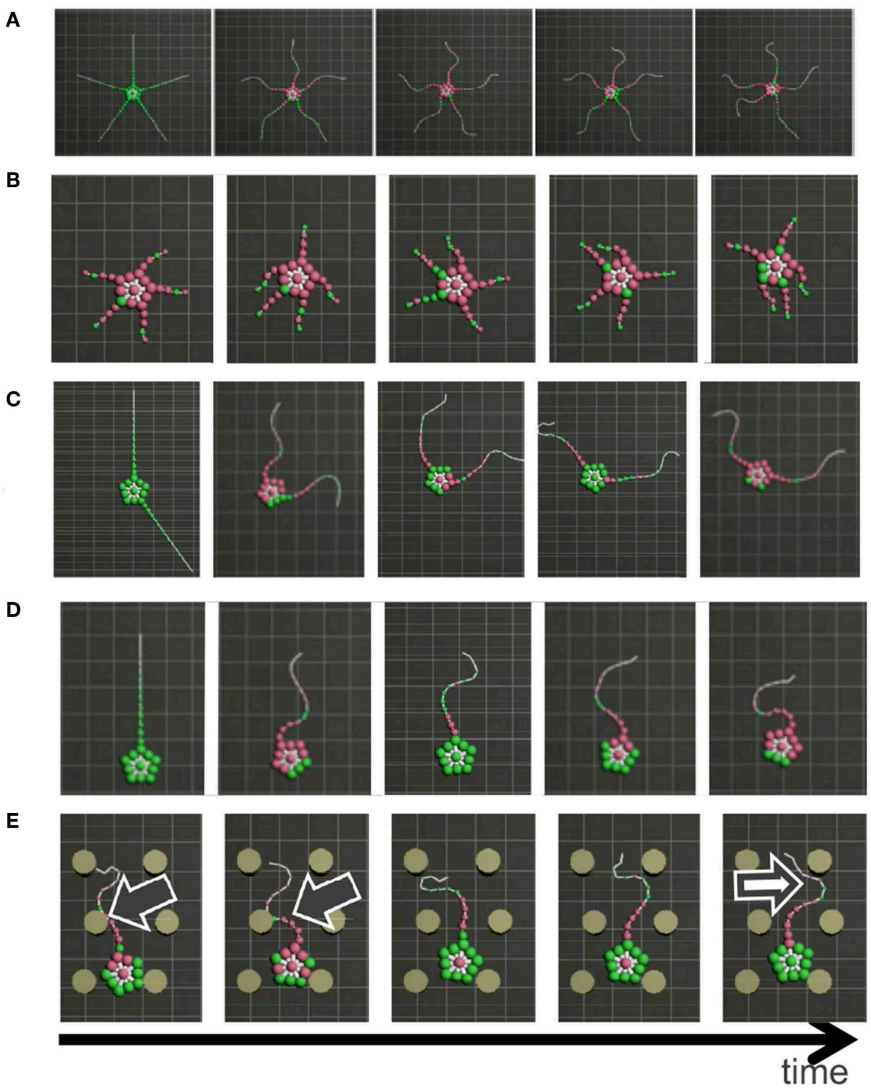

FIGURE 8 | Snapshots of the simulated brittle star: **(A)** an intact brittle star on a flat terrain, **(B)** a brittle star with five shortened arms on a flat terrain, **(C)** a brittle star with two arms on a flat terrain, **(D)** a brittle star with one arm on a flat terrain, and **(E)** a brittle star with one arm on a flat terrain with several circular objects. Black and white arrows denote points where the arms exploit and avoid objects, respectively. Mass points on and off the ground are colored by green and purple, respectively.

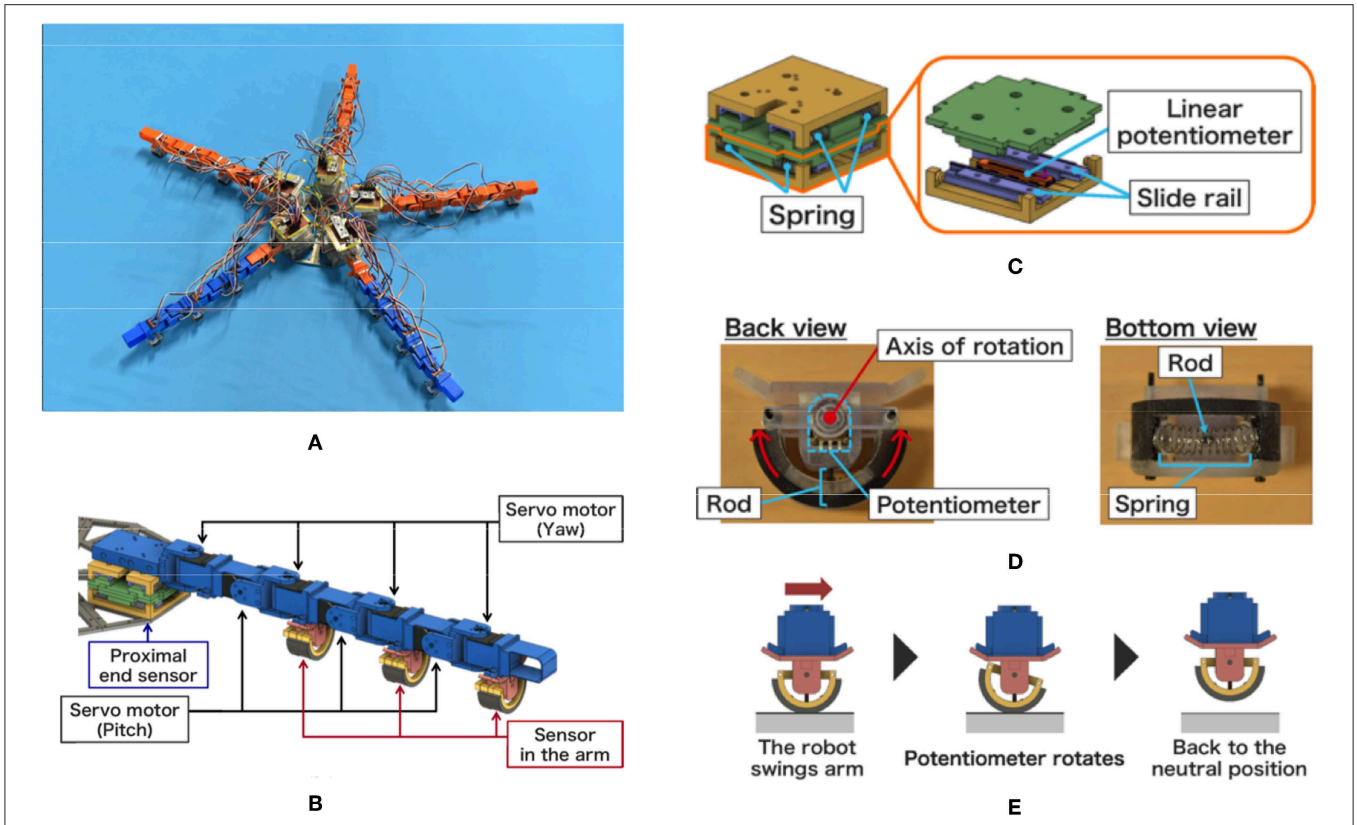

FIGURE 10 | Brittle star-like robot developed. **(A)** Overview of the robot. **(B)** CAD image for the arrangement of servo motors and sensors within an arm. **(C)** Proximal end sensor. **(D)** Back view and bottom view of the sensor. **(E)** Sensing mechanism.

pitch joints were embedded alternatively in each arm, and they were driven by servo motors (Futaba Co., RS-303MR) (**Figure 10B**). The position control, instead of the torque control, was adopted for controlling the motor; thus, the target angles $\bar{\theta}^{y}_{i,j}$ and $\bar{\theta}^{p}_{i,j}$ were determined according to Equations (5) and (6), and we did not use Equations (3) and (4), which are used to determine the joint torques. While the mass and the gain of the actuation torque of the distal segments were smaller than those of the proximal segments in the simulation model, they were identical in the developed robot. In each arm, a microcomputer (STMicroelectronics : NUCLEO-L432KC) and a control circuit board was embedded to determine the moving direction, to detect sensor values, and to determine the target angles of the motors.

Figure 10C shows the sensor mechanism for detecting internal forces at the proximal ends of the arms. Two combinations of slide rails, springs, and a linear potentiometer (Alps Alpine Co. Ltd., RDC10320RB) were layered perpendicularly. Because it was difficult to measure the internal force directly, we simply assumed that the components of the internal force vector were proportional to the displacement of the two linear potentiometers. Thus, the sensor values of the two linear potentiometers were directly used as the components of the vector $\mathbf{F}_i$.

Figures 10D,E show the sensor mechanism detecting external forces from the environment. This mechanism consists of a semicircular rod, a potentiometer (Alps Alpine Co. Ltd., RDC506002A), and a spring. It was implemented at the bottom of servo motors that drive the yaw joints (**Figure 10D**). **Figure 10E** shows how this mechanism works. The semicircular structure at the bottom rotates when it receives external forces (e.g., frictional forces) from the right or left, and its rotational angle is measured by the potentiometer. When the arm lifts off the ground, the displacement of the potentiometer decreases due to the spring. Because it was difficult to directly measure the external force, we assumed that the external force vector was proportional to the displacement of the potentiometer for the sake of convenience. Thus, the sensor value of the linear potentiometer was directly used as the value of the external force $f^{R/L}_{i,j}$.

5.2. Experimental Results

We performed experiments using the experimental robot. **Table 2** shows the parameter values, which were individually adjusted by trial-and-error for each body configuration shown in **Figures 2A–D**. The frictional property of the floor was also chosen by trial-and-error so that the robot successfully moves.

The result is shown in **Figure 11** (**Supplementary Movie**). When all segments are present (**Figure 11A**), the arms pushed themselves against the ground to move effectively, which is qualitatively similar to real brittle stars (**Figure 11A**). When all arms were shortened (**Figure 11B**), the robot moved in a manner similar to a "breaststroke" pattern of real brittle stars (**Figure 2B**).

When two arms remained (**Figure 11C**), the arms were often anchored to the ground, and then they pushed themselves against the anchored points to move effectively, like with real brittle stars (**Figure 2C**). When only one arm remained (**Figure 11D**), the robot moved in a qualitatively similar manner as real brittle stars (**Figure 2D**) although the central disc did not anchor well to the ground and was often pushed backward during arm extension. Thus, although there existed a slight discrepancy between the robot and real brittle stars, the behavioral findings were qualitatively reproduced.

TABLE 2 | Parameter values used for the experimental robot.

Variable	Dimension	Figure 11A	Figure 11B	Figure 11C	Figure 11D
σ^y	[deg]	45.0	55.0	45.0	45.0
σ^p	[deg]	25.0	25.0	25.0	25.0
n_d		3	3	3	3
n_p		3	3	3	3
γ		1.0×10^3	1.0×10^3	1.0×10^3	1.0×10^3
τ	[s]	6.0×10^{-2}	6.0×10^{-2}	6.0×10^{-2}	0.15

6. CONCLUSION AND FUTURE WORK

We focused on the locomotion of brittle stars that move by coordinating their five flexible arms. Based on behavioral findings of brittle stars with various morphologies in various environments, we proposed a simple decentralized control model that incorporates both inter- and intra-arm coordination mechanisms. We demonstrated, via simulations, that the proposed model reproduces the behavioral findings qualitatively. Moreover, we developed a brittle star-like robot and performed real-world experiments; the robot moved in a qualitatively similar manner as the real brittle stars.

Previous studies that used learning or trial-and-error techniques (Bongard et al., 2006; Mahdavi and Bentley, 2006; Mostafa et al., 2010; Koos et al., 2013; Christensen et al., 2014;

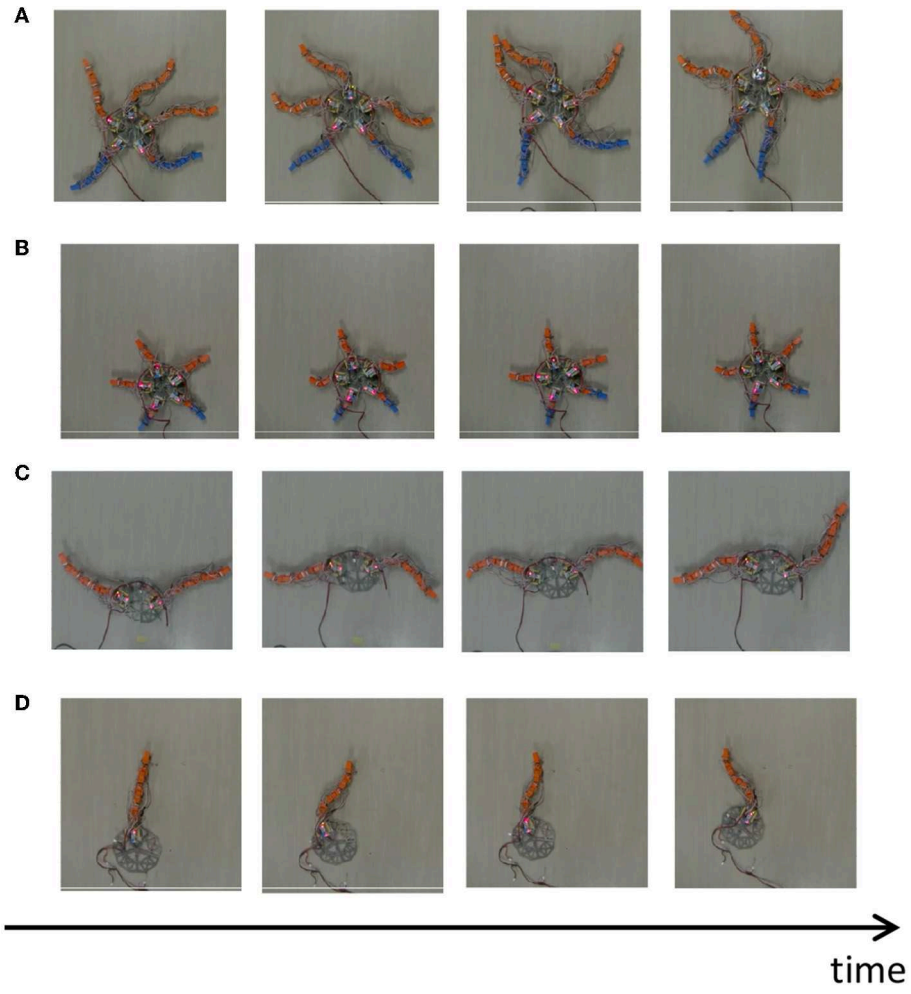

FIGURE 11 | Snapshots of the brittle star-like robot **(A)** with five flexible arms, **(B)** with five shortened arms, **(C)** with two flexible arms, and **(D)** with one flexible arm. All experiments were performed on a flat terrain.

Ren et al., 2014; Cully et al., 2015; Rubio et al., 2018, 2019; Yen et al., 2018) required a considerable amount of time (more than several tens of seconds) to respond to unexpected physical damage. Meanwhile, we have recently developed a brittle star-like robot that can immediately adapt to unexpected physical damage (Kano et al., 2017), yet the number of degrees of freedom within the body was still small. In contrast, this study succeeded in considerably increasing the number of bodily degrees of freedom since our previous work (Kano et al., 2017), thereby paving the way to developing robots that can coordinate a large number of bodily degrees of freedom adapting to unpredictable circumstances in real-time.

This study is also significant from a scientific viewpoint because we succeeded in capturing the essence of the inter- and intra-arm coordination mechanism in brittle stars. Moreover, we believe that our finding imparts novel insights into the essential mechanism of animals' adaptive locomotion from a general perspective. In fact, the proposed mechanism has things in common with other animals. For example, in insect locomotion, local positive feedback mechanism works depending on whether the leg supports locomotion or not (Schmitz et al., 2008), which is similar to the control mechanism proposed in this study.

However, there are limitations in this study. First, we had to fine-tune parameters for each body configuration as well as to carefully choose frictional property of the floor. Second, the robot did not move as effectively as real brittle stars. In particular, the locomotion of the robot with only one arm was extremely slow. Third, we could not reproduce locomotion on a terrain with several objects (**Figure 2E**) with the robot. These limitations originate from mechanical and control issues. Concerning mechanical aspects, the reaction force was not properly measured by the current sensor system used. Additionally, the mass distribution of the robot and the friction between the body and the ground were not optimal. Regarding control, the proposed control scheme is not able to fully mimic the brittle stars' locomotion owing to its simplicity, even though it likely captures the essence of the locomotion. More complex control schemes may improve performance. Solving these issues remain as future work.

Another future direction of this work is the realization of a fully autonomous brittle star-like robot. For this, from the viewpoint of mechanics, the robot must contain batteries. From the viewpoint of control, the moving direction needs to be automatically determined. In our previous works, we performed behavioral experiments wherein the nerve ring was partially damaged (Clark et al., 2019), and based on this, we proposed a mathematical model for the nerve ring and succeeded in determining the moving direction in a self-organized manner (Kano et al., 2019). We believe that the control scheme for the fully autonomous brittle star-like robot can be developed by combining the model proposed in this paper with that for the nerve ring (Kano et al., 2019).

DATA AVAILABILITY STATEMENT

The raw data supporting the conclusions of this manuscript will be made available by the authors, without undue reservation, to any qualified researcher.

AUTHOR CONTRIBUTIONS

TK and AI contributed the initial conception. TK, TO, HA, and AI proposed the mathematical model. TO performed simulations. DK developed the robot and performed experiments. TK wrote the manuscript. DK, TO, HA, and AI contributed to manuscript revision.

FUNDING

This work was supported by the Japan Science and Technology Agency CREST (No. JPMJCR14D5), the Grant-in-Aid for Scientific Research (B) (No. 16KT0099) from the Ministry of Education, Culture, Sports, Science and Technology (MEXT), Japan, and the Cooperative Research Program of Network Joint Research Center for Materials and Devices.

ACKNOWLEDGMENTS

The authors would like to thank Professor Ryo Kobayashi of Hiroshima University, Dr. Elizabeth Clark of Yale University, Dr. Akira Fukuhara, Kotaro Yasui, Shura Suzuki, Taishi Mikami of Tohoku University for their helpful suggestions. The authors would like to thank Dr. Masahiro Shimizu of Osaka University for providing part of the source code.

SUPPLEMENTARY MATERIAL

The Supplementary Material for this article can be found online at: https://www.frontiersin.org/articles/10.3389/fnbot.2019.00104/full#supplementary-material

Supplementary video which summarizes the research. Micro CT images were reproduced from the supplementary video Kano et al. (2017).

Data Sheet 1 | Simulation source code. It is written in C++. "Monitor.cpp" and "Monitor.hpp" were mainly written by Dr. Masahiro Shimizu of Osaka University.

REFERENCES

Antonelli, G., Fossen, T., and Yoerger, D. (2008). *Springer Handbook of Robotics*. Berlin; Heidelberg: Springer.

Arshavskii, Y., Kashin, S., Litvinova, N., Orlovskii, G., and Fel'dman, A. (1976a). Coordination of arm movement during locomotion in ophiurans. *Neurophysiology* 8, 404–410.

Arshavskii, Y., Kashin, S., Litvinova, N., Orlovskii, G., and Fel'dman, A. (1976b). Types of locomotion in ophiurans. *Neurophysiology* 8, 398–404.

Astley, H. (2012). Getting around when you're round: quantitative analysis of the locomotion of the blunt-spined brittle star, *ophiocoma echinata*. *J. Exp. Biol.* 215, 1923–1929. doi: 10.1242/jeb.068460

Bongard, J., Zykov, V., and Lipson, H. (2006). Resilient machines through continuous self-modeling. *Science* 314, 1118–1121. doi: 10.1126/science.1133687

Carnevali, M. (2006). Regeneration in echinoderms: Eepair, regrowth, cloning. *Inverteb. Surviv. J.* 3, 64–76.

Christensen, D., Larsen, J., and Stoy, K. (2014). Fault-tolerant gait learning and morphology optimization of a polymorphic walking robot. *Evolv. Sys.* 5, 21–32. doi: 10.1007/s12530-013-9088-3

Clark, E. G., Kanauchi, D., Kano, T., Aonuma, H., Briggs, D. E. G., and Ishiguro, A. (2019). The function of the ophiuroid nerve ring: how a decentralized nervous system controls coordinated locomotion. *J. Exp. Biol.* 222:jeb192104. doi: 10.1242/jeb.192104

Cobb, J., and Stubbs, T. (1981). The giant neurone system in ophiuroids i. the general morphology of the radial nerve cords and circumoral nerve ring. *Cell Tissue Res.* 219, 197–207.

Cully, A., Clune, J., Tarapore, D., and Mouret, J. (2015). Robots that can adapt like animals. *Nature* 521, 503–507. doi: 10.1038/nature14422

Glaser, O. (1907). Movement and problem solving in ¥ it Ophiura brevispina. *J. Exp. Zoo.* 4, 203–220.

Ijspeert, A. (2014). Biorobotics: using robots to emulate and investigate agile locomotion. *Science* 346, 196–203. doi: 10.1126/science.1254486

Kano, T., Kanauchi, D., Aonuma, H., Clark, E. G., and Ishiguro, A. (2019). Decentralized control mechanism for determination of moving direction in brittle stars with penta-radially symmetric body. *Front. Neurorobot.* 13:66. doi: 10.3389/fnbot.2019.00066

Kano, T., Sato, E., Ono, T., Aonuma, H., Matsuzaka, Y., and Ishiguro, A. (2017). A brittle star-like robot capable of immediately adapting to unexpected physical damage. *Roy. Soc. Open Sci.* 4:171200. doi: 10.1098/rsos.171200

Kano, T., Suzuki, S., Watanabe, W., and Ishiguro, A. (2012). Ophiuroid robot that self-organizes periodic and non-periodic arm movements. *Bioinspir. Biomimet.* 7:034001. doi: 10.1088/1748-3182/7/3/034001

Koos, S., Cully, A., and Mouret, J. (2013). Fast damage recovery in robotics with the t- resilience algorithm. *Int. J. Robot. Res.* 32, 1700–1723. doi: 10.1177/0278364913499192

Mahdavi, S., and Bentley, P. (2006). Innately adaptive robotics through embodied evolution. *Auto. Robots* 20, 149–163. doi: 10.1007/s10514-006-5941-6

Matsuzaka, Y., Sato, E., Kano, T., Aonuma, H., and Ishiguro, A. (2017). Non-centralized and functionally localized nervous system of ophiuroids: evidence from topical anesthetic experiments. *Biol. Open* 6, 425–438. doi: 10.1242/bio.019836

Mostafa, K., Tsai, C., and Her, I. (2010). Alternative gaits for multiped robots with leg failures to retain maneuverability. *Int. J. Adv. Robot. Sys.* 7, 31–38. doi: 10.5772/10487

Murphy, R. (2004). Trial by fire. *Robot. Automat. Mag.* 11, 50–61. doi: 10.1109/MRA.2004.1337826

Nagatani, K., Kiribayashi, S., Okada, Y., Otake, K., Yoshida, K., Tadokoro, S., et al. (2013). Emergency response to the nuclear accident at the fukushima daiichi nuclear power plants using mobile rescue robots. *J. Field Robot.* 30, 44–63. doi: 10.1002/rob.21439

Patané, L. (2019). Bio-inspired robotic solutions for landslide monitoring. *Energies* 12:1256. doi: 10.3390/en12071256

Ren, G., Chen, W., Dasgupta, S., Kolodziejski, C., Wörgötter, F., and Manoonpong, P. (2014). Multiple chaotic central pattern generators with learning for legged locomotion and malfunction compensation. *Info. Sci.* 294, 666–682. doi: 10.1016/j.ins.2014.05.001

Rubio, J. J. (2016). Structure control for the disturbance rejection in two electromechanical processes. *J. Franklin Inst.* 353, 3610–3631. doi: 10.1016/j.jfranklin.2016.07.001

Rubio, J. J. (2018). Robust feedback linearization for nonlinear processes control. *ISA Transact.* 74, 155–164. doi: 10.1016/j.isatra.2018.01.017

Rubio, J. J., García, E., Aquino, G., Aguilar-Ibánez, C., Pacheco, J., and Meda-Campana, J. A. (2019). Recursive least squares for a manipulator which learns by demonstration (mínimos cuadrados recursivos para un manipulator que aprende por demostración). *Revista Iberoamericana de Automática e Informática Industrial* 16, 147–158. doi: 10.4995/riai.2019.8899

Rubio, J. J., Garcia, E., Aquino, G., Aguilar-Ibanez, C., Pacheco, J., and Zacarias, A. (2018). Learning of operator hand movements via least angle regression to be teached in a manipulator. *Evol. Syst.* doi: 10.1007/s12530-018-9224-1

Sanderson, K. (2010). Mars rover spirit (2003–10). *Nature* 463:600. doi: 10.1038/463600a

Schilling, M., Hoinville, T., Schmitz, J., and Cruse, H. (2013). Walknet, a bio-inspired controller for hexapod walking. *Biol. Cybern.* 107, 397–419. doi: 10.1007/s00422-013-0563-5

Schmitz, J., Schneider, A., Schilling, M., and Cruse, H. (2008). No need for a body model: positive velocity feedback for the control of an 18-dof robot walker. *Appl. Bion. Biomechatr.* 5, 135–147. doi: 10.1080/11762320802221074

Skold, M., and Rosenberg, R. (1996). Arm regeneration frequency in eight species of ophiuroidea (echinodermata) from european sea areas. *J. Sea Res.* 35, 353–362.

Sun, Y., Qiang, H., Mei, X., and Teng, Y. (2018). Modified repetitive learning control with unidirectional control input for uncertain nonlinear systems. *Neural Comput. Appl.* 30, 2003–2012. doi: 10.1007/s00521-017-2983-y

Takamatsu, A., Tanaka, R., Yamada, H., Nakagaki, T., Fujii, T., and Endo, I. (2001). Spatio-temporal symmetry in rings of coupled biological oscillators of physarum plasmodium. *Phys. Rev. Lett.* 87:078102. doi: 10.1103/PhysRevLett.87.078102

Watanabe, W., Kano, T., Suzuki, S., and Ishiguro, A. (2012). A decentralized control scheme for orchestrating versatile arm movements in ophiuroid omnidirectional locomotion. *J. Roy. Soc. Interface* 7, 102–109. doi: 10.1098/rsif.2011.0317

Wilkie, I. (1978). Functional morphology of the autotomy plane of the brittlestar ¥ it Ophiocomina Nigra (abildgaard) (ophiuroidea, echinodermata). *Zoomorphologie* 91, 289–305.

Yen, V. T., Nan, W. Y., and Cuong, P. V. (2018). Recurrent fuzzy wavelet neural networks based on robust adaptive sliding mode control for industrial robot manipulators. *Neural Comput. Appl.* 31, 6945–6958. doi: 10.1007/s00521-018-3520-3

Conflict of Interest: The authors declare that the research was conducted in the absence of any commercial or financial relationships that could be construed as a potential conflict of interest.

frontiers in Neurorobotics

ORIGINAL RESEARCH
published: 19 December 2019
doi: 10.3389/fnbot.2019.00106

Toward a Gecko-Inspired, Climbing Soft Robot

Lars Schiller, Arthur Seibel and Josef Schlattmann*

Workgroup on System Technologies and Engineering Design Methodology, Hamburg University of Technology, Hamburg, Germany

In this paper, we present a gecko-inspired soft robot that is able to climb inclined, flat surfaces. By changing the design of the previous version, the energy consumption of the robot could be reduced, and at the same time, its ability to climb and its speed of movement could be increased. As a result, the new prototype consumes only about a third of the energy of the previous version and manages to climb slopes of up to 84°. In the horizontal plane, its velocity could be increased from 2 to 6 cm/s. We also provide a detailed analysis of the robot's straight gait.

Keywords: mobile soft robots, fast pneu-nets, apriltags, gecko-inspired robot, climbing robot

1. INTRODUCTION

In the last decade, soft robotics has become an established field in the robotics sciences, and is still growing rapidly. This discipline utilizes the properties of soft materials and structures for developing new types of machines showing a compliance similar to that of living organisms (Majidi, 2014). Examples of biological models include worms, caterpillars, and cephalopods (Kim et al., 2013).

Typically, soft robots are designed either for locomotion or for grasping and manipulation (Rus and Tolley, 2015). In the context of locomotion, typical principles are crawling, walking, running, jumping, flying, and swimming (Calisti et al., 2017). The zoo of soft robots includes representatives of all these principles. Climbing—a combination of locomotion and adhesion (Chu et al., 2010)—, however, is largely unexplored, besides a few exceptions (Gu et al., 2018; Tang et al., 2018; Qin et al., 2019). A great advantage of flexible machines is that they can hardly endanger themselves or their environment due to their softness. This raises the question why there are no universal, climbing soft robots, as they can easily survive a fall—Universal in the sense that they can move in any direction. In Seibel and Schiller (2018), we therefore introduced a soft robot that is specifically designed for climbing. **Figure 1A** shows a slightly modified version of the robot presented therein. Its design is based on the use of fast pneu-net bending actuators (Mosadegh et al., 2014) as the primary element and its locomotion is inspired by the gecko (Autumn et al., 2006). The attachment of the soft robot to the ground during gait is realized by suction cups as feet. The robot presented therein is able to climb surfaces up to 50° inclination.

However, the robot is linked to an external pressure source by supply tubes. In order to enable autonomous movements, it would have to carry its pressure source with it. Therefore, its movements should be as energy efficient as possible so that a potentially more lightweight pressure source can be used. In this paper, we investigate how the energy consumption of the robot can be reduced by constructive measures. This is an important step in the direction of mobile, untethered soft robotics.

OPEN ACCESS

Edited by:
Poramate Manoonpong, University of Southern Denmark, Denmark

Reviewed by:
Tin Lun Lam, The Chinese University of Hong Kong, China
Luca Patané, University of Catania, Italy

****Correspondence:***
Lars Schiller
lars.schiller@tuhh.de

Received: *08 April 2019*
Accepted: *03 December 2019*
Published: *19 December 2019*

Citation:
Schiller L, Seibel A and Schlattmann J (2019) Toward a Gecko-Inspired, Climbing Soft Robot. Front. Neurorobot. 13:106. doi: 10.3389/fnbot.2019.00106

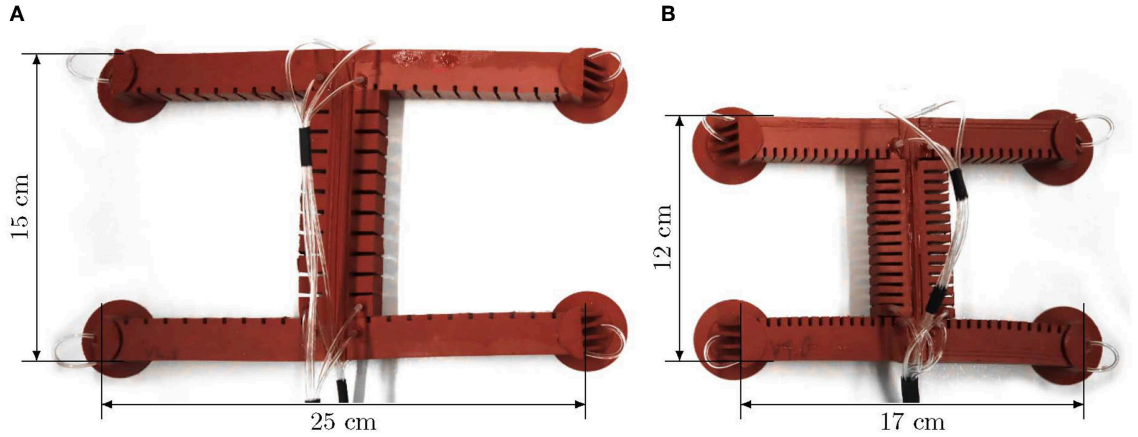

FIGURE 1 | Current prototypes of the gecko-inspired soft robot. **(A)** Large prototype, **(B)** small prototype.

2. NEW PROTOTYPE OF THE ROBOT

The new prototype of our gecko-inspired soft robot is designed in terms of a reduction of its pneumatic energy consumption. This is mainly achieved by downscaling the previous version. Therefore, the new prototype is denoted as small version and the previous one as large version. In the following, the robot's redesign process is described in detail.

2.1. Energy Consumption

The energy consumption of a pneumatic system is strongly related to its air demand, which can be calculated by multiplying the volume of the pneumatic system by the applied pressure. For a qualitative comparison, the energy consumption is considered equal to the air demand, as the used control unit is identical for both prototypes, and therefore, other factors affect both versions in the same fashion. In order to obtain a meaningful value for the energy consumption E of the robot, the air demand is set in relation to the shift in position:

$$\frac{E}{\Delta x} = \frac{n_{\text{cyc}} \sum_i^N p_i V_i n_i}{x_{\text{end}} - x_{\text{start}}} . \tag{1}$$

Here, p_i describes the applied pressure in the ith actuator (from a total of N actuators) with the volume V_i, and n_i is the number of actuations of this actuator within a gait cycle. Furthermore, n_{cyc} describes the number of cycles necessary to move from the start position x_{start} to the end position x_{end}. With a constant distance Δx traveled, there are three ways to reduce the energy consumption:

- Maximize the shift in position per cycle and thus minimize the required number of cycles n_{cyc},
- Reduce the required pressures p_i for the actuators while keeping the shift in position per cycle constant.
- Reduce the inner volumes V_i of the actuators.

The shift in position per cycle can be approximately estimated with one body length, as we will see in **Figure 6** and Equation (5). In order to increase the shift in position, all six actuators of the robot have to be increased in size, which only has an effect by a factor of one on the shift in position, but by a factor of six on the air demand. Therefore, it is more promising to reduce the volume and the required pressure than to increase the shift in position per cycle.

2.2. Design Parameters and Realization of the Small Prototype

The most effective way to reduce the internal volume of a fast pneu-net actuator is to increase the number of chambers. This not only reduces the inner volume, but also increases the self-reinforcing effect of the actuator and thus also reduces the required pressure, as experimentally studied in Mosadegh et al. (2014) (and approved by own experiments documented in the **Supplementary Data**). From simulations in Polygerinos et al. (2013), it is also known that thinner walls lead to less required pressure and increased force output. Additionally, increasing the chamber height increases the force output. From these findings, it can be concluded that an actuator with many chambers, thin inner walls, and a big chamber height is desirable for best performance.

The design of the large prototype is based on the actuator dimensions from the Soft Robotics Toolkit (Website, 2019). In order to reduce the volume of the actuator, only the overall length ℓ_{act} and the number of chambers n_{ch} should be adjusted so that the fittings to the suction cups are not changed. The width w_{ch} and height h_{ch} of the chambers should therefore remain constant. The manufacturing process (3D printed molds, manual injection molding with Elastosil) makes it difficult to achieve wall thicknesses of less than 1 mm. Therefore, the inner wall thickness $t_{\text{w,i}}$ is not varied either. The total length chosen is $\ell_{\text{act}} = 76.5$ mm. Own experiments have shown that a leg of this length has an advantageous stiffness to be integrated into the robot. As many chambers as possible are arranged on this length, which is $n_{\text{ch}} = 15$. The limiting factor here is the fragility of the 3D-printed molds. The inner volume V of an actuator can now be calculated

TABLE 1 | Design parameters of the large and the small prototype of the gecko-inspired soft robot.

Design parameters		Large prototype	Small prototype	
Number of chambers	n_{ch}	11	15	1
Actuator length	ℓ_{act}	112	76.5	mm
Bottom layer height	h_{bot}	5	5	mm
Outer wall thickness	$t_{w,o}$	2	2	mm
Inner wall thickness	$t_{w,i}$	1	1	mm
Chamber height	h_{ch}	15	15	mm
Chamber width	w_{ch}	11	11	mm
Chamber length	l_{ch}	6	1.43	mm
Air channel height	h_{air}	2	2	mm
Air channel width	w_{air}	2	2	mm
Air channel length	l_{air}	4	4	mm
Inner volume	V	0.01105	0.0038	m^3

using the following equation:

$$V = n_{ch}(h_{ch} \cdot w_{ch} \cdot \ell_{ch}) + (n_{ch} - 1)(h_{air} \cdot w_{air} \cdot \ell_{air}), \quad (2)$$

where h_{air}, w_{air}, and ℓ_{air} describe the height, width, and length of the air channel, respectively. It should be noted that this equation only describes the inner volume of an actuator at rest. If the actuator is actuated, the volume increases. However, for a qualitative comparison between the two versions, this approximation should be sufficient. **Table 1** shows all necessary parameters for the design of both the large and the small version.

The design of the small prototype is basically the same as described in Seibel and Schiller (2018). In addition to the size variation, two more details have changed. The supply tubes for the front feet and legs no longer lie in the torso's middle layer, but outside the robot. This allows the middle layer of the torso to be designed with minimal thickness, and the torso is more flexible overall, requiring less pressure to deform it. In addition, there is a dovetail at the ends of the legs and a groove at the ends of the torso to make the process of joining the torso and legs more precise and easier. **Figure 2** shows an exploded view of the small prototype. All parts of the robot have to be manufactured individually and joined afterwards. A photograph of the small prototype is shown in **Figure 1B**. In order to be able to make a meaningful comparison between the two versions, the large prototype of the robot was also manufactured with external supply tubes and dovetail joints (see **Figure 1A**).

3. EXPERIMENTS

The robot consists of fast pneu-net bending actuators that take pressure as input. In most cases, however, the robot should take on a certain pose, that is, its limbs should have particular bending angles. For this reason, the angular input must be converted into pressure references. **Figure 3** illustrates the control scheme for a single actuator. In A, the block diagram is shown. The angular reference r_α is converted into a reference pressure r_p by a mapping function $p(\alpha)$, depicted in B, which must be determined by an experiment. In comparison with the actual pressure, the PID controller C is fed, which in return generates the control signal u for the proportional directional valve G_1. The pressure p is measured by a digital pressure sensor at the valve outlet. In the quasi-static case, this is the pressure inside the actuator G_2, whose output is the bending angle α. A system of six of these channels connected in parallel to a compressor is required to operate all limbs of the robot. Control of the suction cups is realized by direct acting solenoid valves that are connected in parallel to a vacuum pump. All components required for control are combined in a compact, universal control board. In order to measure the bending angles of the robot, a camera is mounted above the walking plane (acrylic glass plate with an adjustable slope), as shown in **Figure 4A**. Apriltags (Wang and Olson, 2016) are attached to the feet and the torso ends of the robot (see **Figure 4B**). The position and orientation of the individual tags (and thus the position and orientation of the robot limbs) can now be detected in the camera images. In this way, the bending angles of the individual limbs can be calculated as follows:

$$\hat{\alpha}(\boldsymbol{r}_1, \boldsymbol{r}_2) = \begin{cases} \varphi_1 = \text{atan2}(r_{y,1}, r_{x,1}) \\ \tilde{\boldsymbol{r}}_2 = \boldsymbol{R}(-\varphi_1)\boldsymbol{r}_2 \\ \hat{\alpha} = \text{atan2}(\tilde{r}_{y,2}, \tilde{r}_{x,2}) \end{cases}, \quad (3)$$

where $\boldsymbol{r}_1$ describes the apriltag's orientation of one and $\boldsymbol{r}_2$ of the other end of a limb. Furthermore, $\boldsymbol{R}$ is the two-dimensional rotation matrix. The orientation angle of the robot ε is defined as the angle between the x-axis and the vector from the rear to the front end of the torso:

$$\varepsilon = \hat{\alpha}(\boldsymbol{e}_x, \boldsymbol{p}_1 - \boldsymbol{p}_4). \quad (4)$$

Here, $\boldsymbol{e}_x$ describes the unit vector in x-direction, $\boldsymbol{p}_1$ the position of the front end, and $\boldsymbol{p}_4$ the position of the rear end of the torso. All of the following experiments were repeated at least five times. In the following graphs, solid curves represent the mean value and the standard deviation is represented by an area, unless stated otherwise. Note that the measured bending angles are only used for analysis. The locomotion of the robot itself is controlled only by the pressure and the corresponding mapping function. The control scheme is intentionally kept as simple as possible in order to have as few dependencies on measurement systems as necessary and thus be able to run outside laboratory conditions.

3.1. Determining the Transient Time

The diameter and length of the supply tubes as well as the control hardware and software are identical for both versions. However, since the inner volume of the actuators is different, the small version requires comparatively less air to be transported through the tubes. This requires correspondingly less time and reduces the robot's movement phase, and thus also the cycle time. **Figure 5** shows the step response for a reference pressure of $p_{ref} = 0.75$ bar of a small (green) and a large (purple) actuator. The bending angle of the small version reaches its equilibrium position after about one second, while the transient time of the large version lasts ∼3 s.

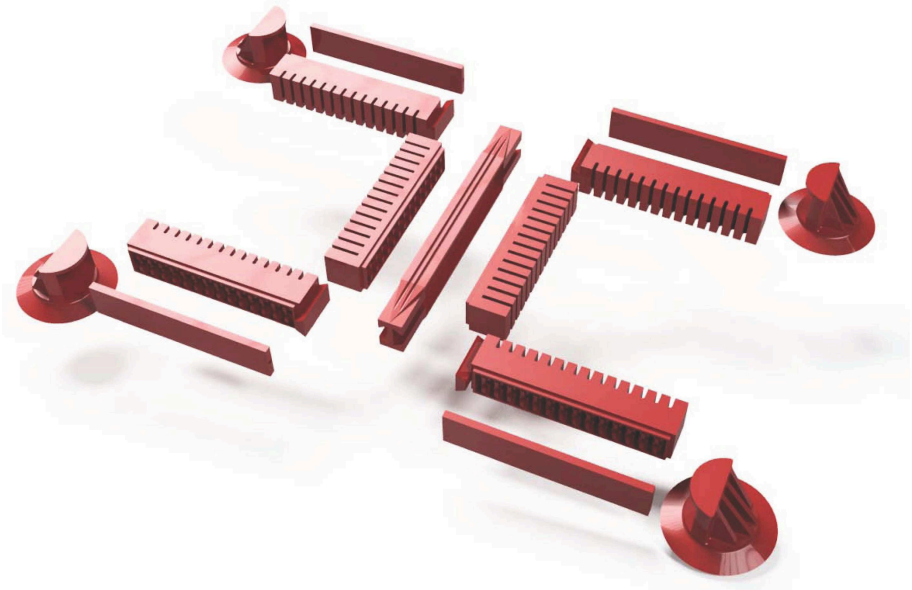

FIGURE 2 | Explosion view of the small prototype of the gecko-inspired soft robot.

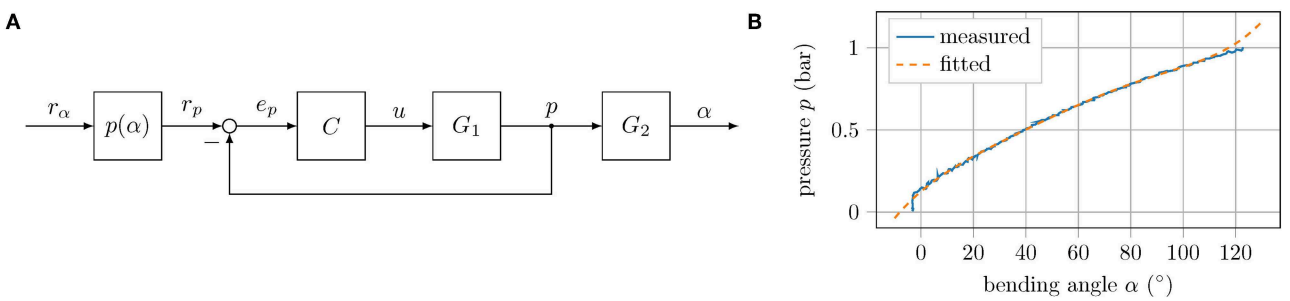

FIGURE 3 | Control scheme: **(A)** Block diagram of the control loop for a single actuator. The block $p(\alpha)$ maps angle to pressure coordinates, C is the implemented PID controller, G_1 describes the dynamics of the proportional valve, and G_2 represents the dynamics of the tube and actuator. **(B)** Measured and fitted relation between bending angle and applied pressure in the horizontal plane of the left front leg of the small version.

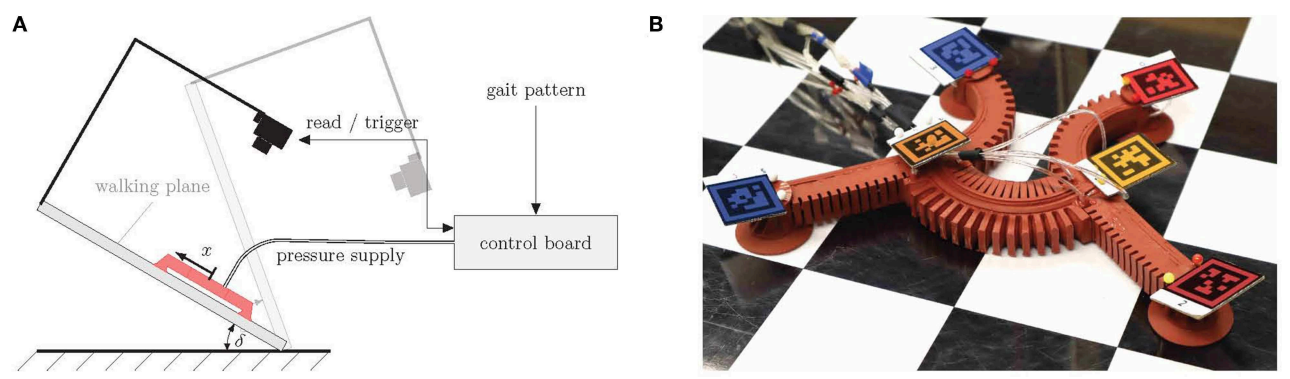

FIGURE 4 | Experimental setting. **(A)** Principal sketch, **(B)** apriltags attached to the robot's feet and torso's ends. The individual tags are indicated by different colors (red—front left, dark red—front right, orange—front center, dark orange—rear center, blue—rear left, dark blue—rear right).

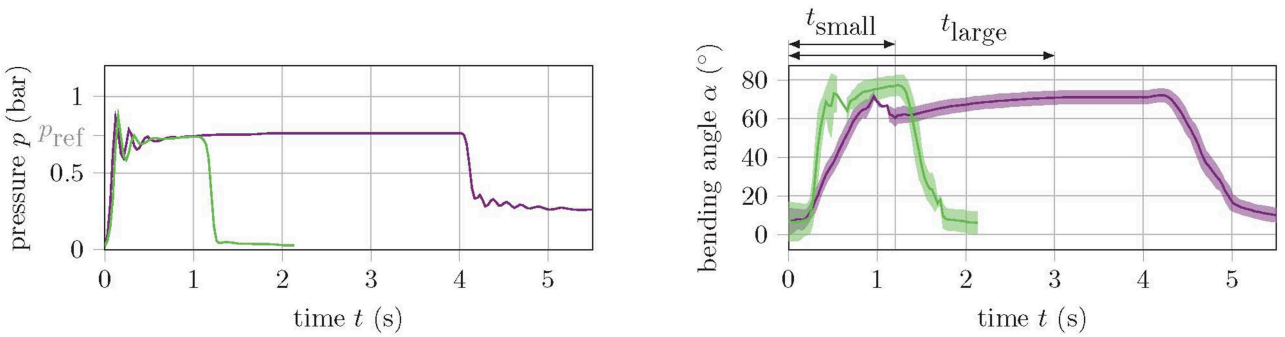

FIGURE 5 | Step response of a small (green) and a large (purple) soft actuator for a reference pressure of $p_{\text{ref}} = 0.75$ bar. The left graph shows the pressure and the right graph shows the angle response.

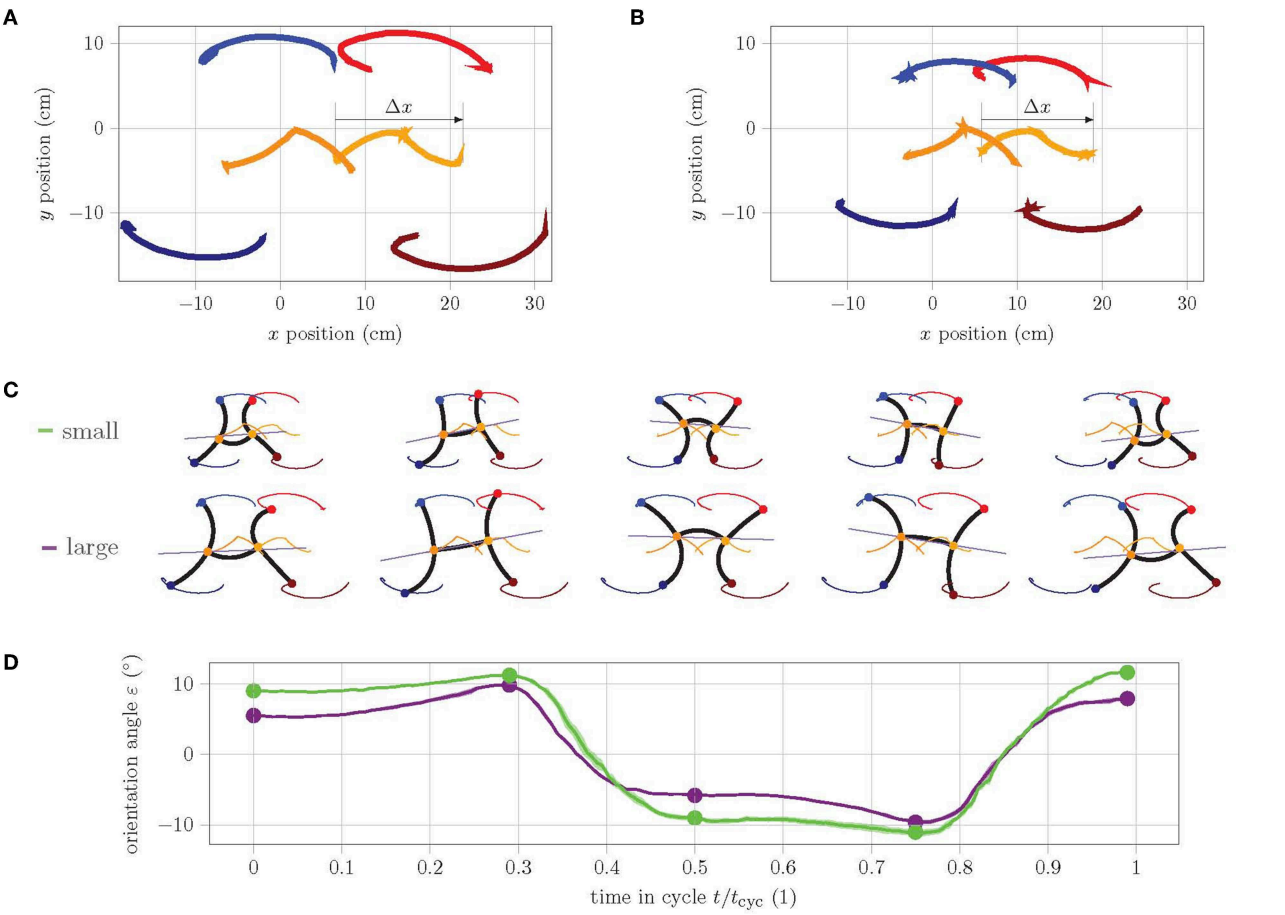

FIGURE 6 | Analysis of the track of feet during one cycle of straight gait in the horizontal plane. **(A)** Track of large prototype, **(B)** track of small prototype. **(C)** Single frames show the abstraction of pose at the extreme points as well as in the start, middle, and end position during cycle. **(D)** Graph of orientation angle ε during cycle of small (green) and large (purple) prototype.

3.2. Experiments on the Horizontal Plane

In a first experiment, the behavior of the two robot versions in the horizontal plane is analyzed. The aim of this experiment is to understand and compare the motion within a cycle. In order to obtain measurement data for the entire cycle, the gait pattern is slowed down since the camera images are smeared when the movements are too fast and the tags can no longer be detected. **Figure 6** shows the track of the tags placed on the

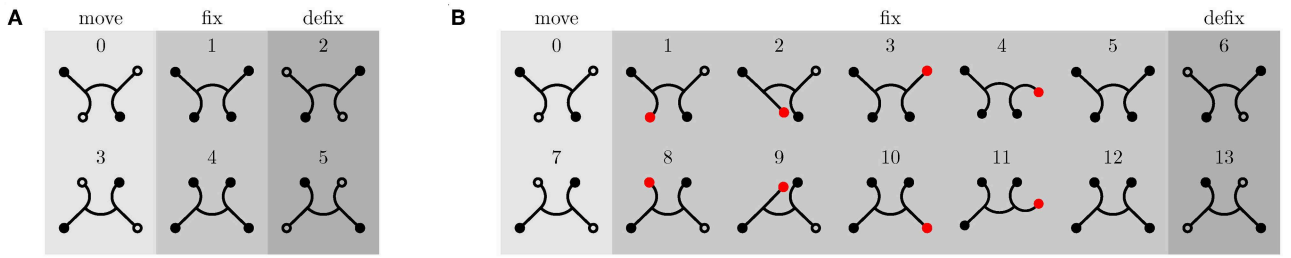

FIGURE 7 | Gait patterns for straight movement of the robot. Fixed feet are indicated by filled circles and unfixed feet by unfilled circles. **(A)** Gait pattern for inclination angles $\delta < 70°$. **(B)** Climbing pattern for high inclinations ($\delta \geq 70°$). Vacuum is applied to red and black filled feet. Black filled feet are fixed to the ground, whereas red feet do not necessarily have to be. In order to secure the fixation, the foot to be fixed is swinged back and forth once.

large (**Figure 6A**) and small (**Figure 6B**) prototype during a cycle. Apart from the dimensions, both robots have a very similar motion quality. However, the overlaps of the track of the torso ends (orange and dark orange) as well as the left feet (red and blue) are much larger in the small version. In fact, the small version has a much better ratio of shift in position within a cycle Δx to body length $\ell_{\text{bl}} = \ell_{\text{act}} + 2(h_{\text{ch}} + h_{\text{bot}} + t_{\text{w,o}})$:

$$\frac{\Delta x_{\text{small}}}{\ell_{\text{bl,small}}} \approx \frac{12.5}{12.05} = 1.04 > 0.96 = \frac{15}{15.6} \approx \frac{\Delta x_{\text{large}}}{\ell_{\text{bl,large}}} . \quad (5)$$

This is mainly due to the fact that the torso of the small version has a better bending performance, as can be seen in the single frames of start, middle, and end pose in **Figure 6C**. Furthermore, the y-symmetry of the track of the torso ends is notable. Apparently, the rear torso end in the second half of the cycle qualitatively performs the same movement as the front torso end in the first half. Similarly, the movement of the rear torso end in the first half of the cycle is complementary to the movement of the front end in the second half. This necessarily results in a change of the orientation angle ε within a cycle. **Figure 6D** shows the history of ε during one cycle of straight gait. It can clearly be seen that the change in orientation within a cycle for the small version is larger than for the large version. The linear model for straight gait from Seibel and Schiller (2018) predicts the maximum displacement of the fixed feet for the poses at 25% and 75% of cycle time (i.e., approximately at the points of maximum orientation). This reveals how the problem of the model is solved in reality: the robot changes its orientation. The larger change of the small version is explained by the fact that the ratio of body length to leg length $\lambda = \ell_{\text{bl}}/\ell_{\text{act}}$ is comparatively larger:

$$\lambda_{\text{small}} = 1.58 > 1.40 = \lambda_{\text{large}} . \quad (6)$$

For a larger ratio λ, the linear model predicts a larger displacement of the fixed feet. Since a displacement of the fixed feet is physically not possible, this theoretically larger displacement results in a larger change of orientation. This effect can be seen very well in the selected poses in **Figure 6C**.

3.3. Experiments on the Inclined Plane

The gait pattern for the robot's straight gait consists of a total of six phases, of which two are complementary. This results in three categorical phases: movement phase, fixation phase, and release phase. **Figure 7A** shows the poses the robot should take within these phases. Based on the determination of the transient time in the previous section, the duration of the movement phase of the large version is set to three seconds and that of the small version to one second. The fixation phase lasts 0.1 seconds and the release phase also 0.1 seconds. Both are the same for both versions of the robot.

Within these phases, the reference bending angle for all limbs is either 0° or 90°. This angle corresponds in the horizontal plane and without external load to a certain pressure: the reference pressure (compare to **Figure 3B**). In the horizontal plane, the gravity force is perpendicular to the direction of movement. As the inclination angle δ increases, however, the gravity acts increasingly against the direction of movement of the robot, and therefore, the reference pressure must be adjusted in order to correspond to a bending angle of 90°. This means that the mapping function $p(\alpha)$ of each actuator must be recalibrated for each inclination.

In the following experiment, the velocity and energy consumption of the two robot versions are determined for different inclination angles δ. First, the same reference pressures are used for all the inclinations, without recalibrating the mapping function. Then, the reference pressures are adjusted according to the inclination angle, so that the bending angles in the extreme positions correspond as closely as possible to 90°. **Figures 8A,B** show how the maximum bending angles of the front legs and the torso decrease with increasing inclination, while the bending angles of the rear feet increase, when using the same pressure references (dashed curve). This is, however, to be expected since the front legs and torso need to operate against gravity, while the actuation of the rear legs is supported by gravity.

The solid curves in **Figures 8A,B** show the maximum bending angles for the recalibrated reference pressures. In **Figures 8C,D**, the values for the reference pressures are shown for each inclination. Especially the torso is more pressurized, while the reference pressures in the legs are slightly decreased. This indicates that the shift in position comes mainly from the torso,

which is consistent with the finding from Fischer and Witte (2007) of the torso as the main organ of locomotion. The high standard deviation is mainly due to the fact that in some cases, the feet are not fixed immediately during the fixation phase, but rather during the subsequent movement phase. This results in a foot position that does not correspond to the gait model, and may not allow the corresponding limb to bend by 90°.

However, as the angle of inclination increases, not only does the load increase (due to the counteracting gravity force), but the normal force, which pushes the feet against the walking plane, decreases to the same extent. Due to the small normal force at high slopes ($\delta > 70°$), the sealing lip of the suction cup may not be in contact with the walking plane over the entire circumference, which may results in a gap. In this case, the suction cup cannot grip despite vacuum being applied. Therefore, a new gait pattern for high inclinations is introduced, as depicted in **Figure 7B**. The movement and release phases remain identical, but the fixation phase is extended by four additional poses. Before the two supporting feet are released, the potentially unfixed rear leg is first swung forwards and backwards once, in the expectation that the corresponding foot will be fixed during this motion. Afterwards, the same happens to the potentially unfixed front leg. Then, both supporting feet are released and the next movement phase begins. In the **Supplementary Video** (from 1:34 min on), it can be seen that the foot to be fixed is sucked into a random location within the swinging motion. With additional pressure

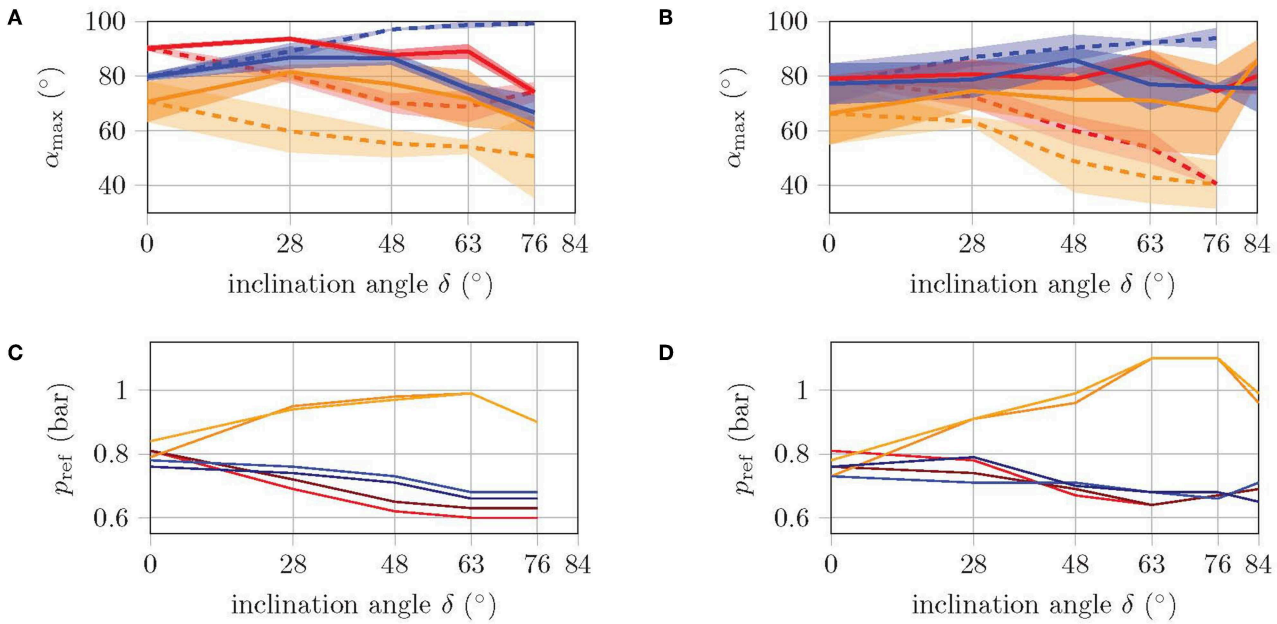

FIGURE 8 | Maximum bending angle **(A,B)** and corresponding reference pressures **(C,D)** of front legs (red), rear legs (blue), and torso (orange) during a cycle. By applying the same pressure reference for different inclination angles (i.e., different loads), the dashed curves are obtained. The solid curves are obtained from the recalibrated pressure references, such that the bending angles match 90° as good as possible. Left diagrams are for large prototype and right diagrams for small prototype.

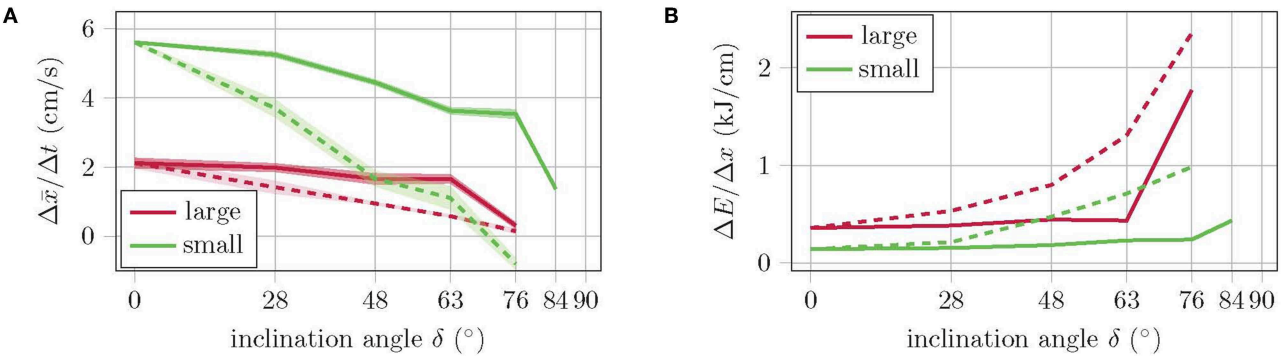

FIGURE 9 | (A) Walking performance and **(B)** energy consumption for various inclination angles. Dashed curves show the values for constant and solid curves for recalibrated pressure references.

TABLE 2 | Comparison of the large and the small prototype of the gecko-inspired soft robot.

	Large prototype	Small prototype	
Speed on horizontal plane	2 (0.13)	6 (0.5)	cm/s (ℓ_{bl}/s)
Energy consumption on horizontal plane	0.36	0.13	kJ/cm
Total weight	200	150	g
Average applied pressure	0.80	0.76	bar
Ability to climb	76	84	°

sensors, it would be possible to detect whether a foot is fixed or not. Through this feedback, the execution of the swing phase of an already fixed leg can be avoided or the swing phase could be repeated if the first run did not have the desired effect. But as the experiments show, the one-time execution of the swing phase is sufficient, and the time saving by avoiding unnecessary swing phases is not particularly large. Therefore, this hardware upgrade has been omitted so far.

The experiment with constant reference pressures shows that the velocity linearly decreases with increasing inclination angle, while the energy consumption increases, see **Figure 9**. The small version has about twice the velocity with half the energy consumption. Both versions manage to climb slopes of up to 63° without falling. At a slope of 76°, the large version does not come from the spot, while the small one even slides backwards. In the experiment with recalibrated reference pressures, the velocity and energy consumption of the large version remain almost constant up to an inclination angle of 63°. This is because the number of cycles required remains the same, while the applied pressure increases only slightly [refer Equation (1)]. With the climbing pattern for high inclinations (see **Figure 7B**), the large version manages to climb inclinations of up to 76°. Higher inclination angles, however, are not possible with this version as the torso cannot reach the corresponding bending angles without running into danger of bursting due to the required applied pressure. The velocity of the small robot version with recalibrated reference pressures is significantly higher compared to the performance with constant pressure references, but decreases with increasing inclination. Energy consumption is also comparatively lower. The small version even manages to master inclinations of up to 84° and is therefore very close to the goal of climbing a vertical wall. A further increase of the inclination, however, does fail here due to a lack of fixation. The normal force is simply too small to bring the suction cups close enough to the walking plane to allow them to suck. Since the robot cannot actively push its feet against the plane of movement, no further variation of the gait pattern will help at this point. A mechanism is needed that pushes the feet against the plane.

The complete data set of the experiments on the inclined plane is provided in the **Supplementary Data**.

4. CONCLUSION

The goal of this paper was to develop a new version of the gecko-inspired soft robot from Seibel and Schiller (2018) that consumes less energy in order to take another step in the direction of an untethered, soft climbing robot. By reducing the volume and increasing the self-reinforcing effect of the bending actuators, not only this goal could be achieved, but also the velocity of the robot was significantly increased (by 300%), as well as its ability to climb. **Table 2** summarizes the results of this study. The large version has major difficulties in reaching the reference pose at all when climbing high inclinations, that is, the actuators do not provide enough force to bend to the desired angle under high load. Increasing the reference pressure would exceed the actuator's capability and cause it to burst. For the small version, however, climbing is not limited by a lack of force, but by a lack of fixation. Reaching the reference pose is no challenge for this version, even under high load. In order to improve the fixation, only a mechanism is needed that allows the robot to actively push its feet to the plane of movement. With such a mechanism, the robot could easily climb vertical walls.

Compared to other robots, this robot can move extremely fast. Qin et al. (2019) summarize the speeds of different soft crawling robots and introduces a novel robot with special emphasis on rapid locomotion, since its speed is much higher than of previous soft robots. Without a payload, this robot moves at a speed of about 0.1 ℓ_{bl}/s, while our robot can run five times the speed related to its body length.

In order to free the robot from its umbilical cord, a suitable on-board pressure and vacuum source must be found. Even though research is ongoing (Adami and Seibel, 2019), this task is still open. In any case, reducing energy consumption to 36% compared to the previous version brings this goal closer.

DATA AVAILABILITY STATEMENT

The datasets `exp_incl_plane` and `exp_slow_track` for this study can be found in the collection Research Data TUHH [https://doi.org/10.15480/336.2519].

AUTHOR CONTRIBUTIONS

LS and AS initiated the study and wrote the manuscript. LS redesigned the robot, performed the experiments, and discussed the results. LS, AS, and JS revised the manuscript. AS and JS supervised the project.

FUNDING

The publication of this work was supported by the German Research Foundation (DFG) and Hamburg University of Technology (TUHH) in the funding programme Open Access Publishing.

ACKNOWLEDGMENTS

We thank Aravinda Paniyoor Bhari, Fynn Knudsen, and Brian Alphonse Pinto for the inspiration and preliminary work.

SUPPLEMENTARY MATERIAL

The Supplementary Material for this article can be found online at: https://www.frontiersin.org/articles/10.3389/fnbot.2019.00106/full#supplementary-material

Supplementary Video | The video supporting the conclusions of the experiments is included as additional file.

Supplementary Data | A pdf containing a experimental design parameter study and all relevant data measured during the experiments on the inclined plane is also included as additional file.

REFERENCES

Adami, M., and Seibel, A. (2019). On-board pneumatic pressure generation methods for soft robotics applications. *Actuators* 8:2. doi: 10.3390/act8010002

Autumn, K., Hsieh, S. T., Dudek, D. M., Chen, J., Chitaphan, C., and Full, R. J. (2006). Dynamics of geckos running vertically. *J. Exp. Biol.* 209, 260–272. doi: 10.1242/jeb.01980

Calisti, M., Picardi, G., and Laschi, C. (2017). Fundamentals of soft robot locomotion. *J. Roy. Soc. Interf.* 14:20170101. doi: 10.1098/rsif.2017.0101

Chu, B., Jung, K., Han, C.-S., and Hong, D. (2010). A survey of climbing robots: locomotion and adhesion. *Int. J. Precis. Eng. Manufact.* 11, 633–647. doi: 10.1007/s12541-010-0075-3

Fischer, M. S., and Witte, H. (2007). Legs evolved only at the end! *Philos. Trans. Roy. Soc. A Math. Phys. Eng. Sci.* 365, 185–198. doi: 10.1098/rsta.2006.1915

Gu, G., Zou, J., Zhao, R., Zhao, X., and Zhu, X. (2018). Soft wall-climbing robots. *Sci. Robot.* 3:eaat2874. doi: 10.1126/scirobotics.aat2874

Kim, S., Laschi, C., and Trimmer, B. (2013). Soft robotics: a bioinspired evolution in robotics. *Trends Biotechnol.* 31, 287–294. doi: 10.1016/j.tibtech.2013.03.002

Majidi, C. (2014). Soft robotics: a perspective—current trends and prospects for the future. *Soft Robot.* 1, 5–11. doi: 10.1089/soro.2013.0001

Mosadegh, B., Polygerinos, P., Keplinger, C., Wennstedt, S., Shepherd, R. F., Gupta, U., et al. (2014). Pneumatic networks for soft robotics that actuate rapidly. *Adv. Funct. Mater.* 24, 2163–2170. doi: 10.1002/adfm.201303288

Polygerinos, P., Lyne, S., Wang, Z., Nicolini, L. F., Mosadegh, B., Whitesides, G. M., et al. (2013). "Towards a soft pneumatic glove for hand rehabilitation," in *2013 IEEE/RSJ International Conference on Intelligent Robots and Systems (IROS)* (Tokyo), 1512–1517. doi: 10.1109/IROS.2013.6696549

Qin, L., Liang, X., Huang, H., Chui, C. K., Yeow, R. C., and Zhu, J. (2019). A versatile soft crawling robot with rapid locomotion. *Soft Robot.* 6, 455–467. doi: 10.1089/soro.2018.0124

Rus, D., and Tolley, M. T. (2015). Design, fabrication and control of soft robots. *Nature* 521, 467–475. doi: 10.1038/nature14543

Seibel, A., and Schiller, L. (2018). Systematic engineering design helps creating new soft machines. *Robot. Biomimet.* 5:5. doi: 10.1186/s40638-018-0088-4

Tang, Y., Zhang, Q., Lin, G., and Yin, J. (2018). Switchable adhesion actuator for amphibious climbing soft robot. *Soft Robot.* 5, 592–600. doi: 10.1089/soro.2017.0133

Wang, J., and Olson, E. (2016). "Apriltag 2: efficient and robust fiducial detection," in *2016 IEEE/RSJ International Conference on Intelligent Robots and Systems (IROS)* (Daejeon), 4193–4198.

Website (2019). *Soft Robotics Toolkit*. Avaialble online at: http://softroboticstoolkit.com/ (accessed: Febuary 02-25, 2019).

Conflict of Interest: The authors declare that the research was conducted in the absence of any commercial or financial relationships that could be construed as a potential conflict of interest.

frontiers in Neurorobotics

ORIGINAL RESEARCH
published: 21 February 2020
doi: 10.3389/fnbot.2020.00008

SAUV—A Bio-Inspired Soft-Robotic Autonomous Underwater Vehicle

Fabian Plum[1,2], *Susanna Labisch*[1,3] *and Jan-Henning Dirks*[1,3,4]*

[1] Department of Biomimetics, Hochschule Bremen - City University of Applied Sciences, Bremen, Germany, [2] Department of Bioengineering, Imperial College London, London, United Kingdom, [3] Biomimetic-Innovation-Centre, Hochschule Bremen - City University of Applied Sciences, Bremen, Germany, [4] Max-Planck-Institute for Intelligent Systems, Stuttgart, Germany

Autonomous and remotely operated underwater vehicles allow us to reach places which have previously been inaccessible and perform complex repair, exploration and analysis tasks. As their navigation is not infallible, they may cause severe damage to themselves and their often fragile surroundings, such as flooded caves, coral reefs, or even accompanying divers in case of a collision. In this study, we used a shallow neural network, consisting of interlinking PID controllers, and trained by a genetic algorithm, to control a biologically inspired AUV with a soft and compliant exoskeleton. Such a compliant structure is a versatile and passive solution which reduces the accelerations induced by collisions to 56% of the original mean value acting upon the system, thus, notably reducing the stress on its components and resulting reaction forces on its surroundings. The segmented structure of this spherical exoskeleton protects the encased system without limiting the use of cameras, sensors or manipulators.

Keywords: exoskeleton, genetic algorithm, compliant structure, shock absorbability, cave diving

OPEN ACCESS

Edited by:
Poramate Manoonpong, Nanjing University of Aeronautics and Astronautics, China

Reviewed by:
Grégoire Danoy, University of Luxembourg, Luxembourg
Yanwu Zhang, Monterey Bay Aquarium Research Institute (MBARI), United States
Khoshnam Shojaei, Islamic Azad University of Najafabad, Iran

***Correspondence:**
Jan-Henning Dirks
jan-henning.dirks@hs-bremen.de

Received: *14 June 2019*
Accepted: *29 January 2020*
Published: *21 February 2020*

Citation:
Plum F, Labisch S and Dirks J-H (2020) SAUV—A Bio-Inspired Soft-Robotic Autonomous Underwater Vehicle. Front. Neurorobot. 14:8. doi: 10.3389/fnbot.2020.00008

INTRODUCTION

In recent years the use of Autonomous Underwater Vehicles (AUVs) and Remotely Operated Vehicles (ROVs) has become increasingly popular in marine biology and underwater exploration. These vehicles enable humans to reach depths and areas which would otherwise be too dangerous for divers or simply inaccessible (Hudson et al., 2005). Yet especially when having to navigate in complex or confined spaces, such as flooded caves, shipwrecks or coral reefs, conventional ROVs still show significant practical limitations. Most ROVs are trivially underactuated and therefore incapable of precisely maneuvering under such circumstances in the first place. The need for a cable connecting to a control station further reduces an ROVs ability to freely move in confined spaces. AUVs are free of this restriction, however, due to their limited on-board signal processing and navigation, they are still often unfit for the interaction with fragile surroundings or are themselves prone to take damage from unintentional collisions (Hudson et al., 2005; Hernández-Alvarado et al., 2016). Especially in fragile confined spaces such as underwater caves, a rigid object colliding with the environment can cause the release of debris or even rocks.

So far, these limitations were addressed using computationally, expensive technical solutions. Typical implementations include adding a multitude of sensors in order to capture the state of the system more accurately when planning its trajectory and additionally carrying out local behavior based strategies (Warren, 1990; Estes et al., 1996; Valavanis et al., 1997; Chyba et al., 2009). However, any active technical systems can fail, and, in these cases, a passive structure or mechanism should prevent severe consequences to the system and especially its environment. As a result, there is an increasing need for a fail-safe, computationally and economically inexpensive solution to allow safe maneuverability of underwater vehicles in fragile and confined environments.

Biological Inspiration

In evolutionary terms there are two possible concepts to respond to mechanical stress: either increase the rigidity of your protective layer, e.g., an exoskeleton or shell, to prevent any deformation, or tolerate certain levels of deformation to minimize the risk of lasting damage (Vincent and Wegst, 2004; Dirks and Taylor, 2012; Wegst et al., 2015).

Especially in unicellular organisms such as ciliates, bacteria or algae, the "tolerate" principle is dominant (King and Beams, 1941; Stocker, 2011; Persat et al., 2015; Sumpio, 2017). These organisms are only separated from their environment by a single membrane or mostly unsclerotised cell walls. Most of these small organisms are also unable to avoid collisions actively; however, due to their small mass and since their "skeleton" is mostly ductile and flexible, they remain unharmed (Persat et al., 2015). The underlying idea of compliance instead of rigidity is applied in soft robotics and modern prosthetics (Trivedi et al., 2008; Belter et al., 2013; Coyle et al., 2018). For underwater vehicles and diving equipment compliance has been used for different actuation strategies (Arienti et al., 2013; Kim et al., 2013; Cianchetti et al., 2015; Laschi et al., 2016), however not yet for structural-skeletal concepts to enhance existing systems. A great advantage of this passively compliant mechanism is its versatility in possible shapes, allowing virtually any system to be equipped with these segmented structures. Here, we show how such a soft and compliant exoskeleton can improve the longevity of an underwater vehicle and reduce the stress, acting upon the system and its environment, in case of a collision.

An additional challenge, which a truly bio-inspired robust system faces, is the ability to compensate for a changing environment, varying carried load, or potential partial system failure. The growing interest in the application of AUVs for exploratory, survey, and economic purposes has led to the development of numerous control strategies, attempting to improve the robustness of such systems to time-variable ocean currents or waves (Elhaki and Shojaei, 2018; Zhong et al., 2018; Shojaei, 2019; Wang et al., 2019; Xia et al., 2019). Recently, the use of neural networks has become increasingly widespread in such control applications to account for changing weight distributions of moving manipulators and otherwise unmodeled hydrodynamics (Hernández-Alvarado et al., 2016; Elhaki and Shojaei, 2018; Shojaei, 2019). During the last century, extensive work in the field of biologically inspired adaptive control models has led to a set of principles that enable computation or decision making procedures which are otherwise impractical for traditional mathematical approaches (Lin and Liu, 2010; Hernández-Alvarado et al., 2016; Meena and Devanshu, 2017). Depending on the task of the system, the feedback-based motor controller needs to be adjusted, to work irrespectively of the attached sensory equipment and additional manipulators. To allow a robust, autonomous control of our AUV, we used a genetic algorithm as a means of tuning a system of interlinking PID controllers as a simple three-layered neural network. As the number of weight parameters in our approach is comparably limited, we attempted to use this directed genetic algorithm as a biologically plausible learning strategy, as opposed to backpropagation methods, which are usually employed in more complex network architectures (Riedmiller and Braun, 1993; Hernández-Alvarado et al., 2016). Using a decaying step-size within a genetic algorithm leads to a rapid convergence in its performance over a comparably small number of generations.

To provide a frame of reference for a successfully auto-tuned system, we compared the performance of this approach to the popular heuristic Ziegler-Nichols method for PID tuning (Ho, 1991; Valério and da Costa, 2006). As a proof of concept, we quantified the stabilization performance of the genetic tuning algorithm for the pitch and roll components of the system. Due to the symmetrical shape and weight distribution of our prototype, its behavior is known to be sufficiently predictable to enable an approximated tuning success when using the classic Ziegler-Nichols method (Ho, 1991). In the following sections, we briefly explain the design choices of our newly developed SAUV, outline the implementation and performance of the employed genetic PID tuning algorithm, and quantify the effectiveness of the biologically inspired soft and compliant exoskeleton.

MATERIALS AND METHODS

To demonstrate the effect of the compliant exoskeleton principle, derived from unicellular organisms, on a larger scale, a fully functional prototype was built. The resulting ability to absorb kinetic energy was experimentally evaluated using this prototype. To be equally agile in six degrees of freedom, we designed a spherical system with six bidirectional thrusters. This almost holonomic design also eliminates the need for a preferable direction of movement as its drag coefficient remains constant, regardless of the system's orientation (Turton and Levenspiel, 1986).

The AUV

The AUV has a total of six NTM Prop Drive 1000 KV brushless motors (by HobbyKing, Hong Kong) which are each connected to a Turnigy MultiStar 30 ampere electronic speed controller (by HobbyKing, Hong Kong). These ESCs were chosen for their ability to reverse the direction of the brushless motors, using the OneShot125 3D protocol. This principle allows generating thrust in either direction when required, especially in the case of rapid descent or aggressive orientation correction. Four motors are positioned in equal distance to each other and the center of mass, facing upwards. To cancel out the angular momentum, neighboring motors spin in opposite directions, as indicated in the control loop diagram, which is explained in detail in **Figure 3**. A further two motors are positioned facing forwards on either side of the system. These motors are required to move the system forwards or backwards without adjusting the pitch and to improve upon the system's ability to turn on the spot. CAD renderings of the complete system are shown in **Figure 1**.

Two ultrasonic distance measuring modules were installed, one in the front, facing forwards, and one in the lower center of the system, facing downwards. These sensors provide the system with readings necessary for primitive obstacle avoidance and,

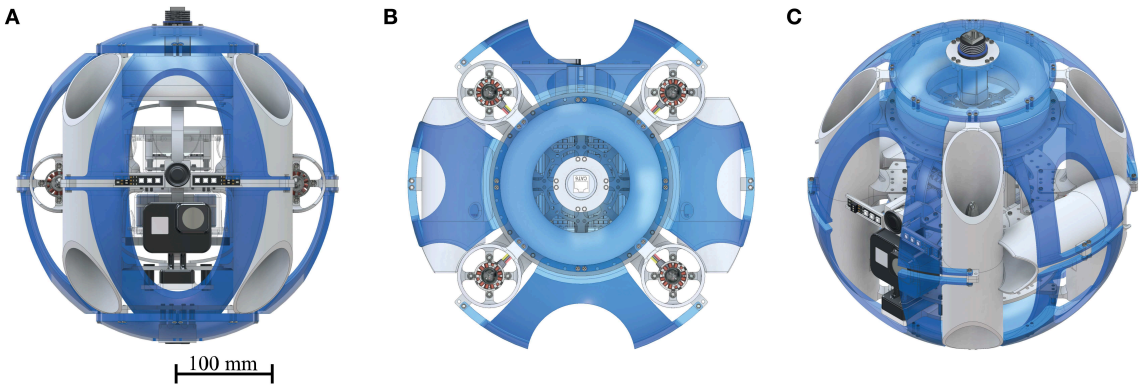

FIGURE 1 | Renderings of constructed SAUV: Soft Autonomous Underwater Vehicle with the compliant exoskeleton (blue, transparent) fitted around it. **(A)** front view, **(B)** top view, **(C)** isometric view. Up to four cameras may be mounted in the lower section of the SAUV. The system is connected to a ground station via a water proof CAT6 connector during the conducted trials to visualize current sensor readings and start the control protocol.

if desired, to keep a constant relative position to the floor. In addition, an altimeter (MS5803 _ 14BA by Sparkfun, Boulder, Colorado, United States) is located in the back of the system to monitor the actual depth relative to the water level by measuring the current water pressure. Two 11.3 V lithium polymer batteries, connected in parallel, are located in a water-sealed container (HPL806 by iSi Deutschland GmbH, Solingen, Germany) in the lower section of the AUV. All other electronic components are contained in a secondary container of the same type in the upper section.

The entire system, at its current stage, is controlled by a Raspberry Pi 3 Model B (by Raspberry Pi Foundation, Cambridge, United Kingdom, Debian release V9.2) which is used to read all sensor input and send motor output commands using i²c protocol. For ease of handling, in all experiments conducted underwater, the Raspberry Pi was placed outside the towing tank and connected via a data transmission cable. During the experiments, however, there was no interaction with any of the control components.

Genetic Algorithm and Preliminary Trials

The stabilization and position tracking are achieved through a shallow neural network consisting of 4 interlinking PID controllers which were tuned through a simple genetic algorithm following to a $(1, 5)^{20}$ evolution strategy (Rechenberg, 1989, 2000) (**Figure 2**). These 4 PID controllers are responsible for correcting and stabilizing the systems (1) pitch & roll, (2) yaw, (3) depth, and (4) frontal distance to an obstacle or object of interest. Due to the spherical shape of the system, the weights of the pitch and roll components are shared and thus tuned simultaneously. In general, our tuning approach is executed for one control segment at a time. In this genetic tuning algorithm an "individual," is represented by a set of corresponding weights for each PID controller within the control loop, and an associated fitness, based on the resulting position tracking performance. The strategy itself can be divided into four distinctive steps: (i) *Reproduction.* Five copies of the fittest offspring of the previous generation are generated. (ii) *Mutation.*

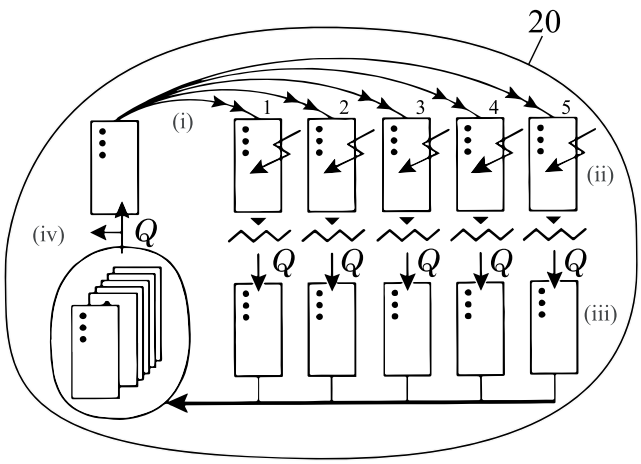

FIGURE 2 | Employed $(1, 5)^{20}$ Evolutionary strategy, depicted using symbols by Rechenberg (Rechenberg, 1989, 2000). **(i)** A single set of variables is duplicated 5 times to produce a new generation. **(ii)** Each offspring is mutated and **(iii)** its fitness is computed based on the *MSE* (Equation 3.2) of the position tracking performance. **(iv)** From this population the offspring with the lowest *MSE* is selected and used as the parent of the next generation. This process is repeated over 20 generations at which point the best performing set of the last generation is determined and the tuning process ends.

Each new offspring is randomly mutated, following Equation 3.1. A randomly generated value $-1 \leq M \leq 1$ divided by the number of generations and multiplied by the range specific to the component ($R_p = 100$, $R_i = 10, R_d = 10$) is added to the previous weight $w_{j_{gen-1}}$ of the set, respectively. (iii) *Evaluation.* After generating these sets, each is applied to the network of controllers and the system, and the fitness of the set is computed over an interval of 5 s in terms of the resulting Mean Squared Error (*MSE*) in the position or angular tracking performance Equation 3.2. The controller error, e_{ctrl}, used in this function corresponds to the currently tuned controller, e.g., $e_{pitch} + e_{roll}$, when pitch and roll weights are tuned. (iv) *Selection.*

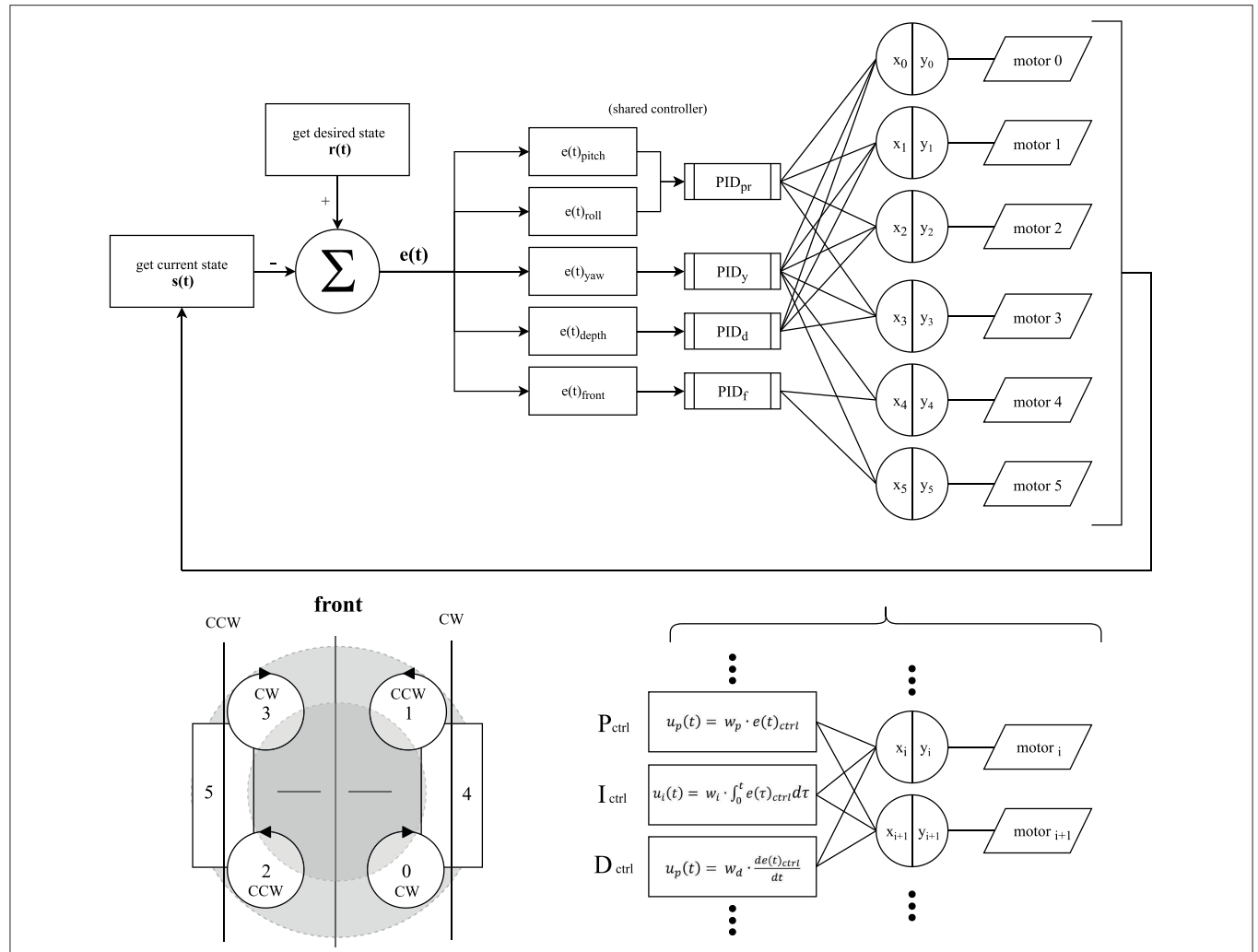

FIGURE 3 | Control diagram of the developed system, consisting of 4 interlinking PID controllers, to allow for accurate position tracking in pitch & roll (PID_{pr}), yaw (PID_y), depth (PID_d) and distance to an obstacle or object of interest in front of the SAUV (PID_f). At the beginning of each increment of the control loop the current state of the system in terms of the vector $s(t)$ and the desired, or reference, state $r(t)$ is determined. The reference state can either be the result of direct user input via a gamepad, a pre-programmed route to follow, or a state to maintain. The deviation from the desired state yields the current error of the system $e(t)$, consisting of the respective values for each controller to correct for. The responses are then mapped to each motor according to the motors' rotation direction (**lower left**) by converting the summed outputs of the PID block x_i into pulse width modulated signals for each ESC denoted as y_i. (**lower right**) Each PID controller consists of three components: a proportional P_{ctrl}, an integral I_{ctrl}, and a derivative D_{ctrl} component. Their respective weights w_p, w_i, w_d are tuned by a genetic algorithm, depicted in **Figure 2**.

The individual containing the set of values resulting in the lowest *MSE* is selected as the fittest offspring and becomes the parent of the successor generation. The process is then repeated over 20 generations in total. As this selection method is purely based on the system's accelerometer, gyroscope, ultrasonic and altimeter measurements, it does not require manual tracking or user input to execute the tuning process.

$$w_{j_{gen}} = w_{j_{gen-1}} + \frac{M \cdot R_j}{gen} \tag{3.1}$$

$$MSE\,(e_{ctrl}) = \frac{\sum_{i=0}^{n} (e_{ctrl})^2}{n} \tag{3.2}$$

To demonstrate the effectiveness of the genetic algorithm, a set of preliminary trials were conducted in a custom-built 60 × 60 × 80 cm (width × length × height) aquarium. This setup was chosen to test the algorithm, as in case of unstable behavior, the system could be easily recovered. In front of the aquarium, at a distance of 52 cm between the lens and the front-facing wall of the aquarium, a GoPro Hero 5 Black (by GoPro Inc., San Mateo, United States) on a tripod was positioned in portrait mode (vertically oriented) to record the prototype system within the aquarium (1,920 × 1,080 px at 59,94 fps). To compensate for the lens distortion, all footage was recorded with the integrated field of view set to linear. For later visual tracking of the system within the aquarium, a set of colored 4 × 4 Lego bricks

were attached to the top of the horizontally facing tubes o the prototype.

The system was calibrated outside of the water on a level surface before being lowered into the aquarium. Afterwards, the training program loop was executed, and all sensor data and the fittest PID weights of each generation were saved directly onto the Raspberry Pi. The desired state of the system, in this case, was a constant vertical position, 30 cm above the floor of the aquarium, and a level orientation, without changes in the pitch or roll axis. This mode is referred to as "Hold Position." After 20 successfully executed generations over the course of 8 min and 20 s, the program was terminated automatically, and the system was lifted out of the water and onto the level surface again. For the next iteration, the system was recalibrated, its batteries recharged and it began with a newly randomized set of input weights. This process was repeated until five iterations had been executed without interference.

For comparison, the heuristic Ziegler-Nichols PID Tuning method (Ziegler and Nichols, 1942) was used as a reference point to which the performance of the genetic algorithm was compared for the pitch and roll components of the controller network. To this end, the respective weights of the pitch and roll nodes were initially set to $w_{pr_d} = w_{pr_i} = 0$ with the exception of the proportional gain being set to $w_{pr_p} = 1$. This value was continuously increased until the system reached a stable oscillation, denoted by the constant K_u , the ultimate gain.

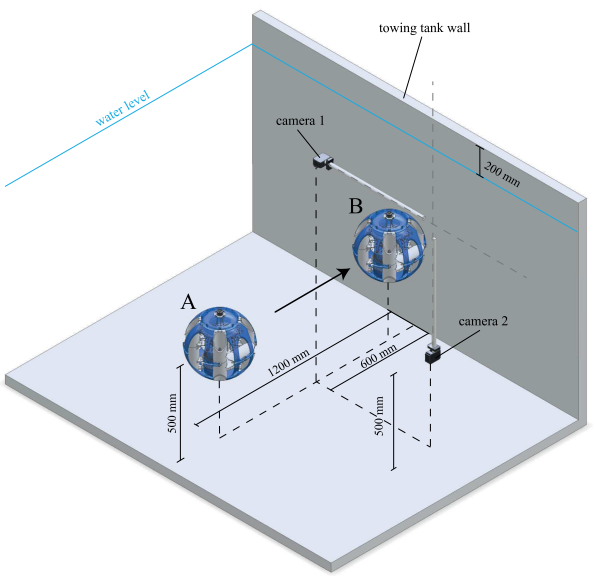

FIGURE 4 | Depicted is a cell shaded rendering of the experimental setup for the conducted *"wet"* impact trials. The SAUV is lowered into the towing tank at position **(A)** and records all IMU data while accelerating toward position **(B)** where it collides with the towing tank wall. After registering the impact, the SAUV stops its motors and backs away from the wall before ascending to the water surface for the following trial. These trials are recorded by two cameras; **camera 1**—GoPro Hero 3+ silver, located 200 mm above the water level, **camera 2**—GoPro Hero 5 black, located underwater at the same depth as the SAUV.

Afterwards, the individual gains for the controller are calculated as described in the original publication (Ziegler and Nichols, 1942) by determining T_u, the period of the oscillation at K_u from the recorded video.

$$w_{pr_p} = 0.6 \cdot K_u \tag{3.3}$$

$$w_{pr_i} = T_i \cdot w_{pr_p} = \frac{T_u}{2} \cdot 0.6 \cdot K_u \tag{3.4}$$

$$w_{pr_d} = T_d \cdot w_{pr_p} = \frac{T_u}{8} \cdot 0.6 \cdot K_u \tag{3.5}$$

To compare the position-tracking performance of the two tuning methods, the system was recalibrated, lowered into the aquarium, and the "*Hold position*" script is executed. The program loop was then initiated, and after 10 s the recording was started. This time is required, as the system propels itself upwards from the aquarium floor and settles at the desired position. From this point on, the video was recorded over a duration of 10 s, resulting in 599 images for each run. Furthermore, a second condition was tested, in which the system was to ascend and descend rapidly, named "Alter Position." Under this condition the desired vertical position was switched every 5 s between 30 and 45 cm above the aquarium floor to provoke unstable behavior over a duration of 60 s, resulting in 3,594 images. The performance of all evolutionary iterations after 20 generations and the Ziegler-Nichols method were tested in 5 repetitions in "*Hold Position*" mode. After showing that all iterations converged regarding their resulting position tracking performance (see **Figure 6**), only iteration one and the Ziegler-Nichols method were then compared in 5 repetitions in "*Alter Position*" mode for the second half of the preliminary trials.

Exoskeleton

The model of the soft and compliant exoskeleton consists of a total of 10 interchangeable parts, which, when mounted onto the AUV, lead to an overall spherical shape. These parts were manufactured with a dual extruder 3D printer (Dual Extruder Metal Frame BIBO 2, Bibo Automatic Equipment Co., Ltd, Shaoxing, China) using a thermoplastic polyurethane filament (Flexible TPU Transparent, SainSmart Ltd., Lenexa, USA). Additionally, the thruster ducts of the AUV were elongated to provide connecting points for the exoskeleton whereas the elongated sections were created from the same material as the exoskeleton. These elongated sections ensure an equally elastic and compliant behavior of the system regardless of the direction of impact. All other structural components were 3D printed using a ZoneStar Prusa i3 filament printer (ZoneStar Innovation Technology Co., Ltd, Shenzhen, China) with clear PLA filament (by filamentworld, Neu-Ulm).

The radius of the resulting sphere of constant width was chosen to allow at least 30 mm of deformation in any direction before a rigid component would come into contact with its surroundings. The only exceptions to this rule are the mounting points of the laterally placed thruster ducts, in case of a direct 90° impact from either side. As the area, for which this is the case, is negligibly small, compared to the overall size of the system, a smaller circumference of the exoskeleton was favored.

Evaluation of Exoskeleton Performance

Before conducting velocity and impact trials, the system's motor controller was tuned, using the above described genetic algorithm, with the exoskeleton attached and not retrained for trials without it, as the exoskeleton's effect on the systems total mass is negligible. Furthermore, due to its symmetry, the exoskeleton does not affect the system's center of mass. The total weight of the system, excluding the exoskeleton, is 2,279 g, while the exoskeleton weighs 283 g.

In order to quantify the dampening effect of the soft and compliant exoskeleton, impact trials were conducted in a 1.2 × 2.2 m (depth x width) section of a towing tank. The movement of the AUV was recorded using two synchronized cameras (top, side, 1,920 × 1,080 pixels, 59,94 fps, a shutter speed of 1/120 s, GoPro Hero 5 black and Hero 3+ black, San Mateo, United States). The experimental setup is shown in **Figure 4**.

The recorded video files were imported into Blender (release 2.79b, GNU General Public License, blender foundation) and analyzed using its internal pattern motion tracking. The resulting trajectories of multiple markers with known distances, to compensate for lens distortion when computing the absolute velocity, were then exported as pixel coordinates using a custom plugin (Blender Motion Tracking Export Plugin, MIT license, www.github.com/BiYonic/blenderMotionExport). An automatic analysis tool for this data was then written in Python 3.6 to compute $v_{\max}$ and $t_{v_{\max}}$, as well as to plot the velocity profile of each run.

To determine the maximum velocity, the AUVs motors were set to accelerate to 70% of their maximum velocity to determine $v_{\max}$ and the required time $t_{v_{\max}}$ to reach it. As the voltage of the two LiPo batteries affects the maximum velocity, they were fully recharged in between impact trials with and without the attached exoskeleton. At the beginning of each trial, the AUV was lowered into the towing tank at a distance of approximately 1.2 m from a wall of the tank, facing it directly. The AUV automatically positioned itself at a depth of 0.5 m below the water level and corrected its drift and orientation steadily for 5 s, settling at a steady position before beginning to accelerate toward the wall in front of it. The AUV then set its horizontally oriented thrusters to 70% of their maximum output to allow for yaw corrections while driving forwards and began logging the acceleration and angular velocity of the system from its inertial measurement unit (IMU) at a refresh rate of 59 Hz ± 1.3. The thrust was kept constant until an impact was registered by the IMU which prompted the horizontal motors to stop and then reverse their direction to move away from the wall. After moving backwards for 1 s, the system was set to hold its current position for 5 s before stopping the recording of IMU data and ascending to the water surface to be redeployed for the next trial.

To derive the true net acceleration and to compute the resulting velocity from the recorded IMU data, gravity and orientation compensation was performed according to Nistler and Selekwa (2011) and implemented in python 3.6. This way the effects of the tilt in the pitch, roll, and yaw axes on the acceleration in cartesian space were accounted for and the position relative to the starting point of the system, as well as its velocity, could be computed accurately. Both inertial and gyroscope measurements are required for this correction. The recorded duration of a single trial does not exceed 20 s; thus, no additional filters were applied to compensate for possible sensor drift, as it is negligible. The compared magnitude of the net acceleration, as shown in Equation 3.7 is dependent on the following components: $\ddot{\vec{r}}_{xyz}$, the corrected acceleration vector, $\ddot{\vec{r}}_{XYZ}$, the input acceleration vector including gravity, as recorded by the inertial measurement unit, $\dot{\vec{r}}_{XYZ}$, the computed velocity vector, $\vec{r}_{XYZ}$, the computed relative position vector, and J, the X- Y- Z rotation matrix, in Equation 3.6. For further details, refer to the original publication by (Nistler and Selekwa, 2011).

$$\ddot{\vec{r}}_{xyz} = J\ddot{\vec{r}}_{XYZ} + 2\dot{J}\dot{\vec{r}}_{XYZ} + \ddot{J}\vec{r}_{XYZ} \tag{3.6}$$

$$\left|\ddot{\vec{r}}_{xyz}\right| = \sqrt{\ddot{\vec{r}}_x^{\,2} + \ddot{\vec{r}}_y^{\,2} + \ddot{\vec{r}}_z^{\,2}} \tag{3.7}$$

To quantify the effect of the soft and compliant exoskeleton itself, also "dry" impact trials were conducted with the SAUV as a simple gravity pendulum and a rigid wall, depicted in **Figure 5**. The initial value problem-setup was taken with a length of the pendulum of $l = 75\,cm$, the SAUV itself was

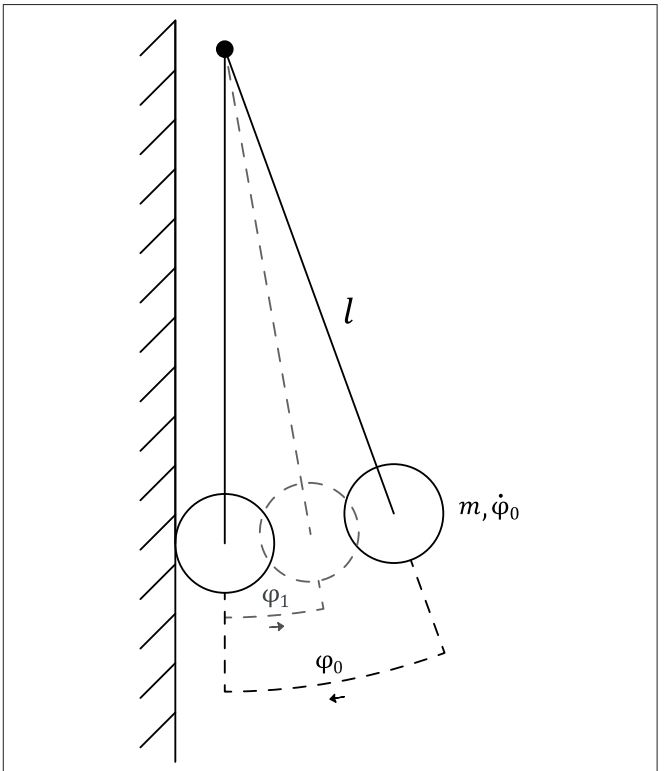

FIGURE 5 | *"dry"* Experimental setup of the gravity pendulum. The SAUV is assumed to be a point mass m, initially at rest prior to release ($\dot{\varphi}_0 = 0$) at an angle of $\varphi_0 = 15° \pm 0.2°$. The maximum angle φ_1 after the impact with a rigid wall is measured to compute the coefficient of restitution of C_R.

assumed to be a point mass and the initial conditions $\varphi_0 = 15 \pm 0.2$ and $\dot{\varphi}_0 = 0$. The impact trials were conducted with and without the attached exoskeleton parts with $n = 5$, respectively, to record the resulting maximum angle after a collision, denoted as φ_1. The true net acceleration was also plotted according to Equations (3.6) and (3.7) with 20 repetitions in each condition.

Statistical Evaluation

During the described preliminary trials, the Shapiro-Wilk test was used to test for normal distribution. Whenever more than two samples were tested for homogeneity of variances, the Levene's test was performed. Otherwise, a two-sample *F*-Test was used. For multi-sample comparison of the mean values, the Kruskal–Wallis rank-sum test was used. If significance occurred either the Dunn's test or the Wilcoxon rank-sum test was used *post-hoc* to identify the responsible subgroups. Whenever normally distributed samples with homogeneity of variances were found between two samples, the Welch Two Sample *t*-test was used to test their mean.

To compare the computed net acceleration and velocities in trials with and without the mounted soft and compliant exoskeleton, the following cascade of tests was performed; The Shapiro–Wilk test was used to test for normal distribution in each data set, followed by the Barnett test to test for homogeneity of variances. Since in all tests, both criteria were met, a two-sample student *t*-test was performed to compare the mean between the two samples. For every velocity and impact test, the sample size was $n \geq 10$ with a significance level of $\alpha = 5\%$. All statistical evaluations were performed in python 3.6, using the library *scipy.stats*.

RESULTS

Genetic Algorithm Performance in Preliminary Trials

Over the course of 20 generations in 5 separate iterations, a total number of 500 individual value sets have been applied and tested in "*Hold Position*" mode during the genetic algorithm tuning phase. The fitness of each individual was determined by its resulting MSE, computed during the runtime of the tuning phase by directly comparing the filtered sensor deviation of the inertial measurement unit within each generation. By comparing the MSE after 20 generations of all iterations in "*Hold Position*" mode to one another, convergence could be shown for the performance of the genetic algorithm tuning (Kruskal–Wallis = 0.81231, $p = 0.9368$), (**Figures 6**, **7**).

During our preliminary trials, for comparison, the system was tuned using the classic Ziegler-Nichols method. Steady oscillation of the system was achieved when the proportional gain of the pitch and roll segment w_{pr_p} reached $Ku = 125$. The oscillation period at that point was determined by an analysis of the footage obtained executing "Hold Position." Tu is therefore equal to 0.825. The approximated deviation (t), in terms of the vertical distance between the rear and front tracking points of the system, can be described by $d(t) = \sin(\frac{2\pi \cdot t}{T_u})$ and a comparison to the recorded video data is shown in **Figure 7A**. After calculating w_{pr_p}, w_{pr_i} , and w_{pr_d}, the stabilization performance in "*Hold Position*" mode led to an MSE

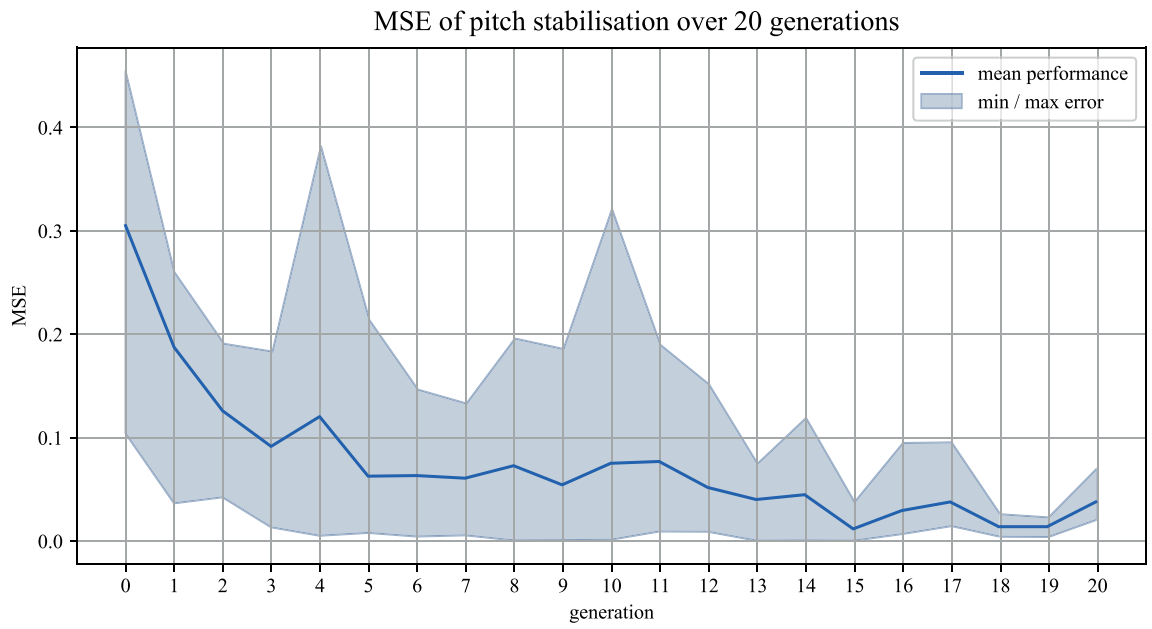

FIGURE 6 | The $MSE(e_{pitch})$ of the best performing parameter sets in the pitch component over 20 generations is shown, recorded during the genetic algorithm tuning process. The light blue area indicates the range of resulting position tracking performances over the 5 repeated iterations and the dark blue line the mean performance in each generation.

of 0.15463 $\pm$ 0.0772. An example of this stabilization method and the performance achieved through the genetic algorithm are shown in **Figure 7B**.

The performance achieved with the use of the genetic algorithm and the Ziegler–Nichols method was significantly different during "*Hold Position*" (Kruskal Wallis $=$ 12.308, $p = 0.00903$, with all Dunn $p < 0.05$). While the MSE over all iterations after 20 generations was between 0.0188 $\pm$ 0.0108 for iteration 3, and 0.0316 $\pm$ 0.0225 for iteration 5, the MSE for the Ziegler-Nichols Method was 0.15463 $\pm$ 0.0772. The MSE for all compared performances, as well as the maximum absolute error e_M are shown in **Figure 7C** and **Table 1**.

Our experiments in "*Alter Position*" mode, with rapid vertical position changes, however, showed no significant difference in the MSE of the pitch and roll stabilization when comparing the genetic tuning method to the Ziegler-Nichols method (Kruskal-Wallis $=$ 3.1527, $p = 0.0758$). A comparison of the MSE is shown in **Figure 7D**. There was also no significant difference between the MSE of iteration 1 in "*Hold Position*" mode and "*Alter Position*" mode (Welch Two Sample t-test $= -2.3097$, $p = 0.0537$), or the MSE of the Ziegler-Nichols Method between "*Hold Position*" mode and "*Alter Position*" mode (Welch Two Sample t-test $= 1.5641$, $p = 0.1685$).

Velocity Profiles

Over a total of 11 initial trials $v_{\max}$ was measured to be 0.168 $\pm$ 0.072 m/s and the required time to accelerate to that velocity $t_{v_{\max}}$ was 3.6 $\pm$ 0.68 s. A representative velocity profile is depicted in **Figure 8**. These results show that when requiring the velocity of the system to be equal to $v_{\max}$ prior to the impact, the distance to the wall must be $\geq$ 0.35 m. As the distance to the wall within the impact trials is $\approx$ 1.2 m the AUV was able to reach the desired velocity in every trial.

The computed average velocity from the IMU data for both setups, with and without the mounted exoskeleton, 2 s before the

TABLE 1 | Experimental results of the pitch and roll controller tuning, quantifying the tracking error e_{ctrl} of the system in hold position and alter position mode.

Mode	Hold position		Alter position	
	GA	**ZN**	**GA**	**ZN**
MSE	0.025	0.155	0.045	0.091
e_M	0.575	0.971	0.741	0.977

The MSE (Mean Squared Error) and e_M (maximum absolute error) are shown. ***GA*** *(Genetic Algorithm) and* ***ZN*** *(Ziegler-Nichols) refer to the employed tuning method.*

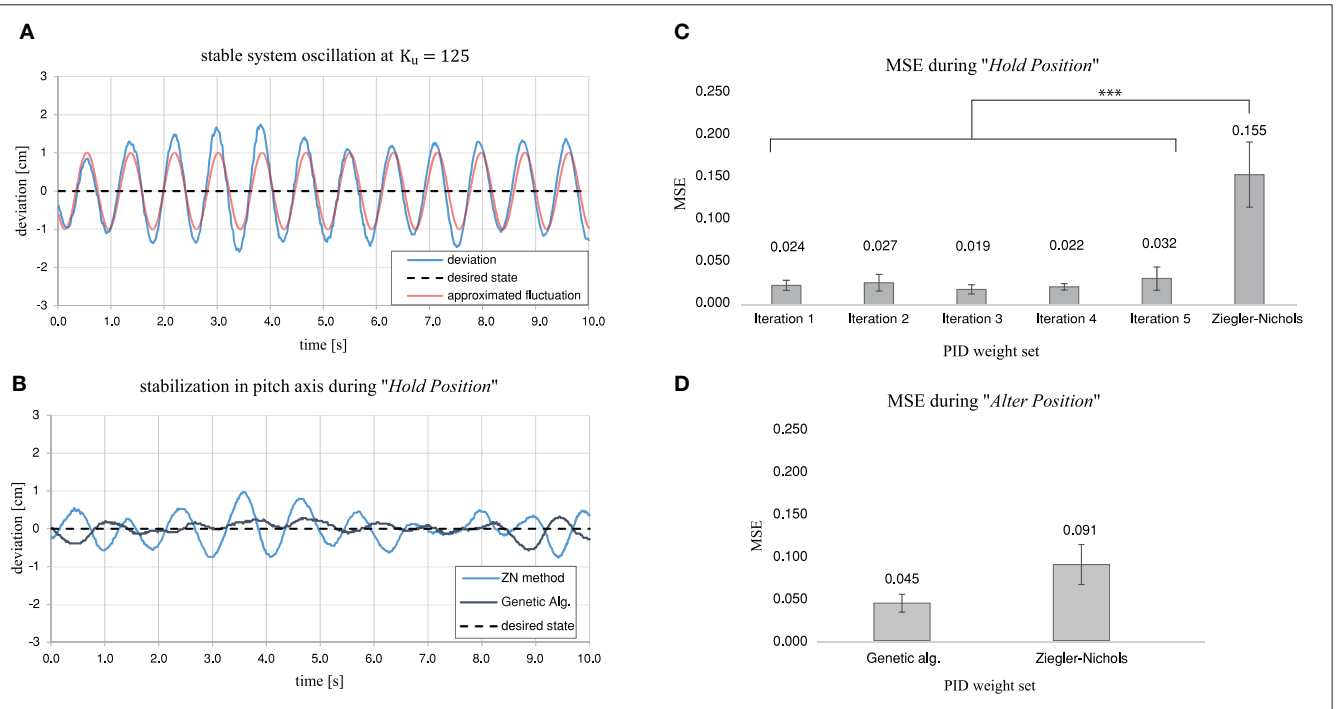

FIGURE 7 | Summarizing the findings of the preliminary trials to evaluate the effectiveness of the genetic algorithm for tuning the nodes related to pitch control. **(A)** The deviation between the front and rear tracking points in centimeters, located on the rims of the horizontal thruster ducts. The stable oscillation achieved during the tuning process of the Ziegler-Nichols algorithm can be approximated by a sinusoidal wave with a period of $Tu = 0.825$. **(B)** Example stabilization in pitch axis over 10 s in "*Hold Position*" mode for the Ziegler-Nichols Tuned nodes compared to the performance of the genetic algorithm after 20 generations. **(C)** Resulting Mean Square Error in stabilization performance in "*Hold Position*" mode for all 5 iterations after 20 generations each compared to the performance of the Ziegler-Nichols method. **(D)** Resulting Mean Square Error in stabilization performance in "*Alter Position*" mode, during rapid vertical position changes, for the genetic algorithm from iteration 1 after 20 generations compared to the performance of the Ziegler-Nichols method.

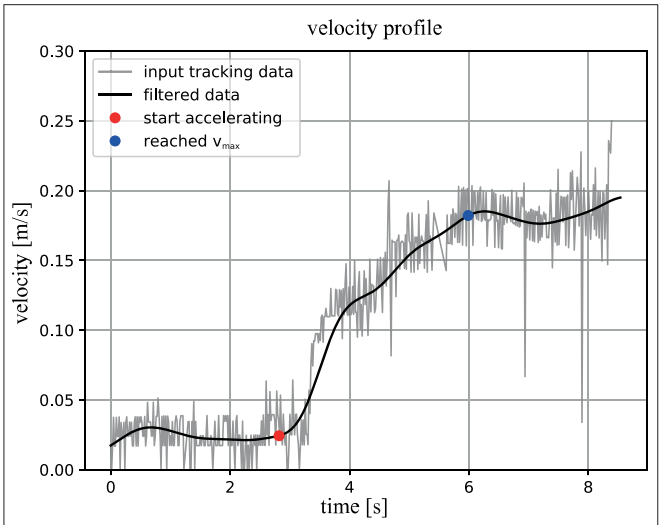

FIGURE 8 | Example velocity profile: the measured absolute velocity of the system is indicated by the gray graph and for the black graph the same data was used, yet a Butterworth frequency filter was applied to account for the noise in the tracking data. The red dot indicates the point in time when the ROV began accelerating and the blue dot marks the instant v_{max} was reached. The interval between these points is equivalent to $\Delta t_{v_{max}}$.

registered impact indicates that this is the case. **Figure 9** shows the velocities measured during this time. The velocity 2 s prior to the impact without the exoskeleton was $0.167 \pm 0.012\, m/s$ and with the exoskeleton $0.160 \pm 0.0049\, m/s$. Both samples are normally distributed and have homogeneous variances. The student t-test returned a p-value of 0.118, indicating no significant difference in the mean velocity with and without the mounted exoskeleton.

Impact Trials

In total, 11 "wet" trials with and without the soft exoskeleton were evaluated. Representative acceleration profiles of the "wet" trials are shown in **Figure 10**. These plots were generated to show the magnitude of the net acceleration, according to Equation 3.7, 1 s before and after the registered impact, over a total span of 2 s. The recorded peak net acceleration in the trials without the soft exoskeleton was $0.616 \pm 0.141\ m/s^2$ and in the trials with the soft exoskeleton $0.347 \pm 0.05\ m/s^2$ as shown in **Figure 9**. Again, both samples are normally distributed and have homogeneous variances. A students t-test shows a significantly lower impact acceleration for the trials with the exoskeleton ($p < 0.001$).

The "dry" trials deliver a maximum angle after a collision of $\varphi_1 = 6.63 \pm 0.75$ for the soft trials and $\varphi_1 = 4.93 \pm 0.38$ for the rigid ones, which lead to a coefficient of restitution of $C_R = 0.432 \pm 0.06$ for the soft and $C_R = 0.329 \pm 0.02$ for the rigid trials. Representative acceleration profiles are shown in **Figure 11**. The recorded peak net acceleration in the "dry" trials without the soft exoskeleton was $4.1 \pm 1.09\ m/s^2$ and in the trials with the soft exoskeleton $2.87 \pm 0.56\ m/s^2$ as shown in **Figure 12**. Because the soft exoskeleton does not substantially affect the mass of the AUV, the acceleration is proportional to the acting force, leading to a factor of nearly 1.5.

DISCUSSION

Inspired by the passive and compliant biological concept, we here present a soft and compliant exoskeleton, fitted to our newly developed SAUV (Soft Autonomous Underwater Vehicle). The SAUVs position tracking is accomplished by a shallow artificial neural network consisting of interlinking PID controllers which are tuned through a genetic algorithm.

Performance of the Genetic Algorithm to Control Motor Outputs

Our results show that using our SAUV as a training platform, application of the Ziegler–Nichols method resulted in an insufficient stabilization compared to the performance of the genetic algorithm. The Ziegler-Nichols PID tuning method is widely used in the controlling of plants, and over the course of the second half of the twentieth century various adjusted versions of it have been published for specific use cases (Ho, 1991; Valério and da Costa, 2006). The classic method used in this research has shown that its aggressive correction due to its high proportional gain leads to an overcompensation which is in itself not consistent yet yields an overall higher Mean Squared Error (MSE).

Other versions of this tuning method take this form of overshoot into account and provide a more appropriate response which can be taken into consideration if revisited in a future study (Ho, 1991). Nevertheless, the fact that such manual tuning methods take a considerable amount of time to perform with uncertain results makes it overall impractical for further use in this scenario. The process of determining Ku at a stable oscillation with adequately small increments as well as the evaluation required to compute T_u took a total of 6 h. Applying the genetic algorithm, following a $(1, 5)^{20}$ evolutionary strategy provided significantly better results within only 8:20 min. Even if a reliable outcome, on par with the genetic algorithm method, could be expected from a heuristically weighted method, the sheer amount of time going into the tuning process would not justify its use. Especially when considering that this method is only applicable in an offline scenario compared to recently published online applications for PID tuning using neural networks (Hernández-Alvarado et al., 2016).

As the learning process itself was performed exclusively during "Hold Position" it is apprehensible that the performance of this method was less accurate under rapidly changing conditions in "*Alter Position*" mode, which aims at producing large disturbances. To a certain extent, this behavior can be interpreted as overfitting of the tuning parameters. The purposely chosen small size of the aquarium might also be the limiting factor at this point, as after a short period of time the creation of vortices within the water could be observed when the system was at work. Because the duration of a single repetition for "*Alter Position*" mode was six times longer than the duration of a "Hold Position" mode repetition, it would have to be

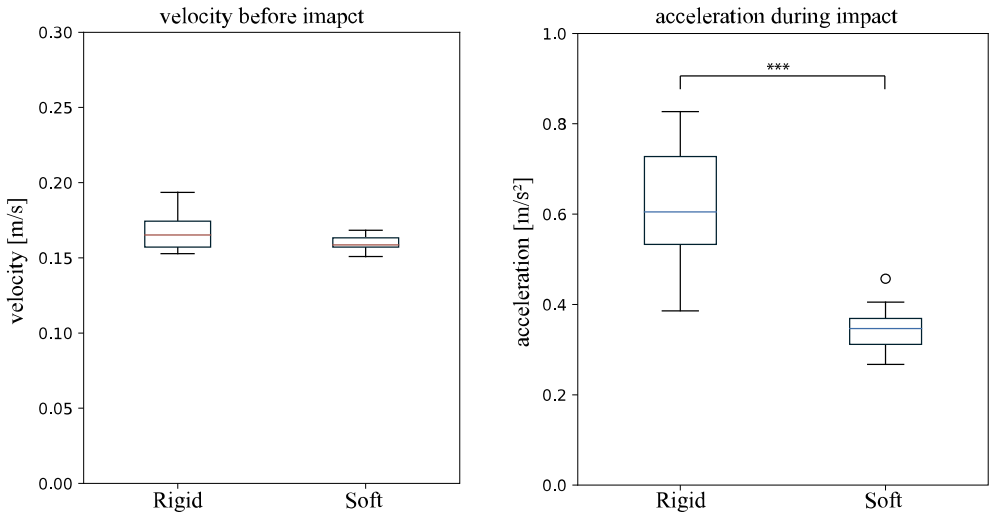

FIGURE 9 | "Wet" Impact trials (conducted underwater in a towing tank). velocity v_{max} (**Left**): The boxplots show the computed velocity in m/s of the system 2 s prior to the registered impact. **Rigid** indicates the data produced by ROV without the mounted soft exoskeleton and **Soft** the data produced with the soft exoskeleton. The computed velocities are not significantly different, indicating there is no effect of the soft exoskeleton on the maximum velocity. Peak net acceleration a_{max} (**Right**): The peak acceleration a_{max} measured during all impact trials with (**Soft**) and without (**Rigid**) the mounted soft exoskeleton. A significant difference between the setup with and without the mounted soft exoskeleton is indicated by *** p returned from a two sample students t-test.

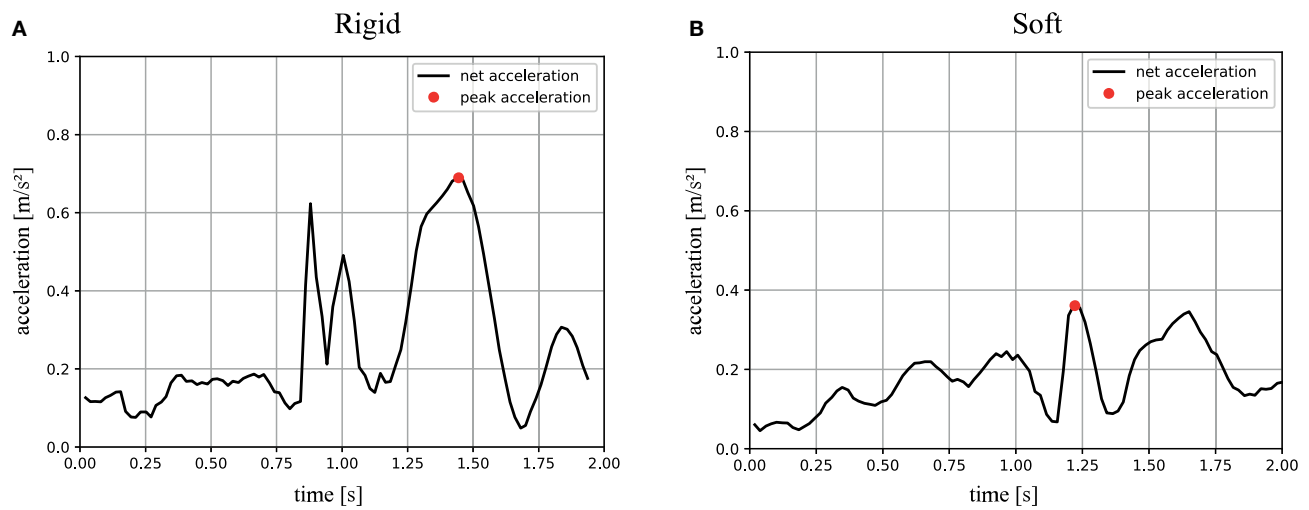

FIGURE 10 | Magnitude of the net acceleration during underwater trials: the black graphs show the magnitude of the net acceleration, corrected for orientation and gravity, of a representative trial, excluding gravity, in m/s during an impact trial without the soft exoskeleton **(A)** and with the soft exoskeleton **(B)**. The data is plotted for 1 s before and after the impact, meaning the onset of the impact was registered by the system at 1 s on the x-axes. The red dots indicate the peak acceleration measured during this time. The constant non-zero magnitude is caused by motor corrections and minor sensor noise.

further investigated whether a decrease in performance could be observed over time which would hint at a negative influence of the testing conditions. It is important to note that the converging performance was not necessarily due to similar combinations of weights but rather multiple local minima of the MSE which all led to acceptable behavior. The simple genetic algorithm, employing a "winner-takes-all" approach paired with fitness function determined by a single dimension of performance, likely needs to include further parameters, training generations, or greater variability in the training conditions to approach a more globally optimal behavior (Lin and Liu, 2010; Jayachitra and Vinodha, 2014; Meena and Devanshu, 2017).

In the future, to improve upon the system's position tracking performance under more complex conditions, control strategies explored in recent publications are to be considered. Especially the current lack of a feed-forward model to control the SAUV, rather than a purely feedback-based control approach needs to

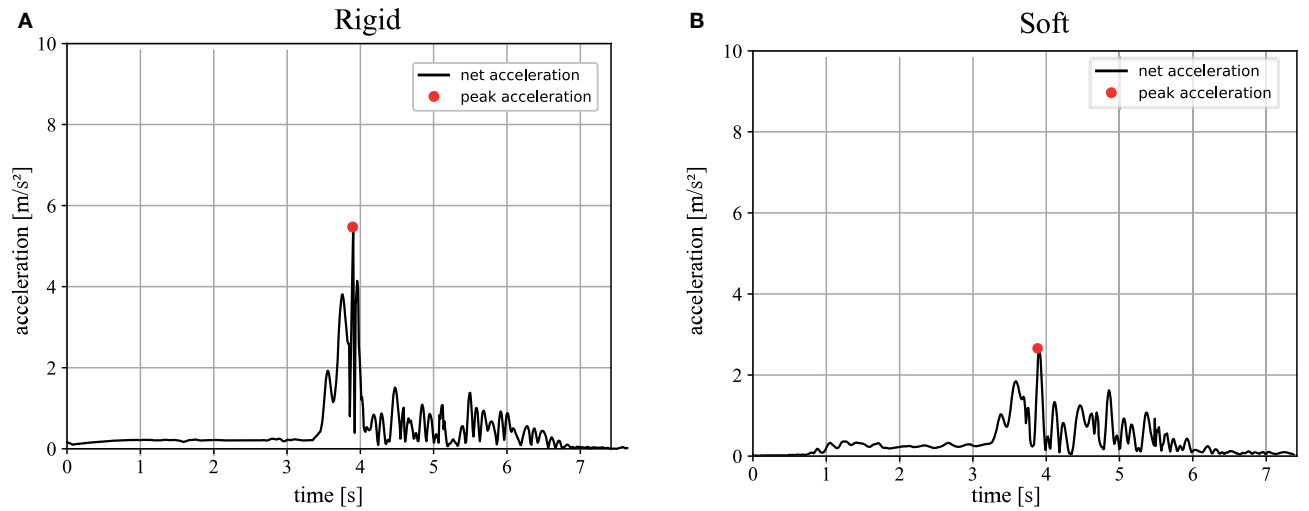

FIGURE 11 | Magnitude of the net acceleration during pendulum trials: the black graphs show the magnitude of the net acceleration, corrected for orientation and gravity, of a representative trial, excluding gravity, in m/s during an impact trial without the soft exoskeleton (**A**) and with the soft exoskeleton (**B**). The data is plotted for the entire duration of the trial, with the release of the system occurring after 3 s and recording until it comes to a rest. The red dots indicate the measured peak acceleration.

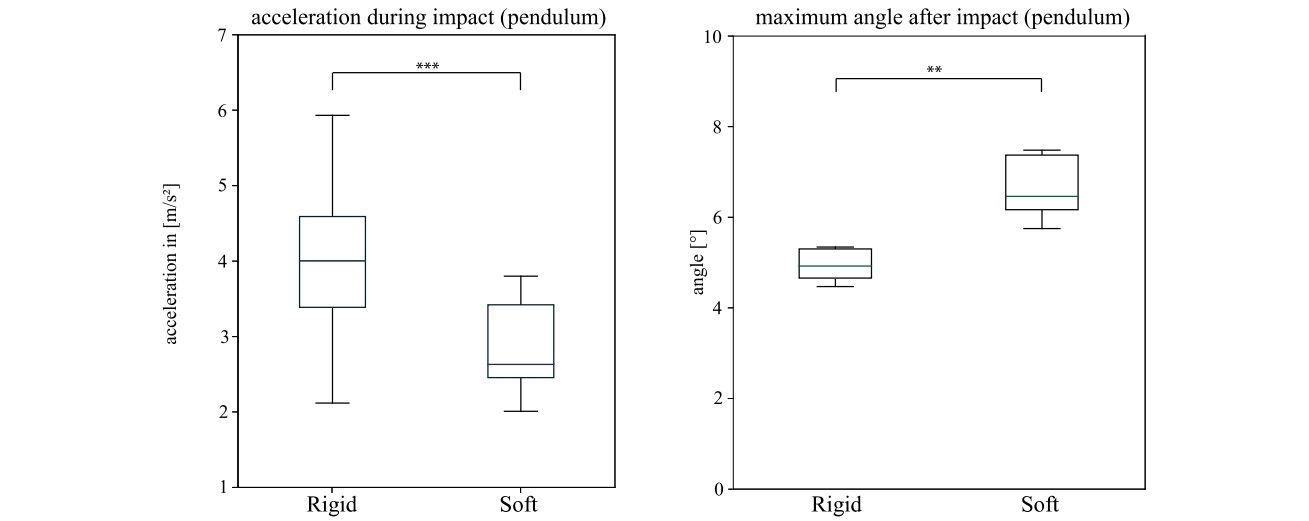

FIGURE 12 | "Dry" Impact trials (gravity pendulum). Comparison Boxplot Peak net acceleration (**Left**): The peak acceleration a_{max} measured during all impact trials with (**Soft**) and without (**Rigid**) the mounted soft exoskeleton. $\varphi_{1\,max}$ (**Right**): The boxplots show the measured maximum assumed angle of the pendulum after the impact of the system. A significant difference between the setup with and without the mounted soft exoskeleton is indicated by ** for a p-value $<$ 0.01 and *** for a p-value $<$ 0.001 returned from a two sample students t-test.

be addressed (Elhaki and Shojaei, 2018; Shojaei, 2019; Wang et al., 2019) as well the potential issue of actuator saturation by utilizing anti-windup compensators (Galeani et al., 2009; Cui et al., 2016; Xia et al., 2019).

In general, the preliminary trials have confirmed the suitability of a biologically plausible genetic algorithm to automatically tune specific sections or the entirety of the controller architecture of such an underwater vehicle. The shallow network structure consisting of interlinking PID controllers can be effectively tuned after comparably few generations and performs significantly better than the heuristic Ziegler-Nichols tuned controller. Major advantages of this implementation include (a) the ability to retrain the system quickly when additional equipment is attached, (b) changing the fitness parameter to include, e.g., the power consumption of the system to select for energetically efficient control strategies, and (c) using the previously adapted parameters to fine-tune the system's response during use. All of the aforementioned advantages are to be explored in-depth as the development of the SAUV continues.

Performance of the Soft and Compliant Exoskeleton

The impact trials in this study clearly show that soft exoskeletons are a viable means to increase the safety and longevity of underwater vehicles while preserving their performance and without limiting the use of sensors or the attached cameras' fields of view. The conducted experiments show that the biologically inspired soft and compliant exoskeleton significantly reduces the net acceleration during an impact without restricting the AUVs performance in terms of its maximum velocity. A lower acceleration indicates lower mechanical stress on the system itself as well as lower reaction forces on its environment. Secondary peaks in the computed net acceleration, as in **Figure 9**, appear whenever there are multiple contact points with the wall during an impact. These peaks are less dominant when the soft exoskeleton is attached as its spherical shape leads to a smaller number of contact points but a larger overall contact area. The higher coefficient of restitution of $C_R = 0.432 \pm 0.06$ for the soft and compliant exoskeleton further indicates a greater reversible deformation. The "dry" trials indicate a reduction in the resulting impact forces of at least 30% when the exoskeleton is mounted on the AUV. Furthermore, in the "dry" trials an increase in the duration of the impact, indicated by the stretched acceleration curves, allows more time for the system to deform. The most striking result lies in the "wet" trials, where a mean reduction of 56% in the occurring peak accelerations can be demonstrated.

To further analyse the effects of an impact on such a system, conducting numerical simulations is a fitting approach. Precise computation of the resulting forces and stresses on the system cannot be performed from IMU data alone, as parameters such as stiffness, damping ratios, as well as contact area vary with the direction and point of impact (Tempelman et al., 2012). Nevertheless, the peak magnitude of the net acceleration is an adequate measure of the severity of an impact.

There is a broad spectrum of applications for this soft exoskeleton. Especially since its use enables divers to safely interact with almost any existing ROV and AUV of any scale as they would no longer have to fear the consequences of an impact by the system. An AUV fitted with a soft exoskeleton may, for example, accompany divers and provide them with lighting of their surroundings or objects in focus to ensure the diver is able to use both of their hands while operating. It is also feasible to send an AUV alongside divers until they reach a machine, crevice or archaeological site which is not directly accessible to the divers. A small AUV with a soft exoskeleton can enter these areas to collect data or perform other tasks. Using our constructed SAUV in a flooded mine, we aim to use it for an automated gathering of omnidirectional video footage for photogrammetry and ultimately an automated 3D reconstruction of previously unmapped or inaccessible cave systems.

Another possible application for such an exoskeleton is the enhancement of scooters and other diving equipment used to propel divers or keep them at a certain depth. Especially when more than one person is operating underwater at the same time, which is a key safety requirement (Buzzacott et al., 2009), the risk of a collision or interference with other machinery must be kept to a minimum. The same principles of the soft exoskeleton may be applied here which make the overall use of these systems safer. In conclusion, the application of our proposed soft exoskeletons results in the following benefits to any underwater vehicle or appliance:

- greatly improves the ability of ROVs and AUVs to operate in an unpredictable environment
- allows for safe operation in close contact with human divers
- reduces the risk of damage to the ROV or AUV
- reduces the risk of damage to the fragile underwater environment
- is a cost-effective means to reduce the need for perfect obstacle avoidance
- is a cost-effective means to upgrade the operational scope and safety of existing systems.

DATA AVAILABILITY STATEMENT

The datasets generated for this study are available on request to the corresponding author.

AUTHOR CONTRIBUTIONS

FP built the AUV, programmed the ANN and collected the experimental data. All authors analyzed the data, interpreted the results, contributed equally to the manuscript and approved the submission.

FUNDING

Open access publication fees were covered by the DFG and the SuUB.

SUPPLEMENTARY MATERIAL

The Supplementary Material for this article can be found online at: https://www.frontiersin.org/articles/10.3389/fnbot.2020.00008/full#supplementary-material

Supplementary Video 1 | (SAUV_Demo.mp4). A short introduction and demonstration of the developed prototype. Footage adapted from Mantismundi (2016) and Smith (2012). Music by Chris Zabriskie (CC BY 4.0).

Supplementary Video 2 | (Comp_Rigid_compressed.mp4). Example recording (top and side view) during an impact trial without the soft and compliant exoskeleton attached.

Supplementary Video 3 | (Comp_Soft_compressed.mp4). Example recording (top and side view) during an impact trial with the soft and compliant exoskeleton attached.

REFERENCES

Arienti, A., Calisti, M., Giorgio-Serchi, F., and Laschi, C. (2013). "PoseiDRONE: design of a soft-bodied ROV with crawling, swimming and manipulation ability," in *2013 OCEANS - San Diego* (San Diego, CA), 1–7.

Belter, J. T., Segil, J. L., Dollar, A. M., and Weir, R. F. (2013). Mechanical design and performance specifications of anthropomorphic prosthetic hands: a review. *J. Rehabil. Res. Dev.* 50, 599–618. doi: 10.1682/JRRD.2011.10.0188

Buzzacott, P. L., Zeigler, E., Denoble, P., and Vann, R. (2009). American cave diving fatalities 1969–2007. *Int. J. Aquatic Res. Educ.* 3:7. doi: 10.25035/ijare.03.02.07

Chyba, M., Haberkorn, T., Singh, S. B., Smith, R. N., and Choi, S. K. (2009). Increasing underwater vehicle autonomy by reducing energy consumption. *Ocean Eng.* 36, 62–73. doi: 10.1016/j.oceaneng.2008.07.012

Cianchetti, M., Calisti, M., Margheri, L., Kuba, M., and Laschi, C. (2015). Bioinspired locomotion and grasping in water: the soft eight-arm OCTOPUS robot. *Bioinspir Biomim.* 10:035003. doi: 10.1088/1748-3190/10/3/035003

Coyle, S., Majidi, C., LeDuc, P., and Hsia, K. J. (2018). Bio-inspired soft robotics: material selection, actuation, and design. *Extreme Mech. Lett.* 22, 51–59. doi: 10.1016/j.eml.2018.05.003

Cui, R., Zhang, X., and Cui, D. (2016). Adaptive sliding-mode attitude control for autonomous underwater vehicles with input nonlinearities. *Ocean Eng.* 123, 45–54. doi: 10.1016/j.oceaneng.2016.06.041

Dirks, J.-H., and Taylor, D. (2012). Fracture toughness of locust cuticle. *J. Exp. Biol.* 215, 1502–1508. doi: 10.1242/jeb.068221

Elhaki, O., and Shojaei, K. (2018). Neural network-based target tracking control of underactuated autonomous underwater vehicles with a prescribed performance. *Ocean Eng.* 167, 239–256. doi: 10.1016/j.oceaneng.2018.08.007

Estes, L. E., Garcia, R., a, and Lizotte, C. D. (1996). Underwater vehicles equipped with laser beacons and tracked from aircraft. *Appl. Opt.* 35, 4843–4849. doi: 10.1364/AO.35.004843

Galeani, S., Tarbouriech, S., Turner, M., and Zaccarian, L. (2009). A tutorial on modern anti-windup design. *Eur. J. Control* 15, 418–440. doi: 10.3166/ejc.15.418-440

Hernández-Alvarado, R., García-Valdovinos, L. G., Salgado-Jiménez, T., Gómez-Espinosa, A., and Fonseca-Navarro, F. (2016). Neural network-based self-tuning pid control for underwater vehicles. *Sensors* 16:1429. doi: 10.3390/s16091429

Ho, W. K. (1991). Refinements of the Ziegler–Nichols tuning formula. *IEE Proc. D Control Theory Appl.* 138, 111–118. doi: 10.1049/ip-d.1991.0015

Hudson, I. R., Jones, D. O. B., and Wigham, B. D. (2005). A review of the uses of work-class ROVs for the benefits of science: lessons learned from the SERPENT project. *Underwater Technol.* 26, 51–56. doi: 10.3723/175605405784426637

Jayachitra, A., and Vinodha, R. (2014). Genetic algorithm based PID controller tuning approach for continuous stirred tank reactor. *Adv. Artif. Int.* 2014, 1–8. doi: 10.1155/2014/791230

Kim, H. J., Song, S. H., and Ahn, S. H. (2013). A turtle-like swimming robot using a smart soft composite (SSC) structure. *Smart Mater. Struct.* 22:014007. doi: 10.1088/0964-1726/22/1/014007

King, R. L., and Beams, H. W. (1941). Some effects of mechanical agitation on *Paramecium caudatum*. *J. Morphol.* 68, 149–159. doi: 10.1002/jmor.1050680108

Laschi, C., Mazzolai, B., and Cianchetti, M. (2016). Soft robotics: technologies and systems pushing the boundaries of robot abilities. *Sci. Robot.* 1, 1–12. doi: 10.1126/scirobotics.aah3690

Lin, G., and Liu, G. (2010). "Tuning PID controller using adaptive genetic algorithms," in *ICCSE 2010 - 5th International Conference on Computer Science and Education, Final Program and Book of Abstracts* (Hefei), 519–523. doi: 10.1109/ICCSE.2010.5593559

Mantismundi (2016). *Amoeba Extends Large Pseudopods or Runs Over Its Prey*. Available online at: https://www.youtube.com/watch?v=D0E_KzOQ7bo (accessed June 14, 2019).

Meena, D. C., and Devanshu, A. (2017). "Genetic algorithm tuned PID controller for process control," in *Proceedings of the International Conference on Inventive Systems and Control, ICISC* (Coimbatore), 1–6. doi: 10.1109/ICISC.2017.8068639

Nistler, J. R., and Selekwa, M. F. (2011). Gravity compensation in accelerometer measurements for robot navigation on inclined surfaces. *Proc. Comput. Sci.* 6, 413–418. doi: 10.1016/j.procs.2011.08.077

Persat, A., Nadell, C. D., Kim, M. K., Ingremeau, F., Siryaporn, A., Drescher, K., et al. (2015). Review the mechanical world of bacteria. *Cell* 161, 988–997. doi: 10.1016/j.cell.2015.05.005

Rechenberg, I. (1989). "Evolution strategy: nature's way of optimization," in *Optimization: Methods and Applications, Possibilities and Limitations: Proceedings of an International Seminar Organized by Deutsche Forschungsanstalt für Luft- und Raumfahrt (DLR), Bonn, June 1989,* ed H. W. Bergmann (Berlin, Heidelberg: Springer Berlin Heidelberg), 106–126.

Rechenberg, I. (2000). Case studies in evolutionary experimentation and computation. *Comput. Methods Appl. Mech. Eng.* 186, 125–140. doi: 10.1016/S0045-7825(99)00381-3

Riedmiller, M., and Braun, H. (1993). "A direct adaptive method for faster backpropagation learning: the RPROP algorithm," in *IEEE International Conference on Neural Networks* (San Francisco, CA), 586–591. doi: 10.1109/ICNN.1993.298623

Shojaei, K. (2019). Three-dimensional neural network tracking control of a moving target by underactuated autonomous underwater vehicles. *Neural Comput. Appl.* 31, 509–521. doi: 10.1007/s00521-017-3085-6

Smith, C. (2012). *Paramecium Feeding Magnified 400X! High Definition!* Available online at: https://www.youtube.com/watch?v=fh_yjLppNAg (accessed June 14, 2019).

Stocker, R. (2011). Reverse and flick: hybrid locomotion in bacteria. *Proc. Natl. Acad. Sci. U.S.A.* 108, 2635–2636. doi: 10.1073/pnas.1019199108

Sumpio, B. E. (2017). Mechanical stress and cell growth. *J. Vasc. Surg.* 10, 570–571. doi: 10.1016/0741-5214(89)90146-8

Tempelman, E., Dwaikat, M. M. S., and Spitas, C. (2012). Experimental and analytical study of free-fall drop impact testing of experimental and analytical study of free-fall drop impact testing of portable products. *Exp. Mech.* 52, 1385–1395. doi: 10.1007/s11340-011-9584-y

Trivedi, D., Rahn, C. D., Kier, W. M., and Walker, I. D. (2008). Soft robotics: biological inspiration, state of the art, and future research. *Appl. Bion. Biomech.* 5, 99–117. doi: 10.1155/2008/520417

Turton, R., and Levenspiel, O. (1986). A short note on the drag correlation for spheres. *Powder Technol.* 47, 83–86. doi: 10.1016/0032-5910(86)80012-2

Valavanis, K. P., Gracanin, D., Matijasevic, M., Kolluru, R., and Demetriou, G. A. (1997). Control architectures for autonomous underwater vehicles. *IEEE Control Syst.* 17, 48–64. doi: 10.1109/37.642974

Valério, D., and da Costa, J. S. (2006). Tuning of fractional PID controllers with Ziegler-Nichols-type rules. *Signal Process.* 86, 2771–2784. doi: 10.1016/j.sigpro.2006.02.020

Vincent, J. F. V., and Wegst, U. G. K. (2004). Design and mechanical properties of insect cuticle. *Arthropod Struct. Develop.* 33, 187–199. doi: 10.1016/j.asd.2004.05.006

Wang, J., Wang, C., Wei, Y., and Zhang, C. (2019). Sliding mode based neural adaptive formation control of underactuated AUVs with leader-follower strategy. *Appl. Ocean Res.* 94:101971. doi: 10.1016/j.apor.2019.101971

Warren, C. W. (1990). A technique for autonomous underwater vehicle route planning. *IEEE J. Ocean. Eng.* 15, 199–204. doi: 10.1109/48.107148

Wegst, U. G. K., Bai, H., Saiz, E., Tomsia, A. P., and Ritchie, R. O. (2015). Bioinspired structural materials. *Nat. Mater.* 14, 23–36. doi: 10.1038/nmat4089

Xia, Y., Xu, K., Li, Y., Xu, G., and Xiang, X. (2019). Improved line-of-sight trajectory tracking control of under-actuated AUV subjects to ocean currents and input saturation. *Ocean Eng.* 174, 14–30. doi: 10.1016/j.oceaneng.2019.01.025

Zhong, Z., Zhu, Y., and Ahn, C. K. (2018). Reachable set estimation for Takagi-Sugeno fuzzy systems against unknown output delays with application to tracking control of AUVs. *ISA Trans.* 78, 31–38. doi: 10.1016/j.isatra.2018.03.001

Ziegler, J. G., and Nichols, N. B. (1942). Optimum setting for automatic controllers. *Transact. ASME* 64, 759–768.

Conflict of Interest: The authors declare that the research was conducted in the absence of any commercial or financial relationships that could be construed as a potential conflict of interest.

frontiers in Neurorobotics

TECHNOLOGY AND CODE
published: 26 February 2020
doi: 10.3389/fnbot.2020.00014

Small-Sized Reconfigurable Quadruped Robot With Multiple Sensory Feedback for Studying Adaptive and Versatile Behaviors

Tao Sun[1], *Xiaofeng Xiong*[2], *Zhendong Dai*[1] *and Poramate Manoonpong*[1,2]*

[1] *Institute of Bio-inspired Structure and Surface Engineering, College of Mechanical and Electrical Engineering, Nanjing University of Aeronautics and Astronautics, Nanjing, China,* [2] *Embodied AI & Neurobotics Lab, SDU Biorobotics, Mærsk Mc-Kinney Møller Institute, University of Southern Denmark, Odense, Denmark*

Self-organization of locomotion characterizes the feature of automatically spontaneous gait generation without preprogrammed limb movement coordination. To study this feature in quadruped locomotion, we propose here a new open-source, small-sized reconfigurable quadruped robot, called Lilibot, with multiple sensory feedback and its physical simulation. Lilibot was designed as a friendly quadrupedal platform with unique characteristics, including light weight, easy handling, modular components, and multiple real-time sensory feedback. Its modular components can be flexibly reconfigured to obtain features, such as different leg orientations for testing the effectiveness and generalization of self-organized locomotion control. Its multiple sensory feedback (i.e., joint angles, joint velocities, joint currents, joint voltages, and body inclination) can support vestibular reflexes and compliant control mechanisms for body posture stabilization and compliant behavior, respectively. To evaluate the performance of Lilibot, we implemented our developed adaptive neural controller on it. The experimental results demonstrated that Lilibot can autonomously and rapidly exhibit adaptive and versatile behaviors, including spontaneous self-organized locomotion (i.e., adaptive locomotion) under different leg orientations, body posture stabilization on a tiltable plane, and leg compliance for unexpected external load compensation. To this end, we successfully developed an open-source, friendly, small-sized, and lightweight quadruped robot with reconfigurable legs and multiple sensory feedback that can serve as a generic quadrupedal platform for research and education in the fields of locomotion, vestibular reflex-based, and compliant control.

Keywords: quadruped robot, multiple sensory feedback, self-organized locomotion, vestibular reflexes, compliant control, flexible configuration

OPEN ACCESS

Edited by:
Florian Röhrbein, Independent Researcher, Winnenden, Germany

Reviewed by:
Dai Owaki, Tohoku University, Japan
Luca Patanè, University of Catania, Italy

***Correspondence:**
Poramate Manoonpong
poma@nuaa.edu.cn

Received: *04 July 2019*
Accepted: *10 February 2020*
Published: *26 February 2020*

Citation:
Sun T, Xiong X, Dai Z and Manoonpong P (2020) Small-Sized Reconfigurable Quadruped Robot With Multiple Sensory Feedback for Studying Adaptive and Versatile Behaviors. Front. Neurorobot. 14:14. doi: 10.3389/fnbot.2020.00014

1. INTRODUCTION

The motor behaviors of animals are characterized by numerous features (Dickinson et al., 2000). Several of these basic features, such as self-organization, vestibular reflexes, and compliance, play fundamental roles in achieving adaptive and versatile locomotion behaviors. Self-organization of locomotion represents the capability of autonomously spontaneous locomotion generation (Taga et al., 1991; Owaki et al., 2013; Tao et al., 2018). Vestibular reflexes and compliance can

extend the functionality of self-organized locomotion in response to unexpected situations, such as abrupt changes in the ground plane and external perturbation. Therefore, understanding the biological principles of these properties contributes to revealing the underlying mechanisms of adaptive locomotion generation (Taga et al., 1991), and the subsequent development of advanced artificial legged robots (Hutter et al., 2017). However, it is not convenient to investigate the locomotor principles by means of animal experiments alone, because, in general, it is difficult to perform repeated measurements of the variables or quantities of unrestrained animal behaviors (Ijspeert, 2014). Fortunately, quadruped robots can serve as useful research tools for studying and validating the mechanisms or hypotheses of the various features of legged locomotion (Ijspeert, 2014; Karakasiliotis et al., 2016).

Over the past decades, several excellent quadruped robots have been developed for researching certain specific locomotion characteristics. For example, several large-sized quadruped robots, such as BigDog (Marc et al., 2008), LS3[1], Wildcat[2], and HyQ serial (Semini et al., 2011, 2016), with masses of over 100 kg and driven by hydraulics, have been developed through studies on high-power actuators, dynamic motions, and navigation (Raibert, 1986). The purpose of these studies focused on developing high-performance artificial machines for mobility in natural environments through engineering approaches. However, despite the performance of the robots shedding significant light on legged robotic applications in the transport field, thus far, they have not been used to investigate the mechanisms of self-organized locomotion generation and basic research. Moreover, their heavy weight and large size may result in a high-operation complexity as well as pose dangers for handlers or researchers who may use them as a legged platform for studying bio-inspired locomotion control (Eckert et al., 2018).

Therefore, several moderate-sized robots (with masses between 20 and 50 kg), such as the MIT Cheetah (Seok et al., 2013; Wensing et al., 2017; Bledt et al., 2018), ANYmal (Hutter et al., 2016), Spotmini[3], and Laikago[4], have been developed for researching the specific issue of quadrupedal locomotion, which includes proprioceptive actuators, electrically powered actuators, as well as learning agile and dynamic motor skills (Hwangbo et al., 2019). These robots have exhibited such stable and dynamic locomotor capabilities that they are quite suitable for studying high-level application techniques (for example, path planning, navigation, and transportation). However, it remains somewhat challenging to use these robots for investigating middle-level locomotion control (such as self-organized locomotion generation, reflex mechanisms, and compliant control), because their powerful actuators [that of the MIT Cheetah is ∼230 Nm (Bledt et al., 2018)] still pose a danger to single researchers while directly manipulating their joints (Eckert et al., 2018). Furthermore, the development and hardware costs of these robots are quite high.

[1]https://www.bostondynamics.com/ls3
[2]https://www.bostondynamics.com/wildcat
[3]https://www.bostondynamics.com/spot-classic
[4]https://www.unitree.cc

Consequently, small-sized, in detail, lightweight and compact, quadruped robots would offer an excellent option for studying adaptive locomotion generation. Several existing studies in this field have been presented to date. For example, Fukuoka et al. constructed a series of Tekken robots (Kimura and Fukuoka, 2004; Fukuoka and Kimura, 2009) and the Spinalbot robot (Fukui et al., 2019) to investigate bio-inspired adaptive locomotion mechanisms [central pattern generators (CPGs) and reflexes mechanism] with predefined interlimb coordination. Although their robots exhibit dynamic locomotion and gait transition, it is hard to use them for studying self-organized interlimb locomotion owing to their binary foot contact sensors, as the self-organized interlimb coordination is a continuous and dynamic interaction process among continuous sensory feedback, neural control, and body-environment dynamics (Owaki et al., 2013; Tao et al., 2018).

To overcome this problem, a series of the OSCILLEX robots (Owaki et al., 2012, 2013; Owaki and Ishiguro, 2017) were developed by Owaki et al. These robots were equipped with analog force sensors to obtain continuous foot contact feedback. They were used to investigate self-organized interlimb coordination for self-organized locomotion based on decoupled CPGs. With a simple robot structure in which each leg has two degrees of freedom (DOFs), OSCILLEX can autonomously perform adaptive locomotion patterns according to the walking speed and weight distribution. Nevertheless, it is difficult to use OSCILLEX with fixed leg configurations to investigate the effectiveness and generalization of self-organized locomotion regarding various leg configurations. Typically, existing small-sized quadruped robots lack sufficient sensory feedback (i.e., body inclination, joint current, and joint voltage) to investigate vestibular reflexes, compliance, and other adaptive and versatile behaviors in various expected situations. Moreover, they are not an open-source platform; therefore, limited access is offered to the community for rebuilding robots in their own studies. Therefore, to explore the features of quadrupedal locomotion (i.e., self-organized locomotion, vestibular reflexes, compliance, and their interactions, a small-sized, lightweight, and affordable quadruped robot) as a friendly research tool, with flexible configurations and sufficient sensory feedback, is a significant necessity for our research community.

In this study, we highlight our efforts to develop an open-source, small-sized, affordable quadruped robot, called Lilibot, in simulation and hardware, with flexibly reconfigurable leg orientations and multiple sensory feedback. The compact Lilibot was flexibly organized using lightweight modular components. These features enabled it to serve as a friendly quadrupedal platform. Furthermore, an adaptive neural controller was implemented to test Lilibot performance. The test included: (1) self-organized locomotion under flexibly reconfigurable leg orientations; (2) vestibular reflexes for stabilizing the body posture on a tiltable plane; and (3) compliant behaviors regarding an external load. Details on Lilibot and its adaptive neural control are provided in section 2. The performance examination of Lilibot is presented in section 3. Finally, section 4 provides a discussion of the experimental results and conclusion.

2. METHODOLOGY

In this section, we briefly introduce the main approaches and processes of Lilibot design, of which the basic restrictions are the small size, in detail, light weight, robust, and compactness but rich sensory feedback. To meet these requirements, selection and sizing of high-end small servo motors with comparative torque density were firstly considered. Secondly, according to the motor dimensions (XM430 from ROBOTIS[5]) and a template model (Full and Koditschek, 1999) of a mammal (i.e., dog), we determined the kinematics and link structures of the leg. The leg should have a large workspace for flexible leg configurations, as well as sufficient proprioceptive sensory feedback for compliant control. Thirdly, the legs were appropriately organized using a trunk, in which several necessary electrical devices for supporting the vestibular reflex control were installed. The final step was to optimize the mechanics of Lilibot iteratively through physical simulation controlled by specific algorithms in the virtual robot experimentation platform (V-REP) (Rohmer et al., 2013).

2.1. System Overview

In this quadrupedal locomotion research system, the real Lilibot and its simulated model in the V-REP are controlled by an adaptive neural controller (**Figure 1**) through the Robot Operation System (ROS) (Quigley et al., 2009). The ROS serves as a framework for linking the three components (simulated robot, controller, and real robot) and providing their communication channels through the ROS interfaces. In the simulation (**Figure 2A**), various values [i.e., motor commands from the controller, sensory signals from the simulated robot, and outputs of all sub-control modules (**Figure 2B**)] of the system can easily be monitored using the graph tools of the V-REP. The parameters of the monitored values can be easily adjusted through the user interface (UI) of the V-REP. Moreover, kinematics and dynamics modules as well as scene objects (i.e., force sensors) of the V-REP can be used to inspect the leg workspace and joint forces of Lilibot. The measurements can be regarded as estimations to iteratively optimize the leg structure design before constructing a physical one (**Figure 2C**). From this point of view, we can improve the robot development efficiency and save the development cost. In the Lilibot system (**Figure 1**), we can first develop and evaluate an adaptive neural controller in the simulation and then directly test it on the real robot without any modifications. The details of the real Lilibot and the adaptive neural controller are presented in the following parts.

2.2. Robot Development

2.2.1. Specifications of Lilibot

The final version of Lilibot, following optimization by means of simulation in the V-REP, is presented in **Figure 3**. With reference to the current proficient template [SLIP (Poulakakis and Grizzle, 2009; Yu et al., 2012)] and anchor (for example, Spotmin and Laikago) of quadrupedal locomotion, Lilibot was designed with four identical legs, namely the right front (RF) leg, right hind (RH) leg, left front (LF) leg, and left hind (LH) leg. Each leg consists of three links, namely the hip, femur, and tibia, and has three active joints (hip 1 joint, hip 2 joint, and knee joint), which are driven by smart servo motors (4.2 Nm, XM430 from ROBOTIS). The tibia link is connected to a foot with a shape resembling a "T" that provides a large support area. The main components of the leg are illustrated in **Figure 3C**, and are constructed using 3D printing or made of carbon fiber. The four legs are attached to a rigid trunk that carries an inertial measurement unit (IMU), an onboard PC, and a Li-ion battery (14.8 V–4 Ah), which could supply Lilibot as a compact mobile platform to run for more than an hour. With a payload of ∼1.25 kg, Lilibot can walk for up to 30 min[6]. The weight and dimensions of Lilibot are presented in **Table 1**. Detailed information regarding the leg configurations and multiple sensory feedback is provided in the following subsection. The open source (including the code for the interface and 3D CAD model) of Lilibot can be viewed at https://gitlab.com/neutron-nuaa/lilibot. The total hardware cost of Lilibot is 5,381 USD.

2.2.2. Flexibly Reconfigurable Leg Orientations

Different species of four-limbed mammals, such as dog, infant, and horse, particularly with varying size scales, have distinct skeleton topologies, especially in the legs. Therefore, when researchers have modeled their structures for building real robots (anchor models) to study quadrupedal locomotion, various leg orientations (joint/leg configurations) have appeared in certain impressive robots (Marc et al., 2008; Fukuoka and Kimura, 2009; Semini et al., 2011; Sprowitz et al., 2013; Wensing et al., 2017; Bledt et al., 2018). Several researchers have specifically studied the influence of multiple leg orientations on the movement performance. For instance, Xiuli et al. demonstrated that centrosymmetric joint configurations (i.e., outward and inward pointing, **Figure 4**) are beneficial for avoiding slipping to increase stability (Xiuli et al., 2005). Moreover, Meek et al. argued that appropriate leg configurations could achieve optimal stabilization in specific situations, such as a simulated quadruped robot with inward-pointing configuration has the lowest pitching motion compared to other three configuration types (Meek et al., 2008). Therefore, it is necessary to construct Lilibot with flexible leg configurations, thereby facilitating studies on the effectiveness and generalization of locomotion control under the different configurations.

Based on the assumptions, we developed Lilibot with flexible leg configurations. This advantage results from each joint of the legs having extensive rotation ranges, which provide the legs with a large and symmetric workspace (**Figure 4A**). Hence, Lilibot can flexibly reconfigure its leg orientations. **Figures 4B–E** present Lilibot with four configuration types using different leg orientations. With reference to Xiuli et al. (2005), we called these the all-elbow, all-knee, outward-pointing, and inward-pointing configurations. The configurations have been used in various classical robots; for example, the all-elbow and all-knee configurations were applied to certain small- and moderated-sized robots [Spotmini, Laikago, and MIT cheetah (Seok et al.,

[5]http://www.robotis.us/

[6]http://www.manoonpong.com/Lilibot/video0.mp4

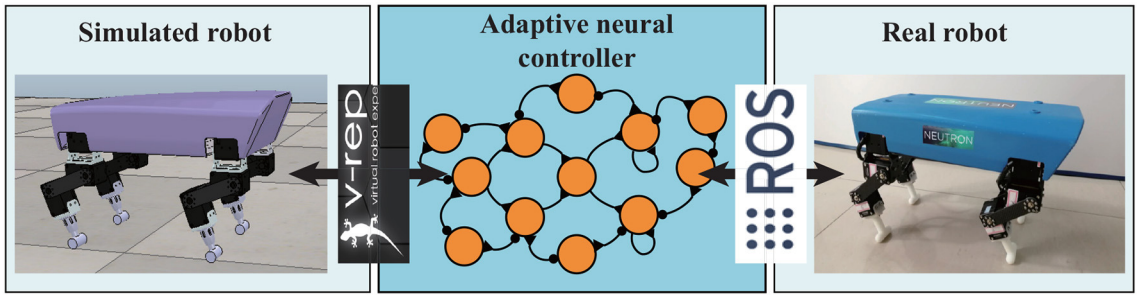

FIGURE 1 | System overview of Lilibot. The adaptive neural controller is implemented in ROS such that it can directly communicate with both the simulated robot in the V-REP simulation and the real robot. The simulated and real robots were consistently developed, such that the simulation demonstrates a good estimation of the actual performance. A video showing a comparison between the simulated and real robot behaviors can be seen at http://www.manoonpong.com/Lilibot/video6.mp4.

2013)], while the inward-pointing configuration was applied to several large-sized quadruped robots [including HyQ (Semini et al., 2011) and BigDog (Marc et al., 2008)], and the outward-pointing configuration was applied to the very heavy robot LS3.

2.2.3. Multiple Sensory Feedback

Abundant sensory feedback plays a vital role in the successful implementation of various control strategies in robots. Thus, we installed as many sensors as possible on this relatively small robot to investigate adaptive and versatile behaviors (see **Table 2**). As a result, a nine-axis IMU and twelve smart actuators with encoders and analog-to-digital converters were installed in Lilibot. The IMU (JY901 of ZNJ) can measure the body inclination, angular velocities, and velocities around three axes. Moreover, each actuator with an encoder and one analog-to-digital converters on the joint can detect and feed the joint position, velocity, current, and voltage. Furthermore, considering the simplification of the foot structure, we utilized the current feedback of the servo motors at the knee joints to reflect the ground reaction force (GRF) quantity by means of an indirect conversion algorithm. The mechanism of the algorithm is that the GRF of a leg, which indicates the load on the leg, has a positive correlation with the keen joint current. The algorithm is given by the following equations:

$$f_i = \begin{cases} 0, 0 \geq g_i \\ g_i, 0 < g_i < f_{\text{limit}} \\ f_{\text{limit}}, g_i \geq f_{\text{limit}} \end{cases}, f_{\text{limit}} = 1.2, \quad (1)$$

$$g_i = k_i \tau_i + b_i(v), \quad (2)$$

$$k_i = \begin{cases} 1.1, i = 0, 1 \\ -1.1, i = 2, 3 \end{cases}, \quad (3)$$

$$b_i(v) = \begin{cases} -0.3 + 1.2v, i = 0, 3 \\ -0.25 + 1.2v, i = 1, 2 \end{cases}, \quad (4)$$

where f_i represents the indirect GRF of the leg i, which is normalized into a range (0, 1). τ_i is the current feedback of the servo motor at the knee joint, while k_i and b_i are the slope and intercept of the linear function g_i, respectively. f_{limit} is the threshold of the indirect GRF, and v is the joint velocity. A measured GRF (obtained from the custom-designed force plate platform for legged robots) is used as a baseline for tuning the model parameters. One can observe a positive correlation between the keen joint current signal and the GRF signal. The signals show high activation (>0.0) when the leg is in a stance phase and low activation (around 0.0) when it is in a swing phase. An experiment for tuning the parameters of the model can be seen in **Figure S1**. This algorithm not only decreases the robot structural complexity, but also increases the stability of the perceptive system of Lilibot, owing to removing the extra force sensors on its legs and, hence, reducing complex signals acquisition and communication tasks.

Although Lilibot exhibited a small size and compact space, the onboard PC (NUC7 from Intel Inc.) can simultaneously acquire 61 sensory feedback signals (see **Table 1**) at a frequency of 180 Hz. The rich sensory feedback and compact actuators enable Lilibot to be a compact and generic legged platform for supporting various control modes (e.g., position control, velocity control, and compliant control, as well as vestibular reflex control). In addition to the existing sensors, additional USB ports of the onboard PC provide available interfaces for including other sensors.

2.3. Adaptive Neural Controller

To test the performance of Lilibot as a friendly quadrupedal platform, particularly for studying adaptive and versatile behaviors, including vestibular reflexes and leg compliance, it is necessary to implement control. For this purpose, by exploring bio-inspired approaches with sensorimotor loop (Hülse et al., 2007) and referring to Owaki et al. (2013), an adaptive neural controller (**Figure 5**) was developed[7]. It consists of three sub-control modules: (I) decoupled CPGs control; (II) vestibular reflex control; and (III) compliant control. The decoupled CPGs control can be used to validate whether Lilibot could perform self-organized locomotion, derived from the self-organized

[7] In this paper, we briefly describe the controller since it is not the main focus of the paper, but it is necessary for demonstrating the performance of our open-source platform Lilibot (which is our main focus).

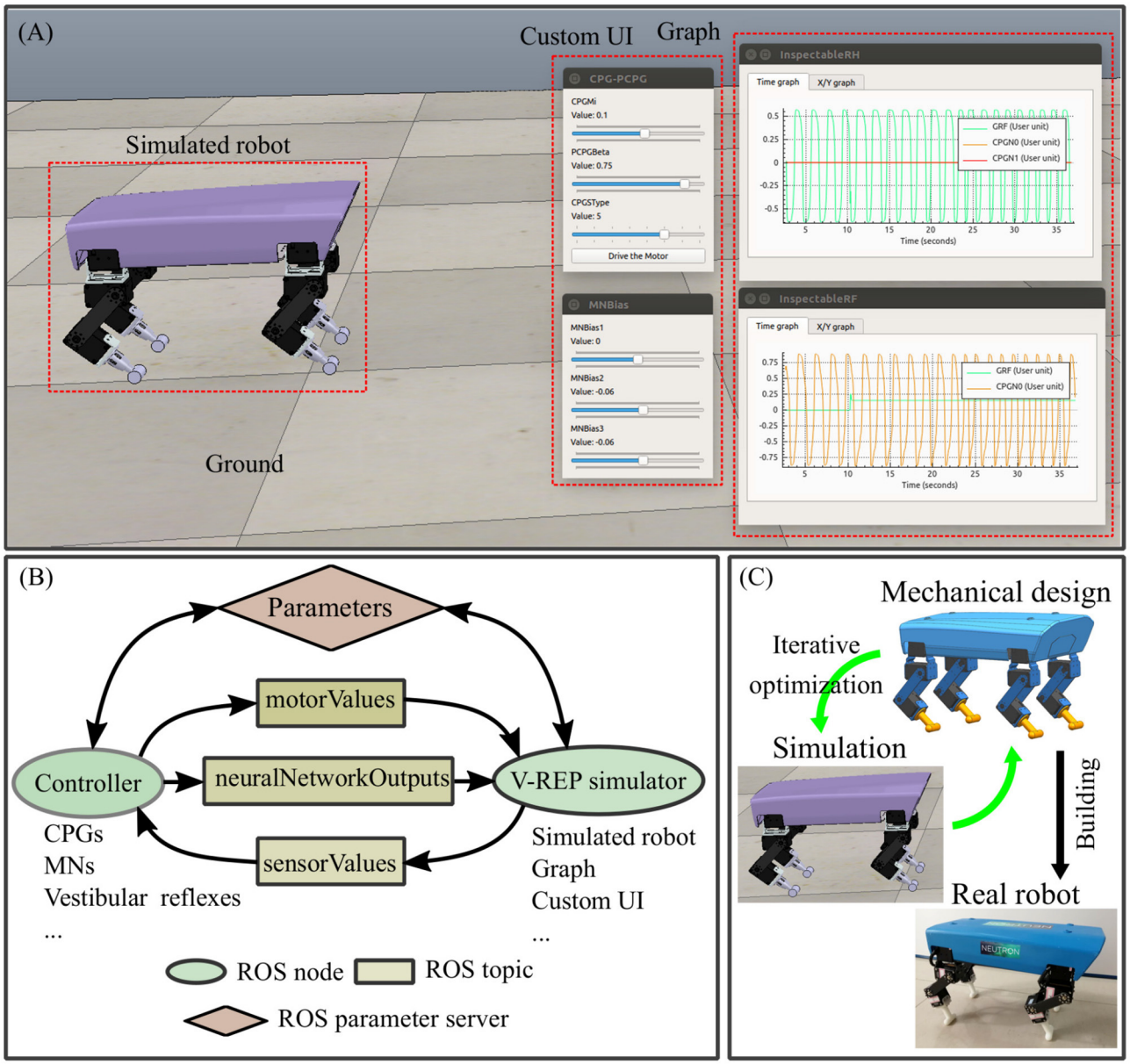

FIGURE 2 | Lilibot simulation and its developmental process. **(A)** The virtual robot experimentation platform (V-REP) (Rohmer et al., 2013) simulation scene of Lilibot. The mechanical model of Lilibot is loaded into the V-REP to create a simulated robot in a virtual environment. The V-REP provides the graph tools to monitor various signals (including motor commands, outputs of the sub-control modules, and sensory signals). Besides, the custom UI of the V-REP can be used to adjust the control parameters [such as in this study, CPG frequency and amplitude as well as sensory feedback strength of the decoupled CPGs control (see Tao et al., 2018) and the weight parameters of the vestibular reflex control (**Figure 7**)]. **(B)** The simulator is based on the V-REP and the robot operation system (ROS) (Quigley et al., 2009). The communication between the controller (ROS node1) and the simulator (ROS node2) is accomplished through three ROS topics and a parameter server. The topics include (1) a "motorValues" topic transmitting motor commands of joints from the controller to the simulated robot; (2) a "sensorValues" topic transmitting sensory signals of the simulated robot to the controller; (3) a "neuralNetworkOutputs" topic transmitting the outputs of the sub-control modules. The parameters of the controller are accessed through a ROS parameter server. The communication between the controller (ROS node1) and the real robot (ROS node3) is also performed in the same manner through the ROS topics and the parameter server. **(C)** The mechanical design is iteratively optimized using the V-REP simulation.

interlimb coordination, as well as its effectiveness under different leg orientations. The vestibular reflex control was designed to validate whether Lilibot could adaptively stabilize the body posture on a tiltable plane. The compliant control based on the hybrid torque-position control principle was designed to test whether Lilibot could exhibit compliant behaviors when responding to an external load. Both the decoupled CPGs and vestibular reflex control modules output the desired positions of all joints. The desired positions are transmitted to the compliant control module (low-level control). Thereafter, the compliant

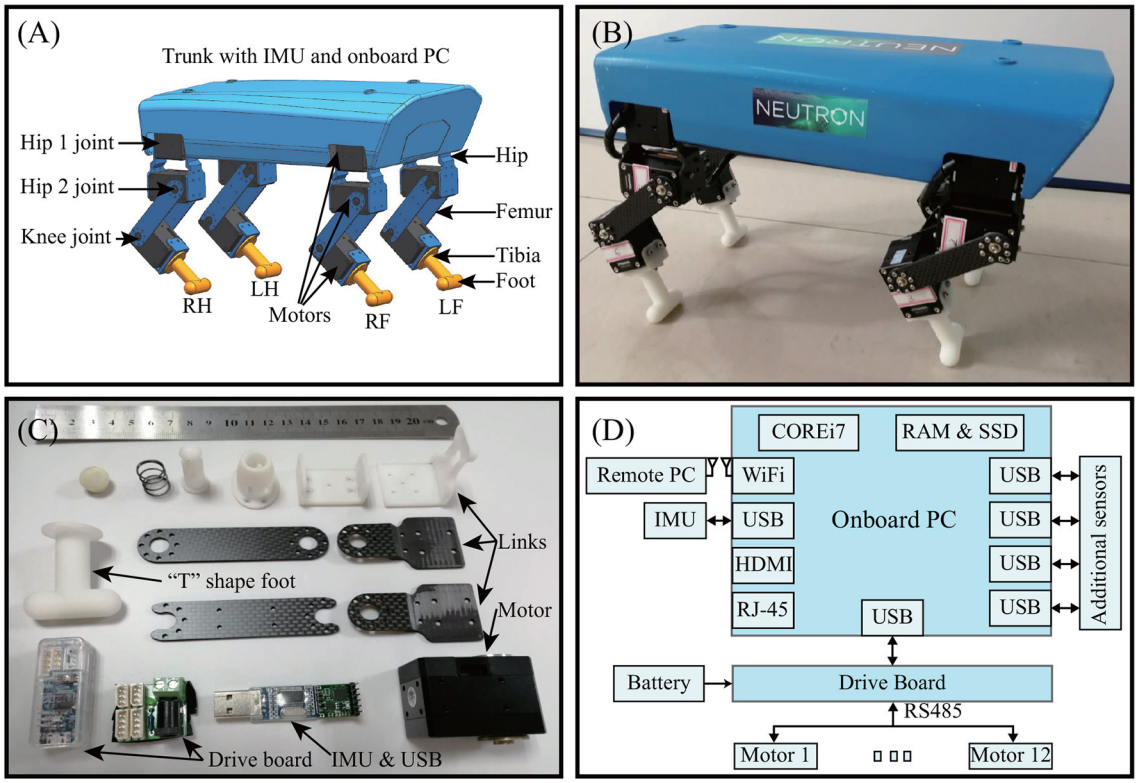

FIGURE 3 | Lilibot. **(A)** CAD model. **(B)** Real robot with a weight of 2.5 kg. Its length, width, and height are 30, 17.5, and 20 cm, respectively, when it stands. **(C)** Main components of one leg. **(D)** Mobile processor system.

TABLE 1 | The weight and dimensions of Lilibot.

Weight	2.5 kg
Length	30 cm
Width	17.5 cm
Height	20 cm

control transforms the desired positions into the desired currents that finally drive the robot as torque control.

2.3.1. Decoupled CPGs Control

The details of the decoupled CPGs control are illustrated in **Figure 6**. The control has four identical and decoupled neural SO(2) oscillators (Pasemann et al., 2003) (acting as CPGs). A single leg of Lilibot is controlled by the decoupled CPG consisting of two fully connected standard additive time-discrete neurons, N1 and N2, both using a sigmoid transfer function. Although there is no connection between the CPGs, their outputs interact through their corresponding/local foot contact feedback, i.e., GRFs. The GRFs shape the outputs of the CPGs such that proper phases between the CPGs emerge to obtain a stable gait. The two outputs with a phase shift of $\pi/2$ are transmitted to control the actuators of the hip 2 and knee joints of the leg (**Figure 3**). As a result, the two joints of each leg move with a phase shift of $\pi/2$. In this manner, for each leg, the knee joint flexes first and is followed by the hip 2 joints generating forward leg motion in the swing phase. During the stance phase, the knee joint extends to allow the foot to touch the ground before the hip 2 joint moves backward. Note that the hip 1 joints of all legs are set to fixed positions for the sake of simplicity. This intralimb movement coordination guarantees ground clearance during the swing phase and ground contact during the stance phase.

To achieve stable gaits, a self-organized method is applied by means of physical communication based on local sensory feedback (namely, GRF) (Tao et al., 2018). In this manner, the GRFs are fed to the corresponding CPGs to modulate their phases. Owing to the GRF differences among the four legs when the robot wriggles on the ground, the effectiveness of the modulations is diverse, and thereby, the phase shifts among the four CPGs emerged autonomously. This results in phase differences in the limb movements. As the phase differences converge, a self-organized locomotion gait is generated.

2.3.2. Vestibular Reflex Control

Inspired by natural vestibular reflex behaviors, our neural reflex mechanism (Tao et al., 2018) was extended to vestibular reflexes for testing the performance of the IMU inclination measurement on Lilibot, as well as the capability of Lilibot to stabilize its body posture. In this case, four distributed vestibular reflexes (**Figure 7**) were implemented to control the legs depending on the body pitch and roll inclination. For example, when there is

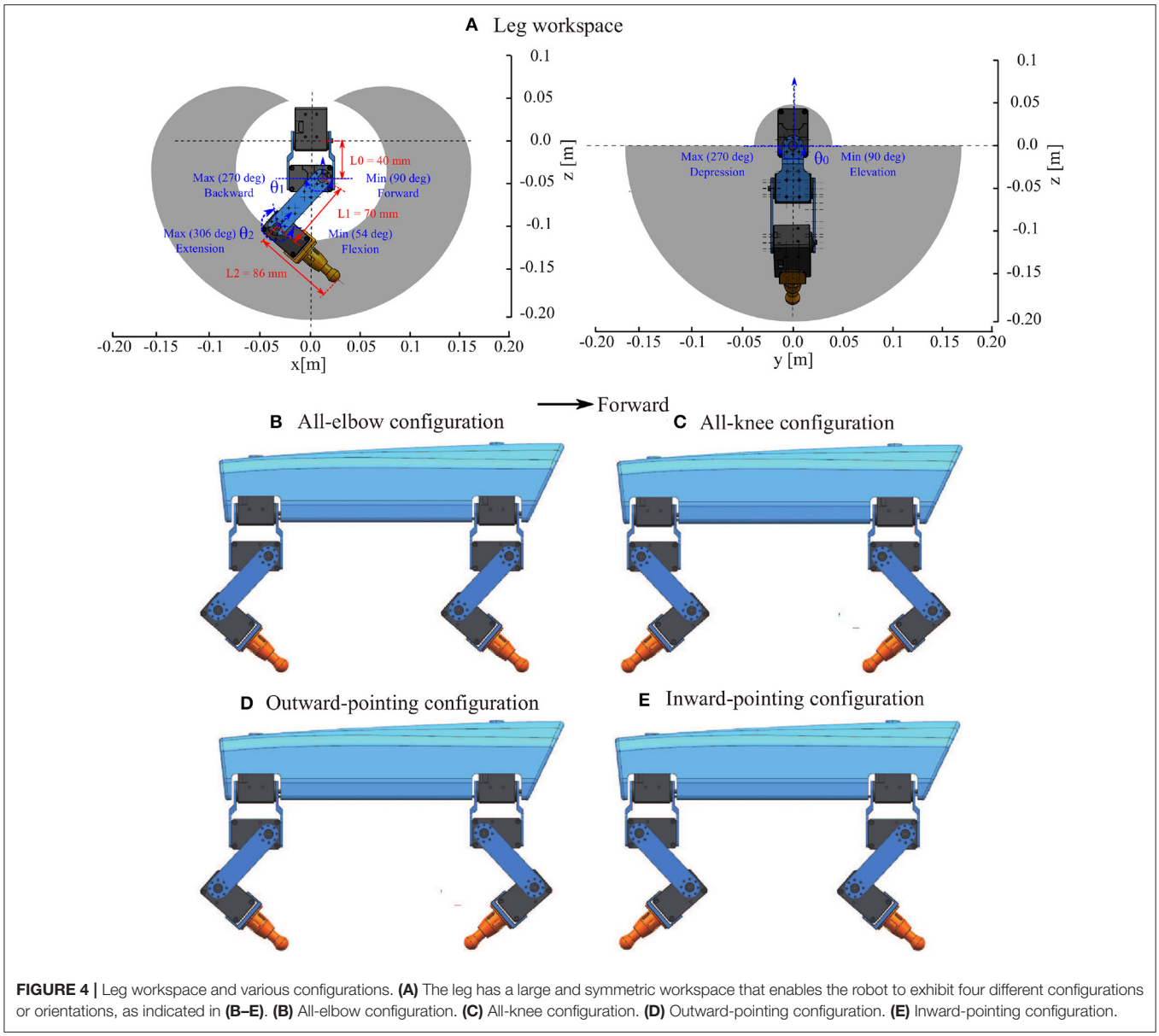

FIGURE 4 | Leg workspace and various configurations. **(A)** The leg has a large and symmetric workspace that enables the robot to exhibit four different configurations or orientations, as indicated in **(B–E)**. **(B)** All-elbow configuration. **(C)** All-knee configuration. **(D)** Outward-pointing configuration. **(E)** Inward-pointing configuration.

a detected inclination in the pitch or roll plane, the downward-inclined and upward-inclined legs would be controlled to extend and flex, respectively.

The single vestibular reflex is realized by a feedforward neural network with four layers composed of six neurons. Their transfer functions are hyperbolic tangent functions, except for those of N5 and N6, which are linear functions. The weights w_{1r} and w_{1p}, are specified in the table in **Figure 7**, and determine the interlimb coordination of the responding movements. Although the neural network has non-linear transforms, for the sake of simplification, the functionality of the transformation can be considered as a combination of several multiplication and addition operations because the inputs (body inclination) of the neural network are scaled into the linear interval of the transfer functions. The neural network outputs two coordinative signals, which are transmitted to the hip 2 and knee joints of a leg through low-level control (e.g., compliant control), thereby manipulating the leg to extend or flex depending on the body inclination.

TABLE 2 | All sensors and amount of sensory feedback of Lilibot.

Sensors	Feedback	Quantity/61
IMU	Body inclinations	3
	Angular velocities	3
	Velocities	3
Encoder	Joint positions	12
	Joint velocities	12
AD	Joint currents	12
	Joint voltages	12
Indirection measurement	Foot contact force	4

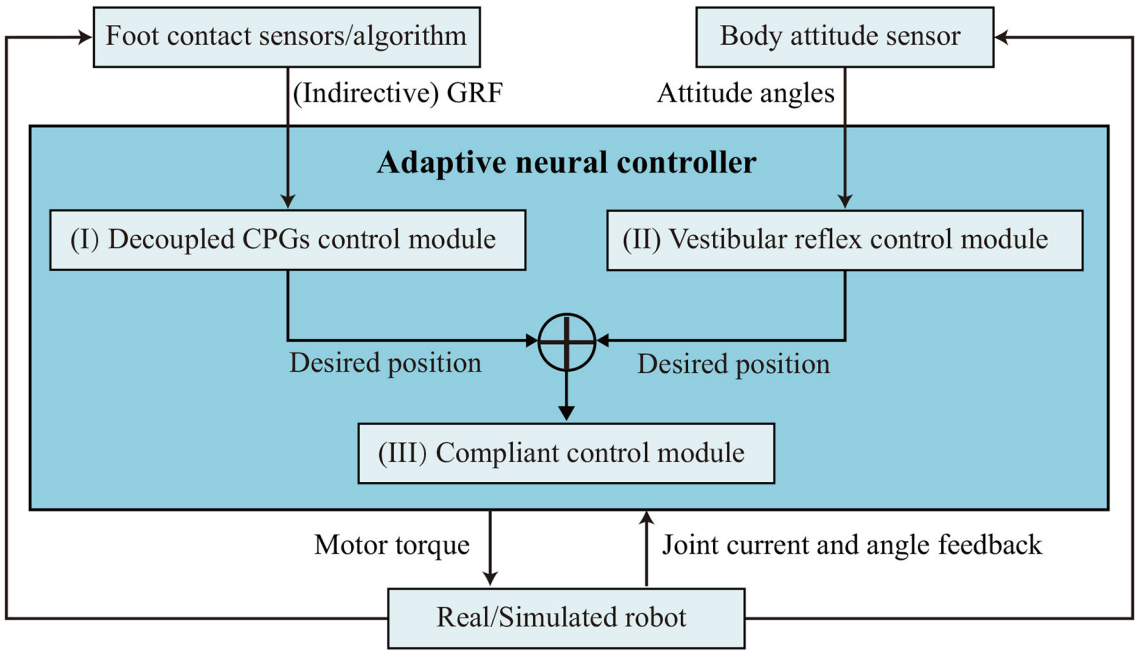

FIGURE 5 | Framework of adaptive neural controller.

2.3.3. Compliant Control

As a low-level control, compliant control (**Figure 8**) is implemented to control actuators precisely and gently when the robot encounters unexpected external perturbation. It has three control loops: (1) feedforward control for rapid response to the desired position, (2) high gain proportional derivative (PD) control for position control with feedback to reduce the position error, and (3) current PD control for torque control. The outputs of the position control are the desired inputs of the torque control. The control framework was implemented on Lilibot to demonstrate compliance for negotiating external loads, as detailed in subsection 3.3.

3. EXPERIMENTS AND RESULTS

Four sets of experiments were performed to test the performance of Lilibot, implemented with the presented adaptive neural controller, as a quadrupedal platform. The three control modules (decoupled CPGs control, compliant control, and vestibular reflex control) in the adaptive neural controller were conducted separately first for clearly demonstrating the functionality of the different features of Lilibot. Subsequently, a combination of the vestibular reflex and compliant controls was executed to evaluate their integrated functions. Therefore, the experiments consisted of: (1) self-organized locomotion under different leg orientations, driven by the decoupled CPGs control, (2) leg compliance to compensate for an unexpected external load, driven by the compliant control, (3) body stabilization on a tiltable plane, driven by the vestibular reflex control, and (4) body stabilization and payload compensation on a tiltable plane, driven by the combination of the vestibular reflex and compliant controls.

3.1. Self-Organized Locomotion Under Different Leg Orientations

Four experiments were performed to test whether Lilibot could exhibit self-organized locomotion driven by the decoupled CPGs control under the four leg orientation types (four leg configurations (see **Figures 4B–E**). In all experiments, the decoupled CPGs were initialized to output in phase with the same parameters, while the robot was held in the air at the beginning [see the stage (i) in **Figure 9**]. We observed that as soon as the robot was placed on the ground [see stage (ii) in **Figure 9**], the representation feedback of the GRFs on the feet was fed to the CPGs to modulate their neural activities, thereby adapting the phases of the CPGs' outputs [see stage (iii) in **Figure 9**]. Consequently, a trot gait autonomously emerged in stage (iv). In the gait diagram (see **Figure 9**), the black regions represent the stance phases, which are detected by the GRFs. For example, if a GRF is higher than a threshold value, a stance phase is indicated. Thin stripes in the gait diagram represent oscillations of the GRFs data around the threshold value. According to the results, such a quadruped-like gait was generated in a self-organized manner under the four leg orientation types when using our decoupled CPGs. A video clip of this experiment was recorded (at http://www.manoonpong.com/Lilibot/video1.mp4).

To evaluate the energetic cost of the locomotion under the four leg configurations, the specific resistance was used. It is defined as the ratio between the consumed energy and the transferred gross weight times the distance traveled (Manoonpong et al., 2016):

$$\epsilon = \frac{E}{mgd}, \tag{5}$$

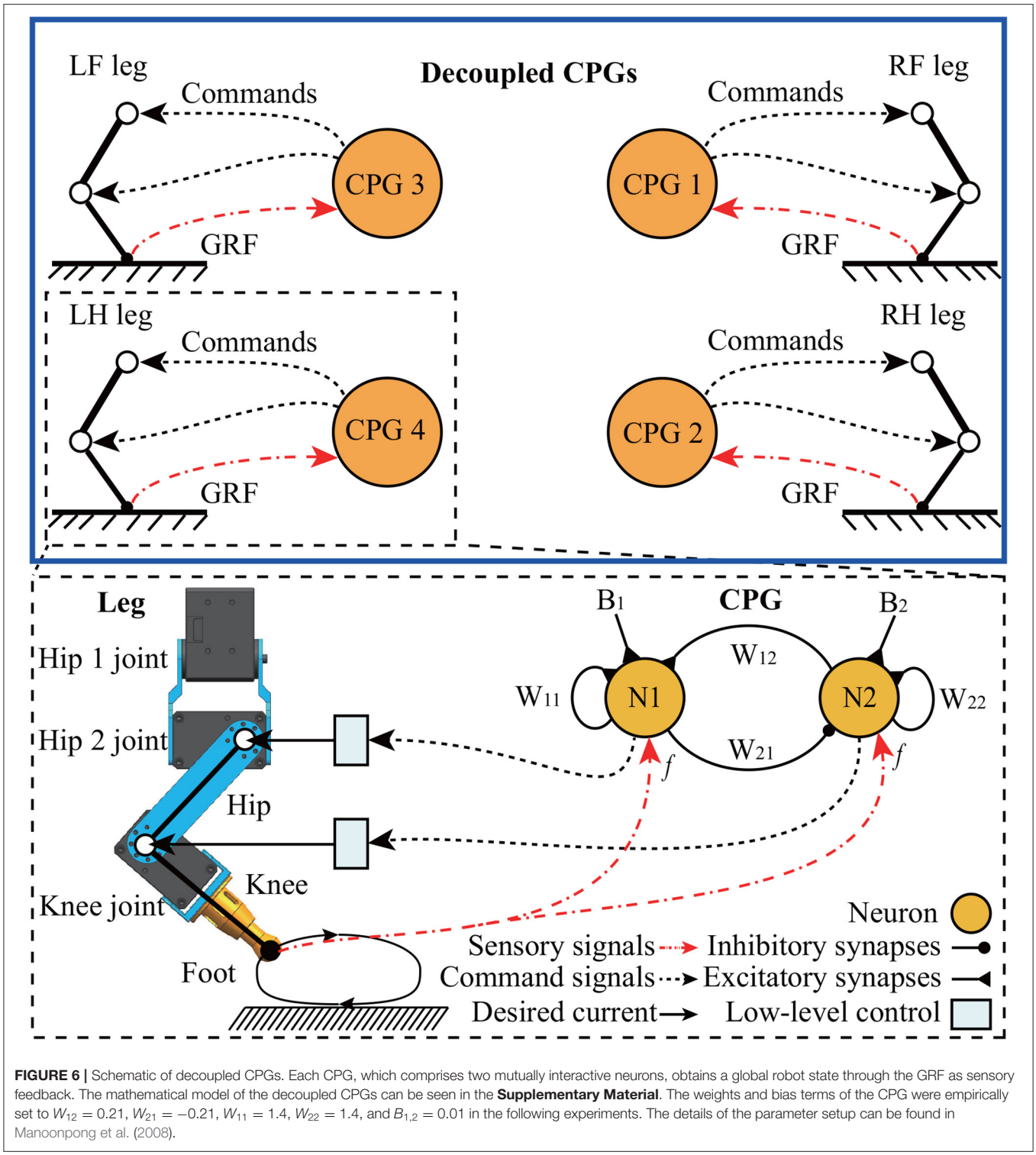

FIGURE 6 | Schematic of decoupled CPGs. Each CPG, which comprises two mutually interactive neurons, obtains a global robot state through the GRF as sensory feedback. The mathematical model of the decoupled CPGs can be seen in the **Supplementary Material**. The weights and bias terms of the CPG were empirically set to $W_{12} = 0.21$, $W_{21} = -0.21$, $W_{11} = 1.4$, $W_{22} = 1.4$, and $B_{1,2} = 0.01$ in the following experiments. The details of the parameter setup can be found in Manoonpong et al. (2008).

where E is the consumed energy of the robot motors when the robot walks a distance d (i.e., 1 m) and mg is the weight of the robot. The energy is estimated from: $E = IVt$, where I and V are the electric current and voltage, respectively. They can be acquired from the joint current and voltage sensors. t is the time the robot uses when it walks a distance d. The average specific resistances of Lilibot under the four leg configurations (all-elbow, all-knee, outward-pointing, and inward-pointing) are $\sim 3.57 \pm 0.12$, 3.32 ± 0.43, 5.16 ± 0.32, and 3.82 ± 0.30, respectively. A low ϵ corresponds to high energy-efficient walking. Thus, the results indicate that the all-elbow and all-knee configurations have relative high energy efficiency and the outward-pointing

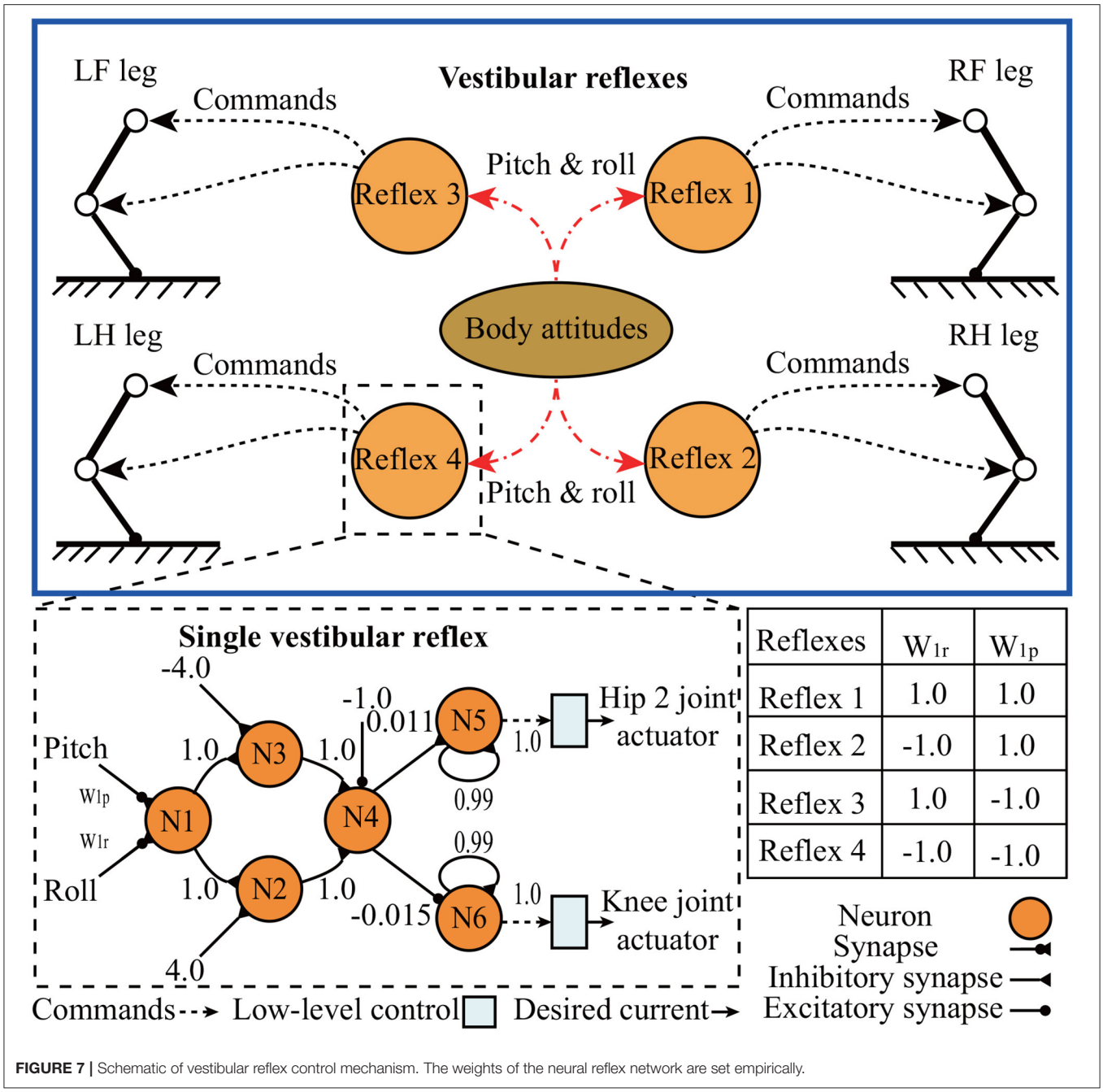

Reflexes	W_{1r}	W_{1p}
Reflex 1	1.0	1.0
Reflex 2	-1.0	1.0
Reflex 3	1.0	-1.0
Reflex 4	-1.0	-1.0

FIGURE 7 | Schematic of vestibular reflex control mechanism. The weights of the neural reflex network are set empirically.

configuration exhibits the lowest energy efficiency. The details of the experiment can be seen in **Figure S2**.

3.2. Compliant Behavior for Unexpected Load Compensation

Compliance is an important function that allows a robot to effectively deal with unexpected load or large perturbation. In this experiment, we demonstrated that Lilibot could deal with an unexpected load (i.e., hand loading) based on the presented compliant control (**Figure 10**). To clearly demonstrate the effect of the compliant control, we switched off the decoupled CPGs and vestibular reflex control (high-level control) by setting their outputs to zeros (see **Figure 5**). At the beginning of the experiment, the robot stood on the ground in stage (i), in which all joints stayed in their normal positions. The normal positions as a reference were inputted into the compliant control as the desired positions (see **Figure 8**). Thereafter, we pushed the robot body by a hand in stage (ii) from ∼3 to 8.2 s, and instead of the rigid status controlled only by highly stiff position control, the robot actively exhibited softness. When the push was withdrawn in stage (iii), the robot returned to its initial

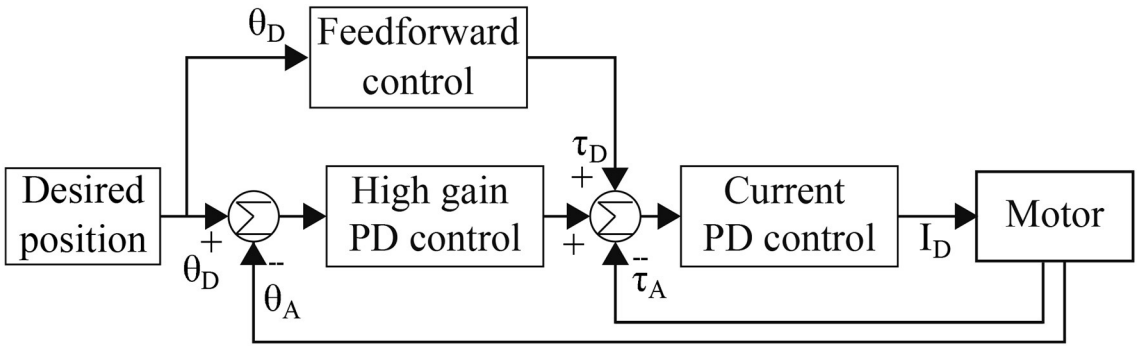

FIGURE 8 | Block diagram of compliant control mechanism loop: θ_D and θ_A represent the desired and actual joint positions, respectively; τ_D and τ_A are the desired and actual motor torques; and I_D is the desired current for driving the motor.

standing posture. As an example, the angle feedback of the right front leg joints is depicted in **Figure 10**, reflecting the active compliant movement of the joints responding to the external hand load. Consequently, it was concluded that Lilibot is capable of exhibiting compliant leg behavior based on our controller. A video clip of this experiment was recorded (at http://www.manoonpong.com/Lilibot/video2.mp4).

3.3. Body Stabilization on a Tiltable Plane

To test the effectiveness of the IMU sensor of Lilibot for body stabilization, an experiment was conducted using the presented vestibular reflexes on Lilibot because the vestibular reflex control can stabilize the robot according to the inclination feedback measured by the IMU. Firstly, Lilibot, with vestibular reflexes, was placed on a tiltable plane (see **Figure 11**). The experiment consists of four procedures [stages (i)–(iv)]. The plane pitch angle was changed in stage (ii), and the robot performed extension or flexion of the legs to stabilize the body, depending on the inclination feedback from the IMU. As a result of the vestibular reflexes, the pitch angles of the body returned to ∼0 following oscillation. Similarly, the changed plane roll angle made the robot extend or flex its legs to maintain its body level in the roll direction during stage (iii). The experimental results demonstrate that the vestibular reflexes could sustain the stabilization of Lilibot on a tiltable plane. Therefore, we also assert that the IMU enabled Lilibot to exhibit vestibular reflexes. A video clip of this experiment was recorded (at http://www.manoonpong.com/Lilibot/video3.mp4).

3.4. Body Stabilization and Payload Compensation on a Tiltable Plane

A combination among the self-organized locomotion, vestibular reflexes and leg compliance plays a crucial role for adaptive locomotion on natural terrains (Fukuoka et al., 2003; Liu et al., 2013). As an example here, we show a combination of the vestibular reflexes and the leg compliance. This combination was applied to demonstrate body stabilization under a complex situation.

To demonstrate the effectiveness of the combination, we performed two comparative experiments: (1) vestibular reflexes with leg compliance and (2) vestibular reflexes without leg compliance. In both experiments, Lilibot was placed on a tiltable plane under a roof (i.e., an upper plane). The roof acts as a payload (>1.0 kg) if the supported tiltable plane is inclined upward (e.g., 20 degrees) where Lilibot hits the roof. Note that a case with only leg compliance was not used because Lilibot without vestibular reflexes cannot keep balance on the plane if it is tilted or inclined. The experimental results are shown in **Figure 12**.

It can be seen that the behaviors of the robot under the two controls were different when it negotiated the payload while standing on the slope. Without leg compliance, Lilibot rigidly resisted the payload; thereby, the knee joints of its front legs drew a substantial amount of current (**Figures 12B,D**). In this situation, the pitch angle of Lilibot also showed a large value (**Figure 12A**). This could result in imbalance. In contrast, with leg compliance, Lilibot could soften or flex its legs (showing compliance behavior) when it encountered the payload. By doing so, the knee joints of its front legs drew less current (**Figures 12B,D**) since the Lilibot did not resist the payload. The results indicate that Lilibot under the combination of the vestibular reflex and compliant controls showed better performance and adaptation compared with pure vestibular reflex control. A video clip of this experiment was recorded (at http://www.manoonpong.com/Lilibot/video4.mp4).

4. DISCUSSION AND CONCLUSION

In this work, we developed a small size, light weight quadruped robot (Lilibot) with flexible configurations and multiple sensory feedback. Lilibot can act as a friendly open-source platform for research and education in the field of locomotion. The features of small size and light weight provide Lilibot with several apparent advantages, such as an easily modular design, and simple yet practical structure. It can be handled with ease to conduct joint control and locomotion generation owing to its appropriate (1) actuator torque (4.2 Nm, which is not dangerous to handlers), (2) size (its length, width, and height are 30, 17.5, and 20 cm, respectively, when it stands), and (3) weight (2.5 kg) for operation. Moreover, it has a considerable endurance capability,

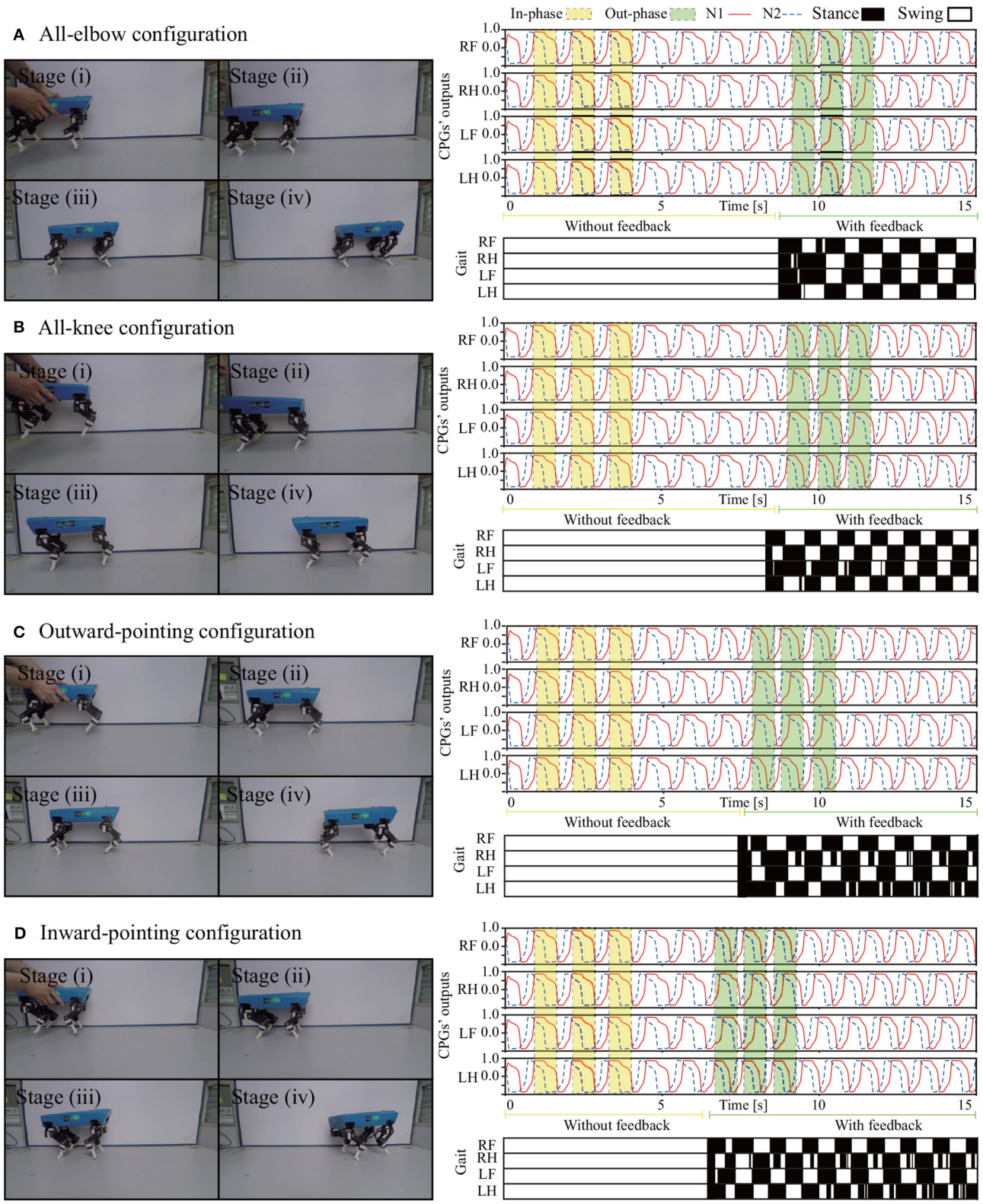

FIGURE 9 | Process of self-organized locomotion generation under four leg orientation types, as indicated in **(A–D)**. **(A)** All-elbow configuration. **(B)** All-knee configuration. **(C)** Outward-pointing configuration. **(D)** Inward-pointing configuration. The outputs of the CPGs started in phase, and once the robot interacted with the ground, the phases began to be adjusted by the GRFs. The gaits quickly emerged within 8 s.

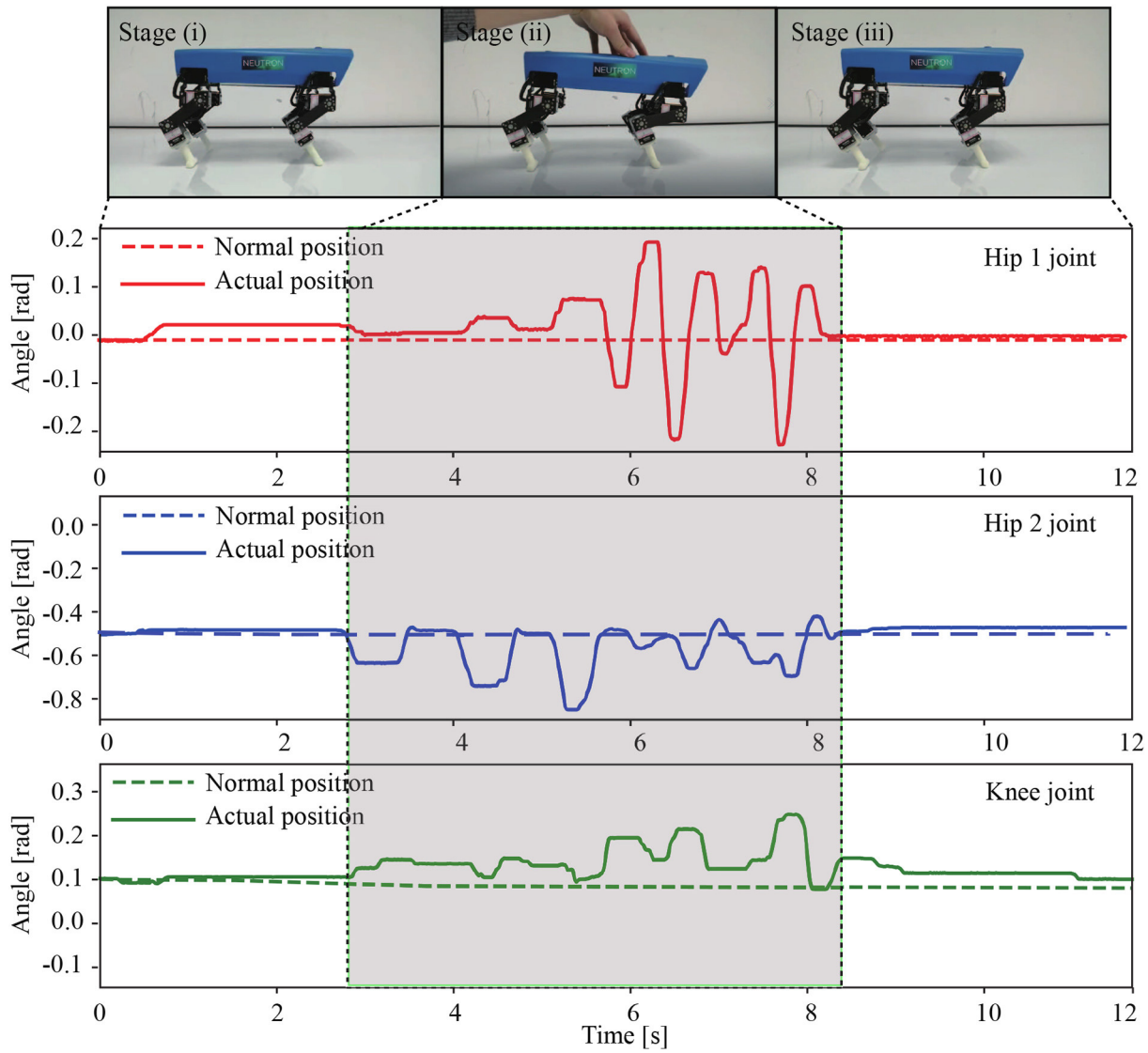

FIGURE 10 | Compliant behavior of Lilibot and angle feedback of the hip 1, hip 2, and knee joints of the RF leg. The normal positions of joints were the desired positions of compliant control. The robot was placed on the ground and was stooding in the initial stage (i). In stage (ii), a hand was used to apply a force on its body, and the robot exhibited compliance to compensate for the perturbation. During stage (iii), the robot returned to its normal position after the load was removed.

which allows it to handle a payload of ∼1.25 kg (50% of its weight) with walking, for up to 30 min. This enables Lilibot to carry extra exteroceptive sensors (e.g., cameras and laser radars for studying motion planning in complex environments). In addition to the real robot, the compatible Lilibot simulation (see **Figure 2**) allows to develop and test controllers before transferring to the real one.

The experimental results show that Lilibot, with its controller, can exhibit three basic functions, including autonomous gait generation under different reconfigurable leg orientations (**Figure 9**), compliance behavior for unexpected load compensation (**Figure 10**), and body stabilization on a tiltable plane (**Figure 11**). The three functions that we focused on have been found in various animals. They play crucial roles in biological legged locomotion (Dickinson et al., 2000; Fukuoka et al., 2003). The functions are fundamental ingredients for developing an advanced artificial legged system with adaptive, autonomous, and self-organized locomotion. In addition, a variety of sensory feedback (see **Table 2**) is required to realize the three functions. Therefore, by exploiting these functions, we can effectively demonstrate the capability of Lilibot serving as a quadrupedal platform for research and education in bio-inspired locomotion. We provide the detailed reasons why the three functions are interesting as follows:

Firstly, self-organization of locomotion, in this study, is considered as an ability of a legged system (e.g., Lilibot) that can form a gait in a self-organized manner, in which its inherent physical properties play a crucial role for interlimb coordination

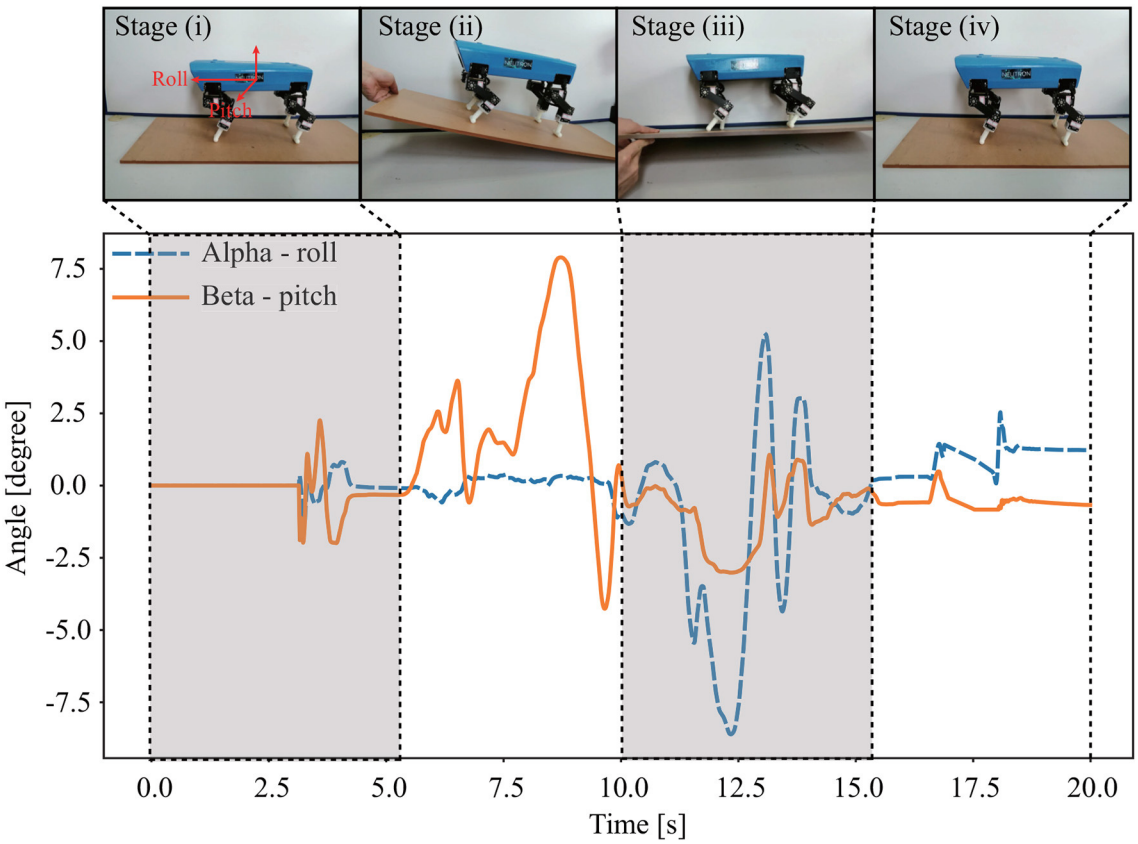

FIGURE 11 | Snapshot and body attitude angles of Lilibot in the experiment, where Lilibot sustained its body attitude stabilization while the supported tiltable plane inclined around the pitch and roll planes in stages (ii) and (iii), respectively.

via sensory feedback (i.e., continuous via interacting with the ground Owaki et al., 2013. The appropriate single leg movement driven by CPG signals can demonstrate the basic motor function of a leg while the formed interlimb coordination driven by decoupled CPGs with GRF modulations can be used to explore the interaction between robot dynamics and the environment (see **Figure 6**). The self-organized locomotion realized on the flexible or reconfigurable structures of Lilibot shows both the adaptation of the decoupled CPGs control to its different leg configurations and the utilization of its motor current feedback to reflect the GRF quantity for gait formation. This elucidates the effectiveness of the robot structure design and the used robot actuators with proprioceptive feedback (e.g., current).

In this work, Lilibot shows trot gaits in the four leg configurations under the decoupled CPGs control with the same initialization. The gaits indicate that specific phase relationships among the four CPGs of the legs emerge automatically. The phases of CPGs are inhibited by their continuous GRFs (see **Figure 6**) if the legs are still on the ground. For example, if a leg is driven to swing by the CPG signals but it cannot swing or lift above the ground, then the GRF will inhibit the CPG signals to make the corresponding leg stay on the ground (stance phase) slightly longer to acquire more GRF. Acquiring more GRF or the maximum GRF during the stance phase of each leg leads to more stable locomotion. A situation that provides maximum GRF at each leg with stable locomotion is when diagonal legs of the robot move at the same phase, e.g., the right front leg and the left hind leg stay on the ground at the same time while the other legs swing in the air and vice versa. This results in a trot gait. This strategy holds for any leg configuration as long as the body can keep balance during a stance phase. An example of the gait generation process can be seen in **Figure S3**.

In the experiments of the self-organized locomotion (shown in **Figure 9**), we used a low frequency of the CPGs (i.e., ∼0.85 Hz). This is to obtain a slow movement for observing the progression of the phase shifts among the decoupled CPGs during the self-organized process with the predefined frequency; therefore, the robot walked slowly. The obtained gaits were static in all leg configurations because we used "T"-shaped feet, which constantly provide large support areas during walking. However, we can also obtain a dynamic gait by increasing the CPG frequency and using an "O"-shaped feet (see http://www.manoonpong.com/Lilibot/video5.mp4).

Consequently, the self-organization of Lilibot in different leg orientations demonstrates the effectiveness of the robot structure design, the GRF model (see Equations 1–4), and the proprioceptive feedback of joints. It also confirms that Lilibot can easily be used to study the functionality of the limb morphology.

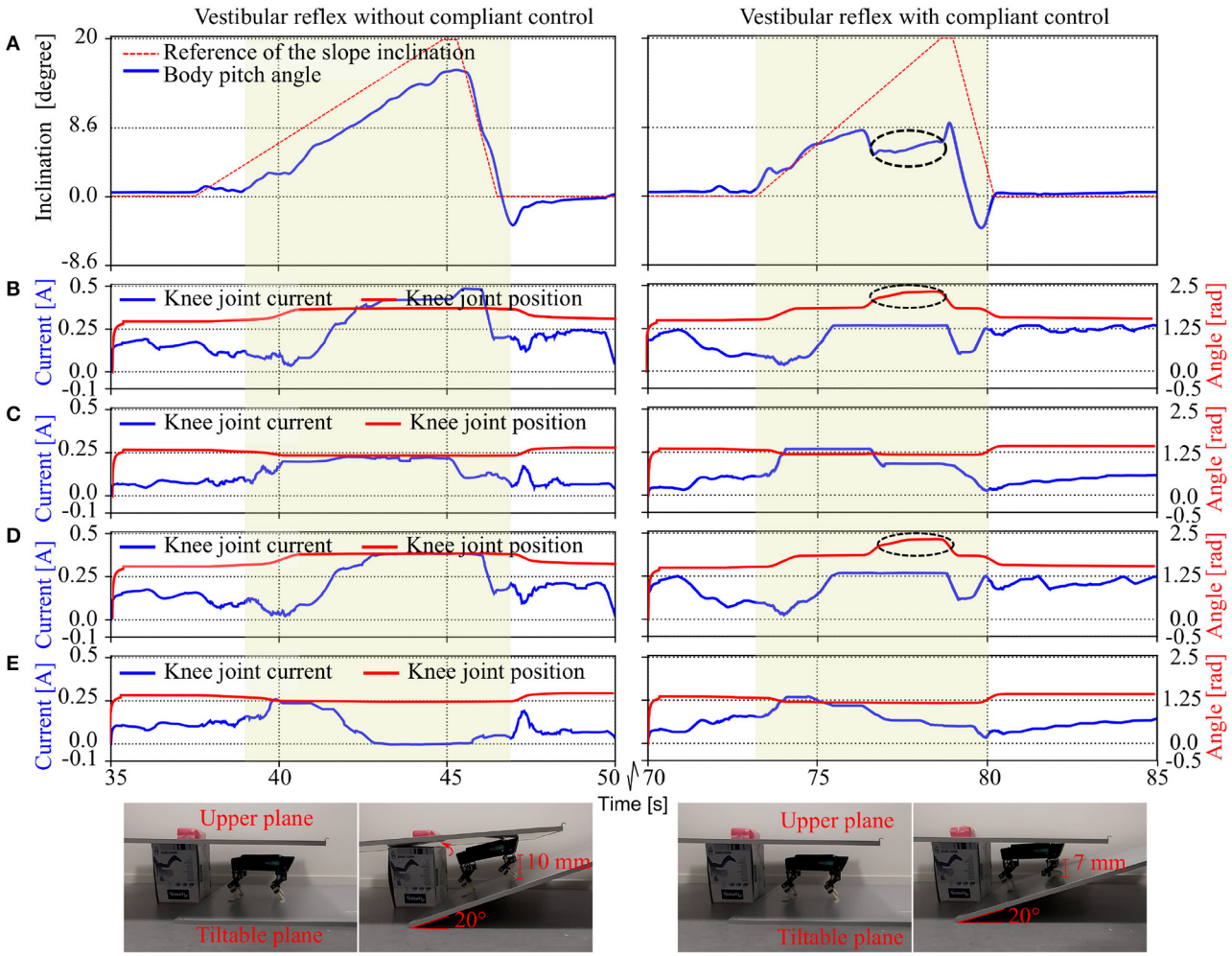

FIGURE 12 | Body stabilization on a tiltable plane with negotiating a payload under vestibular reflex control without and with compliant control. **(A)** The pitch angle of the robot and the reference inclination of the tiltable plane. **(B–E)** are the knee joint positions and currents of the right front (RF), right hind (RH), left front (LF), and left hind (LH) legs, respectively. The yellow colored areas mark the period when the plane was inclined upward. Black circles on the right graphs indicate that the front legs of the robot exhibited compliance to negotiate the payload **(B,D)**. Due to the compliance, the knee joints could flex instead of rigidly resisting the payload, thereby consuming lesser current compared to the case of the pure vestibular reflex control (left graphs). The flexing knee joints could decrease the pitch angle of the robot body [right graph **(A)**], thereby sustaining the body stabilization.

However, the flexibly reconfigurable legs are currently organized by a rigid trunk, which cannot be used to study the functionality of the spine dynamics for self-organized locomotion generation. Thus, in the future, we plan to integrate actuated joints in the trunk to connect the front and rear legs, which will imitate a compliant spine with active stiffness.

Secondly, the vestibular reflexes, which are the fundamental biological principle of legged locomotion, have been demonstrated in many quadruped robots for adapting body posture to maintain balance when facing, e.g., an inclination (slope) (Kimura and Fukuoka, 2004; Liu et al., 2013) or a perturbation (Fukui et al., 2019). For instance, when quadrupeds stand or walk on a slope, they need to actively adjust the normal position of their leg joints to acquire proper body posture, thereby sustaining their balance on the slope (as shown in section 3.3 and Fukuoka et al., 2003). In addition, in the work of Fukui et al., the vestibular feedback was used to modulate CPG activities for producing gait transitions (Fukui et al., 2019). The vestibular feedback was integrated into CPG control to improve the adaptation of the interlimb movement pattern that is originally generated by coupled CPGs with predefined connections. However, in our work, the vestibular reflexes were used to directly modulate the outputs of the decoupled CPGs for body posture stabilization (as shown in section 3.3). Our vestibular reflex mechanism and the CPGs control are independent. Thus, one can remove the reflex mechanism without destroying the self-organized locomotion formed by the decoupled CPGs control. Besides, the achievement of the vestibular reflexes can illustrate the effectiveness of the controlled structure (i.e., Lilibot structure) and the vestibular feedback.

Thirdly, compliance is a vital characteristic of muscles. It allows biological and artificial legged systems to rapidly adapt to external disturbances [such as an unexpected load compensation (as shown in section 3.2) and uneven terrain locomotion (Xiong

et al., 2015)]. Thus, implementing compliance can prevent the robot from being damaged by the disturbance. Moreover, the compliant control can cooperate with vestibular reflex control to realize greater body stabilization when facing a payload on a slope (as shown in section 3.4) and allow for energy efficient locomotion when walking on uneven terrains (Xiong et al., 2015).

Taken together, the self-organization allows a quadruped robot to automatically form adaptive gaits, whereas the vestibular reflexes enable the robot to maintain balance on a non-level ground or slope and the joint compliance can prevent damage as well as lead to energy efficient locomotion (Xiong et al., 2015). A combination of the three functions will be performed in the future as one of our research plans.

In addition to the discussions of the three functions, we review the foot structure of Lilibot here. In contrast to the general foot shapes used previously, the leg structure developed and employed here, with the "T"-shaped feet (see **Figure 3C**) significantly increases the walking stabilization. This is because the "T"-shaped feet provide a higher static stability margin compared to other foot shapes, such as the ball-shaped foot used by Oncilla (Sproewitz et al., 2011) and the half-cylinder-shaped foot used by Tekken (Kimura and Fukuoka, 2004). The "T"-shaped feet allow users to focus on the interlimb coordination of the gait generations, and hence, overcome the problems of intralimb coordination for improving stabilization. However, this shape is not beneficial for lateral stepping due to the smaller lateral contact area, and it is also challenging to adapt to uneven terrain. Therefore, we plan to develop new adaptive compliant feet with a relatively high stability margin and contact area (Canio et al., 2016; Hauser et al., 2018).

In summary, we have successfully developed a small-sized and lightweight quadruped robot, known as Lilibot. The structure of Lilibot, which imitates four-limbed mammals, such as dogs, consists of four identical legs connected by a rigid trunk, as well as "T"-shaped feet with large support areas to provide a higher static stability margin. Each leg has only three active DOFs. Nevertheless, the large joint workspace enables the robot to exhibit flexible leg orientations to imitate various types of mammal morphologies. This characteristic of the robot contributes to studying the adaptation of self-organized locomotion regarding various leg configurations, based on different biological systems (for example, dogs, horses, and infants). This advantage was demonstrated by using decoupled CPGs to control Lilibot under its four leg orientation types in the experiments. Moreover, inspired by a hexapod robot (Mathias et al., 2018), the suitable smart actuators on the joints are employed, which not only simplify the electric system of the robot, but also provide a large variety of sensory feedback (61 sensory feedback signals in total). The sensory feedback allows Lilibot to perform compliant and vestibular reflex controls, thereby demonstrating external load negotiation and body stabilization, respectively. Based on the results, we suggest that Lilibot can be considered as a friendly and generic quadrupedal platform for studying self-organized locomotion, vestibular reflexes, and compliant behavior.

DATA AVAILABILITY STATEMENT

All datasets generated for this study are included in the article/**Supplementary Material**.

AUTHOR CONTRIBUTIONS

TS developed the entire robotic system, performed the experiments, analyzed the data, and drafted the manuscript. XX led the development of compliant control and reviewed the manuscript. ZD provided the general direction of the project and reviewed the manuscript. PM led the development of adaptive neural control, helped with data analysis, drafted the manuscript, and supervised the whole project. All authors contributed to the conception and design of the work, approved the final version of the manuscript, and agree to be accountable for all aspects of the work.

FUNDING

We acknowledge financial support from the research funding of the Recruitment Program for Young Professionals of China and Nanjing University of Aeronautics and Astronautics (NUAA, Grant No. 1005-YQR07001) [PM], NSFC (Grant No. 51861135306) [PM], the National Natural Science Foundation of China (Grant No. 51435008) [ZD], and Chinese Government Scholarship (Grant No. CSC201906830012) [TS].

ACKNOWLEDGMENTS

We thank Weijia Zong and Potiwat Ngamkajornwiwat for their fruitful discussions and Mingyue Lu for recording experimental videos.

SUPPLEMENTARY MATERIAL

The Supplementary Material for this article can be found online at: https://www.frontiersin.org/articles/10.3389/fnbot.2020.00014/full#supplementary-material

REFERENCES

Bledt, G., Powell, M. J., Katz, B., Di Carlo, J., Wensing, P. M., and Kim, S. (2018). "MIT Cheetah 3: Design and control of a robust, dynamic quadruped robot," in *2018 IEEE/RSJ International Conference on Intelligent Robots and Systems (IROS)* (Madrid: IEEE), 2245–2252.

Canio, G. D., Stoyanov, S., Larsen, J. C., Hallam, J., Kovalev, A., Kleinteich, T., et al. (2016). A robot leg with compliant tarsus and its neural control for efficient and adaptive locomotion on complex terrains. *Artif. Life Robot.* 21, 274–281. doi: 10.1007/s10015-016-0296-3

Dickinson, M. H., Farley, C. T., Full, R. J., Koehl, M. A., Kram, R., and Lehman, S. (2000). How animals move: an integrative view. *Science* 288, 100–106. doi: 10.1126/science.288.5463.100

Eckert, P., Schmerbauch, A. E. M., Horvat, T., Söhnel, K., Fischer, M. S., Witte, H., et al. (2018). "Towards rich motion skills with the lightweight quadruped robot serval–a design, control and experimental

study," in *15th International Conference on Simulation of Adaptive Behavior* (Frankfurt), 41–55.

Fukui, T., Fujisawa, H., Otaka, K., and Fukuoka, Y. (2019). Autonomous gait transition and galloping over unperceived obstacles of a quadruped robot with cpg modulated by vestibular feedback. *Robot. Auton. Syst.* 111, 1–19. doi: 10.1016/j.robot.2018.10.002

Fukuoka, Y., and Kimura, H. (2009). Dynamic locomotion of a biomorphic quadruped "tekken" robot using various gaits: walk, trot, free-gait and bound. *Appl. Bionics Biomech.* 6, 63–71. doi: 10.1080/11762320902734208

Fukuoka, Y., Kimura, H., and Cohen, A. H. (2003). Adaptive dynamic walking of a quadruped robot on irregular terrain based on biological concepts. *Int. J. Robot. Res.* 22, 187–202. doi: 10.1177/0278364903022003004

Full, R. J., and Koditschek, D. E. (1999). Templates and anchors: neuromechanical hypotheses of legged locomotion on land. *J. Exp. Biol.* 202, 3325–3332.

Hauser, S., Mutlu, M., Banzet, P., and Ijspeert, A. J. (2018). Compliant universal grippers as adaptive feet in legged robots. *Adv. Robot.* 32, 825–836. doi: 10.1080/01691864.2018.1496851

Hülse, M., Wischmann, S., Manoonpong, P., von Twickel, A., and Pasemann, F. (2007). "Dynamical systems in the sensorimotor loop: on the interrelation between internal and external mechanisms of evolved robot behavior," in *50 Years of Artificial Intelligence* (Ascona: Springer), 186–195.

Hutter, M., Gehring, C., Jud, D., Lauber, A., Bellicoso, C. D., Tsounis, V., et al. (2016). "Anymal–a highly mobile and dynamic quadrupedal robot," in *IEEE/RSJ International Conference on Intelligent Robots & Systems* (Daejeon), 38–44.

Hutter, M., Gehring, C., Lauber, A., Gunther, F., Bellicoso, C. D., Tsounis, V., et al. (2017). Anymal-toward legged robots for harsh environments. *Adv. Robot.* 31, 918–931. doi: 10.1080/01691864.2017.1378591

Hwangbo, J., Lee, J., Dosovitskiy, A., Bellicoso, D., Tsounis, V., Koltun, V., et al. (2019). Learning agile and dynamic motor skills for legged robots. *Sci. Robot.* 4:eaau5872. doi: 10.1126/scirobotics.aau5872

Ijspeert, A. J. (2014). Biorobotics: using robots to emulate and investigate agile locomotion. *Science* 346, 196–203. doi: 10.1126/science.1254486

Karakasiliotis, K., Thandiackal, R., Melo, K., Horvat, T., Mahabadi, N. K., Tsitkov, S., et al. (2016). From cineradiography to biorobots: an approach for designing robots to emulate and study animal locomotion. *J. R. Soc. Interface* 13:20151089. doi: 10.1098/rsif.2015.1089

Kimura, H., and Fukuoka, Y. (2004). "Biologically inspired adaptive dynamic walking in outdoor environment using a self-contained quadruped robot: 'tekken2'," in *IEEE/RSJ International Conference on Intelligent Robots & Systems* (Sendai), 986–991.

Liu, C., Chen, Q., and Wang, G. (2013). Adaptive walking control of quadruped robots based on central pattern generator (CPG) and reflex. *J. Control Theory Appl.* 11, 386–392. doi: 10.1007/s11768-013-1171-6

Manoonpong, P., Pasemann, F., and Woergoetter, F. (2008). Sensor-driven neural control for omnidirectional locomotion and versatile reactive behaviors of walking machines. *Robot. Auton. Syst.* 56, 265–288. doi: 10.1016/j.robot.2007.07.004

Manoonpong, P., Petersen, D., Kovalev, A., Wörgötter, F., Gorb, S. N., Spinner, M., et al. (2016). Enhanced locomotion efficiency of a bio-inspired walking robot using contact surfaces with frictional anisotropy. *Sci. Rep.* 6:39455. doi: 10.1038/srep39455

Marc, R., Kevin, B., Gabriel, N., and Rob, P. (2008). "BigDog, the rough-terrain quadruped robot," in *Proceedings of the 17th World Congress* (Seoul), 10822–10825.

Mathias, T., Larsen, J. C., and Poramate, M. (2018). "Morf–modular robot framework," in *The Second International Youth Conference of Bionic Engineerinbg (IYCBE2018)* (Odense), 21–23.

Meek, S., Kim, J., and Anderson, M. (2008). "Stability of a trotting quadruped robot with passive, underactuated legs," in *IEEE International Conference on Robotics and Automation* (Pasadena, CA: IEEE), 347–351.

Owaki, D., and Ishiguro, A. (2017). A quadruped robot exhibiting spontaneous gait transitions from walking to trotting to galloping. *Sci. Rep.* 7:277. doi: 10.1038/s41598-017-00348-9

Owaki, D., Kano, T., Nagasawa, K., Tero, A., and Ishiguro, A. (2013). Simple robot suggests physical interlimb communication is essential for quadruped walking. *J. R. Soc. Interface* 10:20120669. doi: 10.1098/rsif.2012.0669

Owaki, D., Morikawa, L., and Ishiguro, A. (2012). "Gait transition of quadruped robot without interlimb neural connections," in *Proceedings of Dynamic Walking* (Pensacola, FL).

Pasemann, F., Hild, M., and Zahedi, K. (2003). "So (2)-networks as neural oscillators," In *International Work-Conference on Artificial Neural Networks* (Berlin; Heidelberg: Springer), 144–151.

Poulakakis, I., and Grizzle, J. W. (2009). The spring loaded inverted pendulum as the hybrid zero dynamics of an asymmetric hopper. *IEEE Trans. Autom. Control* 54, 1779–1793. doi: 10.1109/TAC.2009.2024565

Quigley, M., Conley, K., Gerkey, B., Faust, J., Foote, T., Leibs, J., et al. (2009). "ROS: an open-source robot operating system," in *ICRA Workshop on Open Source Software* (Kobe), Number 3.2, 5.

Raibert, M. H. (1986). *Legged Robots That Balance*. London: MIT Press.

Rohmer, E., Singh, S. P., and Freese, M. (2013). "V-rep: a versatile and scalable robot simulation framework," in *2013 IEEE/RSJ International Conference on Intelligent Robots and Systems* (Tokyo: IEEE), 1321–1326.

Semini, C., Barasuol, V., Goldsmith, J., Frigerio, M., Focchi, M., Gao, Y., et al. (2016). Design of the hydraulically actuated, torque-controlled quadruped robot hyq2max. *IEEE/ASME Trans. Mechatron.* 22, 635–646. doi: 10.1109/TMECH.2016.2616284

Semini, C., Tsagarakis, N. G., Guglielmino, E., Focchi, M., Cannella, F., and Caldwell, D. G. (2011). Design of HyQ–a hydraulically and electrically actuated quadruped robot. *Proc. Inst. Mech. Eng. I J. Syst. Control Eng.* 225, 831–849. doi: 10.1177/0959651811402275

Seok, S., Wang, A., Meng, Y. C., and Otten, D. (2013). "Design principles for highly efficient quadrupeds and implementation on the MIT Cheetah robot," in *IEEE International Conference on Robotics & Automation* (Karlsruhe), 3307–3312.

Sproewitz, A., Kuechler, L., Tuleu, A., Ajallooeian, M., D'Haene, M., Moeckel, R., et al. (2011). "Oncilla robot: a light-weight bio-inspired quadruped robot for fast locomotion in rough terrain," in *5th International Symposium on Adaptive Motion of Animals and Machines*, Number CONF (Awaji).

Sprowitz, A., Tuleu, A., Vespignani, M., Ajallooeian, M., Badri, E., and Ijspeert, A. J. (2013). Towards dynamic trot gait locomotion: design, control, and experiments with cheetah-cub, a compliant quadruped robot. *Int. J. Robot. Res.* 32, 932–950. doi: 10.1177/0278364913489205

Taga, G., Yamaguchi, Y., and Shimizu, H. (1991). Self-organized control of bipedal locomotion by neural oscillators in unpredictable environment. *Biol. Cybern.* 65, 147–159. doi: 10.1007/BF00198086

Tao, S., Donghao, S., Zhendong, D., and Poramate, M. (2018). "Adaptive neural control for self-organized locomotion and obstacle negotiation of quadruped robots," in *27th IEEE International Symposium on Robot and Human Interactive Communication (RO-MAN)* (Nanjing), 1081–1086.

Wensing, P. M., Wang, A., Seok, S., Otten, D., Lang, J., and Kim, S. (2017). Proprioceptive actuator design in the MIT Cheetah: impact mitigation and high-bandwidth physical interaction for dynamic legged robots. *IEEE Trans. Robot.* 33, 509–522. doi: 10.1109/TRO.2016.2640183

Xiong, X., Wörgötter, F., and Manoonpong, P. (2015). Adaptive and energy efficient walking in a hexapod robot under neuromechanical control and sensorimotor learning. *IEEE Trans. Cybern.* 46, 2521–2534. doi: 10.1109/TCYB.2015.2479237

Xiuli, Z., Haojun, Z., Xu, G., Zhifent, C., and Liyao, Z. (2005). "A biological inspired quadruped robot: structure and control," in *IEEE International Conference on Robotics and Biomimetics-ROBIO* (Sha Tin: IEEE), 387–392.

Yu, H. T., Li, M. T., Wang, P. F., and Cai, H. G. (2012). Approximate perturbation stance map of the slip runner and application to locomotion control. *J. Bionic Eng.* 9, 411–422. doi: 10.1016/S1672-6529(11)60138-8

Conflict of Interest: The authors declare that the research was conducted in the absence of any commercial or financial relationships that could be construed as a potential conflict of interest.

Advantages of publishing in Frontiers

OPEN ACCESS
Articles are free to read for greatest visibility and readership

FAST PUBLICATION
Around 90 days from submission to decision

HIGH QUALITY PEER-REVIEW
Rigorous, collaborative, and constructive peer-review

TRANSPARENT PEER-REVIEW
Editors and reviewers acknowledged by name on published articles

Frontiers
Avenue du Tribunal-Fédéral 34
1005 Lausanne | Switzerland

Visit us: www.frontiersin.org
Contact us: info@frontiersin.org | +41 21 510 17 00

REPRODUCIBILITY OF RESEARCH
Support open data and methods to enhance research reproducibility

DIGITAL PUBLISHING
Articles designed for optimal readership across devices

FOLLOW US
@frontiersin

IMPACT METRICS
Advanced article metrics track visibility across digital media

EXTENSIVE PROMOTION
Marketing and promotion of impactful research

LOOP RESEARCH NETWORK
Our network increases your article's readership